

# Frequency-Domain Signal Analysis

*Frequency-domain signal analysis* covers a wide variety of techniques involving the Fourier transformation of the signal. The signal's frequency domain representation is then manipulated, decomposed, segmented, classified, and interpreted. One central idea is that of a *filter*: a linear, translation-invariant system that allows one band of frequencies to appear in the output and suppresses the others. Where signal elements of interest occupy a restricted spectrum, filters invariably enter into the early processing of candidate signals. In other ways—often purely theoretical—frequency-domain analysis is important. For example, in this chapter we substantiate the methods of matched filtering and scale-space decomposition, and the Fourier transform plays a crucial role.

The main tools for frequency-domain analysis are of course the discrete signal transforms: the discrete-time Fourier transform (DTFT); its generalization, the  $z$ -transform; and especially the discrete Fourier transform (DFT). Many of the introductory applications proceed from Chapter 1 examples. There are extensions of techniques already broached in Chapters 4 and 6. Modern spectral analysis applications have a digital computer at their heart, and they rely on either the DFT or one of its many fast versions. Some signal filtering applications use infinite impulse response (IIR) filtering methods, implemented using feedback, as discussed in Chapter 2. The DTFT is convenient for obtaining a theoretical understanding of how such filters suppress and enhance signal frequencies. We often begin with an analog filter and convert it to a discrete filter. Thus, we shall have occasion to use the continuous-domain Fourier transform. We also briefly explain how the Laplace transform, a generalization of the Fourier transform, can be used in certain analog filter constructions. The  $z$ -transform figures prominently in this conversion process.

We are generally working with complex-valued signals, but the thresholding, segmentation, and structural decomposition methods that Chapter 4 developed for time-domain signal analysis are just as useful in the frequency domain. For example, to find the spectral region where a source signal contains significant energy, we threshold the signal's magnitude or squared magnitude (power) spectrum. We know that thresholding is often improved by filtering the data, so we are inclined to filter the frequency-domain magnitudes too. This leads directly to the technique of windowing

time-domain signal slices before Fourier transformation. The meaning of the analytical results can be quite different, of course; but as long as we understand the transform relation clearly and capture that in the application design, then the time-domain and frequency-domain procedures are remarkably similar. In some applications, the results of this analysis convey the signal content. For other tasks, an inverse transformation back to the time domain is required. In any case, the principal tools are the Fourier transform and its inverse, in both their analog and discrete formulations.

Our theoretical resources include Chapters 5, 7, and 8. This chapter introduces some further theory, appropriate to the particular applications upon which we focus. Specific applications include tone detection, speech recognition and enhancement, and chirp analysis. Some of these experiments show that the Fourier transform is precisely the tool we need to make the application work. Further reflection reveals problems in applying the Fourier transforms. This motivates a search for frequency transforms that incorporate a time-domain element: time-frequency and time-scale transforms, which are topics for the final three chapters.

Fourier-domain techniques also offer many insights into our earlier material. Scale space and random signals are considered once more, this time from the vantage point of the new frequency-domain methods. The last two sections detail the construction of special filters for frequency analysis and possible structures for their application. Later chapters will draw the link between this approach to signal processing and the notion of a multiresolution analysis of the  $L^2$  Hilbert space.

References on Fourier transforms include Refs. 1–5. Popular signal processing texts that introduce Fourier methods and construct filters from the theory are Refs. 6–10. An older book that concludes its thorough coverage of signal theory with detailed application studies in speech and radar signal analysis is Ref. 11.

**Notation.** The present discussion covers both analog and discrete filters. We use the following notations for clarity:

- (i) *Analog filters*: The impulse response is  $h(t)$ , the radial Fourier transform is  $H(\Omega)$ , and the Laplace transform is  $H_L(s)$ ; in some contexts, we insert the subscript  $a$ :  $h_a(t)$ ,  $H_a(\Omega)$ , and  $H_{L,a}(s)$ .
- (ii) *Discrete filters*: The impulse response is  $h(n)$ , or any FORTRAN-like integer independent variable such as  $h(i)$ ,  $h(k)$ , or  $h(m)$ ; the discrete time Fourier transform is  $H(\omega)$ ; and the discrete Fourier transform is  $H(k)$ .
- (iii) We continue to use  $j^2 = -1$ .

## 9.1 NARROWBAND SIGNAL ANALYSIS

The most basic frequency-domain analysis task involves detecting and interpreting more or less isolated periodic components of signals. For some signals, or at least for some part of their domain, a few oscillatory components contain the bulk of the energy. It is such *narrowband* signals—sinusoids (tones) and dual-tones, mainly, but we could also allow complex-valued exponentials into this category—that we

begin our study of Fourier transform applications. We distinguish narrowband signals from wideband signals, where the energy is spread over many frequencies. A signal that contains sharp edges, for example, will generally have frequency-domain energy dispersed across a wide spectral range.

Although basic, a tone detection application leads to important practical concepts: noise removal, filtering, phase delay, group delay, and windowing. *Filters* are frequency-selective linear translation invariant systems. Filtering a signal can change the time location of frequency components. For instance, a filter might retard a sinusoidal pulse and the signal envelope itself, depending on their frequency. These time lags define the *phase* and *group delay*, respectively. Knowing them is crucial for application designs that must compensate for filter delays. Finally, we often need to analyze signals in chunks, but so doing invariably corrupts the signal spectrum. Only by looking at the signal through a well-constructed *window* can we mitigate this effect. This concept leads directly to the modern theory of the windowed Fourier transform (Chapter 10) and eventually to wavelets (Chapter 11).

Theory from earlier chapters now becomes practice. For designing filters, we employ the discrete-time Fourier transform (DTFT). For implementing filters on a computer, we use the discrete Fourier transform (DFT) or one of its fast Fourier transform (FFT) schemes. Some infinite impulse response filter implementations are particularly powerful, and we visualize their possible recursive implementation on a computer through the  $z$ -transform (Chapter 8). We definitely do not need the continuous-domain Fourier transform (FT), right? Quite wrong: We can obtain very good discrete filters by first designing an analog filter and then converting it into a discrete filter. It is perhaps a surprising fact, but this is the preferred method for constructing high-performance discrete filters. We even use the Fourier series (FS); after a bit of contemplation, we realize that the FS converts an analog  $L^2[0, 2\pi]$  signal into a discrete  $l^2$  signal—just like the inverse DTFT. Indeed, as mathematical objects, they are one and the same.

### 9.1.1 Single Oscillatory Component: Sinusoidal Signals

Let the real-valued signal  $x(n)$  contain a single oscillatory component and perhaps some corrupting noise. We have seen such examples already in the first chapter— $x(n)$  is the Wolf sunspot count, for instance. Now, in earlier chapters, introductory applications explored the discrete Fourier transform as a tool for detecting such periodicities. The source signal's oscillatory component manifests itself as an isolated cluster of large magnitude spectral values. We can usually segment the frequency components with a simple threshold around the maximum value; this is a straightforward application of the DFT.

A tone is a time-domain region of a signal that consists of only a few sinusoidal components. Briefly, detection steps are as follows:

- (i) Select signal regions that may contain tones.
- (ii) For noise removal and frequency selection, processing the signal through various filters may benefit the analysis steps that follow.

- (iii) Fourier transform the signal over such regions.
- (iv) For each such region, examine the spectrum for large concentrations of signal energy in a few frequency coefficients.
- (v) Optionally, once a possible tone has been identified through frequency-domain analysis, return to the time domain to more precisely localize the tone.

The discrete signal sometimes arises from sampling an analog signal  $x_a(t)$ :  $x(n) = x_a(nT)$ , where  $T > 0$  is the sampling period. But perhaps—as in the case of sunspot estimates—the signal is naturally discrete. If we take select a window of signal values,  $0 \leq n < N$ , we can compute the DFT over these  $N$  samples:

$$X(k) = \sum_{n=0}^{N-1} x(n) e^{-\frac{2\pi jkn}{N}}. \quad (9.1)$$

In (9.1),  $X(0)$  represents the direct current (DC), or constant, or zero frequency component. The signal average over the interval  $[0, N - 1]$  is  $X(0)/N$ , and it represents zero cycles per sample (hertz) in the transform. If  $x(n)$  is real, then  $X(k) = X(N - k)$  for all  $1 \leq k \leq N - 1$ . The transform is invertible:

$$x(n) = \frac{1}{N} \sum_{k=0}^{N-1} X(k) e^{\frac{2\pi jkn}{N}}. \quad (9.2)$$

Equations (9.1) and (9.2) are the analysis and synthesis equations, respectively, for the DFT. If  $x_a(t) = \cos(2\pi t/NT)$  is a real-valued analog sinusoid with frequency  $(NT)^{-1}$  hertz, then upon sampling it becomes  $x(n) = x_a(nT) = \cos(2\pi n/N)$ . We can expand  $2x(n) = [\exp(2\pi jn/N) + \exp(2\pi jn(N - 1)/N)]$ , which is a synthesis equation (9.2) for the sinusoid. Thus, the smallest frequency represented by the transform coefficients, the frequency resolution of the DFT, is  $(NT)^{-1}$ . This means that energy from source signal periodicities appears in the transform coefficients in at least two different places. If  $N$  is even, then the highest frequency represented by the transform values is  $1/(2T) = (NT)^{-1} \times (N/2)$  hertz. If  $N$  is odd, then the two middle coefficients share the Nyquist frequency energy.

This section explains the basic methods for applying the discrete Fourier transform (DFT) and discrete-time Fourier transform (DTFT) for detecting oscillatory components of signals. Strictly speaking, the DFT applies to periodic signals and the DTFT to aperiodic signals.

### 9.1.2 Application: Digital Telephony DTMF

Let us consider the problem of recognizing multiple oscillatory components in a source signal. If the source contains multiple periodic components, then the transform exhibits multiple clusters of large values. To spot significant oscillatory signal features, we might invoke the more powerful threshold selection methods covered in Chapter 4, applying them to the magnitude spectrum instead of the signal

amplitude values. Thresholding the magnitude spectrum does work, but it does not take us very far.

This is the limitation of peak finding in the magnitude spectrum: These magnitudes represent frequencies over the entire time domain of the source signal. If oscillations at different times have the same frequency, or those that occur at the same time overlap with others of different wavelengths, then this potentially crucial information for signal understanding is lost in the Fourier transformation. Many applications involve signals with localized frequency components. What complicates such applications is getting the Fourier transform—an inherently global transformation—to work for us in a time localized fashion.

This application—however humble—inspires three general approaches for identifying and localizing signal frequency components:

- Preliminary time-domain analysis, arriving at a segmentation of the signal's values, and subsequent frequency-domain analysis on the segments of promise (Section 9.1.2.2);
- An important tool—the *time-frequency map* or *plane*—which generally decomposes the signal into pieces defined by the time interval over which they occur and the frequencies over which their oscillatory components range (Section 9.1.2.3);
- Another significant tool—the *filter bank*—which directs the signal values into a parallel array of frequency selective linear, translation-invariant (LTI) systems (filters) and analyzes the outputs jointly (Section 9.1.2.4).

It will become clear that these three alternatives couple their time- and frequency-domain analyses ever more closely. Thus, in the first case, algorithms finish the time-domain segmentation and hand the results over to spectral analysis. Using the second alternative's time-frequency plane, in contrast, we decompose the signal into pieces that represent a particular time interval and a particular frequency span. The analyses within the two domains, instead of working in strict cascade, operate simultaneously, albeit through restricted time and frequency windows. Finally, in a filter bank, the signal's values are streamed into the filters in parallel, and application logic interprets the output of the filters. Since this can occur with each signal sample, the output of the interpretive logic can be associated with the particular time instant at which the frequency-domain logic makes a decision. So the filter bank, at least as we sketch it here, comprises a very intimate merging of both time- and frequency-domain signal analysis.

**9.1.2.1 Dual-Tone Pulses in Noise.** Let us review the discrete dual-tone multifrequency (DTMF) pulses that modern digital telephone systems use for signaling [12]. Table 9.1 shows the standard pairs.

True DTMF decoders—such as in actual use at telephone company central offices—must stop decoding DTMF pulses when there is speech on the line. One frequency-domain trait that allows an application to detect the presence of human voices

**TABLE 9.1. DTMF Frequency Pairs<sup>a</sup>**

High (Hz):	1209	1336	1477	1633
Low (Hz):	697	770	852	941
	1	2	3	A
	4	5	6	B
	7	8	9	C
	*	0	#	D

<sup>a</sup>The letter tones are generally reserved for the telephone company's signaling, testing, and diagnostic uses.

voices is that speech contains second and third harmonics [13], which the DTMF tones by design do not [12]. For example, a vowel sound could contain significant energy at 300 Hz, 600 Hz, and 900 Hz. An upcoming speech analysis application confirms this. But note in Table 9.1 that the second harmonic of the low tone at 697 Hz (that would be approximately 1.4 kHz) lies equidistant from the high tones at 1336 Hz and 1477 Hz. Later in this chapter, we will consider mixed speech and DTMF tones and see how to discriminate between control tones and voice. For now, let us return to the basic tone detection problem.

Suppose we represent a DTMF telephony pulse by a sum of two sinusoids chosen from the above table enclosed within a Gaussian envelope. If we sample such an analog signal at  $F_s = 8192$  Hz, then the sampling period is  $T = 8192^{-1}$  s.

Let us briefly cover the synthesis of the dual-tone multifrequency signal used in this example.

The analog sinusoidal signals for a “5” and “9” tone are, respectively,

$$s_5(t) = \sin(2\pi t F_{5,a}) + \sin(2\pi t F_{5,b}), \quad (9.3a)$$

$$s_9(t) = \sin(2\pi t F_{9,a}) + \sin(2\pi t F_{9,b}), \quad (9.3b)$$

where  $F_{5,a} = 770$ ,  $F_{5,b} = 1336$ ,  $F_{9,a} = 852$ , and  $F_{5,b} = 1477$  as in Table 9.1. We need to window these infinite duration signals with Gaussians that—effectively—die to zero outside a small time interval. We take the window width  $L = 50$  ms, let  $\sigma = L/2$ , and use the window functions

$$g_5(t) = e^{-\frac{(t-t_5)^2}{2\sigma^2}}, \quad (9.4a)$$

$$g_9(t) = e^{-\frac{(t-t_9)^2}{2\sigma^2}}, \quad (9.4b)$$

where  $t_5 = 0.125$  s and  $t_9 = 0.375$  s are the centers of the “5” and “9” pulse windows, respectively. Let  $x(t) = s_5(t)g_5(t) + s_9(t)g_9(t) + n(t)$ , where  $n(t)$  is a noise term.

The noise term  $n(t)$  could be genuine noise arduously derived from a real system, such as a radioactive source or galactic background radiation. Or it could be pseudo-random noise conveniently synthesized on a digital computer.<sup>1</sup> In order to control the noise values for the experiments in this section, let us make noise by assuming some realistic distribution functions and using some standard algorithms for the synthesis.

A variety of methods exist for synthesizing noise. For example, an early algorithm for generating a uniform random variable [14] called the *congruential* generator is

$$x(n) = [Ax(n - 1)](\text{mod } M), \tag{9.5}$$

where  $A$  is the *multiplier*,  $M$  is the *modulus*, and the iteration typically starts with a choice for  $x(0)$ , the *seed* value. The method produces values in the range  $[0, M - 1]$  and works better for large  $M$ . For uniform noise on  $[0, 1)$  divide (9.5) by  $M$ .

A better algorithm is the *linear congruential* generator:

$$x(n) = [Ax(n - 1) + C](\text{mod } M), \tag{9.6}$$

where  $C$  is the *increment*. If  $C = 0$ , then (9.6) reduces to (9.5). The following values make the congruential method work well [15]:  $A = 16,807$ ;  $M = 2^{31} - 1$ ; and  $C = 0$ . For the linear congruential iteration, nice choices are  $A = 8,121$ ;  $M = 134,456$ ; and  $C = 28,411$  [16].

There is a standard algorithm for generating pseudo-random normally (Gaussian) distributed sequences [17]. Let  $x_1(n)$  and  $x_2(n)$  be two uniformly distributed random variables on  $(0, 1)$  and define

$$y_1(n) = \cos(2\pi x_2(n))\sqrt{-2\ln(x_1(n))}, \tag{9.7a}$$

$$y_2(n) = \sin(2\pi x_2(n))\sqrt{-2\ln(x_1(n))}. \tag{9.7b}$$

Then  $y_1(n)$  and  $y_2(n)$  are zero-mean normally distributed random variables. References on random number generation include Refs. 18 and 19.

The chapter exercises invite readers to change signal to noise ratios and explore the impact on detection algorithms.

We begin with an analysis of the DTMF signal using the discrete Fourier transform on the entire time interval of  $N = 4096$  points. Let  $x(n) = x_a(nT)$  be the discretized input, where  $T = 8192^{-1}$ s,  $x_a(t)$  is the real-world analog representation, and  $n = 0, 1, \dots, N - 1 = 4095$ . Figure 9.1 (second from top) shows the magnitude of the DFT coefficients (9.1). Even though the presence of DTMF tones in the signal is clear, we cannot be sure when the tones occurred. For example, we detect two low tones, 770 and 852 Hz, and we can see two high tones, 1336 and 1477 Hz, but this global frequency-domain representation does not reveal whether their presence

<sup>1</sup>“Anyone who considers arithmetical methods of producing random digits is, of course, in a state of sin” (John von Neumann). And having repeated the maxim that everyone else quotes at this point, let us also confess that “Wise men make proverbs, but fools repeat them” (Samuel Palmer).

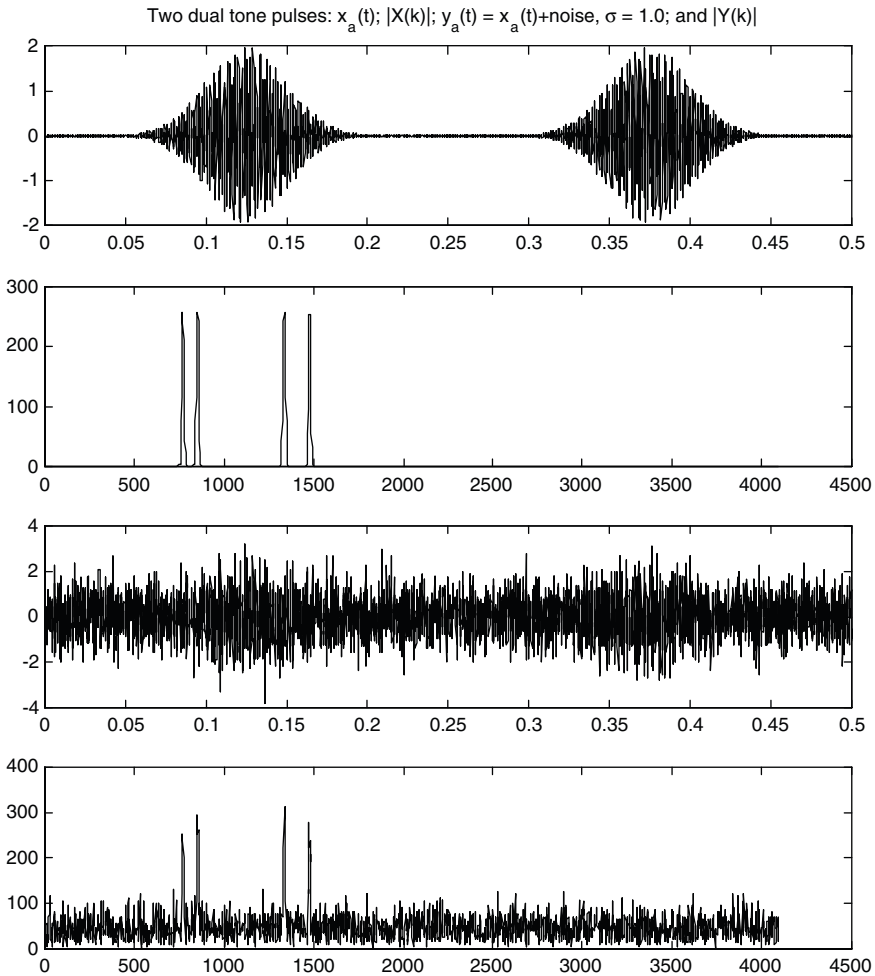


**Fig. 9.1.** DTMF numbers “5” and “9” tones (top). Sampling produces  $x(n) = x_d(nT)$ , where  $T = 8192^{-1}$  s. Discrete Fourier transformation gives  $|X(k)|$  (second). Adding noise of zero mean, normal distribution, and standard deviation  $\sigma = 1$  effectively buries the signal (third). Yet the characteristic peaks remain in the magnitude spectrum of the noisy signal (bottom).

indicates that the time-domain signal contains a “5” pulse, a “9” pulse, a “6” pulse, an “8” pulse, or some invalid combination of tones.

The DFT efficiently detects signal periodicity. Adding a considerable amount of noise to the pure tone signals used above demonstrates this, as can be seen in the lower two panels of Figure 9.1. Should the application need to ascertain the mere existence of a periodicity, obscuring noise is no problem; there is just a question of seeing the spike in  $|X(k)|$ . But it does become a problem when we need to find the

time-domain extent of the tone—when one tone occurs earlier than another. Indeed, high noise levels can confound as simple an application as DTMF detection.

**9.1.2.2 Preliminary Time-Domain Segmentation.** A straightforward approach is to preface frequency-domain interpretation with time-domain segmentation. Chapter 4's diverse thresholding methods, for example, can decide whether a piece of time-domain signal  $x(n)$  merits Fourier analysis. For dual-tone detection, the appropriate steps are as follows:

- (i) Segment the time-domain signal  $x(n)$  into background regions and possible DTMF tone regions.
- (ii) Compute the DFT of  $x(n)$  on possible tone segments.
- (iii) Apply the DTMF specifications and check for proper tone combinations in the candidate regions.

Time-domain signal segmentation methods are familiar from Chapter 4. If we know the background noise levels beforehand, we can assume a fixed threshold  $T_x$ . Of course, the source  $x(n)$  is oscillatory, so we need to threshold against  $|x(n)|$  and merge nearby regions where  $|x(n)| \geq T_x$ . Median filtering may help to remove narrow gaps and small splinters at the edge of high magnitude regions. If we know the probability of DTMF tones, then a parametric method such as the Chow and Kaneko algorithm [20] may be useful. However, if  $x(n)$  contains other oscillatory sounds, such as speech, or the tones vary in length and temporal separation, then a nonparametric algorithm such as Otsu's [21] or Kittler and Illingworth's [22] may work better. In any case, the first step is to produce a preliminary time-domain segmentation into possible tone signal versus noise (Figure 9.2).

Nevertheless, segmentation by Otsu's method fails to provide two complete candidate pulse regions for noise levels only slightly higher than considered in Figure 9.2. It is possible to apply a split and merge procedure to fragmented regions, such as considered in the exercises. However, these repairs themselves fail for high levels of noise such as we considered in the previous section.

Since the high level of noise is the immediate source of our time-domain segmentation woes, let us try to reduce the noise. Preliminary noise removal filtering comes to mind. Thus, we can apply some frequency-selective signal processing to the input DTMF signal before attempting the partition of the source into meaning signal and background noise regions.

Let us try a moving average filter. The motivation is that the zero mean noise locally wiggles around more than the sinusoidal pulses that comprise the DTMF information. So we anticipate that filter averaging ought to cancel out the noise but leave the sinusoidal DTMF pulses largely intact.

The *moving average filter* of order  $N > 0$  is  $h = H\delta$ , where

$$h(n) = \begin{cases} \frac{1}{N} & \text{if } 0 \leq n \leq N-1, \\ 0 & \text{if otherwise,} \end{cases} \quad (9.8)$$

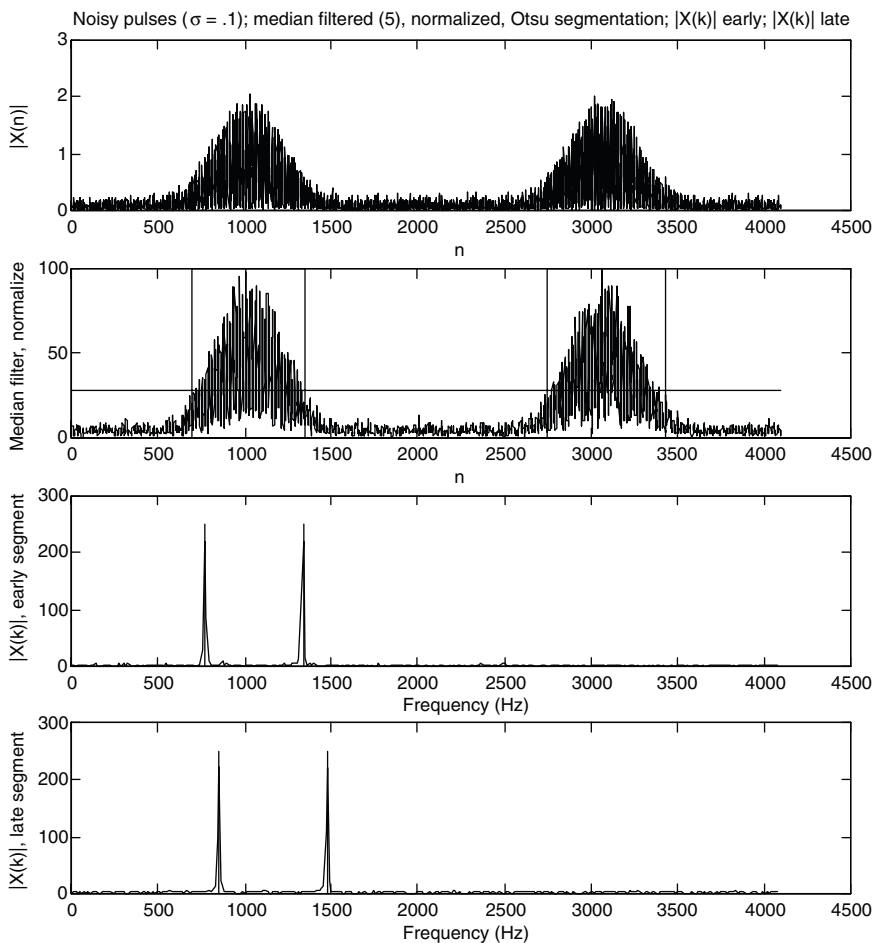


**Fig. 9.2.** Magnitudes of DTMF “5” and “9” tones within noise of zero mean, normal distribution, and moderate  $\sigma = 0.1$  standard deviation. The second panel shows time-domain segmentation via the Otsu algorithm. Here, the magnitude spectra are median-filtered and normalized to a maximum of 100% before histogram construction and segmentation. The horizontal line is the Otsu threshold. The vertical lines are boundaries of the likely pulse regions. The lower panels show the magnitude spectra of DFTs on the two candidate regions. Note that the spikes correspond well to “5” and “9” dual-tone frequencies.

and  $N > 0$  is the *order* of the filter. Let  $x(n)$  be the pure DTMF signal and let us add normally distributed noise of mean  $\mu_x = 0$  and standard deviation  $\sigma_x = 0.8$  (Figure 9.3).

Why the time domain does not seem to aid the segmentation process is evident from examining the various frequency-domain representations. Figure 9.3 shows the spectral effect of filtering this signal with moving average filters of orders 3, 7, and 21. We can see that the smallest order is beneficial in terms of aiding a time-domain

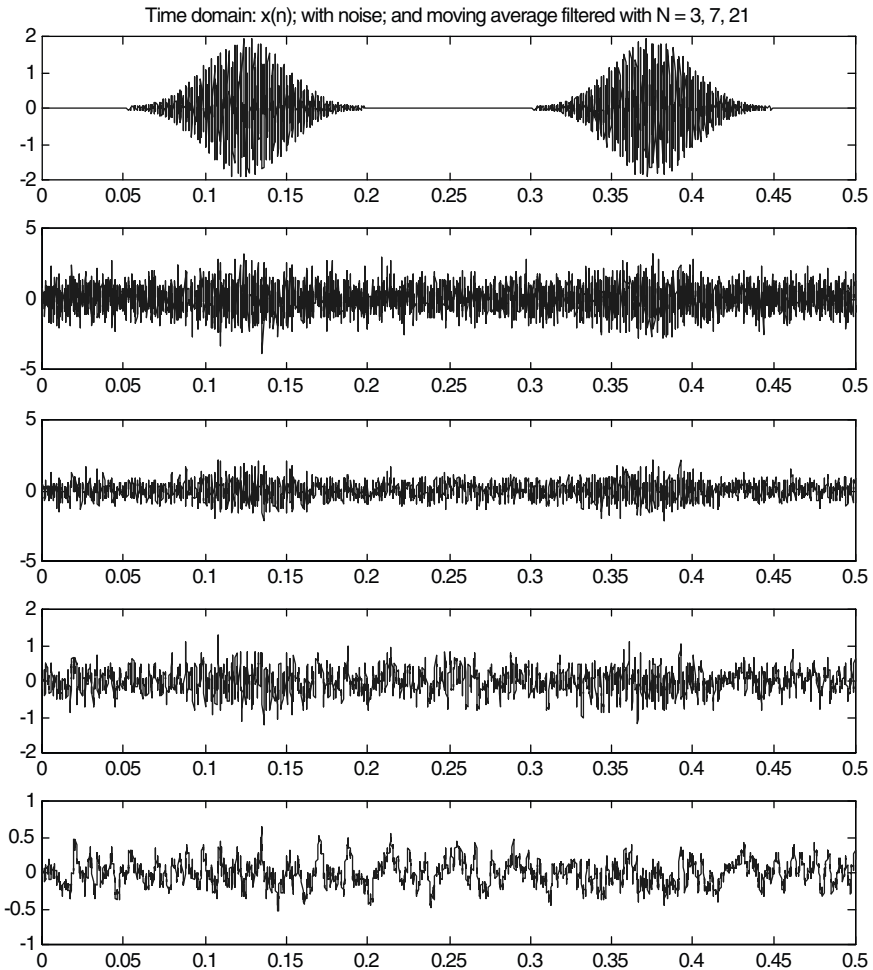


**Fig. 9.3.** Time-domain plots of the pure DTMF signal (top) and with Gaussian noise added,  $\mu_x = 0$  and  $\sigma_x = 0.8$  (second from top). The next three panels show  $y = h*x$ , with  $H$  a moving average filter of order  $N = 3$ ,  $N = 7$ , and  $N = 21$ .

segmentation, but only slightly so. The higher-order filters are—if anything—a hindrance.

We can see that the moving average filter magnitude spectrum consists of a series of slowly decaying humps (Figure 9.4). Frequencies between the humps are suppressed, and in some cases the frequency buckets that correspond to our DTMF pulses are attenuated by the filter. The filter will pass and suppress frequencies in accordance with the DFT convolution theorem:  $Y(k) = H(k)X(k)$ .

This explains in part why the moving average filter failed to clarify the signal for time-domain segmentation. Although it is intuitive and easy, its frequency

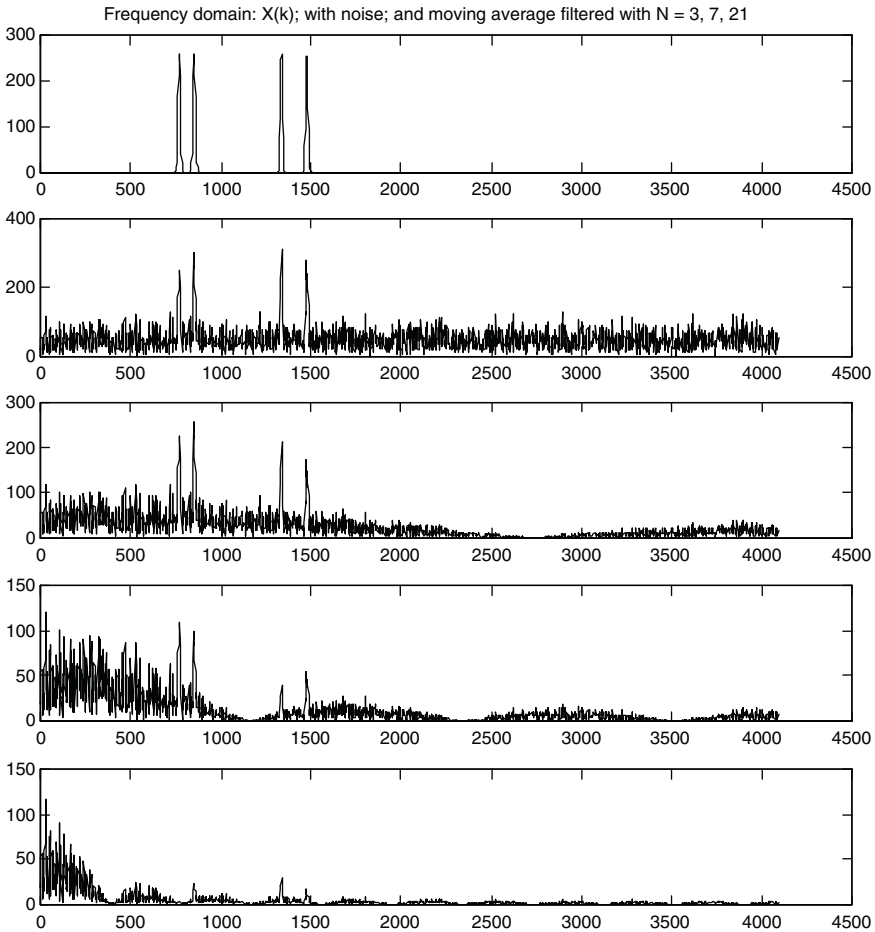


**Fig. 9.4.** Frequency-domain plots of the magnitude spectrum  $|X(k)|$  of DTMF signal  $x(n)$  (top); with Gaussian noise added,  $\mu_x = 0$  and  $\sigma_x = 0.8$  (b); and the final three panels are  $|Y(k)| = |H(k)||X(k)|$ , with  $H$  of order  $N = 3$ ,  $N = 7$ , and  $N = 21$ .

suppression capabilities do not focus well for narrowband tones. We seem to find ourselves designing a raw signal that the moving average filter can improve. Later in this chapter, we shall discover better filters and learn how to build them in accord with the requirements of an application.

In fact, the second method, which applies the time-frequency map to the dual-tone signals, offers some help with the high noise problem.

**9.1.2.3 Analysis in the Time-Frequency Plane.** A time-frequency map is a two-dimensional array of signal frequencies plotted on one axis and their time location plotted on the other axis. This is a useful tool for signal interpretation problems

where the preliminary segmentation is problematic or when there is scant a priori information on frequency ranges and their expected time spans. To decompose a signal into a time-frequency plane representation, we chop up its time domain into intervals of equal size and perform a Fourier analysis on each piece.

Let us explain the new tool using the DTMF application as an example. Application necessity drives much of the design of time-frequency maps. A method appropriate for the DTMF detection problem is as follows.

- (i) Select a fixed window width, say  $N = 256$ . This corresponds to a frequency resolution of 32 Hz at  $F_s = 8192$  Hz and a time-domain width of 31 ms.
- (ii) This DFT length supports efficient calculation of the transform: the Fast Fourier Transform (FFT) algorithm (Chapter 7). Since we may have quite a few time windows, Candidate segments that are too small can be padded with zeros at the end to make, say, 256 points.
- (iii) We can cover longer segments with 256-point windows, overlapping them if necessary.
- (iv) We have to run the FFT computation over a whole set of time-domain windows; hence it may be crucial to use a fast transform and limit overlapping.
- (v) A genuine DTMF application must account for proper pulse time width (23 ms, minimum, for decoding), frequency (within 3.5% of specification), and energy ratio (DTMF tone energy must exceed that of other frequencies present by 30 dB).
- (vi) Once the application checks these details, it can then invoke the logic implied by Table 9.1 and make a final tone decision.

Let us form an array of dual tone energies plotted against time window location (Figure 9.5) and thereby interpret the signal. Sixteen disjoint 256-point windows cover the signal's time domain. Over each window, we compute the FFT. For each of 16 DTMF tones, we calculate the frequency-domain signal energy in the tone frequency range, the energy outside the tone frequency range, and the ratio of the two energies in dB.

Recall that there are two formulas for expressing a gain or ratio  $R_{\text{dB}}$  between signals  $Y_1$  and  $Y_2$  in decibels (dB). We use either magnitude or power (which is proportional to energy, the magnitude squared):

$$R_{\text{dB}} = 20 \log_{10} \left( \frac{M_1}{M_2} \right) = 10 \log_{10} \left( \frac{P_1}{P_2} \right), \quad (9.9)$$

where  $M_i$  and  $P_i$  are the magnitude and power, respectively, of signal  $Y_i$ . For each time window we set  $y(n) = x(n)$  restricted to the window. Let  $Y(k)$  be the 256-point-FFT of  $y(n)$  over the window. Then, for each DTMF tone frequency range in Figure 9.5, we take  $P_1$  to be the sum of squared magnitudes of the transform values that lie within the tone frequency range, considering only discrete frequency values  $0 \leq k < 128$  that lie below the Nyquist value. We set  $P_2$  to be the sum of squared magnitudes that remain; these represent other tones or noise. For example, for DTMF dual tone

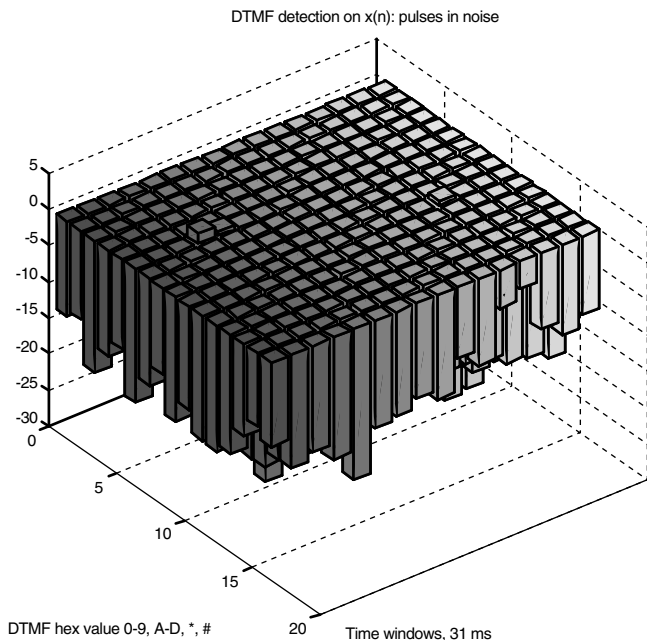


**Fig. 9.5.** A time-frequency array showing DTMF detection on a noisy  $x(n)$ . The DTMF “5” and “9” tones appear as tall blocks, representing high ratios of DTMF tone power to overall signal power (dB). Note, however, that the tones are just barely detectable, by a threshold above 0 dB.

“9,” the energy lies in  $Y(k)$  coefficients  $26 \leq k \leq 27$  (which represent frequencies  $f$  (Hz) of  $26 \times 32 = 832 \leq f \leq 864$ , for the lower tone) and in  $45 \leq k \leq 47$  (which represent frequencies  $1440 \leq f \leq 1504 = 47 \times 32$ ) for the upper tone. Thus, we construct a  $16 \times 16$  array of power ratios, DTMF versus non-DTMF.

Note that the joint frequency and time domain computations involve a tradeoff between frequency resolution and time resolution. When we attempt to refine the time location of a tone segment, we use a lower-order DFT, and the frequency resolution  $(NT)^{-1}$  suffers. Since the sampling rate has been fixed at 8 kHz, on the other hand, improving the frequency resolution—that is, making  $(NT)^{-1}$  smaller—requires a DFT over a larger set of signal samples and thus more imprecision in temporal location.

Let us consider the effect of noise on the time-frequency plane analysis. We have observed that preliminary time domain segmentation works well under benign noise. Heavier noise demands some additional time domain segmentation effort. Noise whose variation approaches the magnitude of the tone oscillations causes problems for segmentation, even though the Fourier analysis can still reveal the underlying tones.

The noisy signal in Figure 9.1 resists segmentation via the Otsu algorithm, for example. Without a time domain segmentation, we can try using small time domain windows and computing an array of coarse frequency resolution magnitude spectra,

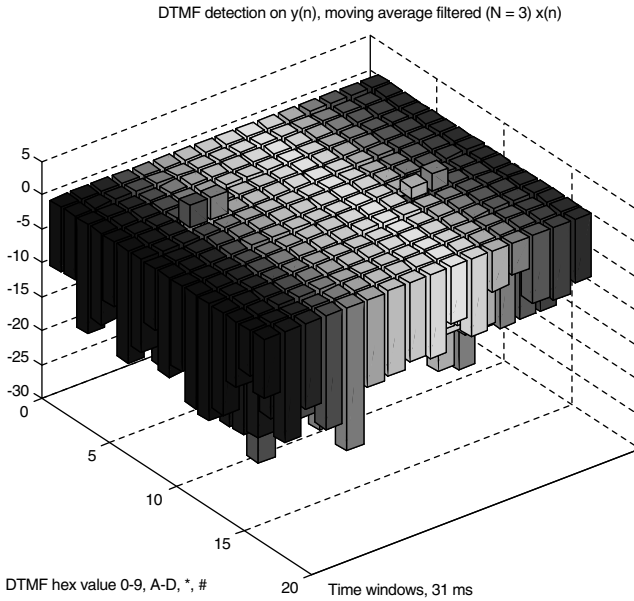


**Fig. 9.6.** A time-frequency array showing DTMF detection on a very noisy  $x(n)$  subject to a moving average noise removal filter. The plot shows the ratio between frequency-domain DTMF power (dB) and non-DTMF power. The time location of the tones is clear, but the frequency discrimination shows little improvement.

such as in Figure 9.5. The problem is that the noisiness of the signal can obscure the tone peaks in the time-frequency array. Let us apply a moving average filter to the signal prior to time-frequency decomposition (Figure 9.6).

The moving average filter’s poor performance is not so surprising. We have already empirically shown that its effectiveness is limited by our lack of control over the lobes that appear in its magnitude spectrum (Figure 9.4). We apparently require a filter that passes precisely the range of our DTMF signals, say from 600 to 1700 Hz, and stops the rest. Such a *bandpass filter* cuts down signal components whose frequencies lie outside the DTMF band.

We can construct such a filter  $H$  by specifying its frequency domain  $H(k)$  as being unity over the discrete DTMF frequencies and zero otherwise. Let  $f_{LO} = 600$  Hz,  $f_{HI} = 1700$  Hz, the sampling rate  $F_s = 8192$  Hz, and suppose  $N = 256$  is the DFT order. The sampling interval is  $T = F_s^{-1}$ , so that the frequency resolution is  $f_{res} = 1/(N \times T)$ . The Nyquist rate is  $f_{max} = (N/2) \times f_{res} = F_s/2 = 4096$  Hz. Hence, let us define  $k_{LO} = (N/2) \times (f_{LO}/f_{max})$  and  $k_{HI} = (N/2) \times (f_{HI}/f_{max})$ . An ideal bandpass filter for this Fourier order is given by

$$H(k) = \begin{cases} 1 & \text{if } k_{LO} \leq k \leq k_{HI}, \\ 1 & \text{if } N - k_{HI} \leq k \leq N - k_{LO}, \\ 0 & \text{if otherwise.} \end{cases} \quad (9.10)$$

Then we find

$$h(n) = \frac{1}{N} \sum_{k=0}^{N-1} H(k) e^{\frac{2\pi jkn}{N}}. \quad (9.11)$$

This creates an  $N$ -point finite impulse response (FIR) filter (Figure 9.7). Except for the DC term  $n = 0$ ,  $h(n)$  is symmetric about  $n = 128$ .

We can filter the noisy  $x(n)$  in either of two ways:

- (i) Set up the filter as a difference equation, for example, using the Direct Form II architecture that we will cover later. This method is appropriate for on-line processing of the signal data.
- (ii) Translate the filter  $g(n) = h(n - 128)$  and perform the convolution  $y(n) = (g*x)(n)$ . This method is suitable for off-line applications, where all of the signal data is available and the noncausal filter  $g(n)$  can be applied to it.

The results of the filtering are shown in the two lower panels of Figure 9.7. Note that the difference equation implementation produces a significant delay in the output

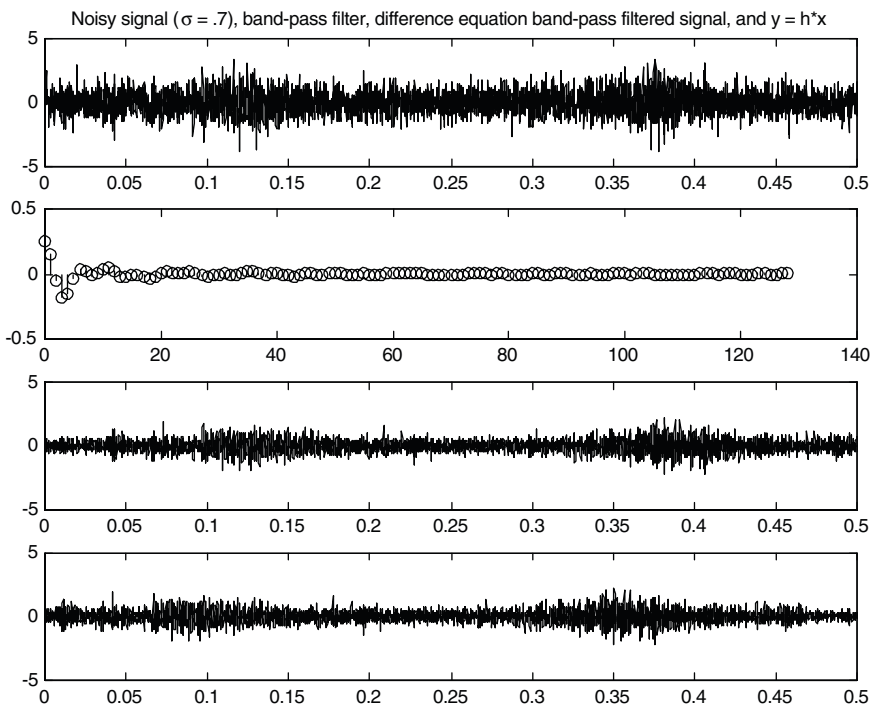


**Fig. 9.7.** Noisy signal  $x(n)$ ,  $\sigma = 0.7$  (top). Bandpass filter  $h(n)$  for  $0 \leq n \leq N/2$  (second from top). Alternative filtering results (lower panels).

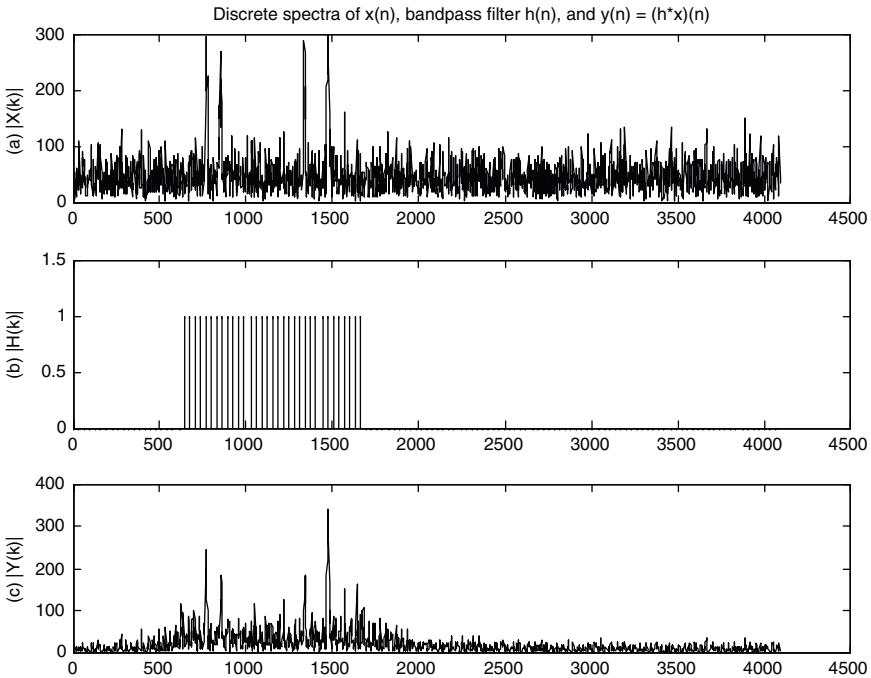


Fig. 9.8. Magnitude spectra from the bandpass filtering operation.

signal. Figure 9.8 shows the frequency-domain magnitude spectra of  $X(k)$ ,  $H(k)$ , and  $Y(k)$ , where  $y(n) = (Hx)(n)$ .

An analysis of the noisy DTMF signal using a time-frequency map is shown in Figure 9.9. Note that the bandpass filter raises the peaks in the time-frequency plane, which potentially helps with detection under severe noise. The drawback is that a few false positive frequency markers appear as well. Why does the bandpass filter not do a clearly superior job compared to the simple moving average filter and analysis without prefiltering? Unfortunately, this bandpass filter is still forgiving to all noise in its pass band—that is, from 600 to 1700 Hz. For example, when the signal of interest is a DTMF “1” dual-tone (697 Hz and 1209 Hz), filtering with the above  $H$  will allow noise from 1.25 to 1.7 kHz into the output.

So bandpass filtering is a promising idea, but cleaning all DTMF tones with a single bandpass filter gives only modest results.

**9.1.2.4 Filter Bank Decomposition and Analysis.** A third approach to dual-tone detection employs a frequency selective filter for each tone in the DTMF ensemble. Constructing, implementing, and applying so many filters seems onerous, but the humble results in the previous two sections encourage alternatives. The appropriate frequency domain tool for this approach is called a *filter bank*. Indeed, this is the conventional approach for DTMF detection, which often calls for online implementation and real-time detection [12].

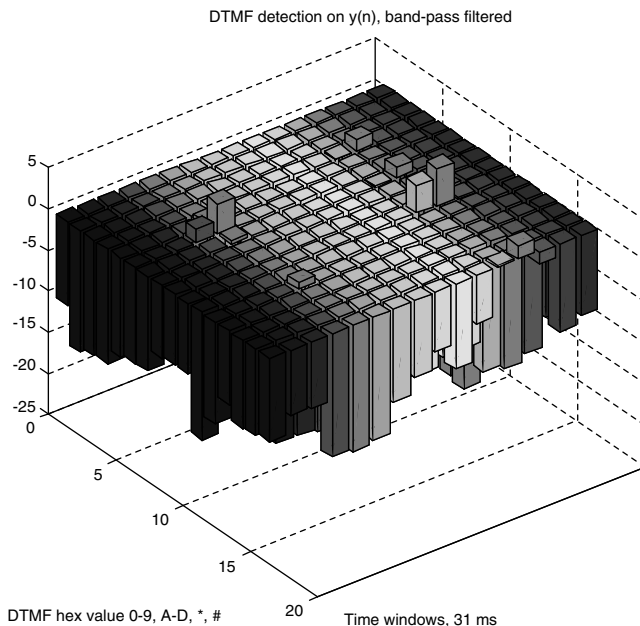


**Fig. 9.9.** Time-frequency map: A DTMF signal after bandpass filtering.

Filter banks have been carefully studied by signal processing researchers for applications involving compression and efficient signal transmission. More recently they have been subject to intense scrutiny because, when combined with subsampling operations, they are related to the theory of wavelets [23–25]. We will consider these ideas at the end of the chapter and follow up on them in the last two chapters especially. However, for now, our purposes are elementary.

We just want to assemble an array of filters whose parallel output might be read out to interpret a signal containing digital telephony dual-tones. Such simple filter banks are suitable for analysis applications where the input signal frequency ranges are generally known in advance, but the time at which they might occur is not known. If the several filters in the bank are implemented as causal filters,  $h(n) = 0$  for  $n < 0$ , then the filter bank can process data as it arrives in real time.

To build a filter bank for the DTMF application, we set up bandpass filters with unit gain passbands centered about the eight (four low and four high) tones of Table 9.1. Each bandpass filter is designed exactly as in (9.10), except that the frequency range is narrowed to within 3.5% of the tone center frequencies. All filters have the same passband width, and the order of the DFT is  $N = 200$  samples (Figure 9.10).

The result of filtering the input signal  $x(n)$ , which contains DTMF tones “5” and “9” as well as normally distributed noise of zero mean and standard deviation  $\sigma = 0.8$ , is shown in Figure 9.11.

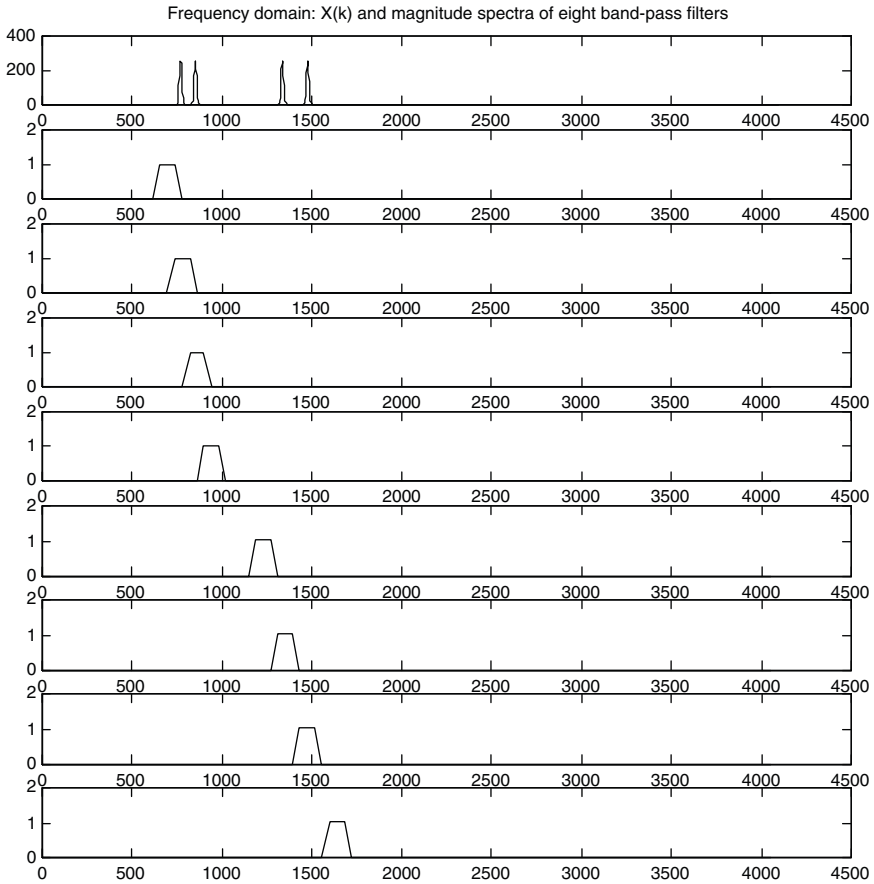


**Fig. 9.10.** Magnitude spectra of pure DTMF tones “5” and “9” (top) and bank of eight bandpass filters.

To complete the application, one could calculate the energy in a certain window of the last  $M$  samples. The dual-tone standard calls for 23 ms for decoding, so at the sampling rate of the example application,  $M = 188$ . If the energy exceeds a threshold, then the tone is detected. A valid combination of tones, one low tone and one high tone, constitutes a dual-tone detection.

The main problem with the filter bank as we have developed it is the delay imposed by the bandpass filters. The shifting of pulses after filtering must be compensated for in the later analysis stages, if there is a need to know exactly when the tones occurred. For example, do we know that the tones are delayed the same amount? If so, then the detection logic will be correct, albeit a little late, depending on the length of the filters. But if different frequencies are delayed different amounts, then we either need to uniformize the delay or compensate for it on a filter-by-filter basis.

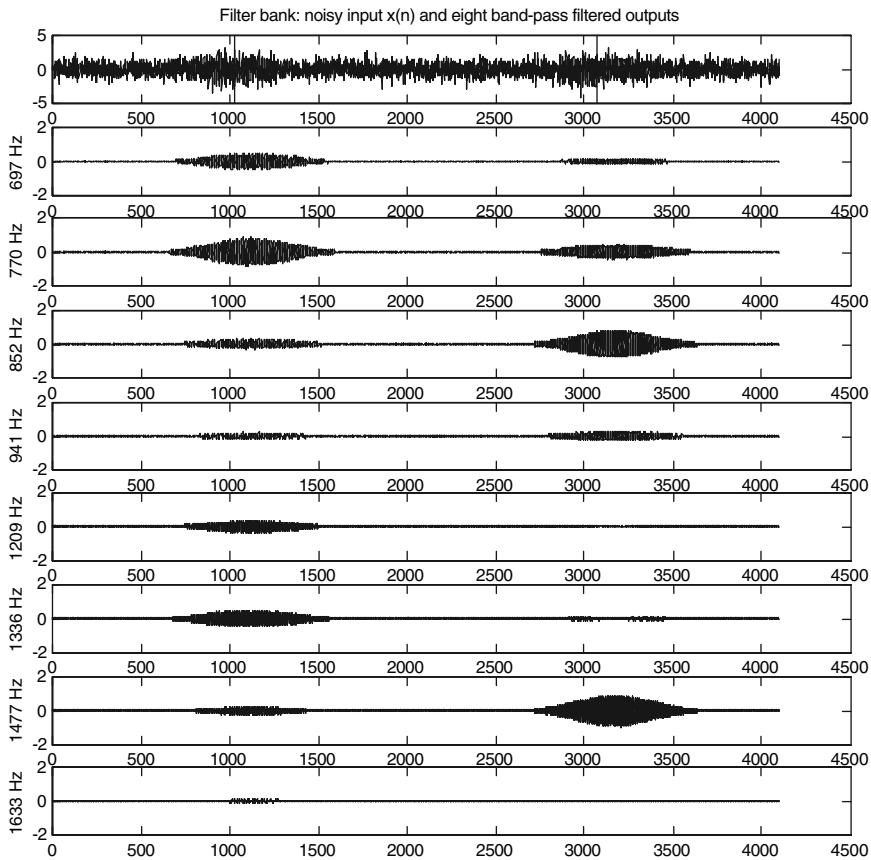


**Fig. 9.11.** Filter bank output, causally implemented. Note the large delay between the center of the input and output pulses. This is a consequence of the length of the filter,  $N = 200$ , and the causal implementation.

### 9.1.3 Filter Frequency Response

When input signals contain oscillatory components that are hidden within noise, the discrete Fourier transform reveals the periodicity as high magnitude spikes in the magnitude spectrum. Even when the signal is so immersed in noise that the time-domain representation refuses to betray the presence of sinusoidal components, this signal transformation is still effective. Though its power is evident for this purpose, the DFT nonetheless loses the time location of oscillations. And for this some time-domain analysis remains. But the noise obscures the time-domain location and extent of the oscillations. This can be a crucial factor in interpreting the signal. By noise removal filtering, however, we can improve visibility into the time-domain and better know the places where the periodicity hides. All of this suggests a theoretical study of the effect of filters on periodic trends in signals.

Consider an exponential signal  $x(n)$  input into a linear, translation-invariant system  $H$ , producing output  $y(n)$ :  $y = Hx$ . If  $\delta(n)$  is the discrete impulse and  $h = H\delta$  is the *impulse response* of  $H$ , then  $y(n) = (x * h)(n)$  is the convolution of  $x(n)$  and  $h(n)$ :

$$y(n) = (x * h)(n) = \sum_{k=-\infty}^{\infty} x(k)h(n-k) = \sum_{k=-\infty}^{\infty} h(k)x(n-k). \quad (9.12)$$

Suppose  $x(n) = e^{j\omega n}$  is the discrete exponential signal with radial frequency  $\omega$  radians per sample. Then

$$y(n) = \sum_{k=-\infty}^{\infty} h(k)e^{j\omega(n-k)} = e^{j\omega n} \sum_{k=-\infty}^{\infty} h(k)e^{j\omega k} = e^{j\omega n} H(\omega), \quad (9.13)$$

where  $H(\omega)$  is the *frequency response* of  $h(n)$ . An exponential input to an LTI system produces an exponential output of the same frequency, except amplified (or attenuated) by the factor  $H(\omega)$ . This basic Chapter 7 result tells us that LTI systems pass exponential signals directly from input to output, multiplied by a complex constant which depends on the signal frequency.

### 9.1.4 Delay

We have observed empirically that noise removal filtering—and by implication, convolutional filtering in general—imposes a delay on input signals. This section explains the theory of two types of signal delay caused by filtering: *phase delay* and *group delay*.

**9.1.4.1 Phase Delay.** Suppose  $x(n)$  is a discrete signal and  $y = Hx$  is a linear, translation-invariant (LTI) discrete system. If  $x(n) = \exp(j\omega n)$  is a pure, complex-valued exponential signal, then  $y(n) = H(\omega)\exp(j\omega n) = H(\omega)x(n)$ , where  $H(\omega)$  is the discrete-time Fourier transform (DTFT) of  $h(n) = (H\delta)(n)$ .

Consider a sinusoidal input signal  $x(n) = \cos(n\omega) = [e^{j\omega n} + e^{-j\omega n}]/2$ . Then

$$\begin{aligned} y(n) &= \frac{H(\omega)e^{j\omega n}}{2} + \frac{H(-\omega)e^{-j\omega n}}{2} = \frac{H(\omega)e^{j\omega n}}{2} + \frac{\overline{H(\omega)}e^{j\omega n}}{2} \\ &= 2\text{Real}\left[\frac{H(\omega)e^{j\omega n}}{2}\right] = \text{Real}[H(\omega)e^{j\omega n}]. \end{aligned} \quad (9.14)$$

But

$$\text{Real}[H(\omega)e^{j\omega n}] = |H(\omega)| \cos[\text{Arg}(H(\omega))e^{j\omega n}]. \quad (9.15)$$

If we set  $\theta(\omega) = \text{Arg}(H(\omega))$ , then

$$y(n) = \text{Real}[H(\omega)e^{j\omega n}] = |H(\omega)| \cos[\omega n + \theta(\omega)] = |H(\omega)| \cos\left[\omega\left(n + \frac{\theta(\omega)}{\omega}\right)\right]. \quad (9.16)$$

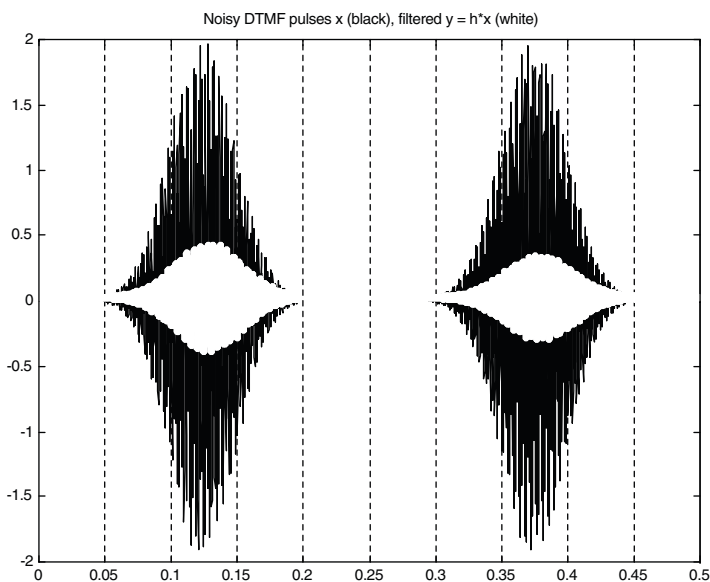


**Fig. 9.12.** Filter phase delay. Noisy DTMF pulses  $x$  (black), filtered  $y = h*x$  (white).

So if the input  $x(n)$  to  $H$  is a sinusoid, then the output  $y(n)$  is a sinusoid too. Signals  $x(n)$  and  $y(n)$  have the same frequency, but  $y(n)$  is scaled by  $|H(\omega)|$  and phase shifted by  $T_H = -\theta(\omega)/\omega$ , which is called the *phase delay* of  $H$  [26].

If we apply a moving average filter of length  $N = 101$  to the noisy DTMF pulses (), then the phase delay imposed by the filter is clearly evident (Figure 9.12).

So sinusoids too, subject to a complex scaling, pass directly through LTI systems. This helps explain the clarity with which the sinusoidal pulses of the DTMF application appear in the frequency domain. Also, we now have a tool, namely the phase delay,  $T_H = -\theta(\omega)/\omega$  in (9.16) for comparing the delays induced by various filters.

**9.1.4.2 Group Delay.** Another type of filter delay occurs when source signals contain sinusoids of nearby frequencies that form an envelope. The superposition of the two sinusoids

$$x(n) = \cos(\omega_1 n) + \cos(\omega_2 n), \quad (9.17)$$

with  $\omega_1 \approx \omega_2$ , creates a long-term oscillation, called a *beat*. This holds as long as the filter  $H$  does not suppress the individual sinusoids; this means that  $\omega_1$  and  $\omega_2$  are in the *passband* of  $H$ .

By trigonometry, we can write  $x(n)$  as a product of cosine functions, one of which gives the envelope, of frequency  $\omega_1 - \omega_2$ , and the other is a sinusoid whose frequency is the mean. Thus,

$$x(n) = 2 \cos\left(n \frac{(\omega_1 - \omega_2)}{2}\right) \cos\left(n \frac{(\omega_1 + \omega_2)}{2}\right), \quad (9.18)$$

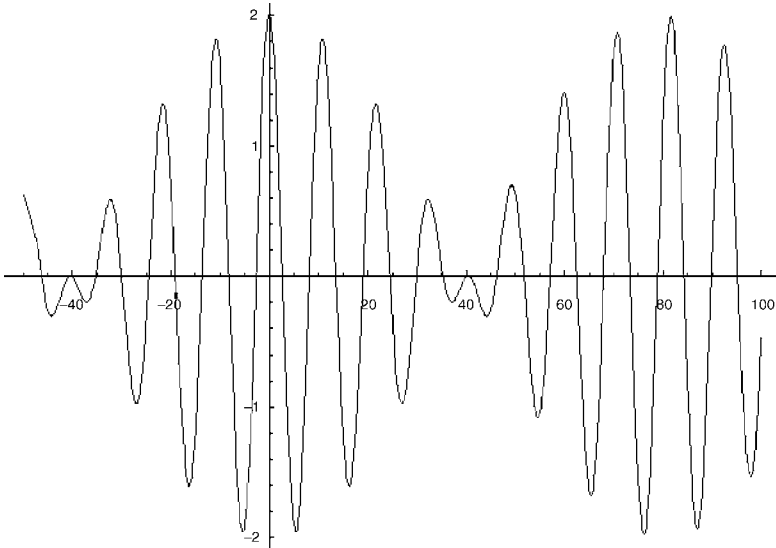


**Fig. 9.13.** Signal envelope formed by two sinusoids of approximately the same frequency.

which explains the amplitude modulated oscillation of Figure 9.13. Now impose a filter  $y(n) = (h*x)(n)$ , with  $h = H\delta$ . Using (9.16) and (9.17) we have

$$y(n) = |H(\omega_1)| \cos(\omega_1 n + \theta(\omega_1)) + |H(\omega_2)| \cos(\omega_2 n + \theta(\omega_2)), \quad (9.19)$$

where  $\theta(\omega) = \text{Arg}(H(\omega))$ . Assume  $\omega_1 \approx \omega_2$  and that these lie in the passband of  $H$ , which is to say  $|H(\omega_1)| \approx |H(\omega_2)| \neq 0$ . Thus,

$$y(n) = |H(\omega_1)| \{ \cos(\omega_1 n + \theta(\omega_1)) + \cos(\omega_2 n + \theta(\omega_2)) \}. \quad (9.20)$$

From trigonometry once again,

$$y(n) = 2|H(\omega_1)| \left\{ \cos \frac{\omega_1 n + \theta(\omega_1) - \omega_2 n - \theta(\omega_2)}{2} \cdot \cos \left( \frac{\omega_1 n + \theta(\omega_1) + \omega_2 n + \theta(\omega_2)}{2} \right) \right\}. \quad (9.21)$$

Rearranging the cosine arguments gives

$$y(n) = 2|H(\omega_1)| \left\{ \cos \left\{ \frac{\omega_1 - \omega_2}{2} \left[ n + \frac{\theta(\omega_1) - \theta(\omega_2)}{\omega_1 - \omega_2} \right] \right\} \cdot \cos \left( \frac{\omega_1 + \omega_2}{2} \left[ n + \frac{\theta(\omega_1) + \theta(\omega_2)}{\omega_1 + \omega_2} \right] \right) \right\}, \quad (9.22)$$

where the first cosine defines the envelope of  $y(n)$ . This envelope is delayed by a factor  $\frac{\theta(\omega_1) - \theta(\omega_2)}{\omega_1 - \omega_2}$ . As  $\omega_1 \rightarrow \omega_2$ , this delay factor becomes a derivative, which is called the *group delay* of the filter  $H$ :  $T_G = -d\theta/d\omega$  [11].

**9.1.4.3 Implications.** Applications that require significant signal filtering must consider the phase and group delay inherent in the system. In our own humble DTMF example above, we noted the phase delay caused by the filter bank. In many scientific and engineering applications, delay considerations affect the actual choice of filters. We shall see later that certain types of finite impulse response (FIR) filters have *linear phase*, so that their group delay is constant. Such filters support signal processing without distortion, an important consideration in communications systems [27].

## 9.2 FREQUENCY AND PHASE ESTIMATION

The dual-tone multifrequency (DTMF) detection problem in the previous section required Fourier transformation of local signal slices in order to find coded tones. With many slices and many frequency bins, we built time-frequency maps. And thus, we were able to ascertain the presence of signal frequency components over the time span of the signal slice by thresholding for large-magnitude Fourier-domain values. In this section, we study the effectiveness of such techniques. Our methods will be limited and introductory, only a small part of the broad and involved theory of *spectral estimation*. In what appear to be obviously correct and quite straightforward approaches to the problem, we shall see that there are some surprising limitations.

This section introduces an important tool: *window functions*. These are special analog or discrete signals that are used to weight a local signal slice. This technique, called *windowing*, helps to suppress artifacts caused by Fourier transformation on a segment of time-domain signal values. Thus, windowing improves the estimation of local signal frequencies. The signal slice itself is called a *window* or a *region of interest*. Sometimes window functions are loosely called “windows” as well. The ideas are easy, and in context the terms are usually clear. In Chapter 10, we consider analog window functions as an instrument with which to generalize the Fourier transform. Here, we pursue signal analysis applications, computerized implementation, and our emphasis is consequently on discrete windowing.

The DTMF tutorial application did not weight the signal values before performing the discrete Fourier transform (DFT). The results were satisfactory, but we shall see later that applying a window function to the values produces a cleaner, easier to analyze time-frequency map. Moreover, we shall see that the window functions and the windowing method provide a straightforward method for designing discrete finite impulse response (FIR) filters.

In the present context, we can hardly do justice to the vast research and engineering literature on spectral estimation [28–31].

## 9.2.1 Windowing

Let us experiment with a simple discrete sinusoid  $x(n)$  and the task of computing its discrete Fourier transform (DFT) on a *window*—that is, over a restricted set of values. Three problematic cases emerge:

- (i) Alignment of the DFT samples with the signal's spectrally significant portion;
- (ii) Signal features that appear to an initial interpretation as frequency characteristics, but in fact arise from wholly different reasons—for example, the presence of an edge;
- (iii) Proper sizing of the DFT for the samples.

The first two points affect one another.

**9.2.1.1 Alignment and Edges.** Let us consider a sinusoidal pulse and its frequency analysis on slices of varying alignments with the pulse event (Figure 9.14).

Windowing involves weighting the samples from the signal slice by window function values before computing the spectrum. We might speculate that Fourier magnitude spectra would be better represented by weighting the central values more

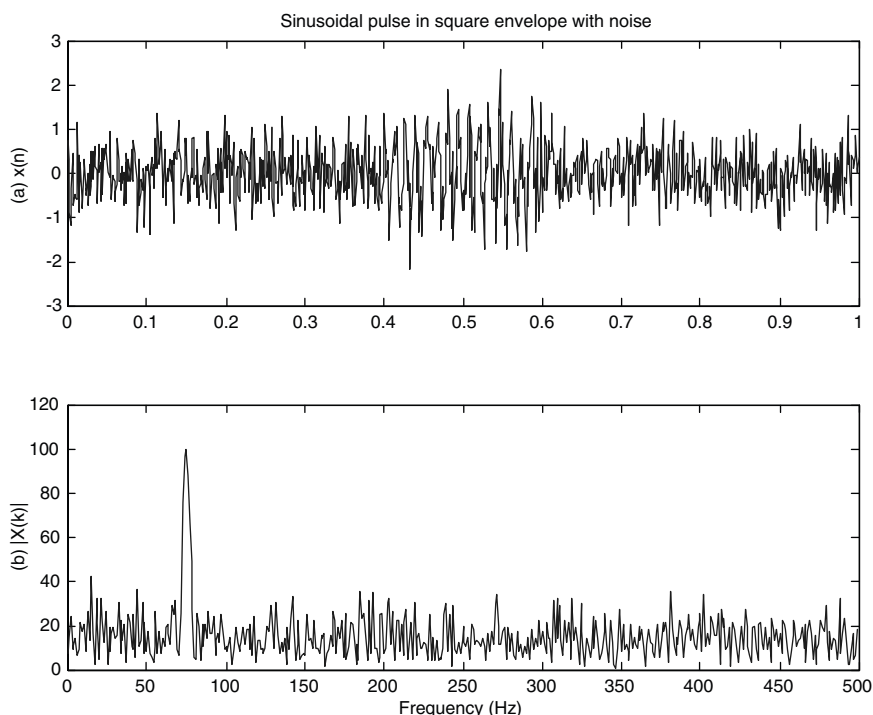


**Fig. 9.14.** Sinusoidal pulse in square envelope (75 Hz, 200 samples wide,  $T = .001$  s) in moderate noise (top) and its magnitude spectrum (bottom).

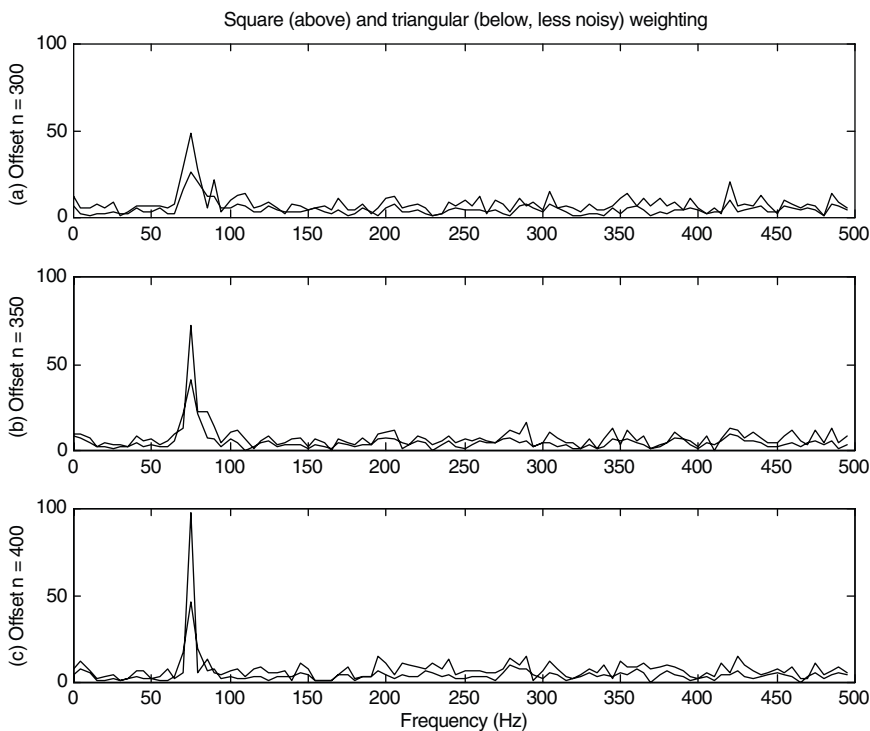


**Fig. 9.15.** Square pulse magnitude spectra, same DFT order ( $N = 200$ ) at three different offsets:  $n = 300$ ,  $n = 350$ , and  $n = 400$  (full alignment).

than the peripheral values with a time slice from an input signal  $x(n)$ . The next experiment (Figure 9.15) shows the result of computing magnitude spectra for square and for triangular-weighted window functions.

The main effect of misalignment of the DFT window with the signal oscillations is a blurring of the magnitude spectrum spike. Improving the alignment—clearly—produces a more distinct spike, and invoking a weighting function (a triangular window) in this case offers only modest improvement.

In many applications, preliminary time-domain segmentation helps avoid this problem. Applications can detect signal edges early and use them to align spectral analysis windows. Sometimes edge detection can be based on signal level changes, but in other cases what constitutes an edge is a change in frequency content.

**9.2.1.2 Window Size.** Now we turn to another anticipated difficulty. Suppose that the signal slice for DFT computation aligns with the oscillation-bearing part of the signal, but the order of the Fourier transformation is a poor choice for the underlying frequency component. We know that a DFT of order  $N$  on data  $x(n)$  sampled at  $F_s = 1/T$  Hz will have frequency resolution  $(NT)^{-1}$  and cover discrete frequencies  $(NT)^{-1}$ ,  $2(NT)^{-1}$ , ...,  $(2T)^{-1}$  as long as  $x(n)$  is real-valued. Adding a pure sinusoid of

one these frequencies—say  $\omega_k = k(NT)^{-1}$ , for  $1 \leq k \leq N/2$ —to  $x(n)$  will alter only  $X(k)$  and  $X(N - k)$  [32]. Superimposing onto  $x(n)$  a sinusoid of frequency  $\omega \neq \omega_k$ , for any  $1 \leq k \leq N/2$ , will perturb all of the  $X(k)$ . The difference caused by adding the sinusoid diminishes in magnitude like  $1/|\omega - \omega_k|$  as  $|\omega - \omega_k|$  increases (exercise).

## 9.2.2 Windowing Methods

Windows are weighting functions that attenuate signals at their discontinuities. When we cut out a piece of a signal and use it to compute its DFT, this effectively periodicizes the signal. The problem is that the signal's early values might differ greatly from the later values in the excised portion. So the effective periodic signal has a huge discontinuity, and this creates large spectral components that are due to the time slicing rather than the trend of the original signal.

The remedy is to suppress the signal slice at its boundaries with a window function. Window functions also serve as a tool for constructing FIR filters. There are a variety of window functions [7–9, 26, 33]:

- The *rectangular* window takes raw signal values without shaping them.
- The *Bartlett*<sup>2</sup> or *triangular* window weights them linearly away from the center.
- The *Hann*<sup>3</sup> window, sometimes called a “Hanning” window, is a modified cosine weighting function.
- The *Hamming*<sup>4</sup> window is also a modified cosine window.
- The *Blackman*<sup>5</sup> window is another modified cosine window.
- The *Kaiser*<sup>6</sup> window uses a Bessel function for shaping the signal slice.

It seems that throughout our experimentation in Section 9.1, we employed the rectangular window. For comparison, Table 9.2 lists the window functions. Note that the window domains  $|n| \leq \frac{N-1}{2}$  of Table 9.2 are convenient for applications not needing causal filters, such as off-line signal analysis tasks. It is also the form that we will use for the analog windows in the next chapter. Since the windows are zero outside this interval, as linear, translation-invariant system impulse responses, the window functions are all weighted moving average filters. They remove high frequencies and preserve low frequencies when convolved with other discrete signals.

<sup>2</sup>After M. S. Bartlett, who used this window to estimate spectra as early as 1950.

<sup>3</sup>Austrian meteorologist Julius von Hann introduced this window. At some point, perhaps due to confusion with Hamming's similar window or to the use of the term “hann” for the cosine windowing technique in general (as in Ref. 32), the name “Hanning” seems to have stuck.

<sup>4</sup>Richard W. Hamming (1915–1998) used this window for improved signal spectral analysis, but the American mathematician is more widely known for having invented error correcting codes (*The Bell System Technical Journal*, April 1950).

<sup>5</sup>After Hamming's collaborator at Bell Telephone Laboratories, Ralph B. Blackman (1904–).

<sup>6</sup>Introduced by J. F. Kaiser of Bell Laboratories in 1974.

**TABLE 9.2. Window Functions for  $N > 0$  Samples<sup>a</sup>**

Name	Definition
Rectangular	$w(n) = \begin{cases} 1 & \text{if }  n  \leq \frac{N-1}{2} \\ 0 & \text{otherwise} \end{cases}$
Bartlett (triangular)	$w(n) = 1 - \frac{2 n }{N-1} \quad \text{if }  n  \leq \frac{N-1}{2}$
Hann	$w(n) = \frac{1}{2} \left[ 1 - \cos \frac{2\pi n}{N-1} \right] \quad \text{if }  n  \leq \frac{N-1}{2}$
Hamming	$w(n) = 0.54 - 0.46 \cos \frac{2\pi n}{N-1} \quad \text{if }  n  \leq \frac{N-1}{2}$
Blackman	$w(n) = 0.42 + 0.5 \cos \frac{2\pi n}{N-1} + 0.08 \cos \frac{4\pi n}{N-1} \quad \text{if }  n  \leq \frac{N-1}{2}$
Kaiser	$w(n) = \frac{I_0 \left( \alpha \sqrt{1 - \left( \frac{2n}{N-1} \right)^2} \right)}{I_0(\alpha)} \quad \text{if }  n  \leq \frac{N-1}{2}$

<sup>a</sup>The table defines the windows as centered about  $n = 0$ . Outside the specified ranges, the windows are zero. It is straightforward to shift them so that they are causal [7]. The Kaiser window is defined in terms of the zeroth-order Bessel<sup>7</sup> function of the first kind (9.23) and a parameter  $\alpha$  given below (9.24).

The summation

$$I_0(t) = 1 + \sum_{n=1}^{\infty} \left[ \frac{1}{n!} \left( \frac{t}{2} \right)^{n-2} \right]^2 \quad (9.23)$$

defines the Bessel function. There is a standard formula [33] for the Kaiser window parameter  $\alpha$ . To ensure a Kaiser window whose Fourier transform suppresses high-frequency components to more than  $-\Delta$  dB, set

$$\alpha = \begin{cases} 0.1102(\Delta - 8.7) & \text{if } \Delta > 50, \\ 0.5842(\Delta - 21)^{0.4} + 0.07886(\Delta - 21) & \text{if } 50 \geq \Delta \geq 21, \\ 0 & \text{if } 21 > \Delta. \end{cases} \quad (9.24)$$

<sup>7</sup>Professor of astronomy, mathematician, and lifelong director of the Königsberg Observatory, Friedrich Wilhelm Bessel (1784–1846) devised the functions bearing his name for analyzing the motions of three bodies under mutual gravitation.

### 9.2.3 Power Spectrum Estimation

The Fourier transform magnitude spectrum has some important drawbacks. Our introductory digital telephony control tones application showed that—under moderate noise—measuring the contributions of frequency components by the relative magnitude of Fourier transform coefficients is effective.

To understand how this comes about, we have to consider signal noise in a mathematically tractable form.

**9.2.3.1 Power Spectral Density.** Let  $\mathbf{x}$  be a discrete random signal; that is,  $\mathbf{x} = \{x_n; n \in \mathbb{Z}\}$  is a family or *ensemble* of *random variables* (Chapter 1). This is an abstract formulation. What it means is that if a signal  $x(n)$  has a random nature, then we do not know exactly what value it may take at any particular time instant  $n \in \mathbb{Z}$ . But we at least know that the values  $x(n)$  might assume at  $n = k$ , for example, are given by a random variable, namely  $x_k \in \mathbf{x}$ . So by a random signal, we understand a signal that is random at all of its measured time instants; it is indeed an ensemble of random variables.

But that is not to say that we know nothing about the random signal  $\mathbf{x}$ . Associated with each random variable  $r = x_n \in \mathbf{x}$  for some  $n \in \mathbb{Z}$  is a *probability distribution function*  $F_r$  and a *probability density function*  $f_r$  such that  $F_r(s) = P(r \leq s)$ , the probability that  $r$  does not exceed  $s \in \mathbb{R}$ . Moreover,

$$F_r(s) = \int_{-\infty}^s f_r(t) dt, \tag{9.25}$$

which is to say that  $\frac{\partial}{\partial s} F_r(s) = f_r(s)$ . To the skeptically inclined individual, these are almost incredible conditions, but they do approximate naturally occurring random signals fairly well. In any case, we need them for the theoretical development.

The distribution and density functions allow us to describe random variables with averages. If  $r = x_n \in \mathbf{x}$  again, then we define its *mean*

$$\mu_r = \int_{-\infty}^{\infty} t f_r(t) dt = E[r] \tag{9.26}$$

and *standard deviation*  $\sigma_r$ , the square root of the *variance*:  $\sigma_r^2 = E[r^2] - \mu_r^2$ .

Generalizing for two random variables,  $u = x_n$  and  $v = x_m$  in  $\mathbf{x}$ , we assume a *joint distribution function*  $F_{u,v}(s, t) = P(u \leq s \text{ and } v \leq t)$  and *joint density function*  $\frac{\partial^2}{\partial s \partial t} F_{u,v}(s, t) = f_{u,v}(s, t)$ . If  $E[uv] = E[u]E[v]$ , then random variables  $u$  and  $v$  are *uncorrelated* or *linearly independent*.

Power spectrum estimation studies how signal power distributes among frequencies. For finite-energy deterministic signals  $x(t)$ , the power of  $x(t)$  in the (unsigned) band  $0 < \Omega_0 < \Omega_1 < \infty$  comes from integrating  $|X(\Omega)|^2$  over  $[-\Omega_1, -\Omega_0] \cup [\Omega_0, \Omega_1]$ .

But for random signals, the mathematical analysis depends on a special class of signals  $x(t)$  that obey the following two conditions:

- (i)  $E[x(t)]$  does not depend on the process variable  $t \in \mathbb{R}$ .
- (ii)  $E[x(t)x(t + \tau)]$  is a function of  $\tau$  and does not depend on  $t \in \mathbb{R}$ .

Such signals are called *wide-sense stationary* (WSS) [34]. We define the *autocorrelation* for a WSS random signal  $x(t)$  to be  $r_{xx}(\tau) = E[x(t)x(t + \tau)]$ . It is easy to show that  $E[x(t)x(s)] = r_{xx}(t - s)$  and that  $r_{xx}(\tau)$  is an even signal. A special type of WSS random signal  $x(t)$  has an autocorrelation function that is an impulse:  $r_{xx}(\tau) = A\delta(\tau)$  for some constant  $A \in \mathbb{R}$ . This means that signal values are completely uncorrelated with their neighbors. Such random signals are called *white noise* processes; we shall explain this colorful terminology in a moment.

In order to study the spectrum of a noisy signal, we have to limit its time-domain extent. So for  $L > 0$  let us define the *localization* of random signal  $x(t)$  to  $[-L, L]$ :

$$x_L(t) = \begin{cases} x(t) & \text{if } -L \leq t \leq L, \\ 0 & \text{if otherwise.} \end{cases} \quad (9.27)$$

so that

$$X_L(\Omega) = \int_{-\infty}^{\infty} x_L(t)e^{-j\Omega t} dt = \int_{-L}^L x(t)e^{-j\Omega t} dt. \quad (9.28)$$

The energy of  $x_L$  is  $\|x_L\|_2^2 = \frac{1}{2\pi}\|X_L\|_2^2 = \frac{1}{2\pi}\int_{-\infty}^{\infty} |X_L(\Omega)|^2 d\Omega$  by Parseval's identity.

The approximate energy of  $x_L$  in a narrow signed frequency band,  $\Delta(\Omega) = \Omega_1 - \Omega_0$ , is thus  $|X_L(\Omega)|^2 \Delta(\Omega)$ . Since frequency is the reciprocal of time,  $|X_L(\Omega)|^2 / (2L)$  has units of energy, which is the product of power and time, or power divided by frequency. Therefore, we may define the *power spectral density* (PSD) for  $x_L(t)$  to be  $\frac{|X_L(\Omega)|^2}{2L}$ . This is a random variable, and its expectation is  $E\left[\frac{|X_L(\Omega)|^2}{2L}\right]$ . It is

tempting to define the PSD of  $x(t)$  as the large time window  $[-L, L]$  limit of such expectations:

$$X_{\text{PSD}}(\Omega) = \lim_{L \rightarrow \infty} E\left[\frac{|X_L(\Omega)|^2}{2L}\right]. \quad (9.29)$$

But some caution is in order. We need to know that the limit (9.29) exists. A famous result shows that the desired limit operation is valid and moreover provides a way to

compute it. The Wiener<sup>8</sup>–Khinchin<sup>9</sup> theorem, says that if  $x(t)$  is a real-valued, WSS random signal with autocorrelation  $r_{xx}(t) \in L^1(\mathbb{R})$ , then

$$X_{\text{PSD}}(\Omega) = R_{xx}(\Omega) = \int_{-\infty}^{\infty} r_{xx}(t) e^{-j\Omega t} dt. \quad (9.30)$$

While the exact values of a random signal are not known, it is a reasonable assumption that the autocorrelation of the signal is available. Indeed, the autocorrelation will tend to resemble a narrow pulse when local signal values  $x(t + \tau)$  correlate poorly with a particular  $x(t)$ , and it will look like a broad pulse when  $x(t + \tau)$  as a trend repeats  $x(t)$ . In any case, for  $\tau$  large,  $r_{xx}(\tau)$  diminishes, and we can often assume a mathematically tractable model for the autocorrelation. For example, from basic physical considerations, we can derive a model for the thermal noise across a resistor in an electric circuit. A purely theoretical example is the aforementioned white noise process. The Wiener–Khinchin theorem implies that the white noise process  $r_{xx}(\tau) = A\delta(t)$  has  $X_{\text{PSD}}(\Omega) = A$ , for  $A \in \mathbb{R}$ . Thus, its frequency spectrum is flat; it contains all “colors,” as it were, and is therefore “white.” It turns out that white noise models the thermal noise across a resistor and that its autocorrelation scales according to the absolute temperature of the circuit elements.

Similar ideas work for discrete random signals. If  $x(n) \in l^2$  is a discrete deterministic signal with DTFT  $X(\omega)$ , then integrating  $|X(\omega)|^2$  over  $[-\omega_1, -\omega_0] \cup [\omega_0, \omega_1]$  gives the power in the band  $0 < \omega_0 < \omega_1 < \pi$ . A *wide-sense stationary (WSS) discrete* random signal satisfies the following:

- (i)  $E[x(n)]$  does not depend on the process variable  $n \in \mathbb{Z}$ .
- (ii)  $E[x(n)x(n + v)]$  is a function of  $v$  and does not depend on  $n \in \mathbb{Z}$ .

The autocorrelation for a WSS random signal  $x(n)$  is  $r_{xx}(v) = E[x(n)x(n + v)]$ . Again,  $E[x(n)x(m)] = r_{xx}(n - m)$  and  $r_{xx}(v)$  is symmetric about  $v = 0$ . Toward analyzing the power spectrum, for  $L > 0$  we define

$$x_L(n) = \begin{cases} x(n) & \text{if } -L \leq n \leq L, \\ 0 & \text{if otherwise.} \end{cases} \quad (9.31)$$

<sup>8</sup>First-generation American mathematician Norbert Wiener (1894–1964) finished the doctoral program at Harvard at age 18, concentrating on philosophy of mathematics and logic. In the tradition of Plato, the great English scholar Bertrand Russell hoped to improve Wiener’s philosophical insights by having him study more mathematics. But later encounters with G. H. Hardy, D. Hilbert, and E. G. H. Landau nudged the prodigy toward mathematical analysis. After some peregrination, Wiener took a ground-floor job as a mathematics instructor at the Massachusetts Institute of Technology. He eventually arose to full Professor, contributed substantially to statistical communication and control theory, and remained at MIT for the rest of his career.

<sup>9</sup>Soviet mathematician Aleksandr Yakovlevich Khinchin (1894–1959) established much of the early theory of stationary stochastic processes. The author of some 150 papers, he took a mathematics professorship at Moscow State University in 1927. He was a patron of the arts and theater. Election to the Soviet Academy of Sciences (1939) recognized Khinchin’s contributions to ranging from probability, number theory, information theory, statistical physics, and quantum mechanics.

The Fourier spectrum of the localized random signal is

$$X_L(\omega) = \sum_{n=-L}^L x(n)e^{-j\omega n} = \sum_{n=-\infty}^{\infty} x_L(n)e^{-j\omega n}. \quad (9.32)$$

We define the PSD for  $x_L(n)$  to be

$$X_{\text{PSD}}(\omega) = \lim_{L \rightarrow \infty} E \left[ \frac{|X_L(\omega)|^2}{2L+1} \right]. \quad (9.33)$$

There is a discrete version of the Wiener–Khinchin theorem. If  $x(n)$  is a real-valued, WSS random signal with an absolutely summable autocorrelation function  $r_{xx}(n)$ , then

$$X_{\text{PSD}}(\omega) = R_{xx}(\omega) = \sum_{n=-\infty}^{\infty} r_{xx}(n)e^{-j\omega n}. \quad (9.34)$$

Thus, for both analog and discrete random variables we are justified in defining the power spectral density, and it can be computed as long as the associated autocorrelation function is respectively  $L^1$  or  $l^1$ . The exercises outline the proofs of both the analog and discrete Wiener–Khinchin theorems.

**9.2.3.2 Periodogram.** Now we consider approximating the power spectral density. The oldest and most straightforward approach is to compute the discrete time Fourier transform on a local time window  $[-L, L]$  of sampled data points  $x(n)$ . Thus, we have

$$\tilde{X}_{L, \text{PSD}}(\omega) = \frac{1}{2L+1} |X_L(\omega)|^2 = \frac{1}{2L+1} \left| \sum_{n=-L}^L x(n)e^{-j\omega n} \right|^2. \quad (9.35)$$

Generally, we would take  $\omega = 2\pi k/T$  for  $-L \leq k \leq L$  and compute (9.35) on a discrete set of frequencies. After all, although we used the discrete Fourier transform magnitude spectrum in the application examples of Section 9.1, we could have equally well used the squared magnitude spectrum. Also, due to the periodicity of the discrete Fourier transforms, we could equally well shift the local window of  $x(n)$  values. In practice, a window of width  $2M$  is chosen to enable a fast Fourier transform computation. In any event, (9.35) is a statistical estimator for the random variable  $X_{\text{PSD}}(\omega)$ . The question before us is how well—for a particular frequency of interest,  $-\pi < \omega \leq \pi$ —the estimate of  $|X(\omega)|^2$  over  $N = 2L + 1$  samples of noisy  $x(n)$  compares to the actual power at that frequency.

Briefly, the problem with the estimated power spectrum  $\tilde{X}_{\text{PSD}}(\omega)$  is twofold:

- (i) As the number of samples is increased, the mean of the estimate does not approach the actual mean; it is a *biased estimator*.
- (ii) As the number of samples is increased, the variance of the estimate does not approach zero; it is an *inconsistent estimator*.

Signal processing [7] and spectrum estimation [29–31] texts explain this theory. Unfortunately, the development would drag us away from our signal analysis focus. We would instead like to emphasize that the problems of the periodogram as an estimator of the PSD can be addressed by applying the window functions we developed earlier in this section along with some straightforward averaging techniques.

**9.2.3.3 Periodogram Improvement.** Fortunately, there are some easy ways to improve the periodogram estimate  $\tilde{X}_{L, \text{PSD}}(\omega)$  of (9.35). We cover some classic methods that use no model of the signal, its spectrum, or its autocorrelation. These *nonparametric* techniques include:

- Bartlett’s method smoothes the time-domain data by breaking the interval into smaller, equally sized segments and averaging the periodograms computed for each segment [35].
- Welch’s algorithm smoothes the time-domain data by breaking the interval into smaller, equally sized segments, applying a window function to each segment, and allowing the windows to overlap [36].
- Another technique, due to Blackman and Tukey [37], relies directly on the Wiener–Khinchin theorem’s identification of the PSD with the Fourier transform of the autocorrelation function.

Bartlett’s method divides a set of  $N = K \times M$  data points of  $x(n)$  into  $K$  subwindows of length  $M$ . Thus, the signal values on subwindow  $k$  are  $x_k(m) = x(kM + m)$ , where  $0 \leq k \leq K - 1$  and  $0 \leq m \leq M - 1$ . For each such subwindow we set

$$\tilde{X}_{k, \text{PSD}}(\omega) = \frac{1}{M} \left| \sum_{m=0}^{M-1} x_k(m) e^{-j\omega m} \right|^2, \quad (9.36a)$$

and then average them all to get the estimate over  $[0, N - 1]$ :

$$\tilde{X}_{N, \text{PSD}}(\omega) = \frac{1}{K} \sum_{k=0}^{K-1} \tilde{X}_{k, \text{PSD}}(\omega), \quad (9.36b)$$

The Welch algorithm improves upon the Bartlett method by

- (i) Allowing the subwindows to overlap.
- (ii) Applying a window function to the individual PSD estimates on the subwindows. The window function can be any of those described in Table 9.2.

The steps in the Blackman–Tukey algorithm are as follows:

- (i) From a body of measured noisy signal data, the autocorrelation function for the random process is estimated.
- (ii) One of the typical window functions—for example, the Hann window—is applied to the autocorrelation estimate.
- (iii) The discrete Fourier transform is applied to windowed autocorrelation values.

Another class of periodogram improvement algorithms—called *parametric* methods—make a model for the noisy signal data. The idea is to assume that the signal arises from a linear system excited by white noise. The exercises cover the concept of noisy inputs to linear systems.

### 9.2.4 Application: Interferometry

An application that involves the precise estimation of signal frequency and phase is interferometry, which is based on the wave nature of electromagnetic radiation [38]. In interferometry, an input optical signal contains light combined from two different sources—for example, reflected from two different surfaces. If the original source of both reflecting beams is coherent (that is, the light waves are in phase with one another, such as from a laser), then the resulting interferogram will contain peaks and valleys of intensity, depending on the path distance of the component light waves. Of course, moving one reflecting surface by a wavelength amount produces the same light combination, and so the intensity only indicates relative changes in position between the two reflecting surfaces.

The technique enables us to measure minute differences in distance. Peaks in the interferogram correspond to when the peak of one sinusoidal wave matches up with the peak of the other. This is the length of the wave; and in the case of light, this value is quite small, from about 400 nm (violet) to 700 nm (red). Thus, optical interferometry is used in precision measurement and manufacture, such as semiconductor integrated circuit fabrication.

We consider a semiconductor manufacturing and control application of interferometry involving chemical mechanical planarization (CMP) of silicon wafers [39]. CMP has become an important process for ensuring the planarity of the wafer surface. A high degree of flatness eliminates flaws in later deposition steps. More importantly for modern integrated circuit manufacture, CMP is used for selectively removing thin layers of material on wafers that do not etch well in plasmas, such as copper.

Evident in the signal trace (Figure 9.16) at the top are:

- (i) The long-term undulations in reflected intensity due to the combination of beams reflected from the surface and Si/SiO<sub>2</sub> interface;
- (ii) Short-term vibrations around  $f = 0.1$  Hz;
- (iii) At the end of the trace, a change in process conditions causing wild instability of the sensor's measured reflectance.

Our interferometric interest is to isolate these three trends. The wavelength of the long-term oscillation, on the order of 0.0085 Hz, will be used to estimate the silicon oxide removal rate (Figure 9.17). The short-term 0.1 Hz oscillation can be removed with a notch filter in order to enhance the estimation of the removal rate. Also, with the short-term oscillation removed by a notch filter, it becomes possible to design a simple algorithm to compute the phase of the long-term reflectance oscillation and use this

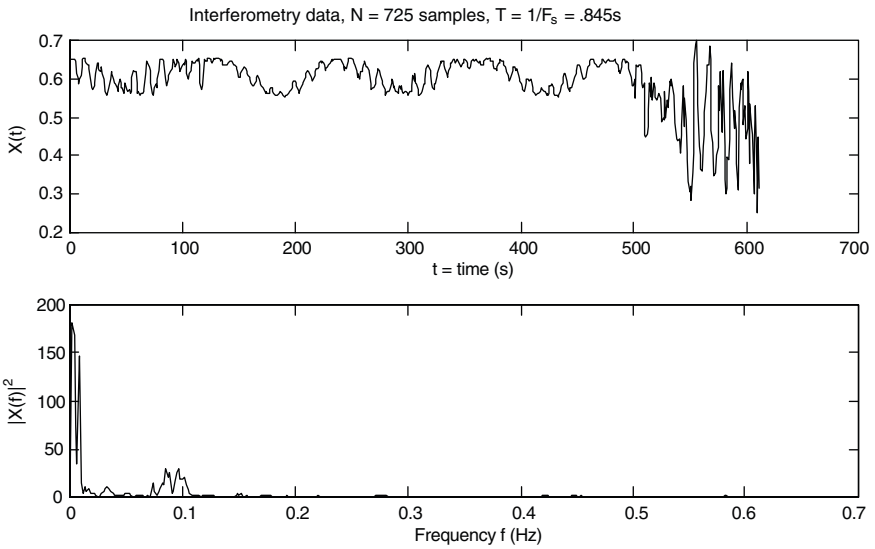


**Fig. 9.16.** Reflectance data from a CMP removal process on a silicon wafer with a surface silicon dioxide film. The upper panel contains the signal trace and the lower panel contains the magnitude spectrum.

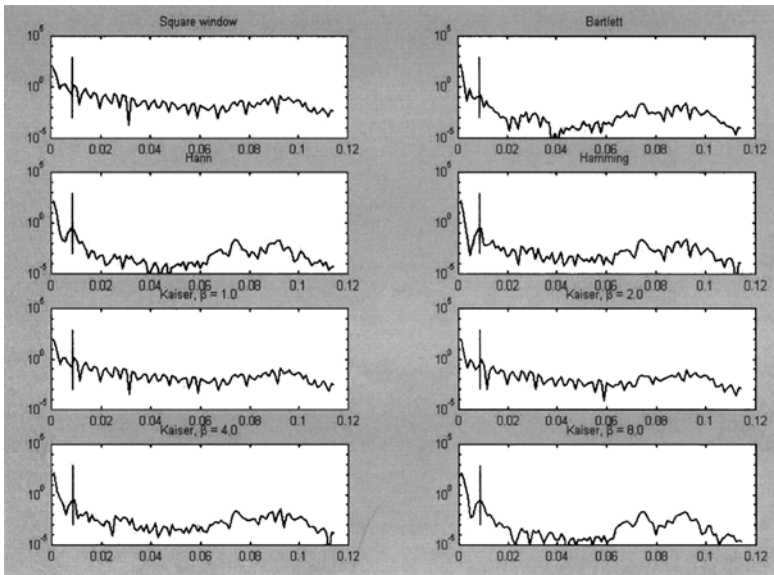


**Fig. 9.17.** Periodograms of several windows applied to the interferometric data from CMP processing of a silicon wafer. Top four periodograms: Square, Bartlett, Hann, and Hamming windows applied to signal before periodogram calculation. The bottom four plots show the efficacy of various Kaiser window parameters. The vertical line marks the frequency of the interference fringes.

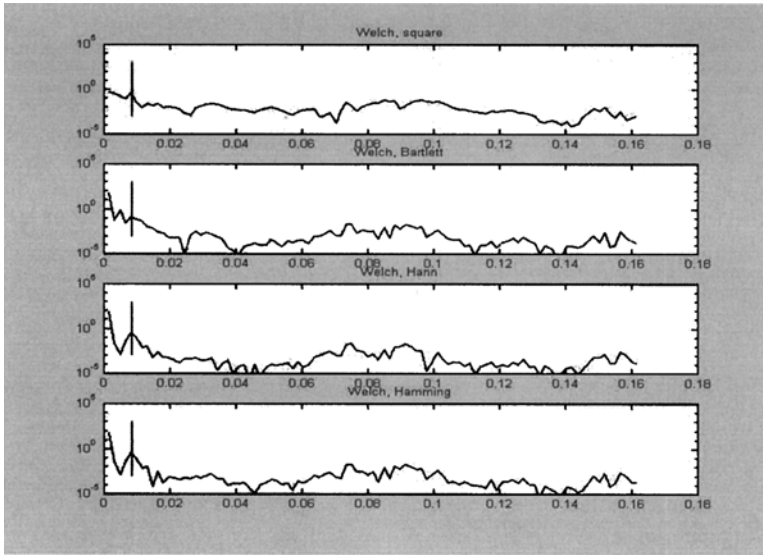


**Fig. 9.18.** Welch's method for periodogram computation.

as a measurement of the amount of top-level film removed. Finally, we are interested in detecting the signal instability at the end of the trace, which is an indication that the oxide has begun to disappear from the wafer, exposing the silicon substrate. This represents polish endpoint.

Let us also investigate one of the spectrogram improvement methods—in this case Welch's method with windows overlapped 50% and a variety of window functions applied before computing the local periodograms. The results are shown in Figure 9.18.

As a practical matter, some goal-directed information needs to be invoked in this example. A peak detector needs to be provided with a limited range in hertz for its search. Once the periodicity of the interferogram fringes is determined from the periodogram algorithm, it is possible to calculate the phase of individual points along the fringe trace. To do this, we would perform a discrete Fourier transform of the proper window size according to the wavelength of the long-term undulations. For the above sampling interval  $T = 0.8451$  s, this would be  $N = 140$  samples. The phase of points along the interference fringe trace could be computed by the complex argument of the first DFT coefficient, for example.

### 9.3 DISCRETE FILTER DESIGN AND IMPLEMENTATION

Discrete filters are suitable for computer implementation, and signal analysis applications depend on them directly. This section reviews some elements of filter theory, the  $z$ -transform, and ideal filters. It also covers the more practical aspects such

as (a) filter approximation and (b) the steps in designing a discrete filter, and it explains basic methods on how to implement discrete filters.

The principal tools for filter design are the discrete Fourier transform (DFT), the discrete-time Fourier transform (DTFT), and the  $z$ -transform. One important design method is to derive a discrete filter from an analog filter. So we shall also use the continuous-domain Fourier transform as well as introduce briefly the Laplace transform. The Fourier transform properties allow us to convert one type of filter into another, considerably simplifying the mechanics of filter construction. For example, we generally design a low-pass filter and then convert it into the required bandpass filter.

### 9.3.1 Ideal Filters

Some applications, such as in the dual-tone multifrequency application above, require fine separation in the frequency domain. Some periodicities we need to pass through for further analysis, such as the DTMF, range from 697 to 1633 Hz. Others, such as high-frequency background noise and low-frequency interference, we prefer to suppress. Offline applications can Fourier transform large time-slices of data and select spectral components according to the frequency resolution of the transform. Online applications, though, must achieve frequency selection as data enters the system, in real time, and then pass the output to interpretation algorithms. Here the filters have to be causal and efficiently implemented. Since no high-resolution Fourier transform of the input data is possible in this situation, it becomes all the more important to design filters that distinguish between nearby frequencies.

**9.3.1.1 Low Pass.** We can eliminate all frequencies above the range of interest to an application by processing input signals through an ideal low-pass filter  $H$ . It is easy to describe such a filter using the discrete-time Fourier transform  $H(\omega)$ :

$$H(\omega) = \begin{cases} 1 & \text{if } |\omega| \leq \omega_c, \\ 0 & \text{if otherwise,} \end{cases} \quad (9.37)$$

where  $\omega_c$  is the *cutoff frequency* of the filter. This filter's perfect cutoff is ideal for separating one frequency from another. The only caveat is that a sufficiently high sampling rate must be chosen so that  $\omega_c$  is close to the frequency of a discrete component.

The inverse DTFT serves as a tool for building discrete filters from such frequency-domain descriptions. The impulse response of the ideal low-pass system (Figure 9.19) is

$$h(n) = \frac{1}{2\pi} \int_{-\pi}^{\pi} H(\omega) e^{j\omega n} d\omega = \frac{1}{2\pi} \int_{-\omega_c}^{\omega_c} e^{j\omega n} d\omega = \frac{\sin(\omega_c n)}{\pi n}. \quad (9.38)$$

Using the inverse DTFT to generate a filter impulse response from description of its ideal frequency-domain representation is elegant and straightforward, but the resulting filters are often—and most particularly in the present case—quite impractical.

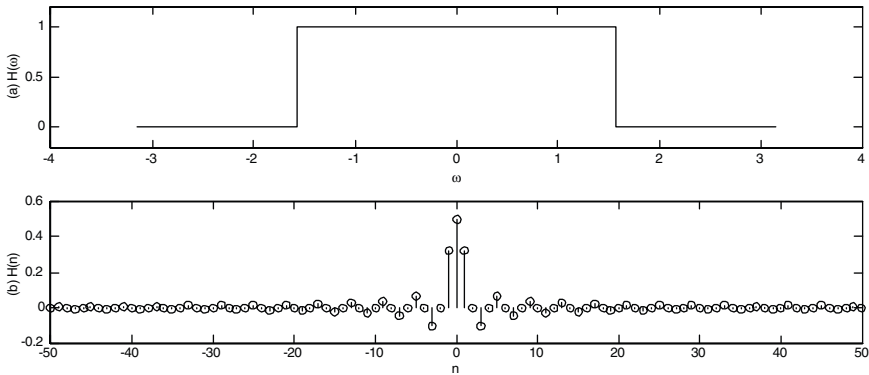


**Fig. 9.19.** Ideal low-pass filter in the frequency-domain (a) and truncation of impulse response in the time-domain (b).

The problems with  $h(n)$  as given by (9.38) are as follows:

- (i) It is an infinite impulse response (IIR) filter.
- (ii) This means that it cannot be implemented by a straightforward convolution in applications.
- (iii) Some IIR filters permit a recursive computation for their implementation, but in this case  $h(n) \neq 0$  for arbitrarily large magnitude  $n < 0$ , so it is in fact unrealizable for applications.
- (iv) The filter is not causal, so its realization requires future signal values and cannot work on real-time data streams.
- (v) The filter is not stable, since its impulse response is not absolutely summable (Chapter 2).

But these problems are not catastrophic. We can truncate  $h(n)$  so that it is supported within some reasonable interval  $[-N, N]$ , say. This is often satisfactory for applications where the raw signals contain high-frequency background noise. The perfect frequency-domain characteristic is lost (Figure 9.19b). We will see how to overcome these problems in a moment.

Next, however, let us look at ideal filters of other types and see how to build them out of low-pass filters.

**9.3.1.2 Other Filters.** Applications require filters with varying frequency-domain characteristics. For example, the DTMF application of Section 9.1 uses a low-pass filter, a simple moving averager, to suppress background noise. In the filter output, this highlights the relatively pure dual tones and improves thresholding results. But an online version of the same application would need filters that select frequency ranges and reject oscillations below and above certain bands. Here we are speaking of a bandpass filter, and we have noted that an array of them in parallel operation can pass filtered signals to the application logic for tone classification.

The mechanics of converting a lowpass filter into one of an alternative frequency-domain behavior are fortunately quite straightforward. We require only a few DTFT properties (Chapter 7).

From a low-pass filter  $h(n) = (H\delta)(n)$ , it is easy to make a high-pass filter  $f(n) = (F\delta)(n)$ . An *all-pass* filter is the discrete impulse  $\delta(n)$  or one of its shifted versions  $\delta(n - n_0)$ . We subtract  $f(n) = \delta(n) - h(n)$  for a high-pass filter  $f(n) = (G\delta)(n)$ .

Two elementary methods exist for building a bandpass filter  $F$ . One way to do this, starting from a low-pass filter  $H$  with cutoff  $\omega_c$ , is to use the frequency shifting property of the DTFT. If we set  $f(n) = e^{j\omega_L n} h(n)$ , then  $F(\omega) = H(\omega - \omega_L)$ .  $F$  is thus a bandpass filter with lower cutoff  $\omega_L$  and upper cutoff  $\omega_H = \omega_L + \omega_c$ . The blemish on this otherwise elegant modification of  $h(n)$  is the fact that  $f(n)$  becomes a complex-valued discrete signal. A second basic technique is to combine a low-pass filter  $H$ , with cutoff  $\omega_c$ , and a high-pass filter  $G$ , with cutoffs  $\omega_L$  and  $\omega_H$ . Typically, we get  $G$  itself by subtracting  $h(n)$  from an all-pass system's impulse response. If our filters satisfy  $\omega_c > \omega_L$ , then the system composition  $F(n) = G(H(n))$  will pass precisely the frequencies that lie in the passband overlap. We know that  $f = F\delta = g * h$ , the convolution of  $g(n)$  and  $h(n)$ . So, if both  $g(n)$  and  $h(n)$  are real-valued, then  $f(n) \in \mathbb{R}$  too. By the convolution theorem for discrete linear, translation-invariant systems, the DTFT of  $f(n)$  is  $F(\omega) = H(\omega)G(\omega)$ . So, if  $H$  and  $G$  are ideal, then  $F$  will be a perfect bandpass filter with lower cutoff  $\omega_L$  and upper cutoff  $\omega_c$ .

We form band-reject or notch filters by subtracting a bandpass filter from an all-pass filter.

### 9.3.2 Design Using Window Functions

A useful discrete FIR filter design method uses the windowing concept from Section 9.2. This is a straightforward way to improve truncated perfect low-pass filters (Section 9.3.1.1). Again, let  $\omega_c$  be the cutoff frequency so that  $h(n)$  is given by

$$h(n) = \left. \frac{1}{2\pi} \int_{-\omega_c}^{\omega_c} e^{j\omega n} d\omega \right]_{-N \leq n \leq N} = \left. \frac{\sin(\omega_c n)}{\pi n} \right]_{-N \leq n \leq N} \tag{9.39}$$

as shown in Figure 9.20(a).

Let  $w(n)$  be a window function, for example the Hann window, of Table 9.2. Set  $g(n) = h(n)w(n)$  as in Figure 9.20c. Using signal multiplication in the time domain is equivalent to convolution in the frequency domain:

$$G(\omega) = \mathcal{F}[h(n)w(n)] = \frac{1}{2\pi} \int_{-\pi}^{\pi} H(\theta)W(\theta - \omega) d\theta. \tag{9.40}$$

Since discrete time Fourier transform of  $w(n)$  has the shape of a weighted averaging function in the frequency domain, convolving it with  $H(\omega)$  effectively smoothes the spectrum of  $h(n)$ . This blends away the Gibbs phenomenon ripples caused by the truncation of the perfect low-pass filter Figure 9.20b. The result is a magnitude spectrum almost completely devoid of the problematic ringing Figure 9.20d.

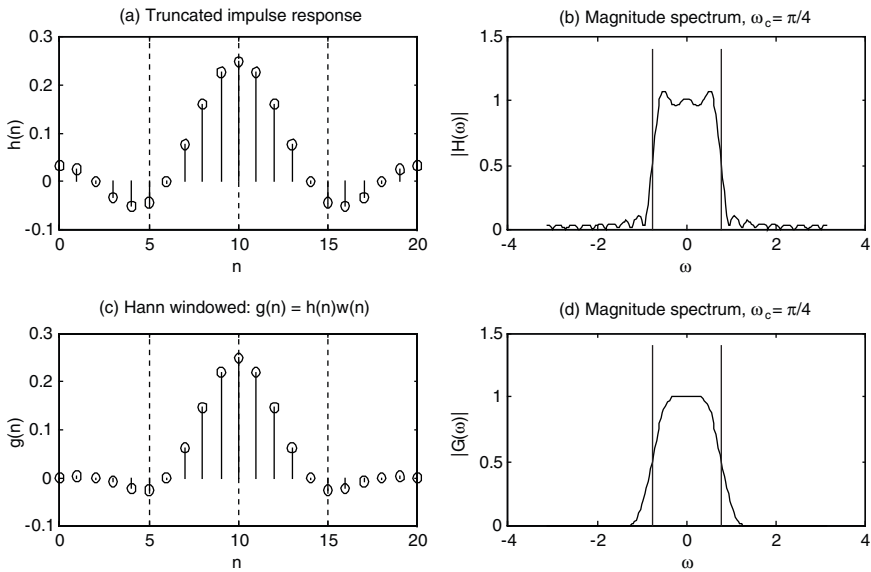


**Fig. 9.20.** FIR filter design using Hann window. Formerly perfect, but now truncated impulse response  $h(n)$  (a). Vertical lines in the magnitude spectrum plot (b) mark the cutoff frequency. Panel (c) shows  $g(n) = h(n)w(n)$ , where  $w(n)$  is a Hann window function having the same support as  $h(n)$ . The final panel (d) shows  $|G(\omega)|$  with the Gibbs phenomenon ringing virtually eliminated.

### 9.3.3 Approximation

This section covers the approximation of ideal filters, the initial step among filter design tasks.

**9.3.3.1 Design Criteria.** Ideal filters are impossible to implement on a digital computer, but a filter that comes close to ideal performance is usually adequate for a signal processing and analysis application. Let us look at the magnitude spectrum of a typical discrete filter—in this case a third-order low-pass elliptic filter, which we will study in Section 9.5. A plot of the magnitude response illustrates design criteria (Figure 9.21).

Referring to Figure 9.21, we assume that the filter  $H$  has been normalized so that it has at most unit gain.

- The *passband* is the region in which the filter in which the magnitude response is near unity. For a low-pass filter, this is an interval around the origin:  $\omega \in [0, \omega_p]$ .
- The *stopband* is the region in which  $H(\omega)$  is near zero:  $\omega \in (\omega_s, \pi]$  for the low-pass filter in the figure.
- Between the passband and the stopband lies the *transition band*:  $\omega \in [\omega_p, \omega_s]$ .

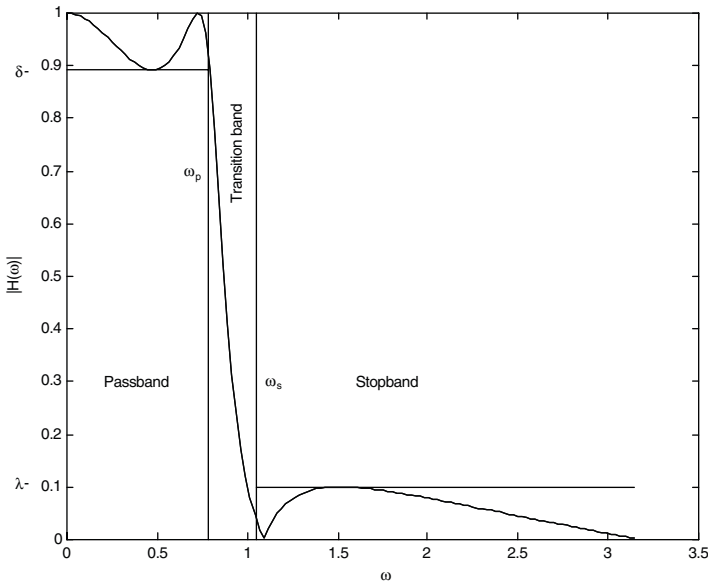


**Fig. 9.21.** Design characteristics of a low-pass filter (third-order low-pass elliptic), showing the positive frequencies  $0 \leq \omega \leq \pi$ .

- The *cutoff frequency*  $\omega_c$  is a transition band value that is somewhat arbitrary, depending on the particular filter, but represents the frequency at which filter suppression begins. For our low-pass example,  $\omega_p \leq \omega_c \leq \omega_s$ .
- *Passband ripple* measures the variation of  $|H(\omega)|$  within the passband. We typically specify a maximum value  $\delta > 0$ , such that  $|H(\omega) - 1| \leq \delta$  for  $\omega \in [0, \omega_p)$ . An equivalent, and sometimes convenient, mode of specification is to express tolerances in decibels (dB). Thus,  $-\Delta \leq 20\log_{10}|H(\omega)| \leq \Delta$ , for some  $\Delta > 0$ .
- *Stopband ripple* measures the variation of  $|H(\omega)|$  within the stopband: There is a  $\lambda > 0$ , such that  $|H(\omega)| \leq \lambda$  for  $\omega \in (\omega_s, \pi]$ . Equivalently, in decibels:  $20\log_{10}|H(\omega)| \leq \Lambda$ , for some  $\Lambda < 0$ .
- *Sharpness* indicates how narrow the transition band is. Applications that require fine frequency discrimination use filters with correspondingly sharp transition bands. One measure of sharpness is the average slope of  $|H(\omega)|$  in the transition band. Another way to specify sharpness is to stipulate a derivative at a representative transition band value, such as  $\omega_c$  or  $(\omega_p + \omega_s)/2$ .

The design criteria for other filters are similar. Thus, in a high-pass filter, the passband is at the upper end of the spectrum:  $\omega_p \leq \omega \leq \pi$ . In a bandpass filter, there are two stop bands (in the neighborhoods of 0 and  $\pi$ ), and there is a single passband. Likewise, the notch filter has two outer passbands and a single inner stopband.

**9.3.3.2 Design Steps.** In signal analysis, our design steps for discrete filters are as follows:

- (i) Determine the type (low-pass, high-pass, bandpass, or band-reject) of filter  $G$  appropriate to the application.
- (ii) Select a low-pass filter that approximates an ideal filter's frequency-domain characteristics.
- (iii) Design a suitable low-pass filter  $h(n) = (H\delta)(n)$ .
- (iv) Convert the low-pass filter  $H$  to the application filter  $g(n) = (G\delta)(n)$  using Fourier transform properties, ensuring that the approximation constraints on  $G$  are not compromised by the conversion.
- (v) For an online application, maintain causality.
- (vi) For IIR filters, maintain stability.
- (vii) Achieve an efficient computer implementation.

It is sometimes feasible to design  $G$  directly, skipping the low-pass starter filter  $H$  and conversion. Once the filter type and approximation questions have been resolved in accord with application constraints—points (i) and (ii), above—the next step is to design a low-pass filter. The  $z$ -transform is the basic tool for working out these remaining design steps.

### 9.3.4 Z-Transform Design Techniques

We recall from the previous chapter that the  $z$ -transform  $X(z)$  of a discrete signal  $x(n)$  is given by

$$X(z) = \sum_{n=-\infty}^{\infty} x(n)z^{-n}, \quad (9.41)$$

where  $z \in \mathbb{C}$ . We recognize that if  $z = e^{j\omega}$ , then (9.41) is the discrete-time Fourier transform of  $x(n)$ . Evaluating the  $z$ -transform on the complex unit circle,  $|z| = 1$ , produces the DTFT. To avoid confusion, we may occasionally use the function notations  $(Zh)(z)$  or  $H_z(z)$  for the  $z$ -transform and continue to use  $H(\omega)$  for the DTFT. The  $z$ -transform came to signal processing from control theory in the early 1960s [40]. It is a staple topic of discrete signal processing books (for example, Refs. 7–11), and there are specialized texts covering the  $z$ -transform [41, 42].

The sum (9.41) converges absolutely on annular regions of the extended complex plane  $\mathbb{C}^+ = \mathbb{C} \cup \{\infty\}$ , called the *region of convergence*,  $\text{ROC}_X$ . The  $z$ -transform expression  $X(z)$  for a signal is not unique; one must also specify  $\text{ROC}_X$ . Both the causal signal  $x(n) = a^n u(n)$  and the anti-causal signal  $y(n) = -a^n u(-n - 1)$ , for example, have the same  $z$ -transforms:  $X(z) = Y(z) = z/(z - a)$ . The difference is that  $\text{ROC}_X = \{z \in \mathbb{C}: |a| < |z|\}$  while  $\text{ROC}_Y = \{z \in \mathbb{C}: |z| < |a|\}$ .

A theoretical subtlety on the region of convergence concerns square-summable signals. We know that discrete signals  $h \in l^2$  have DTFTs, but it is possible

that  $h \notin l^1$ . In fact, the discrete Hilbert space  $l^2$  is isomorphic to the continuous Hilbert space  $L^2[-\pi, \pi]$ , understanding that  $x, y \in L^2[-\pi, \pi]$  are considered identical if they are equal except on a set of Lebesgue measure zero (Chapter 3). Thus, such signals  $h(n)$  possess a discrete-time Fourier transform, even though  $\text{ROC}_H$  does not include the unit circle  $|z| = 1$ .

**9.3.4.1 System Function, Stability, Causality.** If  $H$  is a discrete linear, translation-invariant system, such as we might use for filtering a signal, then the  $z$ -transform  $H(z)$  of its impulse response  $h = H\delta$  is called the *system or transfer function* of  $H$ . The convolution theorem for the  $z$ -transform tells us that if  $y = Hx = h*x$ , then  $Y(z) = H(z)X(z)$ , where  $X(z)$  is the  $z$ -transform of input  $x(n)$ ,  $Y(z)$  is the  $z$ -transform of output  $y(n)$ , and  $H(z)$  is the system function.

Recall that a discrete LTI system  $H$  is *stable* if and only if the impulse response  $h = H\delta$  is absolutely summable:  $h \in l^1$ . But if  $H$  is stable, then  $h(n)$  has a DTFT  $H(\omega)$ . Since  $H(\omega) = H_Z(e^{j\omega})$ ,  $\text{ROC}_H$  evidently contains the unit circle,  $|z| = 1$ . The converse is also true: If  $H_Z(z)$  converges absolutely on a region that contains the unit circle, then  $H$  is stable (exercise).

A signal  $x(n)$  is *right-sided* means that  $x(n) = 0$  for  $n < N \in \mathbb{Z}$ . In this case, its  $z$ -transform  $X(z)$  (9.41) contains at most a finite number of positive powers of  $z$ , and  $\text{ROC}_X$  is the exterior of a circle. If  $N \geq 0$ , then  $\infty \in \text{ROC}_X$ , and  $x(n)$  is *causal*; that is,  $x(n) = 0$  for  $n < 0$ . Similarly, if  $x(n) = 0$  for  $n > N \in \mathbb{Z}$ , then we say that  $x(n)$  is a *left-sided* sequence. The ROC of a left-sided signal is the interior of a circle, omitting perhaps the origin  $z = 0$ .

An LTI system  $H$  is *causal* if its impulse response  $h = H\delta$  is causal:  $h(n) = 0$  for  $n \leq 0$ . Thus,  $h(n)$  is right-sided, and  $\text{ROC}_X$  is the exterior of a circle. If  $H$  is causal and  $y = Hx$ , then

$$y(n) = \sum_{k=0}^{\infty} h(k)x(n-k); \tag{9.42}$$

$y(n)$  can be computed without using future values of the input signal.

**9.3.4.2 Systems Governed by Difference Equations.** A wide variety of discrete systems are defined by a difference equation:

$$y(n) + \sum_{k=1}^N a_k y(n-k) = \sum_{m=0}^M b_m x(n-m). \tag{9.43}$$

Note that (9.43) allows us to compute a new output  $y(n)$  if we know the previous  $N$  output values, the previous  $M$  input values, and the current input value. Thus, for real-time applications, signal filtering prior to frequency domain analysis is often implemented using filters governed by a difference equation. Offline applications, of course, do not worry about this detail, and they commonly employ noncausal filters.

If an LTI system  $H$  is governed by a difference equation, then its transfer function is rational. That is,  $H(z) = P(z^{-1})/Q(z^{-1})$ , where  $P$  and  $Q$  are complex polynomials. We can see this by taking the  $z$ -transform of both sides of (9.43):

$$Y(z) + \sum_{k=1}^N a_k Y(z) z^{-k} = \sum_{m=0}^M b_m X(z) z^{-m}. \quad (9.44)$$

Consequently,

$$Y(z) \left[ 1 + \sum_{k=1}^N a_k z^{-k} \right] = X(z) \sum_{m=0}^M b_m z^{-m}. \quad (9.45)$$

This becomes a rational function in  $z^{-1}$  by computing,

$$\frac{Y(z)}{X(z)} = \frac{\sum_{m=0}^M b_m z^{-m}}{\left[ 1 + \sum_{k=1}^N a_k z^{-k} \right]} = H(z). \quad (9.46)$$

Although the system function is given by the  $z$ -transform convolution theorem as a rational function in the complex variable  $z$ , it is often easier to work in terms of the variable  $z^{-1}$ , which is the  $z$ -transform of a unit delay.

**9.3.4.3 Poles and Zeros Analysis.** Let us continue to consider an LTI system  $H$ , defined by a difference equation. The rational system function  $H(z) = Y(z)/X(z) = P(z^{-1})/Q(z^{-1})$  may also be characterized by its poles and zeros. The *poles* are the zeros of  $Q(z^{-1})$ , and—assuming that common factors are removed from  $H(z)$ —the *zeros* of  $P(z^{-1})$  are those of  $H(z)$  too.

To find the poles and zeros, we must factor  $P(z^{-1})$  and  $Q(z^{-1})$  into products of linear terms. The fundamental theorem of algebra guarantees that every complex polynomial factors into linear terms, unique except for their order. Many readers know the theorem, but if we recount some complex variable theory from Chapter 1, an argument of Liouville<sup>10</sup> proves it fairly easily.

We may assume that some polynomial  $P(z)$  has been reduced to its lowest terms and that it still has degree exceeding unity. If  $P(c) = 0$  for some  $c \in \mathbb{C}$ , then  $(z - c)$  evenly divides  $P(z)$ , so we must have  $P(z) \neq 0$  for all  $z \in \mathbb{C}$ . This means that the reciprocal function  $R(z) = 1/P(z)$  is defined for all  $z \in \mathbb{C}$ . But then  $R(z)$  is everywhere differentiable, since its denominator is differentiable and has no zeros. Further as  $|z|$  gets large,  $|R(z)|$  gets small. So  $R(z)$  is bounded and everywhere differentiable. But, by Liouville's theorem, a bounded, everywhere differentiable (analytic) function is constant (exercise). This means  $R(z)$  is a constant, and we have a

<sup>10</sup>French mathematician Joseph Liouville (1809–1882) authored some 400 papers on number theory, integral equations, and differential geometry.

contradiction. It must be the case that we can always extract another root from a complex polynomial of degree two or more.

Now consider the case of a discrete causal LTI system  $H$  whose transfer function  $H(z)$  is a rational function. Since  $H$  is causal,  $h(n)$  is right-sided:  $h(n) = 0$  for  $n < 0$ .  $\text{ROC}_H$  is the exterior of a circle. Since  $H(z)$  is rational, its denominator is a complex polynomial  $Q(z^{-1})$ . The only values  $z \in \mathbb{C}$  for which  $H(z)$  does not exist are the zeros of  $Q(z^{-1})$ , which are the poles of  $H(z)$ . The number of poles is finite; it is at most the degree of  $Q(z^{-1})$ . Hence, there is a pole of largest modulus  $|p|$ , where  $Q(p) = 0$ . Finally, we conclude that  $\text{ROC}_H$  consists of the exterior of the circle defined by  $|z| = |p|$ . If all the poles of  $H(z)$  are contained within the complex unit circle  $|z| = 1$ , then  $\text{ROC}_H$  contains the unit circle, and  $H$  is a stable system.

How a signal processing application implements a discrete filter on a digital computer depends on the support of its *impulse response*: *finite* (FIR) or *infinite* (IIR).

A simple convolution calculation suffices for an FIR filter. If  $y = Hx$ , and  $h = H\delta$ , then the filtered output  $y(n)$  can be calculated from the input  $x(n)$  via a convolution operation:

$$y(n) = \sum_{k=M}^N h(k)x(n-k). \quad (9.47)$$

Finite impulse response filters are particularly easy to implement. The weighting function  $h(k)$  is the impulse response of the linear, translation invariant discrete filter. The application must store at least  $N - M + 1$  values for this calculation.

The system function for an FIR filter is given by

$$\frac{Y(z)}{X(z)} = \sum_{k=M}^N h_k z^{-k} = H(z), \quad (9.48)$$

where we have written  $h_k = h(k)$ . Since  $H(z)$  has no denominator polynomial, it is an all-zero filter. Thus, another way to characterize FIR and IIR filters is as follows:

- The system function for an FIR filter is an all-zero rational function of  $z^{-1}$ .
- The system function for an IIR filter has at least one pole.

FIR filters tolerate transient inputs. A transient in past  $x(n)$  values eventually falls outside the window  $[M, N]$  over which the sum is computed in (9.47), so an FIR filter's output is never permanently affected by input spikes.

FIR filters behave well. They are clearly stable; that is, a bounded output signal results from filtering a bounded input signal. If  $x(n)$  represents time sampled data with a transient, then eventually the effect of the transient on the output  $y = Hx$  will disappear.

This means that the delay of a sinusoid at the output is proportional to its frequency. This can be important for processing and analysis applications where it is important that tones not be scrambled by the filter. A preliminary filter for a speech recognition system, for example, should not turn a simple spoken word into a grunt followed by a squeak. Later we shall see that some FIR filters have linear phase.

Examples of FIR filters that are implemented as in (9.47) include moving average filters and weighted averaging filters. We explored moving average filters for noise reduction in the dual tone multifrequency detection application. There also we considered windowing the signal in order to obtain a time localized snapshot of its spectral characteristics.

The convolution calculation for an IIR filter is impossible to directly implement. However, a large, powerful, efficient, and therefore important class of IIR filters admits recursive implementation. Recursive filters save prior output values and combine them with current and past input values to produce a current output value. That is, these filters obey a difference equation (Chapters 2 and 8) of the form

$$y(n) + \sum_{k=1}^N a_k y(n-k) = \sum_{m=0}^M b_m x(n-m). \tag{9.49}$$

**9.3.4.4 Implementation.** Recursive implementation can be very efficient. In fact, certain IIR filters, defined by a difference equation, require fewer computations than equally powerful FIR filters. Moreover, these filters have almost linear phase.

To see schematically how we might implement a filter defined by a difference equation on a digital computer, let us consider the system defined by (9.49). We can see that if the blocks symbolized by  $z^{-1}$  store a value for a unit time, then the equation is implemented by the *Direct Form I* architecture [8] shown in Figure 9.22, where

$$y(n) = \sum_{m=0}^M b_m x(n-m) - \sum_{k=1}^N a_k y(n-k) = v(n) - \sum_{k=1}^N a_k y(n-k). \tag{9.50}$$

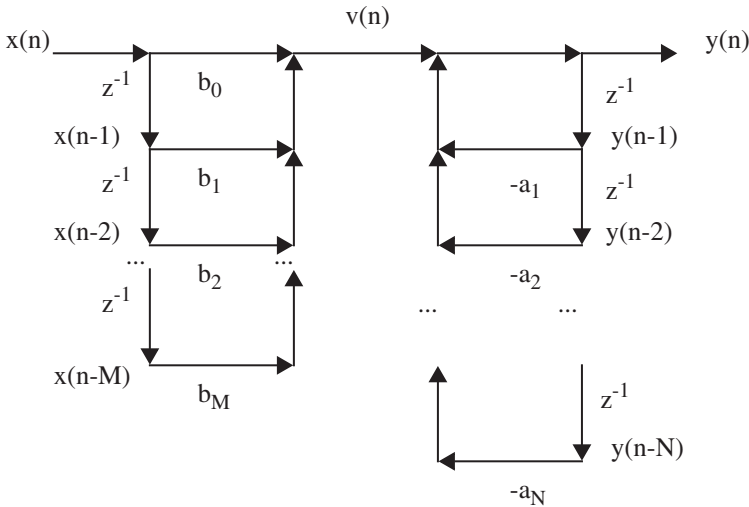


**Fig. 9.22.** Direct Form I implementation of a recursive system, governed by a difference equation.

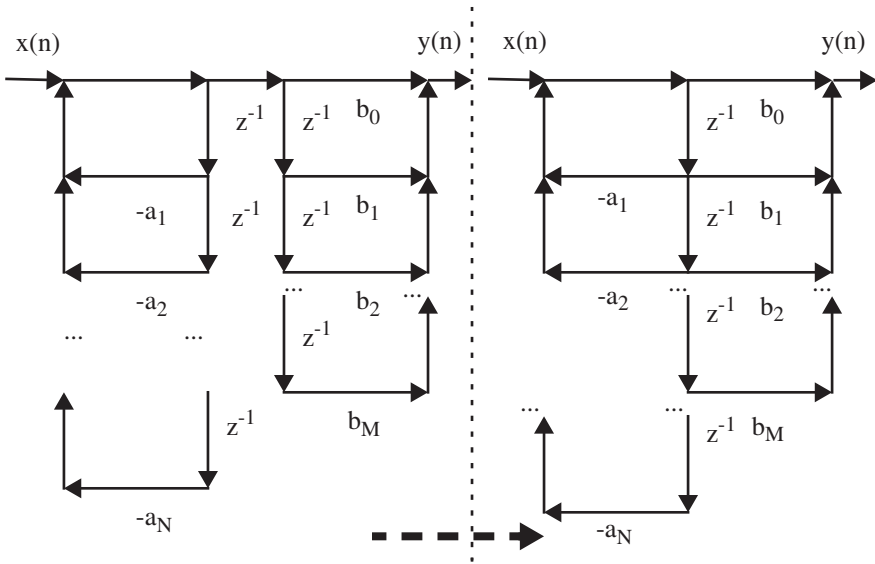


**Fig. 9.23.** The Direct Form II implementation of a recursive system is formed by (i) reversing the order of composition of the subsystems in the Direct Form I arrangement (as on the left) and (ii) then merging the duplicated delay operations (right).

The Direct Form I structure is seldom implemented, because a much more efficient scheme is possible. To see this, note that the lattice structures of Figure 9.22 cascade two LTI systems. One system produces  $v(n)$  from input  $x(n)$ , and the other accepts  $v(n)$  as an input and generates  $y(n)$ . We know from Chapter 2 that the composition of systems is characterized by the convolution of their respective impulse responses. Since convolution is commutative, so is composition. Thus, we can swap the order of the cascaded systems in Figure 9.22. This is shown on the left-hand side of Figure 9.23.

Reversing the order of these two subsystems leaves a network with two identical sets of sequential delays in the middle (Figure 9.23). The insight of the *Direct Form II* architecture is that the nodes across from one another contain the same mathematical result; the two halves can be joined, cutting the number of delay operations and economizing on memory locations. The Direct Form II, on the right-hand side of Figure 9.23, is a commonplace in computer implementations of signal processing systems.

When the difference equation coefficients (9.49) are all real, another efficient filter structure is possible. In this case, the poles and zeros of the system function  $H(z)$  that have nonzero imaginary parts must consist of conjugate pairs. Then  $H(z)$  is the product of terms of the form

$$G_p(z) = b_0 \frac{1 + b_1 p z^{-1}}{1 + a_1 p z^{-1}} \tag{9.51a}$$

and

$$K_q(z) = \frac{1 + b_1 q z^{-1} + b_2 q^2 z^{-2}}{1 + a_1 q z^{-1} + a_2 q^2 z^{-2}}, \quad (9.51b)$$

where all of the coefficients are real. Some coefficients may be zero to account for unequal numbers of poles and zeros. Terms of the form (9.51a) are called *first-order sections*. Terms of the form (9.51b) are called *second-order sections*. We may implement each first- or second-order section as a Direct Form I or Direct Form II network. When we serialize all of them to implement  $H(z)$ , we have the *cascade* architecture for a system defined by a difference equation. Strategies exist for pairing poles and zeros in the cascade architecture so as to minimize round-off error in finite precision arithmetic [11].

### 9.3.5 Low-Pass Filter Design

This section covers several methods for designing discrete low-pass filters. The mechanics of converting an approximate low-pass filter to one of the other types (high-pass, bandpass, or band-reject) are the same as for ideal filters. This section also covers two particularly important procedures for converting continuous domain to discrete filters: the impulse invariance technique and the bilinear transformation.

We have already constructed and applied several ad hoc discrete filters. One obvious method is to use a frequency-domain mask:

- (i) Fourier transform the signal. Thus, from  $x(n)$ , we find  $X(k)$  according to the DFT analysis equation (9.1).
- (ii) Mark out all but the frequencies of interest to the application. In other words, the application determines a binary mask  $H(k) \in \{0, 1\}$  and we set  $Y(k) = H(k)X(k)$ . Note that this is equivalent to convolving  $y(n) = (h*x)(n)$ , where  $h(n)$  is the inverse DFT of  $H(k)$ .
- (iii) Analyze the result  $Y(k)$  by thresholding, segmentation, and classification procedures in the spirit of ordinary time-domain analysis (Chapter 4); or, alternatively, inverse transform  $Y(k)$  to continue time-domain analysis on  $y(n)$ .
- (iv) Finally, interpret the signal.

There are advantages and disadvantages to the obvious approach. It offers perfect control of the filtering, assuming that the sampling rate is high enough. Also, it allows the application designer to work in both domains: time and frequency. This could be pertinent. But one drawback is that it is only feasible for offline applications. Where decisions about the signal must be made while the data arrive, this strategy does not work very well. Even for offline applications, the method could be expensive; the discrete Fourier transform requires a lot of arithmetical operations, and if the data do not naturally come in fast transform-sized chunks, this presents another problem of data windowing and interpretation across the window boundaries.

Another method is to construct low-pass filters intuitively, using weighted averages or recursive, sample-and-hold algorithms. Although it chagrins a signal theorist, probably most of the filters used in analysis applications are of this type. Such adhoc filters are useful for salt-and-pepper noise removal, blending away transients, and preparing signals for derivative or edge finding operations. One can investigate the spectral characteristics of such filters using the discrete Fourier transform, such as we carried out in Section 9.1.

**9.3.5.1 Impulse Invariance.** It is possible to begin with an analog low-pass filter and convert it to a discrete filter. Often, the useful characteristics for an application are known from their analog frequency-domain description. An example is the Gaussian; it is analytically attractive, it decays quickly, and filtering with wider kernels does not create additional time domain structure, as shown by scale-space theory (Chapter 4).

The *impulse invariance* technique is as follows:

- (i) From the application, a specification of the filter's continuous-domain Fourier transform  $H_a(\Omega)$  is generated.
- (ii) The inverse Fourier transform is applied to find  $h_a(t)$ , the impulse response of the analog filter.
- (iii) The analog impulse response is sampled  $h(n) = h_a(nT)$ , where  $T > 0$  is the sampling interval.

Now, impulse invariance is simple and commonly invoked in signal analysis applications. One question, however, is whether the discrete sampling in step (iii) above undoes the frequency-domain behavior that motivated the analog filter's selection in the first place.

The sampling theorem (Chapter 7) answers this question. We can write  $H(\omega)$ , the discrete-time Fourier transform of  $h(n)$ , in terms of  $H_a(\Omega)$ , the analog Fourier transform of  $h_a(t)$ :

$$H(\omega) = \frac{1}{T} \sum_{k=-\infty}^{\infty} H_a\left(\frac{j}{T}[\omega + 2k\pi]\right). \quad (9.52)$$

We recognize the form of (9.52). The DTFT of  $h(n)$  consists of a superposition of scaled (amplified by  $T^{-1}$ ) versions of  $H_a$ , shifted by  $2\pi/T$  and dilated by  $T$ .

Note also that if  $|H_a(\Omega)| \approx 1$  for  $|\Omega| \approx 0$  in (9.52), then  $H(\omega)$  will provide a gain of approximately  $1/T$ . With the sampling rate close to 1 Hz, the effect will be negligible. However, if  $T$  is small—that is, the sampling rate is high—then the discrete filter will have a very high gain. For this reason, it is customary to set  $h(n) = Th_a(nT)$  [7, 40].

**9.3.5.2 Sampling Rational Analog Filters.** An important discrete filter design method is to sample an analog filter whose Fourier transform is a rational

function. It turns out that the impulse invariance method applied to such an analog filter produces a discrete filter governed by a difference equation. Such analog filters are well-known from analog filter theory, and we will develop several of them later. This becomes a very powerful method for designing discrete filters with excellent design characteristics and efficient computer implementations.

Suppose that an analog low-pass filter  $H_a$  has impulse response  $h_a(t)$ . Let the radial Fourier transform of  $h_a(t)$  be a quotient of polynomials in  $\Omega$ :

$$H_a(\Omega) = \int_{-\infty}^{\infty} h_a(t) e^{-j\Omega t} dt = \frac{P(\Omega)}{Q(\Omega)}. \quad (9.53)$$

We can find  $h_a(t)$  using a partial fractions expansion of  $H_a(\Omega)$ . This can be a messy manual computation, but it works just like partial fraction expansions for rational  $z$ -transforms. These are the steps to expand  $H_a(\Omega)$  in partial fractions [10]:

- (i) Normalize the fraction so that the denominator  $Q(\Omega)$  has a leading coefficient of unity.
- (ii) Since  $H_a$  is low-pass, as  $|\Omega| \rightarrow \infty$ , it must also be the case that  $|H_a(\Omega)| \rightarrow 0$ ; the degree of  $Q(\Omega)$  must exceed the degree of  $P(\Omega)$ :

$$H_a(\Omega) = \frac{P(\Omega)}{Q(\Omega)} = \frac{p_{M-1}\Omega^{M-1} + p_{M-2}\Omega^{M-2} + \dots + p_0}{\Omega^M + q_{M-1}\Omega^{M-1} + \dots + q_0}. \quad (9.54)$$

- (iii) Factor the denominator  $Q(\Omega)$  into its roots,  $\omega_m$ ,  $1 \leq m \leq M$ ,

$$Q(\Omega) = \prod_{m=1}^M (\Omega - \Omega_m), \quad (9.55)$$

where we assume for now that the  $\Omega_m$  are distinct. Possibly  $Q(\Omega)$  has a form that allows us to easily derive its roots. In other cases, a computational method of root finding, such as the Traub–Jenkins algorithm may be employed [43].

- (iv) Then  $H_a(\Omega)$  has a partial fractions expansion of the form:

$$H_a(\Omega) = \sum_{m=1}^M \frac{c_m}{\Omega - \Omega_m}, \quad (9.56)$$

where  $c_m$ ,  $1 \leq m \leq M$ , are constants.

- (v) To find  $c_m$ ,  $1 \leq m \leq M$ , note that—having assumed that the denominator's roots  $\Omega_m$  are distinct—we see

$$c_m = [(\Omega - \Omega_m)H_a(\Omega)] \Big|_{\Omega = \Omega_m}. \quad (9.57)$$

The partial fraction expansion enables us to write out the impulse response  $h_a(t)$  of the analog low-pass filter  $H_a$ . Indeed, the inverse radial Fourier transform of  $\frac{c_m}{\Omega - \Omega_m}$  is  $jc_m e^{j\Omega_m t} u(t)$ , where  $u(t)$  is the unit step signal. This transformation is valid so long as the imaginary part of  $\Omega_m$  is positive:  $\text{Imag}(\Omega_m) > 0$ . By Fourier transform linearity, we have

$$h_a(t) = ju(t) \sum_{m=1}^M c_m e^{j\Omega_m t}. \quad (9.58)$$

Now we can discretize the filter by the impulse invariance technique, for instance. Let  $T > 0$  be the sampling interval. Then,

$$h(n) = h_a(nT) = ju(n) \sum_{m=1}^M c_m e^{j\Omega_m nT}. \quad (9.59)$$

Taking the  $z$ -transform of (9.59) gives

$$H(z) = j \sum_{m=1}^M c_m \mathcal{Z}[u(n)e^{j\Omega_m nT}](z) = \sum_{m=1}^M \frac{jc_m}{1 - e^{jT\Omega_m} z^{-1}}. \quad (9.60)$$

The important points about this derivation are as follows:

- Note that (9.60) is already in the form of a partial fractions expansion.
- It has in fact the same partial fractions expansion coefficients as given by (9.56) except for the factor of  $j \in \mathbb{C}$ .
- The poles of  $H(z)$  are at  $\exp(jT\Omega_m)$  for  $m = 1, 2, \dots, M$ .
- The pole at  $\exp(jT\Omega_m)$  will be inside the unit circle if and only if  $\text{Real}(jT\Omega_m) < 0$  and thus if and only if  $\text{Imag}(\Omega_m) > 0$ .
- If we consider  $H(z)$  to be the  $z$ -transform of a causal filter, then  $\text{Imag}(\Omega_m) > 0$  for all  $m = 1, 2, \dots, M$  implies that the region of convergence will be  $\{z \in \mathbb{C}: |z| > a\}$ , for some  $1 > a > 0$ , and the discrete filter  $H$  will therefore be *stable*.
- All of the partial fractions (9.60) are of the form  $\frac{C}{1 - Az^{-1}} = \frac{Cz}{z - A}$ , which is the  $z$ -transform of the LTI system governed by the difference equation  $y(n) = Ay(n-1) + Cx(n)$ .
- Finally, if the sampling rate  $1/T$  differs substantially from unity, then we choose

$$H(z) = \sum_{m=1}^M T \frac{jc_m}{1 - e^{jT\Omega_m} z^{-1}} \quad (9.61)$$

in accord with (9.52) and the remarks thereafter.

Now let us turn to the special case of (9.55) where the denominator  $Q(\Omega)$  has multiple roots. Suppose the root  $\Omega_1$  has multiplicity  $R$  and the remaining  $\Omega_m$ ,  $2 \leq m \leq M$ , are distinct. Then  $H_a(\Omega)$  has a partial fractions expansion of the form

$$H_a(\Omega) = \sum_{r=1}^R \frac{c_{1,r}}{(\Omega - \Omega_1)^r} + \sum_{m=2}^M \frac{c_m}{\Omega - \Omega_m}. \quad (9.62)$$

where  $c_{1,r}$ ,  $1 \leq r \leq R$ , and  $c_m$ ,  $2 \leq m \leq M$ , are constants. The formula for calculating the  $c_{1,r}$  is as follows:

$$c_{1,r} = \frac{\left[ \frac{d^{R-r}}{d\Omega^{R-r}} (\Omega - \Omega_1)^R H_a(\Omega) \right] \Big|_{\Omega = \Omega_1}}{(R-r)!}. \quad (9.63)$$

If there are several multiple roots, then we follow the above procedure, inserting supplemental terms in the partial fractions expansion (9.62) and computing the coefficients with repeated derivatives (9.63).

Notice again that if the analog  $H_a(\Omega)$  has at least one pole, then so will the  $z$ -transform (9.61), and the discrete filter will be IIR.

**9.3.5.3 Laplace Transform Techniques.** Analog filters and discrete filter designs from them are usually approached using the Laplace transform [6–11]. Readers are probably familiar with this tool from continuous-domain systems theory. The Laplace transform plays the same role in analog systems theory that the  $z$ -transform plays in discrete system theory. Let us briefly review how the transform is used with analog filters whose Fourier transform is a rational function. Specialized texts include Refs. 44 and 45.

The Laplace transform  $X_L(s)$  of the analog signal  $x(t)$  is defined by

$$X_L(s) = \int_{-\infty}^{\infty} x(t) e^{-st} dt, \quad (9.64)$$

where  $s \in \mathbb{C}$ . If  $H$  is an LTI system, then the Laplace transform  $H_L(s)$  of its impulse response,  $h = H\delta$ , is also called the *system* or *transfer function* of  $H$ .

Note that if  $x(t)$  has a Fourier transform  $X(\Omega)$ , then  $X_L(j\Omega) = X(\Omega)$ . The Fourier transform is the Laplace transform evaluated on the imaginary axis of the complex plane. If  $s = \sigma + j\omega$ , where  $\sigma \in \mathbb{R}$ , then  $X_L(s)$  is the Fourier transform of  $x(t)e^{-\sigma t}$ . Transform convergence depends on the relation of  $x(t)$  to the exponential factor  $\exp(-\sigma t)$ , and it does not depend on the imaginary part of  $s = \sigma + j\omega$ . Hence, the Laplace transform converges on vertical strips in the complex plane.

A couple of basic examples show that the Laplace transform must be associated with a *region of convergence* (ROC). If  $x(t) = e^{-At}u(t)$ , then  $X_L(s) = 1/(s + a)$  and the  $\text{ROC}_X = \{s \in \mathbb{C}: \text{Real}(s) > -a\}$ . If  $y(t) = -e^{-At}u(-t)$ , then  $Y_L(s) = 1/(s + a)$  and the

$ROC_Y = \{s \in \mathbb{C} : \text{Real}(s) < -a\}$ . Recall that an analog LTI system  $H$  is stable if and only if the impulse response  $h = H\delta$  is absolutely integrable:  $h \in L^1$ . But this means  $h(t)$  has a Fourier transform  $H(\Omega)$ . Since  $H(\Omega) = H_L(j\Omega)$ ,  $ROC_H$  must contain the imaginary axis.

Now suppose  $x(t)$  is *right-sided*:  $x(t) = 0$  for  $t < a \in \mathbb{R}$ . If  $ROC_X$  contains the vertical line  $\text{Real}(s) = b \in \mathbb{R}$ , then  $ROC_X$  contains  $\{s \in \mathbb{C} : \text{Real}(s) \geq \text{Real}(b)\}$ . This is fairly easy to see, because, for such  $s \in \mathbb{C}$ ,  $\exp(-\text{Real}(s)t) \leq \exp(-\text{Real}(b)t)$  for  $t > 0$  and the transform integral (9.64) will still exist. The ROC of a right-sided signal is a right half-plane. Similarly, if  $x(t)$  is *left-sided* ( $x(t) = 0$  for  $t > a \in \mathbb{R}$ ), then  $ROC_X$  is a left half-plane. Now consider the case of a causal LTI system  $H$  whose transfer function  $H_L(s)$  is a rational function. Since  $H$  is causal,  $h(t) = 0$  for  $t < 0$ . In other words,  $h(t)$  is right-sided, and  $ROC_H$  is a right half-plane. Since  $H_L(s)$  is rational, its denominator is a complex polynomial  $Q(s)$ . The only values  $s \in \mathbb{C}$  for which  $H_L(s)$  does not exist are the zeros of  $Q(s)$ , which are the rational function's *poles*. As there are only a finite number of poles of  $H_L(s)$ ,  $ROC_H$  must be the half-plane to the right of the zero of  $Q(s)$  with the largest real part.

We invert the Laplace transform using much the same methods as  $z$ -transform inversion. Rational functions  $X_L(s)$  can be decomposed into a partial-fractions representation and the linearity property applied to elementary transforms to arrive at  $x(t)$ . Table 9.3 lists basic Laplace transform properties.

Let us turn now to the use of the Laplace transform in designing discrete filters from rational analog filters [7]. Let the Laplace transform of  $h_a(t)$  be a quotient of complex polynomials

$$H_L(s) = \int_{-\infty}^{\infty} h_a(t)e^{-st} dt = \frac{P(s)}{Q(s)} \tag{9.65}$$

**TABLE 9.3. Summary of Laplace Transform Properties**

Signal Expression	Laplace Transform or Property
$x(t)$	$X_L(s) = \int_{-\infty}^{\infty} x(t)e^{-st} dt$
$z(t) = ax(t) + by(t)$	$aX_L(s) + bY_L(s)$ (Linearity, $ROC_X \cap ROC_Y \subseteq ROC_Z$ )
$y(t) = x(t - a)$	$e^{-sa}X_L(s)$ (Time shift, $ROC_X = ROC_Y$ )
$y(t) = x(t)\exp(at)$	$X_L(s - a)$ (Frequency shift, modulation, $ROC_Y = \{s : s - a \in ROC_X\}$ )
$y(t) = x(at), a \neq 0$	$\frac{1}{ a }X_L\left(\frac{s}{a}\right)$ (Scaling, dilation, $ROC_Y = \{s : s/a \in ROC_X\}$ )
$y(t) = (x * h)(t)$	$F(s)H(s)$ (Convolution, $ROC_X \cap ROC_H \subseteq ROC_Y$ )

and let its partial fractions expansion be

$$H_L(s) = \sum_{m=1}^M \frac{d_m}{s - s_m}, \quad (9.66)$$

where  $d_m$ ,  $1 \leq m \leq M$ , are constants, and the poles  $s_m$  are distinct. Laplace transform linearity and inversion of the summands in (9.66) implies

$$h_a(t) = u(t) \sum_{m=1}^M d_m e^{s_m t}. \quad (9.67)$$

Impulse invariance applies exactly as above. We set

$$h(n) = h_a(nT) = u(n) \sum_{m=1}^M d_m e^{s_m nT}, \quad (9.68)$$

and the  $z$ -transform of  $h(n)$  is

$$H(z) = \sum_{m=1}^M d_m Z[u(n) e^{d_m nT}](z) = \sum_{m=1}^M \frac{d_m}{1 - e^{T s_m} z^{-1}}. \quad (9.69)$$

Notice that if  $d_m = jc_m$  and  $s_m = j\Omega_m$ , then the two expressions for  $H(z)$ , (9.69) and (9.60), are identical. The conditions for stability and causality are similar too. From a Fourier transform perspective, we need the poles of the rational function

$H_a(\Omega) = \frac{P(\Omega)}{Q(\Omega)}$  to have positive imaginary parts. From the Laplace transform

standpoint, however, we require the poles of  $H_L(s) = \frac{P(s)}{Q(s)}$  to have negative real parts. Of course, if  $\Omega_0$  is a pole of  $H_a(\Omega)$ , then  $j\Omega_0$  is a pole of  $H_L(s)$ .

**9.3.5.4 Bilinear Transformation.** The bilinear transformation obtains a discrete filter from the frequency domain representation of an analog filter by directly mapping the analog frequency values to discrete frequency values. What sort of operation performs such a mapping? Note that analog frequencies can be arbitrarily large,  $-\infty < \Omega < +\infty$ , whereas discrete frequencies are limited to a  $2\pi$ -wide interval:  $-\pi < \omega \leq \pi$ . So we seek a function that maps the real line to the circumference of a circle. The arctangent,  $\tan^{-1}$ , maps  $\mathbb{R}$  to the interval  $(-\pi/2, \pi/2)$ . Let  $T$  be the sampling interval. Then the following relation maps continuous to discrete frequency values:

$$\omega = 2 \tan^{-1} \left( \frac{\Omega T}{2} \right). \quad (9.70)$$

Observe that as  $\Omega \rightarrow \pm\infty$ , the maximum analog frequency values, then  $\omega \rightarrow \pm\pi$ , respectively, the maximum discrete frequency values.

Suppose that  $H_a(\Omega)$  is an analog lowpass filter with cutoff frequency  $\Omega_c$ . Then the bilinear transformation (9.70) allows us to define a discrete low-pass filter as follows:

$$H(\omega) = H_a\left(\frac{2}{T} \tan\left(\frac{\omega}{2}\right)\right). \quad (9.71)$$

The cutoff frequency for  $H(\omega)$  is  $\omega_c = 2 \tan^{-1}\left(\frac{\Omega_c T}{2}\right)$ .

How does the scaling factor  $T$  come to appear in (9.70)? One practical reason is that for small frequencies,  $T$  controls the rate of change of  $\omega$  with respect to  $\Omega$ :  $d\omega/d\Omega \approx T$ . Some authors (e.g., Ref. 46) set  $\omega = \frac{2}{T} \tan^{-1}\left(\frac{\Omega T}{2}\right)$  to ensure that for low frequencies  $\omega \approx \Omega$ . Another way of justifying the frequency mapping (9.70) is to consider the relation between poles of rational analog filters and the discrete filters obtained from them. If  $s = s_m$  is a pole of the Laplace transform  $H_L(s)$  of a filter (9.66), then corresponding to it is a pole  $z = \exp(s_m T)$  of the  $z$ -transform  $H(z)$  (9.69). This suggests a mapping from the Laplace  $s$ -plane to the  $z$ -plane:  $z = e^{sT}$ . Thus,

$$z = e^{sT} = \frac{e^{s(T/2)}}{e^{-s(T/2)}} \approx \frac{1 + s\frac{T}{2}}{1 - s\frac{T}{2}} = \frac{2 + sT}{2 - sT}, \quad (9.72)$$

where we approximate the quotient on the right in (9.72) using the first two Taylor series terms for the exponential function. This implies

$$s \approx \frac{2}{T} \left( \frac{z-1}{z+1} \right), \quad (9.73)$$

which relates the Laplace transform variable to the  $z$ -transform variable. To relate continuous and discrete frequency responses, we use  $z = e^{j\omega}$  and  $s = j\Omega$  in (9.73), treating it as an equality. After a little algebra, (9.70) results (exercise).

### 9.3.6 Frequency Transformations

There are convenient mappings of the independent variable of a filter's system function that convert a low-pass filter to a high-pass, bandpass, bandstop, or even another low-pass filter [7, 11, 33, 47].

**9.3.6.1 Analog.** Consider an analog low-pass filter with Laplace transform  $H_L(s)$  and cutoff frequency  $\Omega_c = 1$ . The transformations are as follows:

- (i) Let  $\phi(s) = s/\Omega_H$ . Then  $H_L(\phi(s))$  is a low-pass filter with cutoff frequency  $\Omega_H$ .
- (ii) Let  $\phi(s) = \Omega_H/s$ . Then  $H_L(\phi(s))$  is a high-pass filter with cutoff frequency  $\Omega_H$ .

(iii) Let  $\phi(s) = \frac{s^2 + \Omega_L \Omega_H}{s(\Omega_H - \Omega_L)}$ . Then  $H_L(\phi(s))$  is a bandpass filter with lower cutoff frequency  $\Omega_L$  and upper cutoff frequency  $\Omega_H$ .

(iv) Let  $\phi(s) = \frac{s(\Omega_H - \Omega_L)}{s^2 + \Omega_L \Omega_H}$ . Then  $H_L(\phi(s))$  is a bandstop filter with lower cutoff frequency  $\Omega_L$  and upper cutoff frequency  $\Omega_H$ .

**9.3.6.2 Discrete.** Consider a discrete low-pass filter with  $z$ -transform  $H(z)$  and cutoff frequency  $\omega_c$ . The transformations are as follows:

(i) Let  $\phi(z^{-1}) = \frac{z^{-1} - \alpha}{1 - \alpha z^{-1}}$ . If we set  $\alpha = \sin\left(\frac{\omega_c - \omega_H}{2}\right) / \sin\left(\frac{\omega_c + \omega_H}{2}\right)$ , then  $H(\phi(z))$  is a low-pass filter with cutoff frequency  $\omega_H$ .

(ii) Let  $\phi(z^{-1}) = \frac{-z^{-1} + \alpha}{1 + \alpha z^{-1}}$ . If  $\alpha = -\cos\left(\frac{\omega_c + \omega_H}{2}\right) / \cos\left(\frac{\omega_c - \omega_H}{2}\right)$ , then  $H(\phi(z))$  is a high-pass filter with cutoff frequency  $\omega_H$ .

(iii) Let  $\phi(z^{-1}) = \frac{-z^{-2} - 2\alpha\beta z^{-1} + \gamma}{\gamma z^{-2} - 2\alpha\beta z^{-1} + 1}$ . If  $\alpha = \cos\left(\frac{\omega_H + \omega_L}{2}\right) / \cos\left(\frac{\omega_H - \omega_L}{2}\right)$ ,

$$\kappa = \cot\left(\frac{\omega_H - \omega_L}{2}\right) \tan\left(\frac{\omega_c}{2}\right), \quad \beta = \kappa / (\kappa + 1), \quad \text{and} \quad \gamma = (\kappa - 1) / (\kappa + 1),$$

then  $H(\phi(z))$  is a bandpass filter with upper cutoff frequency  $\omega_H$  and lower cutoff frequency  $\omega_L$ .

(iv) Let  $\phi(z^{-1}) = \frac{z^{-2} - 2\alpha\beta z^{-1} + \gamma}{\gamma z^{-2} - 2\alpha\beta z^{-1} + 1}$ . If  $\alpha = \cos\left(\frac{\omega_H + \omega_L}{2}\right) / \cos\left(\frac{\omega_H - \omega_L}{2}\right)$ ,

$$\kappa = \tan\left(\frac{\omega_H - \omega_L}{2}\right) \tan\left(\frac{\omega_c}{2}\right), \quad \beta = 1 / (\kappa + 1), \quad \text{and} \quad \gamma = (1 - \kappa) / (\kappa + 1),$$

then  $H(\phi(z))$  is a bandstop filter with upper cutoff frequency  $\omega_H$  and lower cutoff frequency  $\omega_L$ .

**Example (Low-Pass to High-Pass).** Suppose that  $\omega_c = \pi/4$  and  $\omega_H = 3\pi/4$  in (ii) above. Then  $\alpha = \frac{-\cos(\pi/2)}{\cos(-\pi/4)} = 0$  and  $H(\phi(z)) = H(-z)$ .

### 9.3.7 Linear Phase

It is possible to construct causal finite impulse response filters with *linear phase*. Where the analysis steps in an application depend on linear phase during signal

processing steps, this can be factor in favor of using finite impulse response (FIR) filters. Note that it is possible to have infinite impulse response (IIR) filters with linear phase. For example, if  $h = H\delta$  and  $h(n)$  is symmetric about  $n = 0$ , then  $H$  will have zero phase. However, we are interested in filters that are practically implementable, and therefore we require right-sided impulse responses:  $h(n) = 0$  for  $n < N$  for some  $N$ .

**9.3.7.1 FIR Characterization.** Let  $H$  be a linear, translation invariant system, let  $h(n)$  be its impulse response, and let  $H(\omega)$  be its discrete time Fourier transform. If  $H(\omega) = e^{j\phi(\omega)}H_R(\omega)$ , with  $\phi(\omega)$  a linear function of  $\omega$ , and  $H_R(\omega) \in \mathbb{R}$ , then we say  $H$  has linear phase.

The theoretical result we are going to prove is as follows. If  $H$  is a discrete causal FIR filter with impulse response  $h = H\delta$  such that  $h(n) = 0$  for  $n > N - 1$ , then  $H$  has linear phase if and only if for some  $c \in \mathbb{C}$ , with  $|c| = 1$ ,  $h(n) = ch^*(N - 1 - n)$ , where  $h^*$  is the complex conjugate of  $h$ .

To begin, let us assume that  $H$  is causal, FIR, and has linear phase. Let  $H(\omega) = e^{j\phi(\omega)}H_R(\omega)$ , with  $\phi(\omega) = a + b\omega$ , for some  $a, b \in \mathbb{R}$ , and  $H_R(\omega) \in \mathbb{R}$ . Assume that  $\text{Support}(h) = [0, N - 1]$  with  $N > 0$ , so that  $h(0) \neq 0$  and  $h(N - 1) \neq 0$ . Let  $A_H(\omega)$  be the amplitude function for  $H(\omega)$  the DTFT of  $h(n)$ :  $H(\omega) = e^{j\phi(\omega)}A_H(\omega)$ . Then

$$H(\omega) = \sum_{n=-\infty}^{\infty} h(n)e^{-j\omega n} = \sum_{n=0}^{N-1} h(n)e^{-j\omega n}, \tag{9.74}$$

$$H(\omega) = e^{j[2a + 2b\omega - \phi(\omega)]}A_H(\omega) = e^{2ja}e^{2jb\omega}e^{-j\phi(\omega)}A_H(\omega) = e^{2ja}e^{2jb\omega}H^*(\omega). \tag{9.75}$$

Note that  $H(\omega)$  and its complex conjugate  $H^*(\omega)$  are both  $2\pi$ -periodic; we must have  $2b = K \in \mathbb{Z}$  on the right-hand side of (9.75). Let  $c = e^{2ja}$  and  $g(n) = h^*(-n)$ , so that  $G(\omega) = H^*(\omega)$ . Then the discrete signal  $s(n) = cg(n + K)$  has DTFT  $S(\omega) = ce^{jK\omega}G(\omega) = ce^{jK\omega}H^*(\omega) = H(\omega)$ . Because the DTFT is invertible, we must have  $h(n) = s(n) = cg(n + K) = ch^*(-K - n)$ . We know that for  $n < 0$ ,  $h(n) = h^*(n) = 0$ . Also, if  $n > -K$ , we have  $ch^*(-K - n) = h(n) = 0$ . Thus,  $-K = N - 1$  because that is the upper limit of the support of  $h(n)$ , and so  $h(n) = ch^*(N - 1 - n)$ , as claimed.

Conversely, suppose  $\text{Support}(h) = [0, N - 1]$  and  $h(n) = ch^*(N - 1 - n)$  for some  $c \in \mathbb{C}$  with  $|c| = 1$ . Applying the DTFT properties gives  $H(\omega) = ce^{-j(N - 1)\omega}H^*(\omega)$ . Let  $c = e^{j\theta}$ . If  $H(\omega) = e^{j\phi(\omega)}A_H(\omega)$ , then  $H^*(\omega) = e^{-j\phi(\omega)}A_H^*(\omega)$ . Putting these together, we have

$$e^{j\phi(\omega)} = e^{j\theta}e^{-j\phi(\omega)}e^{-j(N - 1)\omega}, \tag{9.76}$$

and thus for some  $K \in \mathbb{Z}$ ,

$$\phi(\omega) = \frac{(1 - N)\omega}{2} + \frac{\theta}{2} + \pi K. \tag{9.77}$$

Clearly,  $\phi(\omega)$  is a linear function of  $\omega$ , and we are done.

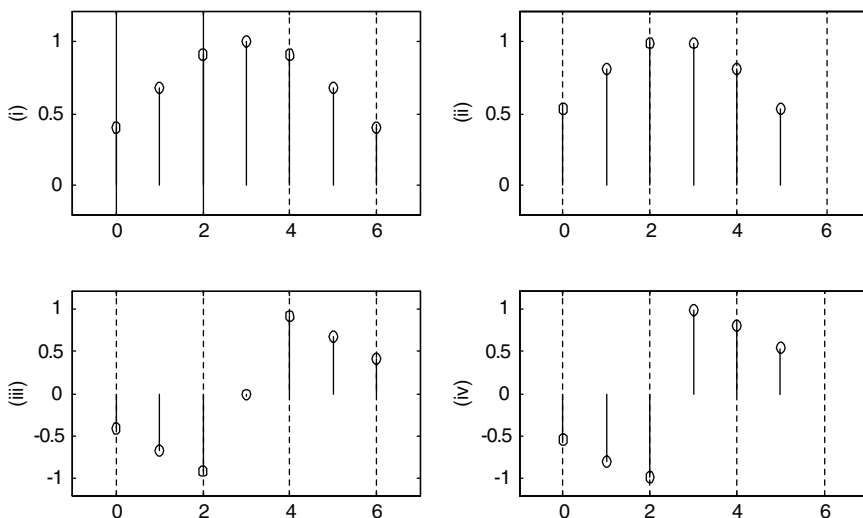


**Fig. 9.24.** Four classes of linear phase FIR filters.

**9.3.7.2 Linear Phase Filter Classes.** For real-valued filters  $h = H\delta$ , where  $h(n)$  has support  $[0, N - 1]$ , with  $N > 0$ , there are four categories of linear phase filters. We showed that a finite impulse response filter  $H$  has linear phase if and only if for some  $c \in \mathbb{C}$ ,  $|c| = 1$ ,  $h(n) = ch^*(N - 1 - n)$ . If  $h(n) \in \mathbb{R}$ , then  $c = 1, -1$ .

We can thus put the filter into one of four classes (Figure 9.24):

- (i)  $c = 1$  and  $N = 2M + 1$  is odd.
- (ii)  $c = 1$  and  $N = 2M$  is even.
- (iii)  $c = -1$  and  $N = 2M + 1$  is odd.
- (iv)  $c = -1$  and  $N = 2M$  is even.

**9.3.7.3 Examples.** We review two cases where the need for linear phase motivates the specific use of FIR filters: electroencephalogram (EEG) interpretation and seismogram interpretation.

The first chapter explained the multichannel EEG [48], a biomedical signal that is often employed in studying brain functions and diagnosing injuries and illnesses. Electrodes attached to the scalp record the minute voltages produced by the interactions of large numbers of neurons. The signals are often quite noisy, and successive averaging is often employed to improve the quality of EEG traces. In studying auditory potentials—EEG traces of the part of the brain that is involved in the front-end processing of auditory nerve impulses—linear filtering has been investigated in order to improve upon successive averaging, the efficacy of which diminishes after a large number of sampling epochs. Frequencies above 2 kHz are removed by lowpass filtering, since they cannot be due to neuronal changes, which take place on the order

of 1 ms. The remaining noise is usually at low frequencies, DC to about 150 Hz [49]. The most popular filtering methods for such an application use IIR filters derived from difference equations (Section 9.3.4.2), since they are efficient and generally have better sharpness than FIR filters. But the nonlinear phase response of the causal IIR filters distorts the EEG trace, making linear phase FIR filtering preferable [49].

In seismic processing, the signals are generally quite noisy, composed of many frequency components, which are filtered by their propagation through the earth. These different sinusoidal pulses arrive at the sensing unit—the seismometer—at different times [50], a kind of phase delay. Perhaps the most basic task of earthquake seismology is to estimate the arrival time of an event, so that different seismometer stations can compare seismograms and locate the epicenter. Against the background noise of minor earth movements, impacts from construction equipment, and vehicle traffic vibrations, the seismic station determines the edge of a significant transient. At what time this transient occurs for a seismic station depends on the group delay of Mother Earth acting as a filter. Thus, for automated seismogram interpretation, a signal processing filter that introduces a nonlinear phase delay into the system might distort the signal and cause an error in pinpointing the onset time of a seismic shock. In order to facilitate the comparison of arrival times among different stations with different equipment, it is essential that their diverse noise removal filters not introduce any frequency dependent delays at all. The filtering requirement is even more stringent; successful analysis of the seismogram usually demands *zero phase* filtering [51].

## 9.4 WIDEBAND SIGNAL ANALYSIS

This section considers signals that contain diverse spectral components. These signals include chirps, which consist of rising or falling tones; transient signals, such as seismic pulses; signals with sharp edges; and irregularly shaped signals, such as image object boundaries. Our earlier methods of periodicity detection are successful only with much simpler waveforms.

### 9.4.1 Chirp Detection

A chirp is a signal segment where the frequency rises or falls over time. Strictly speaking, of course, a chirp is not a narrowband signal. But locally, at least, the signal energy is contained in a narrow spectral range. If this is indeed the case, then the task of chirp analysis becomes based upon a series of pure tone detection problems where the detected tones regularly rise or fall. This section considers the case where locally, at least, a signal contains mainly one frequency component, but that the frequency itself is changing over time.

**9.4.1.1 Synthetic Chirps.** Section 6.5 presented the theory of signal modulation, which is the theoretical foundation of chirp signal analysis. Let us first consider

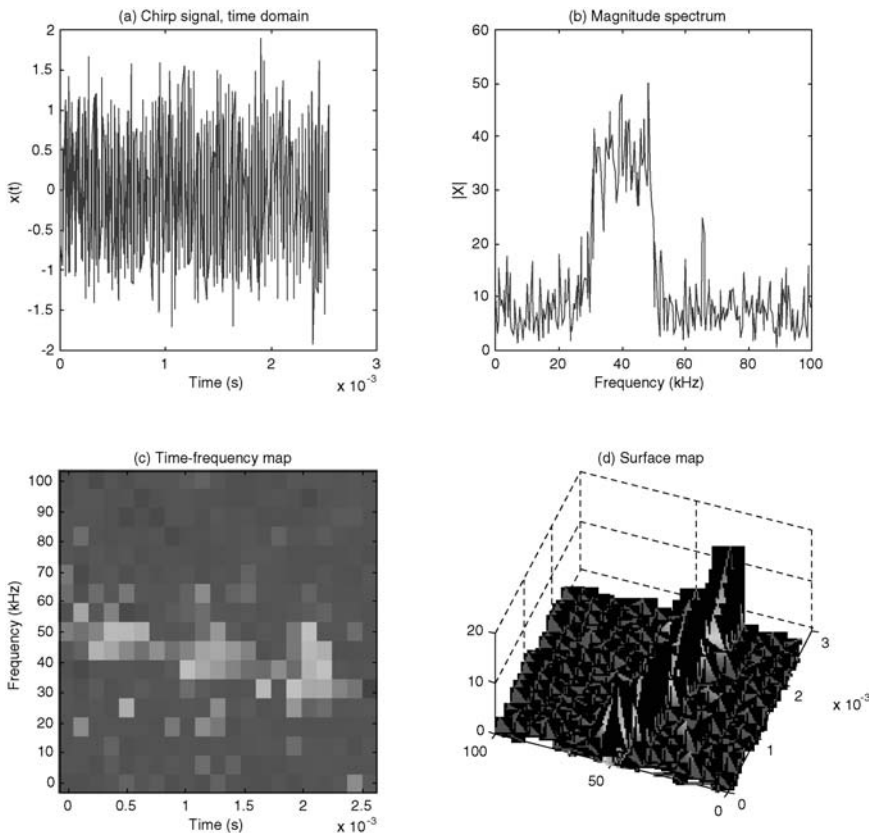


**Fig. 9.25.** Synthetic chirp with noise added (a). Panel (b) shows the magnitude spectrum. A time-frequency map (c) shows how the frequencies change over time. Surface maps (d) are useful aids for visualizing signal structure.

chirp signals for which the change in frequency over time is fairly simple—linear, for instance. Thus, we have  $\omega(t) = t\omega_1 + \omega_0$  as shown in Figure 9.25.

From its time-domain plot Figure 9.25a, it is hard to understand the signal. The magnitude spectrum Figure 9.25b shows that a concentrated range of tones is present, in the range from 30 to 50 kHz, amidst some moderate background noise. But the time evolution of these frequencies and therefore the structure of the signal—itsself remains unclear. We compute a sequence of 32-point discrete Fourier transforms over the time span of the signal. Overlapping the windows by eight samples helps smooth the time-frequency representation. The resulting map, shown in Figure 9.25c, reveals a linear chirp beginning at about 50 kHz and decreasing in frequency in a linear fashion down to about 30 kHz.

As long as its frequency content is, over a certain time interval, basically a tone, a chirp signal can be analyzed using tone detection techniques and a state machine.

Local discrete Fourier transforms carry out the frequency analysis, and some straightforward interpretive logic carry out the chirp discrimination. We can surmise the following steps:

- (i) An order  $N$  for the number of samples for discrete Fourier transformation (DFT) is selected, depending on the sampling rate of the source signal and the range of frequencies expected in the chirp signal.
- (ii) A DFT window overlap is selected.
- (iii) DFT computations are conducted on the source signal within overlapping windows as chosen in (i) and (ii).
- (iv) Where a relatively pure tone in the expected frequency range is found using local Fourier analysis, the state machine enters a tone detected state.
- (v) Step (iv) is carried out again, and if there is a tone in the acceptable spectral range, then the tone is checked for purity, and the machine enters a state of increasing or decreasing tone frequency.
- (vi) Continued local frequency analysis extends the time-domain support of the tone, breaks out of the tone detected state based on an invalid frequency response, or decides that the tone has the proper quality and range to continue the chirp defined in the current machine state.
- (vii) This process continues until the chirp ends or the input signal is exhausted.

The main difficulties with this analysis is that it requires—for the most part—offline data analysis. That is, the DFT windows are applied around a time center value in a noncausal fashion. This could be an expensive operation, and for real-time processing, it may be impossible. One alternative might be to employ a bank of causal filters and seek significant outputs from the banks tuned to increasing or decreasing frequency bands. To achieve this, however, we need to devise filtering methods that are causal and sufficiently efficient for online implementation.

**9.4.1.2 Biological Signals: Bat Echolocation Chirp.** Now let us study the echolocation chirp recorded from a large brown bat (*Eptesicus fuscus*).<sup>11</sup> The sampling period is  $T = 7 \mu\text{s}$ , and there are  $N = 400$  samples in the data set. The time-domain signal oscillates and rises in amplitude, but the plotted values evince few other clues as to its structure (Figure 9.26a). The magnitude spectrum explains a little more. There are frequencies between 20 kHz and 50 kHz, centered more or less strongly around a spectral peak at some 35 kHz. The spectrum appears to be bimodal (Figure 9.26b). From a Fourier domain perspective, we cannot tell whether the modes are frequency components that appear at certain times, one after the other, or whether they substantially overlap and the bimodality is an artifact of relatively weaker middle frequencies.

<sup>11</sup>This data set is available from the signal processing information base (SPIB): <http://spib.rice.edu/spib.html>. The authors wish to thank Curtis Condon, Ken White, and Al Feng of the Beckman Center at the University of Illinois for the bat data and for permission to use it in this book.

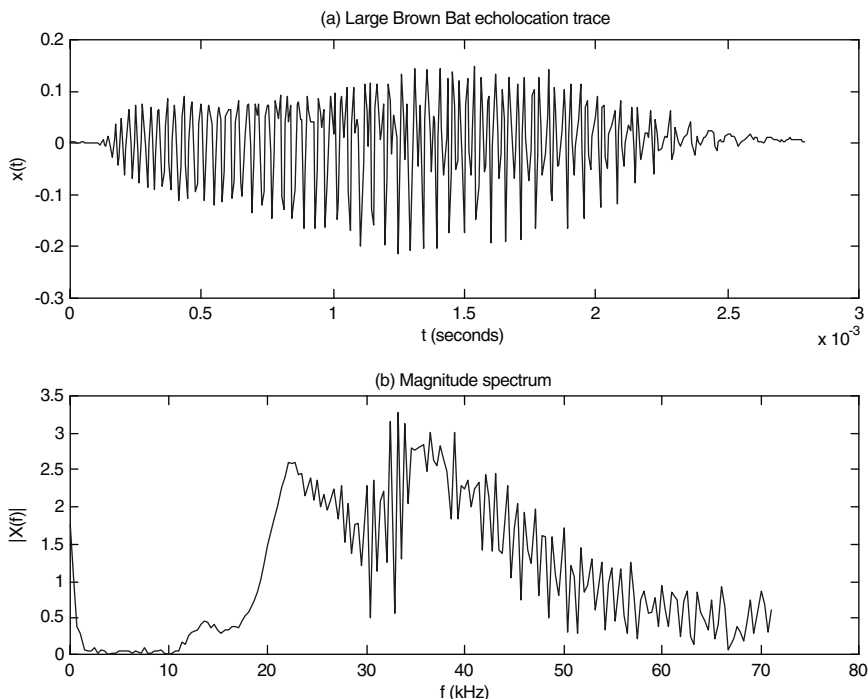


**Fig. 9.26.** Large brown bat echolocation pulse time-domain (a) and frequency-domain (b).

Our knowledge of the echolocation pulse's content changes dramatically when we develop the time-frequency map (Figure 9.27).

We use a boxcar window of width  $N = 128$  to generate the local spectral values, overlapping successive windows by  $M = 120$  samples. This reveals three descending chirps (Figure 9.27a) and shows that the time-frequency plot is at least tri-modal. The bar-shaped artifacts most visible in the lower frequencies appear to correlate with window alignment. We try a Hann window function of length  $N$  and overlap  $M$  to improve the local frequency estimates, as shown in Figure 9.27b. This reduces the time-frequency artifacts, as one might expect. However, Hann windowing has the added benefit of resolving the time-frequency mode of highest initial frequency into two chirps; the echolocation pulse in fact contains four modes.

## 9.4.2 Speech Analysis

Let us now consider some low-level speech signal analysis problems. There is, to be sure, a large research literature on natural language processing from initial filtering methods, detection of utterances in noise, phoneme recognition, word recognition, contextual analysis, and artificial intelligence techniques for computerized speech understanding [13, 52–54].

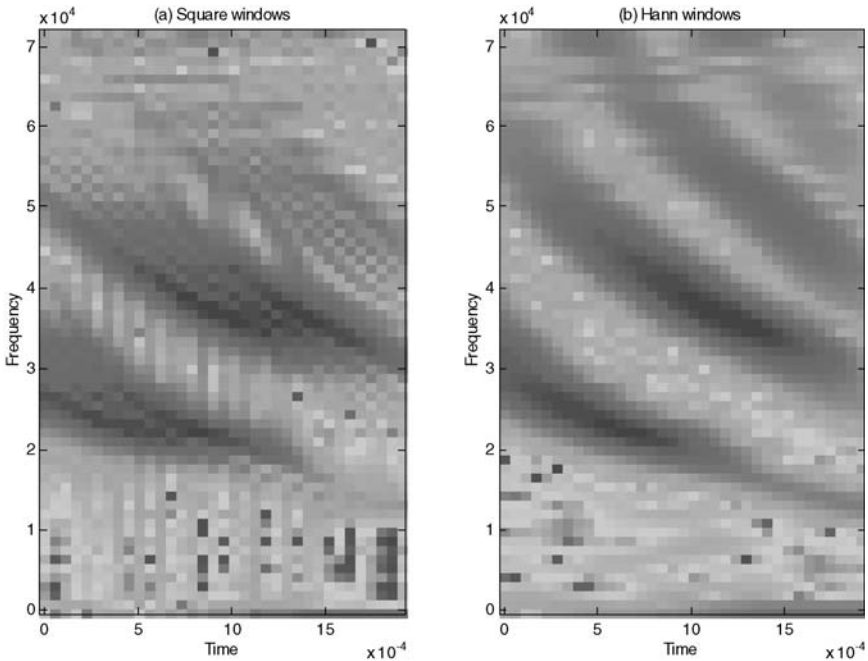


**Fig. 9.27.** The time-frequency map of the large brown bat echolocation pulse evidently has three components (a), each a descending chirp. Instead of a 128-point square window, panel (b) employs a 128-point Hann window to generate the local frequency information.

**9.4.2.1 Formant Detection.** *Formants* are relatively high-energy, tone-like components within a spoken word. They appear in the speech spectrum as isolated peaks. Consider, for example, a digitized voice fragment, consisting of a single word (Figure 9.28).

It is possible to discover formants using peak detection in the Fourier magnitude spectrum. The vowel phoneme /a/ in Figure 9.28c exhibits three strong peaks at approximately 300 Hz, 600 Hz, and 900 Hz. Such harmonics are characteristic of sounds produced in a tube, with a source at one end and open at the other. This crudely models the vocal tract, with the vocal cords at one end and the open mouth at the other. The vowel phoneme /i/ in Figure 9.28e shows three resonant components as well as significant energy in many higher frequencies. Parts of the speech signal that do not contain high-energy tones, such as the /k/ in Figure 9.28b, cannot have formant structures.

Another formant detection task is to identify a *pitch* or *fundamental harmonic frequency* among the significant tones. This is the frequency of vibration of the vocal cords. In real speech recognition systems, this frequency must be identified and tracked, as it varies with the utterance as well as with the gender and emotional

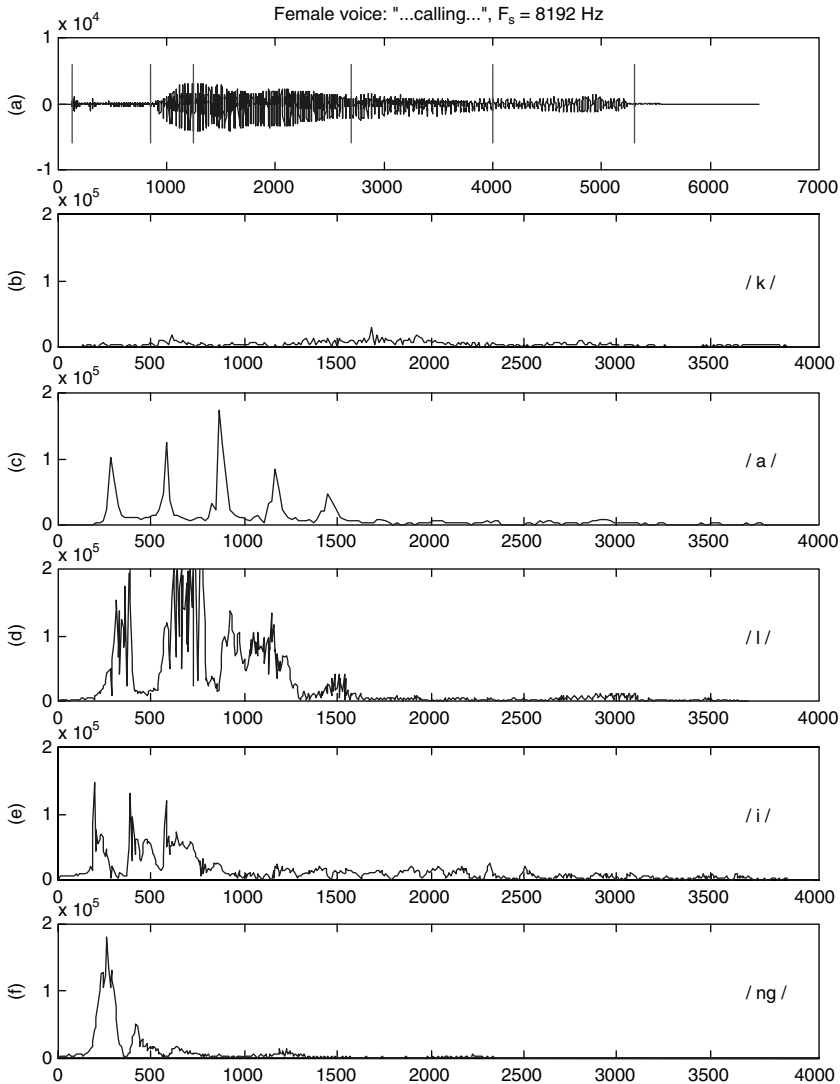


**Fig. 9.28.** Digitized voice (a) of a woman: "...calling...." Vertical lines mark the approximate locations of five phonemes. Panels (b)–(f) show the magnitude spectra for phonemes /k/, /a/, /l/, /i/, and /ng/.

state of the speaker. Some goal-directed information applies here. Pitch ranges from about 60 Hz to 300 Hz in adult males and up to 600 Hz in adult females.

A third formant detection task is to compare the center frequencies of significant tones. If such peaks represent formants, they must be integral multiples of the pitch frequency. Thus, in addition to ordinary peak finding, a formant detection

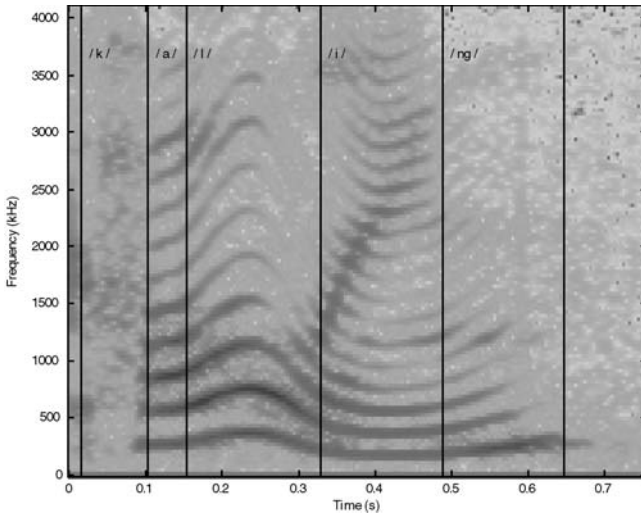


**Fig. 9.29.** Mixed-domain analysis of “calling” speech fragment. Using  $N = 256$  point Hann windows for local frequency estimations centered  $K = 32$  samples apart along the time axis produces the above time-frequency map. In many cases, voiced versus unvoiced speech segments can be found using the time-frequency map.

algorithm must include an assessment of the relative energy contributed by resonant frequencies.

**9.4.2.2 Voice and Unvoiced Speech Determination.** Speech sounds can be divided into *voiced* and *unvoiced* sounds, according to whether the vocal cords vibrate or do not vibrate, respectively (Figure 9.29). Unvoiced sounds split roughly into two categories: fricatives, such as /s/ or /f/, and aspirates, such as /k/.

**9.4.2.3 Endpoint Detection.** An important early speech analysis step involves automatic discrimination between background noise and speech signals. This segmentation procedure is important for automated compilation of speech databases and for detecting word boundaries in speech recognition systems. A fairly old but reliable method uses local energy and zero crossing rate parameters to isolate speech [55]. From a background noise sample, upper- and lower-energy parameters  $E_u$  and  $E_l$ , respectively, and a zero crossing threshold  $Z_c$  are determined. The algorithm refines the boundaries of a speech fragment in three stages as follows:

- (i) The initial energy-based segmentation, say speech exists within  $[M_u, N_u]$ , is given by where local signal energy exceeds  $E_u$ .
- (ii) The refined energy-based segmentation widens this interval to  $[M_l, N_l]$  by searching outside  $[M_u, N_u]$  for the points where energy diminishes to  $E_l$ .

- (iii) Finally, a measure of local signal frequency—the zero crossing rate—is checked outside of  $[M_l, N_l]$ . If the rate exceeds  $Z_c$  three or more times in the 250-ms intervals on either side of  $[M_l, N_l]$ , then the speech fragment boundaries grow again to  $[M_z, N_z]$ , where  $[M_u, N_u] \subseteq [M_l, N_l] \subseteq [M_z, N_z]$ .

Noise versus speech discrimination problems continue to attract experimental researchers [56, 57].

### 9.4.3 Problematic Examples

Let us mention a couple of signal analysis problem domains where Fourier transform-based interpretation techniques begin to break down.

Seismic signals contain oscillations, but these oscillations are of unusually short time domain and are interspersed with transient artifacts that often thwart analysis. The Fourier transform is adequate for long-term periodic signal trends, but its efficiency as a signal descriptor diminishes with the duration of the oscillations. Geophysicists resorted to the short-time or windowed Fourier transform, which we cover in the next chapter, with some success. This theory constructs a time- and frequency-domain transform using the Fourier transform and the windowing techniques of Section 9.2. However, transient components are still problematic. Finally, efforts to get around the difficulties of windowed Fourier methods let to the development of the wavelet transform, which is the subject of Chapter 11.

Another problem area for Fourier methods is shape analysis. It seems that object shapes, however they might be described mathematically, are comprised of parts. One-dimensional methods, such as we develop here, can be applied to object boundaries, and we attempt such applications in the last chapter. There are Fourier transform-based approaches:

- (i) An early method, called Fourier descriptors, approximates image object boundaries with varying numbers of Fourier series components.
- (ii) Another method, the Fourier–Mellin transform, incorporates a temporal parameter into the transform.

These strategies work, but when the bounded object resolves into separate parts, the overall analytic techniques collapse. As a result, automated object recognition systems tend to retreat into structural methods of pattern recognition and cordon off, perhaps giving up on frequency-domain interpretation.

## 9.5 ANALOG FILTERS

Although our present goal is discrete time signal analysis and the frequency selective systems that support it, we have ample reasons for developing a respectable theory of analog filtering.

- (i) While signal analysis is computerized interpretation of signals and therefore assumes a digital implementation, it relies upon discrete theory.

- (ii) However, our ultimate source signals come from analog world.
- (iii) We need to filter incoming analog so as to remove high frequencies that would otherwise cause aliasing during sampling, according to the Nyquist criterion.
- (iv) We may be able to implement cheaper analog filters.
- (v) A lot of discrete filter designs are based on analog filters.
- (vi) We have shown that it is easy to derive discrete filters from analog versions—and especially if the analog filters have a rational transfer function.
- (vii) Thus, if we develop a sound theory of analog filters, then we shall have a correspondingly sound theory of discrete filters.
- (viii) Analog filters are historically prior.
- (ix) The analog theory of continuous theory involves continuous sinusoidal signals, and hence the analog Fourier transform is a convenient theoretical tool. Anyway, this is consonant with our analog-first treatment of the frequency transforms.

Just as the continuous Fourier transform is the natural setting for studying signal frequency, so the class of continuous domain, or analog, filters constitute the right beginning place for our study of frequency-domain signal analysis. Signal analysis usually takes place on a digital computer, but the frequency-selective algorithms that operate on digital signal representations often derive from continuous-domain filters. That is one reason for studying analog filters. But even before signals are digitized and fed to the computer, the signal digitization must often be filtered by analog means so that aliasing (Chapter 7) is minimized. This section presents some basic analog filters, introduces their characteristic descriptors, and outlines the mechanics of converting one filter into another.

Conventional analog filter designs begin by examining the frequency-domain behavior  $X(\omega)$  or the  $s$ -domain behavior  $X_L(s)$  of analog signals  $x(t)$ . System theory texts covering analog filter theory and the Laplace transform include Refs. 6, 58, and 59. Texts that concentrate on the subsequent conversion to discrete time processing are [7–11, 26].

Classical electronics studies networks of electrical components—resistors, capacitors, and inductors—which implement the analog filtering operation in hardware. Circuit design texts cover the electronic circuit designs [60–63]. More modern electrical and computer engineering texts cover the design of hardware for digital filtering [64]. For signal analysis using digital computers, we need digital filters that selectively enhance and suppress signal frequency components of interest to the application. We derive the digital filters from their analog equivalents using some classic methods.

### 9.5.1 Introduction

A *filter* is a frequency-selective linear, translation-invariant system. Analog filtering takes place by virtue of the convolution property:  $Y(\Omega) = H(\Omega)X(\Omega)$ . So, if  $|H(\Omega)|$  is small for values of  $\Omega$  where it is desirable to suppress frequencies in the input  $x(t)$

and  $|H(\Omega)|$  is near unity where it is desirable to preserve frequencies in  $x(t)$ , then convolution with  $h(t)$ ,  $y(t) = (h*x)(t)$  performs the requisite frequency selection operation. To describe system filtering we specify the magnitude spectrum,  $|H(\Omega)|$ , or, equivalently,  $|H(\Omega)|^2$ . We are mainly interested in real-valued filters:  $h(t) \in \mathbb{R}$ . Since  $H(-\Omega) = H^*(\Omega)$  in this case and since  $|H(\Omega)| = |H^*(\Omega)|$ , the filters herein have both positive and negative frequency components. Thus, the magnitude spectra are symmetric about the frequency-domain origin,  $\Omega = 0$ .

This section explains how to construct bandpass and high-pass filters from low-pass filters. The discussion begins with the Gaussian; its Fourier transform is also Gaussian, so it is a natural choice for a low-pass filter. Filter constructions depend on the Fourier transform properties from Chapter 5.

The analog convolution operation is once again denoted by the  $*$  operator:  $y = x*h$ . We define

$$y(t) = (x*h)(t) = \int_{-\infty}^{\infty} x(s)h(t-s) ds. \quad (9.78)$$

Section 6.4.1 introduced ideal analog filter types. One filter missing there is the notch or band-reject filter. It is like a reverse bandpass, and it suppresses rather than preserves a range of frequencies.

## 9.5.2 Basic Low-Pass Filters

Since we can move easily from low-pass filters to any of the other three basic types—high-pass, bandpass, or band-reject—let us consider some examples.

**9.5.2.1 Perfect.** The ideal low-pass filter completely removes all frequencies higher than some given frequency and preserves the rest without amplifying or attenuating them. This is the familiar analog *moving average* or *boxcar* filter.

**9.5.2.2 Gaussian.** The Gaussian

$$g_{\mu, \sigma}(t) = \frac{1}{\sigma\sqrt{2\pi}} e^{-\frac{(t-\mu)^2}{2\sigma^2}} = g(t) \quad (9.79)$$

with mean  $\mu$  and standard deviation  $\sigma$  has Fourier transform

$$G(\Omega) = \int_{-\infty}^{\infty} g(t)e^{-j\Omega t} dt = \exp\left(-\left[\frac{\sigma^2\Omega^2}{2} + j\Omega\mu\right]\right). \quad (9.80)$$

Its magnitude spectrum is also a Gaussian, centered at  $\Omega = 0$ . Thus,  $g(t)$  is the impulse response of an analog low-pass filter. If  $x(t)$  is an analog signal and  $y = Gx = (g * x)(t)$  is the convolution with the Gaussian (9.79), then  $Y(\Omega) = X(\Omega)G(\Omega)$ , where  $G(\Omega) = (\mathcal{F}g)(\Omega)$  is given by (9.80). Gaussians decay rapidly, faster than the inverse of any

polynomial. Thus, the Fourier transform of the system response  $Y(\Omega) = (\mathcal{F}y)(\Omega)$  will contain the  $x(t)$  frequency components near  $\Omega = 0$ , but they will be suppressed by the product with the Gaussian  $G(\Omega)$ . This idea is basic to all low-pass filtering.

Now we also gain a deeper understanding of scale space analysis, introduced in Chapter 4. Recall that we showed that smoothing signals by ever broader Gaussian kernels had the unique property that no structure was created in the process. We understand signal structure to be determined by the concavity regions within the signal. Now (9.80) shows that the wider kernels are actually low-pass filters with smaller passbands. That is, the wider kernels progressively remove the high-frequency components, leaving relatively lower frequency undulations, and—more importantly—not creating additional changes in signal curvature.

A particularly important area of signal analysis is the detection, classification, and recognition of signal features that vary according to the size of their features—according to their *scale*, for instance.

**9.5.2.3 Rational Functions.** We can find other examples based on rational functions. For example, suppose  $H(\Omega) = (1 + \Omega^2)^{-1}$ . The inverse Fourier transform is

$$h(t) = \frac{1}{2\pi} \int_{-\infty}^{\infty} H(\Omega) e^{j\Omega t} d\Omega = \frac{e^{-|t|}}{2}, \quad (9.81)$$

which is easy to see from the forward radial transform  $\mathcal{F}(\exp(-a|t|)) = 2a/(a + \Omega^2)$ . Evidently, convolution with  $h(t)$  performs a weighted averaging on input signal data. In signal analysis applications, the pulse  $h(t)$  is often called a Lorentzian, and it is used to find peaks, valleys, and transients in general by the method of template matching.

**9.5.2.4 Better Low-Pass Filters.** It turns out that very good filters can be built by pursuing the idea of rational functions introduced in the previous example. The important features of such filters are as follows:

- They have superior cutoffs—sharper and more like perfect low-pass filters.
- Upon discrete conversion, they will be causal.
- They are stable.
- They have efficient implementations, relying on difference equations.

For signal analysis applications involving real-time data, such as in speech recognition or industrial control applications, causality is important. Of course, many signal analysis applications do not involve real-time data; that is, they are offline applications, and so causal systems are less critical. Nonetheless, very good filters can be developed for data whose discrete values are only known for the present and past.

### 9.5.3 Butterworth

*Butterworth*<sup>12</sup> filters have maximally flat pass and stop bands. Thus, the filter designer that values, above all else, reduced pass- and stop-band ripple inclines toward this filter.

**9.5.3.1 Conditions for Optimally Flat Filters.** We describe these filters via their frequency-domain representation. Their Fourier transforms are based on rational functions—quotients of continuous domain polynomials. The Butterworth filter specializes the rational function by looking at the Taylor series representations of its numerator and denominator.

Indeed, we have already constructed lowpass filters out of rational functions. The idea is to look at analog filters  $h = H\delta$ , such that their Fourier transform power spectra  $|H(\Omega)|^2$  are rational functions  $B(\Omega)/A(\Omega)$ , where  $A(\Omega)$  and  $B(\Omega)$  are polynomials. We impose conditions on the rational functions so that we achieve our design criteria: passband performance, stopband performance, cutoff frequency, allowable ripple, and required transition band sharpness. Significantly, for signal analysis on digital computers, when the power spectrum of an analog filter is a rational function, then it can be used to derive a discrete filter.

A simple but useful fact is that if  $h(t) \in \mathbb{R}$ , then the squared magnitude spectrum  $|H(\Omega)|^2$  is an even function of  $\Omega$ . To see this, note that Fourier transform symmetry properties imply  $H(-\Omega) = H^*(\Omega)$ . So  $|H(\Omega)|^2 = H(\Omega)H^*(\Omega) = H(\Omega)H(-\Omega)$ . But then  $|H(-\Omega)|^2 = H(-\Omega)H^*(-\Omega) = H(-\Omega)H(\Omega)$  too.

We thus consider  $P(\Omega) = |H(\Omega)|^2 = B(\Omega)/A(\Omega)$ , such that  $P(\Omega)$  is symmetric about  $\Omega = 0$ . This means  $A(\Omega)$  and  $B(\Omega)$  are polynomials in  $\Omega^2$  (exercise). Thus,

$$A(\Omega) = a_0 + a_2\Omega^2 + a_4\Omega^4 \dots + a_{2N}\Omega^{2N}, \quad (9.82a)$$

$$B(\Omega) = b_0 + b_2\Omega^2 + b_4\Omega^4 \dots + b_{2M}\Omega^{2M}, \quad (9.82b)$$

with  $a_0 = b_0$ . We may assume that  $a_0 = b_0 = 1$ . A low-pass filter implies  $|H(\Omega)| \rightarrow 0$  as  $|\Omega| \rightarrow \infty$ , so  $N > M$ . For the filter stopband to be maximally flat as  $\Omega \rightarrow \infty$ , the maximal number of numerator terms in (9.82b) should be zero. Thus,  $b_2 = b_4 = \dots = b_{2M} = 0$ , and we see

$$P(\Omega) = |H(\Omega)|^2 = \frac{1}{A(\Omega)} = \frac{1}{1 + a_2\Omega^2 + a_4\Omega^4 \dots + a_{2N}\Omega^{2N}}. \quad (9.83)$$

Butterworth criteria also require the filter's passband to be maximally flat at  $\Omega = 0$ , which entails  $a_2 = a_4 = \dots = a_{2n-2} = 0$ . We define the cutoff frequency  $\Omega_c$  of the

<sup>12</sup>After S. Butterworth, a British engineer who first analyzed this response profile ["On the theory of filter amplifiers," *Wireless Engineer*, vol. 7, pp. 536–554, 1930]. V. D. Landon later described this same filter as *maximally flat* [Cascade amplifiers with maximal flatness, *RCA Review*, vol. 5, pp. 347–362, 1941].

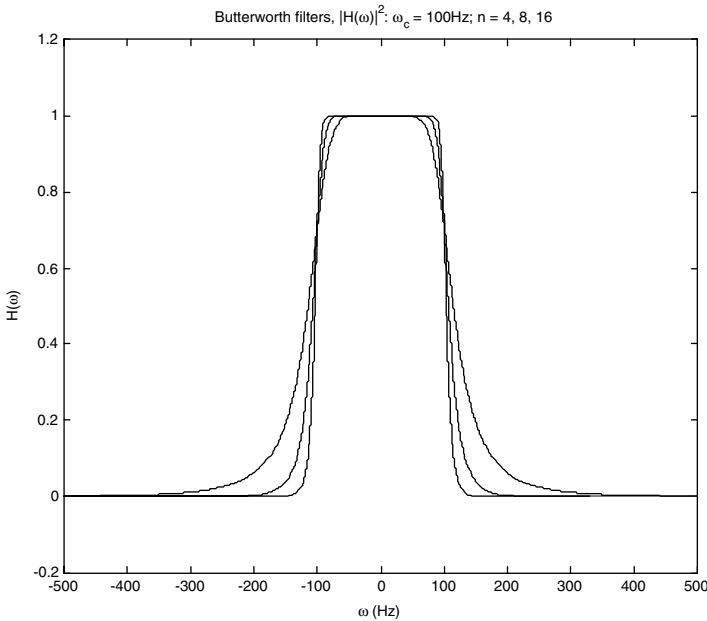


**Fig. 9.30.** Analog Butterworth filters for a few orders.

Butterworth filter by  $(\Omega_c)^{-2n} = a_{2n}$ . Thus, the *Butterworth filter* of order  $N > 0$  is defined by its Fourier transform  $H(\omega)$  (Figure 9.30):

$$H(\Omega) = \frac{1}{\sqrt{1 + \left(\frac{\Omega}{\Omega_c}\right)^{2N}}}; \tag{9.84}$$

an important next step in practical implementation is to decide which square roots to choose for  $H(\Omega)$  in (9.84). Note that  $H(\Omega_c) = 2^{-1/2} \approx 0.707$ , for any filter order.

It is possible to invert the Butterworth filter Fourier transform  $H(\Omega)$ , truncate the impulse response  $h(t)$ , and then sample the result. As we have observed, this would induce some errors due to aliasing into the final filtering result. The filter designer might reduce these errors by preserving a large number of discrete samples. But this necessitates a time-consuming convolution operation. It turns out, however, that because a Butterworth filter has a rational Fourier transform, an efficient discrete implementation is possible using difference equations.

Now let us turn to the approximation problem for the Butterworth filter. The procedure differs depending on how the designer performs conversion from the analog to discrete filter form: impulse invariance or bilinear transformation.

**9.5.3.2 Butterworth Approximation: Impulse Invariance.** Given bounds on how far the filter’s magnitude spectrum can stray from the ideal passband and

stopband, the Butterworth filter approximation finds two parameters: the filter order  $N > 0$  and the radial cutoff frequency  $\Omega_c$  in (9.84). Suppose that we require a discrete low-pass Butterworth filter with unit DC gain:  $|H(\omega)| = 1$  for  $\omega = 0$ , where  $H(\omega)$  is the DTMF of the filter impulse response  $h(n)$ . We assume that the sampling frequency is high enough so that aliasing of  $H_a(\Omega)$ , the filter's (radial) Fourier transform, is not an issue. *This allows us to use the analog filter's magnitude response in the design approximation.*

Suppose that the passband is  $|\Omega| < \Omega_p$  and the application requires that  $|H_a(\Omega)|$  is within  $\delta > 0$  of unity. Suppose the stopband begins at  $\Omega_s > \Omega_p$ , and we need  $|H_a(\Omega)|$  to be within  $\lambda > 0$  of zero. The Butterworth magnitude response is monotone; it suffices to consider the dual constraints:

$$|H(\Omega_p)| = \frac{1}{\sqrt{1 + \left(\frac{\Omega_p}{\Omega_c}\right)^{2N}}} \geq 1 - \delta \approx 1, \quad (9.85a)$$

$$|H(\Omega_s)| = \frac{1}{\sqrt{1 + \left(\frac{\Omega_s}{\Omega_c}\right)^{2N}}} \leq \lambda \approx 0. \quad (9.85b)$$

Filter designers often prefer approximation by differences in decibels. Thus, we say the passband magnitude (dB) is greater than a small negative value ( $\Delta$ ) and the stopband magnitude (dB) is less than a large negative value ( $\Lambda$ ):

$$0 > 10 \log_{10} |H(\Omega_p)|^2 \geq \Delta, \quad (9.86a)$$

$$10 \log_{10} |H(\Omega_s)|^2 \leq \Lambda < 0. \quad (9.86b)$$

The above constraints reduce to

$$1 + \left[\frac{\Omega_p}{\Omega_c}\right]^{2N} \leq R_\Delta = 10^{-\frac{\Delta}{10}} \approx 1, \quad (9.87a)$$

$$1 + \left[\frac{\Omega_s}{\Omega_c}\right]^{2N} \geq R_\Lambda = 10^{-\frac{\Lambda}{10}} \gg 1, \quad (9.87b)$$

but (9.85a) and (9.85b) give similar relations too. Let  $R = \frac{\log(R_\Delta - 1)}{\log(R_\Lambda - 1)}$  so that solving for  $\Omega_c$  gives

$$\log \Omega_c = \frac{R \log \Omega_s - \log \Omega_p}{R - 1}. \quad (9.88)$$

At this point, the filter designer makes choices. We can use (9.87a) to find the Butterworth filter order

$$v = \frac{\log(R_\Delta - 1)}{2\log\left(\frac{\Omega_p}{\Omega_c}\right)}, \quad (9.89)$$

which will generally not be a whole number. Designers usually round the order upward, taking the Butterworth order  $N$  to be the *integral ceiling* of  $v$  in (9.89)—the integer greater than  $v$ , or  $\text{Ceil}(v)$ . Using equality in either (9.87a) or (9.87b), the cutoff frequency must be recomputed. For instance, setting

$$\Omega_{c,N} = \frac{\Omega_p}{2N\sqrt{R_\Delta - 1}} \quad (9.90)$$

establishes a new cutoff frequency based on the upwardly rounded order and the passband constraint. The resulting low-pass Butterworth filter satisfies the passband condition determined by  $\Omega_{c,N}$  and improves upon the stopband condition. This is a good approach for low sampling rates, when the aliasing caused by filter conversion using impulse invariance is a concern [7].

Alternatively, tight application timing constraints might force the designer to round down and choose a smaller  $N$ , the *floor* of  $v$  in (9.89). Perhaps  $N = \text{Floor}(v) \approx v$ , or deviation from the passband and stopband specifications is acceptable. The designer might also opt for a cutoff frequency that favors an exactly met stopband. Assuming that the filter order is rounded upward, the filter then meets a more stringent passband specification. The cost of this option is that it does not counteract the aliasing arising from impulse invariance. The exercises explore these design alternatives.

We determine the  $\omega_p$  and  $\omega_s$  (radians/sample) from the sampling rate  $F_s = 1/T$  and the application's specified analog passband and stopband frequencies (Hz).

**Example (DTMF Passband and Stopband Calculations).** Suppose we require a lowpass filter that removes high-frequency noise for the dual-tone multifrequency application of Section 9.1. Let the digital sampling rate be  $F_s = 8192$  Hz. Then discrete frequency  $\omega = \pm\pi$  corresponds to the Nyquist frequency of  $F_s/2 = 4096$  Hz. DTMF tones range up to 1633 Hz. Thus, the lowpass filter bands could be specified by setting  $\omega_p = (1633/4096) \times \pi \approx 0.3989\pi$ , and, depending upon the desired filter sharpness,  $\omega_s = (1800/4096) \times \pi \approx 0.4395\pi$ .

**Example (Butterworth impulse invariance approximation).** We require a low-pass filter with a passband within 1 dB of unity up to  $\omega_p = \pi/4$  and at least 5 dB below unity beyond  $\omega_s = \pi/3$ . Assume the sampling interval is  $T = 1$ . Thus, we require  $\Delta = -1$ , and  $\Lambda = -5$ . The approximation steps above give  $R_\Delta = 1.2589$ ,  $R_\Lambda = 3.1623$ , and  $R = -1.7522$ . The exact cutoff frequency for this example is  $\Omega_c = 0.9433$ , but we elect to round  $v = 3.6888$  upward to  $N = 4$ . Revising the cutoff frequency, we find  $\Omega_{c,N} = 0.9299$ .

**9.5.3.3 Poles and Zeros Analysis.** Let us continue the design of the Butterworth low-pass filter of order  $N > 0$  by factoring the denominator of the squared magnitude response. Indeed, many analog filters satisfy

$$P_H(\Omega) = |H(\Omega)|^2 = \frac{1}{1 + \left(\frac{\Omega}{\Omega_c}\right)^{2N}} = H(\Omega)H(-\Omega). \quad (9.91)$$

$P_H(\Omega)$  has  $2N$  poles in the complex plane. Let the roots of the denominator in (9.91) be  $\Omega_1, \Omega_2, \dots, \Omega_{2N}$ . In the case of the Butterworth squared magnitude, the roots lie on a circle of radius  $\Omega_c$  in the complex plane. They are in fact the order- $2N$  roots of unity scaled by the cutoff frequency  $\Omega_c$ . All we have to do to find  $H(\Omega)$  that satisfies (9.91) is to select one pole from each pair  $\{\Omega_i, -\Omega_i\} \subset \{\Omega_1, \Omega_2, \dots, \Omega_{2N}\}$ . But a judicious root selection allows us to construct a causal discrete filter governed by a difference equation and therefore having an efficient computer implementation. We can obtain a discrete difference equation from an analog filter that has a rational Fourier transform  $H(\Omega)$  only if its poles have positive imaginary parts (Section 9.2.5.5). (Equivalently, if we are working with the Laplace transform, because  $H(\Omega) = H_L(s)|_{s=j\Omega}$ , this means that the poles of  $H_L(s)$  must have negative real parts.) With causality and difference equation implementation in mind, we retain those roots,  $\Omega_1, \Omega_2, \dots, \Omega_N$ , such that

$$H(\Omega) = \frac{1}{(\Omega - \Omega_1)(\Omega - \Omega_2)\dots(\Omega - \Omega_N)}. \quad (9.92)$$

with  $\text{Imag}(\Omega_i) > 0$ .

Let the partial fractions expansion of (9.92) be

$$H(\Omega) = \sum_{i=1}^N \frac{c_i}{\Omega - \Omega_i}, \quad (9.93)$$

where  $c_i, 1 \leq i \leq N$ , are constants. The results of Section 9.2.5.5 give the corresponding discrete filter's transfer function:

$$H(z) = \sum_{i=1}^N T \frac{jc_i}{1 - e^{jT\Omega_i} z^{-1}}, \quad (9.94)$$

where  $T$  is the sampling interval. We generally compute  $\omega_p$  and  $\omega_s$  using the sampling interval, as explained in the previous section. Then, we derive the order  $N$  and the cutoff frequency  $\Omega_c$  from the Butterworth approximation. The poles and zeros analysis gives a Butterworth filter of order  $N$  with cutoff frequency  $\Omega_c$ , no matter what sampling interval we choose; it is convenient to assume  $T = 1$ . It is usually necessary to scale the coefficients of the discrete filter's impulse response for unit DC gain. Let us see how this works by following through on the previous example.

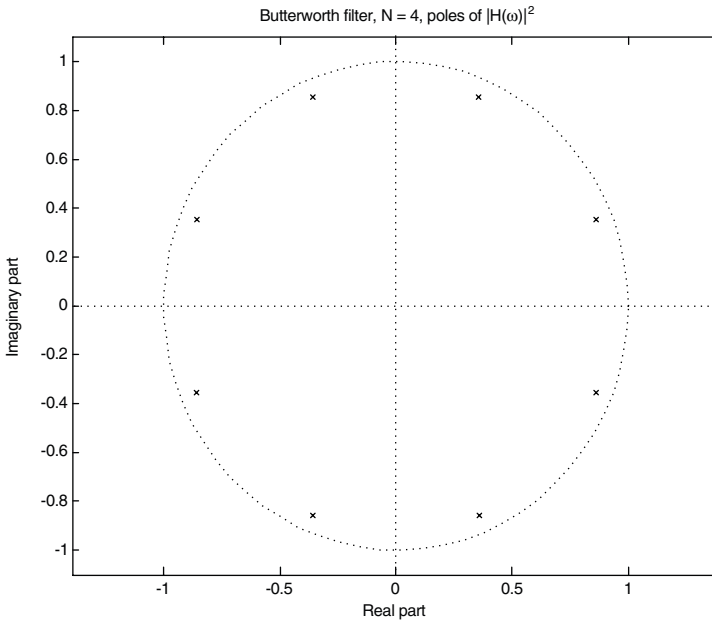


**Fig. 9.31.** Butterworth filter,  $N = 4$ , eight poles of  $|H(\Omega)|^2$ .

**Example (Butterworth impulse invariance design,  $N = 4$ ).** Suppose we require a lowpass filter with order  $N = 4$  and cutoff frequency  $\Omega_c = 0.9299$ , as in the previous example. Figure 9.31 shows the eight roots of the Butterworth squared magnitude function denominator. To find  $H(\Omega)$ , we select poles having a positive imaginary part. This selection corresponds to the poles of  $H_L(s)$  whose real parts are negative, because if  $\Omega_0$  is a pole of  $H(\Omega)$ , then  $H_L(j\Omega_0)$  is a pole of  $H_L(s)$  (Table 9.4).

**TABLE 9.4. Pole Selection in Butterworth Filter Design,  $N = 4$ ,  $\Omega_c = 0.9299$**

Poles of $ H(\Omega) ^2$	Fourier-Selected Poles	Poles of $ H_L(s) ^2$	Laplace-Selected Poles
$-0.8591 + 0.3559j$ $-0.8591 - 0.3559j$	$-0.8591 + 0.3559j$	$-0.3559 - 0.8591j$ $0.3559 - 0.8591j$	$-0.3559 - 0.8591j$
$-0.3559 + 0.8591j$ $-0.3559 - 0.8591j$	$-0.3559 + 0.8591j$	$-0.8591 - 0.3559j$ $0.8591 - 0.3559j$	$-0.8591 - 0.3559j$
$0.3559 + 0.8591j$ $0.3559 - 0.8591j$	$0.3559 + 0.8591j$	$-0.8591 + 0.3559j$ $0.8591 + 0.3559j$	$-0.8591 + 0.3559j$
$0.8591 + 0.3559j$ $0.8591 - 0.3559j$	$0.8591 + 0.3559j$	$-0.3559 + 0.8591j$ $0.3559 + 0.8591j$	$-0.3559 + 0.8591j$

Thus, performing the partial fractions calculations for  $H(z)$  gives

$$H(z) = T \left[ \frac{j(-0.2379 + 0.5745j)}{1 - e^{jT(-0.8591 + 0.3559j)} z^{-1}} + \frac{j(1.3869 - 0.5745j)}{1 - e^{jT(-0.3559 + 0.8591j)} z^{-1}} \right. \\ \left. + \frac{j(-1.3869 - 0.5745j)}{1 - e^{jT(0.3559 + 0.8591j)} z^{-1}} + \frac{j(0.2379 + 0.5745j)}{1 - e^{jT(0.8591 + 0.3559j)} z^{-1}} \right] \quad (9.95)$$

where  $T$  is the sampling interval. Writing  $H(z)$  as a quotient of polynomials in  $z^{-1}$ , we see that (9.46) becomes

$$\frac{\sum_{m=0}^M b_m z^{-m}}{\left[ 1 + \sum_{k=1}^N a_k z^{-k} \right]} = \frac{0.0873z^{-1} + 0.1837z^{-2} + 0.0260z^{-3}}{1 + (-1.7091)z^{-1} + 1.3967z^{-2} + (-0.5538)z^{-3} + 0.0880z^{-4}}. \quad (9.96)$$

Now, finally, we can implement (9.95) with a cascade architecture and (9.96) with a Direct Form II. We can compute the impulse response  $h(n)$  as in Figure 9.32 by feeding a discrete impulse through either of the difference equation architectures or by using (9.68).

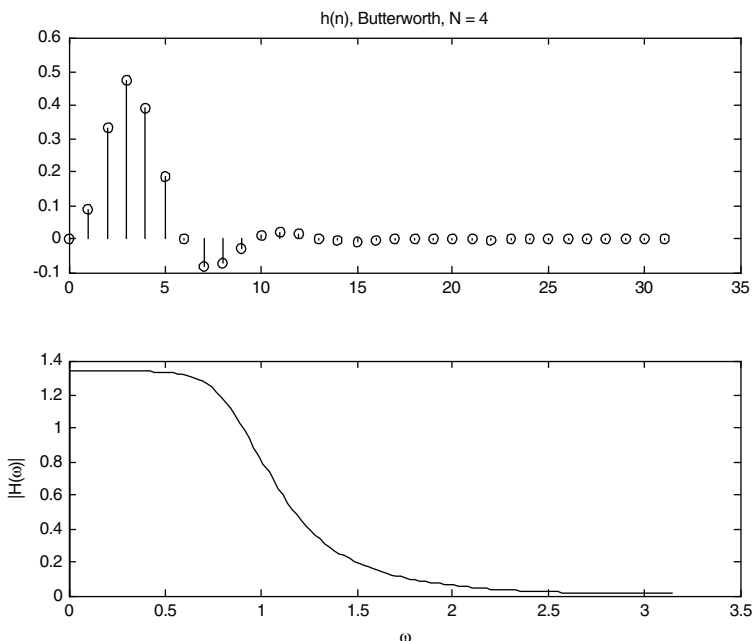


**Fig. 9.32.** Impulse response  $h(n)$  of Butterworth low-pass filter,  $N = 4$ ,  $\Omega_c = 0.9299$  (top), and magnitude response (bottom)  $|H(\omega)|$ . Note that  $H(0) \approx 1.3386$ , so for unit DC gain, we scale  $h(n)$  by  $(1.3386)^{-1}$ .

**9.5.3.4 Butterworth Approximation: Bilinear Transformation.** This section considers the Butterworth low-pass filter approximation using the bilinear transformation. The crucial difference in finding the filter order  $N$  and the cutoff frequency  $\Omega_c$  is the frequency mapping  $H(\omega) = H_a\left(\frac{2}{T}\tan\left(\frac{\omega}{2}\right)\right)$ . Here,  $H(\omega)$  is the DTMF of the desired discrete low-pass filter,  $T > 0$  is the sampling interval, and  $H_a(\Omega)$  is an analog Butterworth low-pass filter whose order  $N$  and cutoff frequency  $\Omega_c$  remain to be found.

Let us suppose specifications on the passband and stopband similar to those with which we began the impulse invariance approximation. Thus,

$$0 > 10\log_{10}|H(\omega_p)|^2 = 10\log_{10}\left|H_a\left(\frac{2}{T}\tan\left(\frac{\omega_p}{2}\right)\right)\right|^2 \geq \Delta, \quad (9.97a)$$

$$10\log_{10}|H(\omega_s)|^2 = 10\log_{10}\left|H_a\left(\frac{2}{T}\tan\left(\frac{\omega_s}{2}\right)\right)\right|^2 \leq \Lambda < 0, \quad (9.97b)$$

where  $\omega_p$  is the discrete passband frequency,  $\omega_s > \omega_p$  is the stopband frequency, and  $\Lambda < \Delta < 0$ . Applying the Butterworth filter condition as before, we calculate

$$\left[\frac{2}{T\Omega_c}\tan\left(\frac{\omega_p}{2}\right)\right]^{2N} \leq 10^{-\frac{\Delta}{10}} - 1 = R_\Delta - 1, \quad (9.98a)$$

$$\left[\frac{2}{T\Omega_c}\tan\left(\frac{\omega_s}{2}\right)\right]^{2N} \geq 10^{-\frac{\Lambda}{10}} - 1 = R_\Lambda - 1. \quad (9.98b)$$

We treat these as equalities and solve for the filter order:

$$v = \frac{\log\left(\frac{R_\Delta - 1}{R_\Lambda - 1}\right)}{2\log\left(\frac{\tan(\omega_p/2)}{\tan(\omega_s/2)}\right)} \quad (9.99)$$

where, in general,  $v$  is not an integer. Typically, we round  $v$  upward:  $N = \text{Ceil}(v)$ . We can use equality in either (9.98a) or (9.98b) to find  $\Omega_c$ . An advantage of bilinear transformation over impulse invariance is that there is no stopband aliasing. Thus, computing  $\Omega_c$  in terms of  $\omega_s$  gives

$$\Omega_c = \frac{2\tan(\omega_s/2)}{T}(R_\Lambda - 1)^{-\frac{1}{2N}}. \quad (9.100)$$

**Example (Butterworth Bilinear Transformation Approximation).** Suppose we require the same low-pass filter:  $\omega_p = \pi/4$ ,  $\omega_s = \pi/3$ ,  $\Delta = -1$ , and  $\Lambda = -5$ . Again,  $R_\Delta = 1.2589$ ,  $R_\Lambda = 3.1623$ , but we calculate  $v = 3.1957$  and choose  $N = 4$ . The exact analog cutoff frequency with  $T = 1$  is  $\Omega_c = 1.048589$ , corresponding to a discrete filter cutoff of  $\omega_c = 0.965788$ . Note that as  $v$  nears its integral floor—in this case  $v \approx 3$ —it might be feasible to round to the *lower* integral order. This could be useful when computing time is a consideration and some cushion exists for passband and stopband specifications.

Having derived the filter order  $N$  and the analog cutoff frequency  $\Omega_c$ , the rest of the bilinear filter design steps are the same as for impulse invariance.

**Example (Butterworth Bilinear Transformation Design,  $N = 4$ ).** For the low-pass filter with order  $N = 4$  and cutoff frequency  $\omega_c = 0.9658$ , as in the previous example, the analog cutoff frequency is  $\Omega_c = 1.0486$ , since  $\Omega_c = \frac{2}{T} \tan\left(\frac{\omega_c}{2}\right)$ . Of the eight poles of

$$|H_a(\Omega)|^2 = \frac{1}{1 + \left(\frac{\Omega}{\Omega_c}\right)^{2N}} = H_a(\Omega)_a H(-\Omega), \tag{9.101}$$

we select those having a positive imaginary part for  $H_a(\Omega)$ . The poles of the Laplace transform  $H_{L,a}(s)$  will thus have negative real parts (Table 9.5).

Thus, using the chosen poles (Table 9.5) the rational Laplace transform is

$$H(s) = \frac{1}{s^4 + 2.7401s^3 + 3.7541s^2 + 3.0128s + 1.2090}. \tag{9.102}$$

Substituting the bilinear transform relation  $s = \frac{2}{T} \left(\frac{z-1}{z+1}\right)$  with  $T = 1$  into (9.102) gives the discrete transfer function,

$$H(z) = \frac{0.0166z^4 + 0.0665z^3 + 0.0997z^2 + 0.0665z + 0.0166}{z^4 - 1.5116z^3 + 1.2169z^2 - 0.4549z + 0.0711}. \tag{9.103}$$

**TABLE 9.5. Pole Selection in Butterworth Filter Design Using Bilinear Transformation,  $N = 4$ ,  $\Omega_c = 0.9658$ .**

$ H_a(\Omega) ^2$ Poles	Fourier Poles Selected	$ H_{L,a}(s) ^2$ Poles	Laplace Poles Selected
$-0.9688 + 0.4013j$	$-0.9688 + 0.4013j$	$-0.4013 - 0.9688j$	$-0.4013 - 0.9688j$
$-0.9688 - 0.4013j$		$0.4013 - 0.9688j$	
$-0.4013 + 0.9688j$	$-0.4013 + 0.9688j$	$-0.9688 - 0.4013j$	$-0.9688 - 0.4013j$
$-0.4013 - 0.9688j$		$0.9688 - 0.4013j$	
$0.4013 + 0.9688j$	$0.4013 + 0.9688j$	$-0.9688 + 0.4013j$	$-0.9688 + 0.4013j$
$0.4013 - 0.9688j$		$0.9688 + 0.4013j$	
$0.9688 + 0.4013j$	$0.9688 + 0.4013j$	$-0.4013 + 0.9688j$	$-0.4013 + 0.9688j$
$0.9688 - 0.4013j$		$0.4013 + 0.9688j$	

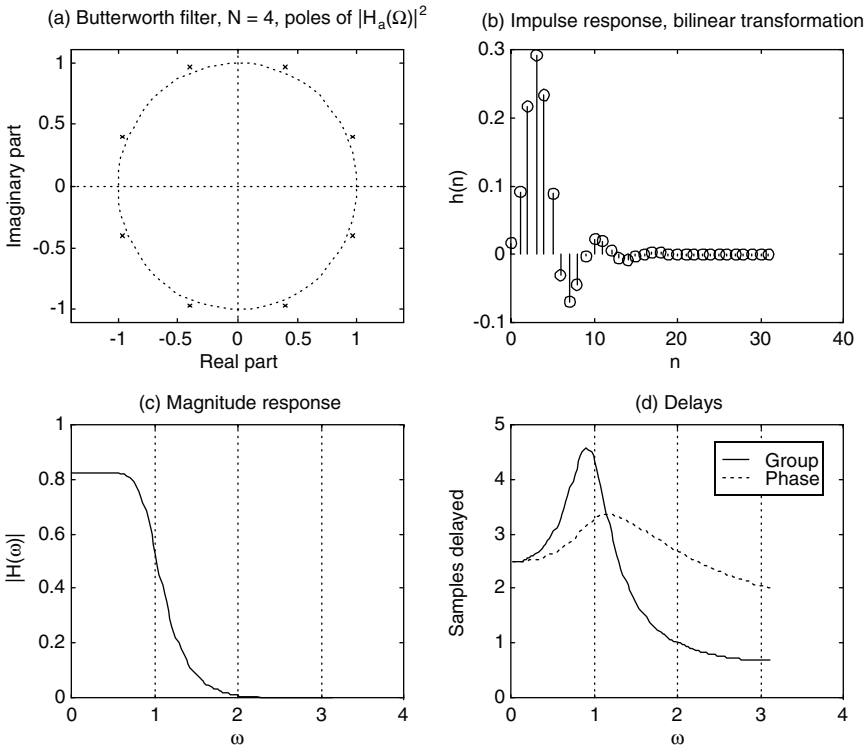


**Fig. 9.33.** Butterworth filter design, bilinear transformation. Pole locations for analog squared magnitude response (a). Impulse response  $h(n)$  of Butterworth low-pass filter,  $N = 4$ ,  $\omega_c = 0.9658$  (b) and (c) magnitude response  $|H(\omega)|$ . Note that  $H(0) \approx 0.8271$ , so for unit DC gain, we scale  $h(n)$  by  $(0.8271)^{-1} \approx 1.2090$ . Panel (d) shows the phase and group delay for this filter.

The partial fraction expansion of  $H(z) = B(z)/A(z)$  is

$$\begin{aligned} \frac{B(z)}{A(z)} = & \frac{-0.3048 + 0.1885j}{1 - (0.4326 + 0.5780j)z^{-1}} + \frac{-0.3048 - 0.1885j}{1 - (0.4326 - 0.5780j)z^{-1}} \\ & + \frac{0.1962 - 1.2480j}{1 - (0.3232 + 0.1789j)z^{-1}} + \frac{0.1962 + 1.2480j}{1 - (0.3232 - 0.1789j)z^{-1}} + 0.2337 \end{aligned} \quad (9.104)$$

The filter has a difference equation implementation (9.49), from which the impulse response follows (Figure 9.33b).

Note that it is possible to skip the approximation step, instead stipulating a discrete cutoff frequency  $\omega_c$  and guessing a filter order  $N > 0$ . After computing the associated analog cutoff  $\Omega_c$ , the above poles and zeros analysis follows. This step produces an impulse response  $h(n)$ , from which one can derive a Fourier magnitude response  $|H(\omega)|$ . Should the passband or stopband not meet the anticipated

constraints, the filter order is incremented and trial-and-error goes on. This is a good use case for a computerized filter design package.

Consider the group and phase delays of the above Butterworth low-pass filter. If  $H(\omega) = e^{j\phi(\omega)}H_R(\omega)$  is a filter's DTFT, where  $H_R(\omega) \in \mathbb{R}$ , and  $\phi(\omega)$  is its phase response, then its group delay is  $-d\phi(\omega)/d\omega$ . Since FIR filters enjoy linear phase (Section 9.3.6), their group delay is constant. Butterworth filters are IIR, so the group delay varies. In fact, Figure 9.33d illustrates that this system's group delay can change as much as four samples over the discrete frequency domain.

## 9.5.4 Chebyshev

Suppose a signal analysis application needs a low-pass filter with an especially sharp cutoff frequency, but tolerates some passband ripple. The Butterworth condition began by hypothesizing flatness in both the pass- and stopbands, so we need to relax one of these constraints. The first type of *Chebyshev*<sup>13</sup> filter approximation achieves a sharper transition than the Butterworth, but it does so at the cost of allowing passband ripple. On the other hand, the stopband is flat, and the designer can easily reduce the ripple to any positive value.

**9.5.4.1 Chebyshev Polynomials and Equiripple Conditions.** For the filter stopband to be maximally flat as  $\Omega \rightarrow \infty$ , any (rational) analog low-pass filter will have a squared Fourier magnitude response with a constant numerator (9.83). If we hope to improve upon the Butterworth filter's sharpness, we have to relax the Butterworth constraints. By the logic of the argument for maximally flat filters in Section 9.5.3.1, we must allow more  $a_{2k}$  to be nonzero. Let  $\varepsilon^2 T(\Omega) = A(\Omega) - 1$  be the nonconstant part of the denominator in (9.83), where  $\varepsilon > 0$  is a parameter controlling the passband ripple height. A low-pass filter with unity gain requires a denominator near unity when  $\Omega = 0$ , so let us stipulate that  $|T(\Omega)| \leq 1$  for  $|\Omega| \leq 1$ . Then a suitable  $\varepsilon$  can always make  $\varepsilon^2 T(\Omega)$  small for  $\Omega$  near zero. Since  $T(\Omega)$  is still a polynomial, its magnitude will get arbitrarily large as  $|\Omega| \rightarrow \infty$ , and so away from the origin,  $P(\Omega) \rightarrow 0$ . Are there such polynomials?

Indeed approximation theory provides us with precisely such polynomials. We set  $T(\Omega) = T_N(\Omega)$ , where  $T_N(\Omega)$  is the *Chebyshev polynomial* of order  $N \geq 0$  [43, 65]. These are defined recursively as follows:  $T_0(\Omega) = 1$ ,  $T_1(\Omega) = \Omega$ , and

$$T_{N+1}(\Omega) = 2\Omega T_N(\Omega) - T_{N-1}(\Omega). \quad (9.105)$$

The Chebyshev polynomials have nice properties, which are explored in the exercises and exploited by our filter designs. It can be shown that

$$T_N(\Omega) = \cos(N \cos^{-1}(\Omega)), \quad (9.106a)$$

<sup>13</sup>In addition to his work on orthogonal functions, Russian mathematician Pafnuty Lvovich Chebyshev (1821–1894) proved Bertrand's conjecture: For  $n > 3$ , there is at least one prime number between  $n$  and  $2n - 2$ .

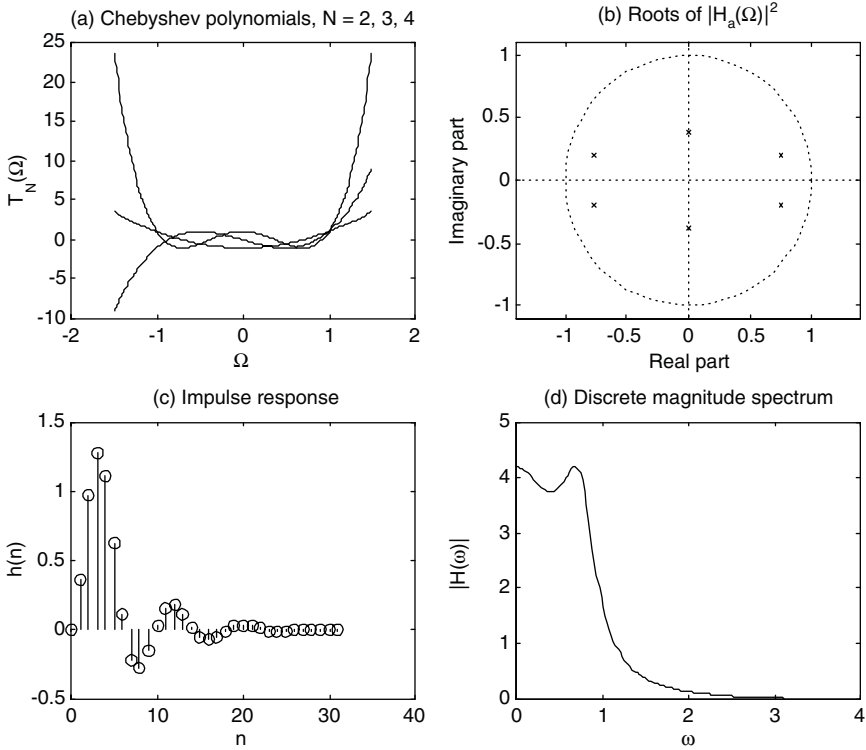


**Fig. 9.34.** Chebyshev polynomials for a few orders (a). Roots of the Fourier squared magnitude response for a third-order low-pass filter (b). Corresponding discrete impulse response (c) and magnitude spectrum (d).

so that indeed  $|T_N(\Omega)| \leq 1$  for  $|\Omega| \leq 1$ . Furthermore, the polynomials are orthogonal on  $[-1, 1]$ . Chebyshev polynomials are also given for  $|\Omega| > 1$  by the relation

$$T_N(\Omega) = \cosh(N \cosh^{-1}(\Omega)), \tag{9.106b}$$

as shown in Ref. 65 (see Figure 9.34).

Importantly for the filter approximation problem:

- If  $1 \leq N$  and  $\Omega \in [-1, 1]$ , then  $T_N(\Omega)$  oscillates between  $-1$  and  $+1$ .
- $T_N(\Omega)$  always achieves the minimum of  $-1$  and the maximum of  $+1$  on  $[-1, 1]$  (for this reason it is called the *equal ripple approximation*).
- $T_N(1) = 1$  for all  $N$ .
- For  $|\Omega| > 1$ ,  $T_N(\Omega)$  is strictly increasing or strictly decreasing.

Thus, the *Chebyshev squared magnitude response* is defined by

$$|H_a(\Omega)|^2 = \frac{1}{A(\Omega)} = \frac{1}{1 + \varepsilon^2 T_N^2(\Omega/\Omega_c)}. \tag{9.107}$$

**9.5.4.2 Impulse Invariance Approximation.** For the Chebyshev low-pass filter approximation using the impulse invariance transformation, we are given a discrete passband frequency  $\omega_p$ , a stopband frequency  $\omega_s$ , an allowable passband ripple, and a required stopband attenuation value. We seek the analog cutoff frequency  $\Omega_c$ , the filter order  $N$ , and the ripple parameter  $\varepsilon$  (9.107).

The Chebyshev polynomials' properties simplify the approximation.  $|T_N(\Omega/\Omega_c)|$  is strictly increasing for  $\Omega > \Omega_c$ , so we can set  $\Omega_c = \omega_p$ . If the passband constraint is  $10\log_{10}|H(\omega_p)|^2 \geq \Delta$ , for some  $\Delta < 0$  as in (9.86a), then the maximum departure from unity will occur for some  $-\Omega_c \leq \Omega \leq \Omega_c$ . Thus, we need  $\varepsilon \geq \sqrt{10^{-\Delta/10} - 1}$ . Here our design assumes that *ripple* is defined by the passband peak-to-valley difference. But some treatments assume that the ripple is half of this value—how far the passband magnitude strays from its mean [26]. So readers should be aware of the differences this assumption can make in the final design specifications. Finally, suppose the stopband specification (9.86b) is  $10\log_{10}|H(\omega_s)|^2 \leq \Lambda$ , for some  $\Lambda < 0$ , and the sampling rate is sufficiently high so that in the stopband,  $|\omega| > \omega_s$ ,

$$|H(\omega)|^2 \approx |H_a(\Omega)|^2 = \frac{1}{1 + [\varepsilon T_N(\Omega/\Omega_c)]^2}. \quad (9.108)$$

Thus, we seek  $N > 0$  such that

$$|H_a(\omega_s)|^2 = 10\log_{10}[1 + [\varepsilon T_N(\omega_s/\Omega_c)]^2]^{-1} \leq \Lambda. \quad (9.109)$$

We solve (9.109) as an equality for  $N$ ,

$$N = \frac{\cosh^{-1}\left(\frac{\sqrt{10^{-\Lambda/10} - 1}}{\varepsilon}\right)}{\cosh\left(\frac{\omega_s}{\Omega_c}\right)}, \quad (9.110)$$

and round upward to the nearest integer.

**Example (Chebyshev Impulse Invariance Approximation).** Suppose we try the Chebyshev approximation on a filter with the same specifications as in the Butterworth impulse invariance design (Section 9.5.3.2). We need a passband within 1 dB of unity for  $\omega < \omega_p = \pi/4$ . This means  $\Delta = -1$ ,  $\Omega_c = \pi/4$ , and  $\varepsilon = 0.5088$ . We need a stopband that is 5 dB or more below unity for  $\omega > \omega_s = \pi/3$ . We have  $\Lambda = -5$ , and (9.110) gives  $N = 2.1662$ , which we round up to  $N = 3$ . Thus, the Chebyshev approximation gives a third-order IIR filter, whereas the Butterworth approximation needed a fourth-order system—a benefit from allowing passband ripple.

**Example (Chebyshev Impulse Invariance design,  $N = 3$ ).** Let us continue the previous example:  $N = 3$ ,  $\Omega_c = \pi/4$ , and  $\epsilon = 0.5088$ . The poles of  $|H_a(\Omega)|^2$  are  $-0.7587 \pm 0.1941j$ ,  $0.7587 \pm 0.1941j$ , and  $\pm 0.3881j$ . They lie on an ellipse in the complex plane [26] as shown in (Figure 9.34b). To find  $H_a(\Omega)$ , we select the three poles with positive imaginary parts. (Equivalently, for the Laplace transform-based filter derivation, these are  $-0.1941 \pm 0.7587j$  and  $-0.3881$ .) Figure 9.34c shows the resulting impulse response. Figure 9.34d shows the discrete magnitude spectrum.

**9.5.4.3 Bilinear Approximation.** In a bilinear transformation,  $\Omega_c = 2 \tan\left(\frac{\omega_p}{2}\right)$  gives the cutoff frequency. The frequency mapping does not alter the passband ripple, so we can calculate  $\epsilon$  just as with impulse invariance. For the filter order, the stopband condition says

$$10 \log \left[ \left[ 1 + \left[ \epsilon T_N \left( \frac{2}{\Omega_c} \tan \left( \frac{\omega_s}{2} \right) \right) \right]^2 \right]^{-1} \right] \leq \Lambda, \tag{9.111}$$

which implies

$$N \geq \frac{\cosh^{-1} \left( \frac{\sqrt{10^{-\Lambda/10} - 1}}{\epsilon} \right)}{\cosh^{-1} \left( \frac{2}{\Omega_c} \tan \left( \frac{\omega_s}{2} \right) \right)}. \tag{9.112}$$

**Example (Chebyshev Bilinear Approximation).** Let us turn to the bilinear transformation method for the same filter design problem as above:  $\omega_p = \pi/4$ ,  $\omega_s = \pi/3$ ,  $\Delta = -1$ ,  $\Lambda = -5$ , with sampling interval  $T = 1$ . Thus,  $\Omega_c = 2 \tan\left(\frac{\omega_p}{2}\right) = 0.8284$ , using the bilinear frequency mapping. The ripple factor is  $\epsilon = 0.5088$ . Solving (9.112) as an equality gives  $N \approx 2.0018$ , but we opt for the integral ceiling, setting  $N = 3$ .

Note that for the present design criteria, the Chebyshev filter comes very close to reducing the required filter order to  $N = 2$ . In fact, unless the application parameters are unusually rigid, this is an attractive possibility. The lesson is twofold:

- For the same filter order the Chebyshev filter has faster (sharper) rolloff than the equivalent Butterworth filter.
- It is possible to achieve the same rolloff as the equivalent Butterworth filter using a Chebyshev filter with a smaller order.

For a quicker rolloff, the Chebyshev suffers some passband ripple. Its transient response is also worse than the Butterworth, as shown below (Section 9.5.4.5).

**Example (Chebyshev Bilinear Design,  $N = 3$ ).** Let us continue the above approximation:  $N = 3$ ,  $\epsilon = 0.5088$ , and  $\Omega_c = 0.8284$ . The poles of  $|H_a(\Omega)|^2$  are  $-0.8003 \pm 0.2047j$ ,  $0.8003 \pm 0.2047j$ , and  $\pm 0.4094j$  (Figure 9.35a). The Laplace transform poles of choice are therefore  $-0.2047 \pm 0.8003j$  and  $-0.4094$ . The analog system function is

$$H_{L,a}(s) = \frac{1}{s^3 + 0.8188s^2 + 0.8499s + 0.2793} \tag{9.113}$$

Inserting the bilinear map  $s = \frac{2}{T} \left( \frac{z-1}{z+1} \right)$  with  $T = 1$  into (9.113) gives

$$H(z) = \frac{0.0754z^3 + 0.2263z^2 + 0.2263z + 0.0754}{z^3 - 1.8664z^2 + 1.4986z - 0.4637} \tag{9.114}$$

$H(z)$  has partial fractions expansion

$$\begin{aligned} \frac{B(z)}{A(z)} = & \frac{-0.6458 - 0.1170j}{1 - (0.6031 + 0.5819j)z^{-1}} + \frac{-0.6458 + 0.1170j}{1 - (0.6031 - 0.5819j)z^{-1}} \\ & + \frac{1.5297}{1 - (0.6602)z^{-1}} - 0.1627. \end{aligned} \tag{9.115}$$

Figure 9.35 shows the impulse (b) and magnitude responses (c).

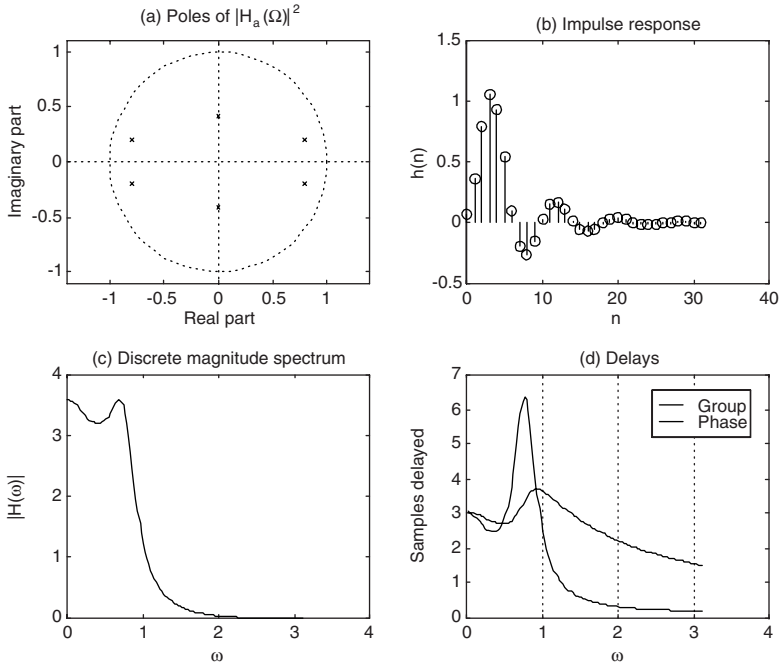


**Fig. 9.35.** Chebyshev low-pass filter, bilinear transformation. Pole locations (a), unnormalized discrete impulse response (b), magnitude response (c) and phase and group delay (d).

**9.5.4.4 Phase and Group Delay of IIR Filters.** Let us compare the group delay of Butterworth and Chebyshev filters. Figure 9.35d shows that the group delay of the Chebyshev filter can be as much as six samples for  $\omega \in [0, \pi]$ —worse than the equivalent Butterworth design Figure 9.33d. This is one thing the Chebyshev filter gives up in order to improve its rolloff performance.

**9.5.4.5 Application: Transient Response Comparison.** The Chebyshev filter's better rolloff, compared to the maximally flat filter, also costs it some transient response performance. To see this, let us consider a basic transient filtering application. Observe first that the Chebyshev filter exhibits a sharper rolloff Figure 9.36a.

We apply the Butterworth and Chebyshev low-pass filters ( $N = 3$ ) developed in previous sections to the transient Figure 9.36b. The Chebyshev filter produces a longer delay and the ringing induced by the step edge persists for a longer time interval than with the Butterworth. On the other hand, the pulse's later sloped edge provokes only a little bad behavior from the Chebyshev filter Figure 9.36c.

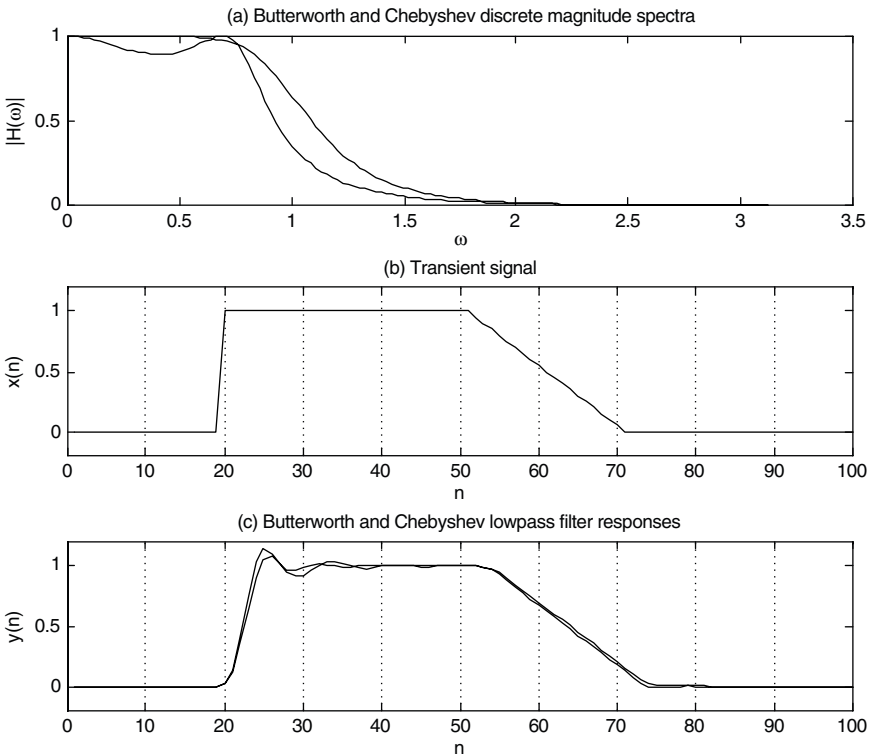


**Fig. 9.36.** Butterworth and Chebyshev comparison. Magnitude spectra (a), transient signal (b), and Butterworth and Chebyshev responses (c).

The following points should be taken into consideration when choosing the Chebyshev over the Butterworth filter for a signal analysis application:

- For less computational overhead with the same frequency discrimination performance, prefer the Chebyshev.
- If the frequencies in the filter passband will be further characterized by their relative strength, then the ripple in the Chebyshev becomes a detriment.
- If the application does not further analyze passband frequencies and is concerned with their mere presence or absence (such as in the DTMF application in Section 9.1) then the Chebyshev should be better.
- This is moreover the case when the application needs to segment relatively close bands of spectral information and sharp rolloff becomes a priority.
- Finally, if the time location of edges is important, and the application needs a crisp response from a crisp input edge to satisfactorily identify and locate the transition, then the Butterworth filter is superior.

### 9.5.5 Inverse Chebyshev

The inverse Chebyshev filter provides a flat passband and an equiripple stopband. This filter is also called the *Chebyshev Type II* filter.

**9.5.5.1 Stopband Equiripple Conditions.** The specification of the filter's squared magnitude response is based on the Chebyshev filter of Section 9.5.4 [26, 65]. The steps (Figure 9.37a) are as follows.

- (i) We begin with the Chebyshev squared magnitude response function

$$|H_a(\Omega)|^2 = \frac{1}{1 + \epsilon^2 T_N^2(\Omega/\Omega_c)} = P(\Omega), \quad (9.116)$$

where  $T_N(\Omega)$  is the order- $N$  Chebyshev polynomial.

- (ii) Subtract this response from unity,  $1 - P(\Omega)$ , to form the squared magnitude response of a high-pass filter having a flat passband and equiripple in the stopband.
- (iii) Reverse the frequency axis to find  $Q(\Omega) = 1 - P(\Omega^{-1})$ :

$$Q(\Omega) = 1 - \frac{1}{1 + \epsilon^2 T_N^2(\Omega_c/\Omega)} = \frac{\epsilon^2 T_N^2(\Omega_c/\Omega)}{1 + \epsilon^2 T_N^2(\Omega_c/\Omega)}, \quad (9.117)$$

which is the squared magnitude response of a low-pass filter. It has a maximally flat passband and puts the Chebyshev equiripple characteristic in the stopband.

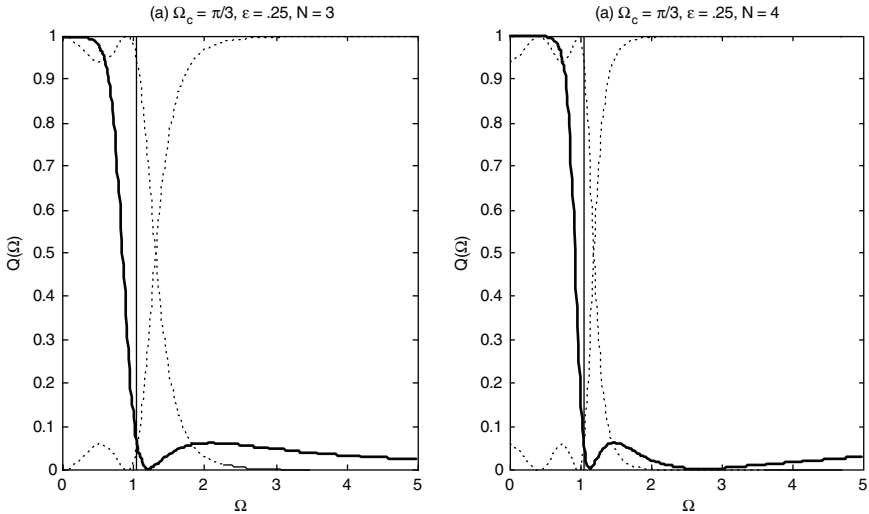


**Fig. 9.37.** Conversion from a Chebyshev to a third-order Inverse Chebyshev squared magnitude response function (a). The dotted traces are intermediate steps. The vertical line is  $\Omega_c$  from (9.117) and represents the stopband frequency. For comparison, panel (b) shows an  $N = 4$  squared magnitude response.

Note that  $Q(\Omega)$  is a rational function in  $\Omega^{-1}$ , but we can write it equivalently as a rational function of  $\Omega$ . The poles of  $Q(\Omega)$  are the reciprocals of the poles of  $P(\Omega)$  (exercise).

**9.5.5.2 Impulse Invariance Approximation.** Consider the impulse invariance approximation for the inverse Chebyshev low-pass filter. Suppose the discrete passband frequency is  $\omega_p$ , the stopband frequency is  $\omega_s$ , the passband is within  $\Delta < 0$  (dB) of unity, and the stopband ripple (dB) does not exceed  $\Lambda < \Delta < 0$ . We need the analog stopband frequency  $\Omega_c$ , the filter order  $N$ , and the ripple parameter  $\epsilon$  (9.117).

As remarked above, the parameter  $\Omega_c$  in (9.117) specifies the analog stopband. So, although for an ordinary Chebyshev filter we took  $\Omega_c = \omega_p$ , now we set  $\Omega_c = \omega_s$ . The stopband condition is  $10\log_{10}Q(\Omega) \leq \Lambda$  for  $\Omega \geq \Omega_c$ . But as long as  $\Omega \geq \Omega_c$  we have  $\Omega_c/\Omega \leq 1$  and so  $1 + \epsilon^2 T_N^2(\Omega_c/\Omega) \leq 1 + \epsilon^2$ . Hence, we can determine the stopband ripple factor  $\epsilon$  from the stopband condition with  $\Omega = \Omega_c$ :  $10\log_{10}Q(\Omega_c) \leq \Lambda$ . Using the elementary Chebyshev polynomial property,  $T_N(1) = 1$  for all  $N \geq 0$ , this reduces to

$$\epsilon \leq \sqrt{\frac{10^{\Lambda/10}}{1 - 10^{\Lambda/10}}}. \tag{9.118}$$

Observe that the ripple parameter does not depend on the filter order. Typically, we solve (9.118) as an equality to obtain  $\varepsilon$ .

The passband condition gives the analog filter order. If the discrete sampling rate is high enough, this means that for  $\Omega < \omega_p < \omega_s = \Omega_c$  we can assume  $10\log_{10}Q(\Omega) \geq \Delta$ . for  $\Omega < \omega_p$ .  $Q(\Omega)$  is strictly increasing as  $\Omega \rightarrow 0$ . Thus, we know that the passband condition applied to  $\Omega = \omega_p$  is a worst case. The usual algebra boils this down to

$$\cosh\left[N \cosh^{-1}\left(\frac{\Omega_c}{\omega_p}\right)\right] = T_N\left(\frac{\Omega_c}{\omega_p}\right) \geq \frac{1}{\varepsilon} \sqrt{\frac{10^{\Delta/10}}{1 - 10^{\Delta/10}}}. \quad (9.119)$$

The familiar steps of taking (9.119) as an equality, solving for  $N$ , and rounding upward give the filter order.

**Example (Inverse Chebyshev, Impulse Invariance,  $N = 3$ ).** We require a low-pass filter with a passband within 1 dB of unity up to  $\omega_p = \pi/4$  and at least 5 dB below unity beyond  $\omega_s = \pi/3$ . Again, we see  $\Delta = -1$  and  $\Lambda = -5$  and assume  $T = 1$ . As above, we set  $\Omega_c = \omega_s = \pi/3$ . From (9.118) we find  $\varepsilon = 0.680055$ . Solving (9.119) as an equality produces  $N = 2.1662$ . This value we round up to  $N = 3$ . Since  $T_3^2(\theta) = 16\theta^6 - 24\theta^4 + 9\theta^2$ , it must be the case that

$$Q(\Omega) = \frac{16\Omega_c^6 - 24\Omega_c^4\Omega^2 + 9\Omega_c^2\Omega^4}{16\Omega_c^6 - 24\Omega_c^4\Omega^2 + 9\Omega_c^2\Omega^4 + \frac{\Omega^6}{\varepsilon^2}}, \quad (9.120)$$

where we have expressed  $Q(\Omega)$  in positive powers of  $\Omega$  (Figure 9.38a).

**9.5.5.3 Poles and Zeros Analysis.** Unlike the others we have already considered, this filter has finite zeros in the extended complex plane. For  $H_a(\Omega)$  we select the poles of  $Q(\Omega)$  which have positive imaginary parts. In general, among the zeros of a squared magnitude response function, we select one each of the numerator's conjugate roots.

**Example (Inverse Chebyshev, Impulse Invariance,  $N = 3$ ).** Let us continue with the poles and zeros analysis of the previous example, for which the squared magnitude response is given by (9.117). The poles of  $Q(\Omega)$  are  $\pm 2.5848j$ ,  $-1.0581 \pm 0.2477j$ , and  $1.0581 \pm 0.2477j$ . The selected Laplace transform poles are thus  $-2.5848$ ,  $-0.2477 - 1.0581j$ , and  $-0.2477 + 1.0581j$ . The zeros of  $Q(\Omega)$  are  $-1.1885 \pm 0.1276j$  and  $1.1885 \pm 0.1276j$ . They all have the same magnitude, so we can choose Laplace transform zeros to be  $-0.1276 - 1.1885j$ , and  $-0.1276 + 1.1885j$ . The poles and zeros plot for  $Q(\Omega)$  is shown in Figure 9.38b.

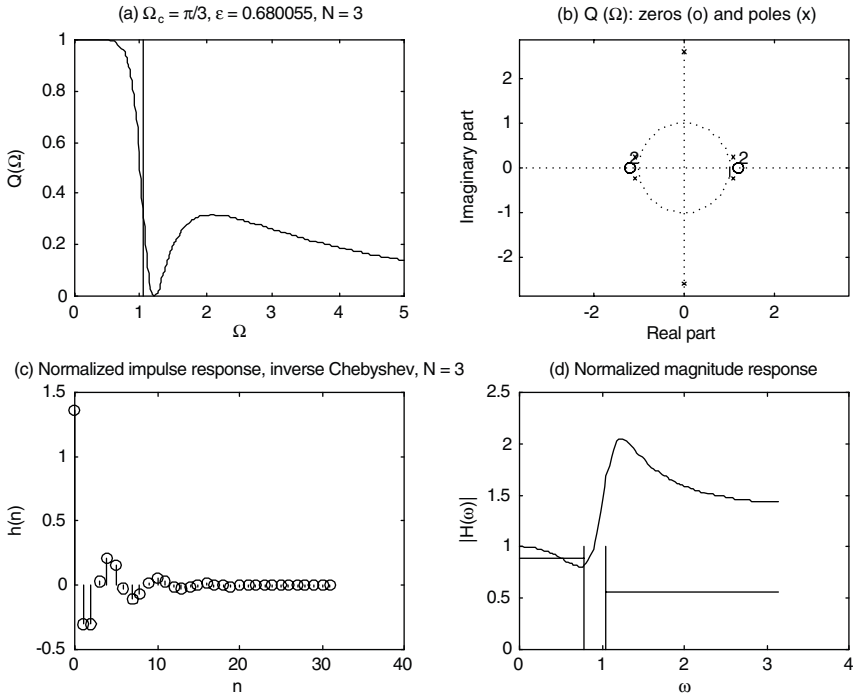


**Fig. 9.38.** The squared magnitude response  $Q(\Omega)$  for an  $N = 3$  analog filter approximated using the impulse invariance method (a). Associated poles and zeros (b), extracted discrete impulse response (c), and magnitude response (d). In panel (d), vertical lines mark the discrete passband and stopband,  $\pi/4$  and  $\pi/3$ , respectively. The horizontal lines are the level criteria associated with the  $\Delta$  and  $\Lambda$  parameters.

As a quotient of polynomials in  $z^{-1}$ , the discrete system function  $H(z)$  is thus given by

$$\frac{\sum_{m=0}^M b_m z^{-m}}{\left[ 1 + \sum_{k=1}^N a_k z^{-k} \right]} = \frac{1 - 0.7624z^{-1} + 0.6826z^{-2}}{1 + (-0.8412)z^{-1} + 0.6671z^{-2} + (-0.0460)z^{-3}} \quad (9.121)$$

Figure 9.38(c) shows the impulse response. Note that it consists of an impulse and some low magnitude correction terms.

The magnitude response Figure 9.38d shows the effect of the rather loose stopband ripple constraint for this example. The filter sharpness is adequate, as can be seen from the bounds in the figure. However, there are high frequencies present in the analog filter, because of the allowed stopband ripple. Because of impulse invariance sampling, aliasing occurs and the derived discrete magnitude response does

not satisfy the required stopband criterion. It might appear that increasing the sampling rate should reduce the aliasing. But unfortunately this causes the cutoff frequency of the analog filter to increase as well [7]. The best choice is to adjust the design parameters so as to meet the discrete filter's stopband criterion. The filter order may be increased, the ripple parameter may be reduced, or the bilinear approximation may be worthwhile.

**9.5.5.4 Bilinear Approximation.** Let us consider the bilinear approximation for the inverse Chebyshev low-pass filter. Suppose the discrete passband frequency is  $\omega_p$ , the stopband frequency is  $\omega_s$ , the passband is within  $\Delta < 0$  (dB) of unity, and the stopband ripple (dB) does not exceed  $\Lambda < \Delta < 0$ . We need the analog stopband frequency  $\Omega_c$ , the filter order  $N$ , and the ripple parameter  $\varepsilon$  (9.117) in order to specify the analog filter.

We know from our study of the inverse Chebyshev squared magnitude response that the  $\Omega_c$  parameter governs the analog stopband frequency. Thus,  $\Omega_c = \frac{2}{T} \tan\left(\frac{\omega_s}{2}\right)$  using the bilinear transformation. The passband and stopband conditions on the desired discrete filter are

$$0 > 10 \log_{10} |H(\omega)|^2 = 10 \log_{10} \left| Q\left(\frac{2}{T} \tan\left(\frac{\omega}{2}\right)\right) \right|^2 \geq \Delta, \quad (9.122a)$$

for  $\omega < \omega_p$ , and

$$10 \log_{10} |H(\omega)|^2 = 10 \log_{10} \left| Q\left(\frac{2}{T} \tan\left(\frac{\omega}{2}\right)\right) \right|^2 \leq \Lambda < 0, \quad (9.122b)$$

for  $\omega > \omega_s$ , where  $Q(\Omega)$  is the analog squared magnitude response (9.117). By Chebyshev polynomial properties,  $Q(\Omega)$  achieves its stopband maximum at the analog stopband value  $\Omega = \Omega_c$ . From (9.122b) we have  $\varepsilon \leq \sqrt{\frac{10^{\Lambda/10}}{1 - 10^{\Lambda/10}}}$ , as in the impulse invariance approximation (9.118). We assume an equality to compute the ripple parameter. In the passband constraint (9.122a) we use  $\Omega = \Omega_p = \frac{2}{T} \tan\left(\frac{\omega_p}{2}\right)$  as a worst case. This entails

$$T_N(\Omega_c/\Omega_p) = \cosh^{-1}[N \cosh(\Omega_c/\Omega_p)] \geq \frac{1}{\varepsilon} \sqrt{\frac{10^{\Lambda/10}}{1 - 10^{\Lambda/10}}}. \quad (9.123)$$

Changing this relation to an equality, solving for  $N$ , and rounding to the integral ceiling gives the filter order.

**Example (Inverse Chebyshev, Bilinear Approximation,  $N = 3$ ).** For a low-pass filter with a passband within 1 dB of unity for  $\omega < \omega_p = \pi/4$  and at least 5 dB of attenuation for  $\omega > \omega_s = \pi/3$ , we again have  $\Delta = -1$ ,  $\Lambda = -5$ . Let  $T = 1$  be the sample

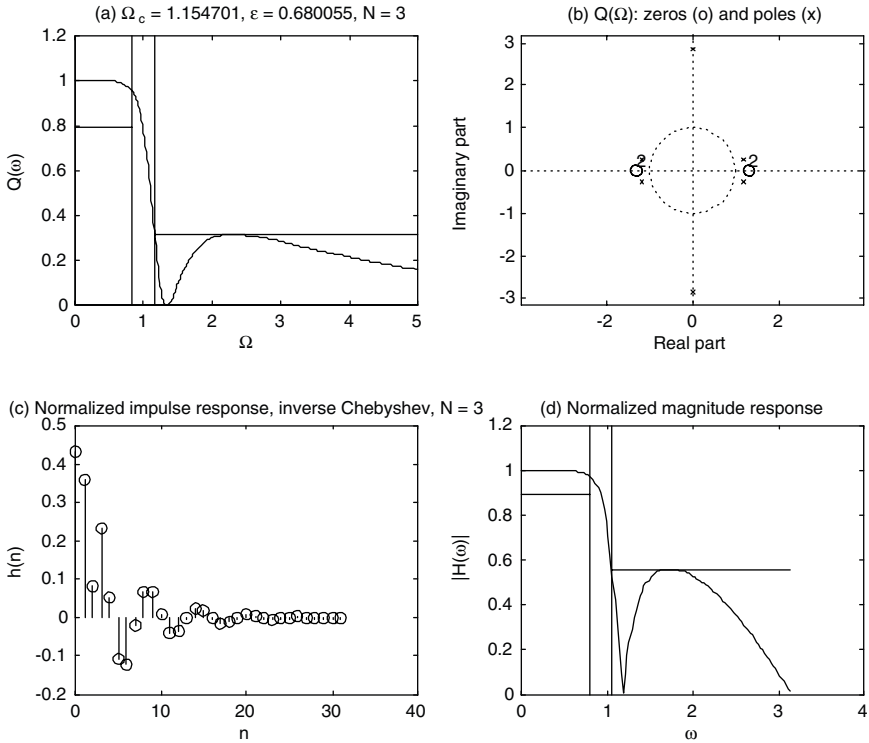


**Fig. 9.39.** The squared magnitude response  $Q(\Omega)$  for an  $N = 3$  analog filter approximated using the bilinear transformation method (a). Panel (b) shows the associated poles and zeros. Note that the zeros are second order. In (c), after normalization, is the impulse response. Finally, there is the normalized magnitude response (d). In panel (d), vertical lines mark the discrete passband and stopband,  $\Omega_p$  and  $\Omega_c$ , respectively. The horizontal lines are the level criteria associated with the  $\Delta$  and  $\Lambda$  parameters.

distance. We find  $\Omega_c = 2 \tan(\omega_s / 2) \approx 1.154701$  and  $\Omega_p \approx 2 \tan(\omega_p / 2) \approx 0.8284$ . Again, from (9.118) we get  $\epsilon = 0.680055$ . Solving (9.123) as an equality produces  $N = 2.0018$ , and although we are breathtakingly close to a second order filter, we prudently round up to  $N = 3$ . The three estimates,  $\Omega_c$ ,  $\epsilon$ , and  $N$ , give the squared magnitude response  $Q(\Omega)$  (Figure 9.39a).

**9.5.5.5 Poles and Zeros Analysis.** Among the poles of  $Q(\Omega)$ , we select those having positive imaginary parts to form  $H_a(\Omega)$ . After bilinear transformation, this filter too has finite zeros in the extended complex plane.

**Example (Inverse Chebyshev, Bilinear Transformation,  $N = 3$ ).** Let us wrap up the previous example. In the squared magnitude response (9.117). The poles of  $Q(\Omega)$  are  $\pm 2.8657j$ ,  $-1.1817 \pm 0.2550j$ , and  $1.1817 \pm 0.2550j$ . The good Laplace transform poles are thus  $-2.8657$ ,  $-0.2550 - 1.1817j$ , and  $-0.2550 + 1.1817j$ . The

zeros of  $Q(\Omega)$  are  $\pm 1.3333$  and each has order two. The Laplace transform zeros must be  $\pm 1.3333j$ . Figure 9.39b shows the poles and zeros plot for  $Q(\Omega)$ . Thus,

$$H_{L,a}(s) = \frac{s^2 + 1.7778}{s^3 + 3.3757s^2 + 2.9228s + 4.1881}. \quad (9.124)$$

Applying the bilinear map  $s = \frac{2}{T}[(z-1)/(z+1)]$  with  $T=1$  to (9.124) gives

$$H(z) = \frac{0.1832z^3 + 0.0423z^2 + 0.0423z + 0.1832}{z^3 - 0.6054z^2 + 0.5459z + 0.1219}. \quad (9.125)$$

The  $z$ -transform  $H(z)$  has partial fractions expansion

$$H(z) = \frac{-0.0821 - 0.0082j}{1 - (0.3917 + 0.7293j)z^{-1}} + \frac{-0.0821 + 0.0082j}{1 - (0.3917 - 0.7293j)z^{-1}} + \frac{-1.1551}{1 - (-0.1779)z^{-1}} + 1.5026 = \frac{B(z)}{A(z)}. \quad (9.126)$$

Feeding a discrete impulse  $\delta(n)$  through the difference equation implementation for (9.126) gives the unnormalized impulse response. This we scale (Figure 9.39c) by a factor of  $(0.4245)^{-1}$  so that the magnitude response has unit DC value, as shown in Figure 9.39d.

### 9.5.6 Elliptic Filters

The fourth common transfer function—the *elliptical*, or *Cauer*<sup>14</sup> (1958), filter—has ripple in both the passband and stopband, nonlinear phase response, and the fastest rolloff from passband to stopband for a given IIR filter order [26, 66, 67].

The squared magnitude response function for the elliptic or Cauer filter<sup>14</sup> is

$$|H_a(\Omega)|^2 = \frac{1}{1 + \varepsilon^2 R^2(\Omega)} = \frac{B(\Omega)}{A(\Omega)}, \quad (9.127)$$

where  $R(\Omega) = U(\Omega)/V(\Omega)$  is a rational function,  $\varepsilon > 0$  is a parameter,  $R(0) = 0$ , and the Degree( $U$ ) > Degree( $V$ ).

The rational function approximations (9.127) for the elliptic filter response are derived from the analytic properties of the Jacobi elliptic functions, which are encountered in the study of nonlinear oscillations. This oscillatory behavior gives rise to the passband and stopband ripple associated with the elliptic filter transfer function. Under certain conditions, the elliptic functions are qualitatively similar to

<sup>14</sup>German circuit theorist Wilhelm Cauer (1900–1945) invented and patented elliptic filters in the mid-1930s. While on his way to his office to get some papers, Cauer was arrested and executed by troops taking control of Berlin at the end of World War II. A short note on Cauer's life and accomplishments is given by A. Fettweis, Fifty years since Wilhelm Cauer's death, *IEEE Transactions on Circuits and Systems—I: Fundamental Theory and Applications*, vol. 42, no. 4, pp. 193–194, April 1995.

the trigonometric sine and cosine. But they have advanced general features which, when properly manipulated, give rise to better rolloff characteristics—for a given filter order—than the Chebyshev filter. Since the reader may have only minimal exposure to the elliptic functions, we will describe the analytical background for Cauer’s elliptic filter prescription prior to developing the rational function approximations implied by (9.127).

**9.5.6.1 Elliptic Functions and Integrals.** Just as the Chebyshev filter response had an analytic description in terms of the circular functions (e.g., (9.106a)), the general elliptic filter response,

$$|H_a(\Omega)|^2 = \frac{1}{1 + \varepsilon^2 R_N^2(\Omega)}, \tag{9.128}$$

can be described in terms of a class of analytic functions known as the *Jacobi elliptic sine*, designated  $sn(z, m)$ , where the parameter  $0 \leq m < 1$  is the modulus, and  $z \equiv u + jv$  is the argument, which may be complex-valued. The Cauer design calls for a function of the form

$$R_N(\Omega) = sn(f \cdot z + c, m), \tag{9.129}$$

where the argument consists of a factor  $f$ ; a constant additive offset  $c$ —both of which can be specified to give the desired filter response; and a variable  $z$  that is the inverse of a Jacobi elliptic sine,

$$z = sn^{-1}(\Omega/\Omega_c, m). \tag{9.130}$$

The *Jacobi*<sup>15</sup> *elliptic sine* of modulus  $m$  is defined by

$$sn(z, m) = \sin(\phi(z, m)). \tag{9.131}$$

The argument  $u$  is described by the *elliptic integral of the first kind*:

$$u(\phi, m) = \int_0^\phi \frac{1}{\sqrt{1 - m^2 \sin^2 \theta}} d\theta, \tag{9.132}$$

where the modulus is restricted to the interval  $0 \leq m < 1$ . The function  $\phi(u, m)$  the inverse of the  $u(\phi, m)$ , for fixed modulus  $m$ , and when we refer to a specific value we denote  $\phi$  as the amplitude of the elliptic integral [33]. For the special case of amplitude  $\phi = \pi/2$ , the elliptic integral of the first kind is a function only of the modulus and reduces to the *complete elliptic integral of the first kind* (Figure 9.40),

$$K(m) = \int_0^{\pi/2} \frac{1}{\sqrt{1 - m^2 \sin^2 \theta}} d\theta. \tag{9.133}$$

<sup>15</sup>Carl Gustav Jacobi (1804–1851), along with Gauss and Legendre, contributed to the early theory.

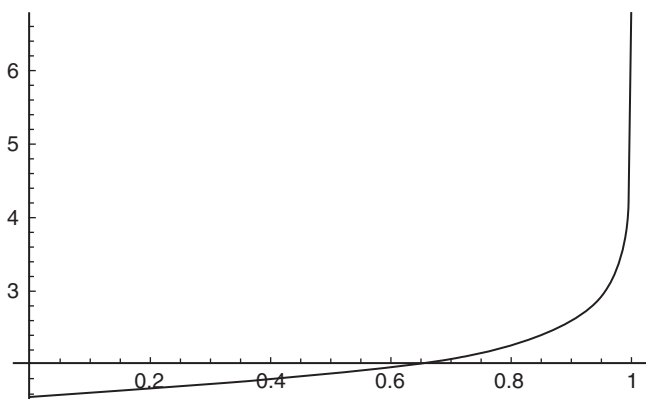


**Fig. 9.40.** The complete elliptic integral as a function of the modulus  $m$ . It is real-valued, but becomes singular as  $m \rightarrow \infty$ .

The complement to this integral is defined

$$K'(m) = \int_0^{\pi/2} \frac{1}{\sqrt{(1-m_1^2 \sin^2 \theta)}} d\theta, \quad (9.134)$$

where  $m_1 = 1 - m$ . (We follow the usual convention and denote the complement by a prime, but emphasize that it has nothing to do with differentiation.) From (9.134) it is obvious that

$$K(m_1) = K'(m) \quad (9.135)$$

and we will use these interchangeably.

In the real-valued interval  $x \in [0, \infty]$ , the Jacobi elliptic sine is qualitatively similar to a sine wave: It is real-valued, restricted in amplitude to the interval  $[-1, 1]$ , and exhibits oscillations which qualitatively resemble a pure sinusoid, as illustrated in Figure 9.41. As this illustration suggests,  $K(m)$  is one-fourth of a full period of the elliptic sine. For this reason it is also known as the *real quarter period*.

The Jacobi elliptic sine exhibits a richness that surpasses the simpler pure sinusoid. The most important new property is double periodicity,

$$\text{sn}(z + r \cdot 4K + s \cdot 4K', m) = \text{sn}(z, m), \quad (9.136)$$

where  $r$  and  $s$  are arbitrary integers. In Figure 9.42 and Figure 9.43 we illustrate the elliptic sine along other important intervals of the complex plane.

The validity of the Cauer's construction of the elliptic filter response is dependent upon the value of the Jacobi elliptic sine at several strategic points in the complex plane. For convenience, these points are listed in table Table 9.6. This table applies to both even- and odd-order elliptic filters.

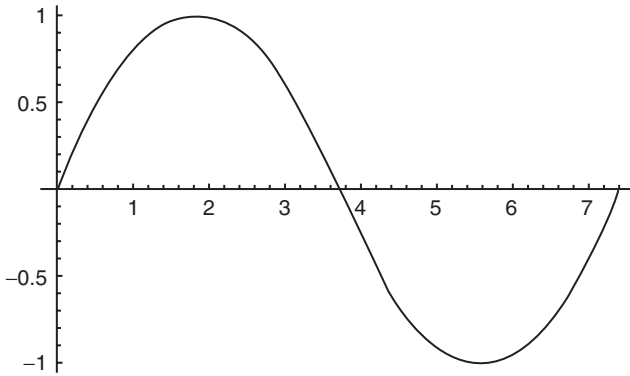


**Fig. 9.41.** The Jacobi elliptic sine  $sn(x, m)$  on the interval  $x \in [0, 4K]$ . The case  $m = 0.5$  is shown.

The foregoing illustrations were selected because they will aid in the understanding of Cauer's design of the elliptic filter response. Note that along these chosen intervals,  $sn(z; m)$  is real-valued, although the argument itself may acquire nonzero real and imaginary parts. Although excursions from the intervals selected here may result in generally complex values for  $sn(z; m)$ , Cauer's design conveniently limits us to these intervals in which the elliptic sine remains real-valued. With suitable manipulation of the free constants  $f$  and  $c$  in (9.129), we can ensure continuity of the response at the transition points between the pass- and stopbands. The third column in Table 9.6 gives the points in the frequency plane at which the conditions in the first two columns are applied. These issues are considered in the next section.

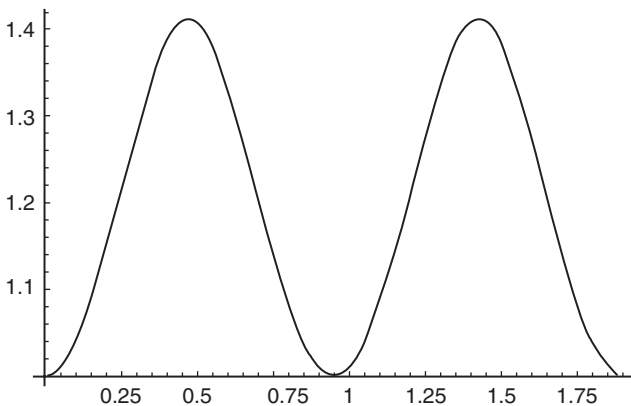


**Fig. 9.42.** The Jacobi elliptic sine  $sn(K + jy, m)$  on the interval  $y \in [0, 4K]$ . The case  $m = 0.5$  is shown.

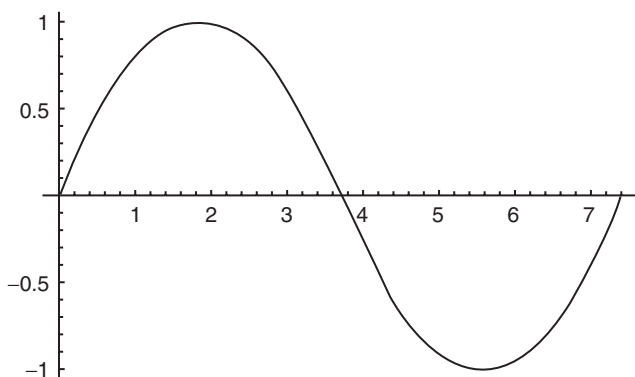


**Fig. 9.43.** The Jacobi elliptic sine  $sn(x + 4jK', m)$  on the interval  $x \in [0, 4K]$ , shown for  $m = 0.5$ .

**9.5.6.2 Elliptic Filter Response.** For the elliptic low-pass filter approximation using the impulse invariance transformation, we are given a discrete passband frequency  $\Omega_p$ , a stopband frequency  $\Omega_s$ , an allowable passband ripple, and a required stopband attenuation value. We seek the filter order  $N$  and the ripple parameter  $\epsilon$ . As in the case of the Chebyshev response, it is not possible to specify a specific set of parameters  $\{\Omega_p, \Omega_s, N, \epsilon\}$  that are identically satisfied by a low-pass elliptic filter response, but an allowable upper bound on the passband ripple and a lower bound on the stopband attenuation can be achieved, with both pass- and stopbands exhibiting a flat response.

The design of an elliptic filter response involves the specification of parameters  $m$ ,  $p$ , and integer  $N$  such that these specific acceptable bounds can be achieved. At the same time, the filter response must be continuous at  $\Omega = \Omega_p$  and  $\Omega = \Omega_s$  while also satisfying acceptable bounds at  $\Omega = 0$  and in the limit  $\Omega \rightarrow \infty$ . Continuity can be achieved by proper specification of the constants  $f$  and  $c$  (see (9.129)), while the proper bounds arise naturally from the behavior of the elliptic sine. The following relations are imposed by the design process and hold for arbitrary positive integer  $N$ . First,

$$m = \Omega_p^2 / \Omega_s^2 \tag{9.137}$$

**TABLE 9.6. The Argument  $z$  and the associated value of the Jacobi Elliptic Sine as the Frequency  $\Omega$  Traverses the Passband, Transition Band, and stopband of a Causer Elliptic Filter<sup>a</sup>**

$z$	$sn(z;m)$	$\Omega$
0	0	0
$\beta K(m)$	1	$\Omega_p$
$\beta K(m) \pm j\gamma K'(m)$	$m^{-1/2}$	$\Omega_s$
$\alpha K(m) \pm j\gamma K'(m)$	$\infty$	$\infty$

<sup>a</sup>The integer  $\alpha$  is even, the integers  $\beta$  and  $\gamma$  are odd.

which ensures that  $m \in [0, 1]$ , as required by the elliptic sine. Second, we define

$$f \equiv N \frac{K(p)}{K(m)} = \frac{K(p_1)}{K(m_1)}. \quad (9.138)$$

The second equality in (9.138) is imposed (it is not an identity) and gives the *flatness condition*,

$$N = \frac{K(m) K(p_1)}{K(p) K(m_1)}. \quad (9.139)$$

Since parameter  $m$  is specified by the filter rolloff in (9.137), and the order  $N$  of the filter is typically specified in advance, relation (9.139) amounts to a default specification of the unknown parameter  $p$ . We note that (9.139) must be satisfied to give identically flat pass- and stopband ripple. In practice, deviations from an integer lead to good flatness provided they are small, and we will find it necessary to finesse the pass- and stopband ripple levels  $a_1$  and  $a_2$  to achieve something close to (9.139).

The value of remaining unknown, namely the additive offset  $c$ , depends on whether the filter is of odd or even order. We will now consider these cases in turn. For *odd* filter order  $N$ , the design process will result in a filter response having the following general characteristics  $|H(\Omega/\Omega_p)|^2$  at selected critical frequencies:

$$|H(0)|^2 = 1, \quad (9.140)$$

$$|H(1)|^2 = \frac{1}{1 + a_1^2}, \quad (9.141)$$

$$|H(\Omega_s/\Omega_p)|^2 = \frac{1}{1 + a_2^2}, \quad (9.142)$$

$$|H(\infty)|^2 \rightarrow 0. \quad (9.143)$$

For filters of an *even* order  $N$ , the DC value of the response will be

$$|H(0)|^2 = \frac{1}{1 + a_1^2} \quad (9.144)$$

but the other three points are the same as given in (9.141)–(9.143). In an actual design problem, the real-valued parameters  $a_1$  and  $a_2$  will be specified according to the desired acceptable ripple and will be adjusted so as to leave the ripple within specified bounds while also providing a flat response in the pass- and stopbands.

*Remark.* Readers consulting further references on elliptic filter design may encounter alternative design procedures which result in a filter response with asymptotic

behavior which deviates from that specified in (9.140) and (9.143), especially when consulting prepackaged tables or routines. Unless otherwise noted, we confine ourselves to the limits defined here.

**Case of N Odd.** For an elliptic filter of odd order we stipulate

$$c = 0. \quad (9.145)$$

Consider the conditions at the stopband  $\Omega = \Omega_s$ , as laid out in Table 9.6. Expressing (9.29), we have

$$R_N(\Omega_s/\Omega_p) = sn\left(N\frac{K(p)}{K(m)} \cdot (K(m) + jK(m_1)), m\right), \quad (9.146)$$

where we have also used expression (9.135). After straightforward algebra this reduces to

$$R_N(\Omega_s/\Omega_p) = sn(NK(p) + jK(p_1), p) = 1/\sqrt{p}. \quad (9.147)$$

Similarly, the passband edge at  $\Omega = \Omega_p$  leads to

$$R_N(1) = sn(NK(p), p) = 1. \quad (9.148)$$

Substitution of (9.147) and (9.148) into the expression for the filter characteristics leads to the relations,

$$|H(\Omega_s/\Omega_p)|^2 = \frac{1}{1 + \left(\frac{\varepsilon}{p}\right)} = \frac{1}{1 + a_2^2} \quad (9.149)$$

and

$$|H(1)|^2 = \frac{1}{1 + \varepsilon} = \frac{1}{1 + a_1^2}. \quad (9.150)$$

Combining these lead to expressions for  $\varepsilon$  and the parameter  $p$  in terms of the pass- and stopband ripple:

$$\varepsilon = a_1^2, \quad (9.151)$$

$$p = \frac{a_1^2}{a_2}. \quad (9.152)$$

*Remark.* In the design of an elliptic characteristic for specified  $\Omega_p$  and  $\Omega_s$ , the essential relations are (9.139), (9.151), and (9.152). A successful design will involve juggling of  $a_1$  and  $a_2$  (within acceptable bounds) such that  $p$  from (9.152) will lead to close agreement with the flatness criterion (9.139). This can be done graphically utilizing packaged math routines, as we will do in the following example.

**Example (Cauer Elliptic Filter,  $N = 3$ ).** Consider a specification calling for the design of an  $N = 3$  elliptic filter with  $\Omega_p = 0.9$ ,  $\Omega_s = 1.39$ , a maximum passband ripple of  $-2.0$  dB, and a stopband ripple not exceeding  $-25.0$  dB. As a first pass, one can barely make the ripple tolerances by setting  $a_1 = 0.763$  and  $a_2 = 17.9$ , which lead to

$$10 \cdot \log[1/(1 + a_1^2)] = -1.99253, \tag{9.153}$$

$$10 \cdot \log[1/(1 + a_2^2)] = -25.0706. \tag{9.154}$$

However, the “integer” is given by

$$N = \frac{K(p_1)}{K(m_1)} \cdot \frac{K(m)}{K(p)} = 2.68387, \tag{9.155}$$

The effect of the deviation from the ideal value of 3 is to cause a departure from flatness, which is particularly notable in the stopband, as illustrated in Figure 9.44.

The problem can be alleviated by reducing the passband ripple such that  $a_1 = 0.445$  and

$$N = \frac{K(p_1)}{K(m_1)} \cdot \frac{K(m)}{K(p)} = 3.00271, \tag{9.156}$$

which is close to the ideal target of 3. The reduction in passband ripple required to achieve this exceeds 1 dB, since

$$10 \cdot \log[1/(1 + a_1^2)] = -0.784659. \tag{9.157}$$

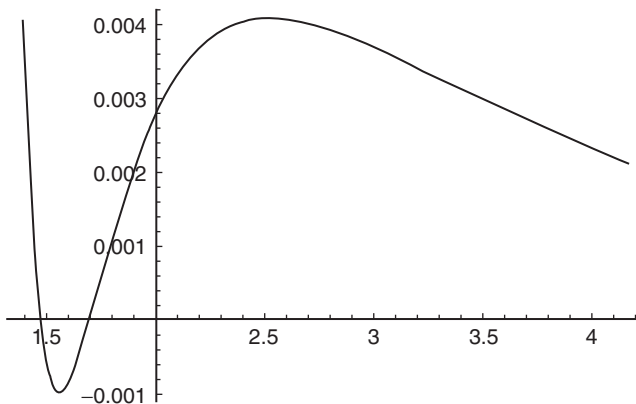


**Fig. 9.44.** Detail of the stopband response when the integer flatness condition is not met. Note that the characteristic becomes negative in a small region of the spectrum.

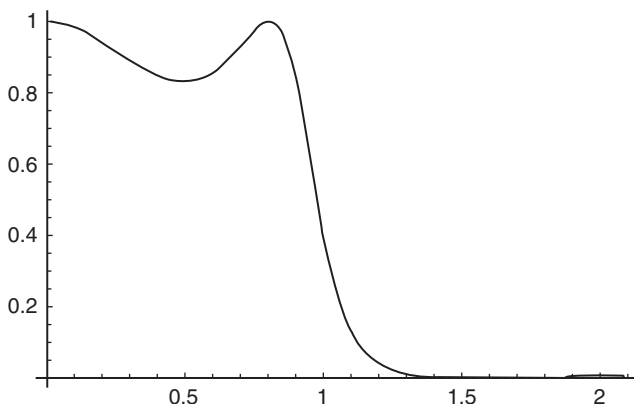


**Fig. 9.45.** The  $N = 3$  elliptic filter response after the parameters have been adjusted to obtain pass- and stopband flatness.

However, the result is the desired flat elliptic filter response representing (9.128), as shown in Figure 9.45.

*Remark.* In practice, deviations from the integer ideal  $N$  have the greatest effect on the stopband response. This includes the flatness, as noted, but even small deviations can induce a small imaginary part to  $H(\Omega)$ . When setting up a plot, it is useful to specify the real part to eliminate the small but unwanted imaginary component.

**Case of  $N$  Even.** For an elliptic filter of even order we apply a nonzero offset to the argument,

$$c = K(p). \quad (9.158)$$

At the passband edge  $\Omega = \Omega_p$  it is easy to show, since  $N + 1$  is an odd number,

$$R_N(1) = sn((N + 1)K(p), p) = 1. \quad (9.159)$$

Likewise, at the stopband edge,

$$R_N(\Omega_s/\Omega_p) = sn((N + 1)K(p) + iK(p_1), p) = 1/\sqrt{p}. \quad (9.160)$$

The effect of the nonzero offset (9.158) is to give edge conditions (9.159) and (9.160) identical to their counterparts in the odd-order case. The offset will have the effect of changing the elliptic filter response at zero frequency, but otherwise the even order characteristic resembles that of the odd-order case. These points are illustrated in the following example.

**Example (Cauer Elliptic Filter,  $N = 4$ ).** Consider the specifications laid out in the example for  $N = 3$ , but suppose we require faster rolloff by specifying  $\Omega_s = 1.12$ . By increasing the order of the filter to 4, and setting  $a_1 = 0.39$  and  $a_2 = 23.9$ , we obtain

$$10 \cdot \log[1/(1 + a_1^2)] = -0.614902, \quad (9.161)$$

$$10 \cdot \log[1/(1 + a_2^2)] = -27.5756, \quad (9.162)$$

and

$$N = \frac{K(p_1)}{K(m_1)} \cdot \frac{K(m)}{K(p)} = 4.01417, \quad (9.163)$$

which leads to a nominally flat response shown in Figure 9.46. Note that by increasing the order of the filter we have achieved the desired faster rolloff and brought the stopband ripple under the specification by more than 1.5 dB.

*Remark.* Note that the even-order elliptic response has the low-frequency limit,

$$|H(0)|^2 = \frac{1}{1 + a_1^2} = 0.86798. \quad (9.164)$$

This outcome is the legacy of the nonzero offset specified in (9.158): At  $\Omega = 0$ , the argument of the Jacobi elliptic sine is no longer zero, as it was in the odd-order construction.

### 9.5.7 Application: Optimal Filters

Finally, let us consider the problem of designing a filter that conditions a signal so that later processing preserves just the desired features of the input. To be more precise, suppose that an analog signal  $x(t)$  contains an original trend  $s(t)$  and an

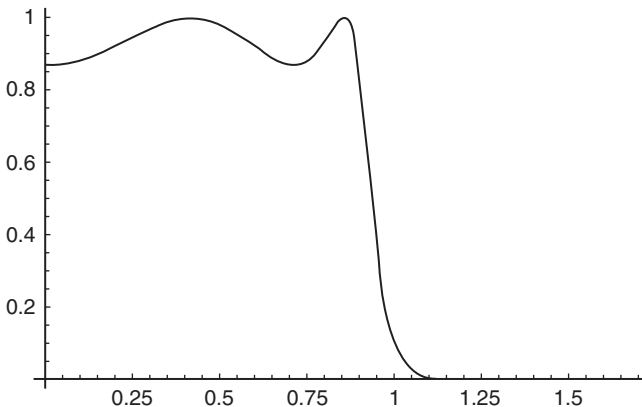


**Fig. 9.46.** The  $N = 4$  elliptic filter response. The result is flat in the pass- and stopbands.

unknown corrupting noise component  $n(t)$ :  $x(t) = s(t) + n(t)$ . The signal  $x(t)$  passes through a linear, translation-invariant system  $H$ ,  $y(t) = (Hx)(t)$ . Assume all signals are real-valued. We seek the best  $H$  with real impulse response  $h(t)$  so that  $(x*h)(t)$  is optimally close to  $s(t)$ .

Frequency-domain methods provide a solution: the *optimal* or *Wiener*<sup>16</sup> filter [68]. Arguing informally, let us use the  $L^2$  norm as a measure of how close  $y(t)$  is to  $s(t)$ . For an optimal noise removal filter, then, we seek to minimize

$$\|y - s\|^2 = \frac{1}{2\pi} \|Y - S\|^2 = \frac{1}{2\pi} \int_{-\infty}^{\infty} |S(\omega) - S(\omega)H(\omega) - H(\omega)N(\omega)|^2 d\omega, \quad (9.165)$$

where we have used Parseval's result and the convolution theorem for the radial Fourier transform (Chapter 5). The integrand on the right-hand side of (9.165) is

$$\begin{aligned} & S(\omega)\overline{S(\omega)}[1 - H(\omega)][\overline{1 - H(\omega)}] - \overline{H(\omega)N(\omega)}[1 - H(\omega)]S(\omega) \\ & - H(\omega)N(\omega)[\overline{1 - H(\omega)}]\overline{S(\omega)} + N(\omega)\overline{N(\omega)}H(\omega)\overline{H(\omega)}. \end{aligned} \quad (9.166)$$

The noise  $n(t)$  is random, so it is uncorrelated with  $s(t)$ , and integrating products involving their respective Fourier transforms gives zero:

$$\|y - s\|^2 = \frac{1}{2\pi} \int_{-\infty}^{\infty} (|S(\omega)|^2|1 - H(\omega)|^2 - |H(\omega)N(\omega)|^2) d\omega, \quad (9.167)$$

To find the minimum of  $\|y - s\|^2$ , we must minimize the integral in (9.167). Thus, we must minimize its integrand, and—arguing informally—the criterion for this is that the function  $f(H) = |S|^2|1 - H|^2 - |HN|^2$  has zero derivative. Taking the derivative with respect to  $H$  gives  $\frac{\partial f}{\partial H} = H[|S|^2 + |N|^2] - |S|^2$ . Setting  $\frac{\partial f}{\partial H} = 0$  and solving gives

$$H = \frac{|S|^2}{|S|^2 + |N|^2}, \quad (9.168)$$

which is the Fourier transform of the optimal or Wiener filter for removing noise from the signal  $x(t)$ .

## 9.6 SPECIALIZED FREQUENCY-DOMAIN TECHNIQUES

This section introduces and applies some signal analysis methods arising from Fourier transform theory.

<sup>16</sup>Although it had been developed in 1942, Wiener's optimal filter was made public only in 1949, when the first edition of Ref. 68 was published. The theory had remained classified during World War II, because of its application to radar.

### 9.6.1 Chirp-z Transform Application

In many applications, the frequencies of interest within candidate signals are known in advance of their processing. Such a priori information can simplify the design of the analysis system. For instance, instead of computing a broad range of spectral values using the discrete Fourier transform, the engineer may elect to compute only a small portion of the spectrum, namely that part that might contain useful signal information. One way to focus in on a spectral interval without computing large numbers of useless coefficients is the use the *chirp-z transform* (CZT), introduced in the previous chapter (Section 8.3.1).

Let us first recall the basic ideas of the CZT. The CZT computes  $z$ -transform on a spiral contour in the complex plane [11]. It is determined by two parameters:  $A$  and  $W$ —the spiral starting point and arc step, respectively. Via an example, we shall see how to apply it to zoom in on DFT frequency components. As in Chapter 8, we take the notation of Rabiner and Gold [11]. Suppose that  $A = A_0 \exp(2\pi j \theta_0)$ ;  $W = W_0 \exp(2\pi j \phi_0)$ ;  $M, N$  are positive natural numbers;  $x(n) = 0$  outside  $[0, N - 1]$ ; and  $z_k = AW^{-k}$  for  $0 \leq k < M$ . The chirp  $z$ -transform of  $x(n)$  with respect to  $A$  and  $W$  is

$$X_{A,W}(k) = \sum_{n=0}^{N-1} x(n) z_k^{-n} = \sum_{n=0}^{N-1} x(n) A^{-n} W^{nk}. \quad (9.169)$$

The exercises of Chapter 8 explained that the CZT reduces to the DFT of order  $N$  when  $A = 1$ ,  $M = N$ , and  $W = \exp(-2\pi j/N)$ .

Let us return to the speech fragment considered earlier, “calling” in a female voice. The fundamental frequency range of the /a/ phoneme for a woman is from about  $F_{lo} = 100$  Hz to  $F_{hi} = 400$  Hz. We would like to design a CZT detector for this spectral range and apply it to the digitized speech sample. From a manual segmentation of the speech sample in question (Figure 9.28), we know that the /a/ phoneme occurs from samples  $n = 800$  to  $n = 1200$ . It also degrades off into the /l/ sound immediately following.

To set up the CZT for this formant detection application, we set the sliding disjoint windows to consist of  $N = 400$  samples. The sampling frequency  $F_s = 8192$  Hz. Also,

$$A = \exp\left[\frac{2\pi j F_{lo}}{F_s}\right], \quad (9.170a)$$

$$W = \exp\left[-2\pi j \left(\frac{F_{hi} - F_{lo}}{NF_s}\right)\right]. \quad (9.170b)$$

Applying the algorithms of Chapter 8, we find the first six detection windows (Figure 9.47).

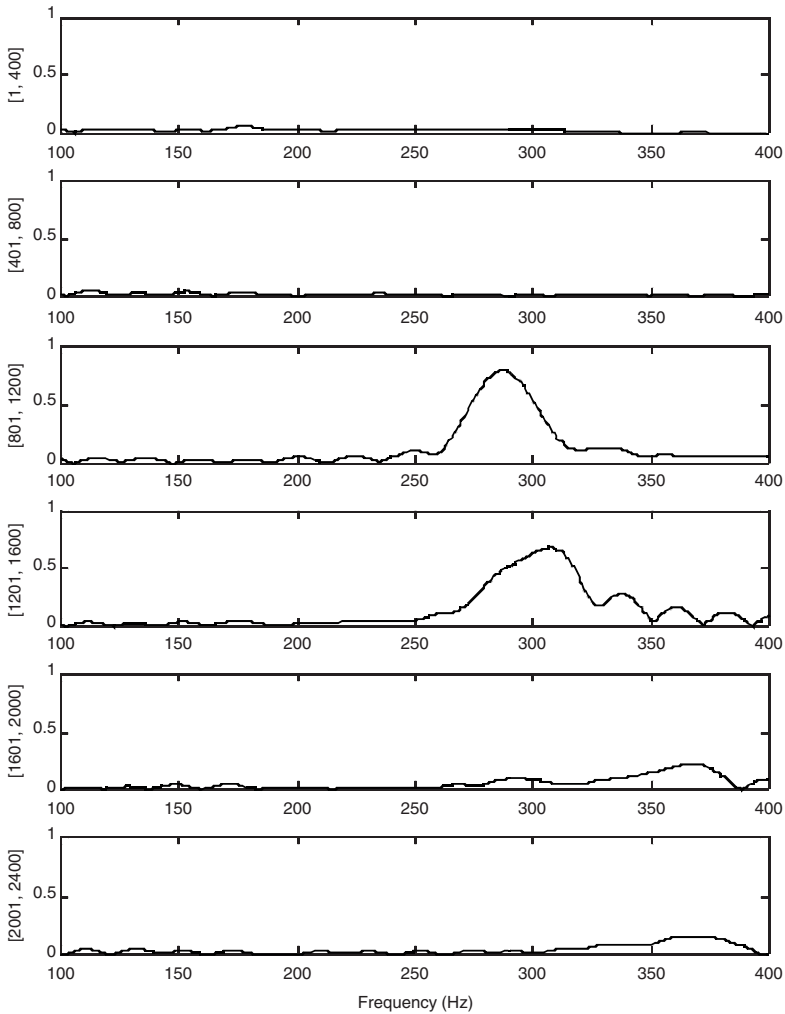


**Fig. 9.47.** Fundamental frequency detector for the /a/ phoneme based on the chirp- $z$  transform. A lone peak rises in the third window, which concurs with a manual segmentation of the speech sample.

### 9.6.2 Hilbert Transform

The Hilbert transform<sup>17</sup> is a powerful technique that can be used to:

- (i) Find the envelope of a signal.
- (ii) Find the instantaneous phase of a signal.

<sup>17</sup>David Hilbert originated the idea in his papers on integral equations, reprinted in the book *Grundzüge einer allgemeinen Theorie der linearen Integralgleichungen*, Leipzig and Berlin: Teubner, 1912.

- (iii) Find the instantaneous frequency of a signal.
- (iv) Suppress one of the sidebands in order to create a single sideband (SSB) modulation of a signal.

The Hilbert transform has rich theory and many interesting properties [7, 69, 70]. We shall skim the theoretical material and show how the transform works in another speech analysis application.

**9.6.2.1 Definition and Properties.** There are analog and discrete Hilbert transforms. The *analog Hilbert transform* of a signal  $x(t)$  is defined to be

$$x_H(t) = \frac{1}{\pi} \int_{-\infty}^{\infty} \frac{x(s)}{t-s} ds = (\mathcal{H}x)(t). \tag{9.171}$$

The integral, due to the singularity of its integrand at  $t = s$ , must be interpreted in a special way in order to make sense. The standard way to define the integral is by the Cauchy principal value [71]:

$$PV \int_{-\infty}^{\infty} \frac{x(s)}{t-s} ds = \lim_{\epsilon \rightarrow 0^+} \left[ \int_{-\infty}^{\epsilon} \frac{x(s)}{t-s} ds + \int_{\epsilon}^{\infty} \frac{x(s)}{t-s} ds \right], \tag{9.172}$$

which is valid as long as the limit of the sum of the two partial integrals exists. The principal value is written with a PV before the integral sign to signify that a special, augmented form of the Lebesgue integral is supposed. Note that the individual limits of the integrals inside the square brackets of (9.172) may not exist. It is in general not permissible to move the limit operation inside the brackets when using the principal value of the integral.

**Example (Square Pulse).** Consider the signal  $x(t) = u(t + 1) - u(t - 1)$ . The function  $h(t) = t^{-1}$  defies integration on  $[-1, 1]$ , because of the singularity at the origin. But using the Cauchy principal value, we can still compute  $x_H(0)$ :

$$x_H(0) = PV \int_{-\infty}^{\infty} \frac{x(s)}{0-s} ds = - \lim_{\epsilon \rightarrow 0^+} \left[ \int_{-\infty}^{-\epsilon} \frac{1}{s} ds + \int_{\epsilon}^{\infty} \frac{1}{s} ds \right] = 0. \tag{9.173}$$

Consequently, we can interpret the transform integral as a special kind of convolution. Let us investigate how the Hilbert transform system affects an analog signal. Let  $h(t) = (\pi t)^{-1}$ . Then  $x_H(t) = (x^*h)(t)$ . The generalized Fourier transform of  $h(t)$  is

$$H(\Omega) = \int_{-\infty}^{\infty} \frac{1}{\pi t} e^{-j\Omega t} dt = -j \operatorname{sgn}(\Omega) = \begin{cases} -j & \text{for } \Omega > 0, \\ 0 & \text{for } \Omega = 0, \\ j & \text{for } \Omega < 0, \end{cases} \tag{9.174}$$

The *duality principle* of the Fourier transform explains (9.174). If  $x(t)$  has radial Fourier transform  $y(\Omega)$ , then  $y(t)$  will have Fourier transform  $2\pi x(-\Omega)$ . From Chapter 6, we know that the Fourier transform of  $(j/2)\text{sgn}(t)$  is  $\Omega^{-1}$ . Hence by duality,  $t^{-1}$  transforms to  $(j/2)(2\pi)\text{sgn}(-\Omega)$ , and (9.174) follows.

The Hilbert transform system  $x(t) \rightarrow x_H(t)$  is also called a  $90^\circ$  phase shift or *quadrature filter* [50]. To see why, we look at the system's frequency-domain effect. The Fourier transform of  $x_H(t)$  is  $X_H(\Omega) = X(\Omega)H(\Omega) = -jX(\Omega)\text{sgn}(\Omega)$ . This operation multiplies positive spectral components by the factor  $-j = \exp(-j\pi/2)$  and negative spectral components by  $j = \exp(j\pi/2)$ . These correspond to phase shifts of  $-\pi/2$  and  $\pi/2$ , respectively. Thus, the Hilbert transform converts sines to cosines and vice versa. Let us examine at these basic transformations.

**Example (Sinusoids).** Consider  $x(t) = \cos(\Omega_0 t)$  and  $y(t) = \sin(\Omega_0 t)$ . The generalized Fourier transforms of  $x(t)$  and  $y(t)$  are  $X(\Omega) = \pi[\delta(\Omega - \Omega_0) + \delta(\Omega + \Omega_0)]$  and  $Y(\Omega) = (\pi/j)[\delta(\Omega - \Omega_0) - \delta(\Omega + \Omega_0)]$ . Note that  $\delta(\Omega - \Omega_0)$  is a positive frequency impulse, whereas  $\delta(\Omega + \Omega_0)$  lives across the origin, in  $\Omega < 0$  land. The Fourier transform of  $x_H(t)$  is  $X_H(\Omega) = F(x_H)(\Omega) = -j\pi\text{sgn}(\Omega)[\delta(\Omega - \Omega_0) + \delta(\Omega + \Omega_0)]$ . But this is  $(\pi/j)[\delta(\Omega - \Omega_0) - (\pi/j)[\delta(\Omega + \Omega_0)]] = Y(\Omega)$ . Evidently,  $x_H(t) = y(t)$ . As an exercise, we leave the other relation  $y_H(t) = -x(t)$  to the reader.

Typically, then, we compute the Hilbert transform of a signal  $x(t)$  by examining the frequency domain product  $X(\Omega)H(\Omega)$ . This is usually much simpler than evaluating the Cauchy principal value integral (9.172), although the results can be counter-intuitive. The generalized Fourier transform of the signal  $x(t) = 1$  is the Dirac  $2\pi\delta(\Omega)$ , for instance. Multiplication by  $-j\text{sgn}(\Omega)$  therefore gives zero.

We summarize analog Hilbert transform properties in Table 9.7 and leave the derivations as exercises. Note that if  $X(0) = 0$ , then the inverse transform is  $\mathcal{H}^{-1} = -\mathcal{H}$ . Also, many algebraic properties of the Fourier transform carry through to the Hilbert transform.

**9.6.2.2 Discretization.** Moving toward computer applications, let us now consider how to define a discrete Hilbert transform. Again, the frequency-domain behavior is the key; we seek a discrete  $90^\circ$  phase shift system. Such a system would turn each cosine component  $\cos(\omega n)$  in a signal  $x(n)$  into a  $\sin(\omega n)$  term and each  $\sin(\omega n)$  into a  $-\cos(\omega n)$ .

First, we consider the case of aperiodic discrete signals  $x(n)$ . The appropriate  $90^\circ$  phase shift system should have a frequency response  $H(\omega)$  given by

$$H(\omega) = \sum_{n=-\infty}^{\infty} h(n)e^{-j\omega n} = -j\text{sgn}(\omega) = \begin{cases} -j & \text{for } \omega > 0, \\ 0 & \text{for } \omega = 0, \\ j & \text{for } \omega < 0. \end{cases} \quad (9.175)$$

**TABLE 9.7. Some Analog Hilbert Transform Properties**

Signal Expression	Hilbert Transform or Property
$x(t)$	$x_H(t) = \frac{1}{\pi} PV \int_{-\infty}^{\infty} \frac{x(s)}{t-s} ds = (\mathcal{H}x)(t)$ (Analysis equation)
$x_H(t)$	$(\mathcal{H}x_H)(t) = -x$ (Inverse, synthesis equation)
$ax(t) + by(t)$	$ax_H(t) + by_H(t)$ (Linearity)
$dx/dt$	$dx_H/dt$ (Derivative)
$\langle x, x_H \rangle = \int_{-\infty}^{\infty} x(t)\overline{x_H(t)} dt = 0 \quad x \in L^2(\mathbb{R})$	Orthogonality
$\ x\ _2 = \ x_H\ _2 \quad x \in L^2(\mathbb{R})$	Energy conservation

The inverse DTFT computation gives

$$h(n) = \frac{1}{2\pi} \int_{-\pi}^{\pi} H(\omega)e^{j\omega n} d\omega = \frac{j}{2\pi} \int_{-\pi}^0 e^{j\omega n} d\omega + \frac{-j}{2\pi} \int_0^{\pi} e^{j\omega n} d\omega = \begin{cases} 0 & \text{if } n \text{ is even,} \\ \frac{2}{n\pi} & \text{if } n \text{ is odd.} \end{cases} \tag{9.176}$$

So the above discrete Hilbert transform system is neither causal nor FIR. Now let us consider a discrete  $x(n)$  with period  $N > 0$ .

Let  $X(k)$  be the DFT of a real-valued signal  $x(n)$  defined on  $[0, N - 1]$ . So corresponding to each positive discrete frequency  $k \in [1, N/2)$  there is a negative frequency  $N - k \in (N/2, N - 1]$ . The DFT coefficients  $X(0)$  and  $X(N/2)$ —corresponding the DC and Nyquist frequency values—are both real. Mimicking the analog Hilbert transform, let us therefore define the system function of the discrete Hilbert transform to be

$$H(k) = \begin{cases} 0 & \text{if } k = 0, \\ -j & \text{if } 1 \leq k < \frac{N}{2}, \\ 0 & \text{if } k = N/2, \\ j & \text{if } \frac{N}{2} < k \leq N - 1. \end{cases} \tag{9.177}$$

We claim this works. For if  $x(n) = A\cos(2\pi k_0 n/N)$ , then its representation in terms of the inverse DFT is  $x(n) = (A/2)\exp[2\pi j k_0 n/N] + (A/2)\exp[2\pi j(N - k_0)n/N]$ . That is,

$X(k) = (A/2)\delta(k - k_0) + (A/2)\delta(k - (N - k_0))$ . Multiplying by  $H(k)$  gives  $X(k)H(k) = (-jA/2)\delta(k - k_0) + (jA/2)\delta(k - (N - k_0))$ . Applying the inverse DFT, this becomes  $y(n) = (-jA/2)\exp[2\pi jk_0n/N] + (jA/2)\exp[2\pi j(N - k_0)n/N] = A\sin(2\pi k_0n/N)$ . So  $y(n) = x_H(n)$ , as claimed. Similarly, discrete Hilbert transformation of  $A\sin(2\pi k_0n/N)$  gives  $-A\cos(2\pi k_0n/N)$ .

Note that the Hilbert transform  $x_H(n)$  of a discrete signal  $x(n)$  on  $[0, N - 1]$  loses the energy of both the DC term and the Nyquist frequency term. To find the impulse response of the discrete Hilbert transform system, we calculate the inverse DFT of (9.177) to get  $h(n)$ . This allows us to implement discrete Hilbert transforms on a digital computer. However, the value of Hilbert transform applications revolves around the related concept of the analytic signal, which the next section covers.

**9.6.2.3 Analytic Signal.** Given an analog signal  $x(t)$  and its Hilbert transform  $x_H(t)$ , the associated *analytic signal* [72, 73] is

$$x_A(t) = x(t) + jx_H(t). \quad (9.178a)$$

Although replacing a real-valued with a complex-valued signal may make things seem needlessly complicated, it does allow us to define the following related—and quite valuable—concepts. The *signal envelope* is

$$|x_A(t)| = \sqrt{x^2(t) + x_H^2(t)}. \quad (9.178b)$$

Thus, we can write the analytic signal as

$$x_A(t) = |x_A(t)|e^{j\phi(t)}, \quad (9.178c)$$

where the *instantaneous phase*  $\phi(t)$  is

$$\phi(t) = \tan^{-1} \left[ \frac{x_H(t)}{x(t)} \right]. \quad (9.178d)$$

In the first chapter, we argued that the derivative of the phase with respect to time is a reasonable way to define the *instantaneous radial frequency*. Hence, we set

$$\omega(t) = \frac{d}{dt}\phi(t). \quad (9.178e)$$

We may also define discrete versions of these notions. Notice that the signal envelope for a sinusoid is precisely its amplitude. Thus, the definition of signal envelope (9.178b) gives us a definition that applies to aperiodic signals, but reduces to what we should expect for the case of sinusoids. The imaginary part of the analytic signal (9.178a) fills in the gaps, as it were, left in the signal by its fine scale oscillations (Figure 9.48).

In many ways, the analytic signal is more important than the Hilbert transform itself. It is possible to show that the analytic signal satisfies the Cauchy–Riemann

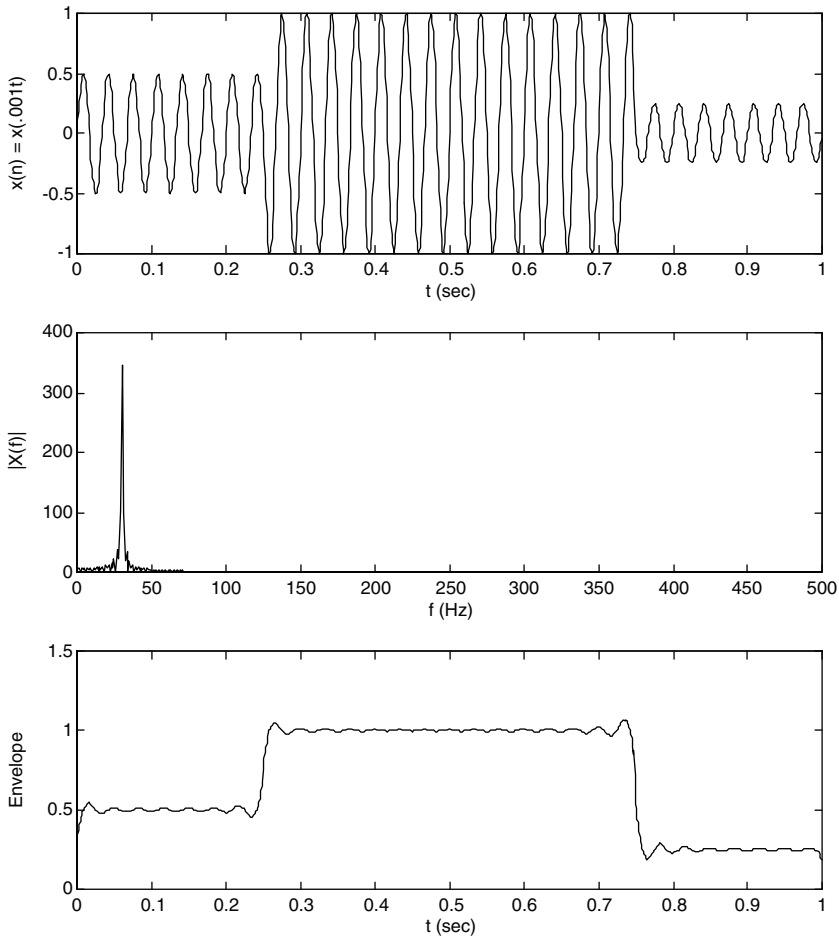


**Fig. 9.48.** Signal  $x(t)$  contains a unit amplitude 30-Hz sinusoid that has been attenuated in the first and last 250 ms of its domain (top). Magnitude spectrum (middle panel). Signal envelope (bottom).

equations, so that it can be extended to an analytic function of a complex variable  $x(z)$  [71, 74]. The next section contains an example of envelope computation on a speech signal.

**9.6.2.4 Application: Envelope Detection.** An important early task in speech analysis is to segment the input signal into regions containing utterances and those holding only background noise. The utterance portions can be further broken up into separate words, although this is by no means a simple task. One tool in either segmentation procedure is the signal envelope. Here, as an example, we compute the envelope of the speech signal considered earlier, namely, the “calling” clip.

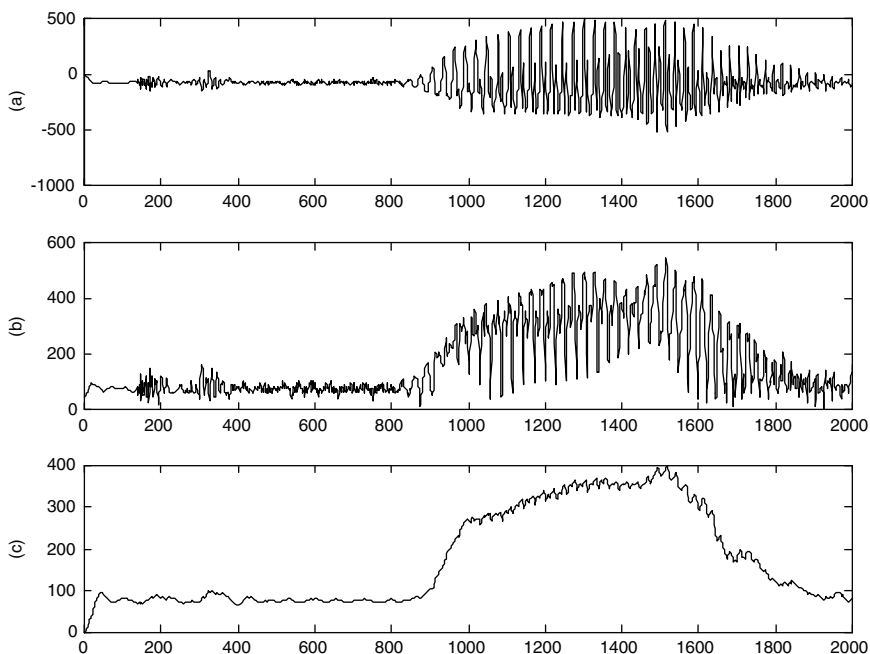


Fig. 9.49. Speech signal (a), its envelope (b), and its filtered envelope (c).

Working on the first 2000 speech samples (Figure 9.49a), we can compute the Hilbert transform, analytic signal, and envelope (Figure 9.49b). The problem is that the envelope remains rather jagged and therefore problematic for segmentation purposes.

One way to improve the envelope is to apply low-pass filter. In Figure 9.49c we created a third order Chebyshev Type II low-pass filter with stopband attenuation of 20 dB. The speech sampling rate is 8 kHz for this example, so the Nyquist rate is 4 kHz, and the cutoff frequency for the low-pass filter is 200 Hz.

In general, envelope detection problems can be improved with such smoothing filters. Even simple sample-and-hold filters with  $H(z) = z/(z - a)$  may prove adequate for envelope amelioration.

Signal analysis applications requiring instantaneous phase or frequency computations—such as interferometry, for instance—may demand more refined filtering. A typical strategy is to use filters based on fitting methods, such as the Savitzky–Golay filters to the raw signal envelope before computing the phase and its derivative.

### 9.6.3 Perfect Reconstruction Filter Banks

In this chapter's first section we considered simple signal analysis problems using an array of filters selective of different frequency ranges. By examining the energy outputs of the separate filters, the frequency content according to time location of signals could be ascertained. This section investigates filter banks more deeply, and,

in particular, takes up the problem of reconstructing the original signal from its separately filtered versions.

Why should this matter? There are two basic reasons:

- If a signal can be broken down into separate components and perfectly (or approximately) reconstructed, then this provides a basis for an efficient signal transmission and compression technology.
- There is also the possibility of constructing signal libraries for detection and interpretation purposes that support a coarse-to-fine recognition methodology but provide a compact library of signal prototypes.

One more involved reason is that a perfect reconstruction filter bank is closely related to a type of time-scale transform, the orthogonal wavelet transformation, which we shall cover in Chapter 11.

**9.6.3.1 Laplacian Pyramid.** An early and innovative approach combining signal scale and frequency-domain analysis is the Laplacian pyramid decomposition. Constructing hierarchical image decompositions was employed by Ref. 75 in their development of the Laplacian pyramid. They approached the problem of managing the sheer volume of information in a pixel image by making two points: First, the gray-scale pixel values are highly correlated in natural scenes; second, it is possible to decompose the original image into both a coarse representation which contains the gross features of the image and a difference image which contains sufficient information to reconstruct the original image from the coarse representation. Their objective was to remove the correlations that typically exist between neighboring pixels in natural scenes. This is a primary goal of image compression.

Burt and Adelson used a discrete filter, which in certain instances closely resembles a Gaussian, to derive the coarse images. The filtered representations are subsampled at twice the unit distance of the previous image to obtain new levels in the pyramid. The authors call this the Gaussian pyramid. This process for one-dimensional signals, passes the original signal at resolution level 0,  $f(n)$ , given by the digitizer, to the first coarser level of the Gaussian pyramid. The filter coefficients,  $w(n)$ , are chosen to have an approximately Gaussian shape by Burt and Adelson, although the technical conditions the authors impose on the  $w(n)$  allow some quite different filters to arise [75].

To extract a difference signal from two successive layers of the Gaussian pyramid, Burt and Adelson began by inserting zeros between the values of the coarse pyramid level. This is necessary because the coarser level contains pixels whose unit of size is twice that of the finer level. The addition of zero elements causes extra high frequency components to be added to the signal when this up-sampling operation is performed. This requires a second smoothing operation. The new smoothed signal, the values of which are now taken at unit intervals, can be subtracted from the original signal. Figure 9.50 illustrates these operations on the signals. The coarse images are obtained by Gaussian-like filtering and the difference images are

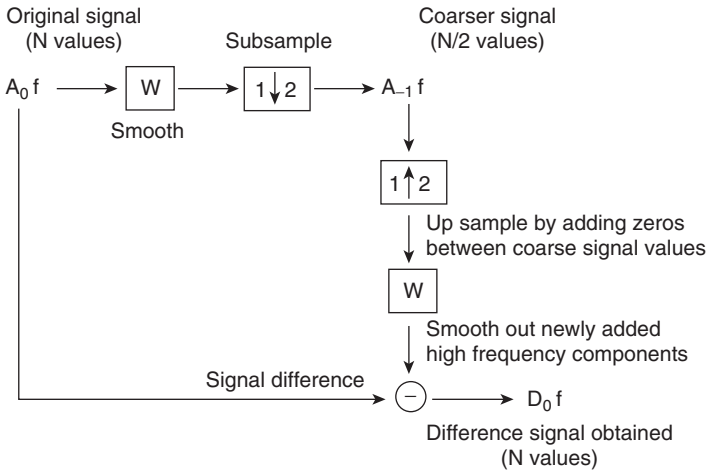


Fig. 9.50. Signal processing diagram of the Laplacian pyramid decomposition.

obtained by subtracting such filtered representations. Since the difference of two Gaussians so closely resembles the Laplacian of a Gaussian operation studied by Marr [77], Burt and Adelson called their construction the Laplacian pyramid.

The signal operations of Figure 9.50 may be repeated. Successive difference signals are produced together with a final coarse, or approximate, signal. The Laplacian pyramid, then, consists of  $D_0, D_{-1}, D_{-2}, \dots, D_{-j}, A_{-j}$ . As is evident from the simple decomposition procedure shown in Figure 9.50, the finer resolution layers of the pyramid may be recovered from the appropriate difference and coarse signals.

When a one-dimensional signal with  $N$  samples is hierarchically analyzed with a Laplacian pyramid, the number of coefficients required increases to approximately  $2N$ . This is evident from the diagram (Figure 9.50).

The Laplacian pyramid provides a scale-based signal recognition strategy. Notice that quasi-Gaussian filters of identical shape applied at differing scales and basic arithmetic operations between the levels of the pyramid to decompose and

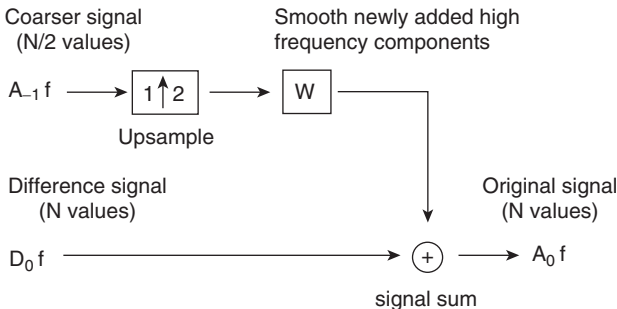


Fig. 9.51. Laplacian pyramid reconstruction of signal.

reconstruct the original image. The computational strategies of the Laplacian pyramid have been implemented in a series of special-purpose vision machines [76].

**9.6.3.2 Exact Reconstruction Filter Banks.** There is a type of pyramid decomposition that allows perfect signal reconstruction but does not increase the amount of data required for storing the decomposition components. Of course, this is an ideal feature for signal compression applications. But it can also be applied for progressive signal transmission as well as for coarse-to-fine recognition applications. Here we introduce the theory. We shall have occasion to refer back to it when we cover wavelet transforms in the last two chapters.

Consider a real-valued signal  $a_0(n)$ . The decomposition and reconstruction scheme resembles the Laplacian pyramid's signal flow (Figure 9.52). For the present and the sequel (Chapter 11, in particular) it is useful to set up the following notations. Given the filter impulse responses  $h(n)$  and  $g(n)$ , we set  $\bar{h}(n) = h(-n)$  and  $\bar{g}(n) = g(-n)$  to be their reflections in time. Observe that  $\bar{H}(\omega) = H^*(\omega)$ .

Also, we have  $a_1(n) = (a_0 * \bar{h})(2n)$ , which is the original signal convolved with  $h(-n)$  and subsampled. Similarly, we have  $d_1(n) = (a_0 * \bar{g})(2n)$ . Typically, we shall select  $h(n)$  to be a low-pass filter and  $g(n)$  to be a high-pass filter. In terms of the classic paper [78],  $a_1(n)$  and  $d_1(n)$  are the first-level approximate and detail signals, respectively, in the decomposition of source signal  $a_0(n)$ . Furthermore, we obtain  $a'_1(n)$  by upsampling  $a_1(n)$  and then  $b'_1(n)$  by filtering with  $h'(n)$ . Similarly,  $c'_1(n)$  comes from filtering  $d'_1(n)$  with  $g'(n)$ , where  $d'_1(n)$  is an upsampled version of  $d_1(n)$ . Finally,  $a'_0(n) = (a'_1 * h')(n) + (d'_1 * g')(n)$ . We seek conditions that will guarantee  $a_0(n) = a'_0(n)$ .

Let us note some properties of the upsampling and downsampling operations. First, let  $x(n)$  be a discrete signal and  $y(n) = x(2n)$ . Then

$$Y(2\omega) = \sum_{n=-\infty}^{\infty} x(2n)e^{-2jn\omega} = \frac{X(\omega) + X(\omega + \pi)}{2}. \tag{9.179}$$

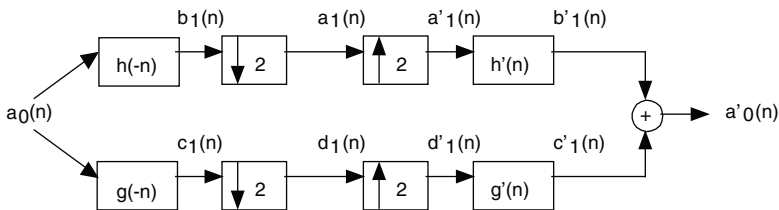


**Fig. 9.52.** Decomposition and reconstruction signal paths. With the proper choice of filters, the original signal can be recovered and yet its decomposition does not increase the amount of data to be stored.

The second term on the right in (9.179) is called the *folding* or *aliasing* term. This is what wrecks the desired exact reconstruction. Next, if  $y(n)$  comes from  $x(n)$  by upsampling and inserting zeros,

$$y(n) = \begin{cases} x(m) & \text{if } n = 2m, \\ 0 & \text{if otherwise.} \end{cases} \quad (9.180)$$

then  $Y(\omega) = X(2\omega)$ . We leave the straightforward proofs as exercises. The next result is due to Ref. 79.

**Theorem.** Let  $h(n)$  and  $g(n)$  be real-valued impulse responses for discrete filters. Then the decomposition and reconstruction filter bank (Figure 9.52) performs perfect reconstruction if and only if

- (i)  $H^*(\omega + \pi)H'(\omega) + G^*(\omega + \pi)G'(\omega) = 0$  and
- (ii)  $H^*(\omega)H'(\omega) + G^*(\omega)G'(\omega) = 2$ .

**Proof:** Referring to Figure 9.52, let us calculate the frequency response of the reconstructed signal  $a_0'(n)$ . We know that  $B_1(\omega) = A_0(\omega)\bar{H}(\omega)$  and  $C_1(\omega) = A_0(\omega)\bar{G}(\omega)$ . Thus,

$$\begin{aligned} 2A_1(2\omega) &= B_1(\omega) + B_1(\omega + \pi) = A_0(\omega)\bar{H}(\omega) + A_0(\omega + \pi)\bar{H}(\omega + \pi) \\ &= A_0(\omega)H^*(\omega) + A_0(\omega + \pi)H^*(\omega + \pi) \end{aligned} \quad (9.181a)$$

and similarly,

$$2D_1(2\omega) = A_0(\omega)G^*(\omega) + A_0(\omega + \pi)G^*(\omega + \pi). \quad (9.181b)$$

On the reconstruction side of the diagram, we have

$$A_0'(\omega) = B_1'(\omega) + C_1'(\omega) = A_1(2\omega)H'(\omega) + D_1(2\omega)G'(\omega). \quad (9.182)$$

Substituting (9.181a) and (9.181b) into (9.182) and simplifying leads to

$$\begin{aligned} A_0'(\omega) &= \frac{1}{2}A_0(\omega)[H^*(\omega)H'(\omega) + G^*(\omega)G'(\omega)] \\ &\quad + \frac{1}{2}A_0(\omega + \pi)[H^*(\omega + \pi)H'(\omega) + G^*(\omega + \pi)G'(\omega)]. \end{aligned} \quad (9.183)$$

Inspecting (9.183), we see that the only way that  $A_0'(\omega)$  can equal  $A_0(\omega)$  is if the nonaliased term is doubled, and the aliased term is zero. These are precisely the conditions (i) and (ii) of the theorem's statement. ■

The theorem gives a necessary and sufficient condition on the reconstruction filters  $h'(n)$  and  $g'(n)$  so that the decomposition scheme provides exact reconstruction.

**Theorem.** Let  $h(n)$  and  $g(n)$  be as in the previous theorem. Then the decomposition and reconstruction scheme (Figure 9.52) performs perfect reconstruction only if

$$H^*(\omega)H'(\omega) + H^*(\omega + \pi)H'(\omega + \pi) = 2. \tag{9.184}$$

**Proof:** After taking complex conjugates, we may write the result of the previous theorem

$$(iii) \ H(\omega + \pi)H'^*(\omega) + G(\omega + \pi)G'^*(\omega) = 0 \text{ and}$$

$$(iv) \ H(\omega)H'^*(\omega) + G(\omega)G'^*(\omega) = 2.$$

Let us rewrite these relations in matrix form as follows:

$$\begin{bmatrix} H(\omega) & G(\omega) \\ H(\omega + \pi) & G(\omega + \pi) \end{bmatrix} \begin{bmatrix} H'^*(\omega) \\ G'^*(\omega) \end{bmatrix} = \begin{bmatrix} 2 \\ 0 \end{bmatrix}. \tag{9.185}$$

If the determinant is nonzero, (9.185) can be solved,

$$\begin{bmatrix} H'^*(\omega) \\ G'^*(\omega) \end{bmatrix} = \frac{2}{\Delta(\omega)} \begin{bmatrix} G(\omega + \pi) \\ -H(\omega + \pi) \end{bmatrix}, \tag{9.186}$$

where  $\Delta(\omega) = H(\omega)G(\omega + \pi) - G(\omega)H(\omega + \pi)$ . Note too that  $\Delta(\omega + \pi) = -\Delta(\omega)$ . From (9.186) we get

$$H'^*(\omega + \pi) = \frac{2G(\omega + 2\pi)}{\Delta(\omega + \pi)} = \frac{-2G(\omega)}{\Delta(\omega)}, \tag{9.187}$$

implying

$$G(\omega)G'^*(\omega) = \frac{\Delta(\omega)H'^*(\omega + \pi)(-2)H(\omega + \pi)}{-2\Delta(\omega)} = H'^*(\omega + \pi)H(\omega + \pi). \tag{9.188}$$

Using the complex conjugate of (9.188) with (ii) of the previous theorem gives (9.184) above. ■

**Corollary.** Under the theorem's assumptions,

$$G^*(\omega)G'(\omega) + G^*(\omega + \pi)G'(\omega + \pi) = 2. \tag{9.189}$$

**Proof:** Exercise. ■

**Definition (Quadrature Mirror Filters).** If the decomposition filter is the same as the reconstruction filter  $h(n) = h'(n)$ , then it is called a *quadrature mirror filter* (QMF) or *conjugate mirror filter* (CMF).

**Corollary.** If  $h(n)$  is QMF, then

$$|H(\omega)|^2 + |H(\omega + \pi)|^2 = 2. \tag{9.190}$$

**Proof:** From (9.184). ■

## 9.7 SUMMARY

This chapter explored a variety of frequency domain signal analysis applications, developed several related tools, explained how to construct and implement filters for frequency selective input processing, and studied the theoretical issues that arose in the course of experimentation.

We can divide analysis applications according to whether the source signals are basically narrowband or wideband:

- (i) Narrowband signals are interpretable—at least locally—via pulse detection in the Fourier magnitude spectrum.
- (ii) Wideband signals, on the other hand, demand more complicated procedures, multicomponent, and shape-based techniques.

For narrow band signals we developed three basic approaches:

- (i) Time-domain segmentation, based on the histogram for example, prior to frequency-domain analysis.
- (ii) Local windowing using a short (say  $N = 256$ ) DFT in many locations, thus forming a time-frequency map.
- (iii) The filter bank.

Either of the first two methods work well under moderate noise. Under heavy noise, or faced with real-time processing and interpretation constraints, a bank of carefully crafted filters, operating in parallel and equipped with decision logic at their output, can provide satisfactory results.

We significantly extended filter bank theory at the end of the chapter. We showed that subsampling combined with low- and high-pass filtering can be used to decompose signals for analysis. Moreover, under certain conditions on the filters, the filter bank supports an exact reconstruction algorithm using upsampling and filtering. We will revisit these ideas in Chapters 11 and 12, showing that there is a link between filter banks and the theory of orthogonal wavelets—a time-scale signal analysis technique.

The concepts of phase and group delay arose in frequency-domain signal analysis applications where discrete filters were necessary. Applications that filter incoming signals for noise removal, frequency selection, or signal shaping and then analyze the output must take into account the delay characteristics of the filter. We observed the phase delay of sinusoidal tones in the DTMF filter bank application, for example. Other applications involve group delay, such as speech analysis and edge detection.

Many applications require that the filters provide linear, or nearly linear, phase. In communication systems, for example, the information is carried on the envelope and the carrier has a constant frequency. Thus, nonlinear phase delay could well stretch and compress the frequencies in the signal so that the distortions render the signal unintelligible. Important aspects of seismic signal processing are to properly

measure the time delays between different signal components. Thus, linear phase is crucial when filtering; and for this reason, finite impulse response (FIR) filters, which we proved to have linear phase, are preferred.

## REFERENCES

1. J. S. Walker, *Fourier Analysis*, New York: Oxford University Press, 1988.
2. G. B. Folland, *Fourier Analysis and Its Applications*, Pacific Grove, CA: Wadsworth and Brooks/Cole, 1992.
3. R. E. Edwards, *Fourier Series: A Modern Introduction*, vol. I, New York: Holt, Rinehart and Winston, 1967.
4. T. W. Körner, *Fourier Analysis*, Cambridge: Cambridge University Press, 1988.
5. D. C. Champeney, *A Handbook of Fourier Theorems*, Cambridge: Cambridge University Press, 1987.
6. H. Baher, *Analog and Digital Signal Processing*, New York: Wiley, 1990.
7. A. V. Oppenheim and R. W. Schaffer, *Discrete-Time Signal Processing*, Englewood Cliffs, NJ: Prentice-Hall, 1989.
8. J. G. Proakis and D. G. Manolakis, *Digital Signal Processing: Principles, Algorithms, and Applications*, 2nd ed., New York: Macmillan, 1992.
9. R. A. Roberts and C. T. Mullis, *Digital Signal Processing*, Reading, MA: Addison-Wesley, 1987.
10. A. V. Oppenheim, A. S. Willsky, and S. H. Nawab, *Signals and Systems*, 2nd ed., Upper Saddle River, NJ: Prentice-Hall, 1997.
11. L. R. Rabiner and B. Gold, *Theory and Application of Digital Signal Processing*, Englewood Cliffs, NJ: Prentice-Hall, 1975.
12. P. Mock, Add DTMF generation and decoding to DSP- $\mu$ P designs, *Electronic Design News*, March 21, 1985; also in K.-S. Lin, ed., *Digital Signal Processing Applications with the TMS320 Family*, vol. 1, Dallas: Texas Instruments, 1989.
13. J. L. Flanagan, *Speech Analysis, Synthesis, and Perception*, 2nd ed., New York: Springer-Verlag, 1972.
14. D. H. Lehmer, Mathematical methods in large-scale computing units, *Proceeding of the 2nd Symposium on Large-Scale Digital Calculating Machines*, Harvard University Press, pp. 141–146, 1951.
15. S. K. Park and K. W. Miller, Random number generators: Good ones are hard to find, *Communications of the ACM*, vol. 31, no. 10, pp. 1192–1201, 1988.
16. W. H. Press, B. P. Flannery, S. A. Teukolsky, and W. T. Vetterling, *Numerical Recipes in C*, Cambridge: Cambridge University Press, 1988.
17. G. E. Box and M. E. Muller, A note on the generation of random normal deviates, *Annals of Mathematical Statistics*, vol. 29, pp. 610–611, 1958.
18. D. E. Knuth, *Seminumerical Algorithms*, 2nd ed., Reading, MA: Addison-Wesley, 1981.
19. L. Devroye, *Non-Uniform Random Variate Generation*, New York: Springer-Verlag, 1986.
20. C. K. Chow and T. Kaneko, Automatic boundary detection of the left ventricle from cineangiograms, *Computers and Biomedical Research*, vol. 5, pp. 388–410, 1972.

21. N. Otsu, A threshold selection method from gray-level histograms, *IEEE Transactions on Systems, Man, and Cybernetics*, vol. SMC-9, no. 1, pp. 62–66, January 1979.
22. J. Kittler and J. Illingworth, On threshold selection using clustering criteria, *IEEE Transactions on Systems, Man, and Cybernetics*, vol. SMC-15, pp. 652–655, 1985.
23. R. E. Crochiere and L. R. Rabiner, *Multirate Digital Signal Processing*, Englewood Cliffs, NJ: Prentice-Hall, 1983.
24. A. N. Akansu and R. A. Haddad, *Multiresolution Signal Decomposition: Transforms, Subband, and Wavelets*, Boston: Academic, 1992.
25. M. Vetterli and J. Kovacevic, *Wavelets and Subband Coding*, Upper Saddle River, NJ: Prentice-Hall, 1995.
26. T. W. Parks and C. S. Burrus, *Digital Filter Design*, New York: Wiley, 1987.
27. L. W. Couch II, *Digital and Analog Communication Systems*, 4th ed., Upper Saddle River, NJ: Prentice-Hall, 1993.
28. R. B. Blackman and J. W. Tukey, *The Measurement of Power Spectra*, New York: Dover, 1958.
29. S. M. Kay, *Modern Spectral Estimation: Theory and Application*, Englewood Cliffs, NJ: Prentice-Hall, 1988.
30. L. L. Scharf, *Statistical Signal Processing: Detection, Estimation, and Time Series Analysis*, Reading, MA: Addison-Wesley, 1991.
31. D. G. Childers, ed., *Modern Spectral Analysis*, New York: IEEE Press, 1978.
32. C. Bingham, M. D. Godfrey, and J. W. Tukey, Modern techniques of power spectrum estimation, *IEEE Transactions on Audio and Electroacoustics*, vol. AU-15, pp. 56–66, June 1967. Also in Refs. 31, pp. 6–16.
33. A. Antoniou, *Digital Filters: Analysis and Design*, New York, McGraw-Hill, 1979.
34. A. Papoulis, *Probability, Random Variables, and Stochastic Processes*, 2nd ed., New York: McGraw-Hill, 1984.
35. M. S. Bartlett, Smoothing periodograms from time series with continuous spectra, *Nature (London)*, vol. 161, pp. 686–687, 1948.
36. P. D. Welch, The use of fast Fourier transform for the estimation of power spectra: A method based on time averaging over short, modified periodograms, *IEEE Transactions on Audio and Electroacoustics*, vol. AU-15, no. 2, pp. 70–73, 1967. Also in Refs. 31, p. 17–20.
37. R. B. Blackman and J. W. Tukey, *Measurement of Power Spectra from the Point of View of Communications Engineering*, New York: Dover, 1959.
38. D. Malacara, *Optical Shop Testing*, New York: Wiley-Interscience, 1992.
39. J. M. Steigerwald, S. P. Murarka, and R. J. Gutmann, *Chemical Mechanical Planarization of Microelectronic Materials*, New York: Wiley, 1997.
40. J. F. Kaiser, Design methods for sampled data filters, *Proceedings of the 1st Allerton Conference on Circuit and System Theory*, pp. 221–236, 1963. Also in L. R. Rabiner and C. M. Rader, eds., *Digital Signal Processing*, New York: IEEE Press, 1972.
41. E. I. Jury, *Theory and Applications of the Z-Transform Method*, Malabar, FL: Krieger, 1982.
42. R. Vich, *Z Transform Theory and Applications*, Boston: D. Reidel, 1987.
43. A. Ralston and P. Rabinowitz, *A First Course in Numerical Analysis*, New York: McGraw-Hill, 1978.

44. R. Beals, *Advanced Mathematical Analysis*, New York: Springer-Verlag, 1983.
45. E. D. Rainville, *The Laplace Transform: An Introduction*, New York: Macmillan, 1963.
46. F. J. Taylor, *Digital Filter Design Handbook*, New York: Marcel Dekker, 1983.
47. A. G. Constantinides, Spectral transformations for digital filters, *Proceedings of the IEE*, vol. 117, no. 8, pp. 1585–1590, August 1970.
48. M. Akay, *Biomedical Signal Processing*, San Diego, CA: Academic Press, 1994.
49. M. Granzow, H. Riedel, and B. Kollmeier, Linear phase filtering of early auditory evoked potentials, in A. Schick and M. Klatte, eds., *Seventh Oldenburg Symposium on Psychological Acoustics*, pp. 39–48, 1997.
50. J. F. Claerbout, *Fundamentals of Geophysical Data Processing with Applications to Petroleum Prospecting*, New York: McGraw-Hill, 1976.
51. F. Scherbaum, *Of Poles and Zeros: Fundamentals of Digital Seismology*, Dordrecht, The Netherlands: Kluwer, 1996.
52. T. Parsons, *Voice and Speech Processing*, New York: McGraw-Hill, 1987.
53. F. J. Owens, *Signal Processing of Speech*, New York: McGraw-Hill, 1993.
54. L. Rabiner and B.-H. Juang, *Fundamentals of Speech Recognition*, Englewood Cliffs, NJ: Prentice-Hall, 1993.
55. L. R. Rabiner and M. R. Sambur, An algorithm for determining the endpoints of isolated utterances, *Bell System Technical Journal*, vol. 54, no. 2, pp. 297–315, 1975.
56. L. Lamel et al., An improved endpoint detector for isolated word recognition, *IEEE Transactions on Acoustics, Speech, and Signal Processing*, vol. 29, pp. 777–785, Aug. 1981.
57. J. Junqua et al., A robust algorithm for word boundary detection in the presence of noise, *IEEE Transactions on Speech and Audio Processing*, vol. 2, no. 3, pp. 406–412, July 1994.
58. R. E. Ziemer, W. H. Tranter, and D. R. Fannin, *Signals and Systems: Continuous and Discrete*, 3rd ed., New York: Macmillan, 1993.
59. L. B. Jackson, *Signals, Systems, and Transforms*, Reading, MA: Addison-Wesley, 1991.
60. E. A. Guillemin, *Synthesis of Passive Networks*, New York: Wiley, 1957.
61. J. E. Storer, *Passive Network Synthesis*, New York: McGraw-Hill, 1957.
62. M. E. Van Valkenburg, *Analog Filter Design*, New York: Holt, Rinehart and Winston, 1982.
63. L. Weinberg, *Network Analysis and Synthesis*, Huntington, NY: Kreiger, 1975.
64. V. K. Madiseti, *VLSI Digital Signal Processors*, Piscataway, NJ: IEEE Press, 1995.
65. R. W. Daniels, *Approximation Methods for Electronic Filter Design*, New York: McGraw-Hill, 1974.
66. W. Cauer, *Synthesis of Linear Communication Networks*, vols. I and II, New York: McGraw-Hill, 1958.
67. D. A. Calahan, *Modern Network Synthesis*, vol. 1, New York: Hayden, 1964.
68. N. Wiener, *Extrapolation, Interpolation, and Smoothing of Stationary Time Series*, New York: Technology Press of MIT and Wiley, 1957.
69. R. N. Bracewell, *The Fourier Transform and Its Applications*, New York: McGraw-Hill, 1978.
70. S. L. Hahn, *Hilbert Transforms in Signal Processing*, Norwood, MA: Artech House, 1996.
71. L. V. Ahlfors, *Complex Analysis*, 2nd ed., New York: McGraw-Hill, 1966.

72. S. L. Marple, Computing the discrete-time “analytic signal” via FFT, *IEEE Transactions on Signal Processing*, vol. 47, no. 9, pp. 2600–2603, September 1999.
73. D. Gabor, Theory of communication, *Journal of the IEE*, vol. 93, pp. 429–457, 1946.
74. L. Cohen, *Time-Frequency Analysis*, Englewood Cliffs, NJ: Prentice-Hall, 1995.
75. P. J. Burt and E. H. Adelson, The Laplacian pyramid as a compact image code, *IEEE Transactions on Communication*, vol. 31, no. 4, pp. 532–540, April 1983.
76. P. J. Burt, Smart sensing within a pyramid vision machine, *Proceedings of the IEEE*, vol. 76, no. 8, pp. 1006–1015, August 1988.
77. D. Marr, *Vision*, New York: W. H. Freeman, 1982.
78. S. Mallat, A theory for multiresolution signal decomposition: The wavelet representation, *IEEE Transactions on Pattern Analysis and Machine Intelligence*, vol. 11, no. 7, pp. 674–693, July 1989.
79. M. Vetterli, Filter banks allowing perfect reconstruction, *Signal Processing*, vol. 10, no. 3, pp. 219–244, April 1986.

## PROBLEMS

- Suppose an analog signal is sampled  $x(n) = xa(nT)$ , where  $T$  is the sampling period. A discrete Fourier transform of order  $N$  follows:  $X(k) = (\mathcal{F}_x)(k)$ . Find the frequency resolution, the Nyquist frequency, and the highest frequency represented by the DFT coefficients:
  - $N = 80$ ,  $T = 0.02$ ;
  - $N = 10$ , sampling frequency  $F = 1$  kHz;
  - $N = 21$ ,  $T = 1$ ;
  - $N = 256$ , sampling frequency = 8192 Hz.
- Which of the following finite impulse response (FIR) filters have linear phase? zero phase?
  - $x(n) = u(n + 2) - u(n - 2)$ , where  $u(n)$  is the discrete unit step signal.
  - $y(n) = u(n + 2) - u(n - 3)$ .
  - $v(n) = (-1)^n x(n)$ .
  - $w(n) = (-1)^n y(n)$ .
  - Can an IIR filter have linear phase?
- Provide sketches of all four types of linear phase filters  $H$  with  $h(n) \in \mathbb{R}$  [26].
- Let  $r_{xx}(\tau) = E[x(t)x(t + \tau)]$  be the autocorrelation for a wide-sense stationary (WSS) analog random signal  $x(t)$ . Prove:
  - $E[x(t)x(s)] = r_{xx}(t - s)$ .
  - $r_{xx}(\tau) = r_{xx}(-\tau)$ .
  - If  $x = Ay$  for some constant  $A$ , find  $r_{yy}(\tau)$ .
  - State and the corresponding properties for the autocorrelation  $r_{ss}(\kappa) = E[s(n)s(n + \kappa)]$  of a discrete WSS random signal  $s(n)$ .

5. Suppose data from a noisy signal is collected for two seconds at a sampling rate of 8 kHz.
  - (a) If a periodogram is calculated for the entire data set, what is its frequency resolution? What is the Nyquist frequency?
  - (b) Suppose that Bartlett's method is tried for the purpose of improving the periodogram. The data is partitioned into sixteen disjoint windows. Now what is the frequency resolution? What is the Nyquist frequency?
  - (c) It is decided to try Welch's method using windows of a larger size than in part (b), but to overlap them by fifty percent. How many windows are needed to cut the frequency resolution in half? Sketch your window layout.
  
6. Let  $H$  be a discrete LTI system, let  $H(z)$  be its system function, and let  $\text{ROC}_H$  be the region of convergence of  $H(z)$ .
  - (a) Show that if  $H$  is *stable* (if the input  $x(n)$  is bounded, then the output  $y(n) = (Hx)(n)$  is also bounded), then this implies that  $\text{ROC}_H$  contains the unit circle  $|z| = 1$  of the complex plane.
  - (b) Suppose that  $\{z \in \mathbb{C}: |z| = 1\} \subset \text{ROC}_H$ . Show that  $H$  is stable.
  - (c) Given: an example of a discrete signal  $h(n)$  that has a discrete-time Fourier transform  $H(\omega)$ , but  $\text{ROC}_H$  does not include the unit circle. Under this circumstance, can the system  $y = Hx = h*x$  be causal, anti-causal, or both?
  
7. Let  $H$  be a discrete LTI system,  $h(n)$  its impulse response,  $H(z)$  its transfer function, and  $\text{ROC}_H$  the region of convergence of  $H(z)$ .
  - (a) Show that if  $H$  is stable, then  $\text{ROC}_H$  contains the unit circle  $|z| = 1$ .
  - (b) Show the converse: If  $\text{ROC}_H \supset \{z \in \mathbb{C}: |z| = 1\}$ , then  $H$  is stable.
  
8. Let  $x(n)$  be a discrete signal,  $X(z)$  its  $z$ -transform, and  $\text{ROC}_X$  the region of convergence.
  - (a) Show that  $x(n)$  is right-sided implies that  $\text{ROC}_X$  is the exterior of a circle in the complex plane.
  - (b) More particularly, if  $x(n)$  is causal, show that  $\infty \in \text{ROC}_X$ .
  - (c) If  $x(n)$  is left-sided, show that  $\text{ROC}_X$  is the interior of a circle and may or may not include 0.
  - (d) Give a condition on a left-sided signal  $x(n)$  so that  $0 \in \text{ROC}_X$ .
  - (e) Give a characterization in terms of  $\text{ROC}_H$  for causal, stable LTI systems  $y = Hx$ .
  
9. Let  $x(t)$  have Fourier transform  $X(\Omega)$  and Laplace transform  $X_L(s)$ .
  - (a) Show that  $X_L(j\Omega) = X(\Omega)$ , for  $\Omega \in \mathbb{R}$ .
  - (b) Let  $s = \Sigma + j\Omega$ , where  $\Sigma \in \mathbb{R}$ . Show that  $X_L(s)$  is the Fourier transform of  $x(t)e^{-\Sigma t}$ .
  - (c) Show that Laplace transform convergence does not depend on the imaginary part of  $s = \Sigma + j\Omega$ .
  - (d) Conclude that  $X_L(s)$  converges on vertical strips in the complex plane.

10. Let  $x(t) = \exp(-a|t|)$  be the Lorentzian function, where  $a > 0$ .
- Show that  $X(\Omega) = 2a/(a + \Omega^2)$ .
  - Sketch  $x(t)$  for  $a = 1, 2, 3$ .
  - Explain how convolution with  $x(t)$  performs a weighted averaging of input signal data.
11. Suppose we map the Laplace  $s$ -plane to the  $z$ -plane via  $z = e^{sT}$ , where we shall assume equality in (9.72).
- Show that this implies  $s = \frac{2}{T} \left( \frac{z-1}{z+1} \right)$ , the bilinear relation between the Laplace and  $z$ -transformations.
  - Let  $z = e^{j\omega}$  and  $s = j\Omega$  in (a) and derive the bilinear mapping (9.70).
12. Derive the Laplace transform properties given in Table 9.3.
13. Let  $T_N(\Omega)$  be the Chebyshev polynomial of order  $N \geq 0$ .
- Show that  $T_N(1) = 1$  for all  $N$ .
  - Show  $T_N(\Omega)$  is even if  $N$  is odd, and  $T_N(\Omega)$  is odd if  $N$  is even.
  - Show all the zeros of  $T_N(\Omega)$  lie on the open interval  $(-1, 1)$ .
  - Show that  $|T_N(\Omega)| \leq 1$  on  $[-1, 1]$ .
14. Let  $P(\Omega)$  and  $Q(\Omega)$  be the squared magnitude response for the Chebyshev and inverse Chebyshev low-pass filters, respectively.
- Show that the poles of  $Q(\Omega)$  are the reciprocals of the poles of  $P(\Omega)$ .
  - Find  $P(\Omega)$  for IIR filters of order 2 and 3.
  - Find  $Q(\Omega)$  for IIR filters of order 2 and 3.
  - Under what conditions is  $Q(\Omega)$  an all-pass filter? Explain.
  - Find the zeros of  $Q(\Omega)$ .
  - Show that the zeros of  $Q(\Omega)$  do not depend on the stopband ripple function.
15. Compute the Hilbert transform  $x_H(t)$  for the following signals:
- $x(t) = \cos(2\pi t)$ .
  - $x(t) = \sin(-3\pi t)$ .
  - $x(t) = \cos(5\pi t) + 2\sin(2\pi t)$ .
  - $x(t) = \delta(t)$ , the Dirac delta.
  - $x(t) = C_0$ , a constant signal.
  - $x(t) = u(t)$ , the unit step signal.
  - $x(t) = u(t+1) - u(t-1)$ .
16. Let  $x(t) = \cos(\Omega_0 t)$  and  $y(t) = \sin(\Omega_0 t)$ .
- Show that  $y_H(t) = -x(t)$ , where  $y_H(t)$  is the Hilbert transform of  $y(t)$ .
  - Compute the analytic signal  $x_A(t)$ .
  - Compute the signal envelope for  $x(t)$ .
  - Compute the instantaneous phase  $\phi(t)$ .
  - Compute the instantaneous frequency  $\omega(t)$ .

17. Show that the Hilbert transform is linear: If  $x(t)$  and  $y(t)$  are analog signals and  $z(t) = Ax(t) + By(t)$ , then  $z_H(t) = Ax_H(t) + By_H(t)$ .
18. Let  $x(n)$  be discrete with period  $N > 0$ . Show that the discrete Hilbert transformation of  $A\sin(2\pi k_0 n/N)$  is  $-A\cos(2\pi k_0 n/N)$ .
19. Suppose the discrete filter  $H$  has impulse responses  $h(n)$ . Suppose  $\bar{h}(n) = h(-n)$  and let  $\bar{H}(\omega)$  be its DTFT.
- (a) Show that  $\bar{H}(\omega) = H^*(\omega)$ , the complex conjugate of  $H(\omega)$ .
- (b) Let  $y(n) = x(2n)$ . Show that  $Y(2\omega) = [X(\omega) + X(\omega + \pi)]/2$ .
- (c) Let  $y(n) = x(n/2)$ . Show that  $Y(\omega) = X(2\omega)$ .
20. Let  $h(n)$  and  $g(n)$  be discrete filters that provide an exact reconstruction scheme as in Figure 9.52. Show that  $G^*(\omega)G'(\omega) + G^*(\omega + \pi)G'(\omega + \pi) = 2$ .

Advanced problems and projects:

21. This problem outlines a proof of the Wiener–Khinchin theorem for discrete random signals. Assume the notation from Section 9.2.3.1.
- (a) First show that

$$\sum_{n=-L}^L \sum_{m=-L}^L x(n)x(m)e^{-j\omega(n-m)} = |X_L(\omega)|^2, \quad (9.191)$$

where  $X_L(\omega)$  is the local discrete time Fourier transform of real-valued WSS random signal  $x(n)$ , and we assume that the autocorrelation function  $r_{xx}(v)$  is absolutely summable:  $r_{xx}(v) \in l^1$ .

- (b) Apply the expectation operator to both sides of (9.191) to get

$$\begin{aligned} E[|X_L(\omega)|^2] &= \sum_{n=-L}^L \sum_{m=-L}^L E[x(n)x(m)]e^{-j\omega(n-m)} \\ &= \sum_{n=-L}^L \sum_{m=-L}^L r_{xx}(n-m)e^{-j\omega(n-m)}. \end{aligned} \quad (9.192)$$

- (c) Divide by  $2L + 1$  and take limits on both sides of (9.192). From the absolute summability of  $r_{xx}(v)$ , argue that the equal limits of the double summation can be replaced with independent limits to get

$$\begin{aligned} \lim_{L \rightarrow \infty} \frac{1}{2L+1} E[|X_L(\omega)|^2] &= \lim_{L \rightarrow \infty} \frac{1}{2L+1} \sum_{n=-L}^L \sum_{m=-L}^L r_{xx}(n-m)e^{-j\omega(n-m)} \\ &= \lim_{L \rightarrow \infty} \frac{1}{2L+1} \sum_{n=-L}^L \lim_{K \rightarrow \infty} \sum_{m=-K}^K r_{xx}(n-m)e^{-j\omega(n-m)}. \end{aligned} \quad (9.193)$$

(d) Conclude as follows:

$$\begin{aligned} X_{\text{PSD}}(\omega) &= \lim_{L \rightarrow \infty} \frac{1}{2L+1} \sum_{n=-L}^L R_{xx}(\omega) \\ &= \lim_{L \rightarrow \infty} \frac{2L+1}{2L+1} R_{xx}(\omega) = R_{xx}(\omega). \end{aligned} \quad (9.194)$$

22. This problem outlines a proof of the Wiener–Khinchin theorem (9.30) for WSS analog random signals  $x(t)$ . Assume the notation from Section 9.2.3.1.

(a) By interchanging the order of integration, show that

$$E \left[ \int_{-\infty}^{\infty} \int_{-\infty}^{\infty} x_L(t)x_L(s)e^{-j\omega(t-s)} ds dt \right] = E[|X_L(\omega)|^2], \quad (9.195)$$

where  $X_L(\omega)$  is the local radial Fourier transform of  $x(t)$ .

(b) Use the results of probability theory:  $E[ax + by] = aE[x] + bE[y]$  and  $r_{xx}(t-s) = E[x(s)x(t)]$ . Show that the expectation operation may be moved inside the integral in (9.195) and therefore that

$$\int_{-\infty}^{\infty} \int_{-\infty}^{\infty} E[x_L(t)x_L(s)e^{-j\omega(t-s)}] ds dt = \int_{-L}^L \int_{-L}^L r_{xx}(t-s)e^{-j\omega(t-s)} ds dt. \quad (9.196)$$

(c) Let  $u = t - s$  for a change of integration variable in (9.196) and show that

$$\text{the iterated integral becomes } \int_{-2L}^{2L} r_{xx}(u)e^{-j\omega u} [2L - |u|] du.$$

(d) Put the above expressions together and take limits to get

$$\lim_{L \rightarrow \infty} \frac{1}{2L} E[|X_L(\omega)|^2] = \lim_{L \rightarrow \infty} \int_{-2L}^{2L} r_{xx}(u)e^{-j\omega u} \left[ \frac{2L - |u|}{2L} \right] du. \quad (9.197)$$

(e) Show that the integrand on the right-hand side of (9.197) is bounded by  $|r_{xx}(u)|$  so that Lebesgue's dominated convergence theorem (Chapter 3) applies.

(f) Since the the limit and integration operations can be interchanged, show

$$X_{\text{PSD}}(\omega) = \int_{-\infty}^{\infty} r_{xx}(u)e^{-j\omega u} \left\{ \lim_{L \rightarrow \infty} \left[ \frac{2L - |u|}{2L} \right] \right\} du = R_{xx}(\omega), \quad (9.198)$$

where  $R_{xx}(\omega)$  is the radial Fourier transform of  $r_{xx}(t)$ .

23. Consider a linear system  $y = Hx$ , where the WSS random signal  $x(t)$  is the input and  $y(t)$  is the corresponding output. Let  $r_{xx}(\tau) = E[x(t)x(t + \tau)]$  and  $r_{yy}(\tau) = E[y(t)y(t + \tau)]$ .

(a) Show that the cross correlation  $r_{xy}(\tau) = r_{xx}(\tau) * \overline{h(-\tau)}$ .

- (b) Show that  $r_{yy}(\tau) = r_{xy}(\tau) * h(\tau)$ .
- (c) Show that  $Y_{\text{PSD}}(\Omega) = X_{\text{PSD}}(\Omega)|H(\Omega)|^2$ , where  $H(\Omega)$  is the radial Fourier transform of  $h(t)$ .
24. Suppose that real-valued discrete signal  $x(n)$  is sampled at  $F_s = 1/T$  Hz. We select a window of  $N > 0$  values and compute the DFT of order  $N$ . Thus, the DFT  $X(k)$  has frequency resolution  $(NT)^{-1}$  and its coefficients represent discrete frequencies  $(NT)^{-1}, 2(NT)^{-1}, \dots, (2T)^{-1}$ .
- (a) Show that adding a pure sinusoid of one these frequencies—say  $\omega_k = kF_s/N$ , for  $1 \leq k \leq N/2$ —to  $x(n)$  will alter only  $X(k)$  and  $X(N - k)$ .
- (b) Verify experimentally using that  $y(n) = x(n) + \cos(2\pi nk/N)$  a sinusoid of frequency  $\omega \neq \omega_k$ , for any  $1 \leq k \leq N/2$ , will perturb all of the  $X(k)$ .
- (c) Show that the difference caused by adding the sinusoid diminishes in magnitude like  $1/|\omega - \omega_k|$  as  $|\omega - \omega_k|$  increases [32].
25. This problem motivates use of the sampling interval  $T$  in the bilinear transformation (9.70). The derivation closely follows [33]. Consider the analog integrator system with impulse response

$$h(t) = \begin{cases} 0 & \text{if } t < 0, \\ 1 & \text{if } t \geq 0. \end{cases} \quad (9.199)$$

- (a) Let  $y = Hx$ , so that  $y(t) = (h*x)(t)$  and show that for  $0 < a < b$ ,

$$y(b) - y(a) = \int_a^b x(t) dt. \quad (9.200)$$

- (b) Argue that as  $a \rightarrow b$ ,

$$y(b) - y(a) \approx \frac{b-a}{2}[x(a) + x(b)]. \quad (9.201)$$

- (c) Let  $a = nT - T$  and  $b = nT$  so that (9.201) becomes a discrete integrator and show that

$$Y(z) - z^{-1}Y(z) = \frac{T}{2}[z^{-1}X(z) + X(z)]. \quad (9.202)$$

- (d) Show that the discrete integrator has  $z$ -transform

$$H(z) = \frac{T(z+1)}{2(z-1)}. \quad (9.203)$$

- (e) Show that the Laplace transform of the analog integrator is  $H(s) = s^{-1}$ .
- (f) Argue that an analog system defined by a difference equation (9.65) can be implemented using adders, amplifiers, and integrators.

- (g) Replace every analog element by its corresponding discrete element and conclude that the discrete transfer function corresponding to (9.65) is given by

$$s = \frac{2(z-1)}{T(z+1)}. \quad (9.204)$$

26. Prove Liouville's theorem, which we used to justify the fundamental theorem of algebra. Let  $|f(z)| \leq B$  on  $\mathbb{C}$  be everywhere differentiable, or *analytic*.

- (a) Show that the Cauchy Residue Theorem (Chapter 1) implies

$$f(z) = \frac{1}{2\pi j} \oint_C \frac{f(s)}{s-z} ds, \quad (9.205)$$

where  $C$  is a large circular contour centered about  $z \in \mathbb{C}$ .

- (b) Show that

$$f'(z) = \frac{1}{2\pi j} \oint_C \frac{f(s)}{(s-z)^2} ds. \quad (9.206)$$

- (c) If  $C$  has radius  $R > 0$ , show that

$$|f'(z)| \leq \frac{B}{R}. \quad (9.207)$$

- (d) Since the radius of  $C$  may be arbitrarily large, conclude that  $f'(z) = 0$  and  $f(z) \equiv \text{constant}$ .

27. Suppose a rational function  $P(\Omega) = B(\Omega)/A(\Omega)$  is even:  $P(\Omega) = P(-\Omega)$  for all  $\Omega \in \mathbb{R}$ . Show that  $A(\Omega)$  and  $B(\Omega)$  have no terms of odd degree.

28. Consider the analog Lorentzian signal  $h(t)$  with rational (radial) Fourier transform.  $H(\Omega) = (1 + \Omega^2)^{-1}$ .

- (a) Show that  $h(t)$  is given by

$$h(t) = \frac{1}{2\pi} \int_{-\infty}^{\infty} H(\Omega) e^{j\Omega t} d\Omega = \frac{e^{-|t|}}{2}. \quad (9.208)$$

- (b) Using synthetic signals, evaluate the performance of  $h(t)$  as a peak, valley, and transient detector.

- (c) Evaluate the signal analysis performance of  $h(t)$  for detecting the same signal features in the presence of synthetic additive noise.

- (d) Identify suitable real data sets and report on the Lorentzian's capabilities for detecting these same features.

29. Develop software for a Butterworth filter design tool.

- (a) Given a discrete cutoff frequency  $\omega_c$  and filter order  $N > 0$ , compute the analog cutoff  $\Omega_c$ .

- (b) Find the above poles of the analog squared Fourier magnitude response function.
- (c) Select poles in order to ensure a stable filter.
- (d) Derive the discrete impulse response  $h(n)$ .
- (e) Compute the discrete magnitude response  $|H(\omega)|$ .
- (f) Compute the margin by which the filter  $H$  passes or fails the passband and stopband constraints.
- (g) Provide an approximation feature that computes the filter order given  $\omega_c$  as well as passband and stopband criteria.

## Time-Frequency Signal Transforms

Time-frequency signal transforms combine traditional Fourier transform signal spectrum information with a time location variable. There results a two-dimensional transformed signal having an independent frequency variable and an independent time variable. Such a signal operation constitutes the first example of a *mixed-domain signal transform*.

Earlier discussions, many applications, and indeed our entire theoretical approach considered signal analysis strategies based upon time, frequency, or scale. *Time-domain* methods are adequate for tasks such as edge detection, elementary segmentation, correlation-based shape recognition, and some texture analysis problems. But in many situations, the inherent periodicity within signal regions pushes us toward a decomposition of the signal according to its *frequency content*.

Frequency—or *spectral*—analysis enters the picture as a tool for discovering a signal's sinusoidal behavior. But this is an inherently global approach. Standard spectral analysis methods, which the Fourier transform in both its analog and discrete guises completely typifies, suffer signal interpretation difficulties when oscillations of interest exist only within a limited signal region. As we discovered in the previous chapter, windowing the signal improves local spectral estimates.

Another approach takes a standard signal shape element, shrinks or expands it into a library of local signal forms, and then considers how well different regions of the signal match one or another such local prototypes. This is an analysis based on *signal scale*. The first chapter provided tutorial sketches of all three approaches. Later chapters built up theoretical tools, demonstrated their applications, and discovered some limitations. So far we have worked out much theory and many applications involving time- and frequency-domain techniques, but we have not formalized the notion of a scale-based analysis.

We now have a sufficient theoretical foundation and practical motivation to explore combined methods. The idea is to mix time-domain methods with either the frequency- or the scale-domain approach. Both combinations provide avenues for structural signal decomposition. The theory is rich and powerful. It has developed rapidly in the last few years. We elect to start with the methods that are most intuitive and, in fact, historically prior: the time-frequency transform techniques.

The Fourier transform is the fundamental tool for frequency-domain signal analysis. It does allow us to solve some problems that confound time-domain techniques. The mapping  $X(\omega) = \mathcal{F}[x(t)]$  lays out the frequency content of a signal  $x(t)$ , albeit in complex values, and its large magnitude  $|X(\omega)|$  indicates the presence of a strong sinusoidal component of frequency  $\omega$  radians per second in  $x(t)$ . We can construct filters and assemble them into filter banks in order to search for spectral components in frequency ranges of interest. All such strategies stem from the convolution theorem, which identifies time-domain convolution—and hence linear, time-invariant processing—with frequency-domain multiplication. The caveat is that standard Fourier techniques depend on a knowledge of the entire time-domain extent of a signal. Even the filter bank highlights ranges of frequencies that existed in the signal for all time: past, present, and future.

But many signals have salient periodic features only over limited time intervals. Although a global analysis is theoretically possible, it may not be practical or efficient. Consider, for example, an orchestra that must play a two-hour symphony, and let us fancy that the composer employs a Fourier transform music style that assigns each instrument just one tone for the entire duration of the performance. The superposition of the various tones, each constantly emitted for two hours by the musicians, does indeed produce the composer's envisioned piece. Of course, the orchestra has but a finite number of musicians, so what is in effect here is really a Fourier series music synthesis. The conductor's job is greatly simplified, perhaps reducing to a few minor pre-concert modifications to the chosen tones. Concert hall owners could well be drawn to encourage such an artform; it would allow them to hire low-paid, unskilled musicians and cut the conductor's hours. The problem of course is that it would be nearly impossible to get the right tonal mix to compose a Fourier symphony. A few hertz too far in this or that direction generates not a symphony but a cacophony instead. Localizing the tones works much better. The composer uses a local frequency synthesis, assigning tones to moments in time; the musicians—they must be artists of supreme skill and dedication—read the musical notation and effect the appropriate, time-limited tones; and the conductor orchestrates the entire ensemble, setting the tempo and issuing direction as the performance proceeds. The composition of the signal in terms of time-localized tones is far easier to understand, communicate, replicate, and modify.<sup>1</sup>

## 10.1 GABOR TRANSFORMS

The previous chapter studied the strategy of time-limiting, or windowing, a signal before calculating its spectrum. This technique—of which there are many variants—furnishes better estimates of the signal's spectrum, because it restricts the signal

<sup>1</sup>Interestingly enough, there is a musical composition style that combines long-term tones to produce desired harmonies: "spectral music." Its resonances evolve slowly, retain a distinctly synthetic character, and thereby differ greatly from traditional 12-tone music. French composer Gérard Grisey (1946–1998), winner of the Rome prize, pioneered this form.

values to those over which the relevant oscillatory signal features should appear. The spectrogram of the signal  $x(t)$  relative to the window function  $w(t)$  is the squared magnitude of the Fourier transform of the product  $s(t) = x(t)w(t)$ :  $|\mathcal{F}[s(t)]|^2 = |\mathcal{F}[x(t)w(t)]|^2 \geq 0$ . Applications can therefore compare or threshold spectrogram values in order to decide whether one frequency is more significant than another or whether an individual frequency is significant, respectively. With the spectrogram, of course, the application design may need to search through possible time locations as well as through possible frequency ranges when seeking local spectral components. That is, Fourier applications tend to be one-dimensional, in contrast to short-time Fourier applications, which are inherently two-dimensional in nature.

We first explore the basic ideas of the transform, working with its original analog formulation. Section 10.1.2 develops the idea of the time-frequency plane. The Gabor transform partitions the  $(t, \omega)$ -plane into equally sized regions, which Gabor dubbed “logons,” from the ancient Greek word *logos*, meaning *word* or *account*. Logons are now generally called *time-frequency windows* or *atoms*. These time-frequency cells contain the signal’s local frequency information, and their derivation provides a structural interpretation. Time-frequency windows with smaller  $t$ -dimensions provide higher signal time resolution, and those with tighter  $\omega$ -dimensions have better signal frequency resolution. So small time-frequency cells are good, but we will eventually discover that a lower limit on cell size exists.

We generalize the Gabor transform further in Section 10.2 to include general window functions. It is proven, however, that among the many short-time Fourier techniques, the Gabor transform has smallest time-frequency windows. A Gaussian window, therefore, provides a joint time and frequency resolution superior to all other window functions: Hanning, Hamming, Kaiser, Bartlett, and so on. Finally, we derive the discretization of the Gabor transform in Section 10.3.

The Gabor transform uses a Gaussian window to create a window of time from which the spectrum of the local signal values are computed. Gaussian signals possess a magic property: Their Fourier transform is also a Gaussian. And this fact imparts an utterly elegant mathematical development to the study of the transform. But elegance is not the only reason for starting our study of short-time Fourier methods with the Gabor transform. In a sense that we will make precise momentarily, the Gabor transform is in fact the optimal short-time Fourier transform.

Carefully note that the width of the Gaussian window, as measured by its variance, is fixed throughout the transformation. Allowing it to vary has proven useful in many applications, but doing so undermines the essence of the transform as a time-frequency tool. It could indeed be argued that varying the window width makes it more like a time-scale transform. The location of the time-domain window, on the other hand, does change and becomes a variable of the two-dimensional, complex valued, Gabor transform function.

After Gabor’s original paper [1], occasional research contributions related to Gabor transforms appeared sporadically in the scientific and engineering literature over the next 30 years. Interest in mixed-domain transforms accelerated with the discovery of the wavelet transform in the mid-1980s. There are now a variety of tutorial articles [2–4] on time-frequency transforms. Books devoted to Gabor analysis and

the broader category of time-frequency transforms include Refs. 5–9. Their introductory chapters and those concentrating on the short-time Fourier transforms—of which the Gabor transform, by using a Gaussian window, is a particular case—are the most accessible. Treatments of time-scale transforms, or wavelets, often contain material introducing time-frequency transforms; we have found the material in Refs. 10–13 to be particularly useful.

### 10.1.1 Introduction

The Gabor transform picks a particular time-limiting window—the Gaussian—and generalizes the windowed spectrum computation into a full signal transform. The goal is to capture both the frequency components of a signal and their time locality in the transform equation. Of course, a Gaussian window is not truly finite in extent; its decay is so fast, however, that as a practical computation matter it serves the purpose of localizing signal values. Finite windows are possible with species [14–18].

**Definition (Gabor Transform).** Let  $g(t)$  be some Gaussian of zero mean:

$$g(t) = Ae^{-Bt^2}, \tag{10.1}$$

where  $A, B > 0$ . If  $x(t) \in L^2(\mathbb{R})$  is an analog signal, then its *Gabor transform*, written  $X_g(\mu, \omega)$ , is the radial Fourier transform of the product  $x(t)g(t - \mu)$ :

$$X_g(\mu, \omega) = \int_{-\infty}^{\infty} x(t)e^{-\frac{(t-\mu)^2}{2\sigma^2}} e^{-j\omega t} dt. \tag{10.2}$$

We will occasionally use the “fancy  $G$ ” notation for the Gabor transform:  $X_g(\mu, \omega) = \mathcal{G}_g[x(t)](\mu, \omega)$ . The windowing function  $g(t)$  in (10.1) remains fixed for the transform. If its parameters are understood—for instance, it may be the Gaussian of zero mean and standard deviation  $\sigma > 0$ —then we may drop the subscript  $g$  for the windowing function.

No reader can have overlooked the fact that we define the Gabor transform for  $L^2(\mathbb{R})$  signals. Analog Fourier analysis (Chapter 5) shows that square-integrable signals have Fourier transforms which are also in  $L^2(\mathbb{R})$ . Thus, if  $x(t) \in L^2(\mathbb{R})$  and  $g(t)$  is a Gaussian, then  $x(t)g(t - \mu) \in L^2(\mathbb{R})$  also, and the Fourier transform integral (10.2) therefore exists. Now for each  $\mu$ ,  $\mathcal{F}[x(t)g(t - \mu)](\omega) \in L^2(\mathbb{R})$ , and this will therefore enable us to find a Gabor inverse transform, or synthesis formula.

It is possible to specify a particular normalization for the Gaussian window used in the Gabor transform. For example, we might choose  $\|g(t)\|_1 = 1$  or  $\|g(t)\|_2 = 1$ , where  $\|\cdot\|_p$  is the norm in the Banach space  $L^p(\mathbb{R})$  of Chapter 3. Gaussian signals belong to both spaces. Either choice makes some Gabor transform properties look

nice but not others. We generally normalize the window with respect to the  $L^1(\mathbb{R})$  norm, so that our windowing functions are zero-mean Gaussians of standard deviation  $\sigma > 0$ ,  $g_{0,\sigma}(t)$ :

$$X_g(\mu, \omega) = \frac{1}{\sigma\sqrt{2\pi}} \int_{-\infty}^{\infty} x(t) e^{-\frac{(t-\mu)^2}{2\sigma^2}} e^{-j\omega t} dt. \quad (10.3)$$

The exercises explore how these alternative Gabor transform normalizations affect various transform properties.

Observe that the Gabor transform, unlike the analog Fourier transform, is a function of two variables. There is a time-domain variable  $\mu$ , which is the center or mean of the window function, and a frequency-domain variable,  $\omega$ . Since a time-domain variable—namely the location of the window's center,  $\mu$ —is a parameter of the transform, the inverse Gabor transform involves a two-dimensional, or iterated integral. Figure 10.1 shows the Gabor transform scheme.

It is also possible to vary the width of the window, which is determined by  $\sigma$ , the standard deviation of the Gaussian. However, this changes the fundamental analytical nature of the transform operation, and our theory endeavors to avoid this. If  $\sigma$  changes while  $\omega$  remains fixed, then the effect of the transform is to find oscillatory components of radial frequency  $\omega$  over signal regions of varying width. But this is the defining characteristic of a scale-based signal analysis. The size of the prototype signal changes. When  $\omega$  and  $\sigma$  both vary, we lapse into a hybrid scale and frequency approach. This does aid some applications. But our present purpose is to reveal the strengths and weaknesses of pure time-frequency methods, and therefore we fix  $\sigma$  for each particular Gabor transform formulation.

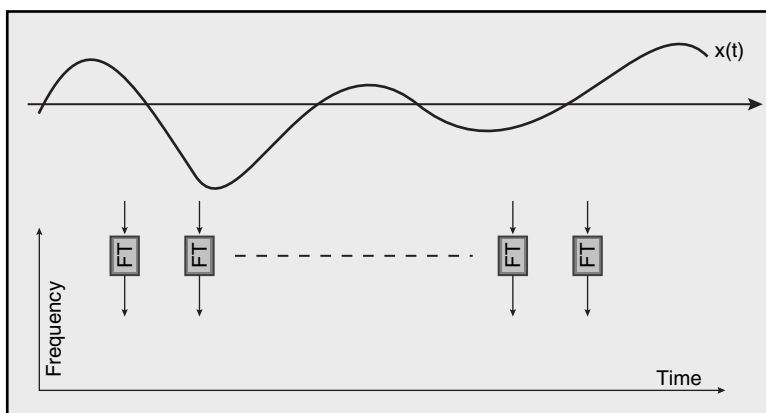


**Fig. 10.1.** The Gabor transform finds the spectral content of  $x(t)$  within a Gaussian window  $g(t - \mu)$ . The two-dimensional transform function takes parameters  $\mu$ , the window's center, and  $\omega$ , the frequency of the exponential  $\exp(j\omega t)$ .

### 10.1.2 Interpretations

There are several fruitful ways to interpret the resulting Gabor transform:

- The most immediate way to visualize  $X_g(\mu, \omega)$  is to see it as the Fourier transform of the windowed—and therefore essentially time-limited—signal  $x(t)g(t - \mu)$ .
- Secondly, in resonance with our physical concept of the Fourier transform, we can think of  $X_g(\mu, \omega)$  as an inner product relation that measures the similarity of  $x(t)$  to the pulse  $g(t)\exp(j\omega t)$ , a Gabor elementary function (GEF).
- Parseval's theorem provides yet a third interpretation: an inner product measure of the similarity of the Fourier transforms of  $x(t)$  and  $g(t)\exp(j\omega t)$ .
- Finally, the Fourier transform's convolution theorem shows that the Gabor transform is a filtering operation on  $X(\omega)$ , the Fourier transform of  $x(t)$ .

So the idea of windowing a signal  $x(t)$  with a Gaussian and making the location of the window a parameter of the transform richly interconnects concepts in signal spaces and transforms. In fact, we encounter two more interpretations of this many-faceted transform later in the chapter! But these first four carry us a long ways, so let us further investigate them.

The most immediate observation is that the Gaussian function  $g(t)$  windows signal values of  $x(t)$  in a neighborhood of around the point  $t = \mu$ . This springs right out of the definition. The windowing effect suppresses oscillatory components of  $x(t)$  distant from  $t = \mu$ . The Gabor transform of  $x(t)$ ,  $X_g(\mu, \omega)$ , is thus the frequency content of  $x(t)$  in this Gaussian-trimmed region.

Another perspective on the Gabor transform follows, if we recall that the product  $g(t)\exp(-j\omega t)$  in the integrand (10.2) is the complex conjugate of a Gabor elementary function,<sup>2</sup> introduced in Chapter 1. Thus, if  $x(t) \in L^2(\mathbb{R})$ , then for each  $\omega \in \mathbb{R}$ , the Gabor transform integral is an inner product:  $\langle x(t), g(t - \mu)\exp(j\omega t) \rangle$ . Or, if the Gaussian has zero mean and standard deviation  $\sigma > 0$ , then  $X_g(\mu, \omega) = \langle x(t), g_{\mu, \sigma}(t)\exp(j\omega t) \rangle$ . Beginning with elementary vector spaces, through abstract inner product spaces, and finally with Hilbert spaces, the inner product relation continues to serve as our yardstick for establishing signal similarity. Hence, the Gabor transform  $X_g(\mu, \omega)$  measures the similarity between  $x(t)$  and the Gabor elementary function  $g(t - \mu)\exp(j\omega t)$ —an important idea which leads directly to the next point and figures prominently in the sequel.

Our third view of the Gabor transform follows from applying Parseval's formula to inner product relation:

$$\langle x(t), g(t - \mu)e^{j\omega t} \rangle = \frac{1}{2\pi} \langle X(\theta), \mathcal{F}[g(t)e^{j\omega t}] \rangle = X_g(\mu, \omega). \quad (10.4)$$

<sup>2</sup>Gabor actually used the Hertz formulation of the Fourier transform in his landmark 1946 paper. He applied the results to human hearing, observing that, up to about 1 kHz and independent of pulse width, we can distinguish some 50% of audible GEFs. Above that frequency, our sense rapidly deteriorates; Gabor concluded that cheaper means of transmission—although perhaps hampered by a poorer frequency, response—might replace more faithful and expensive systems [19].

Note that we are fixing  $\omega$  so that the Gabor elementary function  $g(t)\exp(j\omega t)$  is a pure function of  $t$ . The dummy variable for  $\mathcal{F}[x(t)](\theta) = X(\theta)$  in (10.4) changes from the usual  $\omega$  to avoid a conflict. Thus, the Gabor transform is a (scaled) similarity measure between the Fourier transforms of  $x(t)$  and the GEF  $g(t - \mu)\exp(j\omega t)$ .

The convolution theorem for the radial Fourier transform provides a fourth insight into the Gabor transform. Convolution in time is equivalent to multiplication in frequency. And, reversing the transform direction, convolution in frequency corresponds to termwise multiplication in time. Therefore, if  $y(t) = g(t)\exp(j\omega t)$ , it follows that

$$X_g(\mu, \omega) = \langle x(t), g(t - \mu)e^{j\omega t} \rangle = \frac{1}{2\pi}(X*Y)(\theta) = \frac{1}{2\pi} \int_{-\infty}^{\infty} X(\zeta)Y(\theta - \zeta) d\zeta. \quad (10.5)$$

Gabor transforming a signal  $x(t)$  is the same as filtering  $X(\theta)$  with the Fourier transform of the Gabor elementary function  $y(t) = g(t - \mu)\exp(j\omega t)$ .

These several interpretations lead us to further study the Gaussian, the GEFs, inner products, and convolution operations in both the time and frequency domains.

### 10.1.3 Gabor Elementary Functions

By now, Gabor elementary functions  $y(t) = g(t - \mu)\exp(j\omega t)$  are quite familiar. We introduced them as early as Chapter 1, noted their applicability to spectral analysis of signal texture in Chapter 4, and considered them as amplitude-modulated sinusoidal carrier signals in Chapter 5. They have other names, too: Gabor atoms or windowed Fourier atoms. Now we have seen that  $y(t)$  is a signal *model*—or *prototype*—to which the Gabor transform compares  $x(t)$ . This section continues our investigation of these important signal prototypes.

In the time domain,  $y(t) = g(t)\exp(j\omega t)$  is a complex exponential that is amplitude modulated by a Gaussian  $g(t)$ . The Gaussian envelope—let us say it has mean  $\mu$  and standard deviation  $\sigma$ — $g_{\mu,\sigma}(t)$  amplitude modulates the real and imaginary parts of  $\exp(j\omega t)$ . From a communications theory standpoint, the latter are sinusoidal carrier signals. The real part of  $y(t)$  is  $\cos(\omega t)$ -modulated by  $g_{\mu,\sigma}(t)$ ; hence,  $\text{Real}[g_{\mu,\sigma}(t)\exp(j\omega t)]$  is even. And its imaginary part is  $\sin(\omega t)$  inside the same envelope, making  $\text{Imag}[g_{\mu,\sigma}(t)\exp(j\omega t)]$  an odd signal. The GEFs exhibit more or less oscillations as the frequency of the exponential carrier signal increases or decreases, respectively, under a modulating Gaussian pulse of constant width. This changes the shape of the model signal as in Figure 10.2.

Altering the spread of the Gaussian envelope (given by its width parameter  $\sigma$ ) while leaving  $\omega$  constant also produces prototype signals of different shapes. The large sinusoidal oscillations persist over a wider time-domain region (Figure 10.3). This behavior typifies time-scale analysis methods, which depend upon comparing source signals with models of variable time-domain extent, but similar shape. Unless we tie the frequency  $\omega$  to the Gaussian's standard deviation  $\sigma$ , then the Gabor elementary functions will exhibit different basic shapes as  $\sigma$  changes. This

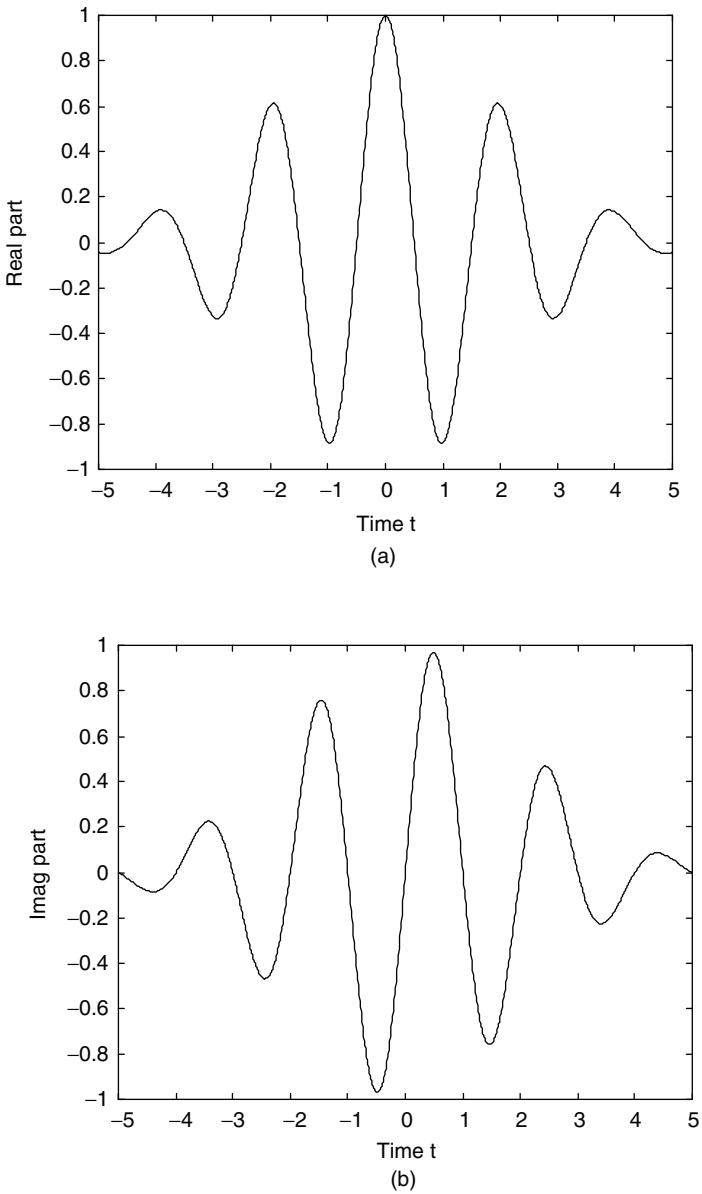


**Fig. 10.2.** Gabor elementary functions. The cosine term (a) represents the real part of a GEF and is an even signal. The sine term represents the imaginary part and is an odd signal (b). Panels (c) and (d) show the effect of frequency doubling.

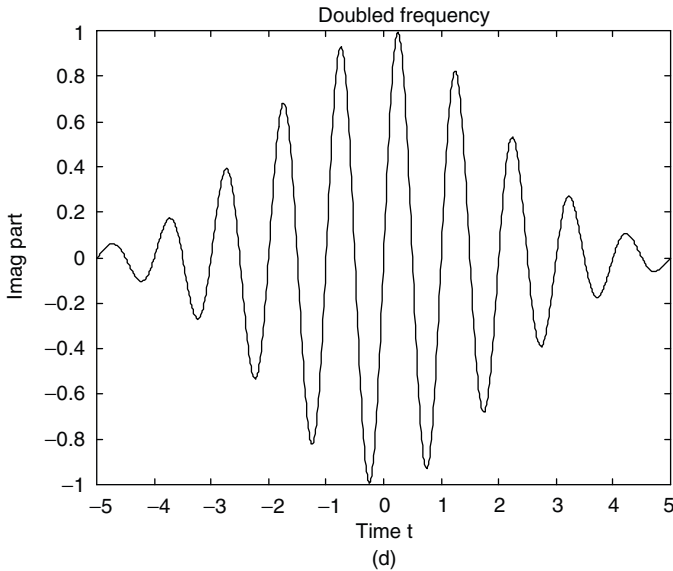
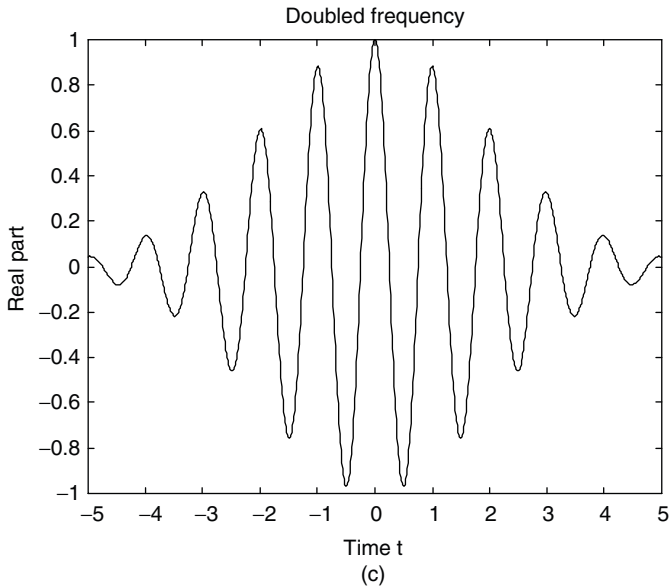
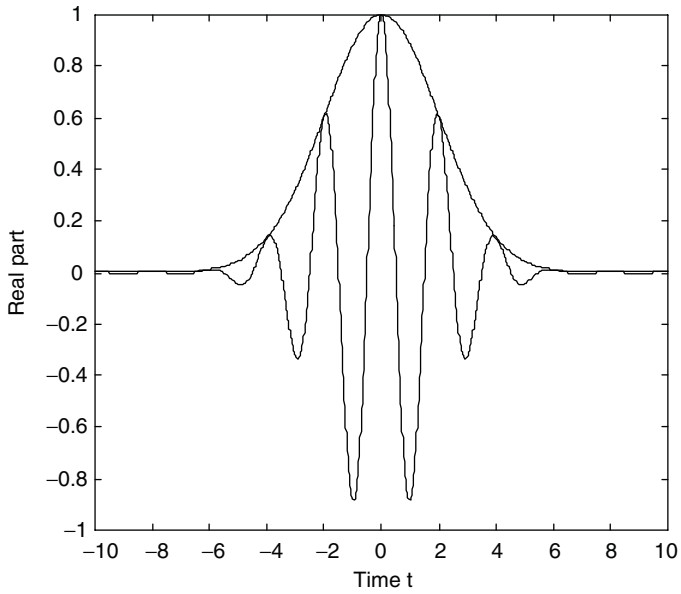
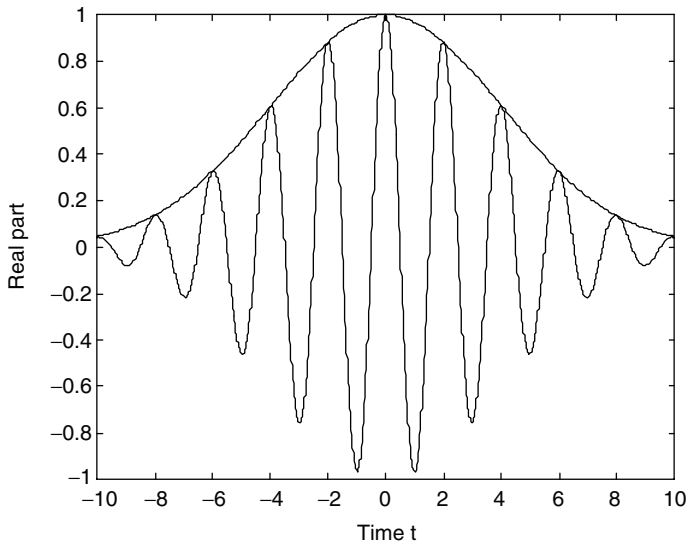


**Fig. 10.2** (Continued)

technique is often called the *adaptive Gabor transform*. But a bona fide time-frequency transform should be able to reveal all frequencies within a local signal region; we cannot mathematically link  $\omega$  and  $\sigma$ . Consequently, to preserve the time-frequency nature of the Gabor transform and short-time Fourier tools in general, we avoid flexible windows. Time-scale transforms (Chapter 11) use dilation to



(a)



(b)

**Fig. 10.3.** Window size variation. With the radial frequency  $\omega$  fixed, the shape of a Gabor elementary function signal (a) changes as the window expands (b).

maintain a basic shape while changing the size of a prototype signal. This chapter’s exercises preview this idea.

Now let us consider the frequency-domain representation of Gabor elementary functions. The formula for the Fourier transform of  $y(t) = g_{\mu,\sigma}(t)\exp(j\omega_0 t)$  derives from the radial Fourier transform’s properties (Chapter 5).

**Proposition (Fourier Transform of Gabor Elementary Function).** Let  $\sigma > 0$  and suppose  $g(t) = g_{\mu,\sigma}(t)$  is the Gaussian with mean  $\mu$  and standard deviation  $\sigma$ . Let  $y(t) = g(t)\exp(j\omega_0 t)$  be a Gabor elementary function with envelope  $g(t)$  and radial frequency  $\omega_0$ . Then

$$Y(\omega) = \frac{1}{2\pi} \exp\left[-\frac{\sigma^2}{2}(\omega - \omega_0)^2 + j(\omega - \omega_0)\mu\right]. \tag{10.6}$$

**Proof:** In Chapter 5 we calculated the radial Fourier transform of the Gaussian; there results a Gaussian once more:  $\mathcal{F}[\exp(-t^2)](\omega) = \pi^{1/2}\exp(-\omega^2/4)$ . The Fourier transform properties allow us to write out the Fourier transform for  $g(t) = g_{\mu,\sigma}(t)$ :

$$G(\omega) = \int_{-\infty}^{\infty} g(t)e^{-j\omega t} dt = \exp\left(-\left[\frac{\sigma^2\omega^2}{2} + j\omega\mu\right]\right) \tag{10.7}$$

whose magnitude  $|G(\omega)|$  is a Gaussian centered at  $\omega = 0$ . Applying the generalized Fourier transform handles the exponential factor:  $\mathcal{F}[\exp(j\omega_0 t)](\omega) = \delta(\omega - \omega_0)$ . A termwise multiplication  $y(t) = x_1(t)x_2(t)$  in time has Fourier transform  $Y(\omega) = X_1(\omega)*X_2(\omega)/(2\pi)$ . This implies  $\mathcal{F}[g(t)\exp(j\omega_0 t)] = G(\omega)*\delta(\omega - \omega_0)/(2\pi)$ , the convolution of a Gaussian with a shifted Dirac delta. Making  $\theta$  the integration variable for continuous-domain convolution, we compute:

$$\begin{aligned} Y(\omega) &= \mathcal{F}[g(t)e^{j\omega_0 t}] = \frac{1}{2\pi} \int_{-\infty}^{\infty} \delta(\theta - \omega_0) e^{-[\sigma^2(\omega - \theta)^2 + j(\omega - \theta)\mu]} d\theta \\ &= \frac{1}{2\pi} e^{-[\sigma^2(\omega - \omega_0)^2 + j(\omega - \omega_0)\mu]} \end{aligned} \tag{10.8}$$

We use the Sifting Property of the Dirac delta in (10.8), the last expression of which is precisely the value (10.6). ■

*Remarks.* In (10.8) observe that  $|Y(\omega)|$  is a scaled (amplified or attenuated) Gaussian pulse centered at  $\omega = \omega_0$  in the frequency domain (Figure 10.4). To find the Fourier transform of  $\text{Real}[y(t)]$ , we write  $\cos(\omega_0 t) = [\exp(j\omega_0 t) + \exp(-j\omega_0 t)]/2$ . Its spectrum is a pair of impulses at  $|\omega| = \omega_0$ ; hence, a convolution like (10.8) produces a sum of two Gaussians. A similar procedure (exercises) works for the imaginary part of  $\exp(j\omega_0 t)$  and gives us the Fourier transform of  $\text{Imag}[y(t)]$ .

Simple experiments demonstrate that for the Gabor elementary function a reciprocal relationship apparently exists between time- and frequency-domain window widths (Figure 10.4). Further elucidation requires us to formalize the concept of window width, which is a topic covered in Section 10.2.4.

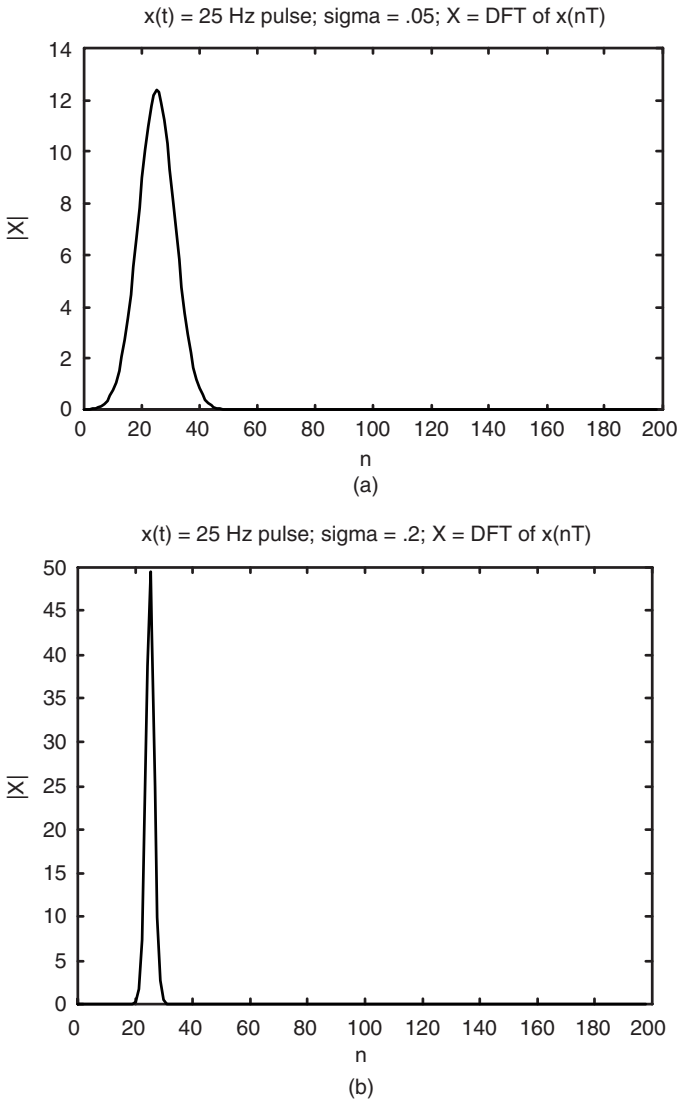


**Fig. 10.4.** Fourier transform of a Gabor elementary function. A narrow time-domain signal,  $y(t) = g_{\mu,\sigma}(t)\exp(j\omega_0 t)$ , has a wide magnitude spectrum (a). As the time-domain width of the Gaussian envelope grows, the frequency-domain window width shrinks (b).

### 10.1.4 Inversion

Recalling that all of the analog and discrete versions of the Fourier transform of Chapters 5 and 7 have inverse relations, let us consider the same problem for the Gabor transform. Suppose we transform with respect to a Gaussian window

$g(t) = g_{\mu,\sigma}(t)$ . We call the forward transform relation,  $X(\omega) = \mathcal{F}[x(t)]$ , the *analysis equation*, and we call the inverse Fourier transform relation,  $x(t) = \mathcal{F}^{-1}[X(\omega)]$ , the *synthesis equation*. Of course,  $X_g(\mu, \omega)$  is the radial Fourier transform of the windowed signal  $x(t)g_{\mu,\sigma}(t)$ , so its synthesis equation produces not  $x(t)$ , but  $x(t)g_{\mu,\sigma}(t)$  back again. How can we get  $x(t)$  from  $X_g(\mu, \omega)$ ? Because  $X_g(\mu, \omega)$  is a function of two variables, we can integrate a second time, letting the Gaussian's location  $\mu$  vary and using it as an integration variable.

We divide our efforts according to whether the Gabor transform of  $x(t)$  is integrable. As with the Fourier transform development in Chapter 5, if  $X_g(\mu, \omega) \in L^1(\mathbb{R})$ , then we can freely interchange integration limits. If we assume  $x(t) \in L^2(\mathbb{R})$  and nothing more, then a limiting argument is once again necessary.

**10.1.4.1 Assuming Transform Integrability.** The following lemma is a direct consequence of our choice of  $g_{\mu,\sigma}(t)$  for the Gabor transform windowing signal. It shows that, for each  $\mu$ , the Gabor transform  $X_g(\mu, \omega)$  represents a local piece of  $\mathcal{F}[x(t)]$ . Independent variable  $\omega$  corresponds to the spectral frequency, and  $\mu$  represents the spectral fragment's time location. Indeed, when we integrate all of these pieces together (10.9), the result is the full signal spectrum  $X(\omega)$ .

**Lemma.** Suppose  $x(t) \in L^2(\mathbb{R})$ ;  $\mu, \sigma \in \mathbb{R}$ ,  $\sigma > 0$ ;  $g(t) = g_{\mu,\sigma}(t)$  is the Gaussian window with mean  $\mu$  and standard deviation  $\sigma$ ; and let  $X_g(\mu, \omega) \in L^1(\mathbb{R})$  be the Gabor transform of  $x(t)$ . Then,

$$X(\omega) = \int_{-\infty}^{\infty} X_g(\mu, \sigma) d\mu. \quad (10.9)$$

**Proof:** Let us expand the integrand in (10.9):

$$\int_{-\infty}^{\infty} X_g(\mu, \sigma) d\mu = \int_{-\infty}^{\infty} \left( \int_{-\infty}^{\infty} x(s)g(s)e^{-j\omega s} ds \right) d\mu = \int_{-\infty}^{\infty} x(s)e^{-j\omega s} \left( \int_{-\infty}^{\infty} g_{\mu,\sigma}(s) d\mu \right) ds. \quad (10.10a)$$

Fubini's theorem [11, 12] states that if an iterated integral's integrand is absolutely integrable, then it is identical to the double integral, and the order of iteration is irrelevant. The interchange of limits (10.10a) is possible by applying Fubini's theorem, which is possible because the integrand is absolutely integrable. The inner integrand is unity, since  $\|g\|_1 = 1$ . Consequently,

$$\int_{-\infty}^{\infty} X_g(\mu, \sigma) d\mu = \int_{-\infty}^{\infty} x(s)e^{-j\omega s} ds = X(\omega). \quad (10.10b)$$

Now we can prove an initial inverse Gabor transform relationship for the situation where  $X_g(\mu, \omega)$  is integrable. ■

**Theorem (Inverse Gabor Transform or Synthesis Equation).** Suppose  $\sigma > 0$ ;  $x(t) \in L^2(\mathbb{R})$ ;  $g(t) = g_{\mu,\sigma}(t)$  is the Gaussian window with mean  $\mu$  and standard deviation  $\sigma$ ; and let  $X_g(\mu, \omega) \in L^1(\mathbb{R})$  be the Gabor transform of  $x(t)$ . Then,

$$x(t) = \frac{1}{2\pi} \int_{-\infty}^{\infty} \left( \int_{-\infty}^{\infty} X_g(\mu, \omega) e^{j\omega t} d\omega \right) d\mu. \tag{10.11}$$

**Proof:** Using the definition of the Gabor transform for  $x(t)$ , we have

$$\frac{1}{2\pi} \int_{-\infty}^{\infty} \left( \int_{-\infty}^{\infty} X_g(\mu, \omega) e^{j\omega t} d\omega \right) d\mu = \frac{1}{2\pi} \int_{-\infty}^{\infty} e^{j\omega t} \left( \int_{-\infty}^{\infty} X_g(\mu, \omega) d\mu \right) d\omega. \tag{10.12}$$

We use the assumption that  $X_g(\mu, \omega) \in L^1(\mathbb{R})$  to infer  $X_g(\mu, \omega)\exp(j\omega t) \in L^1(\mathbb{R})$  as well; Fubini’s theorem then implies (10.12). Using the lemma to evaluate the parenthesized integral on the right-hand side of (10.12) gives

$$\frac{1}{2\pi} \int_{-\infty}^{\infty} e^{j\omega t} \left( \int_{-\infty}^{\infty} X_g(\mu, \omega) d\mu \right) d\omega = \frac{1}{2\pi} \int_{-\infty}^{\infty} e^{j\omega t} X(\omega) d\omega = x(t) \tag{10.13}$$

as desired. ■

The next result is a time-frequency version of Plancherel’s theorem. It shows that the Gabor transform preserves signal energy. We do not have a perfect proportion, since the equation depends on the  $L^2(\mathbb{R})$  norm of the window function.

We interpose a lemma that shows how to compute the Fourier transform of a Gabor transform.

**Lemma (Fourier Transform of Gabor Transform).** Suppose  $\sigma > 0$ ;  $x(t) \in L^2(\mathbb{R})$ ;  $g(t) = g_{\mu,\sigma}(t)$  is the Gaussian window with mean  $\mu$  and standard deviation  $\sigma$ ; and let  $X_g(\mu, \omega) \in L^1(\mathbb{R})$  be the Gabor transform of  $x(t)$ . Then, for each  $\omega \in \mathbb{R}$  we can Fourier transform the signal  $X_g(\mu, \omega)$ , viewing it as a function of  $\mu$ . So,

$$\int_{-\infty}^{\infty} X_g(\mu, \omega) e^{-j\mu\theta} d\mu = \frac{1}{2\pi} X(\omega + \theta) G(\theta) = \frac{1}{2\pi} X(\omega + \theta) e^{-\frac{\theta^2 \sigma^2}{2}}, \tag{10.14}$$

where  $G(\theta)$  is the radial Fourier transform of  $g(t)$ .

**Proof:** Expanding  $X_g(\mu, \omega)$  in the integrand (10.14) gives

$$\begin{aligned} \int_{-\infty}^{\infty} \left[ \int_{-\infty}^{\infty} x(t) g(t) e^{-j\omega t} dt \right] e^{-j\mu\theta} d\mu &= \int_{-\infty}^{\infty} \left( \left[ \int_{-\infty}^{\infty} x(t) g_{0,\sigma}(t - \mu) e^{-j\omega t} dt \right] \right) e^{-j\mu\theta} d\mu \\ &= \int_{-\infty}^{\infty} \left( \left[ \int_{-\infty}^{\infty} x(t) g_{0,\sigma}(t - \mu) e^{-j\omega t} e^{j\omega\mu} dt \right] \right) e^{-j\mu\theta} e^{-j\omega\mu} d\mu. \end{aligned} \tag{10.15}$$

The algebraic manipulations in (10.15) aim to change the expression's form into a convolution of  $x(t)$  with the Gabor elementary function  $y(s) = g_{0,\sigma}(s)\exp(j\omega s)$ . Because  $g_{0,\sigma}(t - \mu) = g_{0,\sigma}(\mu - t)$ ,

$$\begin{aligned} \int_{-\infty}^{\infty} \left[ \int_{-\infty}^{\infty} x(t)g(t)e^{-j\omega t} dt \right] e^{-j\mu\theta} d\mu &= \int_{-\infty}^{\infty} \left[ \int_{-\infty}^{\infty} x(t)g_{0,\sigma}(\mu - t)e^{j\omega(\mu - t)} dt \right] e^{-j\mu\theta} e^{-j\omega\mu} d\mu \\ &= \int_{-\infty}^{\infty} (x^*y)(\mu)e^{-j\mu(\theta + \omega)} d\mu, \end{aligned} \quad (10.16)$$

which exposes a convolution integral,  $(x * y)(\mu)$ . But now the outer integral in is evidently a radial Fourier transform; invoking the convolution theorem,

$$\begin{aligned} \int_{-\infty}^{\infty} \left[ \int_{-\infty}^{\infty} x(t)g(t)e^{-j\omega t} dt \right] e^{-j\mu\theta} d\mu &= \int_{-\infty}^{\infty} (x * y)(\mu)e^{-j\mu(\theta + \omega)} d\mu \\ &= X(\omega + \theta)Y(\omega + \theta). \end{aligned} \quad (10.17)$$

Now,  $X(\omega + \theta)$  is the Fourier transform of  $x(t)$  evaluated at  $\omega + \theta$ , as the lemma requires.  $Y(\phi) = \mathcal{F}[y(s)](\phi) = \mathcal{F}[g_{0,\sigma}(s)\exp(j\omega s)](\phi)$  is the Fourier transform of a Gabor elementary function. In (10.8) we found  $Y(\phi) = (2\pi)^{-1}\mathcal{F}[g_{0,\sigma}(s)](\phi - \omega)$ . If  $\mu = 0$ , then  $\mathcal{F}[g_{\mu,\sigma}(s)](\phi) = \exp(-\sigma^2\phi^2/2)$ . So  $Y(\omega + \theta) = (2\pi)^{-1}\mathcal{F}[g_{0,\sigma}(s)](\omega + \theta - \omega) = (2\pi)^{-1}\mathcal{F}[g_{0,\sigma}(s)](\theta)$ . Finally,

$$X(\omega + \theta)Y(\omega + \theta) = X(\omega + \theta)\mathcal{F}[g_{0,\sigma}(t)e^{j\omega t}](\omega + \theta) = \frac{X(\omega + \theta)}{2\pi}e^{-\frac{\sigma^2\theta^2}{2}}, \quad (10.18)$$

and the proof is complete. ■

**10.1.4.2 Two-Dimensional Hilbert Spaces in Brief.** Our next result is the time-frequency version of the Plancherel formula. Now, this theorem depends on the two-dimensional  $L^2(\mathbb{R})$  norm. “You are so unaccustomed to speak in images,” Adeimantus ironically remarks to Socrates in the Republic,<sup>3</sup> and we too have been—intentionally—so unaccustomed! The  $L^2(\mathbb{R})$  norm applies to analog *images*, and up until now we have been deliberately partial to one-dimensional signal theory. Nonetheless, time-frequency methods, and mixed-domain techniques in general, often transgress into multidimensional or *image* analysis. This is to be expected, since the transforms do encode both time and frequency information as independent variables in the transformed signal. The theoretical extensions are gratefully straightforward. In fact,  $L^2(\mathbb{R} \times \mathbb{R})$  is a Hilbert space also, and its theoretical development follows from our one-dimensional endeavors in Chapter 3. We do not need to spend a lot of time developing that multidimensional theory here; nevertheless, the concepts of the  $L^2(\mathbb{R}^2)$  space and its norm are worth reviewing.

<sup>3</sup>Republic, vol. II, B. Jowett, translator, Oxford: Clarendon Press, 1964.

**Definition ( $L^2(\mathbb{R}^2)$ ).** A two-dimensional signal  $x(s, t)$  is *square-integrable* or has *finite energy* if

$$\int_{-\infty-\infty}^{\infty-\infty} \int |x(s, t)|^2 ds dt < \infty. \tag{10.19}$$

We denote the set of all such signals by  $L^2(\mathbb{R}^2)$  or  $L^2(\mathbb{R} \times \mathbb{R})$ . If  $x(s, t) \in L^2(\mathbb{R}^2)$ , then

$$\left[ \int_{-\infty-\infty}^{\infty-\infty} \int |x(s, t)|^2 ds dt \right]^{\frac{1}{2}} = \|x\|_{2, L^2(d\mathbb{R}^2)} \tag{10.20}$$

is its  $L^2(\mathbb{R}^2)$  norm. If the context is clear, then we omit the subscripted  $L^2(\mathbb{R}^2)$  in (10.20). If  $x(s, t)$  and  $y(s, t)$  are in  $L^2(\mathbb{R}^2)$ , then we define their inner product by

$$\langle x, y \rangle_{L^2(\mathbb{R}^2)} = \int_{-\infty-\infty}^{\infty-\infty} \int x(s, t) \overline{y(s, t)} ds dt. \tag{10.21}$$

In a clear context, we drop the subscript and write (10.21) as  $\langle x, y \rangle$ . The exercises further cover the ideas of two-dimensional signal spaces.

**Theorem (Gabor Transform Plancherel’s).** Suppose  $\sigma > 0$ ;  $x(t) \in L^2(\mathbb{R})$ ;  $g(t) = g_{\mu, \sigma}(t)$  is the Gaussian with mean  $\mu$  and standard deviation  $\sigma$ ; and let  $X_g(\mu, \omega) \in L^1(\mathbb{R})$  be the Gabor transform of  $x(t)$ . Then

$$\|x\|_2 = \sqrt{2\pi} \frac{\|X_g(\mu, \omega)\|_{2, L^2(\mathbb{R}^2)}}{\|g\|_2}. \tag{10.22}$$

**Proof:** Fubini’s theorem applies to the double integral that defines the  $L^2(\mathbb{R}^2)$  norm:

$$\|X_g(\mu, \omega)\|_{2, L^2(\mathbb{R}^2)}^2 = \int_{-\infty-\infty}^{\infty-\infty} \int |X_g(\mu, \omega)|^2 d\mu d\omega = \int_{-\infty-\infty}^{\infty-\infty} \left[ \int |X_g(\mu, \omega)|^2 d\mu \right] d\omega. \tag{10.23}$$

Since the inner integral is a function of the time domain variable  $\mu$ , we can Fourier transform its integrand with respect to  $\mu$ . An application of the Fourier transform Plancherel formula is then feasible:

$$\|X_g(\mu, \omega)\|_{2, L^2(\mathbb{R}^2)}^2 = \int_{-\infty}^{\infty} \frac{1}{2\pi} \left[ \int_{-\infty}^{\infty} |\mathcal{F}[X_g(\mu, \omega)](\theta)|^2 d\theta \right] d\omega. \tag{10.24}$$

Let  $H(\theta) = \mathcal{F}[g_{0,\sigma}(t)](\theta)$ , so that by the Lemma we find

$$\begin{aligned} \|X_g(\mu, \omega)\|_{2, L^2(\mathbb{R}^2)}^2 &= \frac{1}{2\pi} \int_{-\infty}^{\infty} \left[ \int_{-\infty}^{\infty} \left| \frac{1}{2\pi} X(\omega + \theta) H(\theta) \right|^2 d\theta \right] d\omega \\ &= \frac{1}{2\pi} \int_{-\infty}^{\infty} \frac{1}{(2\pi)^2} \left[ \int_{-\infty}^{\infty} |X(\omega + \theta)|^2 |H(\theta)|^2 d\theta \right] d\omega. \end{aligned} \quad (10.25)$$

To evaluate the iterated integral (10.25), we swap the order of integration and use Plancherel two more times. The last expression above becomes

$$\begin{aligned} \|X_g(\mu, \omega)\|_{2, L^2(\mathbb{R}^2)}^2 &= \frac{1}{2\pi} \int_{-\infty}^{\infty} \frac{|H(\theta)|^2}{2\pi} \left[ \int_{-\infty}^{\infty} \frac{|X(\omega + \theta)|^2}{2\pi} d\omega \right] d\theta \\ &= \frac{\|x\|_2^2}{2\pi} \int_{-\infty}^{\infty} \frac{|H(\theta)|^2}{2\pi} d\theta = \frac{\|x\|_2^2}{2\pi} \|g_{0,\sigma}\|_2^2. \end{aligned} \quad (10.26)$$

■

**10.1.4.3 For General Square-Integrable Signals.** This section develops the Plancherel and inverse results for square-integrable signals, dropping the assumption of integrability on the Gabor transform. We begin with a form of the Parseval theorem.

**Theorem (Gabor Transform Parseval's).** Suppose  $\sigma > 0$ ;  $x(t), y(t) \in L^2(\mathbb{R})$ ;  $g(t) = g_{\mu,\sigma}(t)$  is the Gaussian window with mean  $\mu$  and standard deviation  $\sigma$ ; and let  $X_g(\mu, \omega)$  and  $Y_g(\mu, \omega)$  be the Gabor transforms of  $x(t)$  and  $y(t)$ , respectively. Then

$$2\pi \|g\|_2^2 \langle x, y \rangle = \int_{-\infty}^{\infty} \int_{-\infty}^{\infty} X_g(\mu, \omega) \overline{Y_g(\mu, \omega)} d\omega d\mu = \langle X_g, Y_g \rangle_{L^2(\mathbb{R}^2)}. \quad (10.27)$$

**Proof:** For fixed  $\mu$ , we can apply the Parseval theorem to find

$$\int_{-\infty}^{\infty} X_g(\mu, \omega) \overline{Y_g(\mu, \omega)} d\omega = 2\pi \int_{-\infty}^{\infty} \mathcal{F}^{-1} X_g(\mu, \omega) \mathcal{F}^{-1} \overline{Y_g(\mu, \omega)} d\omega, \quad (10.28)$$

where  $\mathcal{F}^{-1}$  is the inverse radial Fourier transform. Since the inverse Fourier transform of the Gabor transform  $X_g(\mu, \omega)$  is the windowed signal  $x(t)g_{\mu,\sigma}(t)$ , we continue (10.28) as follows:

$$2\pi \int_{-\infty}^{\infty} x(t)g_{\mu,\sigma}(t) \overline{y(t)g_{\mu,\sigma}(t)} dt = 2\pi \int_{-\infty}^{\infty} x(t) \overline{y(t)} g_{\mu,\sigma}^2(t) dt. \quad (10.29)$$

Integrating (10.29) with respect to  $\mu$  produces

$$\begin{aligned} \int_{-\infty-\infty}^{\infty} \int_{-\infty}^{\infty} X_g(\mu, \omega) \overline{Y_g(\mu, \omega)} d\omega d\mu &= 2\pi \int_{-\infty-\infty}^{\infty} \int_{-\infty}^{\infty} x(t) \overline{y(t)} g_{\mu, \sigma}^2(t) dt d\mu \\ &= 2\pi \int_{-\infty}^{\infty} x(t) \overline{y(t)} \int_{-\infty}^{\infty} g_{\mu, \sigma}^2(t) d\mu dt \\ &= 2\pi \|g_{\mu, \sigma}\|_2^2 \langle x, y \rangle. \end{aligned} \tag{10.30}$$

Fubini's theorem and the Schwarz inequality (applied to the inner integral on the top right-hand side of (10.30), which is itself an inner product) allow us to interchange the integration order. ■

The next result shows how to retrieve the original signal  $x(t) \in L^2(\mathbb{R})$  from its Gabor transform  $X_g(\mu, \omega)$ . This is the Gabor transform inverse relation, but it has other names, too. It is sometimes called the *resolution of the identity* or simply the *synthesis equation* for the Gabor transform.

**Theorem (Inverse Gabor Transform).** Suppose  $\sigma > 0$ ;  $x(t) \in L^2(\mathbb{R})$ ;  $g(t) = g_{\mu, \sigma}(t)$  is the Gaussian window with mean  $\mu$  and standard deviation  $\sigma$ ; and let  $X_g(\mu, \omega)$  be the Gabor transform of  $x(t)$ . Then for all  $s \in \mathbb{R}$ , if  $x(t)$  is continuous at  $s$ , then

$$x(a) = \frac{1}{(2\pi \|g\|_2^2)_{-\infty}^{\infty}} \int_{-\infty}^{\infty} X_g(\mu, \omega) g_{\mu, \sigma}(a) e^{j\omega a} d\omega d\mu. \tag{10.31}$$

**Proof:** Consider a family of Gaussians  $h_{a,s}(t)$ , where  $s > 0$ . As  $s \rightarrow 0$ , they approximate a delta function, and, informally, from the sifting property we expect that

$$\lim_{s \rightarrow 0} \langle x(t), h_{a,s}(t) \rangle = x(a) \tag{10.32}$$

when  $x(t)$  is continuous at  $t = a$ . If we set  $y(t) = h_{a,s}(t)$ , then we can apply the prior Plancherel theorem to obtain

$$\langle x, h_{a,s} \rangle = \frac{1}{2\pi \|g\|_2^2} \int_{-\infty-\infty}^{\infty} \int_{-\infty}^{\infty} X_g(\mu, \omega) \left[ \int_{-\infty}^{\infty} h_{a,s}(t) g_{\mu, \sigma}(t) e^{-j\omega t} dt \right] d\omega d\mu. \tag{10.33}$$

We calculate the limit

$$\begin{aligned} \lim_{s \rightarrow 0} \int_{-\infty}^{\infty} h_{a,s}(t) g_{\mu, \sigma}(t) e^{-j\omega t} dt &= \lim_{s \rightarrow 0} \int_{-\infty}^{\infty} h_{a,s}(t) g_{\mu, \sigma}(t) e^{j\omega t} dt \\ &= \int_{-\infty}^{\infty} \lim_{s \rightarrow 0} h_{a,s}(t) g_{\mu, \sigma}(t) e^{j\omega t} dt \\ &= \int_{-\infty}^{\infty} \delta(t-a) g_{\mu, \sigma}(t) e^{j\omega t} dt = g_{\mu, \sigma}(a) e^{j\omega a}. \end{aligned} \tag{10.34}$$

Taking the same limit  $s \rightarrow 0$  on both sides of (10.33) and interchanging limit and integration operations gives

$$\lim_{s \rightarrow 0} \langle x, h_{a,s} \rangle = \frac{1}{2\pi \|g\|_2^2} \int_{-\infty}^{\infty} \int_{-\infty}^{\infty} X_g(\mu, \omega) g_{\mu, \sigma}(a) e^{j\omega a} d\omega d\mu = x(a). \quad (10.35)$$

■

### 10.1.5 Applications

Let us pause the theoretical development for a moment to explore two basic Gabor transform applications: a linear chirp and a pulsed tone. These illustrate the use and behavior of the transform on practical signals. Studying the transform coefficients as dependent on the width of the transform window function will also lead us to important ideas about the relation between the transform's time and frequency resolutions.

**10.1.5.1 Linear Chirp.** This section discusses the Gabor transform for a linear chirp signal. A linear chirp is a sinusoidal function of a squared time variable  $At^2$ , where  $A$  is constant. Thus, as  $|t|$  increases, the signal oscillations bunch up. Signal frequency varies with time in a linear fashion, and we anticipate that the Gabor transform will expose this behavior.

Let us consider the analog signal

$$X_a(t) = \begin{cases} \cos(At^2), & t \in [0, L] \\ 0 & \text{otherwise.} \end{cases} \quad (10.36)$$

The Gabor transform of  $x_a(t)$  is

$$\mathcal{G}[x_a(t)](\mu, \omega) = (X_a)_g(\mu, \omega) = \int_0^L x_a(t) g_{\mu, \sigma}(t) e^{-j\omega t} dt. \quad (10.37)$$

We need to decide upon an appropriate value for the spread of the Gaussian, which is given by its standard deviation  $\sigma$ . Also,  $(X_a)_g$  is a two-dimensional function, so we seek an image representation of the Gabor transform for a range of values,  $\mu$  and  $\omega$ .

We apply Section 7.1.2's ideas for approximating an analog transform with discrete samples. Recall that the discrete Fourier series (DFS) coefficients

$$c(k) = \frac{1}{N} \sum_{n=0}^{N-1} x(n) e^{\frac{-2\pi jnk}{N}}, \quad (10.38)$$

where  $0 \leq k \leq N-1$ , are a trapezoidal rule approximation to the Fourier series integral using the intervals  $[0, T/N]$ ,  $[T/N, 2T/N]$ ,  $\dots$ ,  $[(N-1)T/N, T]$ . Recall as well from

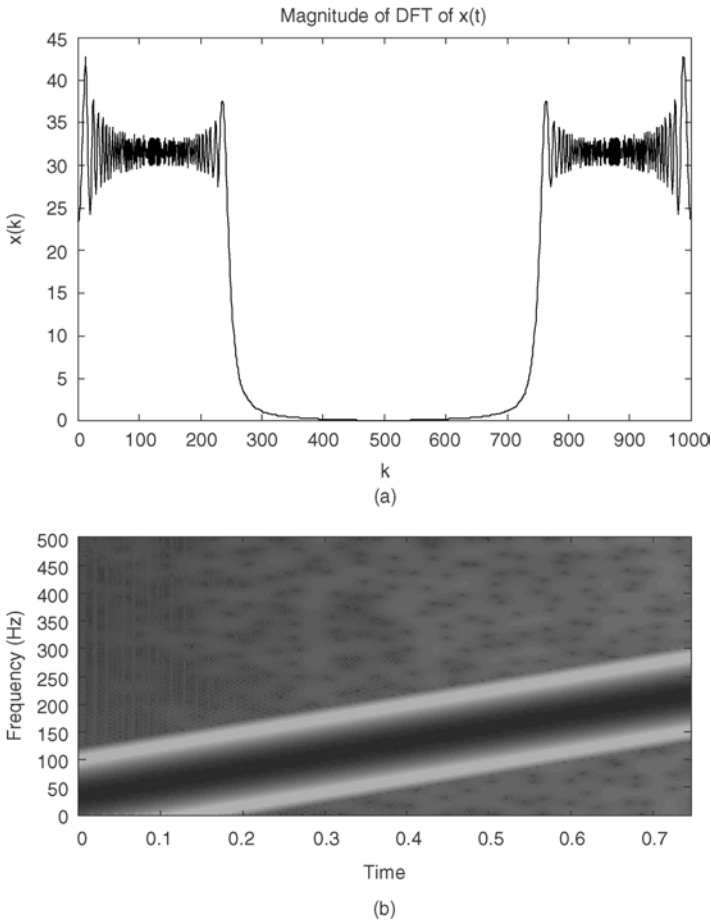


**Fig. 10.5.** Gabor transform of linear chirp, windowing with a Gaussian of  $\sigma = 16$ . The frequency of  $x_d(t) = \cos(At^2)$  rises from 0 to 250 Hz over a 1-s time interval. Its magnitude spectrum  $X(k)$  is shown in panel (a). Note the apparent presence of frequencies between 0 and 250 Hz, but that the time of a particular frequency is lost by the discrete Fourier transform (DFT). The Gabor transform reveals the time evolution of frequencies in  $x(t)$ , as shown in panel (b). Time values are shown along the bottom over the interval  $[0, 1]$ , which represents samples  $n$  from 0 to 255. Image intensities represent Gabor magnitude spectral values  $|\mathcal{G}[x_d](\mu, \omega)|$ ; darker values indicate larger magnitudes.

Chapter 7 that if  $x(n)$  has discrete Fourier transform (DFT) coefficients  $X(k)$  and DFS coefficients  $c(k)$  on  $[0, N - 1]$ , then  $X(k) = Nc(k)$ . Since we have to perform a discrete transform on  $N$  samples over an array of points, we choose that  $N = 2^m$ , for some  $m$ , so that the efficient fast Fourier transform (FFT) algorithm applies. We transform the windowed signal  $x_d(t)g_{\mu,\sigma}(t)$  sampled at  $t = 0, T/N, 2T/N, \dots, (N - 1)T/N$ . Finally,

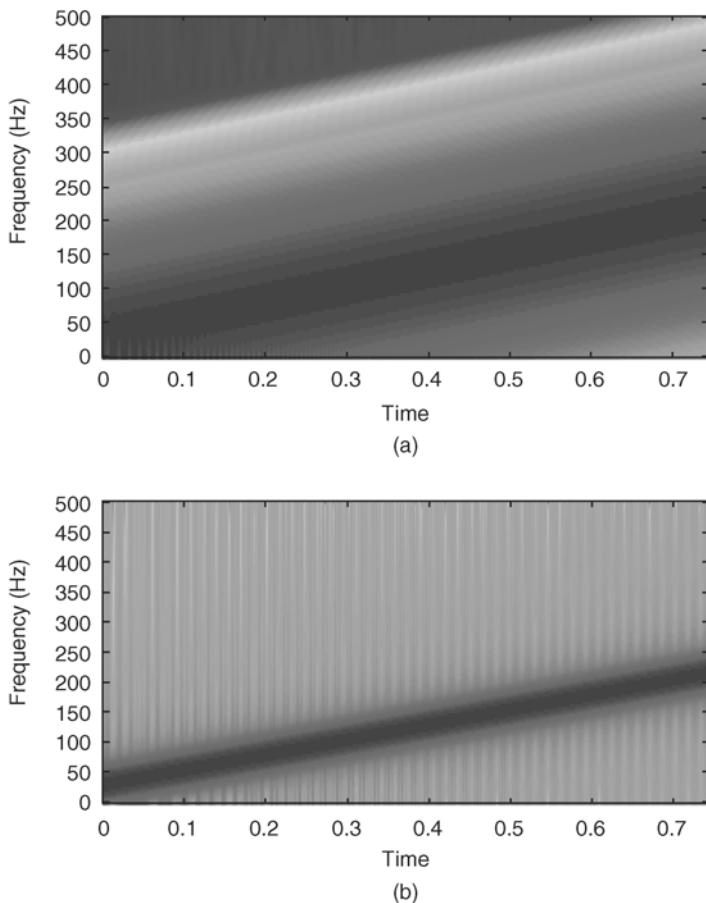


**Fig. 10.6.** Window width effects in the Gabor transform of a linear chirp. Windowing with a Gaussian of  $\sigma = 4$  is shown in panel (a). Panel (b) shows the case of  $\sigma = 64$ .

we select  $\sigma = 16$  as the standard deviation of the Gaussian window function for the transform (Figure 10.5).

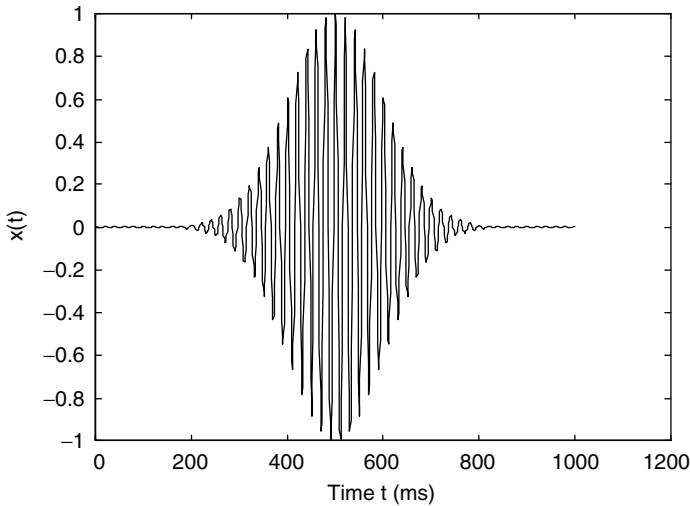
What effect does the decision  $\sigma = 16$  play for the transform? If  $\sigma$  increases, then the band of large transform coefficients shrinks. And decreasing the width of the transform's window function causes the sloping region of large magnitude coefficients to expand.

Carefully note in Figure 10.6 that broadening the time-domain window functions narrows the region of large magnitude values in the transformed signal. Indeed a reciprocal relation is manifest. This is an important characteristic. The next section further explores the link between time- and frequency-domain resolution under Gabor signal transformation.

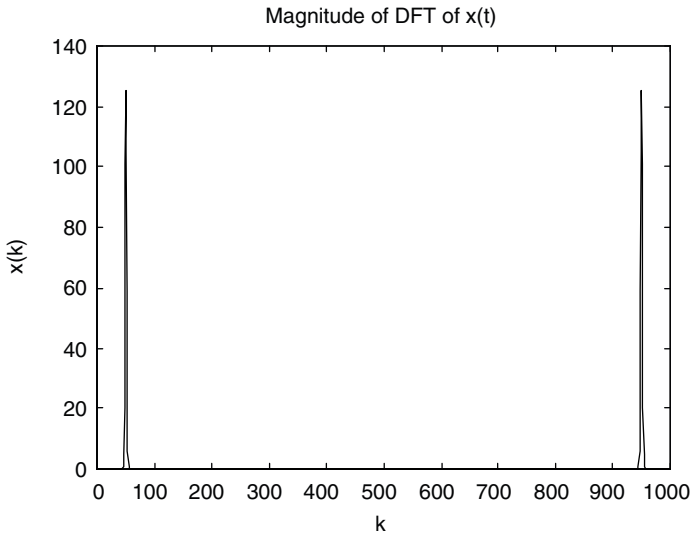
**10.1.5.2 Pulsed Tone.** Now suppose that we begin with a time-domain pulse:

$$x_a(t) = \exp(-Bt^2) \cos(At). \quad (10.39)$$

We shall suppose that the pulse frequency is 50 Hz and consider different time-domain durations of  $x_a(t)$ , which are governed by stretching the Gaussian envelope,  $\exp(-Bt^2)$ . (Figures 10.7 and 10.8).



(a)



(b)

**Fig. 10.7.** Time-frequency localization tradeoff for a pulse tone. (a) The 50-Hz tone pulse rising and decaying in a 600-ms interval about  $t = 0.5$  s. (b) Its Fourier spectrum shows the frequencies present but provides no time information. (c) The Gabor transform.

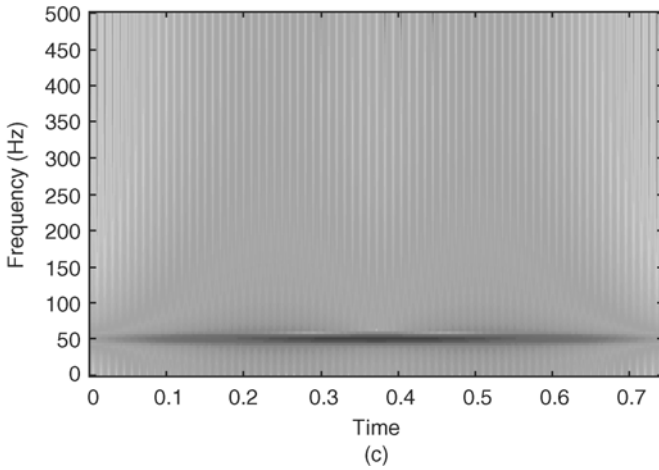


**Fig. 10.7** (Continued)

This elementary experiment reveals that as the time-domain locality of the pulse increases, the frequency-domain locality decreases. In other words, it seems that as we gain a better knowledge of the time span a signal's frequencies occupy, then we lose knowledge of the specific frequencies it contains. This points to a fundamental tradeoff

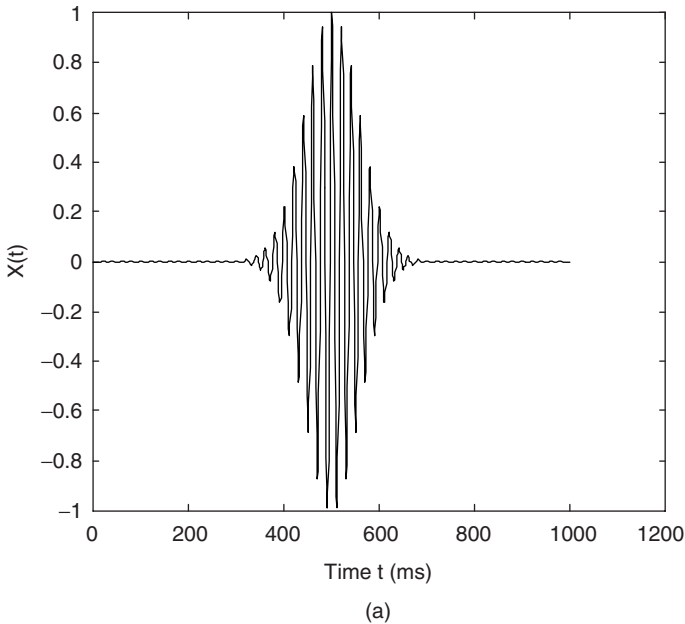


**Fig. 10.8.** Time-frequency localization tradeoff for a pulse tone. Panel (a) shows the 50-Hz tone pulse rising and decaying in a 300-ms interval about  $t = 0.5$  s; (b) the more tightly localized pulse has a Gabor transform that is correspondingly dispersed.

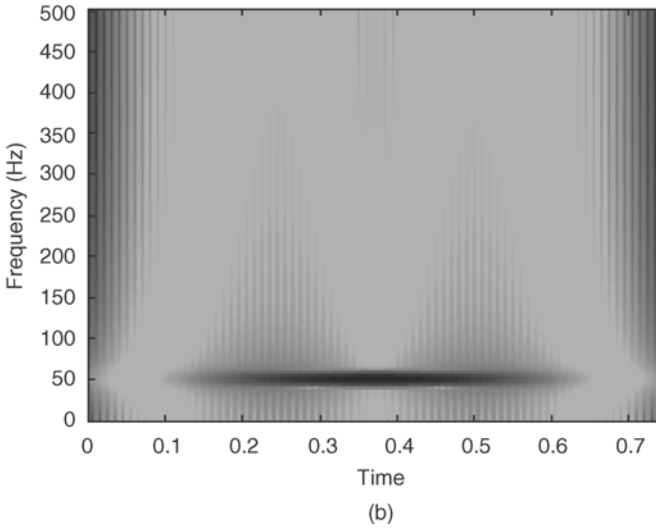


**Fig. 10.8** (Continued)

in time-frequency analysis. It is also closely related to the Heisenberg Uncertainty Principle, which we touched upon in our treatment of frequency-domain analysis.

**10.1.6 Properties**

Table 10.1 summarizes properties of the Gabor transformation, some of which are left as exercises.

**TABLE 10.1. Gabor Transform Properties<sup>a</sup>**

Signal Expression	Gabor Transform or Property
$x(t)$	$X_g(\mu, \omega)$
$ax(t) + by(t)$	$aX_g(\mu, \omega) + bY_g(\mu, \omega)$
$x(t - a)$	$e^{-j\omega a}X_g(\mu - a, \omega)$
$x(t)\exp(j\theta t)$	$X_g(\mu, \omega - \theta)$
$\ x\ _2 = \frac{1}{\sqrt{2\pi}} \frac{\ X_g(\mu, \omega)\ _{2, L^2(\mathbb{R}^2)}}{\ g\ _2}$	Plancherel's theorem
$\langle x, y \rangle = \frac{1}{2\pi\ g\ _2^2} \langle X_g, Y_g \rangle$	Parseval's theorem
$x(t) = \frac{1}{(2\pi\ g\ _2^2)^{-\infty}} \int_{-\infty}^{\infty} X_g(\mu, \omega)g_{\mu, \sigma}(t)e^{j\omega t}d\omega d\mu$	Inverse, resolution of the identity, or synthesis equation

<sup>a</sup>In the table,  $x(t)$  is square-integrable, and  $g(t)$  is a Gaussian of mean  $\mu$  and standard deviation  $\sigma$ .

## 10.2 SHORT-TIME FOURIER TRANSFORMS

A *short-time Fourier transform* (STFT) generalizes the Gabor transform by allowing a general window function. For the supporting mathematics to work, the theory requires constraints on the window functions. These we will elaborate in a moment. Once these theoretical details are taken care of, though, the general transform enjoys many of the same properties as the Gabor transform.

One might well ask whether a window shape other than the Gaussian can provide a better time-frequency transform. The answer is affirmative, but qualified. If the window shape matches the shape of signal regions to be analyzed, then an alternative window function offers somewhat better numerical results in signal detection applications. Thus, choosing the window to have roughly the same shape as the signals to be analyzed improves detection performance. These benefits are usually slight, however.

We know from the experiments with pulses and chirps at the end of the previous section that there is a tradeoff between time and frequency localization when using the Gabor transform. How does the selection of a transform window affect this behavior? It turns out that there is a hard lower limit on the joint time-frequency resolution of windowed Fourier transforms. Constricting the time-domain window so as to sharpen the time domain resolution results in a proportionately broader, more imprecise frequency-domain localization. This is a fundamental limitation on windowed Fourier methods. Its practical import is that signals with both low and high frequencies or with abrupt transients are difficult to analyze with this transform family. In fact, this limitation—which is a manifestation of the famous Heisenberg Uncertainty Principle—stimulated the search for alternative mixed domain transforms and was an impetus behind the discovery of the wavelet transform (Chapter 11).

Among all possible window functions, there is one signal in particular that shows the best performance in this regard: the Gaussian. Thus, the Gabor transform is the short-time Fourier transform with the best joint time-frequency resolution. So despite the benefits a special window may have, the Gabor transform prevails in all but certain specialized STFT-based signal analysis applications.

### 10.2.1 Window Functions

This section specifies those functions that may serve as the basis for a windowed transform. We formally define window functions and the resulting general window transform. We also develop some window function properties. This leads to a criterion for measuring joint time-frequency resolution. We prove the uncertainty principle, and the optimality of the Gabor transform follows as a corollary.

We should note right away that exponential signals modulated by window functions will play the role of structuring elements for signal analysis purposes. The short-time Fourier transform applies this structuring element at different time locations to obtain a set of time-ordered snapshots of the signal at a given frequency. When we later discretize the STFT, this idea will become clearer.

**Definition (Window Function).** If  $x(t) \in L^2(\mathbb{R})$ ,  $\|x(t)\|_2 \neq 0$ , and  $tx(t) \in L^2(\mathbb{R})$ , then  $x(t)$  is called a *window function*.

So,  $x(t)$  is a window function when its squared magnitude,  $|x(t)|^2$ , has a second order moment. This technical condition is necessary for many of the properties of the windowed transform. Of course, the familiar functions we have used to improve signal spectra in Chapter 9 satisfy this definition.

**Example (Gaussian).** The Gaussian  $g(t) = A \exp(-Bt^2)$ , where  $A \neq 0$  and  $B > 0$ , is a window function. The Gaussian has moments of all orders, as we can check by integrating by parts:

$$\begin{aligned} \int_{-\infty}^{\infty} |tg(t)|^2 dt &= A \int_{-\infty}^{\infty} t^2 e^{-2Bt^2} dt = \left( \frac{Ate^{-2Bt^2}}{-4B} \Big|_{-\infty}^{\infty} + \left( \frac{A}{4B} \right) \int_{-\infty}^{\infty} e^{-2Bt^2} dt \right) \\ &= \left( \frac{A}{4B} \right) \int_{-\infty}^{\infty} e^{-2Bt^2} dt. \end{aligned} \quad (10.40)$$

The Fourier transform of a Gaussian is still a Gaussian, and therefore  $G(\omega)$  is a window function in the frequency domain too. But many window functions have Fourier transforms that are not window functions by our definition.

**Example (Square Pulse).** The square pulse of width  $2T > 0$ ,  $w(t) = u(t+T) - u(t-T)$ , is a window function. Indeed any non-trivial compactly supported  $L^2(\mathbb{R})$  signal is a window function. The Fourier transform of  $w(t)$ ,  $W(\omega) = 2T \operatorname{sinc}(T\omega)$ , decays like  $\omega^{-1}$  in the frequency domain. Thus,  $\omega W(\omega) = 2 \sin(T\omega) \notin L^2(\mathbb{R})$ . So a window function does not necessarily have a Fourier transform that is a window function as well. Indeed, this occurs rarely, as the next result shows.

**Lemma (Integrability).** If  $x(t)$  is a windowing function, then  $x(t) \in L^1(\mathbb{R})$ .

**Proof:** (A Schwarz Inequality exercise). ■

**Proposition.** If  $x(t)$  is a discontinuous window function, then  $X(\omega)$  cannot also be a window function.

**Proof:** If  $X(\omega)$  is a window function, then it is absolutely integrable by the lemma, and its inverse Fourier transform  $\mathcal{F}^{-1}[X(\omega)] = x(t)$  is continuous. But this is a contradiction. ■

So constructing double pane windows requires some care. To do so we must find window functions that are continuous, decay quickly, and have Fourier transforms which are continuous with fast decay. Later, we will define the concept of the center and size of a window function. These definitions will lead to the uncertainty principle and the

result that, among the short-time Fourier transforms, the Gabor transform alone possesses a window function with optimal time- and frequency-domain resolution.

### 10.2.2 Transforming with a General Window

It is not hard to generalize the Gabor transform to work with a general window, now that we have introduced the moment condition that a window function must satisfy. We will define the windowed transform for window functions and make the additional assumption that the Fourier transform of the window is also a window function for some of the properties. Drawing inspiration from the Gabor transform formalizations, we can easily draft a definition for a general windowed transform.

**Definition (Short-Time Fourier Transform).** Let  $w(t)$  be a window function and  $x(t) \in L^2(\mathbb{R})$ . The *short-time Fourier transform (STFT) with respect to  $w(t)$* , written  $X_w(\mu, \omega)$ , is the radial Fourier transform of the product  $x(t)w(t - \mu)$ :

$$X_w(\mu, \omega) = \int_{-\infty}^{\infty} x(t)w(t - \mu)e^{-j\omega t} dt. \quad (10.41)$$

The STFT is also known as the *windowed Fourier transform*. There is a “fancy  $W$ ” notation for the short-time Fourier transform:  $X_w(\mu, \omega) = (W'_w)[x(t)](\mu, \omega)$ .

*Remarks.* The windowing function  $w(t)$  in (10.41) remains fixed for the transform, as does the Gaussian in a Gabor transform. Indeed, our definition generalizes the Gabor transform: If  $w(t)$  is a Gaussian, then the short-time Fourier transform with respect to  $w(t)$  of  $x(t)$  is precisely the Gabor transform of  $x(t)$  using the Gaussian  $w(t)$ . We do not demand that the Fourier transform  $(\mathcal{F}w)(\omega) = W(\omega)$  must also be a window function; when we turn to study time-frequency localization using the transform, however, we make this qualification.

**10.2.2.1 Standard Windows.** We can define an STFT for any of the windowing functions used to improve local spectra estimates in Chapter 9. We recall that windowing a signal  $x(t)$  with a tapered window function reduces the size of Gibbs phenomenon sidelobes. Table 10.2 summarizes possible standard analog windows: rectangle, Bartlett (triangle), Hamming, Hanning, and Blackman functions.

Each of the standard window functions above has a discontinuity in a time-domain derivative of some order. We can develop the STFT using  $B$ -splines, however, and achieve smooth time-domain derivatives of arbitrarily high orders.

**10.2.2.2 B-spline Windows.** Another window function appropriate for the STFT involves  $B$ -splines, which we introduced in Section 3.2.5. Splines are popular in applied mathematics [14], computer graphics [15], and signal processing and analysis [16–18]. We recall the definition.

**TABLE 10.2. Short-Time Fourier Transform Window Functions<sup>a</sup>**

Name	Definition
Rectangle	$w(t) = \begin{cases} b & \text{if } ( t  \leq a) \\ 0 & \text{otherwise.} \end{cases}$
Bartlett (triangle)	$w(t) = \begin{cases} \frac{b}{a}t + b & \text{if } -a \leq t \leq 0, \\ -\frac{b}{a}t + b & \text{if } 0 \leq t \leq a, \\ 0 & \text{otherwise.} \end{cases}$
Hanning (von Hann)	$w(t) = \begin{cases} b \cos^2\left(\frac{\pi t}{2a}\right) & \text{if }  t  \leq a \\ 0 & \text{otherwise.} \end{cases}$
Hamming	$w(t) = \begin{cases} 0.54b + 0.46b \cos\left(\frac{\pi t}{a}\right) & \text{if }  t  \leq a \\ 0 & \text{otherwise.} \end{cases}$
Blackman	$w(t) = \begin{cases} 0.42b + 0.5b \cos\left(\frac{\pi t}{a}\right) + 0.08b \cos\left(\frac{2\pi t}{a}\right) & \text{if }  t  \leq a \\ 0 & \text{otherwise.} \end{cases}$

<sup>a</sup>Adjust parameter  $a > 0$  for a window width appropriate to the signal features of interest. Adjust parameter  $b > 0$  in order to normalize the window function.

**Definition (B-spline).** The B-spline of order zero is

$$\beta_0(t) = \begin{cases} 1 & \text{if } -\frac{1}{2} < t < \frac{1}{2} \\ \frac{1}{2} & \text{if } |t| = \frac{1}{2} \\ 0 & \text{if otherwise.} \end{cases} \tag{10.42}$$

and higher-order B-splines are found by successive convolution:

$$\beta_n(t) = \underbrace{\beta_0(t) * \beta_0(t) * \dots * \beta_0(t)}_{n + 1 \text{ times}}. \tag{10.43}$$

The B-splines are clearly window functions;  $\beta_n(t)$  has compact support. Now let us examine the Fourier transform of  $\beta_n(t)$ . Let  $B_n(\omega) = \mathcal{F}(\beta_n)(\omega)$ . The Fourier transform convolution theorem implies

$$B_n(\omega) = \left[ \frac{\sin\left(\frac{\omega}{2}\right)}{\frac{\omega}{2}} \right]^{n+1}. \quad (10.44)$$

So the denominator of (10.44) is  $\omega^{n+1}$ ; in case  $n \geq 1$ , we see  $\omega B_n(\omega) \in L^2(\mathbb{R})$ , so that  $B_n(\omega)$  is indeed a window function.

In Section 10.2.4 we formulate, refine, and quantify the concept of the a windowed Fourier transform's time-frequency localization. A crucial precondition for frequency-domain locality is that the window function's Fourier transform must also be a window function. Note that both the Gabor transform and the B-spline windowed STFT enjoy this condition. Before addressing the idea of joint localization, however, let us cover some STFT properties.

### 10.2.3 Properties

Many of the properties of the Gabor transform carry over directly to the short-time Fourier transform. Like the specialized Gabor transform, the STFT obeys basic properties of linearity, time shift, and frequency shift. We state and leave as exercises the STFT Plancherel, Parseval, and inverse results.

**Theorem (Short-Time Fourier Transform Parseval's).** Suppose  $x(t), y(t) \in L^2(\mathbb{R})$ ;  $w(t)$  is a window function; and let  $X_w(\mu, \omega)$  and  $Y_w(\mu, \omega)$  be the STFTs of  $x(t)$  and  $y(t)$ , respectively, based on windowing with  $w(t)$ . Then

$$2\pi \|w\|_2^2 \langle x, y \rangle = \int_{-\infty}^{\infty} \int_{-\infty}^{\infty} X_w(\mu, \omega) \overline{Y_w(\mu, \omega)} d\omega d\mu = \langle X_w, Y_w \rangle_{L^2(\mathbb{R}^2)}. \quad (10.45)$$

*Proof:* Similar to Gabor transform (exercise). ■

**Theorem (Short-Time Fourier Transform Plancherel's).** Suppose  $\sigma > 0$ ;  $x(t) \in L^2(\mathbb{R})$ ;  $w(t)$  is a window function; and let  $X_w(\mu, \omega)$  be the STFT of  $x(t)$ . Then

$$\|x\|_2 = \sqrt{2\pi} \frac{\|X_w(\mu, \omega)\|_{2, L^2(\mathbb{R}^2)}}{\|g\|_2}. \quad (10.46)$$

*Proof:* Exercise. ■

**Theorem (Inverse Short-Time Fourier Transform).** Suppose  $x(t) \in L^2(\mathbb{R})$ ,  $w(t)$  is a window function, and let  $X_w(\mu, \omega)$  be the STFT of  $x(t)$ . Then for all  $a \in \mathbb{R}$ , if  $x(t)$  is continuous at  $a$ , then

$$x(a) = \frac{1}{(2\pi\|w\|_2^2)} \int_{-\infty}^{\infty} X_w(\mu, \omega) w(a) e^{j\omega a} d\omega d\mu. \quad (10.47)$$

**Proof:** Apply a limit argument to the Parseval formula, as with the Gabor transform (exercise). ■

## 10.2.4 Time-Frequency Localization

How precisely we can locate the frequency values within a signal using the short-time Fourier transform? Section 10.1.5 showed how the Gaussian window width dramatically affects the transform coefficients. Indeed, an improperly chosen window width—determined by the standard deviation  $\sigma$ —can render the transform information useless for interpreting signal evolution through time. The reason is not too hard to grasp. By narrowing the window, we obtain a more precise time frame in which frequencies of interest occur. But if we calculate the transform from discrete samples, then we cannot shrink  $\sigma$  too far; eventually the number of samples within the window are too few to compute the discrete signal frequencies. This is, of course, the threshold governed by the Nyquist rate. As  $\sigma$  decreases, then, the Gabor transform gains time-domain resolution, but it loses frequency-domain resolution at the same time.

**10.2.4.1 Window Location and Size.** To study the tradeoffs between time and frequency-domain resolution requires first of all a standard for measuring a signal's width or extent. The standard deviation of the enclosing Gaussian is a natural choice for the Gabor elementary function,  $y(t) = g_{\mu, \sigma}(t) \exp(j\omega t)$ . Recalling the Gaussian or normal distribution from the probability theory tutorial in Section 1.8, the probability that a normally distributed random variable has a value within one standard deviation of the mean  $\mu$  is approximately 68%. That is, the area under the bell curve from  $\mu - \sigma$  to  $\mu + \sigma$  is about 0.68, whereas the total underlying area is unity. Thus, we propose  $2\sigma$  for the “width” of  $y(t)$ , rather than a single standard deviation. Now, the standard deviation for a normally distributed random variable with density function  $g_{\mu, \sigma}(t)$  is

$$\sigma = \left[ \int_{-\infty}^{\infty} (t - \mu)^2 g_{\mu, \sigma}(t) dt \right]^{\frac{1}{2}}. \quad (10.48)$$

Can we extend this scheme to a general  $x(t) \in L^2(\mathbb{R})$  which we propose to Gabor transform? The answer is, unfortunately, no; we do know that there are signals that have finite energy without being integrable. The canonical example in signal processing is  $\text{sinc}(t) = \sin(t)/t$ . It is square-integrable, because  $\text{sinc}^2(t)$  decays like  $t^{-2}$  at

infinity. However,  $\text{sinc}(t) \notin L^1(\mathbb{R})$ , because, for instance, its Fourier transform is a square pulse, which is not continuous. Another problem is that the second moment integral (10.48) must also be valid. The following definition accounts for both difficulties, but we need a preliminary lemma.

**Lemma.** If  $x(t)$  is a window function, then  $t^{1/2}x(t) \in L^2(\mathbb{R})$ .

**Proof:** This turns out to be a consequence—through the Schwarz inequality—of the square integrability of  $x(t)$  and  $tx(t)$ . We leave this as an exercise. ■

**Definition (Center and Radius).** If  $x(t)$  is a window function, then the *center*  $C_x$  and the *radius*  $\rho_x$  for  $x(t)$  are given by

$$C_x = \frac{1}{\|x\|_2^2} \int_{-\infty}^{\infty} t|x(t)|^2 dt \quad (10.49a)$$

and

$$\rho_x = \left[ \frac{1}{\|x\|_2^2} \int_{-\infty}^{\infty} (t - C_x)^2 |x(t)|^2 dt \right]^{\frac{1}{2}}, \quad (10.49b)$$

respectively. The *diameter* or *width* of a windowing function  $x(t)$  is  $\Delta_x = 2\rho_x$ .

**Remark.** The lemma assures us that the integral (10.49a) exists.

The more highly concentrated a signal  $x(t)$  is about its center  $C_x$ , the smaller is its radius  $\rho_x$ . Let us consider a few examples of window functions before stating some of their basic properties.

**Examples (Window Functions).** Any Gaussian,  $g(t) = A\exp(-Bt^2)$  is a window function as we already showed. All of the standard window functions of Table 10.2 are also window functions. The B-spline functions  $\beta_n(t)$  are also window functions, and, for  $n \geq 1$ ,  $B_n(\omega)$  is a window function.

Now let us work out a few basic properties of window center and radius.

**Lemma (Window Translation and Modulation).** Suppose  $x(t)$  is a window function and  $y(t) = x(t + t_0)$ . Then:

- (a)  $C_y = C_x - t_0$ .
- (b) If  $X = \mathcal{F}x$  and  $Y = \mathcal{F}y$  are the Fourier transforms of  $x$  and  $y$ , respectively, and  $X$  and  $Y$  are window functions, then  $C_X = C_Y$ .
- (c)  $\rho_y = \rho_x$ .
- (d) If  $y(t) = \exp(-jC_X t)x(t + C_X)$  and  $X = \mathcal{F}x$  and  $Y = \mathcal{F}y$  are window functions, then  $C_Y = C_X = 0$  and  $\rho_y = \rho_x$ .

**Proof:** By the Shifting and Modulation Properties of the Fourier transform (exercises). ■

**Lemma (Radius of Derivative).** Suppose  $x(t) \in L^2(\mathbb{R})$  and is differentiable. If  $x'(t) \notin L^2(\mathbb{R})$ , then  $\rho_X = \infty$ .

**Proof:** Use Parseval’s theorem for the radial Fourier transform and the formula for  $\mathcal{F}[x'(t)](\omega)$ . (exercise). ■

**10.2.4.2 Uncertainty Principle.** The next theorem is the classic Heisenberg Uncertainty Principle<sup>4</sup> for the Fourier transform [20, 21]. The theorem says as a signal becomes more concentrated about its time-domain center, it becomes more dispersed about its frequency domain center. Recent tutorials on the Uncertainty Principle include [22, 23].

**Theorem (Heisenberg Uncertainty).** Suppose  $x(t) \in L^2(\mathbb{R})$ ,  $X(\omega) = \mathcal{F}[x](\omega)$  is the radial Fourier transform of  $x(t)$ . Then  $\rho_x \rho_X \geq \frac{1}{2}$ .

**Proof:** We prove the Uncertainty Principle in two steps:

- First, for the happy circumstance that  $x(t)$  obeys a special limit condition at infinity:

$$\lim_{t \rightarrow \infty} \sqrt{|t|} |x(t)| = 0; \tag{10.50}$$

this condition does not necessarily hold for a square-integrable signal, of course; we could have  $x(t) > \epsilon > 0$  on some set  $S$  of measure zero, for example.

- Then, for the general case by writing  $x(t)$  as a limit of such continuous, piecewise smooth signals.

Note that we may assume that  $x(t)$  is a window function; otherwise,  $\rho_x = \infty$ , so that  $\rho_x \rho_X \geq 1/2$ . We assume  $X(\omega)$  is a window function as well, since otherwise  $\rho_X = \infty$  with the same consequence. In either exceptional case, we are done. The Window Translation and Modulation Lemma allows the further simplifying assumption that  $C_x = C_X = 0$ . Therefore,

$$\begin{aligned} \rho_x^2 \rho_X^2 &= \left[ \frac{1}{\|x\|_2^2} \int_{-\infty}^{\infty} t^2 |x(t)|^2 dt \right] \left[ \frac{1}{\|X\|_2^2} \int_{-\infty}^{\infty} \omega^2 |X(\omega)|^2 d\omega \right] \\ &= \frac{1}{\|X\|_2^2 \|x\|_2^2} \left[ \int_{-\infty}^{\infty} |tx(t)|^2 dt \right] \left[ \int_{-\infty}^{\infty} |\omega X(\omega)|^2 d\omega \right]. \end{aligned} \tag{10.51}$$

<sup>4</sup>Werner Heisenberg (1901–1976) discovered that the probable location of a particle trades off against its probable momentum. In 1927, Heisenberg showed that  $\Delta p \Delta x \geq 2h$ , where  $\Delta p$  represents the width of a particle’s momentum distribution,  $\Delta x$  is the width of its position distribution, and  $h$  is Planck’s constant [W. Heisenberg, *Physical Properties of the Quantum Theory*, New York: Dover, 1949].

Using Plancherel's theorem and the radial Fourier transform derivative formula gives

$$\begin{aligned} \rho_x^2 \rho_{f_x}^2 &= \frac{\|x\|_2^{-4}}{2\pi} \left[ \int_{-\infty}^{\infty} |tx(t)|^2 dt \right] \left[ \int_{-\infty}^{\infty} |\mathcal{F}[x'(t)](\omega)|^2 d\omega \right] \\ &= \frac{\|x\|_2^{-4}}{2\pi} \|tx(t)\|_2^2 \|\mathcal{F}[x'(t)](\omega)\|_2^2. \end{aligned} \quad (10.52)$$

That is,

$$\|x\|_2^4 \rho_x^2 \rho_{f_x}^2 = \frac{1}{2\pi} \|tx(t)\|_2^2 \|x'(t)\|_2^2 2\pi = \|tx(t)\|_2^2 \|x'(t)\|_2^2. \quad (10.53)$$

Invoking the Schwarz inequality,  $\|x\|_2 \|y\|_2 \geq \|xy\|_1$ , on (10.53) gives

$$\|x\|_2^4 \rho_x^2 \rho_{f_x}^2 \geq \|tx(t)x'(t)\|_1^2 = \left[ \int_{-\infty}^{\infty} |tx(t)||x'(t)| dt \right]^2 = \left[ \int_{-\infty}^{\infty} |tx(t)\overline{|x'(t)|}| dt \right]^2 \quad (10.54)$$

and, continuing our algebraic duties, we find that

$$\|x\|_2^4 \rho_x^2 \rho_{f_x}^2 \geq \left| \int_{-\infty}^{\infty} \overline{tx(t)} x'(t) dt \right|^2 = (|\langle x'(t), tx(t) \rangle|)^2 \geq (\operatorname{Re} \langle x'(t), tx(t) \rangle)^2. \quad (10.55)$$

Now, we claim the following:

$$(\operatorname{Re} \langle x'(t), tx(t) \rangle) = -\frac{1}{2} \int_{-\infty}^{\infty} |x(t)|^2 dt = -\frac{1}{2} \|x(t)\|_2^2. \quad (10.56)$$

The trick behind the strange looking (10.56) is integration by parts on the inner product integral:

$$\begin{aligned} \int_{-\infty}^{\infty} \overline{tx(t)} x'(t) dt &= \overline{tx(t)} x(t) \Big|_{-\infty}^{\infty} - \int_{-\infty}^{\infty} x(t) [tx'(t) + \overline{x(t)}] dt \\ &= 0 - \int_{-\infty}^{\infty} x(t) [\overline{tx'(t)} + \overline{x(t)}] dt. \end{aligned} \quad (10.57)$$

Note that we have invoked (10.50) to conclude that  $|x(t)|^2 \rightarrow 0$  as  $|t| \rightarrow \infty$ . Separating the bottom of (10.57) into two integrals gives

$$\int_{-\infty}^{\infty} \overline{tx(t)} x'(t) dt = - \int_{-\infty}^{\infty} |x(t)|^2 dt - \int_{-\infty}^{\infty} \overline{tx(t)} x'(t) dt. \quad (10.58)$$

After rearrangement, the claim (10.56) easily follows. We insert the result into the inequality (10.55), thereby finding

$$\|x\|_2^4 \rho_x^2 \rho_{f_x}^2 \geq \frac{\|x\|_2^4}{4} \tag{10.59}$$

and hence  $\rho_x \rho_X \geq \frac{1}{2}$ .

Let us proceed to the second step in the proof: removing the limit assumption (10.50) on the finite energy signal  $x(t)$ . We write  $x(t)$  as the limit of a sequence of signals in the Schwarz space  $S$  of infinitely continuously differentiable, rapidly decreasing signals [21]:

$$x(t) = \lim_{n \rightarrow \infty} x_n(t). \tag{10.60}$$

We introduced the Schwarz space in Chapter 3 and know it to be dense in both  $L^2(\mathbb{R})$  and  $L^1(\mathbb{R})$ . Since for all  $x \in S$ , we have  $t|x(t)|^2 \rightarrow 0$  as  $|t| \rightarrow \infty$ , we have

$$\lim_{n \rightarrow \infty} \int_{-\infty}^{\infty} \overline{tx_n(t)} x_n'(t) dt = \lim_{n \rightarrow \infty} \overline{tx_n(t)} x_n(t) \Big|_{-\infty}^{\infty} - \lim_{n \rightarrow \infty} \int_{-\infty}^{\infty} x_n(t) [\overline{tx_n'(t)} + \overline{x_n(t)}] dt. \tag{10.61}$$

Because  $x_n \in S$ , which decreases faster than any polynomial, the integrands in (10.61) are absolutely integrable and we may interchange the integration and limit operations. Schwarz space elements are also continuous, so the first limit on the right-hand side of (10.61) is still zero. Thus,

$$\int_{-\infty}^{\infty} \lim_{n \rightarrow \infty} \overline{tx_n(t)} x_n'(t) dt = - \int_{-\infty}^{\infty} \lim_{n \rightarrow \infty} x(t) [\overline{tx_n'(t)} + \overline{x_n(t)}] dt. \tag{10.62}$$

But these limits are precisely (10.57). ■

The above proof follows Weyl’s derivation [24], which he published in 1931.<sup>5</sup>

Thus, every windowed Fourier transform has a lower limit on its joint time-frequency resolution. If we work with a transform based on a window function  $w(t)$  whose Fourier transform  $W(\omega)$  is also a window function, then it makes sense to define the time-frequency resolution as the product  $\rho_w \rho_W$ . If we use a standard window function—a Hamming window, for example—whose Fourier transform is not itself a window function, then  $\rho_W$  is infinite. The Uncertainty Principle tells us that this is a hard lower bound:  $\rho_w \rho_W \geq 1/2$ . As a practical consequence, smaller time-domain window sizes result in proportionally large frequency-domain window

<sup>5</sup>The interests of Hilbert’s student, Hermann Weyl (1885–1955), ranged from quantum mechanics to number theory. He showed, for instance, that given an irrational number  $r$ , the fractional parts of  $r, 2r, 3r, \dots$ , etc., lie uniformly distributed on the interval  $(0, 1)$ .

sizes. As we attempt to better locate a signal oscillation, we suffer a corresponding loss of accuracy in estimating the precise frequency of the oscillation.

There are window functions that achieve the lower bound on time-frequency localization given by the Heisenberg Uncertainty Principle. The next section shows that the optimally localizing window is none other than the Gaussian.

**10.2.4.3 Optimally Localized Signals.** The Gabor transform is the short-time Fourier transform with the smallest time-frequency resolution. We identify *time-frequency resolution* with the joint product of the time-domain and frequency-domain radius:  $\rho_x \rho_X$ . To derive this optimality claim, we review the Uncertainty Principle's proof. Our scrutiny shows that inequality arises with its use of the Schwarz inequality [21].

**Corollary (Optimal Time-Frequency Locality).** We have  $\rho_x \rho_X = \frac{1}{2}$  if and only if  $x(t) = ae^{-bt^2}$  for some  $a \in \mathbb{C}$  and  $b \geq 0$ .

**Proof:** We recall that  $\|x\|_2 \|y\|_2 \geq \|xy\|_1$  always, and equality occurs if and only if  $x = cy$  for some constant  $c \in \mathbb{C}$ . In the context of the proof, then, optimally small time-frequency locality coincides with the condition  $x'(t) = ct\overline{x(t)}$ . Are there any  $L^2(\mathbb{R})$  signals satisfying the above differential equation? It is a basic first-order differential equation, but before we note the solution, let us address two problems:

- Since the Uncertainty Principle deals with square-integrable signals  $x(t)$ , we understand this equality as occurring almost everywhere; that is, we require  $x'(t) = ct\overline{x(t)}$  except on some set of measure zero.
- Furthermore, the proof depends on the fact that we can represent a general  $x(t) \in L^2(\mathbb{R})$  as the limit of a sequence  $x(t) = \lim_{n \rightarrow \infty} x_n(t)$ , where  $x_n(t) \in S$ , the Schwarz space of infinitely continuously differentiable, rapidly decreasing signals. We must therefore show that for any  $x(t)$  satisfying the differential equation, which is an  $L^2(\mathbb{R})$  limit of  $x_n(t) \in S$ , that

$$x'(t) = \lim_{n \rightarrow \infty} x_n'(t). \quad (10.63)$$

In the convenient Schwarz space, the second point is straightforward. Indeed, we recall that  $x(t) = y'(t)$  in Lebesgue integration theory means

$$y(t) = \int_0^t x(s) ds + y(0) \quad (10.64)$$

almost everywhere. We have  $x(t) - x(0) = \lim_{n \rightarrow \infty} [x_n(t) - x_n(0)]$ , and the  $x_n(t) \in S$  are infinitely continuously differentiable; thus,

$$x(t) - x(0) = \lim_{n \rightarrow \infty} \int_0^t x_n'(s) ds = \int_0^t x'(s) ds. \quad (10.65)$$

To solve the differential equation, note that  $t^{-1}x'(t) = \overline{cx(t)}$ , whereby

$$\{t^{-1}x'(t)\}' = \{\overline{cx(t)}\}' = \overline{cx'(t)} = c\overline{tx(t)} = |c|^2tx(t). \quad (10.66)$$

If we let  $b = |c|^2$ , then the solutions to this second-order differential equation are of the form  $x(t) = ae^{-bt^2}$ , where  $a \in \mathbb{C}$  is a constant. ■

**Example (STFT based on a B-Spline Window).** Suppose we use a B-spline function  $\beta(t) = \beta_n(t)$ , where  $n \geq 1$ , to define a short-time Fourier transform. We know that  $\omega B_n(\omega) \in L^2(\mathbb{R})$ , so that  $B_n(\omega)$  is indeed a window function. The Uncertainty Principle applies. The Gaussian is not a B-spline, however, and we know therefore that  $\rho_\beta \rho_B > 1/2$ .

## 10.3 DISCRETIZATION

The short-time Fourier transform can also be discretized. There are two possible approaches:

- To compose discrete sums from values of a discrete signal  $x(n)$ , which is covered in Section 10.3.1.
- To sample the ordinary analog STFT analysis equation of an analog signal  $x_a(t)$ —the far more interesting and challenging problem—introduced in Section 10.3.2 and further explored in the sequel.

The second approach is our main emphasis. Its successful development leads to a new structural decomposition of finite-energy analog signals. It was also a focus of Gabor's original paper 1, a preoccupation of a number of later signal analysts, and the wellspring of much of our later insight into the nature of mixed-domain signal interpretation. We shall in fact pursue this idea for the remainder of this chapter.

### 10.3.1 Transforming Discrete Signals

Working with discrete signals, we can formulate a purely discrete theory of windowed Fourier transforms. The results are not difficult to develop, and it turns out that they follow directly from discrete Fourier theorems. We are thus content to explicate only the discrete STFT synthesis and energy conservation equations.

We begin with a discrete signal  $x(n)$  having period  $N > 0$ ,  $x(n) = x(n + N)$ . Alternatively, we may select  $N$  samples  $\{s(n): 0 \leq n < N\}$  from an arbitrary discrete signal  $s(n)$  and consider the periodic extension  $x(n) = s(n \bmod N)$ . We require the discrete window function to be nonzero and have the same period as the signal to be transformed.

**Definition (Discrete Short-Time Fourier Transform).** Let  $x(n)$  and  $w(n)$  be discrete signals of period  $N > 0$ . Further suppose  $w(n)$  is real and not identically zero

on  $[0, N - 1]$ . Then the *discrete short-time Fourier transform* (or *discrete windowed Fourier transform*) of  $x(n)$  with respect to  $w(n)$  is

$$X_w(m, k) = \sum_{n=0}^{N-1} x(n)w(n-m)e^{-2\pi jk\frac{n}{N}}. \quad (10.67)$$

The signal  $w(n)$  is called the *windowing function* for the transform.

**Definition (Discrete Gabor Elementary Function).** Let  $w(n)$  be a discrete signal of period  $N > 0$ , with  $w(n)$  is not identically zero on  $[0, N - 1]$ . Then the *discrete Gabor elementary function* or *discrete Gabor atom* of discrete frequency  $k \in [0, N - 1]$  and location  $m \in [0, N - 1]$  is  $w_{m,k}(n) = w(n - m)\exp(2\pi jkn/N)$ .

As with its analog world counterpart, the discrete STFT can be viewed in several ways. In particular, we may think of (10.67) as giving

- For each  $m \in [0, N - 1]$ , the discrete Fourier transform (DFT) of  $x(n)w(n - m)$ ;
- For each  $k \in [0, N - 1]$ , the inner product on  $[0, N - 1]$  of  $x(n)$  with the discrete GEF  $w_{m,k}(n)$ .

The following theorem gives the synthesis equation for the discrete STFT.

**Theorem (Inverse Discrete STFT).** Let  $x(n)$  and be a discrete signal with period  $N > 0$ ; let  $X_w(m, k)$  be its discrete STFT with respect to the windowing function  $w(n)$ ; and, finally, let  $\|w\|_2$  be the  $l^2$ -norm of  $w(n)$  restricted to the interval  $[0, N - 1]$ :  $\|w\|_2 = [w^2(0) + w^2(1) + \dots + w^2(N - 1)]^{1/2}$ . Then,

$$x(n) = \frac{1}{N\|w\|_2^2} \sum_{m=0}^{N-1} \sum_{k=0}^{N-1} X_w(m, k)w(n-m)e^{2\pi jk\frac{n}{N}}. \quad (10.68)$$

**Proof:** Substituting the definition of  $X_w(m, k)$  into the double summation on the right-hand side of (10.68) gives

$$\sum_{m=0}^{N-1} \sum_{k=0}^{N-1} \sum_{p=0}^{N-1} x(p)w(p-m)e^{-2\pi jk\frac{p}{N}}w(n-m)e^{2\pi jk\frac{n}{N}}. \quad (10.69)$$

Rearrangement of the sums produces

$$\sum_{p=0}^{N-1} x(p) \sum_{m=0}^{N-1} w(p-m)w(n-m) \sum_{k=0}^{N-1} e^{2\pi jk\frac{(n-p)}{N}}. \quad (10.70)$$

Reciting what has become a familiar and fun argument, we note that the final sum in is zero unless  $n = p$ , in which case it is  $N$ . Therefore the entire triple summation is simply

$$Nx(n) \sum_{m=0}^{N-1} w(n-m)w(n-m) = Nx(n) \|w\|_2^2, \quad (10.71)$$

and the theorem follows. ■

**Theorem (Discrete STFT Parseval's).** Let  $x(n)$  and be a discrete signal with period  $N > 0$ ; let  $X_w(m, k)$  be its discrete STFT with respect to the windowing function  $w(n)$ ; and, finally, let  $\|w\|_2$  be as in the previous theorem. Then,

$$\sum_{n=0}^{N-1} |x(n)|^2 = \frac{1}{N \|w\|_2^2} \sum_{m=0}^{N-1} \sum_{k=0}^{N-1} |X_w(m, k)|^2. \quad (10.72)$$

**Proof:** Let us expand the double summation on the right-hand side of (10.72):

$$\sum_{m=0}^{N-1} \sum_{k=0}^{N-1} \left[ \sum_{p=0}^{N-1} x(p)w(p-m)e^{-2\pi jk \frac{p}{N}} \right] \left[ \sum_{q=0}^{N-1} \overline{x(q)w(q-m)} e^{2\pi jk \frac{q}{N}} \right]. \quad (10.73)$$

Interchanging the sums we find that (10.73) becomes

$$\sum_{p=0}^{N-1} \sum_{q=0}^{N-1} x(p)\overline{x(q)} \left[ \sum_{m=0}^{N-1} w(p-m)w(q-m) \right] \left[ \sum_{k=0}^{N-1} e^{2\pi jk \frac{(q-p)}{N}} \right]. \quad (10.74)$$

The final bracketed sum is either  $N$  or  $0$ , depending on whether  $p = q$  or not, respectively. Since only the case  $p = q$  contributes to the sum, we let  $n = p = q$  and reduce the double summation on the left-hand side of (10.74) to a single sum over  $n$ :

$$N \sum_{n=0}^{N-1} x(n)\overline{x(n)} \left[ \sum_{m=0}^{N-1} w(n-m)w(n-m) \right]. \quad (10.75)$$

Finally we see

$$N \|w\|_2^2 \sum_{n=0}^{N-1} x(n)\overline{x(n)} = \sum_{m=0}^{N-1} \sum_{k=0}^{N-1} |X_w(m, k)|^2, \quad (10.76)$$

using the periodicity of  $w(n)$ . ■

### 10.3.2 Sampling the Short-Time Fourier Transform

Now let us turn to the deeper question of what happens we attempt to sample the STFT. We select a time-domain sampling interval  $T > 0$  and a frequency-domain

sampling interval  $\Omega > 0$ . These remain fixed for the discrete transform, and a complex-valued function on pairs of integers results. It might appear that our endeavors here will not differ radically in method and results from the work we did earlier in discretizing the Fourier transform. Quite the opposite turns out to be the case: Discretization of the windowed Fourier transform opens the door to a wealth of intriguing problems in signal analysis.

For one thing, discretizing the transform provides us with a ready breakdown of the signal into time localized frequency components, or time-frequency atoms. Each atom represents a spot in time. Each atom represents a possible frequency component. And—depending on the nature of our atomic signal building blocks—there is a way to measure the quantity of that frequency resident in the signal in the vicinity a discrete time instant. This is a structural decomposition of the signal. Chapters 4 and 9 explored time- and frequency- domain signal analysis, respectively. Among their lessons is the usefulness of a structural decomposition of the signal for purposes of classification, recognition, and interpretation. Time-frequency transforms benefit signal analysis by providing an elegant, formal mathematical theory as well as a relational description of the signal.

Discretization places Gabor's original problem on the agenda [1]. He proposed to model communication signals using families of discretely indexed signal elements, which he called *logons*, but which nowadays are known by various other monikers—*Gabor elementary functions*, *Gabor atoms*, *windowed Fourier atoms*, and so on. Can families of the form  $\{\exp(2\pi jnt)g(t - m) : m, n \in \mathbb{Z}\}$  provide an orthonormal basis for  $L^2(\mathbb{R})$  signals? Their optimal joint time-frequency localization does recommend them, but neither Gabor nor any other signal analyst for decades after his suggestive 1946 paper could substantiate in theory what seemed so tantalizing for practice.

It was a negative answer to Gabor's insightful proposal that began to emerge in the 1980s, a decade marking a watershed of results in time-frequency and time-scale signal analysis. The rest of the chapter elaborates some of these apparently discouraging results for short-time Fourier methods. The next chapter suggests an alternative approach, motivated in part our understanding of the limitations inherent in atomic time-frequency signal decompositions. Chapter 11 does show that transformations that rely on signal scale instead—the wavelet transform in particular—may avoid the weaknesses of short-time Fourier techniques.

**Definition (Discretized Short-Time Fourier Transform).** Suppose that  $X_w(\mu, \omega)$  is the STFT of  $x(t) \in L^2(\mathbb{R})$  with respect to the window function  $w(t)$ . Given  $T > 0$  and  $\Omega > 0$ , the *discretized short-time Fourier transform* is

$$X_w(m, n) = (X_w)_a(m\Omega, nT) = \int_{-\infty}^{\infty} x(t)w(t - mT)e^{-jn\Omega t} dt. \quad (10.77)$$

If distinguishing between the discrete and analog transform signals becomes a problem, then we can append a subscript  $a$  to the analog form, as in (10.77). Note that

we are using the first discrete independent variable of  $X_w(m, n)$  as the time index and are using the second variable as the frequency index.

### 10.3.3 Extracting Signal Structure

If we can find a sufficiently strong mathematical representation, then discretized short-time Fourier transforms provide an attractive means of describing signal structure. We have already covered the broad qualifications for such a representation. It must be able to represent any candidate signal, for otherwise some inputs will avoid our decomposition method. The representation must also be stable, which, informally, means that changing the signal a little bit only perturbs the representation a little bit.

So, the question is, Can windowed Fourier atoms of the form

$$w_{m,n}(t) = e^{jn\Omega t} w(t - mT), \quad (10.78)$$

where  $T > 0$  and  $T\Omega = 2\pi$ , serve as a complete signal representation? The two practical alternatives are that the family  $\{w_{m,n}(t): m, n \in \mathbb{Z}\}$  constitutes either

- An orthonormal basis or
- A frame.

It is hoped that we can discover  $\{w_{m,n}(t): m, n \in \mathbb{Z}\}$  that make up an orthonormal basis. Then every square-integrable signal  $x(t)$  has an expansion in terms of Fourier coefficients, easily calculated as the inner products of  $x(t)$  with the  $w_{m,n}(t)$ :

$$x(t) = \sum_{m,n \in \mathbb{Z}} \langle x(t), w_{m,n}(t) \rangle w_{m,n}(t). \quad (10.79)$$

If we fail to find such a basis, then computing the expansion coefficients (10.79) becomes problematic. Lack of a basis encumbers our signal analysis too. While we might be able to decompose a candidate signal  $x(t)$  into a linear combination of atoms,  $x(t) = \sum c_{m,n} w_{m,n}(t)$ , we do not necessarily know the uniqueness of the expansion coefficients  $c_{m,n}$  for representing  $x(t)$ . So the utility of the expansion coefficients as indicators of some signal component's presence or the lack thereof is very much compromised.

Should a basis not be available, we could search for a frame representation of  $L^2(\mathbb{R})$  signals using the Gabor atoms (10.118). After all, we know from Chapter 3 that frame coefficients can characterize the source signal  $x(t)$ , and they support numerically stable reconstructions. This may be a good redoubt.

**10.3.3.1 Discrete Time-Frequency Plane.** Toward building a structural interpretation of a signal, we can place the expansion coefficients  $c_{m,n}$  into an array. Thus, for a fixed frequency  $n\Omega$ , the rows of the array,  $\{c_{m,n}: m \in \mathbb{Z}\}$ , indicate the relative weight of frequency  $n\Omega$  inside signal  $x(t)$  at all time instants  $mT$ . Similarly, the columns record the frequencies at a given time instant. Refer to Figure 10.9.

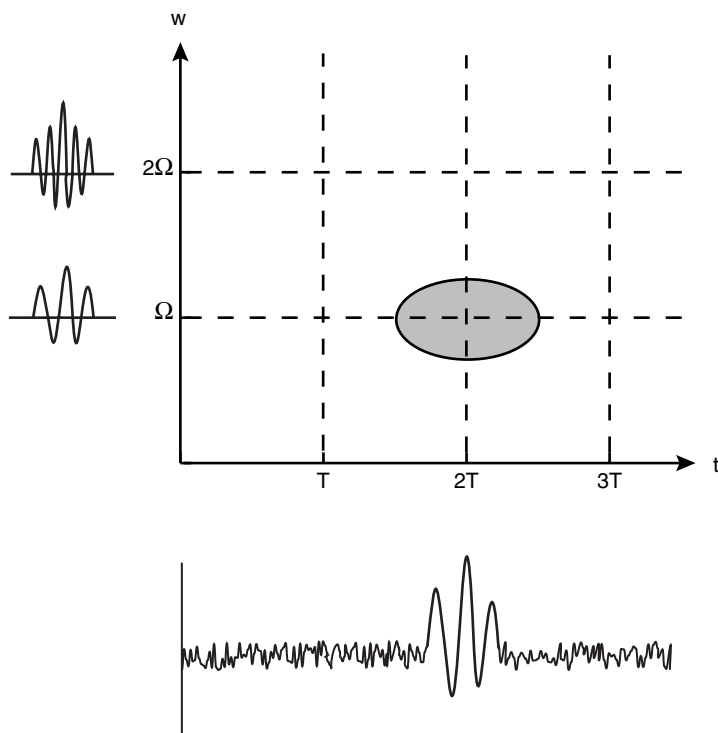


**Fig. 10.9.** Discretized STFT coefficients arranged in a rectangular grid.

Notice that upon discretizing the STFT we have a mathematical signal transform that resolves a signal into finite regions of the time-frequency plane. The Fourier series of Chapter 5, in contrast, can only furnish time-frequency regions of infinite time-domain extent. When we covered discrete Fourier theory in Chapter 7, we studied the sampling theorem by which a band-limited analog signal can be reconstructed from sufficiently dense discrete samples. The sampling theorem too implies a partition of the time-frequency plane, except that its regions have an infinite frequency-domain extent. The STFT therefore marks a theoretical advance within our signal analytic understanding.

As a relational structure, this partition of the time-frequency plane is quite simple. Each region has the same size as its neighbors. We can, however, adjust the size of the regions to be smaller or larger in time or frequency by dilating our windowing function. The Uncertainty Principle imposes the constraint that the area of the STFT regions be no smaller than that given by the Gabor transform. Signal analysis applications based on STFT methods generally search the corresponding time-frequency mesh in order to understand signal content.

Let us consider some examples of how the time-frequency decomposition structure presents itself in applications.

Figure 10.10 illustrates a time-frequency mesh that contains a linear chirp and what is apparently a tone. Chirp signal energy concentration is fairly constant and can

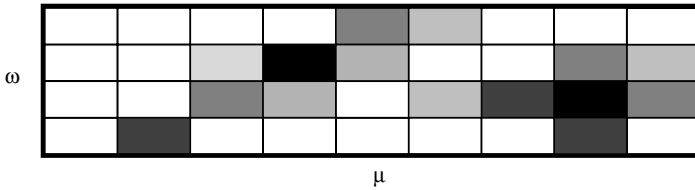


**Fig. 10.10.** Schematic representation of a signal with two components: a linear chirp and an isolated tone.

be tracked as a rising line over time. Tone signal energy concentration remains at a fixed frequency. Clicks or pops are characterized by a narrow time-domain extent and an extended, more or less uniform distribution of signal energy over a wide range of frequencies—a vertical linear structure. A sinusoidal tone is a horizontal linear structure. These ideas are only schematic, but they convey some of the signal varieties that are amenable to time-frequency analysis.

Let us now consider a speech analysis application. We have considered speech signal interpretation already in Chapters 4 and 9. In fact, in Chapter 9 we saw that many speech recognition systems have been developed using the basic technique of windowing the Fourier transform. If  $x(t)$  is a speech signal, for example, then looking for a large percentage of signal energy in a pair of frequencies might indicate the presence of a vowel phoneme. Or, a broad dispersion of signal energy in a range of high frequencies could mark a velar fricative. Time-frequency signal decomposition offers a complete picture of the speech waveform. Figure 10.11 shows a contour diagram of the energies in a speech fragment.

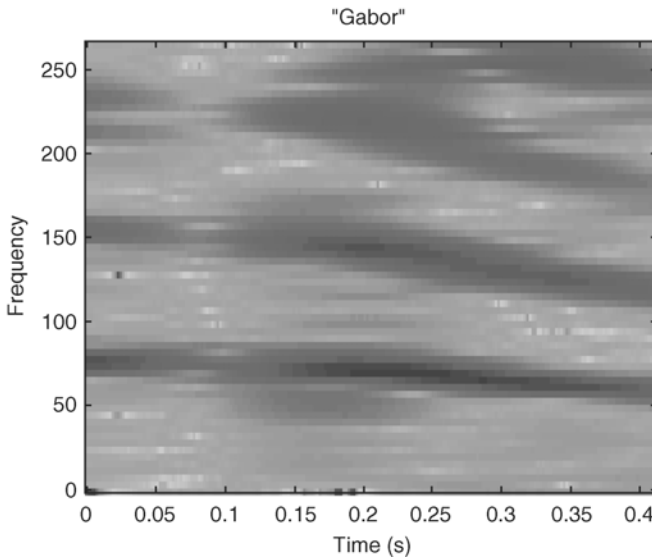


**Fig. 10.11.** The time-frequency decomposition of the word “Gabor.” Lines indicate signal energy contours. Note that the two syllables can be segmented in time according to the distribution of signal energy along the frequency axis.

**10.3.3.2 Identifying Significant Local Frequency Components.** Many of the filtering, enhancement, and thresholding techniques we applied in time-domain signal analysis can help us find localized signal frequency components. For instance, we might use a threshold to indicate a significant frequency component. Furthermore, we might calculate the total amount of energy among all time-frequency cells at a certain time instant and count the number that contain say a majority of the energy. Such quantities can be assembled into feature vectors, for example. All of the methods we employed in Chapter 4 for thresholding signals apply equally well to thresholding values in the two-dimensional time-frequency plane. Indeed, this is an elementary instance of image analysis, and with it, our work in interpreting signal content begins to take advantage of techniques in image processing and computer vision.

### 10.3.4 A Fundamental Limitation

We have observed that the windowed Fourier transform provides an elegant and natural description of signal structure—a two-dimensional array, easily searched along time or frequency axes. With other decomposition techniques, especially those revolving around signal scale, structures may assume the form of a tree or some more general graph. Traversing graph structures consumes computer time. So even though our derived structures may be far simpler than the time-domain signal, we are still concerned to make the graphs sparse and conclude our exhaustive search as quickly as possible. Hence the problem before us is, How large can we choose the time and frequency sampling intervals,  $T$  and  $\Omega$ , so that we still build a family of windowed Fourier atoms that provide an orthonormal basis or exact frame structure?

**10.3.4.1 Nyquist Density.** Our question directly concerns the power of short-time Fourier transforms for signal interpretation. Gabor studied the case  $T\Omega = 2\pi$ , suggesting that the Fourier expansion coefficients could be used to encode a signal for efficient transmission. Note too that for this case the time-domain sampling interval is  $T = 2\pi/\Omega$ . If a signal  $x(t)$  has bandwidth  $\Omega$ , then its highest frequency component is  $\Omega/2$  radians per second, or  $F_{\max} = (\Omega/2)/(2\pi) = \Omega/(4\pi)$  hertz. By the Shannon–Nyquist sampling theorem, it can be reconstructed from discrete samples taken at intervals sampled at a rate not less than  $F = T^{-1} = 2F_{\max} = \Omega/(2\pi)$  hertz. We offer the formal definition.

**Definition (Time-Frequency, Nyquist Densities).** Let  $x(t)$  have bandwidth  $\Omega$  and be sampled at intervals  $T > 0$ . Then we define its *time-frequency density* to be  $(T\Omega)^{-1}$ . The *Nyquist density* is  $(2\pi)^{-1}$ .

In other words, Gabor’s concern was to set the time- and frequency-domain sampling intervals so that  $T\Omega = 2\pi$ —that is, to sample at the Nyquist density. This is equivalent to time sampling at the largest interval allowable, by the sampling theorem, for analog signal reconstruction from discrete samples. Gabor proposed families of windowed Fourier atoms, separated from one another at the Nyquist

limit  $T = 2\pi\Omega^{-1}$ . Our problem is to characterize Gabor’s proposal for each of the three cases:

- (i)  $T\Omega < 2\pi$ , when the sampling interval is less than the Nyquist frequency or, equivalently, when the time-frequency density exceeds the Nyquist density.
- (ii)  $T\Omega = 2\pi$ , the original proposal of Gabor.
- (iii)  $T\Omega > 2\pi$ .

**10.3.4.2 Too Sparse:  $T\Omega > 2\pi$ .** Gabor’s proposal to represent signals using sums of windowed Fourier atoms does not in fact succeed for the sparse case,  $T\Omega > 2\pi$ . This case occurs when the time-domain sampling interval exceeds the maximum allowable for reconstructing an analog signal of bandwidth  $\Omega$  by its discrete samples at times  $mT, m \in \mathbb{Z}$ . That is, families of Gabor atoms  $\{w_{m,n}(t) = \exp(jn\Omega)t w(t - mT): m, n \in \mathbb{Z}\}$  cannot be a frame when  $(T\Omega)^{-1}$  is less than the Nyquist density.

Using the Zak transform, introduced in Chapter 8, this result can be shown for the case where  $(2\pi)^{-1}T\Omega$  is rational and exceeds unity. We will only consider a far simpler case:  $\Omega = 2\pi$  and  $T = 2$ . We recount the following results from Ref. 12.

**Lemma.** Let  $w(t) \in L^2(\mathbb{R}); w_{m,n}(t) = e^{jn\Omega t} w(t - mT)$ , for  $m, n \in \mathbb{Z}; \Omega = 2\pi$ ; and  $T = 2$ . Then there is an  $x(t) \in L^2(\mathbb{R})$  such that  $\|x\|_2 \neq 0$  and  $\langle x(t), w_{m,n}(t) \rangle = 0$  for all  $m, n \in \mathbb{Z}$ .

**Proof:** Let  $t \in [0, 1)$  and define

$$x(t+k) = (-1)^k \overline{w(t-k-1)}, \tag{10.80}$$

where  $k \in \mathbb{Z}$ . It is easily shown (exercise) that

- (i)  $x \in L^2(\mathbb{R})$ .
- (ii)  $\|x\|_2 = \|w\|_2$ .
- (iii)  $\|x\|_2 \neq 0$ .

We contend that  $\langle x(t), w_{m,n}(t) \rangle = 0$  for all  $m, n \in \mathbb{Z}$ . Breaking up the inner product integral reveals

$$\begin{aligned} \langle x(t), w_{m,n}(t) \rangle &= \int_{-\infty}^{\infty} x(t) e^{jn\Omega t} \overline{w(t-2m)} dt \\ &= \int_0^1 e^{-jn\Omega t} \sum_{k=-\infty}^{\infty} x(t+k) \overline{w(k+t-2m)} dt \end{aligned} \tag{10.81}$$

But inserting (10.80), we observe that

$$\sum_{k=-\infty}^{\infty} x(t+k) \overline{w(k+t-2m)} = \sum_{k=-\infty}^{\infty} (-1)^k \overline{w(t-k-1)} \overline{w(t+k-2m)}. \tag{10.82}$$

On the right-hand side of (10.82) consider a summand,

$$(-1)^k \overline{w(t-k-1)} \overline{w(t+k-2m)}, \quad (10.83a)$$

for some  $k \in \mathbb{Z}$ . Let  $i = 2m - k - 1$  and compare the term

$$(-1)^i \overline{w(t-i-m)} \overline{w(t+i-2m)}. \quad (10.83b)$$

The trick is that

$$(-1)^i \overline{w(t-i-m)} \overline{w(t+i-2m)} = (-1)^{-k-1} \overline{w(t-2m+k)} \overline{w(t-k-1)}, \quad (10.84)$$

which is the additive inverse of (10.83a). The upshot is that every summand in is complemented by its additive inverse also inside the summation; the sum is precisely zero! All inner products (10.81) are zero, and we have constructed a nontrivial  $x(t)$  in the orthogonal complement of  $\{w_{m,n}(t): m, n \in \mathbb{Z}\}$ . ■

Now we can prove the theorem. Recall that a frame generalizes the notion of an orthogonal basis, yet provides stable signal reconstruction and complete signal representation. We introduced frame theory in Section 3.3.4.

**Theorem.** Let  $w(t) \in L^2(\mathbb{R})$ ;  $w_{m,n}(t) = e^{jn\Omega t} w(t - mT)$ , for  $m, n \in \mathbb{Z}$ ;  $\Omega = 2\pi$ ; and  $T = 2$ . Then  $\{w_{m,n}(t): m, n \in \mathbb{Z}\}$  cannot be a frame.

**Proof:** Let  $x(t)$  be given by the lemma: nontrivial and orthogonal to all of the  $w_{m,n}(t)$ . If the  $\{w_{m,n}(t): m, n \in \mathbb{Z}\}$  were a frame, then by the definition of frame, there exist  $A > 0$  and  $B > 0$  such that

$$A\|y\|^2 \leq \sum_{m, n = -\infty}^{\infty} |\langle y, w_n \rangle|^2 \leq B\|y\|^2 \quad (10.85)$$

for all  $y(t) \in L^2(\mathbb{R})$ . The frame condition must hold for the lemma's  $x(t)$  as well, but since  $\langle x(t), w_{m,n}(t) \rangle = 0$  for all  $m, n \in \mathbb{Z}$ , we have a contradiction. ■

*Remark.* So there are no frames of windowed Fourier atoms,  $w_{m,n}(t) = e^{jn\Omega t} w(t - mT)$ , when the frequency- and time-domain sampling intervals are  $\Omega = 2\pi$ ; and  $T = 2$ , respectively. This is perhaps not too surprising a result, given the Shannon–Nyquist sampling theorem.

We have shown our result for only a particular instance,  $\Omega = 2\pi$  and  $T = 2$ , of the case  $T\Omega > 2\pi$ . An interesting, but somewhat technical, Zak transform application extends this same argument whenever  $T\Omega > 2\pi$  and  $T\Omega$  is a rational multiple of  $2\pi$  [25]. Using advanced mathematical methods well beyond our present scope, it has been shown that whenever the time-frequency sampling is too sparse—whether either  $T$  and  $\Omega$  are rational or irrational—then there are no frames of windowed Fourier atoms [26].

### 10.3.5 Frames of Windowed Fourier Atoms

Now let us consider another possibility:  $T\Omega < 2\pi$ . This is the dense time-frequency sampling case. Now, from a classic construction [27], it can be shown that we can build frames from windowed Fourier atoms when  $T\Omega < 2\pi$ . Here, we adapt the presentation in Ref. 12 to our own notation and show that collections of Gabor atoms  $\{w_{m,n}(t) = \exp(jn\Omega)t w(t - mT) : m, n \in \mathbb{Z}\}$  can be a frame when  $(T\Omega)^{-1}$  exceeds the Nyquist density,  $(2\pi)^{-1}$ .

**Theorem.** Let  $w(t) \in L^2(\mathbb{R})$ ; let  $w_{m,n}(t) = e^{jn\Omega t} w(t - mT)$ , for  $m, n \in \mathbb{Z}$ ;  $T\Omega < 2\pi$ ; and suppose that  $[-\pi/\Omega, \pi/\Omega] \supset \text{Support}(w)$ . Then for any  $x(t) \in L^2(\mathbb{R})$ ,

$$\sum_{m, n = -\infty}^{\infty} |\langle x, w_{m,n} \rangle|^2 = \frac{2\pi}{\Omega} \int_{-\infty}^{\infty} |x(t)|^2 \left( \sum_{k = -\infty}^{\infty} |w(t - kT)|^2 \right) dt. \tag{10.86}$$

**Proof:** Let us expand the sum on the left-hand side of (10.86) as sums over  $2\pi/\Omega$ -wide intervals:

$$\sum_{m, n = -\infty}^{\infty} |\langle x, w_{m,n} \rangle|^2 = \sum_{m, n = -\infty}^{\infty} \left| \int_0^{\frac{2\pi}{\Omega}} e^{jn\Omega t} \sum_{k = -\infty}^{\infty} x\left(t + \frac{2\pi k}{\Omega}\right) \overline{w\left(t + \frac{2\pi k}{\Omega} - mT\right)} dt \right|^2. \tag{10.87}$$

Notice that the integral in (10.87) is a constant multiple of a Fourier series coefficient. The functions  $\frac{1}{\sqrt{2\pi}} e^{jn\Omega t} = e_n(t)$  are an orthonormal basis for the Hilbert space  $H = L^2[0, 2\pi/\Omega]$ , and we know therefore that  $\|y\|_2^2 = \sum_n |\langle y, e_n \rangle|^2$  for any square-integrable  $y(t)$  in  $H$ . (This is in fact a Parseval result for  $H$ , and its roots extend back to our very early algebraic result from abstract Banach spaces—Bessel’s inequality.) Thus, for each  $m \in \mathbb{Z}$  we are able to replace the sum over  $n \in \mathbb{Z}$  in (10.87) with the square of the  $L^2[0, 2\pi/\Omega]$  norm of the sum in the integrand:

$$\sum_{m, n = -\infty}^{\infty} |\langle x, w_{m,n} \rangle|^2 = \frac{2\pi}{\Omega} \sum_{m = -\infty}^{\infty} \left| \int_0^{\frac{2\pi}{\Omega}} \sum_{k = -\infty}^{\infty} x\left(t + \frac{2\pi k}{\Omega}\right) \overline{w\left(t + \frac{2\pi k}{\Omega} - mT\right)} dt \right|^2. \tag{10.88}$$

Next, observe that for any  $m$  all of the summands over  $k$  inside the integral are zero except for possibly one. This is due to the choice of support for the window function  $w(t)$ . The right-hand side of simplifies, and we see

$$\sum_{m, n = -\infty}^{\infty} |\langle x, w_{m,n} \rangle|^2 = \frac{2\pi}{\Omega} \sum_{m, k = -\infty}^{\infty} \left| \int_0^{\frac{2\pi}{\Omega}} x\left(t + \frac{2\pi k}{\Omega}\right) \overline{w\left(t + \frac{2\pi k}{\Omega} - mT\right)} dt \right|^2. \tag{10.89}$$

We can now reassemble the separate finite integrals to one over the entire real line:

$$\sum_{m, n = -\infty}^{\infty} |\langle x, w_{m, n} \rangle|^2 = \frac{2\pi}{\Omega} \int_{-\infty}^{\infty} |x(t)|^2 \left( \sum_{k = -\infty}^{\infty} |w(t - kT)|^2 \right) dt. \quad (10.90)$$

■

The term in parentheses inside the integral (10.90) is crucial. If we can show that there are constants  $A, B > 0$  such that  $A$  bounds this term below and  $B$  bounds this term above, then we will have found frame bounds and shown that the windowed Fourier atoms  $\{w_{m, n}(t) = \exp(jn\Omega)t w(t - mT): m, n \in \mathbb{Z}\}$  do comprise a frame. The following corollary imposes a reasonable technical condition on the window function  $w(t)$  [27], namely that the window function be continuous and positive on some interval about  $t = 0$ .

**Corollary.** Let  $w(t) \in L^2(\mathbb{R})$  be as in the theorem. Further suppose that  $w(t)$  is continuous and that there are  $\varepsilon > 0$  and  $1 > \delta > 0$  such that  $|w(t)| > \varepsilon$  on  $I = [-\delta\pi/\Omega, \delta\pi/\Omega]$ . Then  $\{w_{m, n}(t) = e^{jn\Omega} w(t - mT): m, n \in \mathbb{Z}\}$  are a frame.

$$\sum_{m, n = -\infty}^{\infty} |\langle x, w_{m, n} \rangle|^2 = \frac{2\pi}{\Omega} \int_{-\infty}^{\infty} |x(t)|^2 \left( \sum_{k = -\infty}^{\infty} |w(t - kT)|^2 \right) dt. \quad (10.91)$$

**Proof:** Since

$$\sum_{m, n = -\infty}^{\infty} |\langle x, w_{m, n} \rangle|^2 = \frac{2\pi}{\Omega} \int_{-\infty}^{\infty} |x(t)|^2 \left( \sum_{k = -\infty}^{\infty} |w(t - kT)|^2 \right) dt, \quad (10.92)$$

by the theorem, we seek positive constants  $\alpha$  and  $\beta$  such that  $\alpha < \sum |w(t - kT)|^2$  and  $\sum |w(t - kT)|^2 < \beta$  for all  $t$ . Then we have

$$\frac{2\pi\alpha}{\Omega} \int_{-\infty}^{\infty} |x(t)|^2 dt \leq \sum_{m, n = -\infty}^{\infty} |\langle x, w_{m, n} \rangle|^2 = \frac{2\pi\beta}{\Omega} \int_{-\infty}^{\infty} |x(t)|^2 dt, \quad (10.93)$$

so that  $A = (2\pi\alpha)/\Omega$  and  $B = (2\pi\beta)/\Omega$  constitute lower and upper frame bounds, respectively, for  $\{w_{m, n}(t)\}$ . By the assumption that  $w(t)$  exceeds  $\varepsilon > 0$  on the proper subinterval  $I$ , we can set  $\alpha = \inf\{|w(t)|^2: t \in I\}$ . Since  $\alpha$  is the greatest lower bound of  $|w(t)|^2$  on  $I$ , and  $|w(t)| > \varepsilon$  on  $I$ , we know  $\alpha \geq \varepsilon > 0$ . The lower frame condition follows easily with bound  $A = (2\pi\alpha)/\Omega$ . To find the upper frame bound, we note that because the support of  $w(t)$  is contained within the interval  $[-\pi/\Omega, \pi/\Omega]$ , only a finite number  $K$  of terms in the sum  $\sum |w(t - kT)|^2$  will be nonzero. Since  $w(t)$  is continuous and supported on  $[-\pi/\Omega, \pi/\Omega]$ , we may let  $M$  be its least upper bound; that is,  $M = \|w\|_{\infty}$ . We can then set  $\beta = \sup\{\sum |w(t - kT)|^2: t \in \mathbb{R}\} \leq KM$ , and with  $B = (2\pi\beta)/\Omega$  we can verify the upper frame bound property. ■

*Remarks.* Recall from our general discussion of frames in Section 3.3.4 that the frame reconstruction algorithm is more efficient when the frame is tight. We can see in the theorem that finding  $w(t)$  so that  $\sum |w(t - kT)|^2$  is constant does provide us with a tight frame:  $A = B = 2\pi(\Omega T)^{-1}$ . In fact, it is fairly straightforward to concoct window functions  $w(t)$  so that this expression is constant. Moreover, the construction method gives windows with compact support arbitrarily good smoothness. We refer the reader to the literature for details [12, 25, 27].

The result of the theorem (10.86) can be used to find examples of windowed Fourier frames from special window functions.

**Example.** Suppose  $w(t) = (1 + t^2)^{-1}$ . Then  $w(t)$  is bounded and absolutely integrable. If  $T > 0$ , then  $\sum |w(t - kT)|^2$  has an upper and lower bound. One can show (exercise) that  $\{w_{m,n}(t) = e^{jm\Omega t} w(t - mT): m, n \in \mathbb{Z}\}$  are a frame if we take  $\Omega$  to be sufficiently small.

**Example.** Now let  $w(t) = g_{\mu,\sigma}(t)$ , the Gaussian with mean  $\mu$  and standard deviation  $\sigma$ . Again,  $\sum |g_{\mu,\sigma}(t - kT)|^2$  is bounded above and below when  $T > 0$ , and we can use the theorem's criterion for showing that Gabor frames exist for a sufficiently small frequency sampling interval.

Before summarizing our results in pursuit of Gabor's problem, let us note an important necessary condition of windowed Fourier frames [12].

**Theorem.** Suppose  $w(t) \in L^2(\mathbb{R}); \Omega, T > 0$ ; and  $\{w_{m,n}(t) = e^{jm\Omega t} w(t - mT): m, n \in \mathbb{Z}\}$  constitute a frame with lower and upper bounds  $A$  and  $B$ , respectively. Then

$$A \leq \frac{2\pi}{\Omega T} \|w\|_2^2 \leq B. \tag{10.94}$$

*Proof:* Exercise. ■

### 10.3.6 Status of Gabor's Problem

We can briefly summarize the status of our search for frames of windowed Fourier atoms. There are three cases, which depend on the time- and frequency-domain sampling intervals,  $T$  and  $\Omega$ , respectively. Our present understanding is as follows:

- (i) When  $T\Omega < 2\pi$  the time-frequency density is higher than the Nyquist density, and we have just constructed frames of windowed Fourier atoms in this case.
- (ii) When  $T\Omega = 2\pi$  the atom are at Nyquist density exactly; this is the alternative proposed by Gabor, and our analysis of it is not yet complete.
- (iii) Finally, when  $T\Omega > 2\pi$  we have noted that windowed Fourier frames do not exist in this situation; we proved a simple instance, and the research literature—portions of which rely on advanced analysis—completely covers the remaining cases.

We will in fact devote a considerable portion of the remainder of this chapter to Gabor's dividing line case. The applicability of the short-time Fourier transform (STFT) when time-frequency localization is of paramount importance hangs on this question. This question also vexed signal processing investigators for a number of years; we are especially interested in fully understanding the impact of windowed Fourier transform discretization when  $T\Omega = 2\pi$ .

Before turning to this question, however, let us consider another approach to time-frequency signal decompositions.

## 10.4 QUADRATIC TIME-FREQUENCY TRANSFORMS

There are classes of time-frequency transforms that do not depend on a windowing function. Instead, the transform relation emerges out of the properties of the analyzed signal. The signal  $x(t)$  enters the transform integral as a quadratic rather than as linear term, as it does in the windowed Fourier transform. This transform family is therefore generally known as the *quadratic* time-frequency transformations. Its principal members are the *Wigner-Ville transform* (WVT) and the closely related *ambiguity function*.

Now, transforming without a window function appears to be quite advantageous, since the resulting procedure eliminates the effect window selection imposes on the transform's behavior. The short-time Fourier transform mixes spectral properties of the analyzed signal  $x(t)$  together with those of the window function  $w(t)$ . Blindly perusing coefficients, we do not know whether their large magnitude results from signal or window properties. On the other hand, we do not often blindly process transform coefficients. Rather, the window function is typically chosen to isolate signal features of expected frequency content and time-domain extent; in the more typical application then, choosing a window function may well be the best first step.

Although avoiding window effects may recommend quadratic transforms, there are some more important considerations. We shall explore three significant properties of these transforms. This transform family:

- More precisely resolves certain standard cases of time-varying frequencies than does the STFT;
- Enjoys special properties called *marginal conditions* that allow them to act as distribution functions for a signal's spectral content;
- Has the significant drawback that transformed signals exhibit certain artifacts called *cross-terms* that hamper higher-level interpretation.

This is in fact a very rich transform family. An entire book could be written about these transforms, and many treatments devote considerable space to these transforms [2, 6, 9]. By our brief sketch we hope that the reader will acquire a more balanced opinion of the windowed Fourier transforms and an interest in further exploring the theory and application of quadratic transforms.

### 10.4.1 Spectrogram

We can base a quadratic time-frequency transform on the STFT. This is in fact just the spectrogram, which we define as follows.

**Definition (Spectrogram).** Let  $x(t) \in L^2(\mathbb{R})$  and let  $w(t)$  be a window function. The *spectrogram with respect to  $w(t)$* , written  $X_{S,w}(\mu, \omega)$ , is

$$X_{S,w}(\mu, \omega) = |X(\mu, \omega)|^2 = \left| \int_{-\infty}^{\infty} x(t)w(t - \mu)e^{-j\omega t} dt \right|^2, \tag{10.95}$$

where  $X_w(\mu, \omega)$ , is the STFT of  $x(t)$  with respect to  $w(t)$ .

Thus, the spectrogram of  $x(t)$  is the squared magnitude of the STFT of  $x(t)$  with respect to  $w(t)$ . The spectrogram is thus a natural generalization of the windowed Fourier methods we have been comfortable in using. However, despite the more intuitive feel, spectrograms are far from being the most popular quadratic time-frequency transforms. For one thing,  $X_{S,w}$  relies on a window function. But it also has some other undesirable traits that have motivated signal theorists to search out other transform techniques. Among these better transforms is the the classic transform of Wigner and Ville which we introduce next; we shall assess the merits of the spectrogram in this context.

### 10.4.2 Wigner–Ville Distribution

The Wigner–Ville distribution (WVD) is the oldest time-frequency transform and the preeminent quadratic signal representation. In fact it dates to the early 1930s when E. Wigner<sup>6</sup> applied it in quantum mechanics [28]. The communication theorist J. Ville<sup>7</sup> introduced the transform to the signal processing community some 16 years later [29].

The transform has been widely studied for signal analysis applications [30, 31]. It has also found use as an important tool in computer vision [32]. The WVD has some distinct advantages over the more intuitive spectrogram. But it is not without its faults.

One difficulty in applying the WVD is the presence of so-called *cross- or interference terms* among the transform coefficients. Indeed, many research efforts in time-frequency theory have concentrated on avoiding or ameliorating the effects of cross-terms when using this type of tool. This problem is covered in the Section 10.4.3.

**10.4.2.1 Definition and Motivation.** The Wigner–Ville distribution takes the Fourier transform of a product of the signal with its complex conjugate. Thus, it resembles the computation of the power spectral density.

<sup>6</sup>The Hungarian chemical engineer Eugene P. Wigner (1902–1996) immigrated to the United States to teach mathematics at Princeton University in 1930. He received the Nobel prize in 1963 for discoveries in atomic and elementary particle research.

<sup>7</sup>French communication researcher J. Ville developed the same transform as Wigner, but for the purposes of clarifying the concept of instantaneous frequency.

**Definition (Wigner–Ville Distribution).** If  $x(t) \in L^2(\mathbb{R})$  is an analog signal, then its *Wigner–Ville distribution*, written  $X_{WV}(\mu, \omega)$ , is the radial Fourier transform of the product  $x(\mu + t/2)x^*(\mu - t/2)$ :

$$X_{WV}(\mu, \omega) = \int_{-\infty}^{\infty} x\left(\mu + \frac{t}{2}\right)\overline{x\left(\mu - \frac{t}{2}\right)}e^{-j\omega t} dt. \tag{10.96}$$

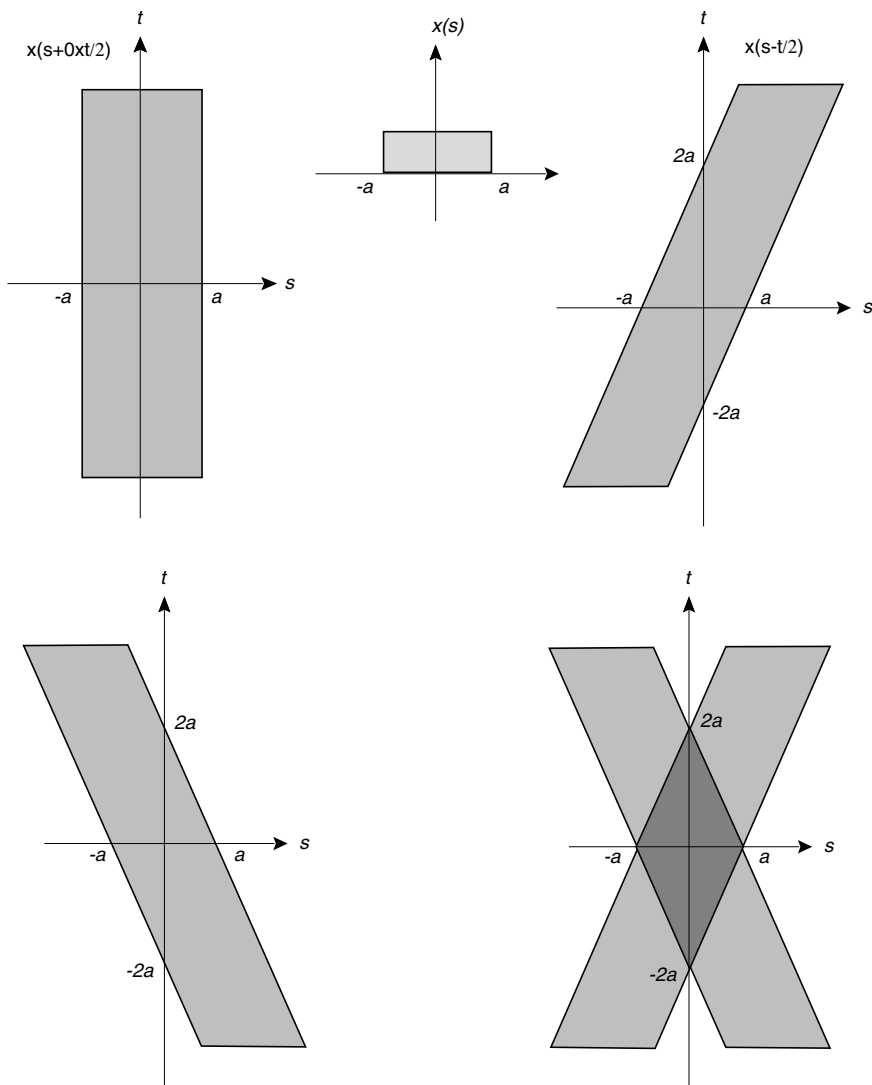


**Fig. 10.12.** Illustrating the support of  $x(s + t/2)x^*(s - t/2)$  in the  $(s, t)$  plane. Panel (a) shows the support of  $x(s)$ . We move to two dimensions in Panel (b), but show the support of the degenerate function  $x(s + 0 \times (t/2))$ . The support of  $x(s - t/2)$  is the parallelepiped region (c) and the product  $x(s + t/2)x^*(s - t/2)$  has support mainly within the diamond (d).

*Remark.* We observe that the integral (10.96) is well-defined. It is the Fourier transform of  $x(\mu + t/2)x^*(\mu - t/2)$ , which must be absolutely integrable. This follows because both factors are in  $L^2(\mathbb{R})$ , and the Schwarz inequality ensures that  $\|x(\mu + t/2)\|_2 \|x^*(\mu - t/2)\|_2 \geq \|x(\mu + t/2)x^*(\mu - t/2)\|_1$ . Of course,  $L^1(\mathbb{R})$  signals have Fourier transforms.

No window function appears in the definition (10.96), but there is an easy way to understand how folding the source signal  $x(t)$  over on itself accomplishes the required time localization. Imagining that a signal’s support lies mainly within the interval  $[-a, a]$ , the local region implied by the WVD transform is a diamond, as shown in Figure 10.12.

**10.4.2.2 Properties.** The properties of this transform are quite remarkable. To begin with, we can show that the Wigner–Ville distribution is *real-valued*.

**Proposition (Real-Valued).** Let  $x(t) \in L^2(\mathbb{R})$  and  $X_{WV}(\mu, \omega)$  be its WVD. Then  $X_{WV}(\mu, \omega) \in \mathbb{R}$ .

*Proof:* We calculate the complex conjugate of (10.96) and make the change of integration variable  $s = -t$ .

$$\begin{aligned} \overline{X_{WV}(\mu, \omega)} &= \int_{-\infty}^{\infty} \overline{x\left(\mu + \frac{t}{2}\right)x\left(\mu - \frac{t}{2}\right)e^{j\omega t}} dt \\ &= - \int_{\infty}^{-\infty} \overline{x\left(\mu - \frac{s}{2}\right)x\left(\mu + \frac{s}{2}\right)e^{-j\omega s}} ds = X_{WV}(\mu, \omega). \end{aligned} \tag{10.97}$$

Because  $X^*_{WV}(\mu, \omega) = X_{WV}(\mu, \omega)$ , it must be real. ■

Already we see that the WVD’s properties are quite unlike those of the Fourier transform or its time-limited versions. However, the time- and frequency-domain shifting properties are familiar, as the next proposition shows. Symmetry properties are covered in the exercises.

**Proposition (Time and Frequency Shift).** Let  $x(t) \in L^2(\mathbb{R})$  and  $X_{WV}(\mu, \omega)$  be its WVD. Then

- (a) If  $s(t) = x(t - a)$ , then  $S_{WV}(\mu, \omega) = X_{WV}(\mu - a, \omega)$ .
- (b) If  $y(t) = e^{j\theta t}x(t)$ , then  $Y_{WV}(\mu, \omega) = X_{WV}(\mu, \omega - \theta)$ .

*Proof:* Exercise. ■

The double product of  $x(t)$  terms in the WVD integral, which is the “quadratic” factor, spoils the transform’s linearity. This is easy to see for the scaling property of the linearity. We let  $y(t) = ax(t)$ , where  $a$  is a constant. Then  $Y_{WV}(\mu, \omega) = |a|^2 X_{WV}(\mu, \omega)$ .

Superposition also fails for the WVD. We use an auxiliary transform as part of the argument.

**Definition (Cross Wigner–Ville Distribution).** If  $x(t), y(t) \in L^2(\mathbb{R})$  are analog signals, then the *Cross Wigner–Ville Distribution*, written  $X_{\text{WV},y}(\mu, \omega)$ , is the radial Fourier transform of the product  $x(\mu + t/2)y^*(\mu - t/2)$ :

$$X_{\text{WV},y}(\mu, \omega) = \int_{-\infty}^{\infty} x\left(\mu + \frac{t}{2}\right) \overline{y\left(\mu - \frac{t}{2}\right)} e^{-j\omega t} dt. \quad (10.98)$$

One can easily show that  $X_{\text{WV},y}(\mu, \omega)$  is the complex conjugate of  $Y_{\text{WV},x}(\mu, \omega)$ . If we set  $s(t) = x(t) + y(t)$ , then  $S_{\text{WV}}(\mu, \omega) = X_{\text{WV}}(\mu, \omega) + Y_{\text{WV}}(\mu, \omega) + 2\text{Real}[X_{\text{WV},y}(\mu, \omega)]$ .

Thus, both component properties of linearity fail for the WVD. The failure of superposition is the more serious deficiency. This defect causes artifacts, called *cross-terms*, in the WVD transform coefficients. The presence of cross-terms leads to difficulties of automatic interpretation, and removing them by various alternative transformations has been a major research goal of the last several years.

The next theorem reveals an interesting symmetry between time and frequency domain representations for the WVD. Besides having an eerie similarity to the inverse Fourier relation, it is also useful in calculations involving the WVD.

**Theorem (Frequency-Domain Representation).** Let  $x(t) \in L^2(\mathbb{R})$ , let  $X(\omega)$  be its Fourier transform, and  $X_{\text{WV}}(\mu, \omega)$  be its WVD. Then

$$X_{\text{WV}}(\mu, \omega) = \frac{1}{2\pi} \int_{-\infty}^{\infty} X\left(\omega + \frac{\theta}{2}\right) \overline{X\left(\omega - \frac{\theta}{2}\right)} e^{j\theta\mu} d\theta. \quad (10.99)$$

**Proof:** The key idea is to write  $X_{\text{WV}}(\mu, \omega)$  as an inner product,

$$X_{\text{WV}}(\mu, \omega) = \left\langle x\left(\mu + \frac{t}{2}\right) e^{\frac{-j\omega t}{2}}, \quad x\left(\mu - \frac{t}{2}\right) e^{\frac{j\omega t}{2}} \right\rangle, \quad (10.100)$$

splitting the exponential between its two terms. We can then apply Parseval's theorem:

$$\begin{aligned} X_{\text{WV}}(\mu, \omega) &= \frac{1}{2\pi} \left\langle \mathcal{F}x\left(\mu + \frac{t}{2}\right) e^{\frac{-j\omega t}{2}}, \mathcal{F}x\left(\mu - \frac{t}{2}\right) e^{\frac{j\omega t}{2}} \right\rangle \\ &= \frac{1}{2\pi} \langle 2X(\omega + 2\phi) e^{j\mu(\omega + 2\phi)}, 2X(\omega - 2\phi) e^{j\mu(\omega - 2\phi)} \rangle. \end{aligned} \quad (10.101)$$

The final inner product in (10.101) simplifies to the integral

$$X_{\text{WV}}(\mu, \omega) = \frac{4}{2\pi} \int_{-\infty}^{\infty} X(\omega + 2\phi) \overline{X(\omega - 2\phi)} e^{4j\phi\mu} d\phi, \tag{10.102}$$

whereupon the substitution  $\theta = 4\phi$  gives (10.99). ■

**Corollary (Fourier Transform of WVD).** Let  $x(t) \in L^2(\mathbb{R})$ , let  $X(\omega)$  be its Fourier transform, and  $X_{\text{WV}}(\mu, \omega)$  be its WVD. Then, with  $\omega$  fixed and viewing  $X_{\text{WV}}(\mu, \omega)$  as a signal with independent time variable  $\mu$ , we have

$$\mathcal{F}[X_{\text{WV}}(\mu, \omega)](\theta) = \int_{-\infty}^{\infty} X_{\text{WV}}(\mu, \omega) e^{-j\mu\theta} d\mu = X\left(\omega + \frac{\theta}{2}\right) \overline{X\left(\omega - \frac{\theta}{2}\right)}. \tag{10.103}$$

**Proof:** Apply the theorem to the WVD term in the integral (exercise).

Table 10.3 summarizes WVD properties. Some of the table’s properties are left as exercises.

**10.4.2.3 Examples.** Let us look at some WVD calculations on standard example signals. These examples are revealing, because they show how the WVD improves upon the frequency resolving capability of the STFT.

**TABLE 10.3. Wigner–Ville Distribution Properties<sup>a</sup>**

Signal Expression	WVD or Property
$x(t)$	$X_{\text{WV}}(\mu, \omega)$
$ax(t)$	$ a ^2 X_{\text{WV}}(\mu, \omega)$
$x(t) + y(t)$	$X_{\text{WV}}(\mu, \omega) + Y_{\text{WV}}(\mu, \omega) + 2\text{Real}[X_{\text{WV},y}(\mu, \omega)]$
$x(t - a)$	$X_{\text{WV}}(\mu - a, \omega)$
$x(t)\exp(j\theta t)$	$X_{\text{WV}}(\mu, \omega - \theta)$
$x(t)\exp(j\theta t^2)$	$X_{\text{WV}}(\mu, \omega - 2\theta\mu)$
$x(t/a)$ , with $a > 0$	$aX_{\text{WV}}(\mu/a, a\omega)$
$X_{\text{WV}}(\mu, \omega) = \frac{1}{2\pi} \int_{-\infty}^{\infty} X\left(\omega + \frac{\theta}{2}\right) \overline{X\left(\omega - \frac{\theta}{2}\right)} e^{j\theta\mu} d\theta$	Frequency-domain representation
$\int_{-\infty}^{\infty} X_{\text{WV}}(\mu, \omega) e^{-j\mu\theta} d\mu = X\left(\omega + \frac{\theta}{2}\right) \overline{X\left(\omega - \frac{\theta}{2}\right)}$	Fourier transform of WVD

<sup>a</sup>In this table,  $x(t)$  and  $y(t)$  are square-integrable.

**Example (Dirac).** Let  $x(t) = \delta(t - a)$ . Then  $X_{\text{WV}}(\mu, \omega) = \delta(\mu - a)$ . To verify this formula, we utilize the Frequency-Domain Representation Theorem. Then.

$$X_{\text{WV}}(\mu, \omega) = \frac{1}{2\pi} \int_{-\infty}^{\infty} e^{-j\left(\omega + \frac{\theta}{2}\right)a} e^{j\left(\omega - \frac{\theta}{2}\right)a} e^{j\theta\mu} d\theta = \frac{1}{2\pi} \int_{-\infty}^{\infty} e^{j(\mu-a)\theta} d\theta = \delta(\mu - a). \quad (10.104)$$

The interesting aspect of this example is that the WVD maps an impulse to an impulse. The time-frequency representation that the WVD provides is just as temporally localized as the original time-domain signal. In the  $(\mu, \omega)$  plane, realm of the WVD, the signal  $\delta(\mu - a)$  is a Dirac knife edge, infinitely high and infinitely narrow, parallel to the  $\omega$ -axis and passing through the point  $\mu = a$ . This stands in stark contrast to the STFT. The windowed Fourier transformation of the same Dirac impulse  $x(t) = \delta(t - a)$  is  $X_w(\mu, \omega) = w(a - \mu)e^{-j\omega a}$ , an exponential modulated by the transform window  $w(t)$  situated over the point  $\mu = a$ .

**Example (Sinusoid).** Let  $x(t) = e^{jat}$ . Then  $X_{\text{WV}}(\mu, \omega) = (2\pi)^{-1}\delta(\omega - a)$ . This can be shown using the WVD properties (Table 10.3) or by direct computation as above.

**Example (Gaussian Pulse).** Now let  $g(t) = g_{\alpha, \sigma}(t)$ , the Gaussian of mean  $\alpha$  and standard deviation  $\sigma$ . Then

$$G_{\text{WV}}(\mu, \omega) = \frac{e^{-(\sigma\omega)^2} e^{-\left(\frac{\mu - \alpha}{\sigma}\right)^2}}{2\pi^{3/2}\sigma}. \quad (10.105)$$

Notice in this example that the WVD of a Gaussian pulse is always positive. The only signals  $x(t)$  for which  $X_{\text{WV}}(\mu, \omega)$  is positive are linear chirps,  $\exp(jbt^2 + jat)$ , modulated by a Gaussian envelope Ref. [7].

**Example (Square Pulse).** Let  $s(t) = u(t + 1) - u(t - 1)$ , the square pulse supported on the interval  $[-1, 1]$ . Then

$$S_{\text{WV}}(\mu, \omega) = \frac{2s(\mu)}{\omega} \sin(2\omega(1 - |\mu|)). \quad (10.106)$$

Thus, although the WVD is real-valued, its values can be negative.

These examples illustrate the trade offs between the windowed Fourier transforms and the WVD. There are still other time-frequency transforms, of course; Ref. 33 compares the frequency resolution efficiencies of several of them.

**10.4.2.4 Densities and Marginals.** Now we turn to an important feature of the Wigner–Ville distribution, a set of properties that distinguish it from the

short-time Fourier transform, namely its density function-like character. What does this mean? In the case of the Fourier transform, we have been content to use fractions of signal energy as an indication that a frequency range is significant within a signal  $x(t)$ . Thus, the energy of  $x(t)$  is  $E_x$ :

$$E_x^2 = \int_{-\infty}^{\infty} |x(t)|^2 dt = \|x\|_2^2 = \frac{1}{2\pi} \int_{-\infty}^{\infty} |X(\omega)|^2 d\omega = \frac{\|X\|_2^2}{2\pi}. \quad (10.107)$$

We may normalize  $x(t)$  or  $X(\omega)$  so that they have unit energy, or we may elect to use the normalized radial Fourier transform and equate time and frequency-domain energies. The exercises explore the use of the Hertz Fourier transform for quantifying energy distributions in both time and frequency-domains. In any case then, like a probability density function, the fraction of signal energy between  $\omega_0$  and  $\omega_1$  is given by

$$E_x^2[\omega_0, \omega_1] = \int_{\omega_0}^{\omega_1} |X(\omega)|^2 d\omega, \quad (10.108)$$

where we have normalized so that  $\int_{-\infty}^{\infty} |X(\omega)|^2 d\omega = 1$ .

Now, we are interested in transform representations of signals that have both a time- and a frequency-domain independent variable. Our question is whether such transforms can have joint density function behavior as well. For this to be the case, we should require that the signal transform assumes non-negative values and obey certain marginal integral conditions.

**Definition (Marginals).** The time-frequency transform  $P(\mu, \omega)$  of  $x(t) \in L^2(\mathbb{R})$  obeys the *marginal conditions* if

$$P(\mu, \omega) \geq 0, \quad (10.109a)$$

$$\frac{1}{2\pi} \int_{-\infty}^{\infty} P(\mu, \omega) d\omega = |x(t)|^2, \quad (10.109b)$$

$$\int_{-\infty}^{\infty} P(\mu, \omega) d\mu = |X(\omega)|^2, \quad (10.109c)$$

where  $X(\omega)$  is the radial Fourier transform of  $x(t)$ .

(These conditions are somewhat imperfect, due to the scaling factor in (10.109b). We can escape the scaling by using a Hertz Fourier transform. All we really require is that the marginal integral with respect to one variable be proportional to the signal

energy with respect to the other variable; see the exercises.) The idea behind the definition is that  $P(\mu, \omega)$  represents a relative amount of the signal per unit time and per unit frequency. Summing the distribution over frequency values should produce a relative amount of signal per unit time. Finally, summing over time should produce a signal strength per unit frequency.

The interpretation of the WVD as a kind of probability density function seems to gain steam from the fact that its values are real; we have already seen from the example of the square pulse, however, that the values can be negative. In contrast, the spectrogram, because it is a squared norm, is always non-negative. However, the WVD does satisfy marginal conditions, which the spectrogram does not.

**Theorem (Marginals).** Let  $x(t) \in L^2(\mathbb{R})$ , let  $X(\omega)$  be its Fourier transform, and let  $X_{\text{WV}}(\mu, \omega)$  be its WVD. Then

$$\int_{-\infty}^{\infty} X_{\text{WV}}(\mu, \omega) d\omega = 2\pi|x(\mu)|^2, \quad (10.110a)$$

$$\int_{-\infty}^{\infty} X_{\text{WV}}(\mu, \omega) d\mu = |X(\omega)|^2. \quad (10.110b)$$

**Proof:** We can directly evaluate the integral (10.110a) as follows:

$$\int_{-\infty}^{\infty} X_{\text{WV}}(\mu, \omega) d\omega = \int_{-\infty}^{\infty} \int_{-\infty}^{\infty} x\left(\mu + \frac{t}{2}\right) \overline{x\left(\mu - \frac{t}{2}\right)} e^{-j\omega t} dt d\omega. \quad (10.111)$$

Interchanging the order of integration on the right-hand side of (10.111) gives

$$\begin{aligned} \int_{-\infty}^{\infty} x\left(\mu + \frac{t}{2}\right) \overline{x\left(\mu - \frac{t}{2}\right)} \int_{-\infty}^{\infty} e^{-j\omega t} d\omega dt &= 2\pi \int_{-\infty}^{\infty} x\left(\mu + \frac{t}{2}\right) \overline{x\left(\mu - \frac{t}{2}\right)} \delta(t) dt \\ &= 2\pi x\left(\mu + \frac{t}{2}\right) \overline{x\left(\mu - \frac{t}{2}\right)} \Big|_{t=0} \\ &= 2\pi x(\mu) \overline{x(\mu)} = 2\pi|x(\mu)|^2. \end{aligned} \quad (10.112)$$

We leave the second marginal as an exercise. ■

Thus, we have shown that the WVD obeys a marginal condition akin to that of a joint probability density function. It is possible to show that employing a Hertz formulation of the WVD produces perfect marginal conditions for the transform. Unfortunately, the spectrogram fails the marginals, precisely because of the window function (exercises).

### 10.4.3 Ambiguity Function

Another quadratic time-frequency signal representation is the ambiguity function. Its formulation is much like the WVD, except that it swaps the time and integration variables in the defining Fourier integral.

**Definition (Ambiguity Function).** If  $x(t) \in L^2(\mathbb{R})$  is an analog signal, then its *ambiguity function*, written  $X_{AF}(\mu, \omega)$ , is the radial Fourier transform of the product  $x(t + \mu/2)x^*(t - \mu/2)$ :

$$X_{AF}(\mu, \omega) = \int_{-\infty}^{\infty} x\left(t + \frac{\mu}{2}\right) \overline{x\left(t - \frac{\mu}{2}\right)} e^{-j\omega t} dt. \tag{10.113}$$

The following result relates the ambiguity function to the WVD.

**Theorem (Ambiguity Function Characterization).** Let  $x(t) \in L^2(\mathbb{R})$  be an analog signal,  $X_{AF}(\mu, \omega)$  its ambiguity function, and  $X_{WV}(\nu, \omega)$  its Wigner–Ville distribution. Then,

$$X_{AF}(\mu, \omega) = \int_{-\infty}^{\infty} \int_{-\infty}^{\infty} X_{WV}(\nu, \theta) e^{-j(\nu\omega + \mu\theta)} d\nu d\theta. \tag{10.114}$$

**Proof:** Let us evaluate the integral on the right-hand side of (10.114) by splitting up the exponential into two one-dimensional Fourier transforms. Then the corollary to the Frequency-Domain Representation Theorem [(10.103) applies.

$$\int_{-\infty}^{\infty} \int_{-\infty}^{\infty} X_{WV}(\nu, \theta) e^{-j(\nu\omega + \mu\theta)} d\nu d\theta = \int_{-\infty}^{\infty} X\left(\omega + \frac{\theta}{2}\right) \overline{X\left(\omega - \frac{\theta}{2}\right)} e^{-j\mu\theta} d\theta. \tag{10.115}$$

Writing the integral on the right-hand side of (10.115) as an inner product and invoking Parseval’s formula, we find

$$\int_{-\infty}^{\infty} X\left(\omega + \frac{\theta}{2}\right) \overline{X\left(\omega - \frac{\theta}{2}\right)} e^{-j\mu\theta} d\theta = \int_{-\infty}^{\infty} x\left(t + \frac{\mu}{2}\right) \overline{x\left(t - \frac{\mu}{2}\right)} e^{-j\omega t} dt. \tag{10.116}$$

But the last integral above is  $X_{AF}(\mu, \omega)$ . ■

*Remark.* Notice that the ambiguity function characterization (10.114) shows that  $X_{AF}(\mu, \omega)$  is the two-dimensional Fourier transform of  $X_{WV}(\mu, \omega)$ .

### 10.4.4 Cross-Term Problems

While the WVD does have several advantages over the spectrogram—among them superior frequency-domain resolution, satisfaction of the marginals, and independence of a windowing function—it does have the misfortune of interference terms.

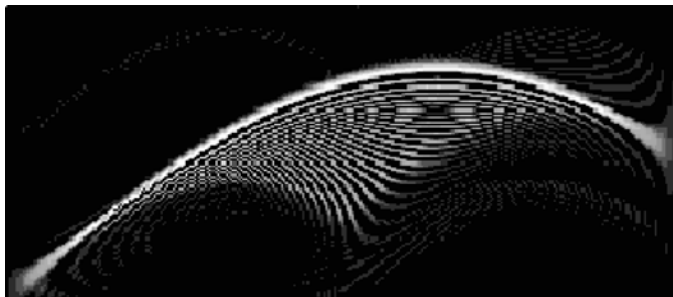


**Fig. 10.13.** An example of the presence of cross-terms in the WVD. The original signal is a chirp, first rising in frequency and then falling. High-energy coefficients appear beneath the main arc of energy in the transform plane, yet the time-domain signal contains no such tones. Higher-level interpretation routines are beset with the problem of separating such artifacts from genuine features of the signal's time evolution.

The cross-terms represent time-frequency domain energy in locations where it is not present in the original signal (Figure 10.13).

Cross-terms in WVD coefficients are, generally speaking, oscillatory in nature. As such, their effect on applications can be mitigated if not removed by filtering in the  $(\mu, \omega)$  plane. The *quid pro quo* is some loss of frequency resolution [9]. The principal approach to removing these oscillatory components is through frequency domain filtering. Thus, one manipulates the Fourier transform of  $X_{WV}(\mu, \omega)$ —the ambiguity function  $X_{AF}(\mu, \omega)$ . Several such methods are compared in Ref. 34. Modification of the ambiguity plane image, a two-dimensional undertaking, is outside our present scope, however.

Although they are in general tolerable, WVD interferences can be extreme in some cases. For example, for each pair of energy concentrations in the time-frequency plane, a possible cross-term region is created. Thus, if there are  $N$  significant temporal-spectral components of  $x(t)$ , then  $X_{WV}(\mu, \omega)$  will have  $N \times (N - 1)$  interference term regions. This combinatorial explosion presents nasty problems for higher-level interpretation algorithms. Furthermore, by the algebraic nature of their origin, cross-term amplitudes can conceivably be double the magnitudes of their source pair of time-frequency energy modes. So how then can a high-level algorithm distinguish meaningful events from meaningless interferences?

#### 10.4.5 Kernel Construction Method

Many of the latest time-frequency signal analysis research efforts have revolved around the problem of finding density-like distributions that obey the marginal conditions, but avoid cross-term effects.

The principal strategy is to introduce a third term into the defining transform integral [35].

**Definition (Kernel-Based or Cohen’s Class of Transforms).** If  $x(t) \in L^2(\mathbb{R})$  is an analog signal, then its *Cohen Class Transform* with respect to  $K$ , written  $X_K(\mu, \omega)$ , is

$$X_K(\mu, \omega) = \int_{-\infty}^{\infty} \int_{-\infty}^{\infty} \int_{-\infty}^{\infty} K(\theta, t) e^{j\theta(s-\mu)} x\left(s + \frac{t}{2}\right) \overline{x\left(s - \frac{t}{2}\right)} e^{-j\omega t} dt ds d\theta. \quad (10.117)$$

The kernel term can be thought of as smoothing the interferences. It is also possible to show that almost all time-frequency transforms, assuming a suitable choice of the kernel function, belong to the Cohen Class [7, 9].

Why resort to such triple integrals for basic one-dimensional signal representation? The spectrogram does not obey the marginals, so signal theorists sought a solution amongst transforms such as the WVD. Hope for a quadratic transform, however, was dashed by Wigner’s theorem [36]. This result states that a quadratic time-frequency transform cannot obey the marginal conditions (10.109a)–(10.109c). Pursuing these very interesting ideas would require quite a bit of multidimensional transform development and take us far afield, however.

We return to the STFT family to answer conclusively the question Gabor posed: Can a critically sampled set of windowed Fourier atoms fully support representation and analysis?

### 10.5 THE BALIAN–LOW THEOREM

This section concludes the chapter by proving a famous result in time-frequency transform theory: the Balian–Low theorem. The theorem applies to the entire class of time-frequency (or windowed-Fourier) transforms. Balian–Low answers a question posed by discretizing the short-time Fourier transform: Can windowed Fourier atoms of the form

$$w_{m,n}(t) = e^{jn\Omega t} w(t - mT), \quad (10.118)$$

where  $T > 0$  and  $T\Omega = 2\pi$  serve as a complete signal representation? We desire good time and frequency localization; we stipulate, therefore, that both  $w(t)$  and its Fourier transform  $W(\omega)$  are window functions. The two practical alternatives are that  $\{w_{m,n}(t): m, n \in \mathbb{Z}\}$  constitutes either

- An orthonormal basis or
- A frame.

It is hoped that we can discover  $\{w_{m,n}(t): m, n \in \mathbb{Z}\}$  that make up an orthonormal basis. Then every square-integrable signal  $x(t)$  has an expansion in terms of Fourier coefficients, easily calculated as the inner products of  $x(t)$  with the  $w_{m,n}(t)$ :

$$x(t) = \sum_{m,n \in \mathbb{Z}} \langle x(t), w_{m,n}(t) \rangle w_{m,n}(t). \quad (10.119)$$

If we fail to find such a basis, then computing the expansion coefficients (10.119) becomes problematic. Lack of a basis encumbers our signal analysis too. While we might be able to decompose a candidate signal  $x(t)$  into a linear combination of atoms,  $x(t) = \sum c_{m,n} w_{m,n}(t)$ , we do not necessarily know the uniqueness of the expansion coefficients  $c_{m,n}$  for representing  $x(t)$ . So the utility of the expansion coefficients as indicators of some signal component's presence or the lack thereof is very much compromised.

Should a basis not be available, we could search for a frame representation of  $L^2(\mathbb{R})$  signals using the Gabor atoms (10.118). After all, frame coefficients can characterize the source signal  $x(t)$ , and they support numerically stable reconstructions. This may be a good redoubt.

In either case, orthonormal basis or frame, we can build a structural interpretation of finite-energy signals  $x(t)$ . The Balian–Low theorem dashes our hopes—both of them. We cover the theorem for the easier-to-prove case of orthonormal bases, first. Then we turn to Balian–Low's rejection of frames. To prove that no such frames exist, we need a special tool, namely the Zak transform. Frames were covered in Section 3.3.5, and the Zak transform was introduced at the end of Chapter 8.

### 10.5.1 Orthonormal Basis Decomposition

The Balian–Low theorem answers Gabor's original problem of finding well-localized signal representations using time-frequency atoms [25, 37–40]. It is also a negative result, for it shows the impossibility of finding well-localized, orthonormal decompositions based on windowed Fourier atoms when  $T\Omega = 2\pi$ .

We begin with a lemma. It is simple, but it allows us to reduce the proof of the theorem for all possible samplings  $T\Omega = 2\pi$ , to the specific case of  $T = 1$  and  $\Omega = 2\pi$ .

**Lemma.** If  $T > 0$ , then the map  $H(x(t)) = T^{1/2}x(Tt)$  is unitary on  $L^2(\mathbb{R})$ ; that is,

- (i)  $H$  is onto;
- (ii)  $H$  preserves inner products,  $\langle Hx, Hy \rangle = \langle x, y \rangle$ .

**Proof:** For (i), let  $y \in L^2(\mathbb{R})$  and choose  $x(t) = T^{-1/2}y(t/T)$ . Then  $(Hx)(t) = y(t)$ . For (ii) we change variables,  $s = Tt$ , in the inner product integral:

$$\langle Hx, Hy \rangle = \int_{-\infty}^{\infty} (Hx)(t) \overline{(Hy)(t)} dt = T \int_{-\infty}^{\infty} x(Tt) \overline{y(Tt)} dt = T \int_{-\infty}^{\infty} \frac{x(s) \overline{y(s)}}{T} ds = \langle x, y \rangle \quad (10.120)$$

This completes the proof. ■

Now we can prove the result of Balian and Low for the orthonormal basis situation.

**Theorem (Balian–Low for Orthonormal Bases).** Let  $T\Omega = 2\pi$ , let  $w(t) \in L^2(\mathbb{R})$ , and let the collection of windowed Fourier atoms  $\{w_{m,n}(t): m, n \in \mathbb{Z}\}$  be given by (10.118). If  $\{w_{m,n}(t): m, n \in \mathbb{Z}\}$  is an orthonormal basis for  $L^2(\mathbb{R})$ , then either

(i)  $w(t)$  is not a window function:

$$\int_{-\infty}^{\infty} t^2 |w(t)|^2 dt = \|tw(t)\|_2^2 = \infty, \quad \text{or} \tag{10.121}$$

(ii)  $W(\omega)$  is not a window function:

$$\int_{-\infty}^{\infty} \omega^2 |W(\omega)|^2 d\omega = \|\omega W(\omega)\|_2^2 = \infty. \tag{10.122}$$

**Proof:** It is sufficient to prove the theorem for the special case  $T = 1$  and  $\Omega = 2\pi$ . We know from the lemma that the scaling map  $H(x(t)) = T^{1/2}x(Tt)$  is unitary on  $L^2(\mathbb{R})$ . If we examine its effect on atoms, we find

$$\begin{aligned} H(w_{m,n}(t)) &= \sqrt{T}w_{m,n}(Tt) = \sqrt{T}e^{jn\Omega Tt} w(Tt - mT) \\ &= e^{2\pi jnt} \sqrt{T}w(T(t - m)) = e^{2\pi jnt} (Hw)(t - m). \end{aligned} \tag{10.123}$$

The map  $H$  takes basis elements  $w_{m,n}(t)$  with time and frequency sampling intervals  $T$  and  $\Omega$ , respectively, to basis elements with corresponding sampling intervals 1 and  $2\pi$ . So it suffices to prove the theorem for this special case—that is, for the image of the set  $\{w_{m,n}(t): m, n \in \mathbb{Z}\}$  under  $H$ .

We note that the derivative  $w'(t) \in L^2(\mathbb{R})$  if and only if  $W(\omega)$  is a window function. We can check this relationship of differentiation to the window condition on  $W(\omega)$  as follows:

$$\|w'(t)\|_2^2 = \frac{1}{2\pi} \|\mathcal{F}w'\|_2^2 = \frac{1}{2\pi} \int_{-\infty}^{\infty} |j\omega W(\omega)|^2 d\omega = \frac{1}{2\pi} \int_{-\infty}^{\infty} \omega^2 |W(\omega)|^2 d\omega. \tag{10.124}$$

Let us assume that both  $w(t)$  and  $W(\omega)$  are window functions. From (10.124) this is equivalent to assuming that  $tw(t)$  and  $w'(t)$  are square-integrable. Our goal is to show that this leads to a contradiction.

From the assumption, we can calculate the pair of inner products  $\langle tw(t), -jw'(t) \rangle$  and  $\langle -jw'(t), tw(t) \rangle$ . Since  $\{w_{m,n}(t): m, n \in \mathbb{Z}\}$  is an orthonormal basis for  $L^2(\mathbb{R})$ , we can expand both inner products as follows:

$$\langle tw(t), -jw'(t) \rangle = \sum_{m,n \in \mathbb{Z}} \langle tw(t), w_{m,n}(t) \rangle \langle w_{m,n}(t), -jw'(t) \rangle, \tag{10.125a}$$

and

$$\langle -jw'(t), tw(t) \rangle = \sum_{m, n \in \mathbb{Z}} \langle -jw'(t), w_{m, n}(t) \rangle \langle w_{m, n}(t), tw(t) \rangle. \quad (10.125b)$$

Let us attend to the first inner product in the summations of (10.125a). We compute

$$\begin{aligned} \langle tw(t), w_{m, n}(t) \rangle &= \int_{-\infty}^{\infty} tw(t) e^{2\pi jnt} \overline{w(t-m)} dt \\ &= \int_{-\infty}^{\infty} (s+m)w(s+m) e^{-2\pi jns} \overline{w(s)} ds, \end{aligned} \quad (10.126)$$

where  $s = t - m$ . Since  $w_{-m, -n}(t) = \exp(-2\pi jnt)w(t+m)$ , we can write the final integral in (10.126) as a sum,

$$\langle tw(t), w_{m, n}(t) \rangle = \int_{-\infty}^{\infty} sw(s+m) e^{-2\pi jns} \overline{w(s)} ds + m \int_{-\infty}^{\infty} w_{-m, -n}(s) \overline{w(s)} ds. \quad (10.127)$$

The final term in (10.127) is zero. It is clearly so if  $m = 0$ , and if  $m \neq 0$ , then it is  $m \langle w_{-m, -n}(t), w(t) \rangle$ . But by the orthogonality of the  $\{w_{m, n}(t)\}$ , of which  $w_{0, 0}(t) = w(t)$ , we get  $\langle w_{-m, -n}(t), w(t) \rangle = 0$ . Thus,

$$\langle tw(t), w_{m, n}(t) \rangle = \int_{-\infty}^{\infty} sw(s+m) e^{-2\pi jns} \overline{w(s)} ds = \langle w_{-m, -n}(s), sw(s) \rangle. \quad (10.128)$$

Now we can rewrite the inner product (10.125a) like this:

$$\langle tw(t), -jw'(t) \rangle = \sum_{m, n \in \mathbb{Z}} \langle w_{-m, -n}(t), tw(t) \rangle \langle w_{m, n}(t), -jw'(t) \rangle. \quad (10.129)$$

Let us now divert our attention to the second inner product expansion (10.125b). We try the same strategy, expand the first inner product in the summation, and use the orthogonality of the  $\{w_{m, n}(t)\}$  to simplify.

$$\langle -jw'(t), w_{m, n}(t) \rangle = -j \int_{-\infty}^{\infty} w'(t) e^{-2\pi jnt} \overline{w(t-m)} dt. \quad (10.130)$$

Integration by parts gives

$$j \langle -jw'(t), w_{m, n}(t) \rangle = w(t) \overline{w(t-m)} e^{-2\pi jnt} \Big|_{-\infty}^{\infty} - I_1(m, n) + I_2(m, n), \quad (10.131)$$

where  $I_1(m, n)$  and  $I_2(m, n)$  are the integrals

$$I_1(m, n) = - \int_{-\infty}^{\infty} (e^{-2\pi jnt} w(t) \overline{w'(t-m)} dt) \tag{10.132a}$$

and

$$I_2(m, n) = 2\pi jn \int_{-\infty}^{\infty} (e^{-2\pi jnt} w(t) \overline{w(t-m)} dt). \tag{10.132b}$$

Since  $w(t) \in L^2(\mathbb{R})$ , the first term on the right-hand side of (10.131) must be zero. The second integral (10.132b) is zero also. To see this, note that

$$I_2(m, n) = 2\pi jn \int_{-\infty}^{\infty} \overline{w(t-m) e^{j2\pi nt}} w(t) dt = 2\pi n \langle w(t), w_{m,-n}(t) \rangle. \tag{10.133}$$

But the final term in (10.133) is zero; either  $n = 0$  or  $\langle w(t), w_{m,-n}(t) \rangle = 0$  by orthogonality of the  $\{w_{m,n}(t)\}$ . Thus,

$$\langle -jw'(t), w_{m,n}(t) \rangle = jI_1(m, n) = j \int_{-\infty}^{\infty} w(t) e^{-2\pi jnt} \overline{w'(t-m)} dt. \tag{10.134}$$

Letting  $s = t - m$  to change integration variables in (10.134) gives

$$\langle -jw'(t), w_{m,n}(t) \rangle = \int_{-\infty}^{\infty} w(s+m) e^{-2\pi jnt} \overline{[-jw'(s)]} ds = \langle w_{-m,-n}(t), -jw'(t) \rangle. \tag{10.135}$$

Thanks to this last result (10.135) we can rewrite the inner product (10.125b) as follows:

$$\langle -jw'(t), tw(t) \rangle = \sum_{m,n \in \mathbb{Z}} \langle w_{-m,-n}(t), -jw'(t) \rangle \langle w_{m,n}(t), tw(t) \rangle. \tag{10.136}$$

Reversing the order of summation in (10.136) produces

$$\langle -jw'(t), tw(t) \rangle = \sum_{m,n \in \mathbb{Z}} \langle w_{m,n}(t), -jw'(t) \rangle \langle w_{-m,-n}(t), tw(t) \rangle. \tag{10.137}$$

This is nothing else but the summation in (10.129); in other words, we have shown that  $tw(t)$  and  $-jw'(t)$  commute under the inner product relation:

$$\langle tw(t), -jw'(t) \rangle = \langle -jw'(t), tw(t) \rangle. \tag{10.138}$$

Contradiction looms. Indeed, computing the integral on the left-hand side of (10.138), we can integrate by parts to find

$$\int_{-\infty}^{\infty} tw(t)\overline{[-jw'(t)]}dt = jt\overline{w(t)w'(t)}\Big|_{-\infty}^{\infty} - j \int_{-\infty}^{\infty} \overline{w(t)}\{w(t) + tw'(t)\} dt. \quad (10.139)$$

Again,  $|w(t)|^2 \rightarrow 0$  as  $t \rightarrow \infty$ , because  $w(t) \in L^2(\mathbb{R})$ . This means

$$j\langle tw(t), -jw'(t) \rangle = \int_{-\infty}^{\infty} \overline{w(t)}w(t) dt - \int_{-\infty}^{\infty} \overline{tw(t)}w'(t) dt = \|w\|_2^2 + \langle -jw'(t), w(t) \rangle. \quad (10.140)$$

Of course,  $\|w\| = \|w_{0,0}\| = 1$  by orthogonality of  $\{w_{m,n}\}$ , and this contradicts (10.138). ■

To illustrate the Balian–Low theorem, we consider two examples of orthonormal bases for  $L^2(\mathbb{R})$ .

**Example (Fourier Basis).** For the first example, we try  $w(t) = u(t) - u(t-1)$ , where  $u(t)$  is the unit step signal, as the window function. Then the family  $\{w_{m,n}(t) = \exp(2\pi jnt)w(t-m): m, n \in \mathbb{Z}\}$  is an orthonormal basis for  $L^2(\mathbb{R})$ . In fact, for any fixed  $m_0 \in \mathbb{Z}$ , we can represent a general signal  $x(t)$  restricted to  $[m_0, m_0 + 1]$  by its Fourier series. And the collection of all such Fourier series suffices to construct  $x(t)$ . Orthogonality follows, of course, from the orthogonality of the exponentials on unit intervals. What does Balian–Low say? Either  $w(t)$  or its Fourier transform  $W(\omega)$  must not be a window function. Indeed the Fourier transform of  $w(t)$  is a sinc function, its Fourier transform decays like  $\omega^{-1}$ , and  $\|\omega W(\omega)\|_2 = \infty$ . So although  $w(t)$  is well-localized in time, it is poorly localized in frequency.

**Example (Shannon Basis).** This example takes the other extreme. We now let  $w(t) = \text{sinc}(\pi t) = (\pi t)^{-1} \sin(\pi t)$ . Then, once again,  $\{w_{m,n}(t) = \exp(2\pi jnt)w(t-m): m, n \in \mathbb{Z}\}$  is an orthonormal basis for  $L^2(\mathbb{R})$ . Although the Fourier transform of this signal is a window function, a square pulse, we now find  $tw(t) \notin L^2(\mathbb{R})$ .

We might yet hope to find an exact frame representation, having shown now that no orthonormal basis of Gabor elementary functions, or more general windowed Fourier atoms, can exist of the case of  $T\Omega = 2\pi$ . Orthonormality is, after all, an extremely strict constraint. And we understand that exact frames can support complete and stable signal representation for analysis purposes. Unfortunately, the looser requirement—that the windowed Fourier decomposition set should form an exact frame—is also impossible. The next section covers this more involved proof.

### 10.5.2 Frame Decomposition

The most elegant and accesible proof of the Balian–Low theorem for frames relies uses the notion of a signal’s Zak transform.

**10.5.2.1 Zak Transform Preliminaries.** Recall from Chapter 8 that the Zak transform maps an analog signal  $x(t)$  to a two-dimensional function having independent variables in both time and frequency. In this sense, it resembles the Gabor transform; however, it looks through no window function, and, much like the discrete-time Fourier transform, it is the limit of an infinite sum involving discrete samples of  $x(t)$ . With parameter  $a = 1$ , we define

$$(Zx)(s, \omega) = \sum_{k=-\infty}^{\infty} x(s-k)e^{2\pi j\omega k}. \tag{10.141}$$

The Zak transform’s properties make it a particularly effective tool for studying frames based on windowed Fourier atoms. Reviews concerning the Zak transform, frames, and windowed Fourier expansions include Refs. 41 and 42.

The Zak transform is a unitary map from  $L^2(\mathbb{R})$  to  $L^2(S)$ , where  $S$  is the unit square  $[0, 1] \times [0, 1]$ . The set of two-dimensional exponentials  $\{e_{m,n}(t) = \exp(2\pi jmt)\exp(2\pi jnt) : m, n \in \mathbb{Z}\}$  is a basis for  $L^2(S)$ . Because of this unitary map, the Zak transform converts questions about frames in  $L^2(\mathbb{R})$  into questions about frames in  $L^2(S)$ , where the answers are generally easier to find. The next proposition shows that Zak transforming a Gabor atom is equivalent to a modulation operation.

**Proposition (Modulation).** Let  $w(t) \in L^2(\mathbb{R})$ ; let  $w_{m,n}(t) = \exp(2\pi jnt)w(t - m)$  for  $m, n \in \mathbb{Z}$ ; and let  $Z: L^2(\mathbb{R}) \rightarrow L^2(S)$  be the Zak transform, where  $S$  is the unit square  $[0, 1] \times [0, 1]$ . Then

$$(Zw_{m,n})(s, \omega) = e^{2\pi jns} e^{-2\pi j\omega m} (Zw)(s, \omega). \tag{10.142}$$

**Proof:** We compute

$$\begin{aligned} (Zw_{m,n})(s, \omega) &= \sum_{k=-\infty}^{\infty} e^{2\pi j\omega k} e^{2\pi jns} e^{-2\pi jnk} w(s-k-m) \\ &= e^{2\pi jns} \sum_{k=-\infty}^{\infty} e^{2\pi j\omega k} w(s-k-m) \end{aligned} \tag{10.143}$$

and find

$$\begin{aligned} (Zw_{m,n})(s, \omega) &= e^{2\pi jns} e^{-2\pi j\omega m} \sum_{k=-\infty}^{\infty} e^{2\pi j\omega(k+m)} w(s-(k+m)) \\ &= (Zw)(s, \omega) e^{2\pi jns} e^{-2\pi j\omega m} \end{aligned} \tag{10.144}$$

as required. ■

**Proposition (Norms).** If  $w(t) \in L^2(\mathbb{R})$ ;  $w_{m,n}(t) = \exp(2\pi jnt)w(t - m)$  for  $m, n \in \mathbb{Z}$ ; and  $Z: L^2(\mathbb{R}) \rightarrow L^2(S)$  is the Zak transform, where  $S$  is the unit square  $[0, 1] \times [0, 1]$ , then

$$\sum_{m, n \in \mathbb{Z}} |\langle x, w_{m,n} \rangle|^2 = \|(Zx)(s, \omega)(Zw)(s, \omega)\|^2. \quad (10.145)$$

**Proof:** From the transform's unitary property and the previous proposition, the sum in (10.145) expands as follows:

$$\begin{aligned} \sum_{m, n \in \mathbb{Z}} |\langle x, w_{m,n} \rangle|^2 &= \sum_{m, n \in \mathbb{Z}} |\langle Zx, Zw_{m,n} \rangle|^2 \\ &= \sum_{m, n \in \mathbb{Z}} \left| \int_0^1 \int_0^1 e^{-2\pi jns} e^{2\pi j\omega m} (Zx)(s, \omega) \overline{(Zw)(s, \omega)} ds d\omega \right|^2. \end{aligned} \quad (10.146)$$

The two-dimensional exponentials are an orthonormal basis for  $L^2(S)$ . Hence, the Bessel relation for Hilbert spaces implies that the final sum in is in fact

$$\sum_{m, n \in \mathbb{Z}} |\langle x, w_{m,n} \rangle|^2 = \iint_{00}^{11} |(Zx)(s, \omega)|^2 |(Zw)(s, \omega)|^2 ds d\omega. \quad (10.147)$$

as desired. ■

The theorem below uses the ideas on Lebesgue measure and integration from Chapter 3.

**Theorem (Bounds).** Let  $w(t) \in L^2(\mathbb{R})$  and suppose  $\{w_{m,n}(t) = e^{2\pi jnt}w(t - m): m, n \in \mathbb{Z}\}$  is a frame, with lower and upper bounds  $A$  and  $B$ , respectively. Then for almost all  $s$  and  $\omega$  we have

$$A \leq |(Zw)(s, \omega)|^2 \leq B. \quad (10.148)$$

**Proof:** The frame property implies

$$0 < A\|x\|^2 \leq \sum_{m, n \in \mathbb{Z}} |\langle x, w_{m,n} \rangle|^2 \leq B\|x\|^2 < \infty \quad (10.149)$$

for any  $x(t) \in L^2(\mathbb{R})$ . By the previous proposition,

$$0 < A\|x\|^2 \leq \iint_{00}^{11} |(Zx)(s, \omega)|^2 |(Zw)(s, \omega)|^2 ds d\omega \leq B\|x\|^2 < \infty \quad (10.150)$$

must hold for all finite energy  $x(t)$  as well. We argue that this entails

$$0 < A \leq \int_0^1 \int |(\mathcal{Z}w)(s, \omega)|^2 ds d\omega \leq B < \infty. \tag{10.151}$$

To see this, let us suppose that, for example,  $|(\mathcal{Z}w)(s, \omega)|^2 < A$  on some subset  $R \subseteq S$  with positive measure:  $\mu(R) > 0$ . Let  $v(s, \omega)$  be the characteristic function on  $S$  and set  $y = \mathcal{Z}^{-1}v$ ; since  $\mathcal{Z}$  is unitary,  $\|y(t)\|^2 = \|v(s, \omega)\|^2 = \mu(R)$ . Consequently,

$$\begin{aligned} A\mu(R) &= A\|y\|^2 < \int_0^1 \int |(\mathcal{Z}y)(s, \omega)|^2 |(\mathcal{Z}w)(s, \omega)|^2 ds d\omega \\ &= \int_0^1 \int |v(s, \omega)|^2 |(\mathcal{Z}w)(s, \omega)|^2 ds d\omega. \end{aligned} \tag{10.152}$$

Now, because  $v(s, \omega) = 1$  on  $R \subseteq S$  and  $v(s, \omega) = 0$  otherwise, this last integral becomes

$$\int_0^1 \int |v(s, \omega)|^2 |(\mathcal{Z}w)(s, \omega)|^2 ds d\omega = \int_R |(\mathcal{Z}w)(s, \omega)|^2 ds d\omega < \int_R A ds d\omega = A\mu(R). \tag{10.153}$$

Together, (10.152) and (10.153) produce a contradiction. By a similar argument, so does the assumption  $B < |(\mathcal{Z}w)(s, \omega)|^2$ . Showing this last step is left as an exercise, which finishes the proof. ■

The next two propositions characterize time- and frequency-domain window functions as having differentiable derivatives of their Zak transforms.

**Lemma (Window Function).** If  $x(t) \in L^2(\mathbb{R})$ , and  $x(t)$  is a window function, then

$$\mathcal{Z}(tx(t))(s, \omega) = s(\mathcal{Z}x)(s, \omega) + \frac{j}{2\pi} \left[ \frac{\partial}{\partial \omega} (\mathcal{Z}x)(s, \omega) \right]. \tag{10.154}$$

**Proof:** Applying the Zak transform (10.141) to  $y(t) = tx(t)$ , this is straightforward:

$$\begin{aligned} (\mathcal{Z}y)(s, \omega) &= \sum_{k=-\infty}^{\infty} (s-k)x(s-k)e^{2\pi j\omega k} \\ &= s \sum_{k=-\infty}^{\infty} x(s-k)e^{2\pi j\omega k} - \sum_{k=-\infty}^{\infty} kx(s-k)e^{2\pi j\omega k}. \end{aligned} \tag{10.155}$$

The first summation on the bottom of (10.155) is  $s(Zx)(s, \omega)$ . Partial differentiation of  $(Zx)(s, \omega)$  with respect to  $\omega$  gives

$$\frac{\partial}{\partial \omega}(Zx)(s, \omega) = \sum_{k=-\infty}^{\infty} 2\pi j k e^{2\pi j k \omega} x(s-k), \quad (10.156)$$

and algebraic manipulation accounts for the second summation in (10.155). ■

**Proposition (Window Function Characterization).** Let  $x(t) \in L^2(\mathbb{R})$  and  $Z$  be the Zak transform  $Z: L^2(\mathbb{R}) \rightarrow L^2(S)$ , where  $S$  is the unit square  $[0, 1] \times [0, 1]$ . Then  $x(t)$  is a window function if and only if

$$\frac{\partial}{\partial \omega}(Zx)(s, \omega) \in L^2[S]. \quad (10.157)$$

**Proof:** If  $x(t)$  is a window function, then the Window Function Lemma applies and (10.154) holds. Since  $s(Zx)(s, \omega) \in L^2(\mathbb{R})$ , necessarily (10.157) holds. Conversely, suppose (10.157). Because both of the final two sums in (10.155) are in  $L^2(S)$ , so is their sum. Following equalities backwards in (10.155), we thereby find that

$$\sum_{k=-\infty}^{\infty} (s-k)x(s-k)e^{2\pi j \omega k} \in L^2(S). \quad (10.158)$$

But (10.158) is none other than the Zak transform expansion for  $tx(t)$ . Thus,  $x(t)$  is a window function. ■

**Lemma (Derivative).** If  $x(t), x'(t) \in L^2(\mathbb{R})$ , then

$$Z(x'(t))(s, \omega) = \frac{\partial}{\partial s}(Zx)(s, \omega). \quad (10.159)$$

**Proof:** By differentiating the Zak transform sum (exercise). ■

**Proposition (Derivative Characterization).** Let  $x(t) \in L^2(\mathbb{R})$ , let  $X(\omega)$  be its radial Fourier transform, and let  $Z$  be the Zak transform  $Z: L^2(\mathbb{R}) \rightarrow L^2(S)$ , where  $S$  is the unit square  $[0, 1] \times [0, 1]$ . Then  $X(\omega)$  is a window function if and only if

$$\frac{\partial}{\partial s}(Zx)(s, \omega) \in L^2[S]. \quad (10.160)$$

**Proof:** The Fourier transform of  $x'(t)$  is  $j\omega X(\omega)$ , so  $x'(t) \in L^2(\mathbb{R})$  if and only if  $\omega X(\omega) \in L^2(\mathbb{R})$ ; that is,  $X(\omega)$  is a window function. Invoking the Derivative Lemma completes the proof (exercise). ■

The proof of the general Balian–Low theorem for frames uses the above Zak transform properties. The bounds theorem, however, implies a weaker version of the theorem, recapitulated from Ref. 13, where it is attributed to Yves Meyer.

**Theorem (Meyer).** Let  $w: \mathbb{R} \rightarrow \mathbb{R}$  be continuous and suppose there are  $\varepsilon > 0$  and  $C > 0$  such that

$$|w(t)| \leq \frac{C}{(1 + |t|)^{1+\varepsilon}}. \tag{10.161}$$

Then  $\{w_{m,n}(t) = e^{2\pi jnt}w(t - m): m, n \in \mathbb{Z}\}$  cannot be a frame.

**Proof:** Since  $|w(t)|$  is dominated by  $C(1 + |t|)^{-1-\varepsilon}$ , its Zak transform sum converges. Moreover, it must converge to a continuous function in  $L^2(S)$ , where  $S$  is the unit square  $[0, 1] \times [0, 1]$ . For the sake of contradiction, now suppose that  $\{w_{m,n}(t) = e^{2\pi jnt}w(t - m): m, n \in \mathbb{Z}\}$  constitute an  $L^2(\mathbb{R})$  frame with lower and upper bounds  $A$  and  $B$ , respectively. Since  $w(t)$  has a Zak transform, the bounds theorem (10.148) entails  $0 < A \leq |(Zw)(s, \omega)|$  for almost all  $(s, \omega) \in S$ . But  $(Zw)(s, \omega)$  is continuous, and therefore  $|(Zw)(s, \omega)| \neq 0$  for all  $(s, \omega) \in S$ .

The trick is to define, for each  $s \in [0, 1]$ , the curve,  $\zeta_s: [0, 1] \rightarrow \mathbb{C}$ :

$$\zeta_s(\omega) = \frac{(Zw)(s, \omega)}{(Zw)(0, \omega)}. \tag{10.162}$$

Note that  $\zeta_0(\omega) = 1$ . Since  $(Zw)(s + 1, \omega) = e^{2\pi j\omega}(Zw)(s, \omega)$ , it follows as well that  $\zeta_1(\omega) = e^{2\pi j\omega}$  for all  $\omega \in [0, 1]$ . But we cannot continuously map the horizontal line segment defined by  $\zeta_0(\omega)$  to the unit circle defined by  $\zeta_1(\omega)$  unless at some  $r \in (0, 1)$  and some  $\omega_0 \in [0, 1]$  we have  $\zeta_r(\omega_0) = 0$ . But then  $(Zw)(r, \omega_0) = 0$ , which contradicts the fact that  $(Zw)(s, \omega) \neq 0$  for all  $(s, \omega) \in S$ . Indeed,  $\{w_{m,n}(t): m, n \in \mathbb{Z}\}$  cannot be a frame. ■

The next section proves the general Balian–Low theorem. We have already shown the result for orthonormal bases and for frames deriving from continuous window functions with a sufficient decay rate. In the general theorem, the window function assumption is much weaker: the windowing function  $w(t)$  of  $\{w_{m,n}(t): m, n \in \mathbb{Z}\}$  need only have finite energy.

**10.5.2.2 General Balian–Low Theorem.** The idea of a frame generalizes the notion of an orthonormal basis. We introduced frames along with the theory of Hilbert spaces of analog signals in Section 3.3.4. Signal analysis using atomic signal models is possible with frames in the sense that such a decomposition:

- Uniquely represents candidate signals;
- Reconstructs a candidate signal in a numerically stable way from its decomposition coefficients.

Frame theory has classic beginnings—Ref. 43–45, for example—and numerous recent texts and papers cover its relationship to mixed-domain signal analysis [27, 42, 46].

We begin with two lemmas on applying the Zak transform to dual frame elements. Recall from basic frame theory (Section 3.3.4.3) that if  $F = \{f_n(t): m, n \in \mathbb{Z}\}$  is a frame in a Hilbert space  $H$ , then the associated *frame operator*  $\mathcal{T}: H \rightarrow l^2(\mathbb{Z})$  is defined by

$$\mathcal{T}(x)(n) = \langle x, f_n \rangle. \quad (10.163)$$

Frame operator  $\mathcal{T}$  is linear; it is bounded; and, in particular, if  $B$  is the upper frame bound, then  $\|\mathcal{T}(x)\|^2 \leq B\|x\|^2$ . Associated to  $\mathcal{T}$  is the operator  $S: l^2(\mathbb{Z}) \rightarrow H$  defined for  $y(n) \in l^2(\mathbb{Z})$  by

$$S(y) = \sum_{n=-\infty}^{\infty} y(n)f_n. \quad (10.164)$$

In fact, we showed that  $S$  is the Hilbert space *adjoint operator* of  $\mathcal{T}$ :  $S = \mathcal{T}^*$ . The composition  $\mathcal{T}^*\mathcal{T}$  happens to be an invertible map  $\mathcal{T}^*\mathcal{T}: L^2(\mathbb{R}) \rightarrow L^2(\mathbb{R})$  given by

$$(\mathcal{T}^*\mathcal{T})(x) = \sum_{n=-\infty}^{\infty} \langle x, f_n \rangle f_n. \quad (10.165)$$

We can thus define the *dual frame* to  $F$  by applying the inverse of  $\mathcal{T}^*\mathcal{T}$  to frame elements:

$$\tilde{F} = \left\{ (\mathcal{T}^*\mathcal{T})^{-1}(f_n) \right\}_{n \in \mathbb{Z}}. \quad (10.166)$$

The dual frame idea is key in signal analysis applications. If the dual frame elements are given by  $\tilde{f}_n = (\mathcal{T}^*\mathcal{T})^{-1}f_n$ , then we have a reconstruction formula for  $x(t)$  from both frame and dual frame elements:

$$x(t) = \sum_{n=-\infty}^{\infty} \langle x(t), f_n(t) \rangle \tilde{f}_n(t) \quad (10.167a)$$

and

$$x(t) = \sum_{n=-\infty}^{\infty} \langle x(t), \tilde{f}_n(t) \rangle f_n(t). \quad (10.167b)$$

If  $x(t), y(t) \in H$ , then these formulas imply

$$\langle x(t), y(t) \rangle = \sum_{n=-\infty}^{\infty} \langle x(t), f_n(t) \rangle \langle \tilde{f}_n(t), y(t) \rangle \quad (10.168a)$$

and

$$\langle x(t), y(t) \rangle = \sum_{n=-\infty}^{\infty} \langle x(t), \tilde{f}_n(t) \rangle \langle f_n(t), y(t) \rangle. \tag{10.168b}$$

Our theory now combines frame and Zak transform concepts. We are also exploiting several different Hilbert spaces:  $L^2(\mathbb{R})$ ,  $L^2([0, 1] \times [0, 1])$ , and  $l^2(\mathbb{Z})$ . Note that although we have formulated these properties for frame elements indexed by a single integral variable, we can specify a one-to-one correspondence between integers and their pairs,  $k \leftrightarrow (m, n)$ . Our families of windowed Fourier atoms  $\{w_{m,n}(t): m, n \in \mathbb{Z}\}$  are doubly indexed, and we thus rewrite (10.163) through (10.166) accordingly. The next lemma shows the relationship between the Zak transform and the frame operator.

**Lemma.** Let  $w(t) \in L^2(\mathbb{R})$ ; let  $F = \{w_{m,n}(t) = \exp(2\pi jnt)w(t - m): m, n \in \mathbb{Z}\}$  be a frame; let  $\mathcal{T}$  be the associated frame operator; and let  $Z: L^2(\mathbb{R}) \rightarrow L^2(S)$  be the Zak transform, where  $S$  is the unit square  $[0, 1] \times [0, 1]$ . If  $x \in L^2(\mathbb{R})$  and  $Zx = y \in L^2(S)$ , then  $[Z(\mathcal{T}^*\mathcal{T})Z^{-1}]y = |Zw|^2y$ .

**Proof:** We have  $[Z(\mathcal{T}^*\mathcal{T})Z^{-1}]y = [Z(\mathcal{T}^*\mathcal{T})]x$ . Since  $(\mathcal{T}^*\mathcal{T})x = \sum \langle x, w_{m,n} \rangle w_{m,n}$ , we have

$$[Z(\mathcal{T}^*\mathcal{T})Z^{-1}]y = \sum_{m,n \in \mathbb{Z}} \langle x, w_{m,n} \rangle Z w_{m,n} = \sum_{m,n \in \mathbb{Z}} \langle Zx, Z w_{m,n} \rangle Z w_{m,n}. \tag{10.169}$$

But

$$\sum \langle Zx, Z w_{m,n} \rangle Z w_{m,n} = \sum \langle y, e^{2\pi jns} e^{-2\pi j\omega m} Z w \rangle e^{2\pi jns} e^{-2\pi j\omega m} Z w, \tag{10.170}$$

by the Modulation Proposition in the previous section. Manipulating the inner product on the right-hand side of (10.170) gives

$$\sum \langle Zx, Z w_{m,n} \rangle Z w_{m,n} = \sum \langle y \bar{Z} w Z w, e^{2\pi jns} e^{-2\pi j\omega m} \rangle e^{2\pi jns} e^{-2\pi j\omega m}. \tag{10.171}$$

Now,  $\bar{Z} w Z w = |Zw|^2$ , and since the two-dimensional exponentials  $e^{2\pi jns} e^{-2\pi j\omega m}$  are an orthonormal basis for  $L^2(S)$ , the last expression is precisely  $|Zw|^2y$ . ■

**Lemma (Dual Frame).** Let  $w(t) \in L^2(\mathbb{R})$ , let  $F = \{w_{m,n}(t) = e^{2\pi jnt}w(t - m): m, n \in \mathbb{Z}\}$  be a frame, and let  $\mathcal{T}$  be the frame operator on  $F$ . Further, let

$$\tilde{w}_{m,n} = (\mathcal{T}^*\mathcal{T})^{-1} w_{m,n} \tag{10.172}$$

be the dual frame elements for  $F$  and  $Z: L^2(\mathbb{R}) \rightarrow L^2(S)$  be the Zak transform, where  $S$  is the unit square  $[0, 1] \times [0, 1]$ . Then

$$(Z\tilde{w}_{m,n})(s, \omega) = \frac{(Zw_{m,n})(s, \omega)}{|(Zw)(s, \omega)|^2} = \frac{e^{2\pi jns} e^{-2\pi j\omega m}}{(Zw)(s, \omega)}. \quad (10.173)$$

**Proof:** By the previous lemma, if  $Zw_{m,n} = y \in L^2(S)$ , then  $[Z(\mathcal{T}^*\mathcal{T})Z^{-1}]y = |Zw|^2 y$ . By definition of the dual frame,  $\tilde{w}_{m,n} = (\mathcal{T}^*\mathcal{T})^{-1}w_{m,n}$ . Fiddling with operators shows

$$Z\tilde{w}_{m,n} = Z(\mathcal{T}^*\mathcal{T})^{-1}w_{m,n} = Z(\mathcal{T}^*\mathcal{T})^{-1}Z^{-1}y = |Zw|^2 y = |Zw|^2 Zw_{m,n}. \quad (10.174)$$

The Bounds Theorem justifies division by  $|Zw|^2$  in (10.174), and (10.173) follows from the Modulation Proposition. ■

These tools allow us to extend the Balian–Low theorem to frames.

**Theorem (Balian–Low for Frames).** Let  $T\Omega = 2\pi$ ,  $w(t) \in L^2(\mathbb{R})$ , and let  $W = \mathcal{F}w$  be the Fourier transform of  $w$ . If the collection of windowed Fourier atoms  $F = \{w_{m,n}(t) = e^{\Omega jnt} w(t - mT) : m, n \in \mathbb{Z}\}$  is a frame, then—once again—either

(i)  $w(t)$  is not a window function:

$$\int_{-\infty}^{\infty} t^2 |w(t)|^2 dt = \|tw(t)\|_2^2 = \infty, \quad \text{or} \quad (10.175)$$

(ii)  $W(\omega)$  is not a window function:

$$\int_{-\infty}^{\infty} \omega^2 |W(\omega)|^2 d\omega = \|\omega W(\omega)\|_2^2 = \infty. \quad (10.176)$$

**Proof:** By a scaling argument, such as we used in proving the theorem for orthonormal bases in Section 10.6.1, it suffices to prove the theorem for  $T = 1$  and  $\Omega = 2\pi$ . Let us suppose that both  $tw(t)$  and  $\omega W(\omega)$  are square-integrable and seek a contradiction.

Let  $Z : L^2(\mathbb{R}) \rightarrow L^2(S)$  be the Zak transform, where  $S = [0, 1] \times [0, 1]$ , and  $\tilde{w} = (\mathcal{T}^*\mathcal{T})^{-1}w$ , where  $\mathcal{T}$  is the frame operator for  $F$ . We claim that

$$t\tilde{w}(t) \in L^2(\mathbb{R}) \quad (10.177a)$$

and

$$\frac{d}{dt}\tilde{w}(t) \in L^2(\mathbb{R}). \quad (10.177b)$$

Indeed, from the assumption that  $tw(t) \in L^2(\mathbb{R})$ , the Window Function Characterization Proposition (10.157) implies  $\frac{\partial}{\partial \omega}(Zw)(s, \omega) \in L^2[S]$ . Likewise, supposing  $\omega W(\omega) \in L^2(\mathbb{R})$  gives  $\frac{\partial}{\partial s}(Zw)(s, \omega) \in L^2[S]$  via the Derivative Characterization Proposition. But extracting derivatives is straightforward using the Dual Frame Lemma (10.173) with  $m = n = 0$ . Thus,  $w_{m,n}(t) = w(t)$ , and we calculate

$$\frac{\partial}{\partial s}(Z\tilde{w})(s, \omega) = \frac{\partial}{\partial s} \frac{(Zw)(s, \omega)}{|(Zw)(s, \omega)|^2} = \frac{\partial}{\partial s} \frac{1}{(Zw)(s, \omega)} = \frac{-\frac{\partial}{\partial s}(Zw)(s, \omega)}{(Zw)(s, \omega)^2} \tag{10.178a}$$

and

$$\frac{\partial}{\partial \omega}(Z\tilde{w})(s, \omega) = \frac{\partial}{\partial \omega} \frac{(Zw)(s, \omega)}{|(Zw)(s, \omega)|^2} = \frac{\partial}{\partial \omega} \frac{1}{(Zw)(s, \omega)} = \frac{-\frac{\partial}{\partial s}(Zw)(s, \omega)}{(Zw)(s, \omega)^2}. \tag{10.178b}$$

Denominators are nonzero almost everywhere in (10.178a) and (10.178b) by the Bounds Theorem on the Zak transform. That is, the expressions on the right-hand sides of (10.178a) and (10.178b) are in  $L^2(S)$ . Hence the partial derivatives  $\frac{\partial}{\partial s}(Z\tilde{w})(s, \omega)$  and  $\frac{\partial}{\partial \omega}(Z\tilde{w})(s, \omega)$  are in  $L^2(S)$ . Hence  $t\tilde{w}(t) \in L^2(\mathbb{R})$  and  $\tilde{w}'(t) \in L^2(\mathbb{R})$  by the Window Function and Derivative Characterization Propositions, respectively.

Now—working toward a contradiction along the same lines we used for the case of orthonormal bases—we claim that

$$\langle \tilde{w}, w_{m,n} \rangle = \langle w, \tilde{w}_{m,n} \rangle = \begin{cases} 1 & \text{if } m = n = 0 \\ 0 & \text{otherwise.} \end{cases} \tag{10.179}$$

To justify the claim, we apply the unitary Zak transform to the inner products of (10.179) and use (10.173) once more:

$$\begin{aligned} \langle w, \tilde{w}_{m,n} \rangle &= \langle Zw, Z\tilde{w}_{m,n} \rangle = \int\int_{00}^{11} (Zw)(s, \omega) \overline{(Z\tilde{w}_{m,n})(s, \omega)} \, dsd\omega \\ &= \int\int_{00}^{11} (Zw)(s, \omega) \frac{e^{-2\pi jns} e^{2\pi j\omega m}}{(Zw)(s, \omega)} \, dsd\omega. \end{aligned} \tag{10.180}$$

Consequently,

$$\langle w, \tilde{w}_{m,n} \rangle = \int\int_{00}^{11} e^{-2\pi jns} e^{2\pi j\omega m} \, dsd\omega, \tag{10.181}$$

which will be unity when  $m = n = 0$  and zero otherwise by the orthogonality of the dual exponentials on the unit square. Showing the same result for  $\langle \tilde{w}, w_{m,n} \rangle$  is left as an exercise.

Our next claim is that

$$\langle tw(t), \tilde{w}'(t) \rangle = -\langle w'(t), t\tilde{w}(t) \rangle. \quad (10.182)$$

Recalling the reconstruction formula for frames (10.167a) and (10.167b), we write

$$\langle tw(t), \tilde{w}'(t) \rangle = \sum_{m,n=-\infty}^{\infty} \langle tw(t), \tilde{w}_{m,n}(t) \rangle \langle w_{m,n}(t), \tilde{w}'(t) \rangle \quad (10.183)$$

and work on inner products within the sum. We compute the first by expanding the inner product integral and using (10.179) (exercise):

$$\langle tw(t), \tilde{w}_{m,n}(t) \rangle = \langle w_{-m,-n}(t), t\tilde{w}(t) \rangle. \quad (10.184)$$

The second inner product in the sum of (10.183) involves integration by parts, and here the proof has much of the uncertainty principle's flavor.

$$\langle w_{m,n}(t), \tilde{w}'(t) \rangle = \int_{-\infty}^{\infty} e^{2\pi jnt} w(t-m) \overline{\tilde{w}'(t)} dt. \quad (10.185)$$

It follows, upon integrating by parts, that

$$\begin{aligned} \langle w_{m,n}(t), \tilde{w}'(t) \rangle &= e^{2\pi jnt} w(t-m) \overline{\tilde{w}(t)} \Big|_{-\infty}^{\infty} - \int_{-\infty}^{\infty} e^{2\pi jnt} w'(t-m) \overline{\tilde{w}(t)} dt \\ &\quad - \int_{-\infty}^{\infty} 2\pi jn e^{2\pi jnt} w(t-m) \overline{\tilde{w}(t)} dt. \end{aligned} \quad (10.186)$$

The first term on the right-hand side of (10.186) is zero. The inner product in the third term,  $2\pi jn \langle w_{m,n}(t), \tilde{w}(t) \rangle$ , is zero unless  $m = n = 0$ , as we proved above, and, thanks to the  $2\pi jn$  factor, the entire term is necessarily zero. Changing the integration variable in the remaining term produces

$$\langle w_{m,n}(t), \tilde{w}'(t) \rangle = - \int_{-\infty}^{\infty} e^{2\pi jnt} w'(t-m) \overline{\tilde{w}(t)} dt = -\langle w'(t), \tilde{w}_{-m,-n}(t) \rangle. \quad (10.187)$$

Substituting (10.184) and (10.187) into (10.183) and reversing the summation, we discover

$$\langle tw(t), \tilde{w}'(t) \rangle = - \sum_{m,n=-\infty}^{\infty} \langle w'(t), \tilde{w}_{m,n}(t) \rangle \langle w_{m,n}(t), t\tilde{w}(t) \rangle = -\langle w'(t), t\tilde{w}(t) \rangle. \quad (10.188)$$

Is this last equality plausible? We claim that it is not, that it leads to a contradiction, and that, therefore, our assumption that  $w(t)$  and  $W(\omega)$  are both window functions is false. To verify this final claim, let us work the integration by parts on the inner product on the left-hand side of (10.188):

$$\langle tw(t), \tilde{w}'(t) \rangle = \int_{-\infty}^{\infty} tw(t) \overline{\tilde{w}'(t)} dt = - \int_{-\infty}^{\infty} w(t) \overline{\tilde{w}(t)} dt - \int_{-\infty}^{\infty} w'(t) \overline{t\tilde{w}(t)} dt. \quad (10.189)$$

The integrals on the right-hand side of (10.189) are inner products, so that

$$\langle tw(t), \tilde{w}'(t) \rangle = - \langle w(t), \tilde{w}(t) \rangle - \langle w'(t), t\tilde{w}(t) \rangle. \quad (10.190)$$

But we know  $\langle tw(t), \tilde{w}'(t) \rangle = - \langle w'(t), t\tilde{w}(t) \rangle$  by (10.188) and  $\langle w(t), \tilde{w}(t) \rangle = 1$  by (10.179). This exposes the contradiction and finishes the proof. ■

*Remark.* Integration by parts for  $x, y \in L^2(\mathbb{R})$ ,  $\int x'y = xy| - \int xy'$ , generally presupposes that  $x'y, xy' \in L^1(\mathbb{R})$ . Using a limit argument, however, we can make only the additional assumptions that the derivatives  $x'$  and  $y'$  are square-integrable [12, 13]. We can specify  $x_n \rightarrow x$  and  $y_n \rightarrow y$ , where  $\{x_n\}$  and  $\{y_n\}$  are Schwarz space elements, for example.

### 10.5.3 Avoiding the Balian–Low Trap

Let us add a final footnote to the saga of Gabor's problem. It is possible to escape the negative conclusion of the Balian–Low theorem only by giving up on some of its suppositions. One of these suppositions is the exponential term in the windowed Fourier atoms. This is something that probably seems quite natural given all the work we have done with signal transforms with the complex exponential at their heart. The idea is to extract orthonormal bases with good time-frequency localization by using *sines and cosines* instead [12].

## 10.6 SUMMARY

The Gabor transform is the most accessible mixed-domain transform tool. It is a representative of a broader class of short-time (or windowed) Fourier transforms (STFT). These transforms invoke a tiling of the time-frequency plane with regions of equal size. The Gabor transform tiles have the minimal area. Tilings of the time-frequency plane are a powerful technique for discovering signal structure, and, developing wavelet theory in the next chapter, we will explore the concept further. In point of fact, equally sized tiles can be a difficulty when analyzing signals that contain feature of different extents and transients; the wavelet transform has time-frequency tiles of varying size, and it was first developed as a transient-capable alternative to the Gabor transform.

Thus, there are some practical and theoretical limitations to the Gabor transform and the STFT in general:

- The size of the signal structures that must be analyzed becomes problematic when the time-domain window has already been fixed for the transform analysis.
- Computationally, the method does not support frames based on windowed Fourier atoms unless the time-frequency density is sufficiently dense.

Natural and synthetic signals have time-limited frequency components. One of the important observations from Chapter 9's study of frequency-domain signal analysis is that standard Fourier transform tools sometimes do a poor job of identifying these localized oscillations. Our principal approach was to trim the source signal  $x(t)$  with a symmetric, decaying window function. This technique time-limits, or windows, a signal before calculating its spectrum. There are many variants, depending on the window's shape. Windowing furnishes better estimates of a signal's spectrum, because it restricts the signal values to those over which the relevant oscillatory waveform features should appear.

The short-time Fourier transform extends this idea of signal windowing to a full transform. It lays out the frequency content of a signal according to the time that the oscillatory components appear. Discretized, the windowed Fourier transform presents a complete structural description of a signal. In Chapters 4 and 9, such constructions were at best ad hoc. Now we can produce a full graphical representation of signal frequency components and the time of their occurrence. Moreover, a rich mathematical theory supports the application of this structural tool.

Of the many feasible window shapes upon which we can found a time-limited Fourier transformation, the one which uses a Gaussian window is the Gabor transform. It is the most natural of the various STFTs, and we introduced it to lead off the chapter. The Gabor transform's Gaussian window function has optimal time and frequency locality—a result of the classic Heisenberg Uncertainty Principle.

Applications generally use the squared norm of the transformed signal, called the spectrogram. We discovered, moreover, that spectrogram performance is satisfactory for many signal analysis tasks. In particular, it has seen wide and largely successful application in speech recognition. It has been the basis for many applications that need time-limited descriptions of signal spectra. The spectrogram of the signal  $x(t)$  relative to the window function  $w(t)$  is the squared magnitude of the Fourier transform of the product:  $|\mathcal{F}[s(t)]|^2 = |\mathcal{F}[x(t)w(t)]|^2$ . This is a non-negative real value. Applications can therefore compare or threshold spectrogram values in order to decide whether one frequency is more significant than another or whether an individual frequency is significant, respectively. With the spectrogram, of course, the application design may need to search through possible time locations as well as through possible frequency ranges when seeking local spectral components. That is, Fourier applications tend to be one-dimensional, in contrast to short-time Fourier applications, which are inherently two-dimensional in nature.

Virtuous in their locality, short-time Fourier transform methods improve upon the necessarily global Fourier transform, but they are not without their problems. The previous chapter found the spectrogram adequate for many important signal analysis tasks. It can perform poorly, however, when signals contain sharply varying frequencies, such as chirps, transients, or unconstrained frequency modulation. This behavior is mitigated in the short-time Fourier transform, but not completely removed. There is still the problem of selecting a window for the transform operation. And there is the fundamental limitation for discrete methods that the Balian-Low theorem enforces. Since their critically sampled collections cannot be frames, and hence cannot provide stable signal reconstruction, we are led to hope that the signal universe is made up of more than just windowed Fourier atoms.

### 10.6.1 Historical Notes

A recent history of time-frequency analysis by one of the principal contributors to the discipline, L. Cohen, is Ref. 47. It includes an extensive bibliography.

The original time-frequency signal analysis technique is the Wigner–Ville distribution. E. Wigner proposed it for application to quantum mechanics [28]. J. Ville used it to explicate the notion of instantaneous frequency for communication theory purposes [29]. The WVD does not rely on a separate window function for generating the transform, using instead a bilinear term involving the original signal. This independence from window selection is at once its strength and weakness. The WVD and its more modern variants have been widely studied and are quite powerful; under certain conditions these transforms are optimal detectors for frequency-modulated signals [48]. It has been used as the cornerstone of a complete approach to biological and computer vision, for example [32].

The WVD has come under critical scrutiny because of the problematic cross-terms that the transform produces [7]. Some conferences have witnessed spirited debates over this transform’s strengths and weaknesses. There are a variety of approaches for reducing cross-term effects, and a number of researchers were already investigating them in the early 1980s. The main line of attack was given by P. Flandrin in 1984 [49].

The general theory of quadratic kernel-based transforms is due to L. Cohen [35]. He introduced the *Cohen class* of distributions for applications in quantum mechanics—an area that has stimulated many original contributions to time-frequency signal theory. Later, Wigner published the result that quadratic time-frequency representations, such as his namesake distribution, cannot be simultaneously non-negative and obey the Marginal Conditions.

The Gabor transform is the most easily accessible time-frequency transform, and this is due to the analytic tractability of the Gaussian window function. Gabor’s 1946 paper studied sets of signal atoms—Gabor elementary functions—with optimal joint resolution in the time and frequency domains. Gabor applied the theory to acoustics [19] and communication theory [1]. Gabor’s conjecture—that optimally localized time-frequency atoms of spatial and spectral sampling intervals satisfying  $T\Omega = 2\pi$  could be a foundation for signal analysis—was seriously

undermined by the Balian–Low theorem. Such windowed Fourier atoms cannot comprise a frame; their signal reconstruction behavior is therefore unstable. Nevertheless, Gabor methods remain the mostly widely applied time-frequency transform.

Researchers in diverse areas—communications theory, speech recognition, seismic signal interpretation, image analysis, and vision research—have had a keen interest in the Gabor transform for many years. One surprise, in fact, issued from investigations into the behavior of neurons in the visual cortex of animals. Research showed that individual neurons respond to certain visual stimuli in ways that resemble the shapes of the real and imaginary parts of GEFs. Chapter 12 outlines these discoveries and provide references to the literature.

We now know from frame theory, largely developed by I. Daubechies and her coworkers [12, 25, 27] that frames of windowed Fourier atoms are possible for sufficiently dense time-frequency samplings. For many years, investigators pondered how to expand a signal with elementary functions based on a particular window function, such as the Gaussian. Sparse samplings preclude windowed Fourier frames, and at the Nyquist density they are only possible given poor time-frequency localization. Therefore, decomposing signals with windowed Fourier atoms was a major problem. The first solution was in fact given many years after Gabor’s paper, by M. Bastianns [50, 51] using the Zak transform. Another strategy for finding expansion coefficients relied upon a neural network for their approximation [52]. Only recently have efficient algorithms for calculating the decomposition coefficients been disclosed [53].

The correct proof of the Balian–Low theorem eluded researchers for a number of years. The result was given independently by Balian [37] and Low [38]. Their proofs both contained the same technical gap, which was corrected several years later for the specific case of orthonormal bases [39] and later extended to frames [25, 40]. It is a hard-won result. Further research in this area produced a workaround for the Balian–Low theorem: Use sinusoids instead of exponentials for the atomic decomposition! Some examples of this approach are [54, 55].

## 10.6.2 Resources

Readers will find the following resources handy for working with time-frequency transforms:

- The Matlab and Mathematica commercial software packages, which we have used to generate many of the figures.
- The Time-Frequency ToolBox (TFTB), available over the web from CNRS in France; this public-domain software package, based on Matlab, contains a variety of tools for performing STFT, WVD, and other time-frequency signal transforms. We have used it for replicating the WVD analysis of the speech sample “Gabor.”
- The small, but very educational, demonstration tool bundled with the treatise [8], the Joint Time-Frequency Analysis (JTFA) package. We have used JTFA to illustrate a number of STFT and WVD concepts in this chapter.

### 10.6.3 Looking Forward

Time-frequency transforms are problematic in certain applications, especially those with transients or local frequency information that defies any *a priori* demarcation of its frequency- and time-domain boundaries. Quadratic methods have better spectral resolution, but interference terms are sometimes hard to overcome. Finally, the Balian–Low theorem enforces a fundamental limitation on the joint time-frequency resolution capability of the windowed Fourier transforms.

This situation led to the discovery of another mixed-domain signal analysis tool—the wavelet transform, one of the great discoveries of mathematical analysis in the twentieth century. As we have already indicated, the wavelet transform uses a signal scale variable instead of a frequency variable in its transform relation. This renders it better able to handle transient signal behavior, without completely giving up frequency selectivity. Readers seeking a popular introduction to wavelet theory, a review of the basic equations, and fascinating historical background will find Ref. 56 useful. A more mathematical treatment focusing on applications is Ref. 57. The next chapter introduces wavelets, and the final chapter covers both time-frequency and time-scale applications.

## REFERENCES

1. D3. Gabor, Theory of communication, *Journal of the Institute of Electrical Engineers*, vol. 93, pp. 429–457, 1946.
2. F. Hlawatsch and G. F. Boudreaux-Bartels, Linear and quadratic time-frequency signal representations, *IEEE SP Magazine*, pp. 21–67, April 1992.
3. L. Cohen, Introduction: A primer on time-frequency analysis, in *Time-Frequency Signal Analysis*, B. Boashash, ed., Melbourne: Longman Cheshire, pp. 3–42, 1992.
4. S. Qian and D. Chen, Joint time-frequency analysis, *IEEE Signal Processing Magazine*, pp. 52–67, March 1999.
5. H. G. Feichtinger and T. Strohmer, eds., *Gabor Analysis and Algorithms: Theory and Applications*, Boston: Birkhäuser, 1998.
6. B. Boashash, ed., *Time-Frequency Signal Analysis*, Melbourne: Longman Cheshire, 1992.
7. L. Cohen, *Time-Frequency Analysis*, Englewood Cliffs, NJ: Prentice-Hall, 1995.
8. S. Qian and D. Chen, *Joint Time-Frequency Analysis: Methods and Applications*, Englewood Cliffs, NJ: Prentice-Hall, 1996.
9. P. Flandrin, *Time-Frequency/Time-Scale Analysis*, San Diego, CA: Academic Press, 1999.
10. C. K. Chui, *An Introduction to Wavelets*, San Diego, CA: Academic Press, 1992.
11. S. Mallat, *A Wavelet Tour of Signal Processing*, San Diego, CA: Academic Press, 1998.
12. I. Daubechies, *Ten Lectures on Wavelets*, Philadelphia: Society for Industrial and Applied Mathematics, 1992.
13. E. Hernandez and G. Weiss, *A First Course on Wavelets*, Boca Raton, FL: CRC Press, 1996.
14. J. H. Ahlberg, E. N. Nilson, and J. L. Walsh, *The Theory of Splines and Their Applications*, New York: Academic Press, 1967.

15. R. H. Bartels, J. C. Beatty, and B. A. Barsky, *Splines for Use in Computer Graphics*, Los Altos, CA: Morgan Kaufmann, 1987.
16. M. Unser, A. Aldroubi, and M. Eden, B-spline signal processing: Part I—theory, *IEEE Transactions on Signal Processing*, vol. 41, no. 2, pp. 821–833, February 1993.
17. M. Unser, A. Aldroubi, and M. Eden, B-spline signal processing: Part II—efficient design and applications, *IEEE Transactions on Signal Processing*, vol. 41, no. 2, pp. 834–848, February 1993.
18. M. Unser, Splines: A perfect fit for signal and image processing, *IEEE Signal Processing Magazine*, vol. 16, no. 6, pp. 22–38, November 1999.
19. D. Gabor, Acoustical quanta and the theory of hearing, *Nature*, vol. 159, no. 4044, pp. 591–594, May 1947.
20. G. B. Folland, *Fourier Analysis and Its Applications*, Pacific Grove, CA: Wadsworth, 1992.
21. H. Dym and H. P. McKean, *Fourier Series and Integrals*, New York: Academic, 1972.
22. J. J. Benedetto, Uncertainty principle inequalities and spectrum estimation, in *Recent Advances in Fourier Analysis and Its Applications*, J. S. Byrnes and J. F. Byrnes, eds., Dordrecht: Kluwer, pp. 143–182, 1990.
23. G. B. Folland and A. Sitaram, The uncertainty principle: A mathematical survey, *Journal of Fourier Analysis and Applications*, vol. 3, pp. 207–238, 1997.
24. H. Weyl, *The Theory of Groups and Quantum Mechanics*, New York: Dutton, 1931; also, New York: Dover, 1950.
25. I. Daubechies, The wavelet transform, time-frequency localization and signal analysis, *IEEE Transactions on Information Theory*, vol. 36, no. 5, pp. 961–1005, September 1990.
26. M. A. Rieffel, Von Neumann algebras associated with pairs of lattices in Lie groups, *Mathematische Annalen*, vol. 257, pp. 403–418, 1981.
27. I. Daubechies, A. Grossmann, and Y. Meyer, Painless nonorthogonal expansions, *Journal of Mathematical Physics*, vol. 27, no. 5, pp. 1271–1283, May 1986.
28. E. Wigner, On the quantum correction for thermodynamic equilibrium, *Physical Review*, vol. 40, pp. 749–759, 1932.
29. J. Ville, Théorie et applications de la notion de signal analytique, *Cables et Transmission*, vol. 2A, pp. 61–74, 1948.
30. F. Hlawatsch and P. Flandrin, The interference structure of the Wigner distribution and related time-frequency signal representations, in *The Wigner Distribution—Theory and Applications in Signal Processing*, W. F. G. Mecklenbrauker, ed., Amsterdam: Elsevier, 1993.
31. T. A. C. M. Claasen and W. F. G. Mecklenbrauker, The Wigner distribution—a tool for time-frequency signal analysis; part I: Continuous-time signals, *Philips Journal of Research*, vol. 35, no. 3, pp. 217–250, 1980.
32. H. Wechsler, *Computational Vision*, San Diego, CA: Academic Press, 1990.
33. B. Boashash, Time-frequency signal analysis, in S. Haykin, ed., *Advances in Spectrum Estimation*, Prentice-Hall, 1990.
34. F. Hlawatsch, T. G. Manickam, R. L. Urbanke, and W. Jones, Smoothed pseudo-Wigner distribution, Choi–Williams distribution, and cone-kernel representation: ambiguity-domain analysis and experimental comparison, *Signal Processing*, vol. 43, pp. 149–168, 1995.

35. L. Cohen, Generalized phase-space distribution functions, *Journal of Mathematical Physics*, vol. 7, pp. 781–786, 1966.
36. E. Wigner, Quantum-mechanical distribution functions revisited, in *Perspectives in Quantum Theory*, W. Yourgrau and A. van der Merwe, eds., New York: Dover, 1971.
37. R. Balian, Un principe d'incertitude fort en theorie du signal ou en mecanique quantique, *C.R. Acad. Sci. Paris*, vol. 292, series 2, pp. 1357–1362, 1981.
38. F. Low, Complete sets of wave packets, in *A Passion for Physics—Essays in Honor of Geoffrey Chew*, C. DeTar, ed., Singapore: World Scientific, pp. 17–22, 1985.
39. G. Battle, Heisenberg proof of the Balian–Low theorem, *Letters on Mathematical Physics*, vol. 15, pp. 175–177, 1988.
40. I. Daubechies and A. J. E. M. Janssen, Two theorems on lattice expansions, *IEEE Transactions on Information Theory*, vol. 39, no. 1, pp. 3–6, January 1993.
41. A. J. E. M. Janssen, The Zak transform: A signal transform for sampled time-continuous signals, *Philips Journal of Research*, vol. 43, no. 1, pp. 23–69, 1988.
42. C. E. Heil and D. F. Walnut, Continuous and discrete wavelet transforms, *SIAM Review*, vol. 31, pp. 628–666, December 1989.
43. B. Sz-Nagy, Expansion theorems of Paley–Wiener type, *Duke Mathematical Journal*, vol. 14, pp. 975–978, 1947.
44. R. J. Duffin and A. C. Schaeffer, A class of nonharmonic Fourier series, *Transactions of the American Mathematical Society*, vol. 72, pp. 341–366, 1952.
45. R. M. Young, *An Introduction to Nonharmonic Fourier Series*, New York: Academic Press, 1980.
46. Y. Meyer, *Wavelets and Operators*, Cambridge: Cambridge University Press, 1992.
47. L. Cohen, Time-frequency analysis, in L. Atlas and P. Duhamel, Recent developments in the core of digital signal processing, *IEEE Signal Processing Magazine*, vol. 16, no. 1, pp. 22–28, January 1999.
48. B. Barkat and B. Boashash, Adaptive window in the PWVD for IF estimation of FM signals in additive Gaussian noise, *Proceedings of the ICASSP*, vol. 3, pp. 1317–1320, 1999.
49. P. Flandrin, Some features of time-frequency representations of multi-component signals, *IEEE International Conference on Acoustics, Speech and Signal Processing*, ICASSP-84, San Diego, CA, pp. 41.B.4.1–41B.4.4, 1984.
50. M. Bastiaans, Gabor's expansion of a signal into gaussian elementary signals, *Optical Engineering*, vol. 20, no. 4, pp. 594–598, July 1981.
51. M. Bastiaans, On the sliding-window representation in digital signal processing, *IEEE Transactions on Acoustics, Speech, and Signal Processing*, vol. ASSP-33, pp. 868–873, August 1985.
52. J. Daugman, Complete discrete 2-D Gabor transforms by neural networks for image analysis and compression, *IEEE Transactions on Acoustics, Speech, and Signal Processing*, vol. 36, July 1988.
53. J. Yao, Complete Gabor transformation for signal representation, *IEEE Transactions on Image Processing*, vol. 2, no. 2, pp. 152–159, April 1993.
54. I. Daubechies, A simple Wilson orthonormal basis with exponential decay, *SIAM Journal of Mathematical Analysis*, vol. 22, pp. 554–572, 1991.
55. H. Malvar, Lapped transforms for efficient transform/subband coding, *IEEE Transactions on Acoustics, Speech, and Signal Processing*, vol. 38, pp. 969–978, 1990.

56. B. B. Hubbard, *The World According to Wavelets*, Wellesley, MA: A. K. Peters, 1996.

57. Y. Meyer, *Wavelets: Algorithms and Applications*, Philadelphia: SIAM, 1993.

## PROBLEMS

- Suppose that  $\mu, \sigma \in \mathbb{R}$ ,  $\sigma > 0$ ; and  $g(t) = g_{\mu, \sigma}(t)$  is the Gaussian signal with mean  $\mu$  and standard deviation  $\sigma$ . Find the Gabor transform with respect to  $g_{0,4}(t)$  of the following signals:
  - $x(t) = \exp(6\pi jt)$
  - $y(t) = \exp(-5\pi jt)$
  - $z(t) = x(t) + y(t)$
  - $\exp(j\omega_0 t)$
  - $\sin(6\pi t)$
  - $\cos(5\pi t)$
- Using the notation of the first problem, find the Gabor transform with respect to  $g_{0,1}(t)$  of the following signals:
  - $x(t) = \delta(t)$ , the Dirac delta
  - $y(t) = \delta(t - 5)$
  - $s(t) = x(t) + y(t)$
  - $z(t) = \delta(t - r)$ , where  $r \in \mathbb{R}$
- Using the notation of the first problem, find the Gabor transform with respect to  $g_{0,1}(t)$  of the following signals:
  - $x(t) = g_{2,4}(t)$
  - $y(t) = g_{2,4}(t)\exp(6\pi jt)$
  - $z(t) = g_{-2,4}(t)\cos(6\pi t)$
  - $s(t) = g_{-2,4}(t)\sin(6\pi t)$
- Let  $x(t) = \exp(j\Omega t^2)$  be a linear chirp signal and  $g(t) = g_{0,\sigma}(t)$  be the zero-mean Gaussian with standard deviation  $\sigma > 0$ .
  - Find the Gabor transform  $X_g(\mu, \omega)$  of  $x(t)$ .
  - Show that the frequency at which  $|X_g(\mu, \omega)|$  reaches a maximum value for  $\mu = T$  is  $\Omega_{\max} = 2T\Omega$ .
  - Let  $\phi(t) = \Omega t^2$ , so that  $\phi(t)$  is the phase of the signal  $x(t)$ ; show that the instantaneous frequency of  $x(t)$ ,  $d\phi/dt$  evaluated at  $t = T$ , is precisely  $\Omega_{\max}$  of part (b).
- Suppose that  $x(t)$  is an analog signal;  $\mu, \sigma \in \mathbb{R}$ ,  $\sigma > 0$ ; and  $g(t) = g_{\mu, \sigma}(t)$  is the Gaussian signal with mean  $\mu$  and standard deviation  $\sigma$ . Show the following:
  - $g(t) \in L^2(\mathbb{R})$ .
  - If  $x(t) \in L^2(\mathbb{R})$ , then  $x(t)g(t) \in L^2(\mathbb{R})$  and the Gabor transform of  $x(t)$ ,  $X_g(\mu, \omega)$  exists.

- (c) Show that if  $x(t) \in L^2(\mathbb{R})$ , then its Gabor transform with respect to the window function  $g(t)$  is the inner product of  $x(t)$  and the Gabor elementary function  $g(t)\exp(j\omega t)$ .
  - (d) Find the norm of  $g(t)$  in  $L^2(\mathbb{R})$ :  $\|g(t)\|_2$ .
6. With the notation of Problem 1, show the following:
- (a) If  $x(t) \in L^1(\mathbb{R})$ , then  $x(t)g(t) \in L^1(\mathbb{R})$  also.
  - (b) If  $x(t) \in L^1(\mathbb{R})$ , then  $X_g(\mu, \omega)$  exists.
  - (c) Find an upper bound for  $\|X_g(\mu, \omega)\|_1$ , the  $L^1(\mathbb{R})$  norm of  $X_g(\mu, \omega)$ .
7. Let  $y(t) = g(t)\exp(j\omega_0 t)$ , using the notation of Problem 1.
- (a) Write the sinusoidal signal,  $\sin(\omega_0 t)$ , as a sum of exponentials and sketch its spectrum using Dirac delta functions.
  - (b) Using the Sifting Property of the Dirac delta, calculate  $Y(\omega)$ .
  - (c) Sketch the magnitude spectrum  $|Y(\omega)|$  and the phase spectrum  $\arg[Y(\omega)]$ .
8. If  $w(t)$  is a window function and  $v(t) = w(t + t_0)$ . Define the center  $C_w$  and radius of  $\rho_w$  of  $w(t)$  by

$$C_w = \frac{1}{\|w\|_{2-\infty}^2} \int t |w(t)|^2 dt, \tag{10.191}$$

$$\rho_w = \left[ \frac{1}{\|w\|_{2-\infty}^2} \int (t - C_w)^2 |w(t)|^2 dt \right]^{\frac{1}{2}}. \tag{10.192}$$

- (a) Show that  $v(t)$  is a window function also.
  - (b) Show  $C_v = C_w - t_0$ .
  - (c) If  $W = \mathcal{F}w$  and  $V = \mathcal{F}v$  are the Fourier transforms of  $w$  and  $v$ , respectively, and  $W$  and  $V$  are window functions, then  $C_W = C_V$ .
  - (d)  $\rho_v = \rho_w$ .
  - (e) If  $x(t) = \exp(-jC_w t)w(t + C_w)$ , then  $C_x = C_x = 0$  and  $\rho_x = \rho_w$ .
9. Let  $w(t)$  be a window function. Show the following:
- (a)  $s(t) = (1 + |t|)^{-1} \in L^2(\mathbb{R})$ .
  - (b)  $v(t) = (1 + |t|)w(t) \in L^2(\mathbb{R})$ .
  - (c) Use the Schwarz inequality for analog Hilbert spaces (Chapter 3) and the previous two results to show that  $w(t) \in L^1(\mathbb{R})$ .
  - (d) Again using the Schwarz inequality, show that  $t^{1/2}w(t) \in L^2(\mathbb{R})$ .
10. This problem explores how our definitions of center and radius accord with the mean and standard deviation of a Gaussian pulse.
- (a) Calculate the center and radius of  $g(t) = g_{\mu, \sigma}(t)$ , the Gaussian with mean  $\mu$  and standard deviation  $\sigma$ . For instance, for  $\rho_x$  we find

$$\int_{-\infty}^{\infty} t |g(t)|^2 dt = \int_{-\infty}^{\infty} \frac{t}{\sigma^2 2\pi} e^{-\frac{(t-\mu)^2}{\sigma^2}} dt. \quad (10.193)$$

(b) Calculate the center and radius of the other standard window functions: the rectangular, triangular, Hanning, Hamming, and Blackman windows.

(c) Calculate the center and radius of the  $B$ -spline windows,  $\beta_n(t)$ .

11. Let  $w(t) \in L^2(\mathbb{R})$  and define the signal  $x(t)$  by

$$x(t+k) = (-1)^k \overline{w(t-k-1)}, \quad (10.194)$$

where  $t \in [0, 1)$  and  $k \in \mathbb{Z}$ . Show the following:

(a)  $x \in L^2(\mathbb{R})$

(b)  $\|x\|_2 = \|w\|_2$

(c)  $\|x\|_2 \neq 0$

12. Let  $x(t) \in L^2(\mathbb{R})$ , and  $x'(t) \notin L^2(\mathbb{R})$ . Show that  $\rho_X = \infty$ . [Hint: Use Parseval's theorem for the radial Fourier transform and the formula for  $\mathcal{F}[x'(t)](\omega)$ .]

13. Consider the two-dimensional  $L^2(\mathbb{R}^2)$  signals  $x(s, t)$ , or *images*, that satisfy

$$\int_{-\infty}^{\infty} \int_{-\infty}^{\infty} |x(s, t)|^2 ds dt < \infty. \quad (10.195)$$

(a) Show that  $L^2(\mathbb{R}^2)$  is a vector space: it is closed under sums and scalar multiplication, and each element has an additive inverse.

(b) What is the zero element of  $L^2(\mathbb{R}^2)$ ? Is it unique? Explain how to rectify this difficulty by establishing equivalence classes of images  $[x] = \{y \in L^2(\mathbb{R}^2) : x(s, t) = y(s, t) \text{ for almost all } (s, t) \in \mathbb{R}^2\}$ . Define vector addition of equivalence classes by  $[x] + [y] = [z]$ , where  $z = x + y$ . Define scalar multiplication analogously. Show that this definition makes sense.

(c) Define a norm on  $L^2(\mathbb{R}^2)$  by

$$\left[ \int_{-\infty}^{\infty} \int_{-\infty}^{\infty} |x(s, t)|^2 ds dt \right]^{\frac{1}{2}} = \|x\|_{2, L^2(\mathbb{R}^2)}. \quad (10.196)$$

Show that  $\|x\|$  in (10.196) is indeed a norm:  $\|x\| > 0$ , unless  $x(t)$  is zero almost everywhere;  $\|ax\| = |a| \cdot \|x\|$ ; and  $\|x\| + \|y\| \geq \|x + y\|$ .

(d) Show that  $L^2(\mathbb{R}^2)$  with norm (10.196) is a Banach space; that is, every Cauchy sequence of finite-energy images converges to a finite energy image.

(e) If  $x(s, t)$  and  $y(s, t)$  are in  $L^2(\mathbb{R}^2)$ , then we define their inner product by

$$\langle x, y \rangle_{L^2(\mathbb{R}^2)} = \int_{-\infty-\infty}^{\infty-\infty} \int x(s, t) \overline{y(s, t)} ds dt. \tag{10.197}$$

Show that  $\langle x, y \rangle$  is an inner product space:  $\langle x + y, z \rangle = \langle x, y \rangle + \langle x, z \rangle$ ;  $\langle ax, y \rangle = a\langle x, y \rangle$ ;  $\langle x, x \rangle \geq 0$ ;  $\langle x, x \rangle = 0$  if and only if  $x(t) = 0$  almost everywhere; and  $\langle x, y \rangle = \overline{\langle y, x \rangle}$ ;

(f) Show that  $L^2(\mathbb{R}^2)$  is a Hilbert space.

14. Prove the Parseval theorem for the short-time Fourier transform. Suppose  $x(t), y(t) \in L^2(\mathbb{R})$ ; suppose  $w(t)$  is a window function; and let  $X_w(\mu, \omega)$  and  $Y_w(\mu, \omega)$  be the STFTs of  $x(t)$  and  $y(t)$ , respectively, based on windowing with  $w(t)$ . Then

$$2\pi \|w\|_2^2 \langle x, y \rangle = \int_{-\infty-\infty}^{\infty-\infty} \int X_w(\mu, \omega) \overline{Y_w(\mu, \omega)} d\omega d\mu = \langle X_w, Y_w \rangle_{L^2(\mathbb{R}^2)}. \tag{10.198}$$

15. Prove the Plancherel formula for the short-time Fourier transform. Let  $x(t) \in L^2(\mathbb{R})$ , let  $w(t)$  be a window function, and let  $X_w(\mu, \omega)$  be the STFT of  $x(t)$ . Then

$$\|x\|_2 = \sqrt{2\pi} \frac{\|X_w(\mu, \omega)\|_{2, L^2(\mathbb{R}^2)}}{\|w\|_2}. \tag{10.199}$$

16. Prove the inversion formula for the short-time Fourier transform. Suppose  $x(t) \in L^2(\mathbb{R})$ , suppose  $w(t)$  is a window function, and let  $X_w(\mu, \omega)$  be the STFT of  $x(t)$ . Then for all  $a \in \mathbb{R}$ , if  $x(t)$  is continuous at  $a$ , then

$$x(a) = \frac{1}{(2\pi \|w\|_2^2)_{-\infty}} \int_{-\infty}^{\infty} X_w(\mu, \omega) w(a) e^{j\omega a} d\omega d\mu. \tag{10.200}$$

17. Provide an example of a signal  $x(t) \in L^2(\mathbb{R})$  that fails to satisfy the special condition we assumed in the first part of the Uncertainty Principle's proof:

$$\lim_{t \rightarrow \infty} \sqrt{|t|} |x(t)| = 0; \tag{10.201}$$

[Hint: Define  $x(t)$  so that  $x(n) = \varepsilon > 0$  on the integers  $\mathbb{Z}$ .]

18. Restate and prove the Uncertainty Principle for the Hertz Fourier transform:

$$X(\omega) = \int_{-\infty}^{\infty} x(t) e^{-2\pi j\omega t} dt. \tag{10.202}$$

19. Let us derive a one-dimensional form of Heisenberg's Uncertainty Principle. Following the quantum mechanical viewpoint, we assume that the position and momentum describe the state of an electron, and a probability density function  $|\phi(x)|^2$  governs its position. The probability that the particle is on the closed real interval  $a \leq x \leq b$  is

$$\int_a^b |\phi(x)|^2 dx, \tag{10.203}$$

where we must have  $\|\phi(x)\|_2 = 1$  so that  $\phi$  is indeed a density. Define a momentum state function  $\psi(\omega)$  as follows:

$$\psi(\omega) = \frac{\Phi\left(\frac{\omega}{h}\right)}{\sqrt{2\pi h}}, \tag{10.204}$$

where  $\Phi(\omega)$  is the radial Fourier transform of  $\phi(x)$ , and  $h$  is a constant (Planck's).

- (a) Show that  $\|\psi(\omega)\|_2 = 1$ , so that  $\psi$  is a density also.
  - (b) Let  $\Delta_\phi = 2\rho_\phi$  and  $\Delta_\psi = 2\rho_\psi$  be the diameters of  $\phi$  and  $\psi$ , respectively, where  $\rho$  is the radius (10.192). Show that  $\Delta_\phi\Delta_\psi \geq 2h$ .
20. Suppose we are interested in time-frequency localization and thus require a short-time Fourier transform based on a window function  $w(t)$  such that  $W(\omega)$  is also a window function.
- (a) Which of the standard window functions, if any, in Table 10.2 supports this requirement?
  - (b) Show that a Gaussian works.
  - (c) Show that any B-spline  $\beta_n(t)$  of order  $n \geq 1$  works too.
21. This problem explores the idea of changing the window width normalization for the Gabor transform. We defined the Gabor transform for an arbitrary Gaussian window  $g_{0,\sigma}(t)$  of zero mean and arbitrary standard deviation  $\sigma > 0$ :

$$X_g(\mu, \omega) = \frac{1}{\sigma\sqrt{2\pi}} \int_{-\infty}^{\infty} x(t) e^{-\frac{(t-\mu)^2}{2\sigma^2}} e^{-j\omega t} dt. \tag{10.205}$$

- (a) Suppose we are Gabor transforming with a window function  $g(t)$  with  $\|g(t)\|_1 = 1$ , where  $\|\cdot\|_1$  is the norm in the Banach space of absolutely integrable signals  $L^1(\mathbb{R})$ . What form do the following Gabor transform properties take in this case: the inverse theorem, the Plancherel theorem, and the Parseval theorem?
  - (b) Suppose instead that we have used a Gaussian  $g(t)$  with  $\|g(t)\|_2 = 1$ . Now what form do these same properties take?
22. Try to prove the bounds theorem for windowed Fourier frames without resorting to Zak transform results. Let  $w(t) \in L^2(\mathbb{R})$  and its windowed Fourier

atoms  $\{w_{m,n}(t) = e^{jn\Omega t}w(t - mT): m, n \in \mathbb{Z}\}$ , constitute a frame. Show that  $A \leq \frac{2\pi}{\Omega T} \|w\|_2^2 \leq B$ , where  $A$  and  $B$  are the lower and upper frame bounds, respectively.

23. Suppose we select the following window function:  $w(t) = (1 + t^2)^{-1}$ .
- (a) Show that  $w(t)$  is bounded (in  $L^\infty(\mathbb{R})$ ) and absolutely integrable (in  $L^1(\mathbb{R})$ ).
  - (b) Let  $T > 0$  be the time-domain sampling interval for discretizing the STFT with respect to  $w(t)$ . Show that  $\sum |w(t - kT)|^2$  has an upper and lower bound.
  - (c) Show that we can find a frequency-domain sampling interval  $\Omega > 0$  such that  $\{w_{m,n}(t) = e^{jn\Omega t}w(t - mT): m, n \in \mathbb{Z}\}$  are a frame. How small must  $\Omega$  be?
  - (d) Repeat the above steps for the Gaussian window  $w(t) = g_{\mu,\sigma}(t)$ , the Gaussian with mean  $\mu$ , and standard deviation  $\sigma$ .
24. Let  $x(t) \in L^2(\mathbb{R})$  and  $X_{WV}(\mu, \omega)$  be its Wigner–Ville distribution. Show the following:
- (a) If  $s(t) = x(t - a)$ , then  $S_{WV}(\mu, \omega) = X_{WV}(\mu - a, \omega)$ .
  - (b) If  $y(t) = e^{j\theta t}x(t)$ , then  $Y_{WV}(\mu, \omega) = X_{WV}(\mu, \omega - \theta)$ .
  - (c) If  $y(t) = ax(t)$ , then  $Y_{WV}(\mu, \omega) = |a|^2 X_{WV}(\mu, \omega)$ .
  - (d) If  $y(t) = x(t/a)$  and  $a > 0$ , then  $Y_{WV}(\mu, \omega) = a X_{WV}(\mu/a, a\omega)$ .
  - (e) If  $y(t) = \exp(j\theta t^2)x(t)$ , then  $Y_{WV}(\mu, \omega) = X_{WV}(\mu, \omega - 2\theta\mu)$ .
25. Let  $x(t) \in L^2(\mathbb{R})$ ,  $X(\omega)$  be its Fourier transform, and  $X_{WV}(\mu, \omega)$  be its WVD. Show the following symmetry properties:
- (a) If  $x(t)$  is real-valued and  $X_{WV}(\mu, \omega) = X_{WV}(\mu, -\omega)$ , then  $X(\omega)$  is even:  $X(\omega) = X(-\omega)$ .
  - (b) If  $X_{WV}(-\mu, \omega) = X_{WV}(\mu, \omega)$  and  $X(\omega)$  is real-valued, then  $x(t)$  is even.
26. Let  $x(t) \in L^2(\mathbb{R})$ ,  $w(t)$  be a window function, and let  $X_{S,w}(\mu, \omega)$  be the spectrogram of  $x(t)$  with respect to  $w(t)$ . Develop a table of properties for  $X_{S,w}(\mu, \omega)$  analogous to Table 10.3.
27. Let  $x(t)$  and  $y(t)$  be finite energy analog signals and let  $X_{WV,y}(\mu, \omega)$  be the cross Wigner–Ville distribution of  $x(t)$  with respect to  $y$ :

$$X_{WV,y}(\mu, \omega) = \int_{-\infty}^{\infty} x\left(\mu + \frac{t}{2}\right) \overline{y\left(\mu - \frac{t}{2}\right)} e^{-j\omega t} dt. \tag{10.206}$$

- (a) Show that  $[X_{WV,y}(\mu, \omega)]^* = Y_{WV,x}(\mu, \omega)$ .
  - (b) If  $s(t) = x(t) + y(t)$ , show then that  $S_{WV}(\mu, \omega) = X_{WV}(\mu, \omega) + Y_{WV}(\mu, \omega) + 2\text{Real}[X_{WV,y}(\mu, \omega)]$ .
  - (c) What is the relation between the cross Wigner–Ville distribution and the short-time Fourier transform?
28. Suppose  $x(t) = e^{jat}$ . Show that  $X_{WV}(\mu, \omega) = (2\pi)^{-1} \delta(\omega - a)$ .
29. Let  $g(t) = g_{\alpha,\sigma}(t)$ , the Gaussian of mean  $\alpha$  and standard deviation  $\sigma > 0$ . Show that

$$X_{WV}(\mu, \omega) = \frac{e^{-(\sigma\omega)^2} e^{-\left(\frac{\mu-\alpha}{\sigma}\right)^2}}{2\pi^{3/2}\sigma}. \tag{10.207}$$

30. Let  $s(t) = u(t + 1) - u(t - 1)$ . Show that

$$S_{WV}(\mu, \omega) = \frac{2s(\mu)}{\omega} \sin(2\omega(1 - |\mu|)). \tag{10.208}$$

31. Let  $x(t) \in L^2(\mathbb{R})$ , let  $X(\omega)$  be its Fourier transform, and let  $X_{WV}(\mu, \omega)$  be its WVD. As a function of  $\mu$ , show that  $X_{WV}(\mu, \omega)$  has the following Fourier transform:

$$\mathcal{F}[X_{WV}(\mu, \omega)](\theta) = \int_{-\infty}^{\infty} X_{WV}(\mu, \omega) e^{-j\mu\theta} d\mu = X\left(\omega + \frac{\theta}{2}\right) \overline{X\left(\omega - \frac{\theta}{2}\right)}. \tag{10.209}$$

32. Complete the proof of the bounds theorem for windowed Fourier frames. Let  $w(t) \in L^2(\mathbb{R})$  and suppose  $\{w_{m,n}(t) = e^{2\pi jnt} w(t - m) : m, n \in \mathbb{Z}\}$  is a frame, with lower and upper bounds  $A$  and  $B$ , respectively. Then for almost all  $s$  and  $\omega$  we have  $|(Zw)(s, \omega)|^2 \leq B$ , where  $Zw$  is the Zak transform (parameter  $a = 1$ ) of  $w$ :

$$(Zx)(s, \omega) = \sum_{k=-\infty}^{\infty} x(s - k) e^{2\pi j\omega k}. \tag{10.210}$$

33. Prove the Zak transform derivative lemma: if  $x(t), x'(t) \in L^2(\mathbb{R})$ , then

$$Z(x'(t))(s, \omega) = \frac{\partial}{\partial s}(Zx)(s, \omega). \tag{10.211}$$

Justify interchanging the summation and differentiation operations when differentiating the Zak transform sum with respect to  $s$ .

34. Complete the proof of the Zak transform derivative characterization. Let  $x(t) \in L^2(\mathbb{R})$ ;  $X(\omega) = \mathcal{F}[x(t)]$  be its Fourier transform; and  $Z$  be the Zak transform  $Z: L^2(\mathbb{R}) \rightarrow L^2(S)$ , where  $S$  is the unit square  $[0, 1] \times [0, 1]$ . Then the following are equivalent:

- (a)  $X(\omega)$  is a window function.
- (b)  $x'(t) \in L^2(\mathbb{R})$ .
- (c)  $\frac{\partial}{\partial s}(Zx)(s, \omega) \in L^2[S]$ .

35. Let  $w(t) \in L^2(\mathbb{R})$ ;  $F = \{w_{m,n}(t) = e^{2\pi jnt} w(t - mT) : m, n \in \mathbb{Z}\}$  be a frame; let  $Z: L^2(\mathbb{R}) \rightarrow L^2(S)$  be the Zak transform, where  $S = [0, 1] \times [0, 1]$ ; and let  $\tilde{w} = (\mathcal{T}^* \mathcal{T})^{-1} w = S^{-1} w$ , where  $\mathcal{T}$  is the frame operator for  $F$ . If  $k \in \mathbb{Z}$ , show that

- (a) Translations by  $k$  and the operator  $S$  commute:

$$(Sw)(t-k) = S(w(t-k)). \tag{10.212}$$

(b) Modulations are also commutative under  $S$  transformation:

$$e^{2\pi jkt}(Sw(t)) = S(e^{2\pi jkt}w(t)). \tag{10.213}$$

(c)  $((\mathcal{T}^* \mathcal{T})^{-1}w)_{m,n} = (\mathcal{T}^* \mathcal{T})^{-1}(w_{m,n})$ .

(d)  $\langle \tilde{w}, w_{m,n} \rangle = \begin{cases} 1 & \text{if } m = n = 0, \\ 0 & \text{otherwise.} \end{cases}$

(e) Show that

$$\langle tw(t), \tilde{w}_{m,n}(t) \rangle = \langle w_{-m,-n}(t), t\tilde{w}(t) \rangle. \tag{10.214}$$

by expanding the inner product integral.

- 36. Develop an experiment with either real or synthetic data showing that an improperly chosen STFT window width can render the transform information useless for interpreting signal evolution through time.
- 37. Develop an experiment with either real or synthetic data showing the presence of cross-terms in the WVD of a signal. Consider the analysis of a linear chirp signal. Devise an algorithm to estimate the rate of change in frequency over time. How do the WVD's cross terms affect this algorithm? Suppose that a quadratic chirp is given, and explore the same issues.
- 38. Obtain or generate signals have significant transient phenomena in addition to localized frequency components. Develop experiments comparing the STFT and the WVD for the purposes of analyzing such signals.
- 39. Define the following Hertz version of the spectrogram:

$$X_{S,w}(\mu, f) = \left| \int_{-\infty}^{\infty} x(t)w(t-\mu)e^{-2\pi jft} dt \right|^2. \tag{10.215}$$

(a) Show that

$$\int_{-\infty}^{\infty} X_{S,w}(\mu, f) df = \int_{-\infty}^{\infty} |s(t)w(t-\mu)|^2 dt. \tag{10.216}$$

(b) Also show

$$\int_{-\infty}^{\infty} X_{S,w}(\mu, f) d\mu = \int_{-\infty}^{\infty} |X(u)W(u-f)|^2 du. \tag{10.217}$$

- (c) Show that the Hertz spectrogram does not satisfy the either the time or frequency marginal conditions.
- (d) Define a Hertz version of the WVD.
- (e) Show that the Hertz WVD satisfies the ideal Marginal Conditions.

## Time-Scale Signal Transforms

Petroleum seismologists discovered the modern form of the continuous wavelet transform in the mid-1980s. For some time, researchers had been using time-frequency transforms—such as the Gabor transform and its broader family of short-time Fourier transforms—for analyzing signals containing localized frequency components. Speech and seismic waveforms are representative examples. Windowed Fourier analysis becomes problematic, however, when the structure of the signal involves transients of varying scale. Then the short-time tools behave more like the global Fourier transform, and their approximations converge poorly. One idea put forward to improve decomposition convergence was to replace the frequency variable with a scale parameter in the transform relation. The basis functions for this new method were shifted and dilated versions of each other. So they looked like little waves: *wavelets*.

This research caught the eye of mathematicians who found that the new technique held a wealth of special properties. It could be discretized. Wavelets were close kin to theoretical tools used in the study of singular integral operators (mathematical physics), the frame signal decomposition structure (harmonic analysis), quadrature mirror filters (communication theory), and the scale space representation (signal and image analysis). And against the intuition of all theoreticians of the time, there were found orthonormal bases for the  $L^2$  Hilbert space that consisted of smooth, rapidly decaying, similarly shaped elements: *orthonormal wavelets*.

This chapter develops both continuous and discrete scale-based transforms. The topics include the continuous wavelet transform; further development of the idea of frames, which we covered in Chapters 3 and 10; the concept of multiresolution analysis; orthogonal wavelets; discrete wavelet transforms; and, finally, the construction of multiresolution analyses and orthogonal wavelets. Wavelet decomposition furnishes an alternative approach for describing signal structure.

There is a rich research literature on wavelet transforms, including a history of the discipline [1] and many excellent introductory treatments [2–12].

## 11.1 SIGNAL SCALE

In a variety of signal analysis applications we have taken note of the problems that arise due to the scale of signal features. The idea is that of the extent of recognizable portions of the signal or the width of regions of interest within the signal may vary over time. The scale of signal features affects the behavior of such signal analysis elements as edge detectors, shape detectors, and local frequency identification algorithms.

From several standpoints we have attempted to interpret signals, and from each of them we had to deal with the issue of scale in a rather informal manner. For instance, in Chapter 4 we pursued time domain techniques for understanding signals. Scale issues affect edge and peak detection, obviously, and even the decision about how wide noise removal filters should be must take into account the size of objects sought within the signal. In Chapter 9 we designed filters to find periodicities within signals. But when such oscillatory components are localized—and so they often are in natural signals—then the extent of the oscillatory phenomenon affects the outcome of the analysis.

The dilation of a function has the same basic shape. For scale-based signal analysis we generally use translations and *dilations* or *scalings* of a basic signal  $\psi(t)$ :

$$\psi_{a,b}(t) = \frac{1}{\sqrt{a}} \psi\left(\frac{t-b}{a}\right). \quad (11.1)$$

In the next section, we shall show, following Grossmann and Morlet [13], that dilations (variations in parameter  $a$ ) and translations (variations in  $b$ ) support a decomposition of a general function  $\psi(t)$ .

In the previous chapter we covered time-frequency transforms, which combine time and frequency information in the transformed signal. These time-frequency transforms achieve local frequency estimation, but the windowed Fourier transforms suffer from a fixed window size. It turns out, as a consequence, that they do not effectively handle signals with transients and components whose pitch changes rapidly. Making the time-domain window more localized (narrower) makes the frequency-domain window less localized (wider) and vice versa. Time-scale transforms can deal with these last problems; indeed we can mark this insight by petroleum geologists as the grand opening of modern wavelet theory. But time-scale transforms too have deficiencies. One such is the lack of translation-invariance. The final chapter explores some signal analysis applications and examines the tradeoffs between pure time-domain, time-frequency, and time-scale methods.

## 11.2 CONTINUOUS WAVELET TRANSFORMS

This section presents the continuous wavelet transform. The wavelet representation for one-dimensional signals was developed by Grossmann and Morlet to overcome the deficiencies of the Gabor transform for seismic applications [13]. Wavelets are special functions whose translations and dilations can be used for expansions of



**Fig. 11.1.** Typical seismic section.

square-integrable functions. In the discussion of the fixed window size implicit in the Gabor representation in Section 2.4, it was noted that the Gabor representation is burdened by the problem of high-magnitude, high-frequency coefficients that is so typical of the Fourier transform.

### 11.2.1 An Unlikely Discovery

Seismic signals contain many irregular and isolated transients (Figure 11.1). The drawback of the Fourier transform is that it represents signal frequencies as present for all time, when in many situations, and in seismic signal interpretation in particular, the frequencies are localized. The Gabor transform and its more general variant, the short-time Fourier transform (STFT), provide local frequency analysis. One feature of the short-time transforms is that the window size remain fixed. This is acceptable as long as the signal frequency bursts are confined to regions approximating the size of the transform window.

However, in seismic applications, even the STFT becomes problematic. The problem is that seismic signals have many transients, and Grossmann and Morlet found the windowed Fourier algorithms to be numerically unstable. That is, a slight change in the input seismic trace results in a quite pronounced change in the decomposition coefficients. Grossmann and Morlet identified the fixed window size as contributing to the difficulty. Their solution was to keep the same basic filter shape, but to shrink its time-domain extent. That is, they resorted to a transform based on *signal scale*.

### 11.2.2 Basic Theory

This section introduces the fundamental ideas behind continuous-domain wavelet transforms.

**11.2.2.1 Definition and Motivation.** Let us begin with a formal definition of a wavelet. The idea is rather recent, and this special signal type passes through the scientific and engineering literature by means of a variety of monikers.

**Definition (Analyzing Wavelet).** The square-integrable signal  $\psi(t)$  is an *analyzing wavelet* if it satisfies the *admissibility condition*

$$C_\psi = \int_{-\infty}^{\infty} \frac{|\Psi(\omega)|^2}{|\omega|} d\omega < \infty, \quad (11.2)$$

where  $\Psi(\omega)$  is the radial Fourier transform of  $\psi(t)$ . The quantity in (11.2) is called the *admissibility factor*. Other names for analyzing wavelets are *basic wavelet*, *continuous wavelet*, *admissible wavelet*, and *mother wavelet*. In some analyses it is convenient to normalize the analyzing wavelet,

$$\sqrt{\langle \psi(t), \psi(t) \rangle} = 1, \quad (11.3)$$

but normalization is not a necessary condition for generating useful time-scale transforms or performing the inverse wavelet transform.

The admissibility condition makes possible the inversion relation for the transform. There are some further consequences, however: Wavelets are bandpass filters with a quick frequency cutoff characteristic and have zero mean in the time domain.

The *wavelet transform* is a time-scale transform that uses a scaled and translated version of the analyzing wavelet in a Hilbert space inner product to convert one-dimensional time-varying signals to a two-dimensional scale and translations space:

**Definition (Wavelet Transform).** Let

$$\Psi_{a,b}(t) = \frac{1}{\sqrt{|a|}} \psi\left(\frac{t-b}{a}\right) \quad (11.4)$$

Let  $f(t)$  be square-integrable. The wavelet transform of  $f(t)$  is defined as the inner product

$$F_\psi(a,b) = \mathcal{W}[f(t)](a,b) = \int_{-\infty}^{\infty} f(t) \overline{\Psi_{a,b}(t)} dt \equiv (f(t), \Psi_{a,b}(t)). \quad (11.5)$$

The wavelet transform is a mapping from the one-dimensional time domain to a two-dimensional space consisting of a scale  $a$  and a translation  $b$  (Figure 11.2).

An inverse wavelet transform synthesizes  $f(t)$  from the two-dimensional  $W[f(t)](a,b)$ :

**Definition (Inverse Wavelet Transform).** The inverse wavelet transform is the two-dimensional integral,

$$f(t) = \frac{1}{C_\psi} \int_{-\infty}^{\infty} \int_{-\infty}^{\infty} W[f(t)](a,b) \psi(t) d\mu, \quad (11.6)$$

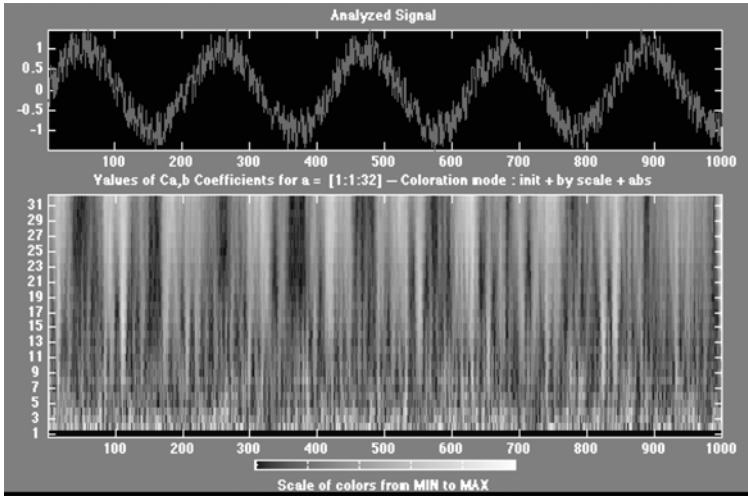


Fig. 11.2. Example of continuous wavelet transform of a noisy sine wave.

where

$$d\mu = \frac{dad b}{a^2} \tag{11.7}$$

and

$$C_\Psi = \int_{-\infty}^{\infty} \frac{|\Psi(\omega)|^2}{|\omega|} d\omega. \tag{11.8}$$

*Remarks.* The definition of a wavelet is fundamentally quite simple, consisting of a *time* criterion (square integrability) and a *frequency* criterion expressed by the admissibility condition. Some references include normalization in the definition of a wavelet, but we emphasize that unit energy is an option, not a necessity. At the present level of development, (11.6) suggests that the admissibility condition (11.2) allows the inverse wavelet transform to be carried out. On cursory inspection the admissibility condition would suggest that the spectrum of an analyzing wavelet should decay rapidly for large  $|\omega|$ , and since wavelets are defined to be square-integrable, this is automatically fulfilled. On the other hand, the presence of  $|\omega|$  in the denominator of (11.8) imposes two further requirements on the time domain behavior of the analyzing wavelet. One is obvious, the other is a bit more subtle, but both are relatively easy to satisfy, as the following discussion demonstrates.

**Proposition.** Let  $\psi(t)$  be an analyzing wavelet as previously defined. Then the admissibility criterion is satisfied if

(i) the analyzing wavelet is of zero mean, that is,

$$\int_{-\infty}^{\infty} \psi(t) dt = 0, \quad (11.9)$$

and

(ii)

$$t\psi(t) \in L^1(\mathbb{R}). \quad (11.10)$$

**Proof:** The first condition is obvious: We require  $\Psi(0) = 0$  to ensure that the integrand in (11.2) remains finite at  $\omega = 0$ . Equation (11.9) simply restates this in terms of the Fourier transform,

$$\lim_{\omega \rightarrow 0} \int_{-\infty}^{\infty} \psi(t) e^{-j\omega t} dt = \int_{-\infty}^{\infty} \psi(t) dt = 0. \quad (11.11)$$

The significance of the second criterion is best demonstrated by dividing the real line into three segments and examining the integral (11.8),

$$C_{\psi} = \int_{-\infty}^{-1} \frac{|\Psi(\omega)|^2}{|\omega|} d\omega + \int_{-1}^1 \frac{|\Psi(\omega)|^2}{|\omega|} d\omega + \int_1^{\infty} \frac{|\Psi(\omega)|^2}{|\omega|} d\omega. \quad (11.12)$$

Our primary interest is the integral over the interval  $t \in [-1, 1]$ . According to the moment theorem developed in Chapter 5, if  $t\psi(t) \in L^1(\mathbb{R})$ , then the first derivative of  $\Psi(\omega)$  exists and is bounded. Designate the maximum value of this derivative in the interval  $|\omega| \leq 1$ :

$$\frac{d}{d\omega} \Psi(\omega) \leq M. \quad (11.13)$$

According to the mean value theorem of differential calculus, if a function  $g(\omega)$  is bounded and continuous on an interval  $[a, b]$ , then

$$\int_a^b g(\omega) d\omega \leq M(b-a). \quad (11.14)$$

Designating  $\frac{d}{d\omega} |\Psi(\omega)| = g(\omega)$ , (11.14) implies

$$|\Psi(\omega)| \leq M \cdot 2|\omega| \quad (11.15)$$

for  $|\omega| \leq 1$ . This bound is actually tighter than implied by (11.15). Since  $\Psi(0) = 0$ , the relevant interval is effectively halved so that

$$|\Psi(\omega)| \leq M \cdot |\omega|. \quad (11.16)$$

Returning to the admissibility condition, we now have

$$\int_{-1}^1 \frac{|\Psi(\omega)|^2}{|\omega|} d\omega \leq \int_{-1}^1 M^2 |\omega| d\omega \leq M, \quad (11.17)$$

thus bounding one portion of the admissibility condition. The remaining two integrals along their respective semi-infinite intervals are easily handled. Since  $\frac{|\Psi(\omega)|^2}{|\omega|} \geq 0$  over  $|\omega| \leq 1$ , it follows that

$$\int_{-\infty}^{-1} \frac{|\Psi(\omega)|^2}{|\omega|} d\omega + \int_1^{\infty} \frac{|\Psi(\omega)|^2}{|\omega|} d\omega \leq \int_{-\infty}^{\infty} \frac{|\Psi(\omega)|^2}{|\omega|} d\omega < \int_{-\infty}^{\infty} |\Psi(\omega)|^2 d\omega. \quad (11.18)$$

This is bounded by virtue of the  $L^2$  Fourier transform. In summary, the overall proposition is proved by virtue of (11.11), (11.17), and (11.18). ■

*Remark.* The conditions (11.9) and (11.10) are not difficult to satisfy. The first criterion,

$$\int_{-\infty}^{\infty} \psi(t) dt = 0 \quad (11.19)$$

implies that a wavelet must oscillate about the time axis—it puts the wave into a wavelet. The stipulation  $t\psi(t) \in L^1(d\mathbb{R})$  can be met if (for example)  $\psi(t) \in L^1(\mathbb{R})$  and has compact support. By definition, this would imply that any function  $\psi(t) \in L^1(\mathbb{R}) \cap L^2(\mathbb{R})$  with zero mean is a wavelet.

**Proposition (Fourier Representation of Wavelet Transform).** Let  $f(t) \in L^2(\mathbb{R})$ . Then for a given scale  $a$ , the wavelet transform is proportional to a Fourier transform into the space of translations:

$$W[f(t)](a, b) = \frac{1}{\sqrt{2\pi}} \mathcal{F}[F(\gamma)](-b), \quad (11.20)$$

where

$$F(\gamma) = \sqrt{|a|} \cdot \mathcal{F}[f(t)](\gamma) \cdot \overline{\mathcal{F}[\psi(t)](a\gamma)}. \quad (11.21)$$

By definition and by Parseval's relation, it readily follows that

$$W[f(t)](a, b) = \langle f(t), \Psi_{a,b}(t) \rangle = \frac{1}{\sqrt{2\pi}} \langle \mathcal{F}[f(t)](\gamma), \overline{\mathcal{F}[\Psi_{a,b}(t)](\gamma)} \rangle. \quad (11.22)$$

However,

$$\mathcal{F}[\Psi_{a,b}(t)](\gamma) = e^{j\gamma b} \mathcal{F}[\Psi_{a,0}(t)](\gamma) = e^{j\gamma b} \sqrt{|a|} \mathcal{F}[\psi(t)](\gamma a) \quad (11.23)$$

so that (11.22) can be expressed in the desired form,

$$W[f(t)](a, b) = \frac{1}{\sqrt{2\pi}} \int_{-\infty}^{\infty} \sqrt{|a|} \cdot \mathcal{F}[f(t)](\gamma) \cdot \mathcal{F}[\psi_{a,b}(t)](\gamma) \cdot e^{-j\gamma b} d\gamma \quad (11.24)$$

and the proposition is proven. ■

This intermediate result is useful for establishing the more important Parseval relation for the wavelet transform.

**Theorem (Wavelet Transform Parseval Relations).** Let  $f(t) \in L^2(\mathbb{R})$  and  $g(t) \in L^2(\mathbb{R})$ , and let  $C_\psi$  be the admissibility coefficient as previously defined. Then

$$\int_{-\infty}^{\infty} \int_{-\infty}^{\infty} W[f(t)](a, b) \overline{W[g(t)](a, b)} d\mu = C_\psi \langle f(t), g(t) \rangle. \quad (11.25)$$

**Proof:** Let  $F(\gamma)$  be defined as in (11.21) and define

$$G(\gamma) \equiv \sqrt{|a|} \cdot \mathcal{F}[g(t)](\gamma) \cdot \overline{\mathcal{F}[\psi(t)](a\gamma)}. \quad (11.26)$$

Then according to the previous proposition,

$$\begin{aligned} & \int_{-\infty}^{\infty} \int_{-\infty}^{\infty} W[f(t)](a, b) \overline{W[g(t)](a, b)} d\mu \\ &= \int_{-\infty}^{\infty} \int_{-\infty}^{\infty} \frac{1}{\sqrt{2\pi}} \mathcal{F}[F(\gamma)](-b) \overline{\frac{1}{\sqrt{2\pi}} \mathcal{F}[G(\gamma)](-b)} d\mu \end{aligned} \quad (11.27)$$

Using the Parseval relation to convert the  $b$ -space Fourier transforms back to  $\gamma$  space, the above integral takes the form

$$\frac{1}{\sqrt{2\pi}} \int_{-\infty}^{\infty} \int_{-\infty}^{\infty} \mathcal{F}[f(t)](\gamma) \overline{\mathcal{F}[g(t)](\gamma)} \cdot |\mathcal{F}[\psi(t)](a\gamma)|^2 d\gamma d\alpha, \quad (11.28)$$

where  $d\alpha \equiv \frac{da}{a}$ .

The integrals over  $a$  and  $\gamma$  can be separated so that (11.28) becomes

$$\frac{1}{\sqrt{2\pi}} \int_{-\infty}^{\infty} |\mathcal{F}[\psi(t)](a\gamma)|^2 d\alpha \int_{-\infty}^{\infty} \mathcal{F}[f(t)](\gamma) \overline{\mathcal{F}[g(t)](\gamma)} d\gamma. \quad (11.29)$$

Applying Parseval's relation to the second of these integrals gives a time-domain inner product:

$$\sqrt{2\pi} \langle f(t), g(t) \rangle. \quad (11.30)$$

The substitution of variables  $\omega = a\gamma$  into the first integral implies  $\frac{da}{a} = \frac{d\omega}{|\omega|}$  so that (11.29) takes the desired form,

$$C_\Psi \langle f(t), g(t) \rangle, \quad (11.31)$$

completing the proof.  $\blacksquare$

**Theorem (Inverse Wavelet Transform).** Let  $f(t)$  be square-integrable. The synthesis problem for the continuous wavelet transform takes the form

$$f(t) = \frac{1}{C_\Psi} \int_{-\infty}^{\infty} \int_{-\infty}^{\infty} W[f(t)](a, b) \Psi_{a, b}(t) d\mu. \quad (11.32)$$

**Proof:** This inversion formula follows directly from the Parseval relation (11.25), which can be written

$$\int_{-\infty}^{\infty} \int_{-\infty}^{\infty} W[f(t)](a, b) \overline{\int_{-\infty}^{\infty} g(t) \Psi_{a, b}(t) dt} d\mu = C_\Psi \langle f(t), g(t) \rangle. \quad (11.33)$$

This can be rearranged in the more suggestive form:

$$\int_{-\infty}^{\infty} \left[ \int_{-\infty}^{\infty} \int_{-\infty}^{\infty} W[f(t)](a, b) \Psi_{a, b}(t) d\mu \right] \overline{g(t) dt} = C_\Psi \langle f(t), g(t) \rangle. \quad (11.34)$$

Since  $g(t)$  is an arbitrary function in  $L^2(\mathbb{R})$ , (11.34) implies (11.25), and the proposition is proven.  $\blacksquare$

*Remark.* Note that the wavelet  $\Psi_{a, b}(t)$  is not conjugated when taking the inverse transform (11.25), in contrast to the forward wavelet transform (11.5).

Since  $\Psi(\omega) \in L^2(\mathbb{R})$ , we must obtain  $\Psi(\omega) \rightarrow 0$  as  $\omega \rightarrow \infty$ ; hence  $y(t)$  is a band-pass filter. The details are left as an exercise.

**11.2.2.2 Algebraic Properties.** As in the case of the Fourier transform, operations such as scaling, translation, and linear combination can be applied to both the analyzing wavelet and the signal waveform. The proofs are straightforward, some are given explicitly in the text, and others are left as exercises. In the following discussion, we assume all signals are square-integrable.

Let us first cover operations on the analyzing wavelet.

**Proposition.** Let  $\alpha, \beta$  be complex constants and  $\psi(t), \phi(t)$  are wavelets. If we define  $\theta(t) = \alpha\psi(t) + \beta\phi(t)$ , then

$$W_\theta[f(t)](a, b) = \bar{\alpha} W_\psi[f(t)](a, b) + \bar{\beta} W_\phi[f(t)](a, b). \quad (11.35)$$

**Proof:** Follows trivially from the linearity of the integral (exercise). ■

**Proposition (Translation of Analyzing Wavelet).** Let  $\gamma$  be a real constant and  $\psi(t)$  be a wavelet. If we define  $\theta(t) = \psi(t - \gamma)$ , then

$$W_{\theta}[f(t)](a, b) = W_{\psi}[f(t)](a, b + \gamma a). \quad (11.36)$$

**Proof:** By definition,

$$W_{\theta}[f(t)](a, b) = \int_{-\infty}^{\infty} f(t) \frac{1}{\sqrt{|a|}} \overline{\psi\left(\frac{t-b}{a} - \gamma\right)} dt = \int_{-\infty}^{\infty} f(t) \frac{1}{\sqrt{|a|}} \overline{\psi\left(\frac{t-(b+\gamma a)}{a}\right)} dt, \quad (11.37)$$

which proves the theorem. ■

**Proposition (Scaling of Analyzing Wavelet).** Let  $\eta > 0$  and  $\psi(t)$  be a wavelet. If  $\theta(t) = \frac{1}{\eta} \psi\left(\frac{t}{\eta}\right)$ , then

$$W_{\theta}[f(t)](a, b) = \frac{1}{\sqrt{\eta}} W_{\psi}[f(t)](a\eta, b). \quad (11.38)$$

**Proof:** Exercise. ■

Now let us turn to signal operations and the resulting wavelet transformations.

**Proposition (Linearity).** Let  $\alpha, \beta$  be complex constants. If we define  $\theta(t) = \alpha\psi(t) + \beta\phi(t)$ , then

$$W_{\theta}[\alpha f(t) + \beta g(t)](a, b) = \alpha W_{\psi}[f(t)](a, b) + \beta W_{\phi}[f(t)](a, b). \quad (11.39)$$

**Proof:** The proof is straightforward and left as an exercise. Note the similarity to, and subtle difference between, this case and the similar operation on the analyzing wavelet. ■

**Proposition (Translation).** Let  $\gamma$  be a real constant. Then

$$W[f(t - \gamma)](a, b) = W[f(t)](a, b - \gamma). \quad (11.40)$$

**Proof:** Exercise. ■

**Proposition (Scaling of Signal).** Let  $\eta > 0$ . Then

$$W\left[\frac{1}{\eta} f\left(\frac{\cdot}{\eta}\right)\right](a, b) = \frac{1}{\sqrt{\eta}} W[f(t)]\left(\frac{a}{\eta}, \frac{b}{\eta}\right). \quad (11.41)$$

**Proof:** By change of variables  $\tau = t/\eta$ , it follows that

$$W\left[\frac{1}{\eta}f\left(\frac{1}{\eta}\right)\right](a, b) = \int_{-\infty}^{\infty} f(\tau) \frac{1}{\sqrt{|a|}} \overline{\Psi\left(\frac{\eta\tau - b}{a}\right)} d\tau = \int_{-\infty}^{\infty} f(\tau) \frac{1}{\sqrt{|a|}} \overline{\Psi\left(\frac{\tau - (b/\eta)}{(a/\eta)}\right)} d\tau. \quad (11.42)$$

Since

$$W[f(t)]\left(\frac{a}{\eta}, \frac{b}{\eta}\right) = \int_{-\infty}^{\infty} f(\tau) \sqrt{\frac{|\eta|}{|a|}} \overline{\Psi\left(\frac{\tau - (b/\eta)}{(a/\eta)}\right)} d\tau \quad (11.43)$$

the desired relation (11.41) follows. ■

**11.2.2.3 Synthesis with Positive Scale.** One final set of properties follows when we restrict the dilation parameter  $a$  to positive values.

Practical signal analysis and synthesis algorithms benefit from the elimination of redundant data. We now demonstrate a condition under which the reconstruction (11.32) (and by inference, the forward wavelet transform) requires only positive values of the dilation. We show that this condition is met by *all real-valued wavelets*, which comprise the vast majority of continuous and discrete wavelets.

**Proposition (Positive Dilation Values).** If

$$\int_0^{\infty} \frac{|\Psi(\omega)|^2}{|\omega|} d\omega = \int_{-\infty}^0 \frac{|\Psi(\omega)|^2}{|\omega|} d\omega, \quad (11.44)$$

then (note the limit on the domain of  $a$ )

$$f(t) = \frac{1}{C_{\Psi}} \int \int_{\Psi_0}^{\infty} W[f(t)](a, b) \Psi_{a, b}(t) d\mu, \quad (11.45)$$

where

$$C_{\Psi} = \int_0^{\infty} \frac{|\Psi(\omega)|^2}{|\omega|} d\omega = \int_{-\infty}^0 \frac{|\Psi(\omega)|^2}{|\omega|} d\omega. \quad (11.46)$$

**Proof:** First, note

$$\int_{-\infty}^{\infty} \frac{|\Psi(\omega)|^2}{|\omega|} d\omega = 2 \int_0^{\infty} \frac{|\Psi(\omega)|^2}{|\omega|} d\omega = 2 \int_{-\infty}^0 \frac{|\Psi(\omega)|^2}{|\omega|} d\omega. \quad (11.47)$$

The overall proof is best carried out by reconsidering the steps leading up to the Parseval relation (11.25). Note that if (11.44) holds, the two auxiliary functions,

$$G(\gamma) \equiv \sqrt{|\gamma|} \cdot \mathcal{F}[g(t)](\gamma) \cdot \overline{\mathcal{F}[\Psi(t)](a\gamma)} \quad (11.48)$$

and

$$F(\gamma) \equiv \sqrt{|a|} \cdot \mathcal{F}[f(t)](\gamma) \cdot \overline{\mathcal{F}[\psi(t)](a\gamma)}, \quad (11.49)$$

display the necessary symmetry in  $a$  so that (11.27) can be reformulated as an integral over positive dilations only:

$$2 \int_{0-\infty}^{\infty} \int_{0-\infty}^{\infty} W[f(t)](a, b) \overline{W[g(t)](a, b)} \, d\mu = 2 \left( \int_0^{\infty} \frac{|\Psi(\omega)|^2}{|\omega|} \, d\omega \right) \langle f(t), g(t) \rangle. \quad (11.50)$$

The factors of 2 cancel and, starting from (11.50), it is straightforward to reproduce the wavelet inversion formula, leading to the desired result (11.45). ■

This proposition is of more than passing interest, as indicated by our next observation.

**Theorem (Real Wavelets).** If  $\psi(t)$  is a real-valued function, then (11.44) is satisfied.

*Proof:* This is easily established from the Fourier transform of  $\psi(t)$ ,

$$\Psi(\omega) = \int_{-\infty}^{\infty} \psi(t) e^{-j\omega t} \, dt. \quad (11.51)$$

If  $\psi(t) \in \mathbb{R}$ , then

$$\Psi(-\omega) = \int_{-\infty}^{\infty} \psi(t) e^{j\omega t} \, dt = \overline{\Psi(\omega)}. \quad (11.52)$$

From here is easy to establish condition (11.44), since

$$\int_{-\infty}^0 \frac{|\Psi(\omega)|^2}{|\omega|} \, d\omega = - \int_0^{-\infty} \frac{|\Psi(\omega)|^2}{|\omega|} \, d\omega. \quad (11.53)$$

With a simple substitution of variables  $\eta = -\omega$ , this can be rearranged to the desired result,

$$- \int_0^{-\infty} \frac{|\Psi(\omega)|^2}{|\omega|} \, d\omega = - \int_{\infty}^0 \frac{|\Psi(\gamma)|^2}{|\gamma|} \, d\gamma = \int_0^{\infty} \frac{|\Psi(\gamma)|^2}{|\gamma|} \, d\gamma. \quad (11.54)$$

■

*Remarks.* Note how the condition (11.52) is explicitly used to establish the first equality in (11.54). Also, the importance of this theorem lies in the implication that all real-valued wavelets can lead to reconstruction on the half-plane  $a \in [0, \infty]$ .

Note that some authors *define* synthesis to occur over this restricted domain, but they are often tacitly restricting the discussion to real-valued  $\psi(t)$ , which form the overwhelming majority of practical wavelets. Selected complex-valued wavelets (to be considered later) may also satisfy (11.45) with a suitable redefinition of  $C_\psi$ , but whenever complex-valued wavelets are under consideration, the reader should exercise caution when performing reconstruction.

Table 11.1 summarizes our results so far.

**11.2.2.4 Wavelets by Convolution.** Convolution is a smoothing operation which preserves any existing localized properties of the functions involved. It is simple to show that under certain reasonable conditions, wavelets generate other wavelets through the convolution operation.

**Theorem (Wavelets Through Convolution).** If  $\psi(t)$  is a wavelet and  $\lambda(t) \in L^1$ , then

$$\phi \equiv \psi * \lambda \tag{11.55}$$

is a wavelet.

**Proof:** We first need to establish that  $\phi \in L^2$ . This can be carried out in the time domain, but it is simpler to consider the frequency domain where

$$\mathcal{F}[\phi(t)](\omega) = \Psi(\omega)\Lambda(\omega). \tag{11.56}$$

**TABLE 11.1. Wavelet Transform Properties<sup>a</sup>**

Signal Expression	Wavelet Transform or Property
$\Psi_{a,b}(t) = \frac{1}{\sqrt{ a }} \psi\left(\frac{t-b}{a}\right)$	Dilation and translation of $\psi(t)$
$C_\psi = \int_{-\infty}^{\infty} \frac{ \Psi(\omega) ^2}{ \omega } d\omega$	Admissibility factor
$f(t)$	$W[f(t)](a,b) = \int_{-\infty}^{\infty} f(t) \overline{\Psi_{a,b}(t)} dt$
$W[f(t)](a,b) = \frac{1}{\sqrt{2\pi}} \mathcal{F}[F(\gamma)](-b)$	Fourier transform representation
$f(t) = \frac{1}{C_\psi} \int_{-\infty}^{\infty} \int_{-\infty}^{\infty} W[f(t)](a,b) \psi(t) \frac{dadb}{a^2}$	Inverse
$\theta(t) = \alpha\psi(t) + \beta\phi(t)$	$W_\theta[f(t)] = \bar{\alpha}W_\psi[f(t)] + \bar{\beta}W_\phi[f(t)]$

<sup>a</sup>In the table,  $\psi(t)$  is square-integrable.

It is easy to establish that this spectrum is  $L^2$ . While we cannot assert that  $\Lambda(\omega)$  is integrable, it is certainly bounded and

$$\int_{-\infty}^{\infty} |\Psi(\omega)\Lambda(\omega)|^2 d\omega = \int_{-\infty}^{\infty} |\Psi(\omega)|^2 |\Lambda(\omega)|^2 d\omega < |\Lambda(\omega)|_{\max}^2 \int_{-\infty}^{\infty} |\Psi(\omega)|^2 d\omega < \infty, \quad (11.57)$$

which proves  $\mathcal{F}[\phi(t)](\omega) \in L^2$ . The inverse Fourier transform maps  $L^2$  to  $L^2$  so that

$$\phi(t) \in L^2. \quad (11.58)$$

The admissibility condition on  $\phi(t)$  follows in a similar manner:

$$\int_{-\infty}^{\infty} \frac{|\Phi(\omega)|^2}{|\omega|} d\omega = \int_{-\infty}^{\infty} \frac{|\Psi(\omega)|^2}{|\omega|} |\Lambda(\omega)|^2 d\omega < |\Lambda(\omega)|_{\max}^2 \int_{-\infty}^{\infty} \frac{|\Psi(\omega)|^2}{|\omega|} d\omega < \infty. \quad (11.59)$$

Conditions (11.58) and (11.59) establish that  $\phi(t)$  is a wavelet. ■

Now let us turn to some examples of analyzing wavelets.

### 11.2.3 Examples

Continuous analyzing wavelets are atomic functions with imposed oscillations. For example, we have seen that the Gaussian time-scale atom is not a wavelet, but operating on a Gaussian by taking one or more derivatives can impose the necessary waviness to ensure that the zero-mean condition (11.19) is satisfied.

**11.2.3.1 First derivative of a Gaussian.** Let us first consider the analyzing wavelet. A bona fide wavelet is created by applying the first derivative to a Gaussian,

$$\psi(t) = A_0 \cdot \left[ -\frac{d}{dt} e^{-t^2} \right] = 2A_0 t e^{-t^2}. \quad (11.60)$$

The normalization constant  $A_0$  can be determined by solving a straightforward Gaussian integral,

$$\int_{-\infty}^{\infty} |\psi(t)|^2 dt = 4A_0^2 \int_{-\infty}^{\infty} t^2 e^{-2t^2} dt \equiv 1, \quad (11.61)$$

which leads to

$$A_0 = \sqrt[4]{2/\pi}. \quad (11.62)$$

The normalization verifies that  $\psi(t)$  is in fact square-integrable and by inspection, due to the odd symmetry of (11.60), the zero-mean condition

$$\int_{-\infty}^{\infty} \psi(t) dt = 0 \quad (11.63)$$

is assured.

Next, we check the admissibility criteria. The Fourier domain is easily handled by applying the time differentiation property,

$$\mathcal{F}[\psi(t)](\omega) = j\omega A_o \sqrt{\pi} e^{-\omega^2/4}. \quad (11.64)$$

Then for  $\omega < 0$

$$\frac{|\Psi(\omega)|^2}{|\omega|} = -A_o^2 \pi \omega e^{-\omega^2/2} \quad (11.65)$$

and for positive frequencies

$$\frac{|\Psi(\omega)|^2}{|\omega|} = A_o^2 \pi \omega e^{-\omega^2/2}. \quad (11.66)$$

The coefficient (11.8) takes the form

$$C_\Psi = -A_o^2 \pi \int_{-\infty}^0 \omega e^{-\omega^2/2} d\omega + A_o^2 \pi \int_0^{\infty} \omega e^{-\omega^2/2} d\omega. \quad (11.67)$$

These integrals defined along the half-line can be evaluated by noting that each integrand can be represented as a derivative, so (11.67) now reads

$$C_\Psi = A_o^2 \pi \int_{-\infty}^0 \frac{d}{d\omega} e^{-\omega^2/2} d\omega - A_o^2 \pi \int_0^{\infty} \frac{d}{d\omega} e^{-\omega^2/2} d\omega \quad (11.68)$$

so

$$C_\Psi = 2\pi A_o^2. \quad (11.69)$$

*Remark.* Note that (11.54) holds for this real-valued analyzing wavelet, as expected. If reconstruction uses only positive values of scale (as per (11.45)), then

$$C_\Psi = \pi A_o^2 \quad (11.70)$$

should be used in place of (11.69).

**Example (Gaussian Transient).** We will generate and discuss the wavelet transform of a Gaussian pulse

$$f(t) = e^{-\alpha t^2}, \quad (11.71)$$

where  $\alpha$  is a positive factor. The analyzing wavelet (11.60) with an applied scale  $a$  and translation  $b$  reads

$$\Psi\left(\frac{t-b}{a}\right) = 2A_0 e^{-b^2/a^2} \cdot \left(\frac{t-b}{a}\right) e^{-\left(\frac{t^2-2bt}{a^2}\right)} \quad (11.72)$$

and the wavelet transform integral breaks down conveniently,

$$W[f(t)](a, b) = \frac{1}{\sqrt{a}} \int_{-\infty}^{\infty} f(t) \Psi\left(\frac{t-b}{a}\right) dt = C(a, b)[I_1 - bI_2], \quad (11.73)$$

where

$$C(a, b) = \frac{2A_0}{a\sqrt{a}} e^{-b^2/a^2} \quad (11.74)$$

and the integrals

$$I_1 \equiv \int_{-\infty}^{\infty} t e^{-(\alpha + (1/a^2))t^2 + (2b/a^2)t} dt = \frac{a\sqrt{\pi}}{\sqrt{a^2\alpha + 1}} \left(\frac{b}{a^2}\right) e^{\left(\frac{b^2}{a^2}\right)\left(\frac{1}{a^2\alpha + 1}\right)} \quad (11.75)$$

and

$$I_2 \equiv \int_{-\infty}^{\infty} e^{-(\alpha + (1/a^2))t^2 + (2b/a^2)t} dt = \frac{a\sqrt{\pi}}{\sqrt{a^2\alpha + 1}} e^{\left(\frac{b^2}{a^2}\right)\left(\frac{1}{a^2\alpha + 1}\right)} \quad (11.76)$$

are evaluated using standard Gaussian integration. The result

$$W[f(t)](a, b) = \frac{-a^2 b \alpha \sqrt{\alpha}}{\sqrt{a(a^2\alpha + 1)}} e^{\left(\frac{b^2}{a^2}\right)\left(\frac{1}{a^2\alpha + 1}\right)} \quad (11.77)$$

is a two-dimensional function of scale and translation shown in Figure 11.3.

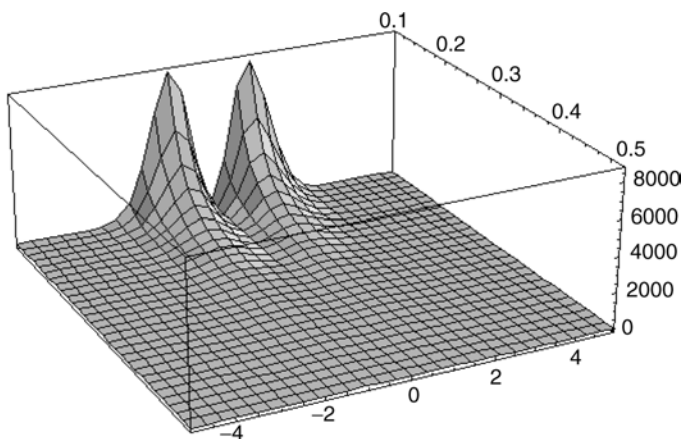


Fig. 11.3. Wavelet transform of Gaussian pulse.

**Example (Rectangular Pulse).** Consider a rectangular pulse of width  $D$  analyzed by the same wavelet as above. The wavelet transform again takes the form

$$W[f(t)](a, b) = \frac{1}{\sqrt{a}} \int_{-\infty}^{\infty} f(t) \psi\left(\frac{t-b}{a}\right) dt = C(a, b)[I_1 - bI_2], \quad (11.78)$$

where as before

$$C(a, b) = \frac{2A_0}{a\sqrt{a}} e^{-b^2/a^2}. \quad (11.79)$$

The integrals now read

$$I_1 \equiv \int_{-D/2}^{D/2} t e^{-(1/a^2)t^2 + (2b/a^2)t} dt \quad (11.80)$$

and

$$I_2 \equiv \int_{-D/2}^{D/2} e^{-(1/a^2)t^2 + (2b/a^2)t} dt. \quad (11.81)$$

The central feature of each integral is the exponential

$$e^{-[f(a)t^2 + g(b)t]}, \quad (11.82)$$

where  $f(a) \equiv 1/a^2$  and  $g(a) \equiv -2b^2/a^2$ . With proper manipulation, (11.81) and (11.82) can be handled analytically. It is a simple matter to complete the square on the argument of the above exponential, transforming it:

$$f(a)t^2 + g(b)t \rightarrow (f(a)t^2 + g(b)t + x) - x, \quad (11.83)$$

where  $x = \frac{1}{4} \frac{g^2(b)}{f(a)}$ . If we let  $y \equiv \sqrt{f(a)}t + \frac{1}{2} \frac{g(b)}{\sqrt{f(a)}}$  and make a substitution of variables, then

$$I_1 \rightarrow \frac{1}{\sqrt{f(a)}} \int_{L_1}^{L_2} \left( y - \frac{1}{2} \frac{g(b)}{\sqrt{f(a)}} \right) e^{-y^2} e^x \cdot \frac{1}{\sqrt{f(a)}} dy, \quad (11.84)$$

where the limits  $L_1 \equiv \frac{-d\sqrt{f(a)}}{2} + \frac{1}{2} \frac{g(b)}{\sqrt{f(a)}}$  and  $L_2 \equiv \frac{d\sqrt{f(a)}}{2} + \frac{1}{2} \frac{g(b)}{\sqrt{f(a)}}$ . This conveniently breaks into two terms,

$$I_1 = \frac{e^x}{f(a)} \left[ \int_{L_1}^{L_2} y e^{-y^2} dy - \frac{1}{2} \frac{g(b)}{\sqrt{f(a)}} \int_{L_1}^{L_2} e^{-y^2} dy \right]. \quad (11.85)$$

Now  $y e^{-y^2} = \left( -\frac{1}{2} \right) \frac{d}{dy} [e^{-y^2}]$  so

$$I_1 = \frac{e^x}{f(a)} \left[ \left( -\frac{1}{2} \right) (e^{-L_2^2} - e^{-L_1^2}) - \frac{1}{2} \frac{g(b)}{\sqrt{f(a)}} [\operatorname{erf}(L_2) + \operatorname{erf}(L_1)] \right]. \quad (11.86)$$

With similar operations, it is easy to show

$$I_2 = \frac{e^x}{\sqrt{f(a)}} [\operatorname{erf}(L_2) + \operatorname{erf}(L_1)]. \quad (11.87)$$

**11.2.3.2 Second Derivative of a Gaussian (“Mexican Hat”).** Taking a further derivative provides an analyzing wavelet

$$\psi(t) = B_0 \cdot \left[ \frac{de^{-t^2}}{dt^2} \right] = -2B_0 [1 - 2t^2] e^{-t^2}. \quad (11.88)$$

It is readily shown that

$$\int_{-\infty}^{\infty} |\psi(t)|^2 dt = 3B_0^2 \sqrt{\frac{\pi}{2}}, \quad (11.89)$$

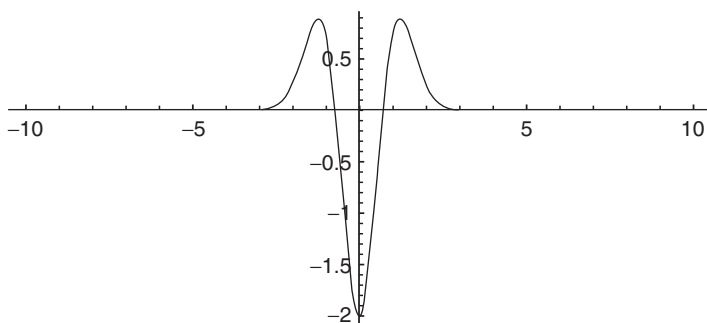


Fig. 11.4. Mexican hat wavelet.

so the normalization constant is

$$B_0 = \frac{1}{\sqrt{3}} \sqrt[4]{2/\pi}. \quad (11.90)$$

This wavelet is shown in Figure 11.4. It has an even symmetry, but equal area above and below the axis, so that (11.9) is satisfied.<sup>1</sup> These details are left as an exercise.

In the Fourier domain, the Mexican hat provides a spectrum

$$\mathcal{F}[\psi(t)](\omega) = -B_0 \omega^2 \sqrt{\pi} e^{-\frac{\omega^2}{4}}, \quad (11.91)$$

and the admissibility coefficient is

$$C_\psi \equiv \int_{-\infty}^{\infty} \frac{|\Psi(\omega)|^2}{|\omega|} d\omega = \frac{2}{3} \sqrt{2\pi}. \quad (11.92)$$

**Example (Gaussian Transient).** Consider the Mexican hat applied to the Gaussian transient of (11.71). The scaled and translated analyzing wavelet is easily found:

$$\psi\left(\frac{t-b}{a}\right) = [d_0 - d_1 t + d_2 t^2] e^{-\frac{b^2}{a^2}} e^{-\left(\frac{t^2 - 2bt}{a^2}\right)}, \quad (11.93)$$

where

$$d_0 = -2B_0 \left[ 1 - 2\frac{b^2}{a^2} \right], \quad (11.94)$$

$$d_1 = \frac{8B_0}{a^2}, \quad (11.95)$$

<sup>1</sup>It might resemble a traditional Mexican *sombrero* in cross section—hence the name.

and

$$d_2 = \frac{4B_0}{a^2}. \quad (11.96)$$

It is left as an exercise to show that the wavelet transform takes the form

$$\mathcal{W}[f(t)](a, b) = \frac{e^{-b^2/a^2}}{\sqrt{a}} [d_0 I_0 - d_1 I_1 + d_2 I_2] \quad (11.97)$$

with

$$I_0 \equiv \int_{-\infty}^{\infty} e^{-(\alpha + (1/a^2))t^2 + (2b/a^2)t} dt = \frac{a\sqrt{\pi}}{\sqrt{a^2\alpha + 1}} e^{\left(\frac{b^2}{a^2}\right)\left(\frac{1}{a^2\alpha + 1}\right)} \quad (11.98)$$

and  $I_1$  as in (11.75), and

$$\begin{aligned} I_2 &\equiv \int_{-\infty}^{\infty} t^2 e^{-(\alpha + (1/a^2))t^2 + (2b/a^2)t} dt \\ &= \frac{a\sqrt{\pi}}{\sqrt{a^2\alpha + 1}} \left( \frac{a^2}{2(a^2\alpha + 1)} \right) \left( 1 + \frac{4(b^2/a^2)}{a^2\alpha + 1} \right) e^{\left(\frac{b^2}{a^2}\right)\left(\frac{1}{a^2\alpha + 1}\right)}. \end{aligned} \quad (11.99)$$

### 11.3 FRAMES

It is much easier to construct frames based upon wavelets than upon the short-time Fourier transform. Building computer applications requires us to work with discrete rather than continuous signal representations. One requirement for signal analysis is that our discrete representation be capable of representing any signal; this is a *completeness* or *spanning* condition. If we also ask that our discrete representation also be *numerically stable*—that is, a small change in a signal results in a small change in its decomposition coefficients—then we must use a *frame* representation.

As a generalization of orthonormal bases, Chapter 3 introduced frames. We remember that  $F = \{f_n : n \in \mathbb{Z}\}$  from a Hilbert space  $H$  is a *frame* if there are  $A, B \in \mathbb{R}$  such that  $A > 0, B > 0$ , and for all  $x \in H$ ,

$$A\|x\|^2 \leq \sum_{n=-\infty}^{\infty} |\langle x, f_n \rangle|^2 \leq B\|x\|^2. \quad (11.100)$$

The frame  $F$  is *tight* if its lower and upper bounds— $A$  and  $B$ , respectively—are equal. Any frame  $F \subset H$  spans  $H$ . A frame  $F$  is *exact* if, when an element is removed from it, it ceases to be a frame. If  $F$  is orthonormal, then  $F$  is tight; in fact,  $A = B = 1$ , and  $F$  is exact.

Recall from Chapter 10 that the Balian–Low theorem imposes strict constraints on the time- and frequency-domain sampling intervals for a frame of windowed Fourier atoms. The time- and frequency-domain sampling intervals,  $T$  and  $\Omega$ , respectively are critical:

- (i) If  $T\Omega < 2\pi$ , then the time-frequency density  $(T\Omega)^{-1}$  exceeds the Nyquist density  $(2\pi)^{-1}$ , and frames of windowed Fourier atoms are possible.
- (ii) If  $T\Omega > 2\pi$ , then we are sampling below the Nyquist density and there are no windowed Fourier frames.
- (iii) If we sample at precisely the Nyquist density,  $T\Omega = 2\pi$ , and  $F = \{w_{m,n}(t) = e^{i\Omega jnt} w(t - mT) : m, n \in \mathbb{Z}\}$  is a frame, then either  $w(t)$  or its Fourier transform  $W(\omega)$  is not well-localized (i.e., not a window function).

In this section we shall see that the wavelet transform is not so restrictive; one can find wavelets  $\psi(t)$  that allow tight frames as long as  $\Omega \neq 0, 1$  and  $T \neq 0$  [14, 15].

### 11.3.1 Discretization

The wavelet discretization procedure is analogous to discretization of time-frequency transforms. Instead of applying a time and frequency increment, we use a time and scale increment on a signal model. The signal model is an admissible wavelet  $\psi(t)$ .

We have noted that the continuous wavelet transform is an inner product. It measures similarity of  $x(t)$  and  $\Psi_{a,b}(t) = \frac{1}{\sqrt{a}}\psi\left(\frac{t-b}{a}\right)$  as follows:

$$X_{\Psi}(a, b) = \langle x, \Psi_{a,b} \rangle = \int_{-\infty}^{\infty} x(t) \overline{\Psi_{a,b}(t)} dt, \quad (11.101)$$

where  $a, b \in \mathbb{R}$ . The wavelet  $\psi(t)$  must satisfy the admissibility condition (11.2). For simplicity, let us consider only the case  $a > 0$  and assume  $\psi(t) \in \mathbb{R}$ . The inner product (11.101) measures the similarity of  $x(t)$  and  $a^{-1/2}\psi_{a,b}(t)$ , which is a dilated version of  $\psi(t)$ , shifted so that it centers at time  $t = b$ .

Suppose we are searching a candidate signal for a prototype shape  $\psi(t)$ . This is a typical signal analysis problem. Perhaps the shape  $\psi(t)$  resembles the signal trace we are trying to detect, or it maybe it responds significantly to some feature—such as an edge—that we can use in a structural description to identify the candidate. If we know the exact location and time-domain extent, we can fix  $a, b \in \mathbb{R}$  and perform the inner product computation. If  $x(t)$  happens to be a scalar multiple (an attenuated or amplified replica) of  $\psi_{a,b}(t)$ , then the Schwarz inequality

$$|\langle x(t), \Psi_{a,b}(t) \rangle| \leq \|x\| \|\Psi_{a,b}\| \quad (11.102)$$

will be an equality. Thus, we threshold the inner product (11.102) as a percentage of  $\|x\| \times \|\psi_{a,b}\|$  to obtain a measure of the match between prototype and candidate signals.

One the other hand, if we do not know the location and time extent—and this is the more common and daunting signal recognition problem—then the task of performing many inner products in (11.102) becomes a computational burden. We can correlate  $\psi_{a,b}(t)$  with local values of  $x(t)$ , say restricted to  $[b - c, b + c]$ , for some  $c > 0$ . But then our inner product varies with the  $L^2$  norm of  $x(t)$  restricted to  $[b - c, b + c]$ . This is conventional normalized cross-correlation, where we divide the inner product by the norm of the candidate signal in a region of interest. Nevertheless, there is in principle a continuous range of scale factors, offsets, and (perhaps) window widths— $a$ ,  $b$ , and  $c$ , respectively. To make the analysis practical, we must choose a discrete set of locations and signal prototype sizes against which we compare the candidate waveform.

Let us start discretization with scale increment  $a_0 > 0$ . Our discussion closely follows [3]. Dyadic decomposition remains the most common. In this case  $a_0 = 2$ , and we have dilation steps  $\psi(t/2)$ ,  $\psi(t)$ ,  $\psi(2t)$ ,  $\psi(4t)$ , and so on. These signal models are, respectively, twice as large, exactly the same, half as large, and one quarter as large in time-domain extent as the root scale element  $\psi(t)$ . If we let  $a = a_0^m$ , then  $\psi(ta_0^{-m})$  is  $a_0^m$  times wider than  $\psi(t)$ .

Now let us decide how to discretize the time domain. A moment's thought shows that we cannot just take  $b = nb_0$  for some  $b_0 > 0$  and  $n \in \mathbb{Z}$ . Note that if  $a_0 = 2$ , then signal prototypes at the scale  $a = a_0^1$  have the shape of  $\psi(t/2)$  and occupy twice the time-domain extent as at unit scale  $a = 1$ . Thus, we should cover the time-domain with step increments that are twice as far apart as at unit scale. That way, the time-domain coverage and overlap between prototypes at unit and double scale is proportional. Similarly, if  $a = a_0^{-1}$ , then models at this scale look like  $\psi(2t)$  and take only half the time-domain width as at unit scale. We could repeat this logic at quadruple and quarter scales, but the point is that time-domain steps for scale  $a = a_0^m$  should be in increments of the product  $b_0 a_0^m$ . For wavelet transform discretization, we employ wavelet atoms of the form

$$\Psi_{m,n}(t) = a_0^{-\frac{m}{2}} \psi\left(\frac{t - nb_0 a_0^m}{a_0^m}\right) = a_0^{-\frac{m}{2}} \psi(a_0^{-m} t - nb_0). \quad (11.103)$$

Note that—in accord with other established notations [3, 10]—we use the first discrete index for the scale variable and use the second for the time variable.

As with the short-time Fourier transform, discretization implies a structural description of a signal. Windowed Fourier transforms produce a tiling of the time-frequency plane by signal atoms that occupy equally sized regions. In contrast, time-scale discretizations, as with wavelets, tile the plane with regions of varying size. Signal atoms tuned to higher frequencies have a more restricted time-domain support (Figure 11.5).

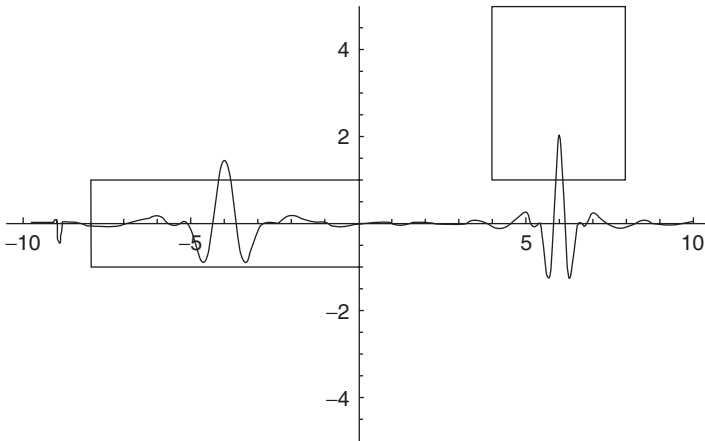


Fig. 11.5. Tiling of the time-frequency plane by a discretized wavelet transform.

### 11.3.2 Conditions on Wavelet Frames

In order for a discretization based on translations and dilations to constitute a frame, certain necessary conditions must obtain. We quote the following theorem.

**Theorem (Necessity of Admissible Wavelet).** Suppose  $\psi(t) \in L^2(\mathbb{R})$ ,  $a_0 > 0$ , and

$$F = \left\{ \Psi_{m,n}(t) = a_0^{-\frac{m}{2}} \psi(a_0^{-m}t - nb_0) \mid m, n \in \mathbb{Z} \right\} \tag{11.104}$$

constitutes a frame with lower and upper bounds  $A$  and  $B$ , respectively. Then

$$Ab_0 \ln a_0 \leq \int_0^\infty \frac{|\Psi(\omega)|^2}{\omega} d\omega \leq Bb_0 \ln a_0 \tag{11.105a}$$

and

$$Ab_0 \ln a_0 \leq \int_0^\infty \frac{|\Psi(\omega)|^2}{\omega} d\omega \leq Bb_0 \ln a_0, \tag{11.105b}$$

where  $\Psi(\omega)$  is the (radial) Fourier transform of  $\psi(t)$ .

**Proof:** Due to Daubechies [3, 15]. ■

*Remark.* Interestingly, for a family of translates and dilates to be a frame,  $\psi(t)$  must be admissible. One might think that the admissibility condition (11.2) is a

technicality, concocted just to make the wavelet transform inversion work. We see now that it is essential for signal analysis using families of scaled, translated atoms—that is, for wavelet frames.

### 11.3.3 Constructing Wavelet Frames

This section covers one method for constructing tight wavelet frames [3, 14, 15]. Let  $v(t)$  be real-valued,  $k$  times continuously differentiable, and approximate the unit step as follows:

$$v(t) = \begin{cases} 0 & \text{if } t \leq 0, \\ 1 & \text{if } t \geq 1. \end{cases} \quad (11.106)$$

An example (Figure 11.6) of  $v \in C^1$  is the following

$$v(t) = \begin{cases} 0 & \text{if } t \leq 0, \\ \sin^2\left(\frac{\pi t}{2}\right) & \text{if } 0 \leq t \leq 1, \\ 1 & \text{if } t \geq 1. \end{cases} \quad (11.107)$$

Now let  $a_0 > 1$  and  $b_0 > 0$ . We will specify two square-integrable signals,  $\psi^+(t)$  and  $\psi^-(t)$ , by their *normalized* radial Fourier transforms,  $\Psi^+(\omega)$  and  $\Psi^-(\omega)$ , respectively. Let  $L = 2\pi[b_0(a_0^2 - 1)]^{-1}$ , define

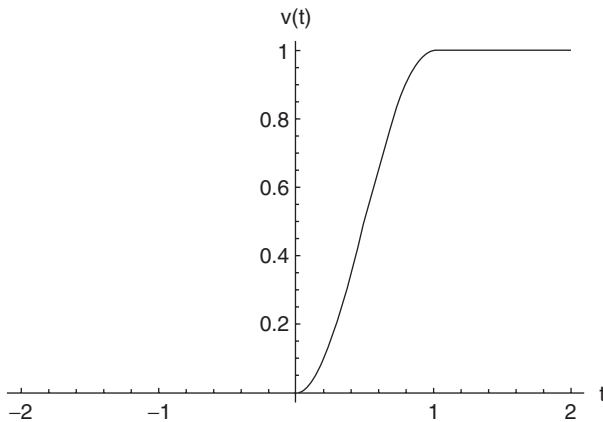
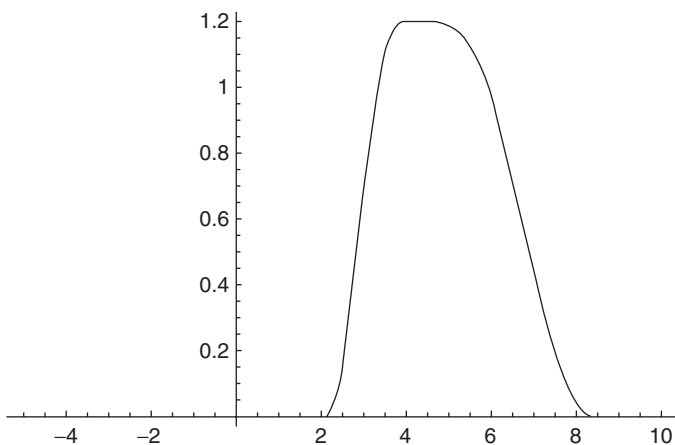
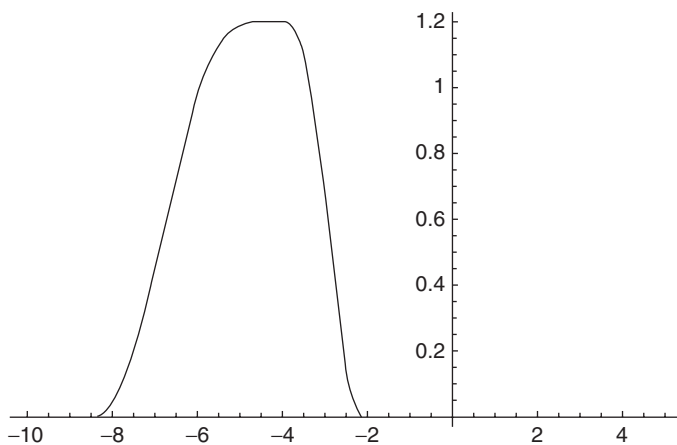


**Fig. 11.6.** Continuously differentiable approximation to the unit step.

$$\Psi^+(\omega) = (\ln a_0)^{-\frac{1}{2}} \begin{cases} 0 & \text{if } \omega \leq L \text{ or } \omega \geq La_0^2, \\ \sin\left(\frac{\pi}{2}v\left(\frac{\omega - L}{L(a_0 - 1)}\right)\right) & \text{if } L \leq \omega \leq La_0, \\ \cos\left(\frac{\pi}{2}v\left(\frac{\omega - La_0}{La_0(a_0 - 1)}\right)\right) & \text{if } La_0 \leq \omega \leq La_0^2 \end{cases} \quad (11.108)$$



(a)



(b)

**Fig. 11.7.** Fourier transforms of atoms used for a tight frame based on translation and dilation: (a)  $\Psi^+(\omega)$  and (b)  $\Psi^-(\omega)$ .

and set  $\Psi^-(\omega) = \Psi^+(-\omega)$ . Then—as Figure 11.7 illustrates for the choices  $a_0 = 2$ ,  $b_0 = 1$ , and  $v(t)$  given by (11.107)— $\Psi^+(\omega)$  is finitely supported on  $[L, La_0^2]$ .

The special construction (11.108) guarantees

$$\sum_{m=-\infty}^{\infty} \left| \Psi^+(a_0^m \omega) \right|^2 = \begin{cases} \frac{1}{\ln(a_0)} & \text{if } 0 < \omega, \\ 0 & \text{if } \omega \leq 0. \end{cases} \tag{11.109}$$

To see this, note that the sequence  $\{a_0^m \mid m \in \mathbb{Z}\}$  decreases toward zero as  $m \rightarrow -\infty$  and increases toward  $\infty$  as  $m \rightarrow \infty$ . If  $\omega > 0$ , then there must be exactly one  $m \in \mathbb{Z}$  such that  $\omega a_0^m \in [L, La_0]$ , the interval of the  $\sin()$  term in (11.108). Then the next summand’s argument  $\omega a_0^{m+1}$  falls in the interval supporting the  $\cos()$  term,  $[La_0, La_0^2]$ . The consequence is that exactly two summands from (11.109) are non-zero: one  $\sin()$  term for  $\omega a_0^m$  and one  $\cos()$  term for  $\omega a_0^{m+1}$ . The sum of their squares is unity justifying (11.109).

We turn to the frame condition. If  $x(t) \in L^2(\mathbb{R})$  and  $X(\omega)$  is its normalized radial Fourier transform,  $X(\omega) = (2\pi)^{-(1/2)} \int x(t) \exp(-j\omega t) dt$ , then following Ref. 3 we find

$$\begin{aligned} & \sum_{m,n=-\infty}^{\infty} \left| \langle x, \Psi^+_{m,n} \rangle \right|^2 \\ &= \sum_{m,n=-\infty}^{\infty} \left| \langle X, \Psi^+_{m,n} \rangle \right|^2 \\ &= \sum_{m,n=-\infty}^{\infty} a_0^m \left| \int_{-\infty}^{\infty} e^{j\omega n b_0 a_0^m} X(\omega) \Psi^+(a_0^m \omega) d\omega \right|^2 \\ &= \sum_m a_0^m \sum_n \left| \sum_k \int_{\frac{k-2\pi}{\Omega}}^{\frac{(k+1)-2\pi}{\Omega}} X(\omega) \Psi^+(a_0^m \omega) e^{j\omega n b_0 a_0^m} d\omega \right|^2. \end{aligned} \tag{11.110}$$

Our strategy has been to break down the integral over  $\mathbb{R}$  in (11.110) into an infinite sum of integrals over a finite interval. Note that we have used the fact that the normalized radial Fourier transform is an isometry:  $\langle x, y \rangle = \langle X, Y \rangle$ . By resorting to the normalized frequency transform, we economize on  $2\pi$  factors. We recall from basic Hilbert space theory that  $\{e_n(t) = (\Omega/2\pi)^{1/2} \exp(jn\Omega t) \mid n \in \mathbb{Z}\}$  is

an orthonormal basis for the Hilbert space  $H = L^2[0, 2\pi/\Omega]$ . Thus, by Chapter 2's abstract version of the Pythagorean theorem,  $\|x\|_2^2 = \sum_n |\langle x, e_n \rangle|^2$ . Above, we set  $\Omega = b_0 a_0^m$ , break up the integral over  $\mathbb{R}$  into sections  $2\pi/\Omega$  wide, and interchange summation and integral. With the substitution  $\omega = \theta + 2\pi \frac{k}{\Omega}$ , (11.110) continues as follows:

$$\begin{aligned} & \left| \sum_m a_0^m \sum_n \left| \int_0^{\frac{2\pi}{\Omega}} e^{j\theta n \Omega} \sum_k X\left(\theta + \frac{2\pi k}{\Omega}\right) \Psi^+\left(a_0^m \theta + \frac{2\pi k}{b_0}\right) d\theta \right|^2 \right. \\ &= \left. \sum_m a_0^m \sum_n \left| \int_0^{\frac{2\pi}{\Omega}} e^{j\theta n \Omega} Y(\theta) d\theta \right|^2 \right. = \sum_m a_0^m \frac{2\pi}{\Omega} \|Y\|_2^2, \end{aligned} \quad (11.111)$$

where  $Y(\theta)$  is the summation in the integrand at the top of (11.111). Having disposed of one summation, we now backtrack, writing the  $\|Y\|_2^2$  term (which is the  $L^2$  norm over  $H$ ) as an integral, first as a sum over a finite interval, and then as over all of  $\mathbb{R}$ :

$$\begin{aligned} \sum_m a_0^m \frac{2\pi}{\Omega} \|Y\|_2^2 &= \frac{2\pi}{b_0} \sum_m \int_0^{\frac{2\pi}{\Omega}} Y(\theta) \overline{Y(\theta)} d\theta \\ &= \frac{2\pi}{b_0} \sum_m \int_{-\infty}^{\infty} |X(\omega)|^2 |\Psi^+(a_0^m \omega)|^2 d\omega = \frac{2\pi}{b_0 \ln a_0} \int_{-\infty}^{\infty} |X(\omega)|^2 d\omega. \end{aligned} \quad (11.112)$$

A similar argument—with a little analytical discomfort but still no pain—gives

$$\sum_{m, n = -\infty}^{\infty} |\langle x, \psi_{m, n}^- \rangle|^2 = \frac{1}{2\pi b_0 \ln a_0} \sum_m \int_{-\infty}^0 |X(\omega)|^2 d\omega, \quad (11.113)$$

where  $\psi^-(t)$  has normalized Fourier transform  $\Psi^-(\omega)$ . Now we claim that  $F = \{\psi_{m, n}^+(t)\} \cup \{\psi_{m, n}^-(t)\}$  is a frame. Indeed, (11.110) through (11.112) and (11.113) imply

$$\sum_{\substack{m, n = -\infty \\ \varepsilon = +, -}}^{\infty} |\langle x, \psi_{m, n}^\varepsilon \rangle|^2 = \frac{2\pi}{b_0 \ln a_0} \int_{-\infty}^{\infty} |X(\omega)|^2 d\omega = \frac{2\pi}{b_0 \ln a_0} \int_{-\infty}^{\infty} |x(t)|^2 dt; \quad (11.114)$$

we see that (11.114) is a tight frame with bounds  $\frac{2\pi}{b_0 \ln a_0}$ .

This construction—albeit clearly contrived—shows how readily we can construct frames for signal analysis based on translations and dilations. We can actually loosen the provisions  $a_0 > 1$  and  $b_0 > 0$  by reviewing the argument. We see that positive and negative integer powers of  $a_0$  were used to justify (11.109). Hence, as long as  $0 < a_0$  and  $a_0 \neq 1$ , the same argument applies (exercise).

Now, it turns out that this frame is not a particularly stellar choice for signal analysis [3]. For one thing, its frame elements do not consist entirely of translations and dilations of a single element; rather, there are two prototype patterns from which the others derive. Worse, however, is the fact that the elements in our special tight frame have poor time-domain decay. Their spectrum has finite support. The consequence is that inner products will have nonzero responses even when the analyzing frame elements are offset some distance away from the candidate signals. The exercises invite the reader to explore these ideas further.

### 11.3.4 Better Localization

We can construct frames based on translations and dilations of a Gaussian root signal. Such frames offer satisfactory time-domain decay. The drawback, however, is that the precise explication of the frame condition is not as elegant as in the previous section’s special construction. There is a sufficient condition for wavelet frames [3], which, despite its ponderous formulation, allows one to estimate frame bounds for  $\psi(t)$  having good time and frequency-domain decay.

**11.3.4.1 Sufficient Conditions for Wavelet Frames.** Let us state some theorems due to Daubechies [3].

**Theorem (Sufficiency).** Suppose  $\psi(t) \in L^2(\mathbb{R})$ ,  $a_0 > 1$ ,  $\Psi(\omega)$  is the (radial) Fourier transform of  $\psi(t)$ , and

$$\beta(s) = \sup_{1 \leq |\omega| \leq a_0} \left( \sum_{m=-\infty}^{\infty} \left| \Psi(a_0^m \omega) \right| \left| \Psi(a_0^m \omega + s) \right| \right). \tag{11.115}$$

Further assume that

$$\inf_{1 \leq |\omega| \leq a_0} \left( \sum_{m=-\infty}^{\infty} \left| \Psi(a_0^m \omega) \right|^2 \right) > 0; \tag{11.116a}$$

$$\sup_{1 \leq |\omega| \leq a_0} \left( \sum_{m=-\infty}^{\infty} \left| \Psi(a_0^m \omega) \right|^2 \right) < \infty; \tag{11.116b}$$

and, for some  $\varepsilon > 0$ ,  $\beta(s)$  decays as fast as  $(1 + |s|)^{-1-\varepsilon}$ . Then there is  $B_0 > 0$  such that for any  $b_0 < B_0$ ,  $F = \{\psi_{m,n}(t) = a_0^{-(m/2)}\psi(a_0^{-m}t - nb_0) \mid m, n \in \mathbb{Z}\}$  is a frame.

**Corollary (Bounds).** With the theorem's assumptions and notation, let

$$C = \sum_{\substack{k=-\infty \\ k \neq 0}}^{\infty} \left[ \beta\left(\frac{2\pi k}{b_0}\right) \beta\left(-\frac{2\pi k}{b_0}\right) \right]^{\frac{1}{2}}, \quad (11.117)$$

and suppose  $b_0 < B_0$ . Then  $F = \{\psi_{m,n}(t) \mid m, n \in \mathbb{Z}\}$  has lower and upper frame bounds,  $A$  and  $B$ , respectively:

$$A = \frac{1}{b_0} \left[ \inf_{1 \leq |\omega| \leq a_0} \left( \sum_{m=-\infty}^{\infty} |\Psi(a_0^m \omega)|^2 \right) - C \right] \quad (11.118a)$$

and

$$B = \frac{1}{b_0} \left[ \sup_{1 \leq |\omega| \leq a_0} \left( \sum_{m=-\infty}^{\infty} |\Psi(a_0^m \omega)|^2 \right) + C \right]. \quad (11.118b)$$

**Proofs:** Again due to Daubechies [3, 15].

*Remark.* These technical conditions will be met, for example, if  $\psi(t)$  obeys the following:

- Its time- and frequency-domain decay rates are not too slow.
- Its spectrum is zero for  $\omega = 0$ :  $\Psi(0) = \int \psi(t) dt = 0$ .

The conditions do imply that  $\psi(t)$  is admissible (11.2). Moreover, under these mild constraints, there will be many combinations of scale and time steps for which  $F$  comprises a frame [3].

**11.3.4.2 Example: Mexican Hat.** Let us consider the Mexican hat function, introduced in Section 11.2.3.2 (Figure 11.4). This signal is the second derivative of the Gaussian:  $\psi(t) = \exp(-t^2/2)$ . Normalizing,  $\|\psi\|_2 = 1$ , gives

$$\psi(t) = \frac{2\pi}{\sqrt{3}} \frac{1}{4} (1 - t^2) \exp\left(-\frac{t^2}{2}\right). \quad (11.119)$$

Table 11.2 repeats some estimates for the lower and upper frame bounds,  $A$  and  $B$ , respectively, for frames based on translations and dilations of the Mexican hat [3].

Notice that as the time domain increment  $b_0$  increases, then frame lower bound  $A$  decreases much faster toward zero; we might interpret this as indicating that there are finite energy signals that are more and more orthogonal to the frame elements. Decreasing the scale domain increment  $a = a_0^{1/k}$ ,  $k = 1, 2, 3, 4$ , etc., mitigates this tendency.

**TABLE 11.2. Lower and Upper Bound Estimates for Frames Based on the Mexican Hat**

$b_0$	$A$	$B$	$a = 2^1$
0.25	13.091	14.183	
0.50	6.546	7.092	
0.75	4.364	4.728	
1.0	3.223	3.596	
1.25	2.001	3.454	
1.50	0.325	4.221	
1.75	—	—	No frame

$b_0$	$A$	$B$	$a = 2^{1/2}$
0.25	27.273	27.278	Nearly exact
0.50	13.673	13.676	
0.75	9.091	9.093	
1.0	6.768	6.870	
1.25	4.834	6.077	
1.50	2.609	6.483	
1.75	0.517	7.276	

$b_0$	$A$	$B$	$a = 2^{1/3}$
0.25	40.914	40.914	Nearly exact
0.50	20.457	20.457	
0.75	13.638	13.638	
1.0	10.178	10.279	
1.25	7.530	8.835	
1.50	4.629	9.009	
1.75	1.747	9.942	

$b_0$	$A$	$B$	$a = 2^{1/4}$
0.25	55.552	55.552	Nearly exact
0.50	27.276	27.276	
0.75	18.184	18.184	
1.0	13.586	13.690	
1.25	10.205	11.616	
1.50	6.594	11.590	
1.75	2.928	12.659	

What time- and scale-domain increments make the best choices? To answer this question, we recall the formula for reconstructing a signal  $x(t)$  from frame elements (Section 3.3.4). Let  $\{\psi_k(t): k \in \mathbb{Z}\}$  enumerate the doubly indexed frame  $F$  of translations and dilations of  $y(t)$ ,  $F = \{\psi_{m,n}(t)\}$ . Then,

$$x = \sum_k \langle x, S^{-1}\psi_k \rangle \psi_k = \sum_k \langle x, \psi_k \rangle S^{-1}\psi_k, \quad (11.120)$$

where  $S = T^*T$ ;  $T$  is the frame operator,  $T_F(x)(k) = \langle x, \psi_k \rangle$ ; and  $T^*$  is the frame operator adjoint,  $T^*(s) = \sum_{k=-\infty}^{\infty} s(k)\psi_k$ , where  $s(k) \in l^2(\mathbb{Z})$ . Now by the Frame Characterization Theorem of Section 3.3.4.3, we can write the frame condition as  $AI \leq S \leq BI$ , where  $I$  is the identity operator on  $L^2(\mathbb{R})$ .

Suppose that the lower and upper frame bounds are almost equal, a condition that several of the alternatives in Table 11.2 allow [3]. As  $B \rightarrow A$ ,  $\varepsilon = B/A - 1 \rightarrow 0$ , and the operator  $S = T^*T$  is close to a midpoint operator between  $AI$  and  $BI$ :  $S \approx \frac{A+B}{2}I$ . Thus,  $S^{-1} \approx \frac{2}{A+B}I$ , and (11.120) becomes

$$x = \sum_k \langle x, S^{-1}\psi_k \rangle \psi_k \approx \frac{2}{A+B} \sum_k \langle x, \psi_k \rangle \psi_k. \quad (11.121)$$

Equation (11.121) is a simple, approximate reconstruction formula for  $x(t)$  that is valid when the frame  $F$  is almost exact. Thus, choosing time and scale dilation factors that provide an almost exact frame facilitates reconstruction of  $x(t)$  from its frame coefficients.

The next section develops wavelet theory that provides not just frames, but orthonormal bases for finite energy signals based on translations and dilations of a single prototype signal.

## 11.4 MULTIREOLUTION ANALYSIS AND ORTHOGONAL WAVELETS

After the publication of Grossmann and Morlet's paper in 1984, wavelet methods attracted researchers—including the present authors—from a broad range of scientific and engineering disciplines.<sup>2</sup> The new scale-based transform posed an alternative to short-time Fourier techniques for seismic applications [13, 16]. It facilitated the construction of frames (Section 11.3), which are necessary for numerically stable signal modeling [14, 15]. Wavelets were used for analyzing sound waves [17] and adapted to multiscale edge detection [18]. Academic meetings were exciting. It was still unclear how powerful this tool could become.

<sup>2</sup>“Such a portentous and mysterious monster roused all my curiosity” (Melville).

The wavelet transform was but one of several mixed domain signal transforms known in the mid-1980s. Among the others were time-frequency techniques such as the short-time Fourier transform and the Wigner distribution (Chapter 10). Wavelet analysis, in contrast, represents a scale-based transform.

Recall that if we set  $\Psi_{a,b}(t) = \frac{1}{\sqrt{a}}\Psi\left(\frac{t-b}{a}\right)$ , then the wavelet transform

$$X_w(a,b) = \langle x, \Psi_{a,b} \rangle = \int_{-\infty}^{\infty} x(t)\overline{\Psi_{a,b}(t)} dt \tag{11.122}$$

measures the similarity of  $x(t)$  and the scaled, shifted wavelet  $\Psi_{a,b}(t)$ . This makes it a multiscale shape detection technique.

Because Grossmann and Morlet’s wavelets are also bandpass filters, the convolution (11.122) effects a frequency selection from the source signal  $x(t)$ . Assuming that  $\psi(t) \in L^2(\mathbb{R})$  is an analyzing wavelet and  $\Psi(\omega)$  is its radial Fourier transform, the inverse wavelet transform is given by

$$x(t) = \frac{1}{C_\Psi} \int_0^\infty \int_{-\infty}^\infty X_w(a,b) \frac{\Psi_{a,b}(t)}{a^2} db da, \tag{11.123}$$

where  $C_\Psi$  is the admissibility factor,  $C_\Psi = \int_{-\infty}^\infty \frac{|\Psi(\omega)|^2}{|\omega|} d\omega < \infty$ . Thus, the transform (11.122) characterizes the signal  $x(t)$  and can be the basis for signal comparisons, matching, and interpretation.

To accomplish wavelet-based signal analysis on a computer requires, of course, that the transform be discretized. For example, we might study transform coefficients of the form  $x_w(m,n) = X_w(m\Delta, nT) = \langle x(t), \Psi_{m\Delta, nT}(t) \rangle$ . This leads to the construction of wavelet frames, which support signal characterization and numerically stable representation. These benefits would be all the stronger if a wavelet frame could be somehow refined into an orthonormal basis.

Nonetheless, it was the intuition of pioneering researchers that—just as they had shown for windowed Fourier expansions—a Balian–Low type of result would hold for wavelets, precluding orthonormal bases. As exciting as the developments of the 1980s had been, the prospects for well-localized short-time Fourier bases appeared quite bleak. The critical time-frequency sampling density,  $T\Omega = 2\pi$ , does not permit frames let alone orthogonal windowed Fourier bases, unless either the windowing function  $w(t)$  or its Fourier transform  $W(\omega)$  fails to be well-localized:  $\|tw(t)\|_2 = \infty$  or  $\|\omega W(\omega)\|_2 = \infty$  (Section 10.5.1). Anticipating equally negative results for the new scale-based transforms too, Meyer [19] tried to prove a version of Balian–Low for wavelets. To his own and everyone else’s surprise, he failed and instead found an orthonormal wavelet basis!

Meyer’s basis [4,19] proceeds from a wavelet  $\psi(t)$  whose normalized Fourier transform is given by

$$\Psi(\omega) = \begin{cases} \frac{j\omega}{\sqrt{2\pi}} \sin \left[ \frac{\pi}{2} \upsilon \left( \frac{3|\omega|}{2\pi} - 1 \right) \right] & \text{for } \frac{2\pi}{3} \leq |\omega| \leq \frac{4\pi}{3}, \\ \frac{j\omega}{\sqrt{2\pi}} \cos \left[ \frac{\pi}{2} \upsilon \left( \frac{3|\omega|}{2\pi} - 1 \right) \right] & \text{for } \frac{4\pi}{3} \leq |\omega| \leq \frac{8\pi}{3}, \\ 0 & \text{otherwise.} \end{cases} \tag{11.124}$$

In (11.124)  $\upsilon(t)$  is a  $C^k$  signal, where  $\upsilon(t) \approx u(t)$ , except on  $(0, 1)$ . It specializes the  $\upsilon(t)$  used earlier; the extra proviso is  $\upsilon(t) + \upsilon(1 - t) = 1$ . Figure 11.8 shows Meyer's wavelet  $\psi(t) = \mathcal{F}^{-1}[\Psi(\omega)](t)$ .

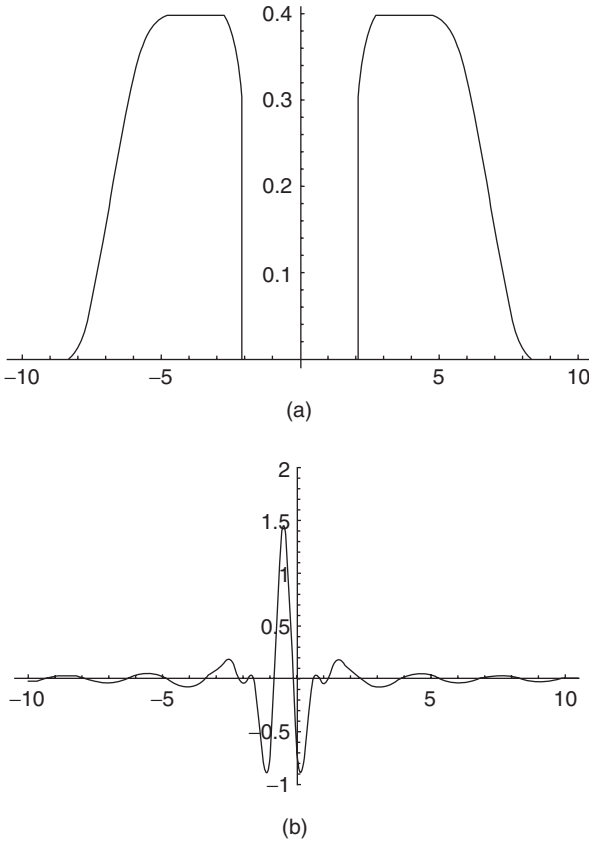


**Fig. 11.8.** Its normalized Fourier transform (a) and the Meyer wavelet (b). Its translations and dilations form an orthonormal basis for  $L^2$  signals.

Until this discovery, mathematicians had more or less given up on finding orthonormal expansions for  $L^2(\mathbb{R})$  using smooth basis elements. It was assumed that there had to be discontinuities in the time domain such as with Haar’s basis, which was discovered some 75 years earlier [20], or in the frequency domain, such as with Shannon’s  $\text{sinc}(t) = \sin(t)/t$  basis of Ref. 21 (Section 3.3.3). A later construction of Strömberg provides another orthonormal basis of continuous functions [22]; it predated Meyer’s function by a few years and had been largely overlooked.

From the desks of several other mathematicians, more examples of orthonormal wavelet bases soon issued. But—except for the intricate calculations, carefully concocted estimations, and miraculous cancellations—there seemed to be no connection between these diverse constructions. Could there be no rules for building them? It was a fascinating mess.

### 11.4.1 Multiresolution Analysis

The unifying breakthrough came when Mallat [23] and Meyer elaborated the concept of a *multiresolution analysis* (MRA) for square-integrable signals. A computer vision researcher, Mallat was especially inspired by the similarities between some of the recent wavelet basis developments and work in pyramid decompositions for signal and image analysis such as the Laplacian pyramid [24], quadrature mirror filter banks employed in communication engineering [25], and scale space decompositions [26–28].

The MRA concept leads to a rich theory of the scale-based structure of signals. As a bonus, the MRA establishes a set of rules for constructing a wide range of orthonormal wavelet bases. Mallat and Meyer found the rules for building orthonormal wavelet bases in a quite unexpected place: the very applied areas of multiscale signal decomposition, image analysis, and efficient communication engineering. The discovery of important theoretical concepts out of utterly practical problems seems to be a distinct characteristic within the new discipline of wavelet analysis.

**11.4.1.1 Definition.** A multiresolution analysis of  $L^2(\mathbb{R})$  is an abstract structure, but it has close links to several signal analysis ideas that we have already covered. We present the formal definition and develop some of the theory of bases made up of translations of a single root signal. The presentation follows closely and may be considered a tutorial on the classic papers [23, 29].

**Definition (Multiresolution Analysis).** A *multiresolution analysis* (or *multiresolution approximation*, MRA) is a chain of closed subspaces  $\{V_i; i \in \mathbb{Z}\}$  in  $L^2(\mathbb{R})$  such that the following conditions hold:

(i) The  $V_i$  are nested within one another:  $\dots \subset V_{-1} \subset V_0 \subset V_1 \subset V_2 \subset \dots$

(ii) The union of the  $V_i$  is dense in  $L^2(\mathbb{R})$ :  $\overline{\bigcup_{n=-\infty}^{\infty} V_i} = L^2(\mathbb{R})$ .

- (iii) The intersection of the  $V_i$  is the signal of zero norm (zero almost everywhere), which we write  $\bigcap_{i=-\infty}^{\infty} V_i = 0$ .
- (iv) Elements of the spaces are dyadically scaled (more precisely, *dilated*) versions of one another:  $x(t) \in V_i \Leftrightarrow x(2t) \in V_{i+1}$ .
- (v) For any  $x(t) \in V_0$  and any  $k \in \mathbb{Z}$ ,  $x(t-k) \in V_0$ .
- (vi) There is an isomorphism from  $V_0$  onto the Hilbert space of square-summable discrete signals  $l^2$ :  $V_0 \rightarrow l^2$  such that for any  $k \in \mathbb{Z}$ , if  $I(x(t)) = s(n) \in l^2$ , then  $I(x(t-k)) = s(n-k)$ .

*Remark.* We give the classic definition and notation for the MRA [23]. It has become common to index the  $V_i$  in the other direction:  $V_i \supset V_{i+1}$ . So readers must pay close attention to an author's  $V_i$  indexing.

Nowadays, many treatments (for instance, Refs. 3, 8, and 9) replace (vi) with the requirement that  $V_0$  has an orthonormal basis of translates of a single finite-energy signal:  $\{\phi(t-n) \mid n \in \mathbb{Z}\}$ . This works. But so early on, it also seems incredible; we prefer to proceed from the apparently weaker criterion. In Section 11.4.2 we demonstrate that there is indeed a special function in  $V_0$ , called a *scaling function*, whose translates comprise an orthonormal basis of  $V_0$ .

Finally, note that by an *isomorphism* in (vi) we mean only a bounded, one-to-one, linear map, with a bounded inverse. Some mathematics texts, for example [30], define the term to mean also  $\langle Ix, Iy \rangle = \langle x, y \rangle$ , which implies an *isometry*; this we do not assume herein. The last MRA property (vi) is very strong, though. The isomorphism is a bounded linear map: There is an  $M$  such that  $\|Ix\| \leq M\|x\|$  for all  $x \in V_0$ . For linear maps this is equivalent to continuity.  $\text{Range}(I)$  is all of  $l^2$ . If it were an isometry, then we would be easily able to show that  $V_0$  has a scaling function; but with our weaker assumption, this requires quite a bit more work.

**11.4.1.2 Examples.** Although it is rich with mathematical conditions, which might appear difficult to satisfy, we can offer some fairly straightforward instances of multiresolution analyses. Here are three examples where the root spaces consist of:

- Step functions;
- Piecewise linear functions;
- Cubic splines.

Note that the root spaces in these examples contain increasingly smooth signals.

**Example (Step Functions).** It is easiest to begin with a root space  $V_0$  comprised of step functions and define the spaces of non-unit scale by dilation of  $V_0$  elements. Let  $u(t)$  be the analog unit step signal and set  $V_0 = \{x(t) \in L^2(\mathbb{R}) \mid \text{for all } n \in \mathbb{Z}, \text{ there is a } c_n \in \mathbb{R} \text{ such that } x(t) = c_n[u(t-n) - u(t-n-1)] \text{ for } t \in (n, n+1)\}$ . So elements of  $V_0$  are constant on the open unit intervals  $(n, n+1)$ . The boundary values of the

signals do not matter, since  $\mathbb{Z}$  is a countable set and thus has Lebesgue measure zero. We define  $V_i = \{y(t) \in L^2(\mathbb{R}) \mid \text{for some } x(t) \in V_0, y(t) = x(2^i t)\}$ . Thus,  $V_i$  signals are constant on intervals  $(n2^{-i}, (n+1)2^{-i})$ , where  $n \in \mathbb{Z}$ . Let us show that each of the MRA properties holds.

- (i) Signals that are constant on  $(n2^{-i}, (n+1)2^{-i})$  for all  $n \in \mathbb{Z}$  will also be constant on subintervals  $(n2^{-i-1}, (n+1)2^{-i-1})$ , so the first property holds.
- (ii) From Chapter 3, we know that the step functions are dense in  $L^2(\mathbb{R})$ ; since arbitrarily narrow steps are contained in  $V_i$  for  $i$  sufficiently large, we know that the  $V_i$  are dense in  $L^2(\mathbb{R})$ .
- (iii) For a nonzero signal to be in all of the  $V_i$ , it would have to have arbitrarily wide steps, so the intersection property must be satisfied.
- (iv) This is how we define the  $V_i$  for  $i \neq 0$ .
- (v) Integral translates of signals in  $V_0$  are obviously in  $V_0$ , since an integral translate is still constant on unit intervals.
- (vi) If  $x(t) \in V_0$ , and  $x(t) = c_n(u(t-n) - u(t-n-1])$  for  $t \in (n, n+1)$ , then we set  $I(x(t)) = s(n)$ , where  $s(n) = c_n$  for all  $n \in \mathbb{Z}$ ; then  $I(x(t-k)) = s(n-k)$ , and  $I$  is an isomorphism. This is left as an exercise.

This MRA is the orthonormal basis of Haar in modern guise [20]. For analyzing blocky signals, this simple MRA is appropriate (Figure 11.9a). But when studying smoother signals, decompositions on the Haar set require quite a few coefficients in

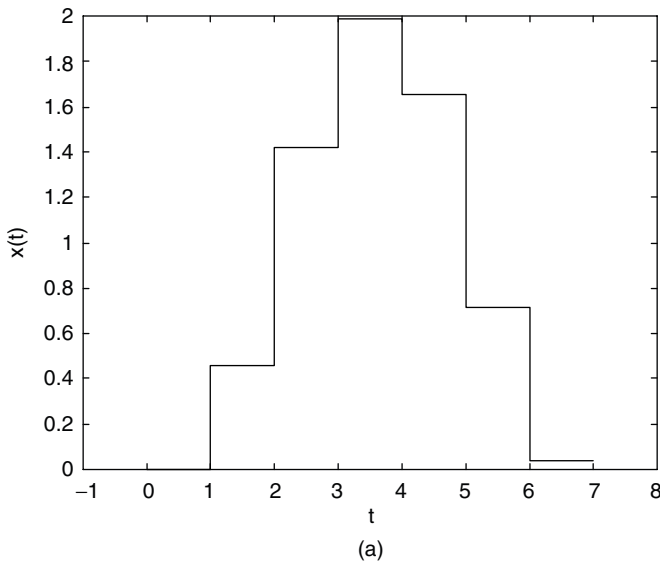


**Fig. 11.9.** Typical elements of an MRA built by step functions (a), piecewise linear functions (b), and cubic splines (c).

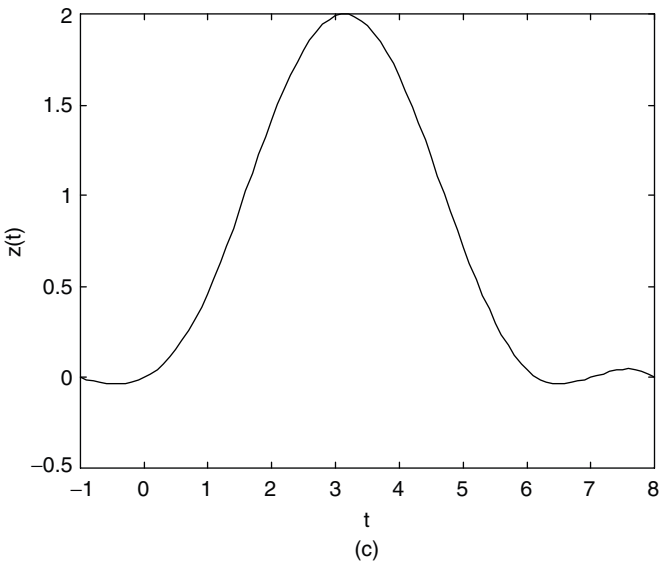
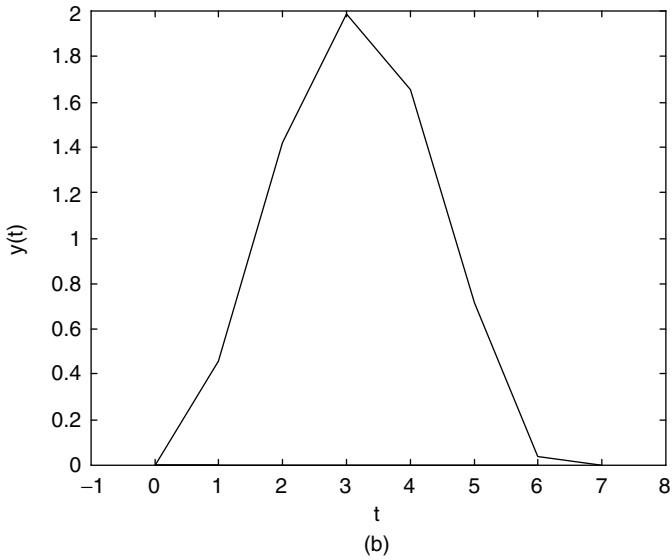


**Fig. 11.9** (Continued)

order to smooth out the discontinuities present in the basis elements. So the approximations are often quite inefficient.

**Example (Piecewise Linear Functions).** Let us refine the multiscale structure so that it employs piecewise continuous signals. MRAs using such functions are better

for signal analysis purposes when we have to interpret signals that do not contain abrupt jumps in value (Figure 11.9b). Let us define  $V_0$  to be the  $L^2(\mathbb{R})$  continuous functions that are piecewise linear on integral intervals  $[n, n+1]$ . We define the remaining spaces via the MRA's dilation property (iv):  $x(t) \in V_i \Leftrightarrow x(2t) \in V_{i+1}$ . The six MRA properties are clear, except perhaps for density (ii) and the isomorphism (vi). Note, however, that a piecewise continuous  $x(t) \in V_0$  is determined uniquely by its values on integers. We define  $I(x(t)) = s(n)$ , where  $s(n) = x(n)$  for all  $n \in \mathbb{Z}$ . We can approximate a step function to arbitrary precision with piecewise linear functions, and the step functions are dense in  $L^2(\mathbb{R})$ , so the second MRA property holds. Strömberg [22] elaborated this MRA's theory.

**Example (Cubic Splines).** A more interesting example relies on cubic splines. Here, the root space  $V_0$  consists of all functions that are twice continuously differentiable and equal to a cubic polynomial on integral intervals  $[n, n+1]$ . Again, dilation defines the other  $V_i$ :  $x(t) \in V_i \Leftrightarrow x(2t) \in V_{i+1}$ . Numerical analysis texts, (e.g., Ref. 31, show that a continuous function can be approximated to any precision with a cubic spline, so the  $V_i$  are dense in  $L^2(\mathbb{R})$ .

As we continue to develop MRA theory, we shall return to these examples.

**11.4.1.3 Links to Signal Analysis Legacy.** Before expounding more theory, let us reflect on how the multiresolution analysis concept echoes many ideas from previous multiscale signal analysis techniques. In fact, stripped of their mathematical formalism, several of the multiresolution analysis properties (i)–(vi) have conceptual precedents in prior multiscale representations. Others embody ideas that were only implicit in the intuitive constructs of earlier methods of interpretation.

For example, the nested sequence of subspaces in (i) embodies the concept of the representations becoming ever finer in resolution. The inclusion property indicates that every coarse representation of a signal may also be considered to be a fine resolution version of some other waveform that has an even coarser shape. The subspaces are closed; each  $V_i$  contains the limit of its convergent function sequences. Coarse resolution representations are useful because:

- Using them can reduce the time required for pattern searches, such as in elementary edge and feature detection applications [32–34].
- Some signal features appear only at certain scales [35].

We need closure to guarantee that given a finite-energy signal  $x(t)$  and an approximation error, there is some  $V_i$  that approximates  $x(t)$  to within the tolerance.

What does the union property (ii) mean? If one looks in a sufficiently fine resolution space, then there is a finite energy signal that is arbitrarily close to any given signal.  $V_i$  signals are only approximations of real signals, but we can choose them to be very good approximations. Notice that (i) and (ii) encapsulate the intuitive notion of earlier researchers that scale is critical for structural decompositions of signals.

To interpret a signal we have to determine either the specific time extents of signal shapes, or we must search for shapes across all scales. This insight is the motivation behind scale space analysis [26–28], which we first considered in Chapter 4.

The intersection property (iii) tells us that, from a scale-based signal analysis standpoint, any meaningful signal must be visible to the MRA at some scale. That is, if a signal is composed of structures that have such a fine scale that it must appear in all the subspaces, then this signal must be the almost everywhere zero signal.

The next property concern resolution. Next, if a function is in space  $V_i$ , then its dilation by a factor of 2 is in the next higher resolution space  $V_{i+1}$ . Furthermore, its dilation by a factor of 1/2 is in the lower resolution space  $V_{i-1}$ . Thus, the implication of (iv) is that one ascends and descends in resolution by means of dilations, such as in the classic Laplacian pyramid construction [24].

The subspace  $V_0$  contains signals that resolve features to the unit of measure. Signals in  $V_0$  may be translated by integral amounts, and we are assured that the result remains in the root space (v).

Lastly, discrete samples characterize the MRA functions that model the signals. Property (vi) formalizes this by requiring an isomorphism between  $V_0$  and the square-summable sequences of real numbers. This discretization has the further property that the discrete representations of functions are translated when the function is translated. Without this invariance, the discrete samples associated with a waveform  $x(t)$  in  $V_0$  might change with the translation of  $x(t)$  by integral steps. For the lower resolution spaces  $V_i$ ,  $i < 0$ , translation invariance does not hold. It will become apparent in applications that the overall situation for translation invariance is far from satisfactory; indeed, it is problematic.

**11.4.1.4 Bases of Translates: Theory.** Our first theoretical result on MRAs comes right out of the sixth criterion. It shows that the root space  $V_0$  has a basis, consisting of integral translates of a single square-integrable signal. Multiresolution analysis exploits the special properties of such bases.

**Proposition (Basis).** If  $\{V_i \mid i \in \mathbb{Z}\}$  is an MRA in  $L^2(\mathbb{R})$ , then there is  $e(t) \in V_0$  such that  $\{e(t - k) \mid k \in \mathbb{Z}\}$  is a basis for  $V_0$ .

**Proof:** Let  $\delta(n - k)$  be the discrete delta signal delayed by  $k \in \mathbb{Z}$ .  $\{\delta(n - k) \mid k \in \mathbb{Z}\}$  is an orthonormal basis for  $l^2$ . Let  $I: V_0 \rightarrow l^2$  be the isomorphism of MRA property (vi). Since  $I$  is onto, we may set  $e_k(t) = I^{-1}(\delta(n - k))$ . Then  $\{e_k(t) \mid k \in \mathbb{Z}\}$  is a basis for  $V_0$ . However,  $I(e_0(t)) = \delta(n)$ , so that the translation-invariance provision of (vi) also implies  $I(e(t - k)) = \delta(n - k)$ , whence  $e_k(t) = e(t - k)$ . ■

The proposition guarantees a basis that is useful for those pattern matching applications where we expect candidate signals containing the shape of the root element. The basis elements comprise our model or prototype signals. For computational purposes, we prefer such bases to be orthonormal, since that simplifies expansion coefficient computations. But, again, orthogonality requires more work. Let us explore some of the theory of such bases.

**Definition (Riesz Basis).**  $E = \{e_n \mid n \in \mathbb{Z}\}$  is an *unconditional* or *Riesz basis* in a Hilbert space  $H$  if

- (i)  $E$  spans  $H$ : For any  $x \in H$ , there is  $s \in \ell^2$  such that

$$x = \sum_{n=-\infty}^{\infty} s(n)e_n. \quad (11.125a)$$

- (ii) There are  $0 < A \leq B < \infty$  such that for any  $s \in \ell^2$ ,

$$A\|s\| \leq \left\| \sum_{n=-\infty}^{\infty} s(n)e_n \right\| \leq B\|s\|. \quad (11.125b)$$

The constants  $A$  and  $B$  are called the *lower* and *upper Riesz basis bounds*, respectively.

Notice how (11.125b) cross-couples the norms of  $H$  and  $\ell^2$ . An orthonormal basis is also a Riesz basis. Note too that the lower bound condition in (11.125b) implies that a Riesz basis is linearly independent (exercises). The next result shows that property (vi) of an MRA is equivalent to  $V_0$  having a Riesz basis.

**Theorem (Riesz Basis Characterization).**  $E = \{e_k \mid k \in \mathbb{Z}\}$  is a Riesz basis in a Hilbert space  $H$  if and only if:

- (i) There is an isomorphism  $I$  from  $H$  onto  $\ell^2$  such that  $I(e_k) = \delta(n - k)$ , where  $\delta(n)$  is the discrete delta.  
 (ii)  $I^{-1}$  is bounded.

**Proof:** Let  $E = \{e_k \mid k \in \mathbb{Z}\}$  be a Riesz basis in  $H$ . Since for any  $x \in H$ , there is  $s \in \ell^2$  such that (11.125a) holds, we may set  $Ix = s$ . This map is well-defined by the linear independence of  $E$ ; that is, for each  $x$ , the coefficient sequence  $\{s(n)\}$  is unique. The linearity follows from the properties of the square-summable sequences, and clearly  $I(e_k) = \delta(n - k)$ . The map is also onto, because any  $s \in \ell^2$  defines an element of  $H$  as in (11.125a). This sum converges in  $H$  by the upper bound inequality in (11.125b). The boundedness of  $I$  follows as well:  $\|Ix\| = \|s\| \leq A^{-1}\|x\|$ . The inverse  $J = I^{-1}$  exists because  $I$  is one-to-one and onto (a *bijection*).  $\|Js\| = \|x\| = \|\sum s(k)e_k\| \leq B\|s\|$  by (11.125b), so  $J$  is bounded too.

Conversely, let  $I: H \rightarrow \ell^2$  be an isomorphism obeying (i) and (ii). Let  $x \in H$ . We need to show that  $x$  is in the closure of  $\text{Span}(E)$ . Let  $Ix = s \in \ell^2$ . In general, it does not necessarily follow that if an isomorphism is bounded, then its inverse is bounded. However, we are assuming  $J = I^{-1}$  is bounded, so it is also continuous [30]. Thus,

$$\lim_{N \rightarrow \infty} J \left( \sum_{k=-N}^N s(k)\delta(n-k) \right) = \sum_{k=-\infty}^{\infty} s(k)J(\delta(n-k)) = \sum_{k=-\infty}^{\infty} s(k)e_k, \quad (11.126)$$

and  $x$  is a limit of elements in  $\text{Span}(E)$ . Let  $\|I\| = A^{-1}$  and  $\|J\| = B$ . Then  $A$  and  $B$  are the lower and upper Riesz bounds for  $E$  (11.125b). ■

**Corollary.** Property (vi) of an MRA is equivalent to  $V_0$  having a Riesz basis of translates.

**Proof:** Since the isomorphism  $I$  in (vi) has a bounded inverse and  $I$  is onto, we may find  $e_k(t)$  such that  $I(e_k(t)) = \delta(n - k)$ , where  $\delta(n)$  is the discrete delta signal. The theorem tells us that  $\{e_k(t) \mid k \in \mathbb{Z}\}$  is a Riesz basis. The translation invariance for  $V_0$  implies that  $e_k(t) = e(t - k)$ . ■

The conditions (11.125a) and (11.125b) for a Riesz basis resemble the criterion for a frame, which we studied in Chapters 3 and 10. Indeed, the following corollary shows that a Riesz basis is a frame. Of course, the converse is not true; a Riesz basis must be linearly independent, while frames can be overcomplete.

**Corollary (Frame).** If  $E = \{e_k \mid k \in \mathbb{Z}\}$  is a Riesz basis in a Hilbert space  $H$ , then  $E$  is a frame.

**Proof:** Let  $I: H \rightarrow l^2$  be the isomorphism promised in the Riesz basis characterization:  $I(e_k) = \delta(n - k)$ . Let  $I^*$  be the Hilbert space adjoint operator for  $I$ . We introduced the adjoint operator in Chapter 3 and therein applied it to the study of frames (Section 3.3.4). The adjoint cross-couples the inner product relations of  $H$  and  $l^2$  so that if  $s(n)$  is square-summable, then  $\langle Ix, s \rangle = \langle x, I^*s \rangle$ . Note that  $I^*: l^2 \rightarrow H$  is an isomorphism, bounded, and in fact  $\|I^*\| = \|I\|$ . For example, to show  $I^*$  is one-to-one, let  $I^*v = I^*w$  for some  $v(n), w(n) \in l^2$ . Then for any  $h \in H$ ,  $\langle h, I^*v \rangle = \langle h, I^*w \rangle$ . But this implies  $\langle Ih, v \rangle = \langle Ih, w \rangle$ . Since  $I$  is onto and  $h$  is arbitrary,  $Ih$  could be any finite-energy discrete signal. In other words,  $\langle s, v \rangle = \langle s, w \rangle$  for all  $s \in l^2$ . But this means  $v = w$  too. We leave the remaining  $I^*$  details as exercises.

Now, let  $f_k = I^*(\delta(n - k))$ . Since  $\delta(n - k) = (I^*)^{-1}(f_k)$  and  $((I^*)^{-1})^{-1} = I^*$  is bounded, the proposition says that  $F = \{f_k \mid k \in \mathbb{Z}\}$  is a Riesz basis in  $H$ . If  $x \in H$ , then by (11.125a) there is  $s \in l^2$  such that  $x = \sum_{k=-\infty}^{\infty} s(k)f_k$ . We see that  $\langle x, e_k \rangle = s(k)$  by calculating  $\langle f_i, e_k \rangle = \langle I^*(\delta(n - i)), e_k \rangle = \langle \delta(n - i), I(e_k) \rangle = \langle \delta(n - i), \delta(n - k) \rangle$ . So

$$\sum_{k=-\infty}^{\infty} |\langle x, e_k \rangle|^2 = \sum_{k=-\infty}^{\infty} |s(k)|^2 = \|s\|_2^2. \quad (11.127)$$

Since  $I^*$  and  $(I^*)^{-1}$  are bounded and  $x = I^*s$ , we have

$$\frac{\|x\|^2}{\|I^*\|^2} \leq \sum_{k=-\infty}^{\infty} |\langle x, e_k \rangle|^2 = \sum_{k=-\infty}^{\infty} |s(k)|^2 \leq \|s\|^2 \|(I^*)^{-1}\|^2, \quad (11.128)$$

which is precisely a frame condition on  $E$ . ■

**Theorem (Orthonormal Translates).** Let  $\phi(t) \in L^2(\mathbb{R})$  and  $\Phi(\omega) = \mathcal{F}[\phi(t)](\omega)$  be its (radial) Fourier transform. The family  $F = \{\phi(t - k) \mid k \in \mathbb{Z}\}$  is orthonormal if and only if

$$\sum_{k=-\infty}^{\infty} |\Phi(\omega + 2\pi k)|^2 = 1 \tag{11.129}$$

for almost all  $\omega \in \mathbb{R}$ .

**Proof:** An interesting application of Fourier transform properties makes this proof work. Let us define  $a_k = \langle \phi(t), \phi(t - k) \rangle$ . Note that—by a simple change of variable in the inner product integral— $F$  is orthonormal if and only if  $a_k$  is zero when  $k \neq 0$  and unity when  $k = 0$ . We calculate

$$a_k = \langle \phi(t), \phi(t - k) \rangle = \frac{1}{2\pi} \langle \Phi(\omega), \Phi(\omega)e^{-jk\omega} \rangle = \frac{1}{2\pi} \int_{-\infty}^{\infty} \Phi(\omega)\overline{\Phi(\omega)}e^{jk\omega} d\omega. \tag{11.130}$$

by the Parseval and shift properties. The right-hand integrand in is  $|\Phi(\omega)|^2 e^{jk\omega}$ . We break up the integral into  $2\pi$ -wide pieces, invoke the exponential’s periodicity, and swap the order of summation and integration to get

$$a_k = \frac{1}{2\pi} \sum_{n=-\infty}^{\infty} \int_0^{2\pi} |\Phi(\omega + 2\pi n)|^2 e^{jk\omega} d\omega = \frac{1}{2\pi} \int_0^{2\pi} e^{jk\omega} \sum_{n=-\infty}^{\infty} |\Phi(\omega + 2\pi n)|^2 d\omega. \tag{11.131}$$

We move the sum into the integral, since  $\Phi = \mathcal{F}\phi \in L^2(\mathbb{R})$ , so that  $|\Phi(\omega)|^2 \in L^1(\mathbb{R})$ . Let us define

$$P_{\Phi}(\omega) = \sum_{n=-\infty}^{\infty} |\Phi(\omega + 2\pi n)|^2. \tag{11.132}$$

Now observe

$$\int_0^{2\pi} \sum_{n=-\infty}^{\infty} |\Phi(\omega + 2\pi n)|^2 d\omega = \int_0^{2\pi} P_{\Phi}(\omega) d\omega = \int_{-\infty}^{\infty} |\Phi(\omega)|^2 d\omega = \|\Phi(\omega)\|_2^2, \tag{11.133}$$

so that  $P_{\Phi}(\omega)$  is finite for almost all  $\omega \in \mathbb{R}$ . This allows us to interchange summation and integration with the Lebesgue integral (Chapter 3) in (11.131). We can say more about  $P_{\Phi}(\omega)$ : It is  $2\pi$ -periodic, and the right-hand side of (11.131) is precisely the expression for its Fourier series coefficient, which is  $a_k$ . Within the inner product there hides nothing less than a Fourier series analysis equation for the special periodic function  $P_{\Phi}(\omega)$ ! We use this periodization argument a lot.

Let us check our claim that  $P_{\Phi}(\omega) = 1$  almost everywhere if and only if the family of translates  $F$  is orthonormal. First, if  $P_{\Phi}(\omega) = 1$ , then (11.131) becomes

$$a_k = \frac{1}{2\pi} \int_0^{2\pi} e^{jk\omega} d\omega = \langle \phi(t), \phi(t-k) \rangle. \quad (11.134)$$

The integral in (11.134) is  $2\pi$  if  $k = 0$  and zero if  $k \neq 0$ . So  $F = \{\phi(t-k)\}$  must be orthonormal. Conversely, suppose  $F$  is orthonormal so that  $a_k = 1$  if  $k = 0$  and  $a_k = 0$  if  $k \neq 0$ . Because (11.131) gives the Fourier series coefficients for the  $2\pi$ -periodic function  $P_{\Phi}(\omega)$ , we know that  $P_{\Phi}(\omega)$  has all zero Fourier series coefficients except for its DC term, which is one. In other words,

$$P_{\Phi}(\omega) = \sum_{k=-\infty}^{\infty} a_k e^{jk\omega} = 1e^0 = 1. \quad (11.135) \quad \blacksquare$$

The following corollary shows that when the translates of  $\phi(t)$  are orthonormal, then its spectrum, as given by the support of  $\Phi(\omega)$ , cannot be too narrow [8]. Scaling functions cannot have simple frequency components. This result uses the Lebesgue measure of a set, an idea introduced in Section 3.4.1.

**Corollary (Spectral Support).** Let  $\phi(t) \in L^2(\mathbb{R})$ ,  $\Phi(\omega) = \mathcal{F}[\phi(t)](\omega)$  be its (radial) Fourier transform, let  $\text{Support}(\Phi) = \{\omega \in \mathbb{R} \mid \Phi(\omega) \neq 0\}$ , and let  $\mu(A)$  be the Lebesgue measure of a measurable set  $A$ . If the family  $F = \{\phi(t-k) \mid k \in \mathbb{Z}\}$  is orthonormal, then  $\mu(\text{Support}(\Phi)) \geq 2\pi$ . Under these assumptions, moreover,  $\mu(\text{Support}(\Phi)) = 2\pi$  if and only if  $|\Phi(\omega)| = \chi_A$ , for some Lebesgue measurable  $A \subset \mathbb{R}$  with  $\mu(A) = 2\pi$ .

**Proof:** Since  $\|\phi\|_2 = 1$ , we know  $\|\Phi\|_2 = (2\pi)^{1/2}$ , by Plancherel's formula. The theorem then implies  $|\Phi(\omega)| \leq 1$  for almost all  $\omega \in \mathbb{R}$ . Consequently,

$$\mu(\text{Support}(\Phi)) = \int_{\text{Support}(\Phi)} 1 d\omega \geq \int_{-\infty}^{\infty} |\Phi(\omega)|^2 d\omega = 2\pi. \quad (11.136)$$

Now suppose (11.136) is an equality, but  $0 < |\Phi(\omega)| < 1$  on some set  $B \subset \mathbb{R}$  with  $\mu(B) > 0$ . Then

$$\int_B |\Phi(\omega)|^2 d\omega < \int_B 1 d\omega = \mu(B) \quad (11.137)$$

and

$$\begin{aligned} \|\Phi\|_2^2 = 2\pi &= \int_{\text{Support}(\Phi)} |\Phi(\omega)|^2 d\omega < \mu(\text{Support}(\Phi) \setminus B) + \mu(B) \\ &= \mu(\text{Support}(\Phi)) = 2\pi \end{aligned} \quad (11.138)$$

a contradiction. Conversely, assume  $F$  is orthonormal and  $|\Phi(\omega)| = \chi_A$ , for some Lebesgue measurable  $A \subset \mathbb{R}$  with  $\mu(A) = 2\pi$ . Then we quickly see that

$$\mu(A) = \mu(\text{Support}(\Phi)) = \|\Phi\|_2^2 = 2\pi. \tag{11.139}$$

■

Here is a second characterization of unconditional bases. In the next section, we use this result to find the scaling function for an MRA. We begin with a lemma [9].

**Lemma.** Suppose  $\phi(t) \in L^2(\mathbb{R})$ ,  $\Phi(\omega) = \mathcal{F}[\phi(t)](\omega)$  is its (radial) Fourier transform,  $F = \{\phi(t - k) \mid k \in \mathbb{Z}\}$ , and we define  $P_\Phi(\omega)$  as above (11.132). If  $s \in l^2$ , then

$$\left\| \sum_{k=-\infty}^{\infty} s(k)\phi(t-k) \right\|_2^2 = \frac{1}{2\pi} \int_0^{2\pi} |S(\omega)|^2 P_\Phi(\omega) d\omega, \tag{11.140}$$

where  $S(\omega)$  is the discrete-time Fourier transform of  $s(k)$ .

**Proof:** Let us consider a linear combination of the  $\phi(t - k)$ ,  $\sum_{k=p}^q s(k)\phi(t - k)$ , where  $s \in l^2$ . Using the above periodization technique, we compute

$$\begin{aligned} \left\| \sum_{k=p}^q s(k)\phi(t-k) \right\|_2^2 &= \frac{1}{2\pi} \left\| \sum_{k=p}^q s(k)e^{-jk\omega} \Phi(\omega) \right\|_2^2 \\ &= \frac{1}{2\pi} \int_{-\infty}^{\infty} \left| \sum_{k=p}^q s(k)e^{-jk\omega} \right|^2 |\Phi(\omega)|^2 d\omega = \frac{1}{2\pi} \int_0^{2\pi} \left| \sum_{k=p}^q s(k)e^{-jk\omega} \right|^2 P_\Phi(\omega) d\omega \end{aligned} \tag{11.141}$$

By assumption,  $s(k)$  is square-summable. Hence its discrete-time Fourier transform exists (Chapter 7), and we may pass to the double summation limit in (11.141). Indeed, as  $p, q \rightarrow \infty$ , the last integrand in (11.141) becomes  $|S(\omega)|^2 P_\Phi(\omega)$ , where  $S(\omega)$  is the DTFT of  $s(k)$ . ■

**Theorem (Riesz Translates Basis Characterization).** Suppose  $\phi(t) \in L^2(\mathbb{R})$ ,  $\Phi(\omega) = \mathcal{F}[\phi(t)](\omega)$  is its (radial) Fourier transform,  $F = \{\phi(t - k) \mid k \in \mathbb{Z}\}$ ,  $0 < A \leq B < \infty$ , and we define  $P_\Phi(\omega)$  as above (11.132). Then the following are equivalent:

- (i)  $F$  is a Riesz basis with lower and upper bounds  $\sqrt{A}$  and  $\sqrt{B}$ , respectively.
- (ii)  $A \leq P_\Phi(\omega) \leq B$  for almost all  $\omega \in \mathbb{R}$ .

**Proof:** Suppose (ii), and let  $s \in l^2$ . Then  $A|S(\omega)|^2 \leq |S(\omega)|^2 P_\Phi(\omega) \leq B|S(\omega)|^2 < \infty$  almost everywhere, too, where  $S(\omega)$  is the DTFT of  $s(k)$ . Integrating on  $[0, 2\pi]$ , we see

$$\frac{A}{2\pi} \int_0^{2\pi} |S(\omega)|^2 d\omega \leq \frac{1}{2\pi} \int_0^{2\pi} |S(\omega)|^2 P_\Phi(\omega) d\omega \leq \frac{B}{2\pi} \int_0^{2\pi} |S(\omega)|^2 d\omega. \tag{11.142}$$

We know that  $2\pi\|s\|^2 = \|S\|^2$ , and so the lemma implies

$$A\|s\|_2^2 \leq \left\| \sum_{k=-\infty}^{\infty} s(k)\phi(t-k) \right\|_2^2 \leq B\|s\|_2^2; \quad (11.143)$$

this is precisely the Riesz basis condition for lower and upper bounds  $\sqrt{A}$  and  $\sqrt{B}$ , respectively.

Now let us assume (i) and try to show  $A \leq P_{\Phi}(\omega)$  almost everywhere on  $[0, 2\pi]$ . Following [9], we set  $Q_{\Phi,a} = \{\omega \in [0, 2\pi]: P_{\Phi}(\omega) < a\}$ . If the Lebesgue measure of  $Q_{\Phi,a}$ ,  $\mu(Q_{\Phi,a})$ , is zero for almost all  $a \in \mathbb{R}$ , then  $P_{\Phi}(\omega)$  diverges almost everywhere, and, in particular,  $A \leq P_{\Phi}(\omega)$ . We can thus suppose that there is some  $a \in \mathbb{R}$  such that  $\mu(Q_{\Phi,a}) > 0$ . Let  $\chi_a$  be the characteristic function on  $Q_{\Phi,a}$ :

$$\chi_a(\omega) = \begin{cases} 1 & \text{if } \omega \in Q_{\Phi,a}, \\ 0 & \text{if } \omega \notin Q_{\Phi,a}. \end{cases} \quad (11.144)$$

By the theory of Lebesgue measure, if a set is measurable, then so is its characteristic function. This entitles us to compute the inverse discrete-time Fourier transform of  $\chi_a(\omega)$ :

$$x_a(n) = \frac{1}{2\pi} \int_0^{2\pi} \chi_a(\omega) e^{j\omega n} d\omega, \quad (11.145)$$

where  $x_a \in l^2$ . From (i) and the lemma we see

$$\begin{aligned} A\|x_a\|_2^2 &\leq \left\| \sum_{k=-\infty}^{\infty} x_a(k)\phi(t-k) \right\|_2^2 = \frac{1}{2\pi} \int_0^{2\pi} |\chi_a(\omega)|^2 P_{\Phi}(\omega) d\omega \\ &= \frac{1}{2\pi} \int_0^{2\pi} \chi_a(\omega) P_{\Phi}(\omega) d\omega = \frac{1}{2\pi} \int_{Q_a} P_{\Phi}(\omega) d\omega. \end{aligned} \quad (11.146)$$

By our choice of  $Q_{\Phi,a}$ ,  $P_{\Phi}(\omega) < a$  for  $\omega \in Q_{\Phi,a}$ , and (11.146) entails

$$A\|x_a\|_2^2 \leq \frac{a}{2\pi} \mu(Q_{\Phi,a}). \quad (11.147)$$

But  $\|x_a\|^2 = (2\pi)^{-1} \|\chi_a\|^2 = (2\pi)^{-1} \mu(Q_{\Phi,a})$ , and, by (11.147),  $A \leq a$ . This gives us a contradiction by the following observation. If  $A \leq P_{\Phi}(\omega)$  almost everywhere on  $[0, 2\pi]$ , then we are done. Otherwise, there must be some  $U \subseteq \mathbb{R}$  such that  $\mu(U) > 0$  and  $P_{\Phi}(\omega) < A$ . But then there must also be some  $a > 0$  such that  $P_{\Phi}(\omega) < a < A$  and  $\mu(Q_{\Phi,a}) > 0$ . But our argument above has just proven that  $A \leq a$ , a contradiction.

Let us continue to assume (i) and try to show  $P_{\Phi}(\omega) \leq B$  for almost all  $\omega \in [0, 2\pi]$ . Define  $P_{\Phi,a} = \{\omega \in [0, 2\pi]: P_{\Phi}(\omega) > a\}$ . Much like before, if  $\mu(P_{\Phi,a}) = 0$  almost everywhere, then  $P_{\Phi}(\omega) = 0$  for almost all  $\omega \in [0, 2\pi]$ , and thus  $P_{\Phi}(\omega) \leq B$ . Assume that some  $a > 0$  gives  $\mu(P_{\Phi,a}) > 0$ . Now the argument parallels the one just given and is left as an exercise [9]. For an alternative proof, see [8]. ■

### 11.4.2 Scaling Function

From our study of bases of translates and Riesz expansions, we can show that every multiresolution analysis  $V = \{V_i\}$  has a special *scaling function*, whose translates form an orthonormal basis for  $V_0$ . The MRA structure is appropriately named; the scaling function property further implies that signals in every  $V_i$  look like combinations of dilated versions of  $V_0$  elements.

**11.4.2.1 Existence.** In the following result, the equalities in (11.148a) and (11.148b) are assumed to hold almost everywhere.

**Proposition (Spanning Translates).** If  $x(t), y(t) \in L^2(\mathbb{R})$ ,  $X(\omega)$  and  $Y(\omega)$  are their respective radial Fourier transforms, and  $s(k) \in l^2$ , then the following are equivalent:

$$y(t) = \sum_{k=-\infty}^{\infty} s(k)x(t-k), \tag{11.148a}$$

$$Y(\omega) = S(\omega)X(\omega), \tag{11.148b}$$

where  $S(\omega)$  is the discrete-time Fourier transform of  $s(k)$ .

**Proof:** Now, assuming (11.148b), we have

$$y(t) = \frac{1}{2\pi} \int_{-\infty}^{\infty} S(\omega)X(\omega)e^{j\omega t} d\omega = \frac{1}{2\pi} \int_{-\infty}^{\infty} \left( \sum_{k=-\infty}^{\infty} s(k)e^{-jk\omega} \right) X(\omega)e^{j\omega t} d\omega. \tag{11.149}$$

Hence,

$$y(t) = \sum_{k=-\infty}^{\infty} s(k) \frac{1}{2\pi} \int_{-\infty}^{\infty} X(\omega)e^{j\omega(t-k)} d\omega = \sum_{k=-\infty}^{\infty} s(k)x(t-k). \tag{11.150}$$

To show the converse, we work backwards through the equalities in (11.150) to the front of (11.149), a Fourier transform synthesis equation for  $y(t)$ . We must have (11.148b) except on a set of Lebesgue measure zero. ■

This section's main result comes from the classic source papers on wavelets and multiresolution analysis [23, 29].

**Theorem (Scaling Function).** If  $\{V_i: i \in \mathbb{Z}\}$  is an MRA, then there is some  $\phi(t) \in V_0$  such that  $\{\phi(t-k): k \in \mathbb{Z}\}$  is an orthonormal basis of  $V_0$ .

**Proof:** By the Riesz Basis Characterization (Section 11.4.1.3), there is some  $g(t) \in V_0$  such that  $F = \{g(t-k) \mid k \in \mathbb{Z}\}$  is a Riesz basis for  $V_0$ . Let us say it has lower and upper bounds  $\sqrt{A}$  and  $\sqrt{B}$ , respectively. The Riesz Translates Basis Characterization implies

$$A \leq \sum_{k=-\infty}^{\infty} |G(\omega + 2\pi k)|^2 \leq B \quad (11.151)$$

for almost all  $\omega \in \mathbb{R}$ , where  $G(\omega)$  is the (radial) Fourier transform of  $g(t)$ . Note that the sum in (11.151) is the  $2\pi$ -periodic function  $P_G(\omega)$ , defined in (11.132). The Riesz bounds on  $P_G(\omega)$  allow us to define (almost everywhere) the  $L^2(\mathbb{R})$  function

$$\Phi(\omega) = \frac{G(\omega)}{\sqrt{P_G(\omega)}}. \quad (11.152)$$

$\Phi(\omega)$  is the Fourier transform of  $\phi(t) \in L^2(\mathbb{R})$ , and our claim is that  $\phi(t)$  works. The previous proposition implies  $\phi(t) \in \overline{\text{Span}\{g(t-k)\}}$ . Since  $V_0$  is closed,  $\phi(t) \in V_0$ , and so  $\phi(t-k) \in V_0$ , by MRA property (v). Equation (11.152) works both ways, and we see that  $F = \{g(t-k) \mid k \in \mathbb{Z}\}$ —which is dense in  $V_0$ —is in the closure of  $\{\phi(t-k) \mid k \in \mathbb{Z}\}$ . Thus,  $\overline{\text{Span}\{\phi(t-k)\}} = V_0$ . It remains to show that the  $\phi(t-k)$  are orthonormal. We calculate

$$\sum_{k=-\infty}^{\infty} |\Phi(\omega + 2\pi k)|^2 = \sum_{k=-\infty}^{\infty} \left| \frac{G(\omega + 2\pi k)}{\sqrt{P_G(\omega + 2\pi k)}} \right|^2 = \sum_{k=-\infty}^{\infty} \frac{|G(\omega + 2\pi k)|^2}{P_G(\omega)} = 1. \quad (11.153)$$

By the Orthonormal Translates criterion (11.129),  $\{\phi(t-k) \mid k \in \mathbb{Z}\}$  is an orthonormal set.

**Corollary.** Let  $\{V_i: i \in \mathbb{Z}\}$  be an MRA, and  $\phi(t) \in V_0$  be given by the theorem. Then,  $\{2^{i/2}\phi(2^i t - k): k \in \mathbb{Z}\}$  is an orthonormal basis of  $V_i$ .

**Proof:** By properties (iv) and (v) of the MRA, the scaled versions of an orthonormal basis for  $V_0$  will constitute an orthonormal basis for  $V_i$ . ■

**Definition (Scaling Function).** Let  $V = \{V_i: i \in \mathbb{Z}\}$  be an MRA and  $\phi(t) \in V_0$  such that  $\{\phi(t-k): k \in \mathbb{Z}\}$  is an orthonormal basis of  $V_0$ . Then  $\phi(t)$ , known from the theorem, is called a *scaling function* of the MRA.

Any translate  $\phi(t - k)$  of a scaling function  $\phi(t)$  is still a scaling function. The next corollary [9] characterizes scaling functions for an MRA.

**Corollary (Uniqueness).** Let  $V = \{V_i: i \in \mathbb{Z}\}$  be an MRA and  $\phi(t) \in V_0$  be the scaling function found in the proof. Then  $\theta(t) \in V_0$  is a scaling function for  $V$  if and only if there is a  $2\pi$ -periodic function  $P(\omega)$  such that

- (i)  $\Theta(\omega) = P(\omega)\Phi(\omega)$ ;
- (ii)  $|P(\omega)| = 1$  almost everywhere on  $[0, 2\pi]$ .

**Proof:** Exercise. ■

**11.4.2.2 Examples.** Let us look at some examples of scaling functions for the three multiresolution analyses that we know.

**Example (Step Functions).** The scaling function for the Haar MRA, for which  $V_0$  consists of constant functions on unit intervals  $(n, n + 1)$ , is just the unit square pulse  $\phi(t) = u(t) - u(t - 1)$ .

**Example (Piecewise Continuous Functions).** Finding this scaling function is not so direct. The continuity of  $V_0$  elements forces us to reflect on how a possible scaling function  $\phi(t)$  might be orthogonal to its translates  $\phi(t - k)$ . It is clear that  $\phi(t)$  cannot be finitely supported. For then we could take the last interval  $(n, n + 1)$  to the right over which  $\phi(t)$  is nonzero, the last interval  $(m, m + 1)$  proceeding to the left over which  $\phi(t)$  is nonzero, and compute the inner product  $\langle \phi(t), \phi(t - (n - m)) \rangle$ . A simple check of cases shows that it is never zero. Evidently,  $\phi(t) \neq 0$  on  $(n, n + 1)$  for arbitrarily large  $|n|$ , and the inner products  $\langle \phi(t), \phi(t - k) \rangle$  involve an infinite number of terms.

But rather than stipulating from the start that  $V_0$  must have a scaling function, we have elected to define our MRAs using the apparently weaker isomorphism condition (vi). The existence of this isomorphism  $I: V_0 \rightarrow l^2$ , which commutes with translations by integral amounts, is equivalent to  $V_0$  having a Riesz basis. This facilitates our study of the Strömberg MRA. If we can find a Riesz basis  $F = \{g(t - k) \mid k \in \mathbb{Z}\}$  for  $V_0$ , then the Scaling Function Theorem (11.152) readily gives the Fourier transform  $\Phi(\omega)$  of  $\phi(t)$ . Let  $g(t) \in V_0$  be the simple triangular pulse with  $g(0) = 1$ ,  $g(t) = t + 1$  on  $(-1, 0)$ ,  $g(t) = 1 - t$  on  $(0, 1)$ , and  $g(t) = 0$  otherwise. Then  $x(t) = \sum a_k g(t - k)$  is piecewise linear, continuous, and  $x(k) = a_k$  for all  $k \in \mathbb{Z}$ . We can define the isomorphism  $I$  by  $(Ix)(k) = a_k$ . This map commutes with integer translations. The Riesz Basis Characterization implies that  $\{g(t - k) \mid k \in \mathbb{Z}\}$  is a Riesz basis. In fact,  $g(t) = I^{-1}(\delta(n))$ , where  $I$  is the isomorphism from  $V_0$  to  $l^2$ , and  $\delta(n)$  is the discrete delta signal. We compute

$$G(\omega) = \int_{-\infty}^{\infty} g(t)e^{-j\omega t} dt = \left[ \frac{\sin\left(\frac{\omega}{2}\right)}{\frac{\omega}{2}} \right]^2 = \text{sinc}^2\left(\frac{\omega}{2}\right). \tag{11.154}$$

Define

$$\Phi(\omega) = \frac{G(\omega)}{\sqrt{P_G(\omega)}} = \frac{\text{sinc}^2\left(\frac{\omega}{2}\right)}{\sqrt{\sum_{k=-\infty}^{\infty} \text{sinc}^4\left(\frac{\omega + 2\pi k}{2}\right)}} = \frac{\text{sinc}^2\left(\frac{\omega}{2}\right)}{4\sin^2(\omega) \sqrt{\sum_{k=-\infty}^{\infty} (\omega + 2\pi k)^{-4}}}. \tag{11.155}$$

We define the utility function  $\Sigma_n(\omega)$  as follows:

$$\Sigma_n(\omega) = \sum_{k=-\infty}^{\infty} (\omega + 2\pi k)^{-n}. \tag{11.156}$$

Though it tests our competence in differential calculus, it is possible [23] to develop closed form expressions for the  $\Sigma_n(\omega)$ , beginning with the standard summation [36]:

$$\Sigma_2(\omega) = \sum_{k=-\infty}^{\infty} (\omega + 2\pi k)^{-2} = \frac{1}{4} \sin^{-2}\left(\frac{\omega}{2}\right). \tag{11.157}$$

Twice differentiating (11.157) gives

$$\frac{d^2}{d\omega^2} \Sigma_2(\omega) = 6 \sum_{k=-\infty}^{\infty} (\omega + 2\pi k)^{-4} = 6\Sigma_4(\omega) = \frac{1}{4} \cot^2\left(\frac{\omega}{2}\right) \csc^2\left(\frac{\omega}{2}\right) + \frac{1}{8} \csc^4\left(\frac{\omega}{2}\right). \tag{11.158}$$

Finally,

$$\Phi(\omega) = \frac{G(\omega)}{\sqrt{P_G(\omega)}} = \frac{\sqrt{6}}{\omega^2 \sqrt{\frac{1}{4} \cot^2\left(\frac{\omega}{2}\right) \csc^2\left(\frac{\omega}{2}\right) + \frac{1}{8} \csc^4\left(\frac{\omega}{2}\right)}}. \tag{11.159}$$

Taking the inverse Fourier transform gives  $\phi(t)$  (Figure 11.10). Notice from its magnitude spectrum that  $\phi(t)$  is an analog low-pass filter.

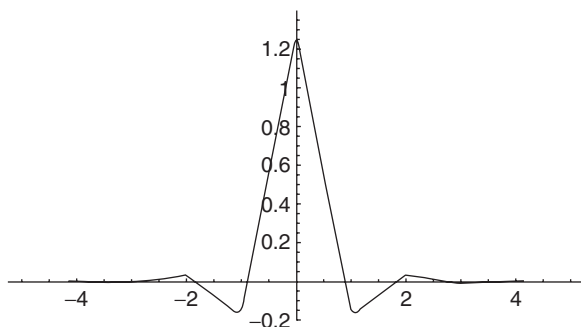


Fig. 11.10. Scaling function for the MRA consisting of continuous piecewise signals.

**Example (Spline Functions).** The procedure for finding this scaling function is similar to the one we use for the piecewise continuous MRA. The root space  $V_0$  contains the  $L^2(\mathbb{R})$  signals that are continuously differentiable and equal to cubic polynomials on each interval  $[n, n + 1]$ , where  $n \in \mathbb{Z}$  [37, 38]. To find a scaling function we need to find a Riesz basis. Let  $g(t) \in V_0$  be the cubic spline that satisfies  $g(0) = 1$  and  $g(n) = 0$  otherwise. This is a rounded tent function. Then  $x(t) = \sum a_k g(t - k)$  is a cubic spline on intervals  $[n, n + 1]$ , continuously differentiable, and  $x(k) = a_k$  for all  $k \in \mathbb{Z}$ . Once again we set  $(Ix)(k) = a_k$  and invoke the Riesz Basis Characterization toward showing  $\{g(t - k) \mid k \in \mathbb{Z}\}$  to be a Riesz basis. We compute the radial Fourier transform of  $g(t)$ :

$$G(\omega) = \left(1 - \frac{2}{3} \sin^2\left(\frac{\omega}{2}\right)\right)^{-1} \text{sinc}^4\left(\frac{\omega}{2}\right). \tag{11.160}$$

We can derive a cubic spline scaling function by the standard formula (11.152):

$$\Phi(\omega) = \frac{G(\omega)}{\sqrt{P_G(\omega)}} = \frac{[\Sigma_g(\omega)]^{\frac{1}{2}}}{\omega^4}, \tag{11.161}$$

where  $\Sigma_n(\omega)$  is given by (11.156). Again, we can compute the  $\Sigma_n(\omega)$  by taking successive derivatives—six actually—of  $\Sigma_2(\omega)$ . With either resolute patience or a symbolic computation software package, we calculate

$$\begin{aligned} \frac{d^6}{d\omega^6} \Sigma_2(\omega) &= \frac{1}{4} \cot^6\left(\frac{\omega}{2}\right) \text{csc}^2\left(\frac{\omega}{2}\right) + \frac{57}{8} \cot^4\left(\frac{\omega}{2}\right) \text{csc}^4\left(\frac{\omega}{2}\right) \\ &+ \frac{45}{4} \cot^2\left(\frac{\omega}{2}\right) \text{csc}^6\left(\frac{\omega}{2}\right) + \frac{17}{16} \text{csc}^8\left(\frac{\omega}{2}\right). \end{aligned} \tag{11.162}$$

Consequently,

$$\Sigma_g(\omega) = \frac{1}{5040} \frac{d^6}{d\omega^6} (\Sigma_2(\omega)) \tag{11.163}$$

and

$$\Phi(\omega) = \frac{1}{\omega^4 \sqrt{\Sigma_g(\omega)}}. \tag{11.164}$$

So once again, we find a scaling function using frequency-domain analysis. The key relationship is (11.152). Inverse Fourier transformation gives  $\phi(t)$  (Figure 11.11). For the cubic spline MRA too, the scaling function is a low-pass filter. In comparison to the MRA for piecewise linear signals, observe the flatter reject band of  $\Phi(\omega)$  for the spline MRA.

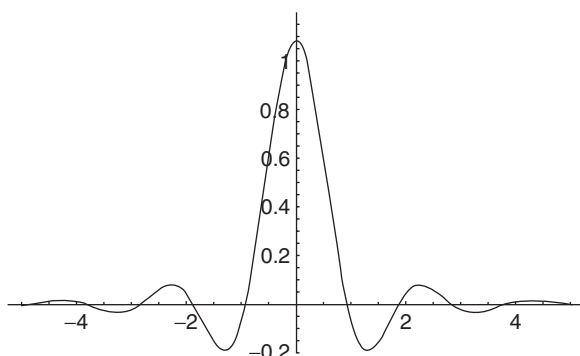


Fig. 11.11. Scaling function for the MRA consisting of cubic splines.

### 11.4.3 Discrete Low-Pass Filter

The scaling function is not the only special function connected with the multiresolution analysis structure. This section shows that for every MRA of finite energy signals we can find a special discrete filter [10, 23, 29]. This filter will prove useful when we discretize our theory and use it in signal analysis applications. In fact, we shall show that it is a low-pass filter. Mathematically thorough introductions to this material include [8, 9].

Suppose  $V = \{V_i : i \in \mathbb{Z}\}$  is an MRA and  $\phi(t) \in V_0$  is its scaling function. Because  $\phi(t/2) \in V_{-1} \subset V_0$  and since integral translates of  $\phi(t)$  span  $V_0$ , we see that

$$\frac{1}{2}\phi\left(\frac{t}{2}\right) = \sum_{n=-\infty}^{\infty} h_n \phi(t-n), \quad (11.165)$$

where the sequence  $\{h_n \mid n \in \mathbb{Z}\}$  is square-summable. Hilbert space theory tells us that

$$h_n = \left\langle \frac{1}{2}\phi\left(\frac{t}{2}\right), \phi(t-n) \right\rangle. \quad (11.166)$$

These observations lead to the following definition.

**Definition (Associated Filter).** The  $\phi(t)$  be the scaling function of an MRA,  $V = \{V_i : i \in \mathbb{Z}\}$ . If  $H_\phi$  is the discrete filter with impulse response  $h_\phi(n) = h_n$ , where  $h_n$  is given by (11.166), then  $H_\phi$  is called the *associated filter* to  $V$  (and to  $\phi(t)$ ).

As we develop the properties of the discrete filter associated to an MRA, we shall see that it is indeed a low-pass filter. When there is no ambiguity, we drop the subscript:  $H = H_\phi$ . The following proposition gives a formula for the discrete-time Fourier transform  $H(\omega)$  of the associated filter [23].

**Proposition.** Let  $\phi(t)$  be the scaling function of an MRA,  $V = \{V_i: i \in \mathbb{Z}\}$ ; let  $\Phi(\omega)$  be its Fourier transform; and let  $H$  be the associated discrete filter with impulse response,  $h(n) = h_n$ , given by (11.166). Then,

$$\Phi(2\omega) = \Phi(\omega)H(\omega), \tag{11.167}$$

where  $H(\omega)$  is the DTFT of  $h(n)$ :  $H(\omega) = \sum_n h(n)e^{-j\omega n}$ .

**Proof:** Apply the radial Fourier transform to both sides of (11.165). ■

*Remark.* The relation shows that  $H(\omega)$  has a low-pass filter characteristic (Figure 11.12). The dilation  $\Phi(2\omega)$  looks just like  $\Phi(\omega)$ , except that it is contracted with respect to the independent frequency-domain variable  $\omega$  by a factor of two. The relation (11.167) shows that a multiplication by  $H(\omega)$  accomplishes this, and the

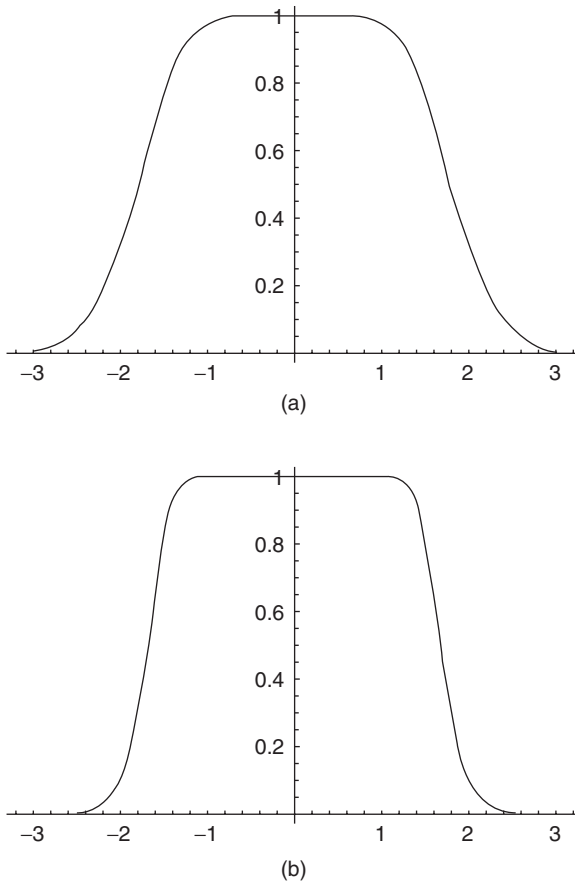


**Fig. 11.12.** Associated low-pass filters for the MRAs consisting of piecewise linear functions (a) and cubic splines (b). Note the better cutoff behavior of the filter based on cubic spline approximations.

only this can be the case, intuitively, is that  $H(\omega)$  is approximately unity around the DC value  $\omega = 0$ , and it falls off to essentially zero halfway through the passband of the spectrum of  $\Phi(\omega)$ . This is not a rigorous argument, but it can be made so by assuming some decay constraints on the scaling function  $\phi(t)$  [23, 29].

**Proposition.** Let  $\phi(t)$  be the scaling function of an MRA,  $V = \{V_i: i \in \mathbb{Z}\}$ ;  $\Phi(\omega)$  its Fourier transform;  $h(n)$  the associated discrete low-pass filter (11.166), and  $H(\omega)$  its DTFT. Then,

$$|H(\omega)|^2 + |H(\omega + \pi)|^2 = 1, \quad (11.168)$$

for almost all  $\omega \in \mathbb{R}$ .

**Proof:** By the Orthonormal Translates Theorem,  $\sum_{k=-\infty}^{\infty} |\Phi(2\omega + 2\pi k)|^2 = 1$ . Inserting (11.167) into this identity gives

$$\sum_{k=-\infty}^{\infty} |\Phi(\omega + \pi k)|^2 |H(\omega + \pi k)|^2 = 1 \quad (11.169)$$

almost everywhere. Next, we split left-hand side of (11.169) into a sum over even integers and odd integers:

$$|H(\omega)|^2 \sum_{k=-\infty}^{\infty} |\Phi(\omega + 2\pi k)|^2 + |H(\omega + \pi)|^2 \sum_{k=-\infty}^{\infty} |\Phi(\omega + 2\pi k + \pi)|^2 = 1, \quad (11.170)$$

where we have used  $H(\omega) = H(\omega + 2\pi)$ . The Orthonormal Translates Theorem tells us that the infinite sums in (11.170) are unity, and (11.168) follows. ■

*Remarks.* Discrete filters satisfying (11.168) are *conjugate* filters, familiar from Chapter 9. Conjugate filters are used to filter a signal in such a way that it can be subsampled and exactly reconstructed later. The Laplacian pyramid technique provides decomposition by filtering and subsampling as well as exact reconstruction [24]. Various efficient signal compression and transmission techniques rely on this idea [25, 39, 40]. What is particularly striking about the MRA structure is that quite disparate signal theoretic techniques such as scale space analysis [26–28], orthogonal bases, and pyramid decompositions all meet together in one place.

The following results [8] link the low-pass filter  $H$  of an MRA,  $V = \{V_i: i \in \mathbb{Z}\}$ , with the low-resolution subspace  $V_{-1} \subset V_0 \in V$ .

**Lemma.** Let  $\phi(t)$  be the scaling function of an MRA, let  $\Phi(\omega)$  be its Fourier transform, and let  $C(\omega) \in L^2[0, 2\pi]$  be  $2\pi$ -periodic. Then  $C(\omega)\Phi(\omega) \in L^2(\mathbb{R})$ .

**Proof:** We compute

$$\begin{aligned} \int_{-\infty}^{\infty} |\Phi(\omega)|^2 |C(\omega)|^2 d\omega &= \sum_{n=-\infty}^{\infty} \int_0^{2\pi} |\Phi(\omega + 2\pi n)|^2 |C(\omega + 2\pi n)|^2 d\omega \\ &= \sum_{n=-\infty}^{\infty} \int_0^{2\pi} |\Phi(\omega + 2\pi n)|^2 |C(\omega)|^2 d\omega, \end{aligned} \tag{11.171}$$

where we have invoked  $C(\omega) = C(\omega + 2\pi)$ . Interchanging summation and integration in (11.171), and again using  $\sum |\Phi(\omega + 2\pi n)|^2 = 1$ , we get

$$\begin{aligned} \int_{-\infty}^{\infty} |\Phi(\omega)|^2 |C(\omega)|^2 d\omega &= \int_0^{2\pi} \sum_{n=-\infty}^{\infty} |\Phi(\omega + 2\pi n)|^2 |C(\omega)|^2 d\omega \\ &= \int_0^{2\pi} |C(\omega)|^2 d\omega = \|C\|_{2, L^2[0, 2\pi]}^2. \end{aligned} \tag{11.172}$$

■

**Proposition (V<sub>0</sub> Characterization).** Let  $V = \{V_i : i \in \mathbb{Z}\}$  be an MRA, let  $\phi(t)$  be its scaling function, and let  $\Phi = \mathcal{F}(\phi)$  be its (radial) Fourier transform. Then the root space  $V_0 \in V$  contains precisely those  $x(t) \in L^2(\mathbb{R})$  such that  $X(\omega) = C(\omega)\Phi(\omega)$  for some  $2\pi$ -periodic  $C(\omega) \in L^2[0, 2\pi]$ , where  $X(\omega) = \mathcal{F}(x)$ .

**Proof:** Let  $x(t) \in V_0$ . Then  $x(t) = \sum c_k \phi(t - k)$  for some  $c(k) = c_k$ , where  $c \in l^2$ . We compute  $X(\omega)$  as follows:

$$\begin{aligned} \int_{-\infty}^{\infty} x(t)e^{-j\omega t} dt &= \int_{-\infty}^{\infty} \sum_{k=-\infty}^{\infty} c_k \phi(t - k)e^{-j\omega t} dt = \sum_{k=-\infty}^{\infty} c_k \int_{-\infty}^{\infty} \phi(t - k)e^{-j\omega t} dt \\ &= \sum_{k=-\infty}^{\infty} c_k e^{-j\omega k} \int_{-\infty}^{\infty} \phi(t)e^{-j\omega t} dt = C(\omega)\Phi(\omega). \end{aligned} \tag{11.173}$$

Now suppose  $X(\omega) = C(\omega)\Phi(\omega)$  for some  $2\pi$ -periodic  $C(\omega) \in L^2[0, 2\pi]$ . By the lemma,  $X(\omega) \in L^2(\mathbb{R})$ , and we can write  $C(\omega) = \sum c_k e^{-j\omega k}$ , where  $c(k)$  is the inverse DTFT of  $C(\omega)$ . Whence the computation (11.173) shows that  $x(t)$  is in the closure of the span of  $\{\phi(t - k) \mid k \in \mathbb{Z}\}$ ; so  $x \in V_0$ . ■

**Corollary.** With the same notation, define the operator  $T: V_0 \rightarrow L^2[0, 2\pi]$  by  $Tx = C$ , where  $C(\omega)$  is the  $2\pi$ -periodic function with  $X(\omega) = C(\omega)\Phi(\omega)$  guaranteed by the proposition. Then:

- (i)  $T$  is linear.
- (ii) If  $x \in V_0$ , then  $2\pi\|x\|_2^2 = \|C\|_{2, L^2[0, 2\pi]}^2$ .
- (iii) If  $x, y \in V_0$ ,  $C = Tx$ , and  $D = Ty$ , then  $2\pi\langle x, y \rangle_{L^2(\mathbb{R})} = \langle C, D \rangle_{L^2[0, 2\pi]}$ .

**Proof:** Linearity (i) is left as an exercise. For (ii), let  $x(t) \in V_0$ , so that  $X(\omega) = C(\omega)\Phi(\omega)$ . Then, the Plancherel's formula for  $L^2(\mathbb{R})$  and (11.172) entail

$$\|X\|_{2, L^2(\mathbb{R})}^2 = \int_{-\infty}^{\infty} |\Phi(\omega)|^2 |C(\omega)|^2 d\omega = \|C\|_{2, L^2[0, 2\pi]}^2 = 2\pi\|x\|_{2, L^2(\mathbb{R})}^2. \quad (11.174)$$

From (11.174) and the polarization identity [8, 30] for inner product spaces (Chapter 2),  $4\langle x, y \rangle = \|x + y\|^2 - \|x - y\|^2 + j\|x + jy\|^2 - j\|x - jy\|^2$ , (iii) follows. ■

**Definition (Canonical Linear Map on  $V_0$ ).** The linear map  $Tx = C$ , where  $C(\omega)$  is the  $2\pi$ -periodic function with  $X(\omega) = C(\omega)\Phi(\omega)$  guaranteed by the corollary, is called the *canonical map* from  $V_0$  to  $L^2[0, 2\pi]$ .

**Proposition ( $V_{-1}$  Characterization).** Let  $V = \{V_i; i \in \mathbb{Z}\}$  be an MRA, let  $\phi(t)$  be its scaling function,  $\Phi = \mathcal{F}(\phi)$ , and let  $H = H_\phi$  the associated low-pass filter. Then the first low resolution subspace  $V_{-1} \in V$  contains precisely those  $x(t) \in L^2(\mathbb{R})$  such that  $X(\omega) = C(2\omega)H(\omega)\Phi(\omega)$  for some  $2\pi$ -periodic  $C(\omega) \in L^2[0, 2\pi]$ , where  $X(\omega) = \mathcal{F}(x)$ .

**Proof:** Let  $x(t) \in V_{-1}$ , so that  $2x(2t) \in V_0$ . Then  $2x(2t) = \sum c_k \phi(t - k)$  for some  $c_k = c(k) \in l^2$ . Thus,

$$2x(t) = \sum_{k=-\infty}^{\infty} c(k) \phi\left(\frac{t}{2} - k\right). \quad (11.175)$$

Taking Fourier transforms again [8]:

$$\begin{aligned} 2X(\omega) &= 2 \sum_{k=-\infty}^{\infty} c_k \int_{-\infty}^{\infty} \phi(s) e^{-j\omega(2s+2k)} ds \\ &= 2 \sum_{k=-\infty}^{\infty} c_k e^{-2j\omega k} \int_{-\infty}^{\infty} \phi(s) e^{-j(2\omega)s} ds = 2C(2\omega)\Phi(2\omega), \end{aligned} \quad (11.176)$$

where we have made the substitution  $s = t/2 - k$ , and  $C(\omega)$  is the DTFT of  $c(k)$ . From (11.167),  $\Phi(2\omega) = H(\omega)\Phi(\omega)$ ; thus,  $X(\omega) = C(2\omega)H(\omega)\Phi(\omega)$ . For the converse, let  $X(\omega) = C(2\omega)H(\omega)\Phi(\omega)$  for some  $2\pi$ -periodic  $C(\omega) \in L^2[0, 2\pi]$ . Since  $C(2\omega)H(\omega)$  is still  $2\pi$ -periodic, the Lemma applies, and  $X(\omega) \in L^2(\mathbb{R})$ . Finally, (11.176) reverses to show  $x(t) \in V_0$ . ■

It is possible to generalize this result (exercise). The next section explains a mathematical surprise that arises from MRA theory.

### 11.4.4 Orthonormal Wavelet

Besides the scaling function and the associated discrete low-pass filter, a third special function accompanies any multiresolution approximation of  $L^2(\mathbb{R})$ : the *orthonormal wavelet* [23, 29]. Our presentation has been guided by the mathematically complete introductions [8, 9].

**Definition (Orthonormal Wavelet).** Let  $\psi(t) \in L^2(\mathbb{R})$ . If its dilations and translations  $\{2^{n/2}\psi(2^n t - m) : m, n \in \mathbb{Z}\}$  are an orthogonal basis of  $L^2(\mathbb{R})$ , then  $\psi$  is an *orthogonal wavelet*. If  $\|\psi\| = 1$ , then  $\psi$  is an *orthonormal wavelet*.

At the beginning of this chapter we considered an extension of the Fourier transform based on scale and location as transform parameters. The transform inversion required a special signal, the *admissible wavelet*, in order to succeed, and we found that admissible wavelets had to be analog band-pass filters. Now, for MRAs it turns out that the special associated orthogonal wavelet too is a band-pass filter. To discover how it is that an MRA supports this extraordinary function, we examine the orthogonal complements of the component spaces  $V_i$  of the multiresolution analysis  $V = \{V_i : i \in \mathbb{Z}\}$ .

**11.4.4.1 Existence.** Consider first  $V_{-1} \subset V_0$ . From Hilbert space theory (Chapters 2 and 3), we know that every element of  $V_0$  can be written uniquely as a sum  $x = v + w$ , where  $v \in V_{-1}$  and  $w \perp v$ . The set of all such  $w \in V_0$  constitute a Hilbert subspace of  $V_0$ ; let us denote it by  $W_{-1}$ . We say that  $V_0$  is the *direct sum* of  $V_{-1}$  and  $W_{-1}$ :  $V_0 = V_{-1} \oplus W_{-1}$ . In general, every  $V_{i+1}$  is the direct sum of  $V_i$  and  $W_i$ , where  $W_i$  is the *orthogonal complement* of  $V_i$  in  $V_{i+1}$ . We know already that the  $V_i$  have orthonormal bases made up of translations and dilations of the scaling function  $\phi(t)$ . We can also find an orthonormal basis of  $W_i$  by the Gram–Schmidt orthonormalization procedure, of course [31]. But this does not imply that the basis elements are translates of one another, and it exposes no relation between the basis elements so found and the rest of the MRA structure. We want a more enlightening theory.

**Lemma (First  $W_{-1}$  Characterization).** Let  $V = \{V_i : i \in \mathbb{Z}\}$  be an MRA; let  $\phi(t)$  be its scaling function; let  $\Phi = \mathcal{F}(\phi)$  be the (radial) Fourier transform of  $\phi(t)$ ; let  $H = H_\phi$  be the associated low-pass filter; and let  $Tx = C$  be the canonical linear map from  $V_0$  to  $L^2[0, 2\pi]$ . Then  $x(t) \in W_{-1} \subset V_0$  if and only if

$$C(\omega)\overline{H(\omega)} + C(\omega + \pi)\overline{H(\omega + \pi)} = 0 \tag{11.177}$$

for almost all  $\omega \in [0, 2\pi]$ .

**Proof:** Let  $y(t) \in V_{-1}$  and let  $Ty = D$ . Then by the  $V_{-1}$  characterization,  $Y(\omega) = A(2\omega)H(\omega)\Phi(\omega)$  for some  $2\pi$ -periodic  $A \in L^2[0, 2\pi]$ . So  $D(\omega) = A(2\omega)H(\omega)$  almost

everywhere on  $[0, 2\pi]$ . By the corollary to the  $V_0$  characterization,  $\langle x, y \rangle = \langle C, D \rangle$ . Thus,  $x(t) \in W_{-1}$  if and only if  $\langle C(\omega), A(2\omega)H(\omega) \rangle = 0$ , for almost all  $\omega \in [0, 2\pi]$ . Writing out the inner product integral [8], we see that this is further equivalent to

$$\int_0^{2\pi} C(\omega) \overline{A(2\omega)H(\omega)} d\omega = \int_0^{\pi} \overline{A(2\omega)} [C(\omega)\overline{H(\omega)} + C(\omega + \pi)\overline{H(\omega + \pi)}] d\omega = 0 \quad (11.178)$$

for almost all  $\omega \in [0, 2\pi]$ . Since  $y(t)$  is any element of  $V_{-1}$ , the  $A(2\omega)$  in the integrand on the right-hand side of (11.178) is an arbitrary  $\pi$ -periodic signal; evidently,  $x(t) \in W_{-1}$  if and only if the  $\pi$ -periodic factor  $C(\omega)\overline{H(\omega)} + C(\omega + \pi)\overline{H(\omega + \pi)} = 0$  almost everywhere on  $[0, \pi]$ . Finally, by the  $2\pi$ -periodicity of  $C(\omega)$  and  $H(\omega)$ , this same expression must be almost everywhere zero on  $[0, 2\pi]$ .

**Lemma (Second  $W_{-1}$  Characterization).** Let  $V = \{V_i; i \in \mathbb{Z}\}$  be an MRA, let  $\phi(t)$  be its scaling function, let  $\Phi = \mathcal{F}(\phi)$  be the Fourier transform of  $\phi$ , let  $H = H_\phi$  be the associated low-pass filter, and let  $Tx = C$  be the canonical map from  $V_0$  to  $L^2[0, 2\pi]$ . Then,  $x(t) \in W_{-1}$  if and only if  $X(\omega) = e^{-j\omega} S(2\omega)\overline{H(\omega + \pi)}\Phi(\omega)$  for some  $2\pi$ -periodic  $S(\omega) \in L^2[0, 2\pi]$ .

*Proof:* Resorting to some linear algebra tricks, we formulate the previous lemma's criterion as a determinant. Thus,  $x(t) \in W_{-1}$  is equivalent to

$$\det \begin{bmatrix} \overline{H(\omega + \pi)} & C(\omega) \\ -\overline{H(\omega)} & C(\omega + \pi) \end{bmatrix} = 0 \quad (11.179)$$

for almost all  $\omega \in [0, 2\pi]$ . This means that the columns of the matrix (11.179) are linearly dependent—that is, they are proportional via a  $2\pi$ -periodic function  $R(\omega)$ :

$$\begin{bmatrix} C(\omega) \\ C(\omega + \pi) \end{bmatrix} = R(\omega) \begin{bmatrix} \overline{H(\omega + \pi)} \\ -\overline{H(\omega)} \end{bmatrix} \quad (11.180)$$

for just as many  $\omega \in [0, 2\pi]$ . Now substitute  $\omega + \pi$  for  $\omega$  in (11.180) to see

$$\begin{bmatrix} C(\omega + \pi) \\ C(\omega) \end{bmatrix} = R(\omega + \pi) \begin{bmatrix} \overline{H(\omega)} \\ -\overline{H(\omega + \pi)} \end{bmatrix} \quad (11.181)$$

whence  $C(\omega) = -R(\omega + \pi)\overline{H(\omega + \pi)}$ . Further putting  $\omega + \pi$  for  $\omega$  in (11.181) gives  $C(\omega) = R(\omega)\overline{H(\omega + \pi)}$ . Evidently,  $R(\omega) = -R(\omega + \pi)$  for almost all  $\omega \in [0, 2\pi]$ . Hence we have shown that  $x(t) \in W_{-1}$  if and only if  $X(\omega) = C(\omega)\Phi(\omega)$ , where

$C(\omega) = R(\omega)\overline{H(\omega + \pi)}$  for some  $2\pi$ -periodic  $R(\omega) \in L^2[0, 2\pi]$  with  $R(\omega) = -R(\omega + \pi)$ . We define  $S(\omega) = \exp(j\omega/2)R(\omega/2)$ . Then  $S(\omega + 2\pi) = S(\omega)$  almost everywhere, and

$$X(\omega) = C(\omega)\Phi(\omega) = R(\omega)\overline{H(\omega + \pi)}\Phi(\omega) = e^{-j\omega}S(2\omega)\overline{H(\omega + \pi)}\Phi(\omega). \tag{11.182}$$

■

**Lemma ( $W_0$  Characterization).** Let  $V = \{V_i; i \in \mathbb{Z}\}$  be an MRA,  $\phi(t)$  its scaling function,  $\Phi = \mathcal{F}(\phi)$  the Fourier transform of  $\phi$ ,  $H = H_\phi$  the associated low-pass filter, and  $Tx = C$  the canonical map from  $V_0$  to  $L^2[0, 2\pi]$ . Then,  $x(t) \in W_0$  if and only if  $X(2\omega) = e^{-j\omega}S(2\omega)\overline{H(\omega + \pi)}\Phi(\omega)$  for some  $2\pi$ -periodic  $S(\omega) \in L^2[0, 2\pi]$ .

**Proof:** We note that  $x(t) \in W_0$  if and only if  $\langle x(t), v(t) \rangle = 0$  for all  $v(t) \in V_0$ , which is equivalent to  $\langle x(t/2), v(t/2) \rangle = 0$ . But any  $f(t) \in V_{-1}$  is of the form  $v(t/2)$ , so this is also equivalent to  $x(t/2) \perp V_{-1}$ ; in other words,  $y(t) = x(t/2) \in W_{-1}$ . The previous lemma says  $Y(\omega) = e^{-j\omega}S(2\omega)\overline{H(\omega + \pi)}\Phi(\omega)$  for some  $2\pi$ -periodic  $S(\omega) \in L^2[0, 2\pi]$ . But  $Y(\omega) = 2X(2\omega)$ . ■

The main result of this section—very probably the main result of this chapter, likely the main result of this book, and arguably the main result of Fourier analysis in the latter half of the twentieth century—is expressed in the following theorem and its corollary [23, 29].

**Theorem (Orthonormal Basis of  $W_0$ ).** Suppose  $V = \{V_i; i \in \mathbb{Z}\}$  is an MRA,  $\phi(t)$  its scaling function,  $\Phi = \mathcal{F}(\phi)$  the Fourier transform of  $\phi$ , and  $H = H_\phi$  is the associated low-pass filter. If  $\psi(t)$  is the finite energy signal whose Fourier transform is given by

$$\Psi(2\omega) = e^{-j\omega}\overline{H(\omega + \pi)}\Phi(\omega), \tag{11.183}$$

then  $\{\psi(t - k) \mid k \in \mathbb{Z}\}$  is an orthonormal basis for  $W_0$ .

**Proof:** We know that the  $W_0$  characterization lemma entails  $\psi(t) \in W_0$ . (In fact,  $\psi(t)$  represents the very straightforward case where the lemma’s  $S(\omega) = 1$  almost everywhere on  $[0, 2\pi]$ .) Let  $x(t) \in W_0$ . Let us show that a linear combination of translates of  $\psi(t)$  is arbitrarily close to  $x(t)$ . The previous lemma says that  $X(2\omega) = e^{-j\omega}S(2\omega)\overline{H(\omega + \pi)}\Phi(\omega)$  for some  $2\pi$ -periodic  $S(\omega) \in L^2[0, 2\pi]$ . Thus,  $X(\omega) = S(\omega)\Psi(\omega)$ , almost everywhere on  $[0, 2\pi]$ . But we know this condition already from the Spanning Translates Proposition of Section 11.4.2.1: It means that

$$x(t) = \sum_{n=-\infty}^{\infty} s(n)\psi(t - n), \tag{11.184}$$

where  $s(n)$  is the inverse discrete-time Fourier transform of  $S(\omega)$ . Verily, the closure of  $\{\psi(t - k) \mid k \in \mathbb{Z}\}$  is all of  $W_0$ .

What about orthonormality? If we attempt to apply the Orthonormal Translates criterion (11.129), then we have

$$\begin{aligned} \sum_{k=-\infty}^{\infty} |\Psi(\omega + 2k\pi)|^2 &= \sum_{k=-\infty}^{\infty} \left| \Phi\left(\frac{\omega}{2} + k\pi\right) \right|^2 \left| H\left(\frac{\omega}{2} + (k+1)\pi\right) \right|^2 \\ &= \sum_{k=-\infty}^{\infty} \left| \Phi\left(\frac{\omega}{2} + 2k\pi\right) \right|^2 \left| H\left(\frac{\omega}{2} + 2k\pi + \pi\right) \right|^2 \\ &\quad + \sum_{k=-\infty}^{\infty} \left| \Phi\left(\frac{\omega}{2} + 2k\pi + \pi\right) \right|^2 \left| H\left(\frac{\omega}{2} + 2k\pi + 2\pi\right) \right|^2. \end{aligned} \quad (11.185)$$

By the orthonormality of  $\{\phi(t-k)\}$ , we have

$$\begin{aligned} \sum_{k=-\infty}^{\infty} |\Psi(\omega + 2k\pi)|^2 &= \sum_{k=-\infty}^{\infty} \left| \Phi\left(\frac{\omega}{2} + k\pi\right) \right|^2 \left| H\left(\frac{\omega}{2} + (k+1)\pi\right) \right|^2 \\ &= \sum_{k=-\infty}^{\infty} \left| \Phi\left(\frac{\omega}{2} + 2k\pi\right) \right|^2 \left| H\left(\frac{\omega}{2} + 2k\pi + \pi\right) \right|^2 \\ &\quad + \sum_{k=-\infty}^{\infty} \left| \Phi\left(\frac{\omega}{2} + 2k\pi + \pi\right) \right|^2 \left| H\left(\frac{\omega}{2} + 2k\pi + 2\pi\right) \right|^2. \end{aligned} \quad (11.186)$$

By the  $2\pi$ -periodicity of  $H(\omega)$ , this becomes

$$\begin{aligned} \sum_{k=-\infty}^{\infty} |\Psi(\omega + 2k\pi)|^2 &= \left| H\left(\frac{\omega}{2} + \pi\right) \right|^2 \sum_{k=-\infty}^{\infty} \left| \Phi\left(\frac{\omega}{2} + 2k\pi\right) \right|^2 \\ &\quad + \left| H\left(\frac{\omega}{2}\right) \right|^2 \sum_{k=-\infty}^{\infty} \left| \Phi\left(\frac{\omega}{2} + 2k\pi + \pi\right) \right|^2 \end{aligned} \quad (11.187)$$

and by Orthonormal Translates applied to the  $\Phi$  summations on the bottom of (11.187), we get

$$\sum_{k=-\infty}^{\infty} |\Psi(\omega + 2k\pi)|^2 = \left| H\left(\frac{\omega}{2} + \pi\right) \right|^2 + \left| H\left(\frac{\omega}{2}\right) \right|^2. \quad (11.188)$$

But this last expression is unity by (11.168), and thus  $\{\psi(t-k) \mid k \in \mathbb{Z}\}$  is orthonormal.

**Corollary (Existence of Orthonormal Wavelet).** With the theorem's assumptions and notation, let  $\psi(t) \in L^2(\mathbb{R})$  be defined as above. Then the dilations and translations  $\{2^{n/2}\psi(2^n t - m) : m, n \in \mathbb{Z}\}$  are an orthonormal basis of  $L^2(\mathbb{R})$ , and so  $\psi$  is an orthonormal wavelet [8–10].

**Proof:** Since  $V_1 = V_0 \oplus W_0$ , dilations of  $x(t) \in W_0$  by  $2^i$  are in  $W_i$ :  $x(2^i t) \in W_i$ . In fact,  $\{2^{i/2}\psi(2^i t - m) : m \in \mathbb{Z}\}$  is an orthonormal basis for  $W_i$ . But,  $V_{i+1} = V_i \oplus W_i$ , so

$B_{i+1} = \{2^{n/2}\psi(2^n t - m) : n < i + 1 \text{ and } m \in \mathbb{Z}\}$  is an orthonormal set inside  $V_{i+1}$ . By the intersection property (iii) of the MRA, though,  $\bigcap_{i=-\infty}^{\infty} V_i = 0$ ;  $B_{i+1}$  must be dense in  $V_{i+1}$ . By the MRA union property (ii),  $\bigcup_{n=-\infty}^{\infty} V_i = L^2(\mathbb{R})$ ;  $L^2(\mathbb{R})$  must be the Hilbert space direct sum of the  $W_i$ :

$$\bigoplus_{i=-\infty}^{\infty} W_i = L^2(\mathbb{R}). \tag{11.189}$$

■

The wavelet  $\psi(t)$  that we have found is essentially unique. The exercises outline an argument that any other  $W_0$  function that is an orthogonal wavelet for square-integrable signals must have a Fourier transform that differs from the formula (11.183) by a factor that is unity almost everywhere on  $[0, 2\pi]$ .

**11.4.4.2 Examples.** Let us show some examples of orthonormal wavelets from the multiresolution analyses of square-integrable signals that we already know.

**Example (Step Functions).** In the Haar MRA [20], the root space  $V_0$  consists of constant functions on unit intervals  $(n, n + 1)$ , and so  $\phi(t) = u(t) - u(t - 1)$ . We compute its Fourier transform by

$$\Phi(\omega) = \int_{-\infty}^{\infty} \phi(t)e^{-j\omega t} dt = e^{-\frac{j\omega}{2}} \frac{\sin(\omega/2)}{\omega/2} \tag{11.190}$$

and the relation  $\Phi(2\omega) = \Phi(\omega)H(\omega)$  gives the associated low-pass filter:

$$H(\omega) = e^{-\frac{j\omega}{2}} \cos(\omega/2). \tag{11.191}$$

From  $\Psi(\omega) = e^{-j\omega} \overline{H(\omega + \pi)}\Phi(\omega)$ , we calculate

$$\Psi(\omega) = -je^{\frac{j\omega}{2}} \frac{\sin^2(\omega/4)}{\omega/4}. \tag{11.192}$$

But (11.192) is the radial Fourier transform of the function

$$\Psi(t) = \begin{cases} -1 & \text{if } -1 \leq t < \frac{1}{2}, \\ 1 & \text{if } -\frac{1}{2} \leq t < 0, \\ 0 & \text{if otherwise.} \end{cases} \tag{11.193}$$

so  $\psi(t)$  above is the orthogonal wavelet for the step function MRA.

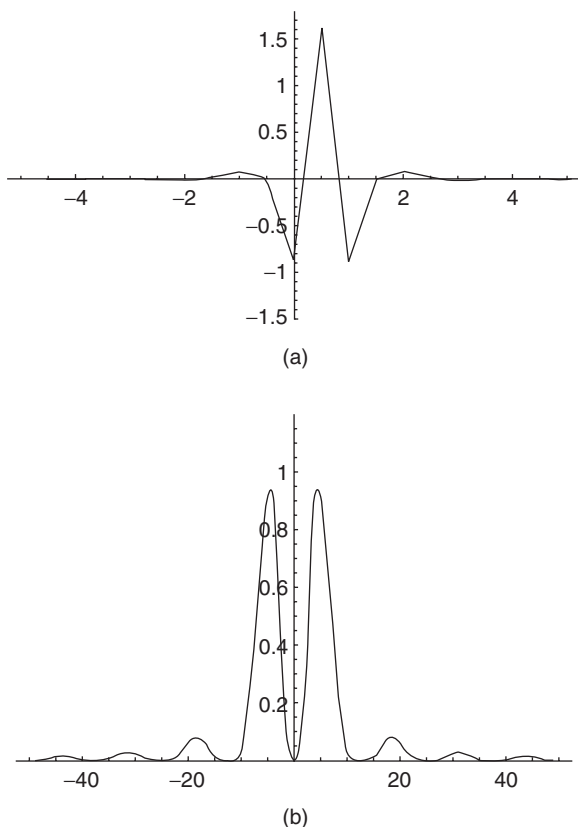


**Fig. 11.13.** For the Strömberg MRA: The orthogonal wavelet, (a) which we compute from a messy, but exact expression for its Fourier transform (b).

**Example (Piecewise Continuous Functions).** We found the scaling function for the Strömberg [22] MRA in Section 11.4.2.2 and the associated low-pass filter in Section 11.4.3. The expression  $\Psi(2\omega) = e^{j\omega} \overline{H(\omega + \pi)} \Phi(\omega)$  as well as (11.159) and (11.167) give us the Fourier transform for the piecewise continuous MRA's wavelet. Then, we can compute  $\psi(t)$  via the inverse transform (Figure 11.13).

**Example (Spline Functions).** In the third MRA we have studied, the root space  $V_0$  contains continuously differentiable, finite-energy signals that are cubic polynomials on unit intervals  $[n, n+1]$ . This MRA was developed by Lemarié [37] and Battle [38]. The same strategy works once more. We know the scaling function's Fourier transform  $\Phi(\omega)$  from (11.164). The discrete-time Fourier transform for the associated low-pass filter is the ratio  $H(\omega) = \Phi(2\omega)/\Phi(\omega)$ . Hence, we find  $\Psi(\omega)$ , and inverse transforming gives the orthogonal wavelet (Figure 11.14).

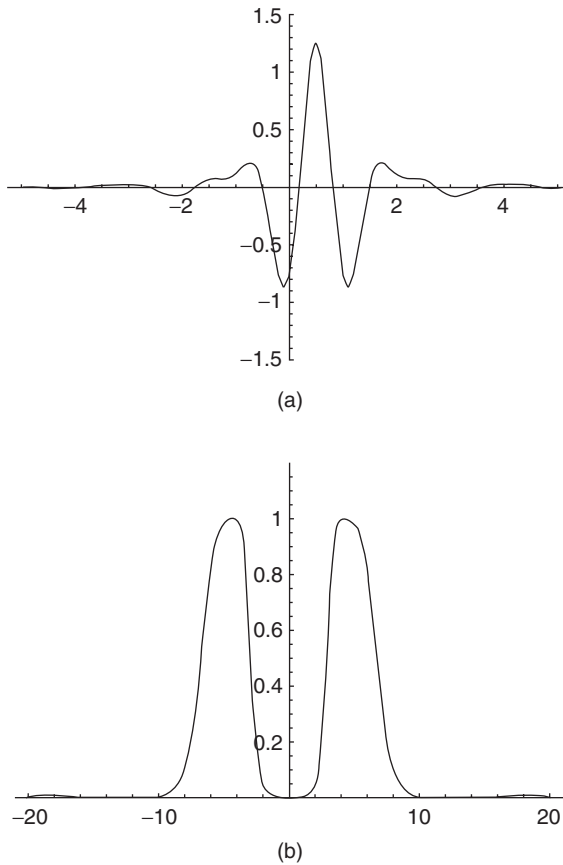


**Fig. 11.14.** For the cubic spline MRA of Lemarié and Battle: The orthogonal wavelet (a) and its Fourier transform (b).

The next chapter provides various examples of mixed domain signal analysis. In particular, it covers the use of the multiresolution analysis structure for combining time- and scale-domain analysis of signals that arise in typical applications.

## 11.5 SUMMARY

For signal analysis, both the continuous wavelet transform and the multiresolution analysis that leads to orthogonal wavelets are attractive and feasible. This chapter covered the signal analytic essentials of wavelet theory. The continuous transform finds more applications in signal understanding, as long as basic facts about input signals—location, scale, spectrum—are known beforehand. The orthogonal transforms, based on multiresolution analysis, tend to find more use in compression. We shall see in the last chapter that there are efficient algorithms for decomposition

using MRAs that lend themselves to efficient signal description, compression, as well as pattern recognition applications.

We omitted the proof of the theorem on the necessity of admissibility for frames based on translation and dilation (Section 11.3.2). The proof itself is somewhat technical, and, besides, in compensation, we later showed that an elegant construction, the MRA, leads to orthogonal wavelets from which efficient algorithms and straightforward frame constructions proceed.

There are three special functions that arise from an MRA,  $V = \{V_i; i \in \mathbb{Z}\}$ :

- The scaling function  $\phi(t)$  whose translates form an orthonormal basis for the root space  $V_0$ ;
- The associated low-pass filter  $H_\phi$ ;
- And, finally, the orthonormal wavelet  $\psi(t)$  whose translations and dilations constitute an orthonormal basis for finite-energy signals.

Some conditions in the definition we give for an MRA are consequences of the others. For example, the third criterion in Section 11.4.1.1—that only the zero signal should appear in all  $V_i$ —follows from the rest. This and other interdependencies were only noted some years later [8, 41].

We provided only a few examples of MRAs, but these suffice for introductory signal analysis applications. Important extensions include compactly supported wavelets [3], approximation theory using wavelets [2], and multidimensional signal analysis using wavelets [10, 23].

Let us remark about how wavelets can be used in image processing and analysis. The principal focus of this book notwithstanding, we should also note that our MRA definition extends from one-dimensional functions (signals) to two-dimensional functions (images). Indeed there are MRA structures for the  $n$ -dimensional Hilbert space  $L^2(\mathbb{R}^n)$ . The technique is identical to that used to extend the Gaussian and Laplacian pyramid constructions to images [24].

We just repeat the definition of Section 11.4.1.1 for functions of two variables,  $x(s, t) \in L^2(\mathbb{R}^2)$ , denoting the subspace chain  $V_{2,n}$ . We can then derive a two-dimensional scaling function  $\phi(s, t)$  as before (exercise). The most common approach, however, is to use a tensor product of one-dimensional MRAs to get an MRA for  $L^2(\mathbb{R}^2)$ :  $V_{2,n} = V_{1,n} \otimes V_{1,n}$ , where  $\{V_n; n \in \mathbb{Z}\}$  is an MRA in  $L^2(\mathbb{R})$ . Then, there is a scaling function for the two-dimensional MRA of  $L^2(\mathbb{R}^2)$ :  $\Phi(x, y) = \phi(x)\phi(y)$ . While there is a single scaling function for the two-dimensional case, there are now three wavelets:  $\Psi_1(x, y) = \phi(x)\psi(y)$ , sensitive to *high vertical frequencies*;  $\Psi_2(x, y) = \psi(x)\phi(y)$ , *horizontal*;  $\Psi_3(x, y) = \psi(x)\psi(y)$ , *diagonal* or *corners*.

This gives an orientation selective decomposition, especially suitable for images with large  $x$ - and  $y$ -direction edge components. A number of applications involve such images: inspection of manufactured materials, remote sensing applications, and seismic signal processing among others.

For a history of wavelets, see Ref. [1]. References 10 and 42 list software resources and toolkits for signal analysis using wavelets.

## REFERENCES

1. B. B. Hubbard, *The World According to Wavelets*, Wellesley, MA: A. K. Peters, 1996.
2. C. Chui, *Introduction to Wavelets*, San Diego, CA: Academic, 1992.
3. I. Daubechies, *Ten Lectures on Wavelets*, Philadelphia: SIAM, 1992.
4. Y. Meyer, *Wavelets: Algorithms and Applications*, Philadelphia: SIAM, 1993.
5. T. H. Koornwinder, ed., *Wavelets: An Elementary Treatment of Theory and Applications*, Singapore: World Scientific, 1993.
6. G. Kaiser, *A Friendly Guide to Wavelets*, Boston: Birkhauser, 1994.
7. M. Holschneider, *Wavelets: An Analysis Tool*, Oxford: Oxford University Press, 1995.
8. E. Hernandez and G. Weiss, *A First Course on Wavelets*, Boca Raton, FL: CRC Press, 1996.
9. P. Wojtaszczyk, *A Mathematical Introduction to Wavelets*, Cambridge: Cambridge University Press, 1997.
10. S. Mallat, *A Wavelet Tour of Signal Processing*, San Diego, CA: Academic, 1998.
11. H. L. Resnikoff and R. O. Wells, Jr., *Wavelet Analysis: The Scalable Structure of Information*, New York: Springer-Verlag, 1998.
12. C. Blatter, *Wavelets: A Primer*, Natick, MA: A. K. Peters, 1999.
13. A. Grossmann and J. Morlet, Decompositions of Hardy functions into square integrable wavelets of constant shape, *SIAM Journal of Mathematical Analysis*, vol. 15, pp. 723–736, 1984.
14. I. Daubechies, A. Grossmann, and Y. Meyer, Painless non-orthogonal expansions, *Journal of Mathematical Physics*, vol. 27, pp. 1271–1283, 1986.
15. I. Daubechies, The wavelet transform, time-frequency localization and signal analysis, *IEEE Transactions on Information Theory*, vol. 36, no. 5, pp. 961–1005, September 1990.
16. P. Goupillaud, A. Grossmann, and J. P. Morlet, Cycle-octave and related transforms in seismic signal analysis, *Geoexploration*, vol. 23, pp. 85–102, 1984.
17. R. Kronland-Martinet, J. P. Morlet, and A. Grossmann, Analysis of sound patterns through wavelet transforms, *International Journal of Pattern Recognition and Artificial Intelligence*, vol. 1, no. 2, pp. 97–126, 1987.
18. A. Grossmann, Wavelet transforms and edge detection, in *Stochastic Processes in Physics and Engineering*, S. Albeverio et al., ed., Dordrecht, Holland: D. Reidel Publishing Company, pp. 149–157, 1988.
19. Y. Meyer, Principe d'incertitude, bases hilbertiennes et algèbres d'opérateurs, *Séminaire Bourbaki*, no. 662, 1985–1986.
20. A. Haar, Zur theorie der orthogonalen Functionensysteme, *Mathematische Annalen*, vol. 69, pp. 331–371, 1910.
21. C. E. Shannon, Communication in the presence of noise, *Proceedings of the Institute of Radio Engineers*, vol. 37, pp. 10–21, 1949.
22. J.-O. Strömberg, A modified Franklin system and higher order spline systems on  $\mathbb{R}^n$  as unconditional bases for Hardy spaces, in *Proceedings of the Conference in Honor of Antoni Zygmund*, vol. II, W. Becker, A. P. Calderon, R. Fefferman, and P. W. Jones, eds., New York: Wadsworth, pp. 475–493, 1981.

23. S. Mallat, "A theory for multiresolution signal decomposition: The wavelet representation," *IEEE Transactions on Pattern Analysis and Machine Intelligence*, pp. 674–693, July 1989.
24. P. J. Burt and E. H. Adelson, The Laplacian pyramid as a compact image code, *IEEE Transactions on Communications*, vol. COM-31, no. 4, pp. 532–540, April 1983.
25. R. E. Crochiere and L. R. Rabiner, *Multirate Digital Signal Processing*, Englewood Cliffs, NJ: Prentice-Hall, 1983.
26. A. P. Witkin, Scale-space filtering, *Proceedings of the 8th International Joint Conference on Artificial Intelligence*, Karlsruhe, W. Germany, 1983. Also in *From Pixels to Predicates*, A. P. Pentland, ed., Norwood, NJ: Ablex, 1986.
27. J. J. Koenderink, The structure of images, *Biological Cybernetics*, vol. 50, pp. 363–370, 1984.
28. T. Lindeberg, Scale space for discrete signals, *IEEE Transactions on Pattern Analysis and Machine Intelligence*, vol. 12, no. 3, pp. 234–254, March 1990.
29. S. G. Mallat, Multiresolution approximations and wavelet orthonormal bases of  $L^2(\mathbb{R}^n)$ , *Transactions of the American Mathematical Society*, vol. 315, no. 1, pp. 69–87, September 1989.
30. E. Kreyszig, *Introductory Functional Analysis with Applications*, New York: John Wiley & Sons, 1989.
31. J. Stoer and R. Bulirsch, *Introduction to Numerical Analysis*, 2nd ed., New York: Springer-Verlag, 1992.
32. A. Rosenfeld and M. Thurston, Edge and curve detection for visual scene analysis, *IEEE Transactions on Computers*, vol. 20, no. 5, pp. 562–569, May 1971.
33. S. Tanimoto and T. Pavlidis, A hierarchical data structure for picture processing, *Computer Graphics and Image Processing*, vol. 4, no. 2, pp. 104–119, June 1975.
34. R. Y. Wong and E. L. Hall, Sequential hierarchical scene matching, *IEEE Transactions on Computers*, vol. C-27, no. 4, pp. 359–366, April 1978.
35. D. Marr, *Vision*, New York: W. H. Freeman and Company, 1982.
36. I. S. Gradshteyn and I. M. Ryzhik, *Table of Integrals, Series, and Products*, Orlando, FL: Academic, 1980.
37. P.-G. Lemarié, Ondelettes à localisation exponentielle, *Journal de Mathématiques Pures et Appliquées*, vol. 67, pp. 227–236, 1988.
38. G. Battle, A block spin construction of ondelettes. Part 1: Lemarié functions, *Communications in Mathematical Physics*, vol. 110, pp. 601–615, 1987.
39. P. P. Vaidyanathan, Multirate digital filters, filter banks, polyphase networks, and applications: A tutorial, *Proceedings of the IEEE*, vol. 78, pp. 56–93, January 1990.
40. O. Rioul and M. Vetterli, Wavelets and signal processing, *IEEE SP Magazine*, pp. 14–38, October 1991.
41. W. R. Madych, Some elementary properties of multiresolution analyses of  $L^2(\mathbb{R}^n)$ , in *Wavelets: A Tutorial in Theory and Applications*, C. K. Chui, ed., Boston: Academic, pp. 259–294, 1992.
42. A. Bruce, D. Donoho, and H. Y. Gao, Wavelet analysis, *IEEE Spectrum*, pp. 26–35, October 1996.

**PROBLEMS**

1. Let  $\psi(t)$  be an analyzing wavelet.
  - (a) Show that  $\Psi(0) = 0$ .
  - (b) Also,  $\int_{-\infty}^{\infty} \psi(t) dt = 0$ .
  - (c) Show that  $\psi(t)$  is a bandpass filter.
2. Provide an example of a bandpass filter that is not an analyzing wavelet.
3. Let  $V = \{V_i; i \in \mathbb{Z}\}$  be a multiresolution analysis of  $L^2(\mathbb{R})$  signals; let  $\phi(t)$  be the scaling function for  $V$ ; let  $\Phi(\omega)$  be the (radial) Fourier transform of  $\phi(t)$ ; and let  $H$  be the associated discrete filter with impulse response,  $h(n) = h_n$ , given by (11.166). Show in detail that  $\Phi(2\omega) = \Phi(\omega)H(\omega)$ , where  $H(\omega)$  is the DTFT of  $h(n)$ .
4. Let  $\alpha, \beta \in \mathbb{C}$  and  $\psi(t), \phi(t)$  be (analyzing) wavelets. If  $\theta(t) = \alpha\psi(t) + \beta\phi(t)$ , then show

$$W_{\theta}[f(t)](a, b) = \bar{\alpha}W_{\psi}[f(t)](a, b) + \bar{\beta}W_{\phi}[f(t)](a, b). \tag{11.194}$$

5. Let  $\eta > 0$ , let  $\psi(t)$  be a wavelet, and let  $\theta(t) = \frac{1}{\eta}\psi\left(\frac{t}{\eta}\right)$ . Show that

$$W_{\theta}[f(t)](a, b) = \frac{1}{\sqrt{\eta}}W_{\psi}[f(t)](a\eta, b). \tag{11.195}$$

6. Let  $\alpha, \beta \in \mathbb{C}$  and define  $\theta(t) = \alpha\psi(t) + \beta\phi(t)$ . Show that

$$W_{\theta}[\alpha f(t) + \beta g(t)](a, b) = \alpha W_{\psi}[f(t)](a, b) + \beta W_{\phi}[g(t)](a, b) \tag{11.196}$$

7. If  $\gamma \in \mathbb{R}$ , then show

$$W[f(t - \gamma)](a, b) = W[f(t)](a, b - \gamma). \tag{11.197}$$

8. Let  $m, n \in \mathbb{Z}; a_0, b_0 > 0$ ; and suppose that

$$\Psi_{m,n}(t) = a_0^{-\frac{m}{2}} \Psi\left(\frac{t - nb_0 a_0^m}{a_0^m}\right) = a_0^{-\frac{m}{2}} \Psi(a_0^{-m} t - nb_0). \tag{11.198}$$

- (a) Find the radial Fourier transform  $\Psi_{m,n}(\omega)$  of  $\Psi_{m,n}(t)$ .
- (b) Defining  $\Psi^-(\omega) = \Psi^+(-\omega)$ , where  $\Psi^+(\omega)$  is given by (11.108), and using the arguments of Section 11.3, show that

$$\sum_{m, n = -\infty}^{\infty} |\langle x, \Psi_{m, n}^- \rangle|^2 = \frac{1}{2\pi b_0 \ln a_0} \sum_m \int_{-\infty}^0 |X(\omega)|^2 d\omega, \quad (11.199)$$

where  $\Psi^-(t)$  is the inverse (radial) Fourier transform of  $\Psi^-(\omega)$ .

9. Let  $H$  be a Hilbert space.
- Show that an orthonormal basis in  $H$  is also a Riesz basis with unit bounds.
  - Show that a Riesz basis is linearly independent.
  - Give an example of a frame in  $L^2(\mathbb{R})$  that is not a Riesz basis.
10. Let  $V = \{V_i\}$  be the Haar MRA which we defined in Section 11.4.1.1. Signals in  $V_i$  are constant on intervals  $(n2^{-i}, (n+1)2^{-i})$ , where  $n \in \mathbb{Z}$ . If  $x(t) \in V_0$ , and  $x(t) = c_n[u(t-n) - u(t-n-1)]$  for  $t \in [n, n+1)$ , then we set  $I(x(t)) = s(n)$ , where  $s(n) = c_n$  for all  $n \in \mathbb{Z}$ .
- Show that  $I$  is an isomorphism, a bounded linear operator that is one-to-one and onto.
  - Show that if  $I(x) = s(n)$  and  $k \in \mathbb{Z}$ , then  $I(x(t-k)) = s(n-k)$ .
  - Is  $I$  an isometry? Explain.
  - Are the elements of  $V_0$  compactly supported? Explain.
11. Let  $W_0$  be the continuous  $L^2(\mathbb{R})$  signals that are piecewise linear on  $[n, n+1]$ ,  $n \in \mathbb{Z}$ . Define  $x(t) \in W_i \Leftrightarrow x(2t) \in W_{i+1}$ .
- Verify MRA properties (i), (iii)–(v) for  $W = \{W_i\}$ .
  - Let  $V = \{V_i\}$  be the Haar MRA of the previous problem. Assuming that step functions are dense in  $L^2(\mathbb{R})$ , argue likewise for  $W$  by showing that given  $v(t) \in V_0$ , then some  $w(t) \in W$  is arbitrarily close to  $v(t)$ . *Moral:* An approximation of an approximation is still an approximation.
  - Let  $w \in W_0$  and set  $Iw = s$ , where  $s(n) = w(n)$ . Show that  $I$  is an isomorphism.
12. Let  $l^\infty(\mathbb{Z})$  be the normed linear space of bounded sequences, with  $\|x\| = \sup\{|x(n)|: n \in \mathbb{Z}\}$ . Define an operator  $Tx = y$  as follows:  $y(n) = x(n)(|n|+1)^{-1}$ . Show that
- $T$  is linear.
  - $T$  is one-to-one.
  - $T$  is onto.
  - $T$  is bounded.
  - $T^{-1}$  is not bounded [30].
13. Let  $I: H \rightarrow K$  be a bounded Hilbert space isomorphism and let  $I^*$  be the Hilbert space adjoint of  $I$ .
- Show that  $\|I^*\| = \|I\|$  [30].
  - Supposing that  $I$  is onto, show that  $I^*$  is an isomorphism.

- (c) Show that if  $E = \{e_k \mid k \in \mathbb{Z}\}$  is a Riesz basis in  $H$ , then there is  $F = \{f_k \mid k \in \mathbb{Z}\}$  such that  $F$  is a Riesz basis and [9]

$$\langle e_m, f_n \rangle = \begin{cases} 1 & \text{if } m = n, \\ 0 & \text{if } m \neq n. \end{cases} \tag{11.200}$$

14. Let  $\phi(t) \in L^2(\mathbb{R})$ , let  $\Phi(\omega) = \mathcal{F}[\phi(t)](\omega)$  be its radial Fourier transform, let  $s \in \ell^2$ ,  $S(\omega)$  be its discrete-time Fourier transform, and set  $P(\omega) = \sum_{n=-\infty}^{\infty} |\Phi(\omega + 2\pi n)|^2$ . Show that

(a)  $\sum_{k=-\infty}^{\infty} s(k)\Phi(t-k) \in L^2(\mathbb{R})$ ;

(b)  $\left\| \sum_{k=-\infty}^{\infty} s(k)\phi(t-k) \right\|_2^2 = \frac{1}{2\pi} \int_0^{2\pi} |S(\omega)|^2 P(\omega) d\omega$ .

15. This problem uses the concept of Lebesgue measure. Let  $P(\omega)$  be defined as above. Define  $P_a = \{\omega \in [0, 2\pi] : P(\omega) > a\}$  and  $Q_a = \{\omega \in [0, 2\pi] : P(\omega) < a\}$ . Referring to Ref. 9, show that:

- (a) If the Lebesgue measure of  $P_a$ ,  $\mu(P_a)$ , is zero for almost all  $a \in \mathbb{R}$ , then  $P(\omega) = 0$  almost everywhere. *Hint:* Suppose not, so that  $P(\omega) > 0$  on  $U \subseteq \mathbb{R}$ . Then  $U = \cup P_{1/n}$ , where  $n > 0$  is a natural number. What is  $\mu(P_{1/n})$ ? Apply the Lebesgue measure to the countable union.
- (b) Similarly, if  $\mu(Q_a) = 0$  for almost all  $a \in \mathbb{R}$ , then  $P(\omega) = \infty$  almost everywhere.

16. Complete the proof of the second Riesz basis characterization theorem [9]. Suppose  $\phi(t) \in L^2(\mathbb{R})$ ,  $\Phi(\omega) = \mathcal{F}[\phi(t)](\omega)$  is its Fourier transform,  $F = \{\phi(t-k) \mid k \in \mathbb{Z}\}$ ,  $0 < A \leq B < \infty$ ,  $P(\omega) = \sum |\Phi(\omega + 2\pi n)|^2$ , and  $F$  is a Riesz basis with lower and upper bounds  $\sqrt{A}$  and  $\sqrt{B}$ , respectively. Show that  $P(\omega) \leq B$  for almost all  $\omega \in \mathbb{R}$ .

- (a) Define  $P_a = \{\omega \in [0, 2\pi] : P(\omega) > a\}$ . Show that if  $\mu(P_a) = 0$  almost everywhere, then  $P(\omega) = 0$  for almost all  $\omega \in [0, 2\pi]$ , and  $P(\omega) \leq B$ . *Hint:* Consider the case  $a = 1/(n+1)$  for  $n \in \mathbb{N}$ .
- (b) Hence, assume that for some  $a > 0$ ,  $\mu(P_a) > 0$ . Let  $\chi_a$  be the characteristic function on  $P_a$  and  $x_a(n)$  be the inverse discrete-time Fourier transform of  $\chi_a(\omega)$ . Show  $\|x_a\|^2 = (2\pi)^{-1} \mu(P_a)$ .
- (c) Show  $\|\sum x_a(k)\phi(t-k)\|^2 \geq a\|x_a\|^2$ .
- (d) Show  $B \geq a$ .
- (e) Conclude that, unless  $B \geq \sum |\Phi(\omega + 2\pi k)|^2$  almost everywhere on  $[0, 2\pi]$ , a contradiction arises.

17. This problem uses Lebesgue measure, but is straightforward. Suppose  $\phi(t) \in L^2(\mathbb{R})$ ,  $\Phi(\omega) = \mathcal{F}[\phi(t)](\omega)$  is its (radial) Fourier transform, and  $F = \{\phi(t - k) \mid k \in \mathbb{Z}\}$  is an orthonormal set.
- (a) Show that  $\|\Phi\|_2 = (2\pi)^{1/2}$ .
  - (b) Show that  $|\Phi(\omega)| \leq 1$  for almost all  $\omega \in \mathbb{R}$ .
18. This problem studies Strömberg MRA [9, 22], wherein  $V_0$  consists of continuous signals that are linear on integral segments  $[n, n + 1]$ .
- (a) Let  $\phi(t)$  be a scaling function for  $V = \{V_i\}$ . Prove that  $\phi(t)$  cannot be finitely supported. Assume that it is finitely supported and derive a contradiction as follows. Take the last interval  $(n, n + 1)$  to the right over which  $\phi(t)$  is nonzero, take the last interval  $(m, m + 1)$  proceeding to the left over which  $\phi(t)$  is nonzero, and compute the inner product  $\langle \phi(t), \phi(t - (n - m)) \rangle$ .
  - (b) Enumerate all of the cases for the inner product, and show that it is never zero.
  - (c) Show that  $\phi(t) \neq 0$  on  $(n, n + 1)$  for arbitrarily large  $|n|$ .
  - (d) Conclude that the inner products  $\langle \phi(t), \phi(t - k) \rangle$  involve an infinite number of terms.
19. Show that the scaling function for an MRA is essentially unique. More precisely, let  $V = \{V_i; i \in \mathbb{Z}\}$  be an MRA and let  $\phi(t) \in V_0$  be its scaling function. Show that  $\theta(t) \in V_0$  is a scaling function for  $V$  if and only if there is a  $2\pi$ -periodic function  $P(\omega)$  such that  $\Theta(\omega) = P(\omega)\Phi(\omega)$  and  $|P(\omega)| = 1$  almost everywhere on  $[0, 2\pi]$ .
20. Let  $V = \{V_i; i \in \mathbb{Z}\}$  be an MRA,  $\phi(t)$  its scaling function,  $\Phi = \mathcal{F}(\phi)$ , and  $H = H_\phi$  the associated low-pass filter. State and prove a generalization of the  $V_{-1}$  Characterization of Section 11.4.3 for any  $V_N \subset V_0$ , where  $N < 0$ .
21. With the same notation as in the previous problem, define the operator  $T: V_0 \rightarrow L^2[0, 2\pi]$  by  $Tx = C$ , where  $C(\omega)$  is the  $2\pi$ -periodic function with  $X(\omega) = C(\omega)\Phi(\omega)$  guaranteed by the  $V_0$  characterization (Section 11.4.3).
- (a) Show that  $T$  is linear:  $T(x + y) = Tx + Ty$  and  $T(ax) = aTx$  for  $a \in \mathbb{C}$ .
  - (b) If  $c(n) \in \ell^2$  is the inverse DTFT of  $C(\omega) = Tx$ , show that  $\|c\| = \|x\|$ .
  - (c) Show that  $T$  is a bounded linear map.
22. This problem uses Lebesgue measure to show that the orthogonal wavelet for an MRA is essentially unique [8]. Suppose  $V = \{V_i; i \in \mathbb{Z}\}$  is an MRA,  $\phi(t)$  is its scaling function,  $\Phi = \mathcal{F}(\phi)$  is the Fourier transform of  $\phi$ , and  $H = H_\phi$  is the associated low-pass filter. Let  $\psi(t) \in W_0$  be an orthogonal wavelet for  $L^2(\mathbb{R})$ .
- (a) Show that there is a  $2\pi$ -periodic  $v(\omega) \in L^2[0, 2\pi]$  such that

$$\Psi(2\omega) = v(2\omega)e^{-j\omega} \overline{H(\omega + \pi)} \Phi(\omega). \tag{11.201}$$

(b) Show that

$$\sum_{k=-\infty}^{\infty} |\Psi(\omega + 2\pi k)|^2 = 1 = |v(\omega)|^2 \sum_{k=-\infty}^{\infty} \left| H\left(\frac{\omega}{2} + \pi k + \pi\right) \right|^2 \left| \Phi\left(\frac{\omega}{2} + \pi k\right) \right|^2. \tag{11.202}$$

(c) Summing over even and odd integers separately, show that the final expression above becomes

$$|v(\omega)|^2 \left( \sum_{k=-\infty}^{\infty} \left| H\left(\frac{\omega}{2} + \pi\right) \right|^2 \left| \Phi\left(\frac{\omega}{2} + 2\pi k\right) \right|^2 + \sum_{k=-\infty}^{\infty} \left| H\left(\frac{\omega}{2}\right) \right|^2 \left| \Phi\left(\frac{\omega}{2} + 2\pi k + \pi\right) \right|^2 \right). \tag{11.203}$$

(d) Prove that

$$1 = |v(\omega)|^2 \left( \left| H\left(\frac{\omega}{2} + \pi\right) \right|^2 + \left| H\left(\frac{\omega}{2}\right) \right|^2 \right) = |v(\omega)|^2 \tag{11.204}$$

for almost all  $\omega \in [0, 2\pi]$ .

(e) Conclude that the Fourier transform of  $\psi(t)$  has the form

$$\Psi(2\omega) = v(2\omega) e^{-j\omega \overline{H(\omega + \pi)}} \Phi(\omega), \tag{11.205}$$

where  $v(\omega)$  is measurable, and has period  $2\pi$ , and  $v(\omega) = 1$  almost everywhere on  $[0, 2\pi]$ .

23. Show that to get an orthonormal basis for  $W_0$  an alternative definition for the Fourier transform of  $\psi(t)$  is

$$\Psi(2\omega) = e^{j\omega \overline{H(\omega + \pi)}} \Phi(\omega). \tag{11.206}$$

Show that with this change of the exponent's sign  $\{\psi(t - k) \mid k \in \mathbb{Z}\}$  is still an orthonormal basis for  $W_0$ .

The following problems involve some extension of concepts in the text, may require some exploration of the research literature, and are generally more difficult than the preceding exercises.

24. Expand the construction of tight wavelet frames in Section 11.3.3 to include the case  $0 < a_0 < 1$ . Show that (11.109) continues to hold.

25. Investigate the application of frames of translations and dilations as constructed in Section 11.3.3. Assume that  $a_0 = 2$  and  $b_0 = 1$ .

- (a) Using a mathematical software package such as Mathematica or Matlab, or by developing your own Fourier transform software in a high-level programming language, find the inverse Fourier transforms for  $\Psi^+(\omega)$  and  $\Psi^-(\omega)$ .
  - (b) As Daubechies remarks [3], this frame is not well-localized, and this becomes a problem for certain signal analysis tasks. By experiments of your own design, justify this claim.
  - (c) Continue your critique of this frame by considering the fact that it consists of translations and dilations of two distinct root elements,  $\psi^+(t)$  and  $\psi^-(t)$ . In particular, explore the consequences of the definition  $\Psi^-(\omega) = \Psi^+(-\omega)$ . What difficulties does this impose on signal analysis applications? Develop experiments that justify your contention.
  - (d) Develop experiments using translations and dilations of the Mexican hat wavelet and compare the performance to the frame in part (c) based on  $\psi^+(t)$  and  $\psi^-(t)$ .
26. Extend the idea of a multiresolution analysis to  $L^2(\mathbb{R}^2)$ .
- (a) Reformulate the definition of Section 11.4.1.1 for functions of two variables,  $x(s, t) \in L^2(\mathbb{R}^2)$ .
  - (b) Let  $\{V_{2,k}: k \in \mathbb{Z}\}$  be an MRA for  $L^2(\mathbb{R}^2)$ . Show that there is a unique image  $\phi(s, t)$  such that  $\{2^k\phi(2^k s - n, 2^k t - m): m, n \in \mathbb{Z}\}$  constitutes an orthonormal basis for  $V_{2,k}$ .

# Mixed-Domain Signal Analysis

This final chapter explains the methods for using time-frequency or time-scale transforms to segment, classify, and interpret signals. The previous two chapters introduced these *mixed-domain* transforms and their application to elementary analysis tasks. The short-time Fourier (or Gabor) transform (Chapter 10) and the wavelet transform (Chapter 11) are the main tools for the applications we discuss. The applications explain their practical and efficient use, spotlight their strengths and weaknesses, and contrast them with pure time- and frequency-domain techniques.

This chapter covers three methods that, together with the local frequency or scale information given by the transforms, are capable of elucidating signal structure:

- A type of structured neural network, which we call the *pattern recognition network*;
- The *hidden Markov model* (HMM), which has become very popular for speech, text, and biological sequence analysis;
- The *matching pursuit*, a Hilbert space search technique for efficient signal description using a dictionary of signal models.

In place of a summary, there is an afterword to the entire book.

## 12.1 WAVELET METHODS FOR SIGNAL STRUCTURE

This section follows up on the theoretical work of the previous chapter. There we discovered a special tool for describing multiscale signal structure, the multiresolution analysis (MRA) of finite-energy signals. Now we want to explain how, working within the framework of a chosen MRA, we can:

- (i) Develop a discrete version of the wavelet transform.
- (ii) Show how an efficient algorithm for signal decomposition arises from the MRA of finite-energy signals.

- (iii) Link this result to the perfect reconstruction filter banks covered in Chapter 9.
- (iv) And, finally, show how to employ these methods for analyzing signal shape across many scales.

### 12.1.1 Discrete Wavelet Transform

Let us assume that we have selected a multiresolution analysis of square-integrable analog signals. Section 11.4 introduced this theory. To recapitulate, an MRA [1] is a chain of subspaces  $\{V_i; i \in \mathbb{Z}\}$  in  $L^2(\mathbb{R})$  such that:

- (i) The  $V_i$  are closed and nested:  $\dots \subset V_{-1} \subset V_0 \subset V_1 \subset V_2 \subset \dots$
- (ii) Their union is dense in  $L^2(\mathbb{R})$ :  $\overline{\bigcup_{n=-\infty}^{\infty} V_n} = L^2(\mathbb{R})$ .
- (iii) The only signal common to all the  $V_i$  is the signal that is zero almost everywhere:  $\bigcap_{i=-\infty}^{\infty} V_i = 0$ .
- (iv) Dilation by a factor of two links the closed subspaces:  $x(t) \in V_i \Leftrightarrow x(2t) \in V_{i+1}$ .
- (v) The root space  $V_0$  is closed under integral translation: If  $x(t) \in V_0$  and  $k \in \mathbb{Z}$ , then  $x(t - k) \in V_0$ .
- (vi) There is a bounded, one-to-one, linear map, with a bounded inverse  $I: V_0 \rightarrow l^2$  that commutes with integral translation: If  $k \in \mathbb{Z}$ , and  $I(x(t)) = s(n) \in l^2$ , then  $I(x(t - k)) = s(n - k)$ .

Property (vi) is equivalent to the existence of a Riesz basis within  $V_0$  (Section 11.4.1.4). The previous chapter provided examples of MRAs: step functions, piecewise linear functions, and cubic spline functions. Most importantly, associated with an MRA  $\{V_i; i \in \mathbb{Z}\}$  are three special signals:

- (i) An analog *scaling function*,  $\phi(t) \in V_0$ , such that  $\{\phi(t - k); k \in \mathbb{Z}\}$  is an orthonormal basis of  $V_0$ .
- (ii) A discrete *associated lowpass filter*  $H_\phi$  with impulse response,  $h(n) = h_n$ , given by  $h_n = \langle \frac{1}{2}\phi(\frac{t}{2}), \phi(t - n) \rangle$ , where  $\phi(t)$  is the scaling function in (i).
- (iii) An analog *orthogonal wavelet*  $\psi(t)$ , defined by its Fourier transform as follows:  $\Psi(2\omega) = e^{-j\omega} H(\omega + \pi) \Phi(\omega)$ , where  $\phi(t)$  is the scaling function of (i),  $\Phi = \mathcal{F}(\phi)$  is the Fourier transform of  $\phi$ , and  $H = H_\phi$  is the associated low-pass filter of (ii).

To make the MRA signal decomposition discrete, we assume that the analog source signals reside in root space  $x(t) \in V_0$  and that we sample them at unit distance to get  $x(n)$ . The scaling function is a lowpass filter, and its expanding dilations—for example,  $\phi(t/2)$ ,  $\phi(t/4)$ ,  $\phi(t/8)$ , and so on—have successively narrower passbands. Filtering  $x(t)$  by these dyadic dilations of  $\phi(t)$  produces approximate versions of  $x(t)$

which are increasingly smooth. Next, since some high frequency detail has been removed from  $x(t)$  by the filtering, we may select samples that are further apart. For example, after the convolution  $x * \phi(t/4)$  removes noise and sharp transitions from  $x(t)$ , sampling occurs on quadruple unit intervals. This idea comes from the Laplacian pyramid decomposition, covered at the end of Chapter 9 [2].

Let us formalize these ideas for the case of the MRA. Following the notation of Ref. 1, let  $x_a(t) = ax(at)$  be the scaled dilation of  $x(t)$  by factor  $a$ . Typically,  $a = 2^i$  for  $i \in \mathbb{Z}$ . Then the *discrete approximate* representation of signal  $x(t)$  at resolution  $2^i$  is

$$(A_i^d x)(n) = (x(t) * \phi_{2^i}(-t))(2^{-i}n). \tag{12.1a}$$

On the other hand, the orthogonal wavelet  $\psi(t)$  is a bandpass filter. Its dilation by various dyadic factors results in filters with narrower passbands and lower center frequencies. Thus, we define the *discrete detail* representation of  $x(t)$  at resolution  $2^i$ :

$$(D_i^d x)(n) = (x(t) * \psi_{2^i}(-t))(2^{-i}n). \tag{12.1b}$$

Although (12.1a) and (12.1b) discretize the decomposition of a square-integrable signal  $x(t)$ , it remains to see how to compute the various analog convolutions that are required.

### 12.1.2 Wavelet Pyramid Decomposition

The *discrete orthogonal wavelet representation* or *wavelet pyramid decomposition* consists of the following filtered and coarsely sampled discrete signals:

$$A_{-J}^d x, D_{-J}^d x, D_{-J+1}^d x, \dots, D_{-1}^d x. \tag{12.2}$$

Notice in (12.2) that only the pyramid maintains all of the detail signals, up to the decomposition level  $-J$ , but only the coarsest approximate representation of  $x(t)$ . Let us turn our attention to the convolution operations needed to derive this special structural description.

**12.1.2.1 Coarse Signal Structure: The Approximate Signal.** We concentrate on deriving the coarse signal approximation,  $A_{-J}^d x$  in the pyramid decomposition (12.2). The next section explains how to derive the detailed structural descriptions.

Again, let  $\{V_i\}_{i \in \mathbb{Z}}$  be a multiresolution analysis of  $L^2(\mathbb{R})$ ,  $\phi \in V_0$  be its scaling function, and  $\psi \in V_1$  be its orthonormal wavelet (Section 11.4.4). We define  $\tilde{h}(n) = h(-n)$  to be the reflection of  $h(n)$ , the impulse response of the associated

low-pass filter  $H = H_\phi$ . (Since a scaling function  $\phi$  is known for the MRA, we drop the subscript.)

We rewrite the convolution (12.1a) as an inner product:

$$(A_i^d x)(n) = 2^i \langle x(t), \phi(2^i t - n) \rangle, \quad (12.3)$$

Now let  $p > 0$  and  $i$  be integers, let  $x \in L^2(\mathbb{R})$ , and let  $H_p$  be the discrete filter with impulse response  $h_p$ :

$$h_p(n) = 2^{-p} \langle \phi(2^{-p} t), \phi(t - n) \rangle = \langle \phi_{2^{-p}}(t), \phi(t - n) \rangle. \quad (12.4)$$

Note that  $h_1(n) = h(n)$ , the impulse response of the quadrature mirror filter associated to the multiresolution analysis  $\{V_i\}$ .

Then we claim that the decomposition for the discrete approximate representation of signal  $x(n)$  at level  $i$  is given in terms of the approximate representation of  $x(n)$  at level  $i + p$  by

$$(A_i^d x)(n) = \sum_{k=-\infty}^{\infty} \tilde{h}_p(2^p n - k) (A_{i+p}^d x)(k). \quad (12.5)$$

This means that we can get completely rid of the analog convolutions through which we originally defined the pyramid. Indeed, if we take  $p = 1$  in (12.5), then each approximate level of representation comes from convolution with  $\tilde{h}_p(n)$  followed by dyadic subsampling. This continues recursively for  $p$  levels to produce the approximate signal structure of  $x(n)$  at level  $i$  from the approximate representation at level  $i + p$ .

To show how this works, we consider the expansion of  $V_i$  signals on the orthogonal basis elements of  $V_{i+p}$ . For any  $i$ , the signals  $\{\phi_{2^i t - 2^{-i} n}\}_{n \in \mathbb{Z}}$  span  $V_i \subset V_{i+p}$ . Indeed, an orthonormal basis of  $V_{i+p}$  is  $\{2^{-(i+p)/2} \phi_{2^{i+p}(t - 2^{-i-p} n)}\}_{n \in \mathbb{Z}}$ . Consequently,

$$\phi(2^i t - n) = 2^{i+p} \sum_{k=-\infty}^{\infty} \langle \phi(2^i s - n), \phi(2^{i+p} s - k) \rangle \phi(2^{i+p} t - k). \quad (12.6)$$

With a change of variables  $s = 2^{-i-p}(t + 2^p n)$ , the inner product in (12.6) is

$$\begin{aligned} \int_{-\infty}^{\infty} \phi(2^i s - n) \phi(2^{i+p} s - k) ds &= 2^{-i-p} \int_{-\infty}^{\infty} \phi(2^{-p} t) \phi(t + 2^p n - k) dt \\ &= 2^{-i-p} \int_{-\infty}^{\infty} \phi(2^{-p} s) \phi(s - (k - 2^p n)) ds. \end{aligned} \quad (12.7)$$

Putting (12.6) back into (12.7), it follows that

$$\langle x(t), \phi(2^i t - n) \rangle = \sum_{k=-\infty}^{\infty} \int_{-\infty}^{\infty} \phi(2^{-p} s) \phi(s - (k - 2^p n)) ds \langle x(t), \phi(2^{i+p} t - k) \rangle. \tag{12.8}$$

From the definition of the impulse response  $h_p$  (12.4), we get

$$\langle x(t), \phi(2^i t - n) \rangle = 2^p \sum_{k=-\infty}^{\infty} \tilde{h}_p(2^p n - k) \langle x(t), \phi(2^{i+p} t - k) \rangle. \tag{12.9}$$

But the inner products in (12.9) are in fact the discrete representations of signal  $x(t)$  at levels  $i$  and  $i + p$ . So (12.5) follows directly.

Let us find the impulse response of the discrete filter  $H_p$ . Since  $\{\phi(t - k)\}_{k \in \mathbb{Z}}$  is a basis for  $V_0$ ,

$$\phi(2^{-p} t) = \sum_{k=-\infty}^{\infty} \langle \phi(2^{-p} s), \phi(s - k) \rangle \phi(t - k). \tag{12.10}$$

Taking radial Fourier transforms on both sides of (12.10) and simplifying,

$$\Phi(2^p \omega) = \sum_{k=-\infty}^{\infty} h_p(k) \int_{-\infty}^{\infty} \phi(t - k) e^{-j\omega t} dt = H_p(\omega) \Phi(\omega). \tag{12.11}$$

The discrete-time Fourier transform of the filter  $H_p$  is

$$H_p(\omega) = \frac{\Phi(2^p \omega)}{\Phi(2\omega)}, \tag{12.12}$$

where  $\Phi(\omega)$  is the radial Fourier transforms of scaling function  $\phi(t)$ . Applying the inverse discrete time Fourier transform to (12.12), gives  $h_p(n)$  (Figure 12.1).

Figure 12.2 shows the  $H_p(\omega)$ . (12.18) lists filter values for the cubic spline MRA. Note that the  $h_p(n)$  are even.

To extract a coarse approximation of a signal's structure using a given MRA, then, the steps are:

- (i) Select a resolution step factor  $p > 0$ .
- (ii) Compute the impulse response  $h_p(n)$  of the filter with discrete time Fourier transform given by (12.12).

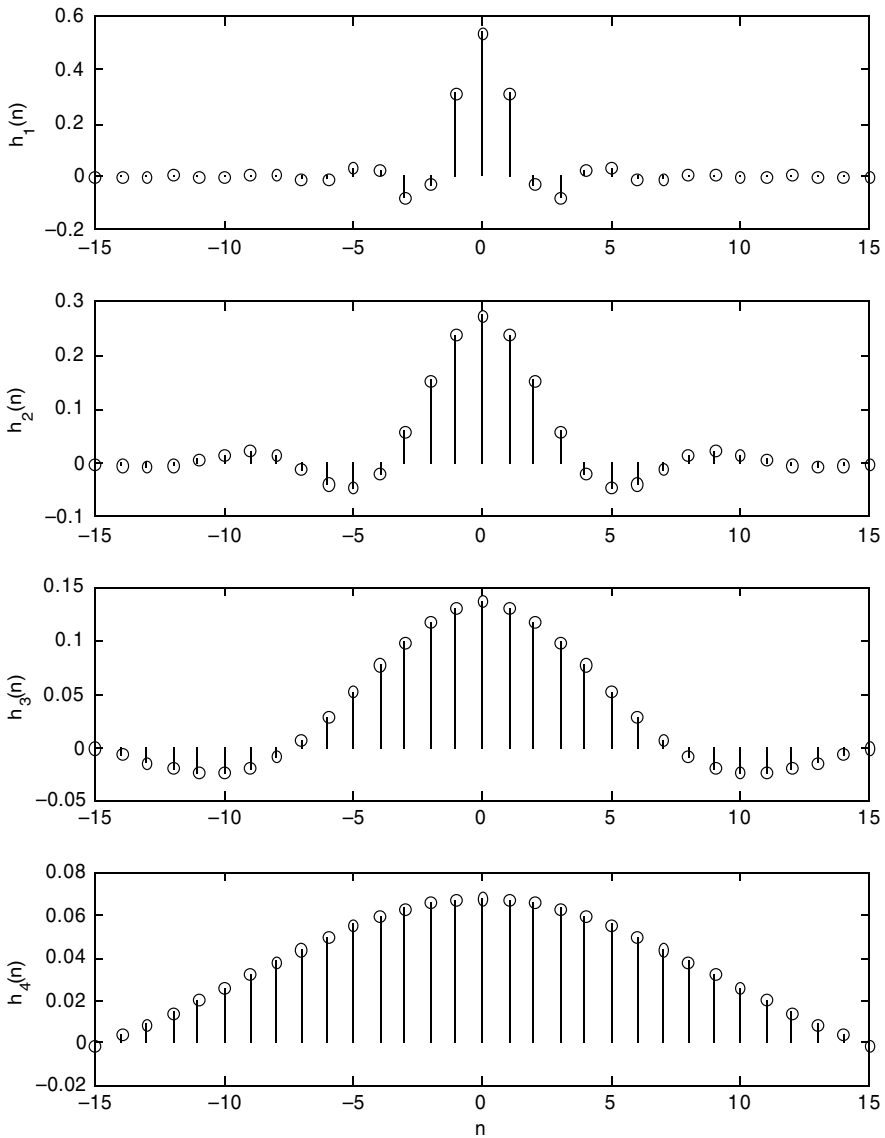


**Fig. 12.1.** Discrete filter impulse response signals  $h_1$ ,  $h_2$ ,  $h_3$ , and  $h_4$  for the cubic spline MRA.

- (iii) Compute the convolution (12.5) on  $2^p$ -wide intervals to get a coarse approximation  $(A_i^d x)(n)$  from  $(A_{i+p}^d x)(n)$ .
- (iv) Employ one of Chapter 4's thresholding methods to the magnitude of the decomposition coefficients, identifying large and small coefficients with significant signal features and background noise, respectively.

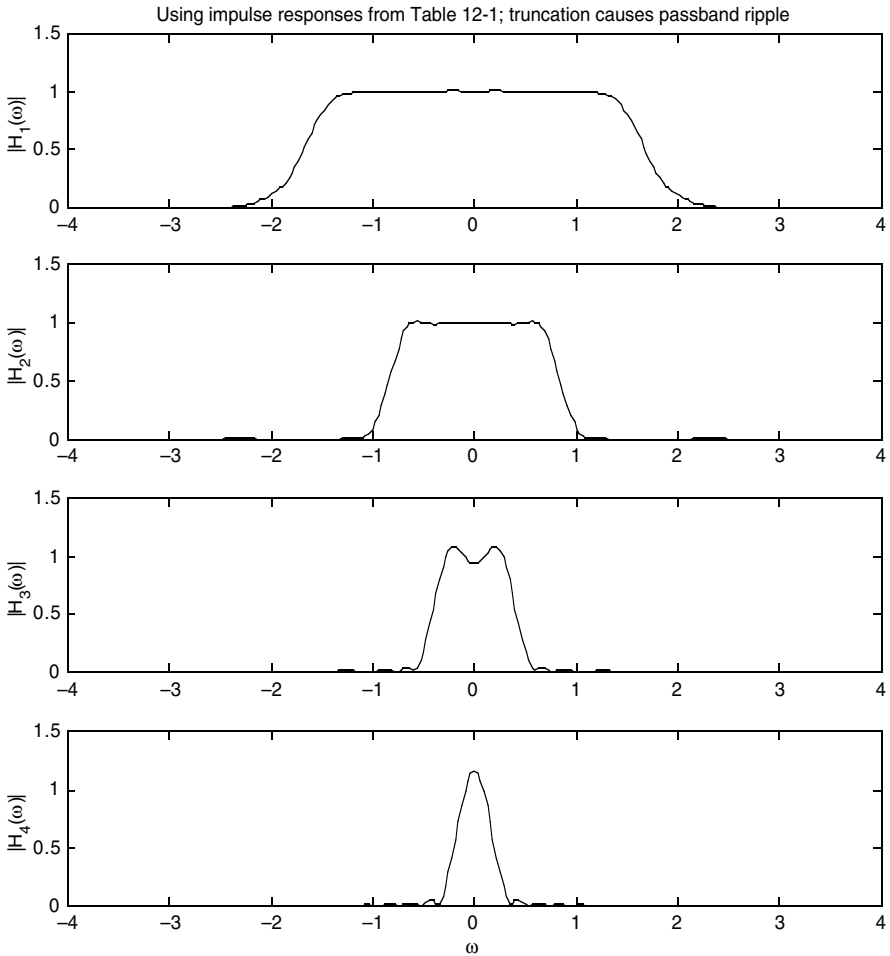


**Fig. 12.2.** Discrete-time Fourier transforms  $H_1, H_2, H_3,$  and  $H_4$  of  $h_1, h_2, h_3,$  and  $h_4$  for the cubic spline MRA.

**12.1.2.2 Fine Signal Structure: The Detail Signal.** A similar derivation gives the signal details at various resolutions. Let  $G_p$  be the discrete filter with impulse response  $g_p$ ,

$$g_p(n) = 2^{-p} \langle \psi(2^{-p}t), \phi(t-n) \rangle, \tag{12.13}$$

and note again that (12.1b) expresses an inner product:

$$(D_i^d x)(n) = 2^i \langle x(t), \psi(2^i t - n) \rangle. \tag{12.14}$$

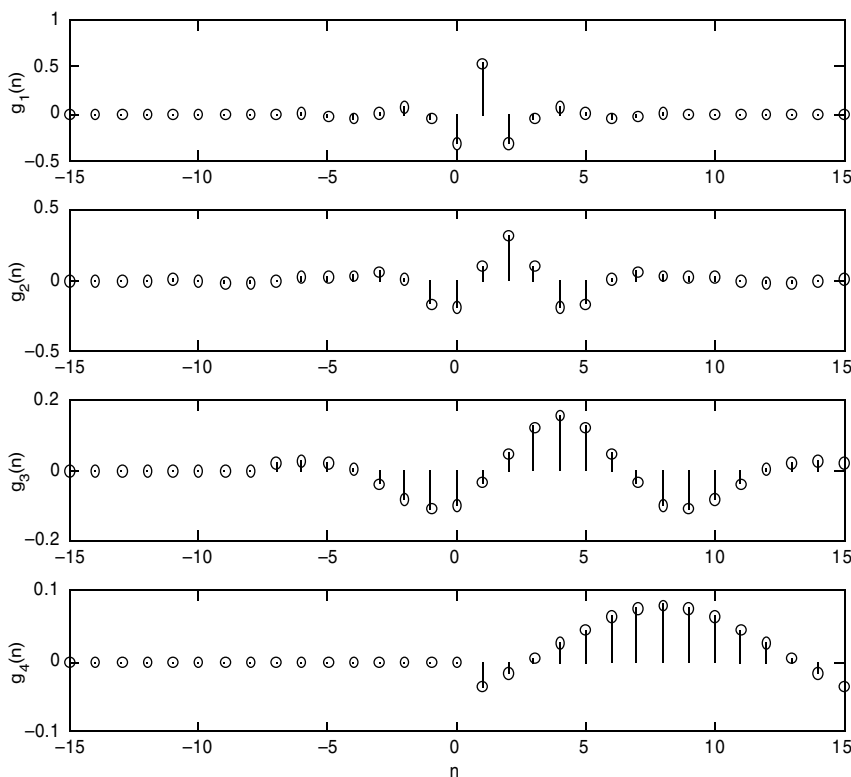


**Fig. 12.3.** Discrete filter impulse response signals  $g_1$ ,  $g_2$ ,  $g_3$ , and  $g_4$  for the cubic spline MRA.

We claim that  $(D_i^d x)(n)$ , the detail signal at level  $i$ , is given in terms of the approximate signal at level  $i + p$  by

$$(D_i^d x)(n) = \sum_{k=-\infty}^{\infty} \tilde{g}_p(2^p n - k)(A_{i+p}^d x)(k). \tag{12.15}$$

To verify this, let  $O_i$  be the orthogonal complement of  $V_i$  inside  $V_{i+1}$ :  $V_i \perp O_i$  and  $V_{i+1} = V_i \oplus O_i$ . The shifted, dilated orthogonal wavelets  $\{\Psi_{2^i t - 2^{-i} n}\}_{n \in \mathbb{Z}}$  span  $O_i \subset V_{i+p}$ . Since  $\{2^{-(i+p)/2} \phi_{2^{i+p}(t - 2^{-i-p} n)}\}_{n \in \mathbb{Z}}$  is an orthonormal basis of  $V_{i+p}$ ,

$$\Psi(2^i t - n) = 2^{i+p} \sum_{k=-\infty}^{\infty} \langle \Psi(2^i s - n), \phi(2^{i+p} s - k) \rangle \phi(2^{i+p} t - k). \tag{12.16}$$

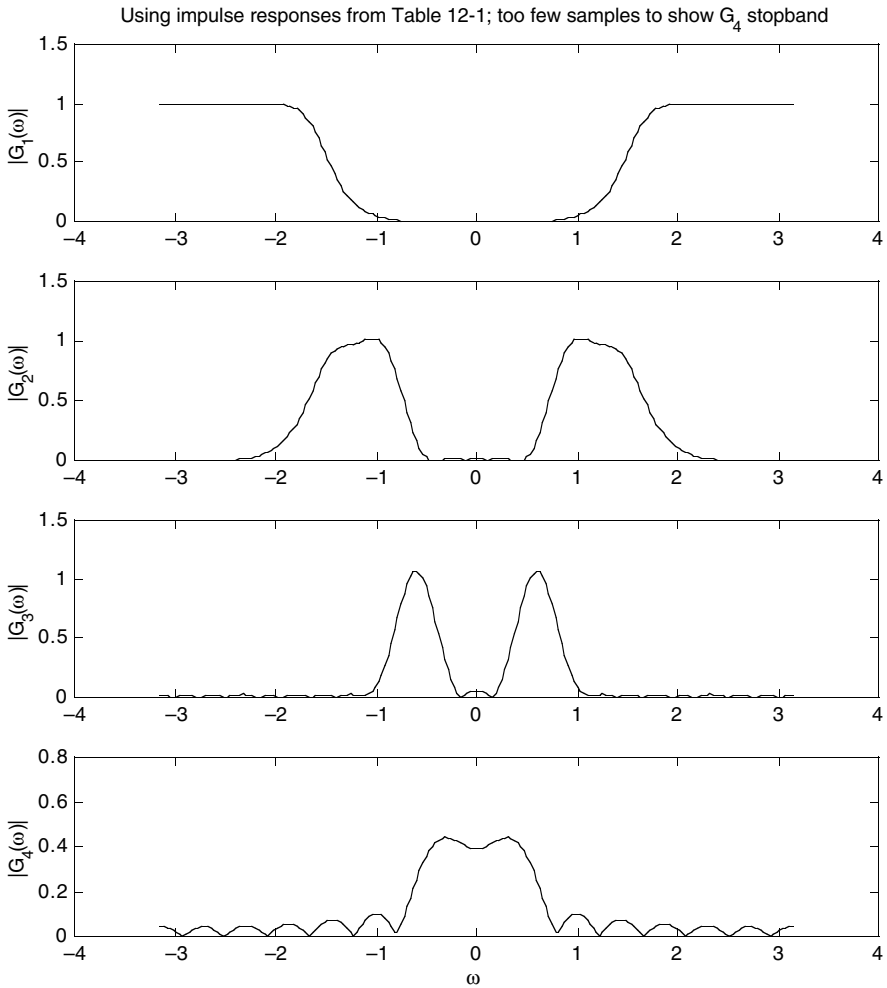


**Fig. 12.4.** Discrete-time Fourier transforms  $G_1, G_2, G_3,$  and  $G_4$  of  $g_1, g_2, g_3,$  and  $g_4$  for the cubic spline MRA.

Then, following the argument about approximate signals from the previous section (exercise) gives

$$\langle x(t), \psi(2^i t - n) \rangle = 2^p \sum_{k=-\infty}^{\infty} \tilde{g}_p(2^p n - k) \langle x(t), \phi(2^{i+p} t - k) \rangle, \quad (12.17)$$

and, consequently,

$$(D_i^d x)(n) = \sum_{k=-\infty}^{\infty} \tilde{g}_p(2^p n - k) (A_{i+p}^d x)(k). \quad (12.18)$$

**TABLE 12.1. Cubic Spline MRA Orthogonal Wavelet Pyramid Filters**

$n$	$h_1(n)$	$h_2(n)$	$h_3(n)$	$h_4(n)$	$g_2(n)$	$g_3(n)$	$g_4(n)$
0	0.542	0.272	0.136	0.068	-0.189	-0.095	-0.048
1	0.307	0.237	0.131	0.067	0.099	-0.035	-0.035
2	-0.035	0.153	0.118	0.066	0.312	0.049	-0.018
3	-0.078	0.057	0.099	0.063	0.099	0.125	0.003
4	0.023	-0.019	0.077	0.059	-0.189	0.157	0.025
5	0.030	-0.047	0.052	0.055	-0.161	0.125	0.045
6	-0.012	-0.039	0.028	0.050	0.005	0.049	0.062
7	-0.013	-0.013	0.007	0.044	0.054	-0.035	0.074
8	0.006	0.012	-0.009	0.038	0.027	-0.095	0.079
9	0.006	0.020	-0.019	0.032	0.018	-0.107	0.074
10	-0.003	0.015	-0.024	0.026	0.017	-0.080	0.062
11	-0.003	0.004	-0.023	0.020	0.000	-0.037	0.045
12	0.002	-0.006	-0.019	0.014	-0.018	0.003	0.025
13	0.001	-0.009	-0.013	0.009	-0.016	0.023	0.003
14	-0.001	-0.006	-0.006	0.004	-0.004	0.027	-0.018
15	-0.001	-0.001	0.000	-0.001	0.003	0.021	-0.035

Seeking the impulse response of the filter  $G_p$ , we expand on  $\{\phi(t-k)\}_{k \in \mathbb{Z}}$ , an orthonormal basis for  $V_0$ :

$$\Psi(2^{-p}t) = \sum_{k=-\infty}^{\infty} \langle \Psi(2^{-p}s), \phi(s-k) \rangle \phi(t-k). \tag{12.19}$$

Fourier transformation of (12.19) produces

$$G_p(\omega) = \frac{\Psi(2^p\omega)}{\Phi(2\omega)}. \tag{12.20}$$

Filters for generating the detail structure of signals via the orthogonal wavelet decomposition are shown in Table 12.1(12.18). We set  $g(n) = g_1(n) = (-1)^{1-n}h(1-n)$ , so it is not shown. Observe that  $g_p(n)$  is symmetric about  $2^{p-1}$ .

**12.1.2.3 Quadrature Mirror Filters.** We have shown that discrete filters,  $H_p$  and  $G_p$ , with impulse responses  $h_p$  and  $g_p$ , respectively, are all that we need for the wavelet pyramid decomposition (12.2). Since we know the Fourier transforms of the wavelet and scaling function, we can compute these impulse responses from the inverse discrete-time Fourier transforms of (12.12) and (12.20). Figure 12.5 shows how the pyramid decomposition occurs by successive filtering and subsampling operations.

From Chapter 11’s theoretical development, we know that the discrete low-pass filter  $H(\omega)$  associated to an MRA satisfies  $|H(\omega)|^2 + |H(\omega + \pi)|^2 = 1$ . Within an amplification factor, this is precisely the perfect reconstruction criterion of Chapter 9. In fact,  $\sqrt{2}h(n)$  is a quadrature mirror filter. We can decompose the signal using

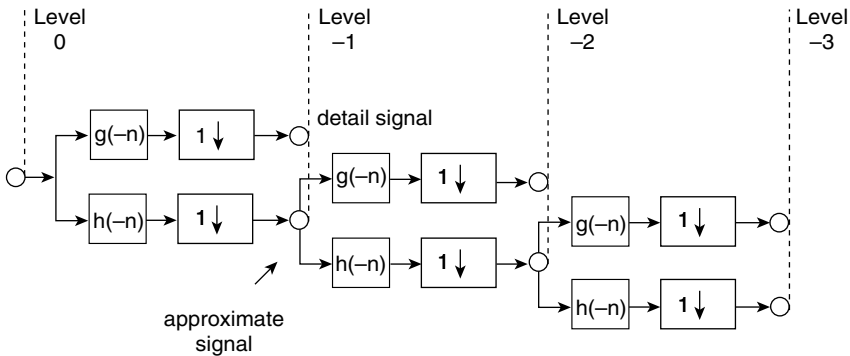


**Fig. 12.5.** Signal decomposition using the orthogonal wavelet pyramid.

this scaled filter, or we can slightly modify the perfect reconstruction scheme of Chapter 9 by supplying an additional amplification factor upon reconstruction [1, 3].

Consider the QMF pyramid decomposition in Figure 12.5. Let  $\tilde{h}(n) = h(-n)$  be the reflection of  $h(n)$  and

$$\tilde{H}(z) = \sum_{n=-\infty}^{\infty} \tilde{h}(n)z^{-n} \tag{12.21}$$

be the  $z$ -transform of  $\tilde{h}(n)$ . Subsampling by two followed by  $\tilde{H}(z)$  filtering is the same discrete system as  $H(z^2)$  filtering followed by subsampling [4] (exercise). Applying the same idea to  $\tilde{g}(n)$ , note that we can directly obtain level  $-2$  coefficients by filtering with  $\tilde{H}(z)H(z^2)$  and  $\tilde{H}(z)\tilde{G}(z^2)$  and subsampling by four. We can compute the impulse response of the filter with transfer function  $\tilde{H}(z)H(z^2)$  by convolving  $\tilde{h}(n)$  with the filter obtained by putting a zero between every  $h(n)$  value.

### 12.1.3 Application: Multiresolution Shape Recognition

This section shows how to use the orthogonal wavelet pyramid decomposition to recognize signal patterns at varying scales. This is one type of pattern recognition application [5]. We seek a known signal pattern, the *model*, in a *sample* signal that—perhaps along with background shapes and noise—contains a dilated version of the model. Moreover, if our pattern comparison algorithm gives localized information, we can attempt to *register* the time-domain position of the model as well. *Registration* is the process of finding the position of a *prototype*, or model, signal within a *candidate*, or sample, signal. For these tasks, signal analysts have relied upon multiple resolution methods for the following reasons.

- If the comparisons between the model and sample proceed pointwise, then the number of computations may become prohibitive—an especially acute problem in multiple dimensions (image analysis, computer vision, video analysis). Hierarchical structures that analyze signals at several resolutions can make the number of computations tractable [6]. Comparisons at coarse scales are iteratively improved in transition to fine scales.
- Coarse representations of signal structure can isolate significant features that are apparent only at certain resolutions [7–9].

When applying pyramid techniques to register a prototype object in a candidate signal, we first decompose both the model pattern and the sample. At the coarsest scale of decomposition, the algorithm compares the model and sample at all possible relative positions. The decomposition coefficients should not change as the model's offset into the sample varies. For otherwise, the decomposition would need to be recomputed for each location; computation time then increases drastically. The model's coefficients will not change if the decomposition procedure is translation-invariant. Of course, the coefficients could change in some simple way that is comparatively inexpensive to compute. Eventually, this produces a set of sufficiently good—or, *feasible*—comparison locations between prototype and candidate. The search continues at the next higher resolution with—hopefully—a greatly confined set of feasible registrations. The best acceptable match at the finest scale gives the final result.

We apply the multiresolution analysis (MRA) of  $L^2(\mathbb{R})$  to the multiscale shape recognition problem [1]. Once a particular MRA is chosen, it leads to simple, compact, and efficient pyramid decompositions using quadrature mirror filter (QMF) banks (Figure 12.5). The algorithms do not increase the amount of memory space required for storing the representations, yet exactly reconstruct the original signal.

We note that the MRA concept extends to two (or more) dimensions for image analysis. In this case, the separable two-dimensional pyramid decomposition distinguishes between horizontal and vertical spatial frequencies, which is useful for texture and image analysis in artificial environments [1]. Supplementary orientation tunings are possible too [10].

Orthogonal wavelet pyramids suffer from the following difficulties in registration and matching applications:

- (i) A registration problem is that the lower resolution coefficients do not translate as the original signal is shifted; in fact, the decomposition coefficients change drastically (Figure 12.6). This greatly complicates the tasks of matching and registration and has inspired research into alternative representations that support pattern matching [11].
- (ii) A second registration difficulty arises from the orthogonality of the representation, a consequence of its derivation from an MRA of  $L^2(\mathbb{R})$ . A registration between prototype and candidate at one resolution may not indicate any correlation between them at a finer scale. Whether this second difficulty appears depends on the nature of the signals acquired by the processing

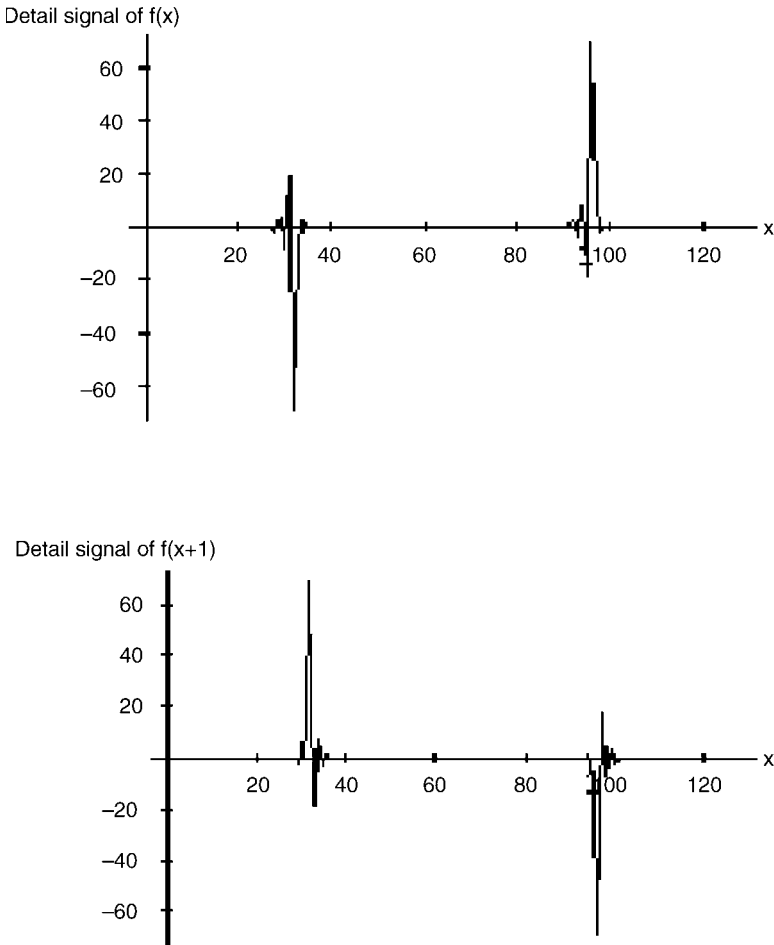


**Fig. 12.6.** Decomposing a prototype square pulse one resolution level using the orthogonal wavelet pyramid decomposition (a). The same pulse, shifted by a unit distance, represents the candidate. Its first coarse representation is shown in (b). This confounds the basic pyramid registration algorithm when it uses raw detail signals. The best registration position of candidate with respect to prototype is to align the left edge of one with the right edge of the other. On the other hand, the registration algorithm succeeds when using the magnitudes to measure of local energy.

system. Below, we describe an algorithm for coarse-to-fine tracking of registrations in orthogonal wavelet pyramids. The exercises suggest a comparison using the Laplacian pyramid [2] representation with the same registration algorithm. We report some earlier results here [5].

- (iii) A problem in multiscale matching is the dyadic dilation factor between pyramid levels. If the modeled object does not happen to be a dyadically scaled version of the candidate's pattern, then it is possible to overlook a match.

In matching applications, we seek instances of model patterns in an acquired signal. Suppose that prototypes are decomposed and stored in a phoneme recognition system, for example. The large number of prototypes needs a compact representation for the model pyramids to trim memory requirements. Applying orthogonal wavelets for such recognition systems is attractive and is a motivation for trying to circumvent the translation of coefficients problem. It is desirable to quickly reject candidate patterns that are not represented by any model. Decomposition of a full pyramid for a candidate pattern is costly when, for instance, only the coefficients at the fourth level of decomposition (1/16 of the total values) are used for comparison with prototypes. If the pattern is accepted, then the time constructing a full pyramid is not lost. It helps obtain a precise registration. But if the pattern is rejected, a full pyramid is built for a candidate even though a tiny fraction of the coefficients find use. One need not derive all pyramid levels, in sequence from finest to coarsest scale of representation, in order to reject or tentatively accept a candidate pattern. We derived formulas for filters that allow us to directly compute coarse pyramid levels in the orthogonal wavelet representation in Sections 12.1.2.1.2.

We use the well-known cubic spline MRA for registration experiments [12]. If  $\{V_i : i \in \mathbb{Z}\}$  is the MRA, then the root space  $V_0$  is all finite-energy continuously differentiable functions that are cubic polynomials on intervals  $[k, k+1]$ . We studied this example of an MRA in Section 11.4. It has a particularly suitable scaling function  $\phi(t) \in V_0$  for signal analysis, with exponential decay in the time domain and polynomial decay of  $\omega^{-4}$  in the frequency domain. We recall that the associated discrete low-pass filter is  $h(n) = \langle \frac{1}{2}\phi(\frac{t}{2}), \phi(t-n) \rangle$ . We set  $g(n) = (-1)^{1-n}h(1-n)$ , which is a discrete high-pass filter.

The registration algorithm begins with a set of *feasible points*, where sufficient correlation exists between the candidate and prototype signals, at the coarsest level of representation. Feasible points at finer scales are found, furnishing *feasible paths* up the pyramid. In order for a feasible point to continue a feasible path from a lower level, it must be close to a previous, coarser registration value. The best complete feasible path to the finest level of representation gives the registration between candidate and prototype patterns.

The algorithm uses the limited shift-invariance in the orthogonal wavelet pyramid representation. The coefficients of the wavelet representation at level  $l < 0$  translate by amount  $k$  when the original signal is translated by amount  $k2^{-l}$ . The steps are:

- (i) The candidate signal is decomposed with the wavelet pyramid (Figure 12.5).
- (ii) The minimum of the registration cost function  $m$  over all registrations  $r$ ,

$$m(r, l) = \sum_i [X_{l,c}(i) - X_{l,p}(i-r)]^2, \quad (12.22)$$

is computed for level  $l = -L$ .  $X_{l,c}$  is the candidate signal decomposition at level  $l$ ,  $X_{l,p}$  is prototype signal decomposition at level  $l$ , and  $i$  varies over candidate signal values. Let  $r_{-L}$  be a registration at which the minimum occurs, and call the minimum  $M_{-L} = m(r_{-L}, -L)$ . We pad arrays with zeros when endpoints overlap.

- (iii) All registrations  $s$  such that  $m(s, -L) \leq Tm(r_{-L}, -L)$ , where  $T > 1$  is a threshold, are the feasible points at level  $-L$ . Call this set of registrations  $FR_{-L}$ , the starting points of feasible paths up the pyramid levels.
- (iv) Steps (ii) and (iii) repeat at higher levels  $-L + k, 1 \leq k < L$ .
- (v) We prune the feasible point sets at the higher levels to retain only feasible points that continue, within an offset tolerance factor, a feasible path coming from a lower level. Thus,  $s \in FR_{-k+1}$  only if  $m(s, -k+1) \leq TM_{-k+1}$  and  $t - \tau \leq s \leq t + \tau$  for some  $t$  in  $FR_{-k}$  and offset tolerance  $\tau$ .
- (vi) Finally, if at level  $-1$  no full feasible path has been found, then registration failed. If at least one feasible path is found, the best is selected as the final registration. In a local neighborhood of the best registration found at level  $-1$ , the original prototype signal and original candidate signal are examined for the best correspondence value.
- (vii) To extend the algorithm to matching, where the scale of the candidate object is unknown, then we allow feasible paths to start and stop at intermediate levels.
- (viii) For matching applications based on coarse signal structure, it is useful to generate low-resolution pyramid levels directly rather than iteratively. The wide filters we developed above (Table 12.1(12.18)) allow us to jump many scales, quickly compare, and tentatively accept or reject candidate signals. This saves the time and memory cost of performing full pyramid decompositions. (12.18) Table 12.1 gives sample coefficients for  $h_p(n)$  and  $g_p(n)$ . We use filters  $g_1(n) = g(n), g_2(n), \dots, g_p(n)$ , and  $h_p(n)$  for an orthogonal wavelet pyramid to level  $-p$ .

For experimentation, we register sections of the Australian coastline. Digitized, it contains 1090 points for the experiments herein. The scale-space representation has been studied in similar experiments [13]. Beginning from a reference zero position, we plot the outline of the Australian coast (Figure 12.7) as ordered pairs  $(x(t), y(t))$ , where  $t$  is the distance along the coastline to the reference position.

To find derivatives, we approximate  $x(t)$  and  $y(t)$  to a quadratic using Lagrange’s interpolation formula. A signed curvature function [14],

$$\kappa(t) = \frac{(x'y'' - y'x'')}{[(x')^2 + (y')^2]^{3/2}}, \tag{12.23}$$

gives the coastline curvature at  $(x(t), y(t))$  (cf. Figure 12.8a). Prototype signal  $\kappa(t)$  is decomposed using the orthogonal wavelet decomposition (Figure 12.9a). The

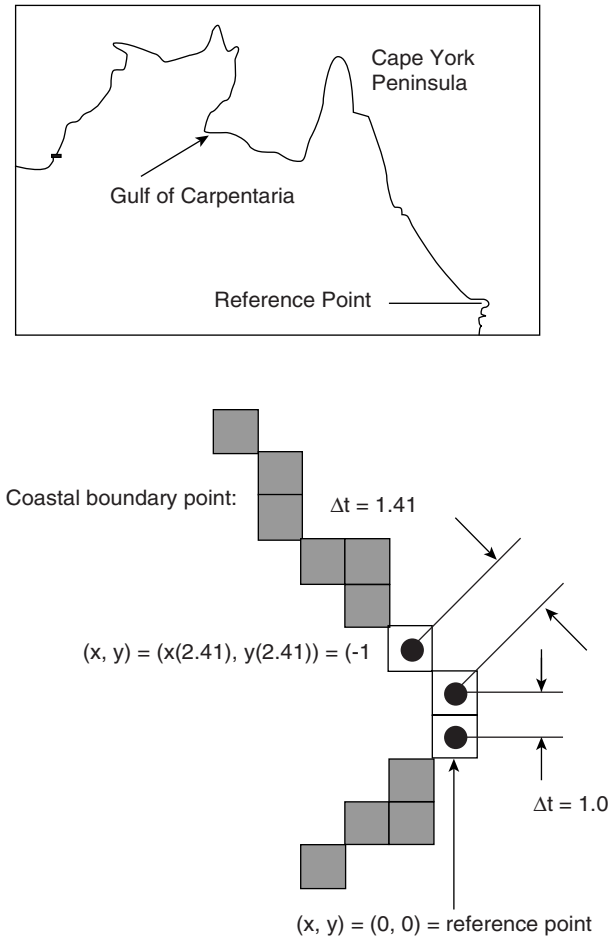


**Fig. 12.7.** Curvature maps of sections of coastline such as the Gulf of Carpentaria and the Cape York Peninsula are registered within an entire boundary curvature map of Australia. The independent variable of the curvature map is the arc-length distance from the reference point.

candidate signals for the experiments are partial curvature maps of coastal sections, for example the Gulf of Carpentaria (Figure 12.8b, Figure 12.9b).

The registration algorithm generates feasible paths through the pyramid (Figure 12.10). Thresholds  $T$  and  $\tau$  depend on the application. For the boundary matching shown here,  $T = 1.2$ , and  $\tau$  in Step (v) was chosen to be  $2^{k+1}$  at level  $-k$ . If the value of  $T$  is too small, the registration can fail at the coarsest level; the  $r_{-L}$  is incorrect, and the neighborhood of the correct registration holds no feasible point. When  $\tau$  is too large, the number of feasible paths to check increases, slowing the coarse-to-fine

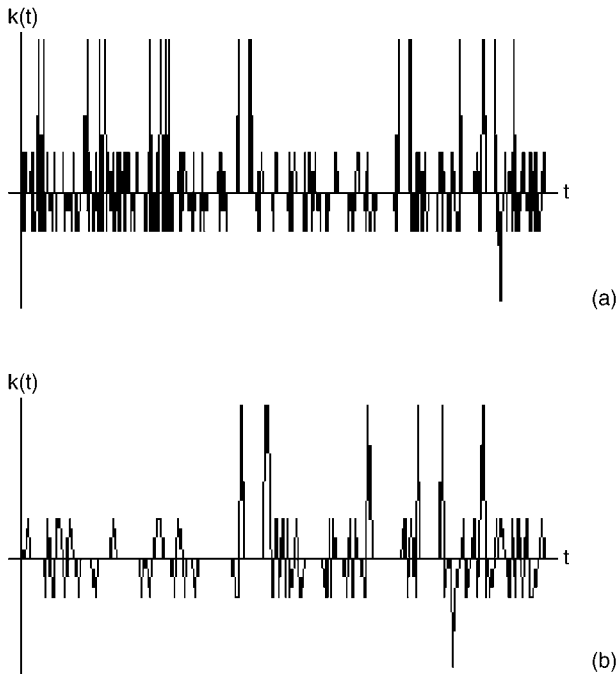


**Fig. 12.8.** Curvature maps. (a) Partial curvature map of Australian coastline. (b) Curvature map of Gulf of Carpentaria. The correct registration is evident.

algorithm. If  $\tau$  is too small, initially correct feasible paths terminate at coarse resolutions. It turns out that this holds for both the Laplacian- and wavelet-based registration schemes [5]. The exercises suggest a comparison of these methods along with the piecewise continuous MRA [15].

Table 12.2 shows experimental results in registering continental boundaries. Over all but the lowest resolution level we rely on the detail signal magnitudes of the candidate and prototype signals. For the coarsest comparisons of structure, the approximate signals are used for matching. We add noise to the candidate curvature maps in some experiments. Note that the mean-square signal-to-noise ratio (SNR) employed here is  $SNR = \sum s^2(t) / \sum N^2(t)$ . Experiments reported in Ref. 5 were performed in which the signals  $X_{l,c}$  and  $X_{l,p}$  in (12.22) were taken to be either the approximate signal, the detail signal, or the absolute value of the detail signal coefficients. The outcome is problematic registration with the raw detail signals, but satisfactory convergence if  $X_{l,c}$  and  $X_{l,p}$  are approximate signals [5]. This is not unexpected, as the algorithm then compares successively low-pass filtered signals. The approximate signals are always used at the coarsest level (here, level  $-4$ ) to generate the initial list of feasible points  $FR_{-4}$ . The feasible paths are robust when the candidate has large support, but smaller candidates of nearly straight coastline can fail to correctly register [5].

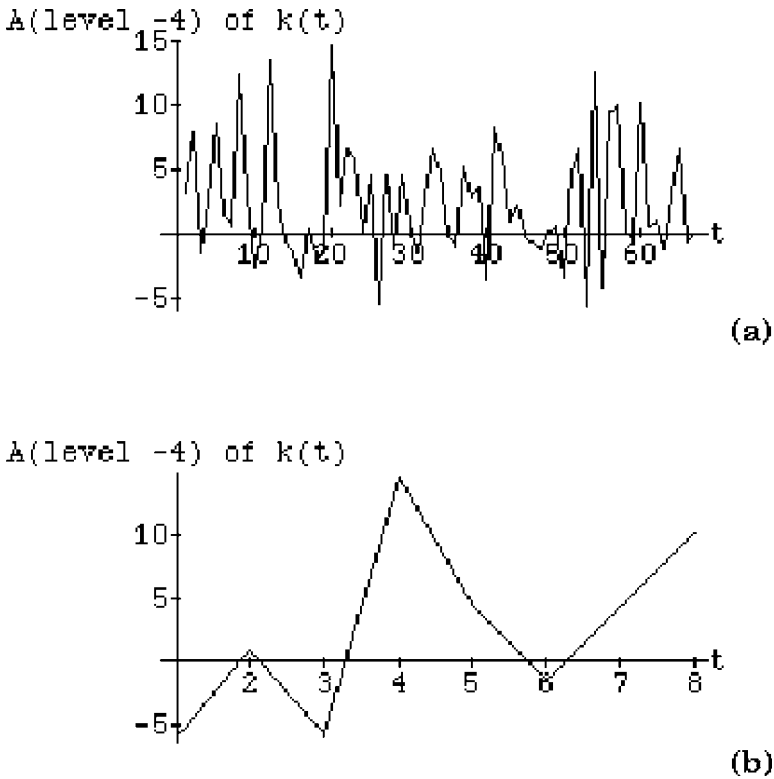
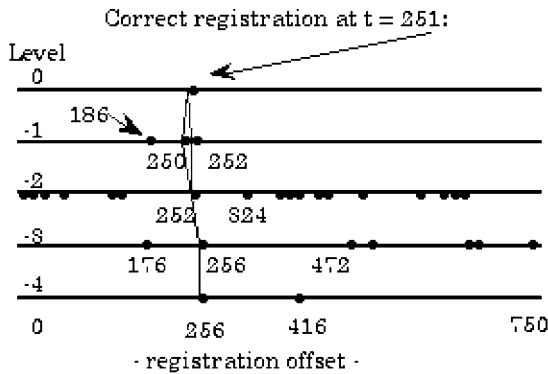


**Fig. 12.9.** Beginning registration of Gulf of Carpentaria at level -4. (a) Australian coastline curvature at resolution 1/16. (b) Gulf of Carpentaria curvature at resolution 1/16. Feasible points are not so evident.



Approximate signals compared at level -4.  
Detail signal magnitudes compared at levels -3, -2, and -1.

**Fig. 12.10.** Registering Gulf segment against Australia boundary: two feasible paths, both ending at the correct registration offset of 251, are found.

**TABLE 12.2. Orthogonal Wavelet Pyramid Algorithm Performance**

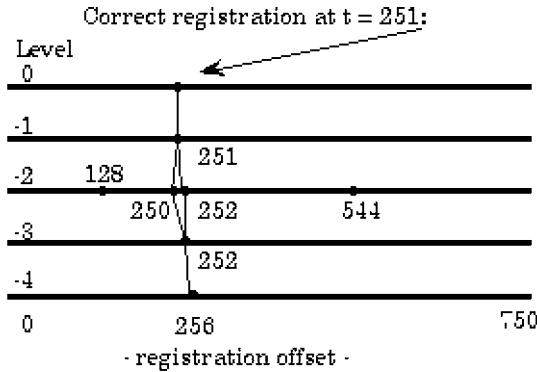
Run	Candidate	Correct Offset	Match Measure	Pyramid Levels	Feasible Points	Success
1.0W	128 point segment of Gulf of Carpentaria	250	Detail signal magnitude	4	19	Yes
1.1W	Same as 1.0W, except shifted	251	Same	4	90	Yes
2.0W	Same as 1.0W, except uniform noise with mean-square SNR of 10.0 added to candidate signal	250	Same	4	87	Yes
2.1W	Same as 2.0W, except shifted	251	Same	4	111	Yes
2.2W	Same as 2.1W, except shifted	252	Same	4	79	Yes

Now, consider the Laplacian pyramid. It analyzes  $N$ -point signals into approximately  $2N$  coefficients and images into  $4N/3$  coefficients. Correlation between levels causes the larger pyramid sizes. Since the orthogonal wavelet and Laplacian pyramid representations are computationally quite alike [1], it is natural to study the registration algorithm using the Laplacian pyramid decomposition. For these experiments, we implemented the Laplacian pyramid using the approximately Gaussian [2] low-pass filter  $\{0.05, 0.25, 0.4, 0.25, 0.05\}$ . We find that raw difference signals of the pyramid (not their magnitudes) suffice for good registration. Figure 12.11 shows the result of the experiment of Figure 12.10 using the Laplacian pyramid decomposition.

Table 12.3 shows the results of the Laplacian-based registration algorithm on the same battery of experiments for which we used orthogonal wavelets.

To summarize the results, registering curvature maps with wavelet pyramids produces many more feasible points and paths. However, some Laplacian pyramid runs produce many feasible points too. Both methods are robust in the presence of noise, although the Laplacian pyramid suffers from very large feasible point counts at coarse resolutions. It turns out that candidate signals with small support often make the wavelet registration fail, whereas the Laplacian pyramid algorithm withstands these same small structures [5]. Overall, the Laplacian pyramid decomposition is somewhat better, since the correlation between levels stabilizes the coarse-to-fine tracking.

It appears that these results do not depend substantially on the type of MRA—and hence the discrete pyramid decomposition filters—chosen for deriving the coarse resolution signal structures. Both the Haar [16] and the Daubechies [17] compactly supported wavelets were used in similar registration experiments [18].



Approximate signals compared at level -4.  
 Difference signals compared at levels -3, -2, and -1.

**Fig. 12.11.** Registering Gulf segment against Australia boundary using the Laplacian pyramid decomposition. Again, two feasible paths arise. The correct registration is found very quickly, at level -1, where the unit distance of the difference signal is the same as the original curvature maps.

These researchers concluded that as long as two or more samples support the signal structure of interest, the approximate signal structures suffice for coarse-to-fine matching and registration. The same authors advise caution with the pyramid's detail signals. Neither method—Haar or Daubechies wavelet pyramids—significantly outperformed the other, although the Haar structures were slightly better when using detail signals [18].

**TABLE 12.3. Laplacian Pyramid Algorithm Performance**

Run	Candidate	Correct Offset	Match Measure	Pyramid Levels	Feasible Points	Success
1.0L	128-point segment of Gulf of Carpentaria	250	Detail signal	4	17	Yes
1.1L	Same as 1.0L, except shifted	251	Same	4	7	Yes
2.0L	Same as 1.0L, except uniform noise with SNR = 10.0 added to candidate	250	Same	4	954	Yes
2.1L	Same as 2.0L, except shifted	251	Same	4	1090	Yes
2.2L	Same as 2.1L, except shifted	252	Same	4	942	Yes

## 12.2 MIXED-DOMAIN SIGNAL PROCESSING

Mixed-domain signal transformations provide some new insights into signal processing tasks. Although this section concerns applications that refine rather than interpret a signal, we observe that these steps are often important ancillary feature of a signal analysis application. Here, we confine our remarks to three areas:

- Compression;
- Filter methods and filter banks;
- Enhancement.

Compression is necessary for constructing large signal databases, such as a model-based recognition system might employ. Filtering is important at the front end of an analysis application. Enhancement can be essential for building signal prototypes. In fact, although it is a purely signal-in, signal-out technology, compression is perhaps the most important commercial application of the orthogonal wavelet transform. We hasten to add that a very large research literature continues to flourish in all of these areas; our present assessment by no means constitutes the final word.

Good compression methods currently employ either the discrete cosine transform (DCT) or orthogonal wavelet transform coding. The idea is that the transform coefficients are statistically far simpler than the original signals or images, and therefore the transformed data can be described with fewer numerical values. Of course, the orthogonality of the wavelet transform and the efficient, perfect reconstruction filter banks that it provides promote its use in compression. After compression, a handful of transform coefficients nonlinearly encode complex signal and image patterns. Perfect reconstruction is, in principle, possible. Even with lossy compression, ratios of one-bit compressed versus one-byte (8-bit) original signal gives excellent reconstruction. When more decomposition coefficients are discarded in compressing the signal and there remains only a single bit versus 4 bytes of source signal, the reconstruction is still fairly good for human perception.

Digital sound, image, and video databases are huge. Whether they support a signal analysis system or not, compression is essential for economy of storage, retrieval, and transmission. The earliest wavelet compression methods were based on the orthogonal wavelet pyramid decomposition (12.2), shown in Figure 12.5 [1]. New compression methods—some of which provide compression ratios of two orders of magnitude—based on wavelet transforms have been reported in the research literature [19–22]. The basic idea is that many detail coefficients carry no useful signal information and can be set to zero without appreciably affecting the result of the pyramid reconstruction algorithm. There are many variations, but typically the steps are as follows:

- (i) Select a multiresolution analysis and a final level of pyramid decomposition  $-L$ , where  $L > 0$ .
- (ii) Decompose the signal  $x(n)$  into its pyramid decomposition (12.2), producing detail coefficients for levels  $-L \leq l \leq -1$  and approximate coefficients for level  $l = -L$ .

- (iii) Apply a threshold to the fine structure signals  $D_{-L}^d x, D_{-L+1}^d x, \dots, D_{-1}^d x$ , so that small magnitude coefficients are set to zero. This is typically a *hard threshold*: If  $s(t)$  is a signal, then its hard threshold by  $T > 0$  is given by

$$s_{T,h}(t) = \begin{cases} s(t) & \text{if } |s(t)| > T, \\ 0 & \text{if } |s(t)| \leq T. \end{cases} \tag{12.24}$$

- (iv) Apply a standard compression technique to the small coarse-resolution trend signal  $A_{-L}^d x$ . Examples include the Karhunen–Loeve compression [23] or—for images, especially—the Joint Photographic Experts Group (JPEG) standard algorithm [24], which derives from the discrete cosine transform (DCT) [25].
- (v) Apply an entropy coding technique, such as simple run-length encoding [26] to the detail signals.
- (vi) Decode the compressed pyramid levels from (iv) and (v) and reconstruct the original signal (with some loss, principally due to the thresholding operations) using the exact reconstruction afforded by the MRA’s quadrature mirror filters;
- (vii) A conservative guideline for hard threshold selection is

$$T = \sigma \sqrt{2 \frac{\log(N)}{N}}, \tag{12.25}$$

where  $\sigma^2$  is the variance of  $x(n)$  at level  $l = 0$  and  $N$  is the number of samples.

Compression ratios of about 25:1 on natural images are possible with the above method. The extension of the orthogonal wavelet pyramid decomposition to two dimensions (images) is necessary for this technique [1], but is unfortunately beyond our present scope. However, Figure 12.12 gives the idea. As with signals, the detail

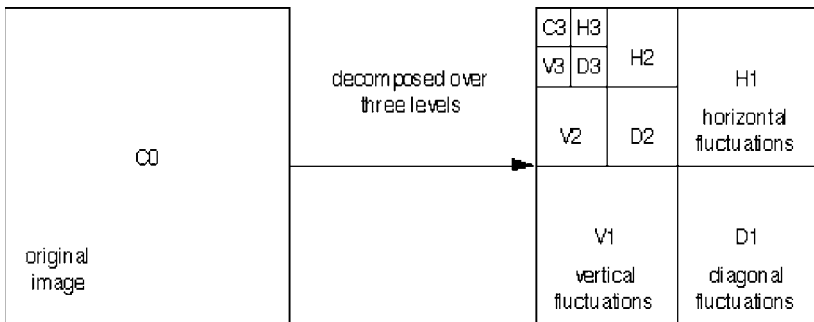


**Fig. 12.12.** Orthogonal wavelet image compression decomposes the original into four uncorrelated subimages. The trend image  $C_1$  is analogous to the one-dimensional approximate signal. The three detail images contain the direction-sensitive fluctuations of the image  $C_0$ . These include vertical details, horizontal details, and diagonal (corner) details. The image pyramid decomposition applies the same algorithm to each coarse structure trend image,  $C_1$ ,  $C_2$ , and so on. This produces more detail images and a final trend image,  $C_3$  above.

images tend to have simple statistics. They can be modeled, quantized, and individually compressed to impressive ratios. The decomposition allows the algorithm designer to tune the vertical, horizontal, and diagonal quantizations so that the direction-sensitive human visual system perceives minimum distortion in the reconstructed image [1, 27].

More recent approaches to signal compression are as follows:

- *Malvar “wavelets”* are in fact a time-frequency signal decomposition [28]. They are an alternative to the time-scale decomposition using wavelet pyramids. This time-frequency compression technique breaks down an image into a sequence of sinusoidally textured atoms, with adjustable leading and trailing borders. The overall size of the atoms is also tunable. Lastly, as we noted briefly in Chapter 10, as an atomic signal decomposition that uses sinusoids instead of complex exponentials may avoid the limitation of the Balian–Low theorem. This flexibility allows Malvar wavelet compression schemes to beat others when tested in constrained problem domains, such as fingerprint images [29].
- *Wavelet packets* are functions of the form  $2^{m/2}W_n(2^m t - k)$ , where  $m$ ,  $n$ , and  $k$  are integers and  $n > 0$  [30,31].  $W_n$  extends only over a finite interval  $[0, M]$ , and it contains the root frequency of its family of atoms. The decomposition scheme is similar to the orthogonal wavelet pyramid, except that the detail signal structures are also composed at every level. Image decomposition uses tensor products of the translations and dilations of the  $W_n$ . A distinct advantage of wavelet packets over Malvar wavelets is that each set of atoms is generated by translation, dilation, and modulation of a single function. This simplifies the construction of algorithms and special-purpose compression hardware. Wavelet packets offer excellent compression ratios, in the realm of 100:1 [19].
- *Structural approaches* to wavelet-based image compression take a two-stage approach. This scheme first extracts edges across several scales. It then encodes the texture representing the difference between the original and the reconstruction from edge information. Combining the texture-coded error image with the edge-coded image gives a perceptually acceptable rendition of the original [20]. Closely related to transform signal compression are mixed-domain processing techniques for noise removal and enhancement.

### 12.2.1 Filtering Methods

Wavelet decompositions provide for methods that remove background noise from a signal but preserve its sharp edges. This can be especially valuable in signal analysis applications where it is necessary to identify local shapes, for example, that may be corrupted by noise, but still obtain a precise registration [29]. We recall from Chapter 9 that low-pass and bandpass filters removed high-frequency components from signals, but as a rule, these convolutional systems blur the edges as well. Once again, there are many alternatives for wavelet-based noise removal. The typical approach follows the compression algorithm, with a twist at the thresholding step [32–34]:

- (i) Select an MRA and final level of decomposition  $-L$ , where  $L > 0$ .
- (ii) Decompose  $x(n)$  according to (12.2).
- (iii) Retain the coarse structure approximate coefficients at  $l = -L$ , but apply a *soft threshold* to  $D_{-L}^d x, D_{-L+1}^d x, \dots, D_{-1}^d x$ : If  $s(t)$  is a signal, then its *soft threshold* by  $T > 0$  is given by

$$s_{T,s}(t) = \begin{cases} \operatorname{sgn}[s(t)](|s(t)| - T) & \text{if } |s(t)| > T, \\ 0 & \text{if } |s(t)| \leq T. \end{cases} \quad (12.26)$$

Soft thresholding results in a continuous signal (Figure 12.13).

- (iv) Reconstruct the original signal.
- (v) Soft threshold selection is either heuristic, based on the hard threshold selection (12.25), or extracted via the Stein unbiased risk estimate (SURE) [33, 35].

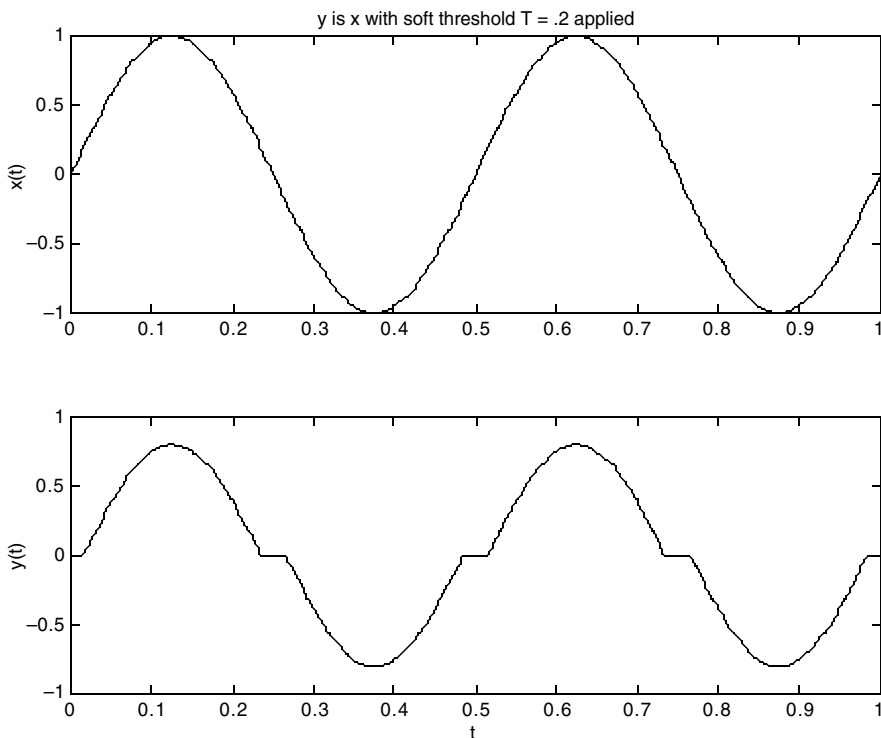


**Fig. 12.13.** Soft thresholding a sinusoidal signal.

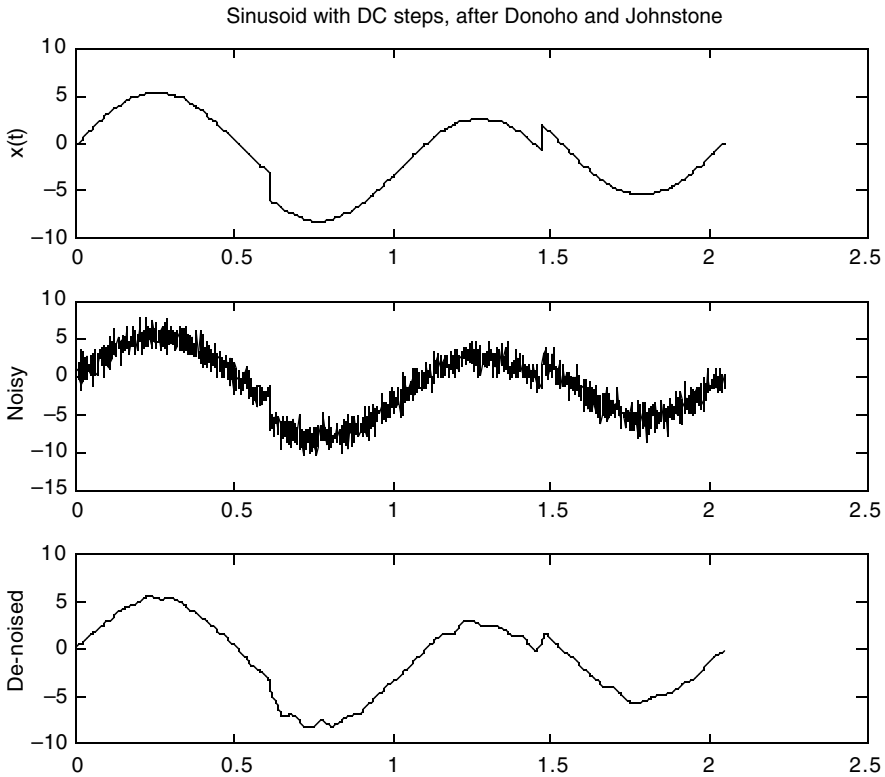


**Fig. 12.14.** Noise removal filtering using wavelets, soft thresholding, and the SURE threshold selection.

Figure 12.14 provides an example.

### 12.2.2 Enhancement Techniques

Let us consider a third processing technique using wavelet transforms. Many signal acquisition and imaging systems use photon detectors, such as the popular charge-coupled device (CCD) or the sensitive photomultiplier tube (PMT), as their data source. Examples are spectrometers used to control plasma etchers in the semiconductor manufacturing industry, an application we considered in Chapter 4; astronomical instruments; remote sensing devices; and photo-optical sensors in general.

CCDs now have become the digital image acquisition device of choice [36]. A *charge well* corresponds to a single pixel. They are small, holding perhaps 800 electrons per micron<sup>2</sup> ( $\mu$ ,  $10^{-6}$ m). This is called the *well capacity*,  $W_c$ . Factors affecting CCD sensor performance include the following:

- Wells have finite capacity, so if exposure time is too long, electrons spill over to adjacent wells, causing *blooming* of the image (bright blurry spots).
- There are three noise sources. These are due to thermal effects,  $N_\theta$ , (also called *dark current*); the quantum nature of light,  $N_\phi$ ; and logic noise during readout,  $N_\rho$ .
- Total noise within the image at a pixel is therefore  $N = N_\phi + N_\theta + N_\rho$ .
- *Dynamic range* of the well is defined as (capacity)/(readout noise level) =  $W_c/N_\rho$ .
- Thermal effects may be mitigated by cooling the sensor; typically, 6 degrees C warmer means twice as much thermal noise; in other words,

$$N_\theta(t) = \int_{t_0}^t K_\theta 2^{\frac{T}{6}} dt, \quad (12.27)$$

where  $T$  is the temperature in degrees Celsius,  $K_\theta$  is a constant, and  $i_\theta$  is the dark current.

- Readout noise rate increases with readout frequency.
- Light flux striking sensor obeys a Poisson distribution, where  $\alpha$  is the parameter of the distribution:

$$p_I(k) = e^{-\alpha} \frac{\alpha^k}{k!} = \text{Prob}(I = k). \quad (12.28)$$

- The mean of a Poisson distributed random variable is  $\mu = \alpha$  and its standard deviation is  $\sigma = \alpha^{1/2}$  in (12.28).

Of the diverse image noise sources, the most troublesome is *quantum noise*,  $N_\phi$ , which arises from the discrete nature of light quanta detection. Its magnitude changes with the light intensity and is thus image-dependent. Toward eliminating this pernicious source of noise in photon imaging systems—so-called *photon noise*—Nowak and Baraniuk [37] have applied an adaptive filtering method, based on the wavelet pyramid decomposition.

We have already observed that in some applications, wavelet pyramids furnish an especially convenient and powerful tool for suppressing noise in signals and images. The decomposition of a signal into a pyramid allows us to design algorithms that eliminate apparent noise in certain frequency bands by simply attenuating (or even zeroing) the coefficients in the suspect pyramid level. When the signal is reconstructed from the modified pyramid, troublesome noise is then absent. Better compression ratios are also obtained, without significant loss in perceptual signal quality.

In Ref. 37, the idea is to adjust pyramid level intensities according to the energy in other parts of the representation. For example, we might decompose to two coarse levels of representation, then attenuate the detail coefficients selectively, where the approximate signals have large magnitudes. Detail signals corresponding to regions where the approximate signal is weak remain the same or are amplified. Then, we reconstruct the profile using the pyramid scheme. A number of the computational experiments in Ref. 37 markedly improve faint, low-contrast medical

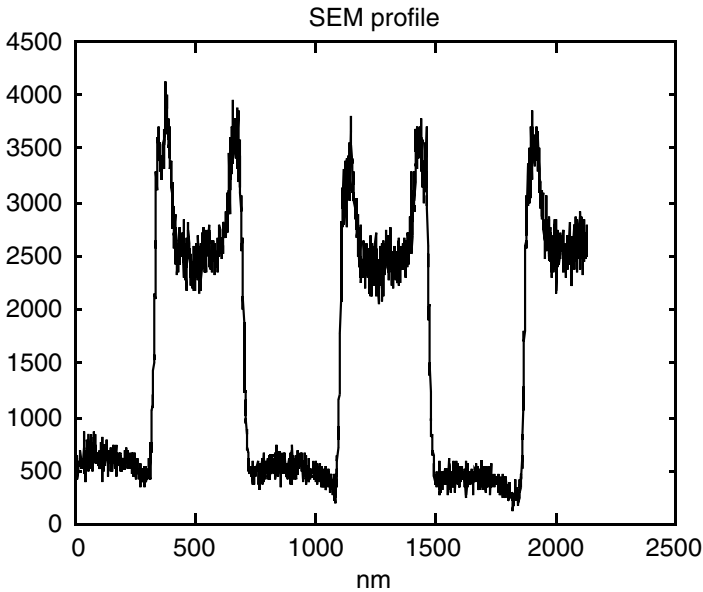


**Fig. 12.15.** Example of scanning electron microscope profile of lines on a test wafer. Noise magnitudes are roughly equal on tops of the high-magnitude lines and at the bottoms of the low-magnitude spaces between them.

and astronomical images. There is also a promise of better histogramming, edge detection, and higher-level image interpretation results. Figure 12.15 and Figure 12.16 show an application of this technique to raster lines from a scanning electron microscope (SEM) image.

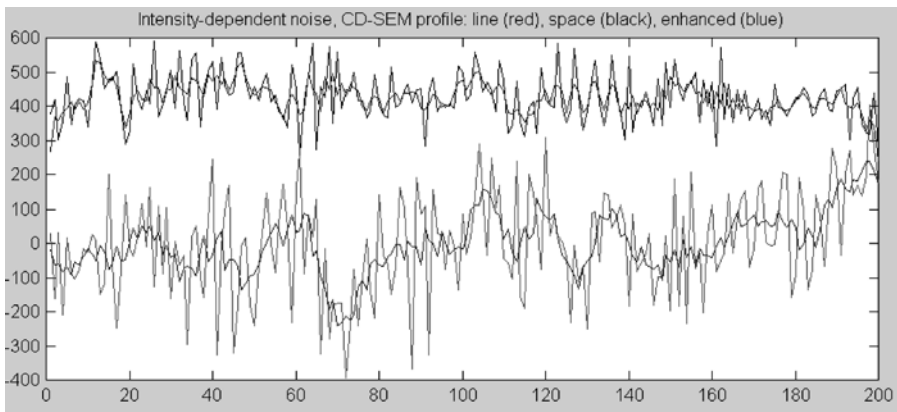


**Fig. 12.16.** After enhancement using the method of Nowak and Baraniuk. Note that noise on the wafer lines (*lower trace*) is reduced, whereas the details on the low magnitude spaces (*upper trace*) tends to be preserved.

## 12.3 BIOPHYSICAL APPLICATIONS

There was a surge of interest in these time-frequency and time-scale transforms in the mid-1980s. Psychophysicists noticed that Gabor elementary signals (Chapter 10) could model some aspects of the brain's visual processing. In particular, the *receptive fields* of adjacent neurons in the visual cortex seem to have profiles that resemble the real and imaginary parts of the Gabor elementary function. A controversy ensued, and researchers—electrical engineers, computer scientists, physiologists, and psychologists—armed with the techniques of mixed-domain signal decomposition continue to investigate and debate the mechanisms of animal visual perception [38, 39].

### 12.3.1 David Marr's Program

Signal concavity remains an important concept in analysis applications. Years ago, the psychologist Attneave [40] noted that a scattering of simple curves suffices to convey the idea of a complex shape, for instance, a cat. Later, computer vision researchers developed the idea of assemblages of simple, oriented edges into complete theories of low-level image understanding [41, 42]. Perhaps the most influential among them was Marr, who conjectured that understanding a scene depends upon the extraction of edge information over a range of visual resolutions [7]. Marr challenged computer vision researchers to find processing and analysis paradigms within biological vision and apply them to machine vision. Researchers investigated concavity and convexity descriptions as well as finding their boundaries at multiple scales. Thus, we might resolve an image into an intricately patterned structure at a fine scale, but coarse representation reveals just a butterfly wing. Marr speculated, but could not prove, that multiscale edges could uniquely describe signals and images. This would imply that the ultimate structural description of a signal would consist of its edge maps across all scales.

Two important early outcomes from Marr's program were scale space theory [8, 9, 43, 44] and optimal multiscale edge detectors [45–48] (Chapter 4). These theoretical results and the practical success of edge-based analysis and description of signal structure, bolstered Marr's conjecture. But wavelets weighed in as well. Mallat tried to use wavelet transform *zerocrossings* [49] as a multiscale structural signal characterization, and showed how the technique could be used for stereometry, but the method suffered from instability. Mallat and Zhong [50] changed strategies and showed that finding wavelet transform *maxima* across scales was equivalent to the Canny edge detector [45]. Then both Berman and Baras [51] and Meyer [29] found counterexamples to Marr's conjecture. In fact, Meyer's example gives a wavelet and a collection of sinusoidal sums that have the same zero crossings when convolved with the wavelet.

### 12.3.2 Psychophysics

Among the research efforts Marr's work inspired are comparisons between biological and computer vision. Such comparisons tend to support the notion that the

particular computer vision innovation being considered is more than an ad-hoc technological trick. When the biological analogies are clear, in fact, it is plausible that the technology is taking advantage of some fundamental physical properties of objects in the world and their possible understanding from irradiance patterns.

While most physiological studies of the visual brain have concentrated on cats and monkeys as experimental subjects [52], the evidence shows many similarities between the function of the cat's visual cortex and that of the monkey. It is therefore reasonable to assume—and the psychophysical studies done on human subjects support this—that the human visual system implements these same principles of cortical organization. Visual information arrives through the retina, and then passes down the optic nerve to the lateral geniculate nucleus (LGN), from which it is relayed to the visual part of the brain, variously known as V1, *area 17*, the *striate cortex*, or the *primary visual cortex*. Some two or three dozen separate visual areas of the brain have been identified according to their visual function [52].

Light impinging on the retina directly stimulates V1 neurons, as well as some other cortical areas. The area of the retina upon which a pattern of irradiance may stimulate a neuron is called the neuron's *receptive field* (RF). In their pioneering work, Hubel and Wiesel [53] differentiated between *simple* cortical neurons and *complex* cortical neurons. A simple cell tends to assume one of two states, “on” or “off,” according to whether special light patterns were directed within its RF. Complex cells, on the other hand, do not exhibit this binary behavior, are prone to have larger RFs than the simple cells, and can be stimulated over a much broader RF area [53]. Studying the cat's visual cortex the researchers further demonstrated that both the simple and complex cells within area V1 have a very high orientation selectivity. Monitoring the responses of cells while slits of light at various angles were flashed onto the RFs of the neurons demonstrated this. Interestingly, such orientation specificity is not shown in the retinal area of the eye or in the LGN, but only appears when the visual information finally reaches the cortex [53]. Campbell and Robson [54] confirmed this property for human subjects through a series of psychophysical experiments.

Campbell and Kulikowski [55] and Blakemore and Campbell [56] described another property showing independent vision channels to exist. These channels have an orientation selectivity in addition to the spatial frequency selectivity. The orientation selectivity exhibited by the independent channels is not well accounted for either in Marr's system [7] or in the Laplacian pyramid algorithms [2]. However, orientation selectivity as well as spatial frequency tuning is a feature of the channels in the two-dimensional wavelet multiresolution representation [1] as shown in Figure 12.12.

Originally, researchers in the animal vision physiology thought that cortical cells were *feature detectors*, activated by the presence of a dot, bar, edge, or corner. Orban [52] emphasizes that it is now clear that cortical cells are actually *filters* and not feature detectors. It is also now possible to identify some visual cortical areas with the animal's behavior. For cats, nearly all neurons of cortical areas 17 (V1), 18, and 19 are orientation-sensitive bandpass filters covering all orientations [52]. Cells in area 17 have the smallest orientation bandwidth and show strong preference for

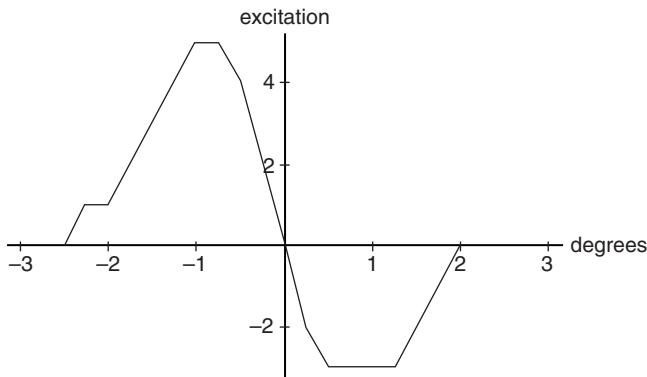


**Fig. 12.17.** RF profile of cortical simple cell #1316 of Ref. 57, odd symmetry.

horizontal and vertical directions. They are therefore most useful for observing stationary objects. The situation in area 19 is less clear. These cells have large receptive fields, broad orientation tuning, and little motion sensitivity. Area 18 cells have very large RFs, are sensitive only to low spatial frequencies, maintain a high orientation bandwidth, and have some velocity sensitivity. These cells work together to provide the animal with motion analysis [52].

To obtain an RF profile for a cortical cell, Jones and Palmer [57, 58] and Jones, Stepnoski, and Palmer [59] plotted neuron firing rate—the cell *activation level*—against the position of a spot of light within a small  $16 \times 16$  grid. According to the widely held view that the simple cells are filters of varying orientation and spatial frequency sensitivity, it should be possible to model the impulse response of the simple cell filter by mapping firing rate versus stimulus position in the RF. In fact, these researchers were able to obtain plots of the spatial and spectral structure of simple RFs in cats. Figure 12.17 and Figure 12.18 are based on cross sections of contour plots of typical cat simple receptive fields provided in Ref. 57.

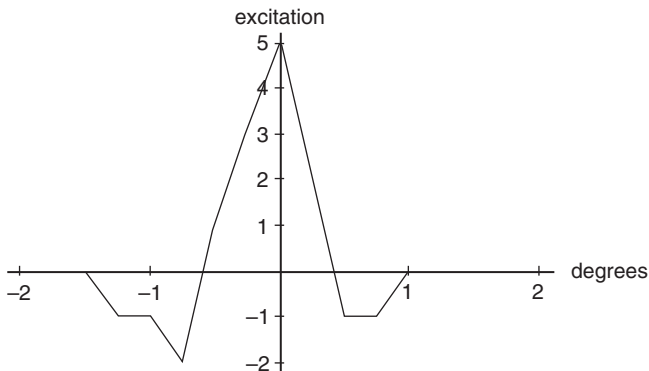


**Fig. 12.18.** RF profile of cortical simple cell #0219 of Ref. 57, even symmetry.

Many cortical simple cells have either an odd or even symmetry. Cells with odd symmetry, such as in Figure 12.17, have areas of excitation and inhibition on opposite sides of the RF center. On the other hand, those cells with even symmetry, such as in Figure 12.18, have a central excitatory (or inhibitory) region that is surrounded by an inhibitory (or excitatory) areas. The two basic types are illustrated in the above figures. In Figure 12.17 and Figure 12.18 the regions of positive excitation represent RF areas where responses to *bright stimuli* were obtained. The regions of negative excitation represent RF positions in which the response was found to correlate with *dark stimuli*. All of their excitation frequency measurements were made by microelectrodes inserted into cortical area 17.

Not long after the profiles of cortical neuron receptive fields became more widely understood, Marcelja [60] showed that the RF profiles were strikingly similar to the graphs of Gabor elementary functions (GEF). Marcelja's paper focused the attention of the computer and biological vision research communities onto the potential applications of these functions in vision research. We recall from Chapter 10 that a GEF is a sinusoid multiplied by a Gaussian. Gabor [61] showed that these functions are optimally localized in the time and frequency domains. The product of their spatial extent and bandwidth is minimal. Further, the functions form a complete mathematical set [62] for expansions of other signals.

When we choose the parameters appropriately and graph the GEF's real and imaginary parts separately, the functions resemble the RF profiles of cortical neurons. More remarkably, Pollen and Ronner [63] discovered that adjacent simple cells are often tuned to similar spatial frequencies, and have similar orientation selectivities, but appear to have phase difference of 90 degrees. That is, it appears that the cosine (even) and sine (odd) components of the GEFs are implemented in the visual cortex by pairs of adjacent simple cells [63]. Not surprisingly, these discoveries in physiological and psychophysical research aroused intense new interest in the study and application of the Gabor functions for computational vision.

Daugman [64] extended Gabor's results [61] to the case of two-dimensions, showing that the resulting two-dimensional elliptical Gaussians were optimally localized in the spatial and spatial frequency domains. Daugman suggested that filters based on the elliptical Gaussians modulated by sinusoids represent a necessary evolutionary compromise for a biological vision system with incompatible high-level goals. The organism must find both spatial information and spatial frequency information from its visual space. The way to accomplish this is to implement in the visual cortex the transform that has the best joint specificity in the spatial and frequency domains. This transform is the Gabor transform [65]. Further, the correspondence remains between the shapes of these two-dimensional Gabor functions and the cortical RFs considered as two-dimensional filters. Thus, by basing themselves on the GEFs as models, vision physiologists are evidently equipped with a formalism that explains the properties of orientation selectivity, spatial frequency selectivity, and the empirically observed quadrature relationship for pairs of cortical simple cells.

Does the visual cortex implement some kind of Gabor transform? The physiological experiments on animals and the psychophysical experiments on humans

seem to overwhelmingly support the view that the simple RFs are filters selective to orientation and frequency. Further, the spatial structure of the simple RFs closely resembles the GEFs. It is no wonder that the Gabor representation, with its optimal localization properties, was seized upon as a candidate model for the functioning of the visual cortex. Mallat questions the choice of the Gabor transform as a model for cortical functions, however [1]. He points out that the simple cells of the visual cortex do not have impulse responses which contain more cycles when the tuning is for a higher frequency. This would be the case if the cells were organized in the form of the logons of the Gabor representation. Instead, Mallat argues, the simple cells have larger RFs when the frequency tuning is lower and smaller RFs when the frequency tuning is correspondingly higher.

The experimental evidence is not completely clear on this issue however. The question at hand is whether simple cells with high-frequency tuning exhibit more cycles within their fields than cells selective of lower spatial frequencies. This is equivalent to saying that the bandwidth in octaves varies with the particular spatial frequency preferred by a cortical simple cell. Pollen and Ronner stress that a variety of bandwidths are typically associated with cells of a given frequency tuning [63].

Nevertheless, the correlations between preferred spatial frequency and bandwidth tend not to support the contention that a full Gabor transform, with its specific requirement of increased cycles in RFs with higher frequency tunings, is implemented in the visual cortex. A model counterposed to the Gabor model of cortical architecture, wherein the RF sizes vary inversely with the frequency tuning of the simple cells, is presented by Kulikowski, Marcelja, and Bishop [39].

Finally, some more recent studies of the visual cortex support the viewpoint that the receptive field sizes vary inversely with preferred spatial frequency. This would be the case if the visual cortex implements a kind of time-scale transform. A case in point is Anderson and Burr's investigations of human motion detection neurons in the visual cortex [66]. The authors discover a regular decrease in RF size as the observed preferred frequency tuning of these cells increases. The RF size was found to progressively diminish from as high as 7 degrees at low spatial frequencies to 2 minutes of arc for cells with the highest preferred frequencies.

As Gabor—and perhaps wavelet—transforms have proven useful in modeling aspects of the human visual system, so have they found applications in studying the auditory system. One can think of the cochlea as a bandpass filter bank (Chapter 9). From measurements of sound sensitivity above 800 Hz, it then turns out that the filter impulse responses are approximately *dilations* of one another [67]. Thus, cochlear sound processing roughly implements a wavelet transform.

## 12.4 DISCOVERING SIGNAL STRUCTURE

Time-frequency and time-scale transforms provide alternative tools for local signal description. The local descriptions can be merged and split, according to application design, resulting in a structural description of a signal. The motivation for this is that the physical processes that produced the signal changed over time and that the

structure of the signal, properly extracted, provides a means for identifying and understanding the mechanism that generated it. Structures may be simple time-ordered chains of descriptors. When there are long-term and short-term variations in the signal's generation, then it may be effective to build a hierarchical graph structure for describing the data.

### 12.4.1 Edge Detection

Let us examine how well the windowed Fourier and wavelet transforms can support basic edge detection signal analysis tasks. Signal edges represent abrupt changes in signal intensity and are a typical initial step to segmenting the signal.

**12.4.1.1 Time-Frequency Strategies.** A simple sawtooth edge experiment demonstrates that the windowed Fourier transform is a problematic edge detector.

The Gabor transform responses indicate local frequencies, and there are indeed high frequency components in the neighborhood of signal edges (Figure 12.19). Locality is poor, however. Shrinking the time width of the Gabor elementary functions provides better resolution. The problem is that this essentially destroys the nature of the transform. Using different window widths makes it more resemble the wavelet transform. Perhaps the most effective application for the short-time Fourier transforms is to indirectly detect edges by locating regions of distinct texture. Indeed, the windowed Fourier transforms are very effective for this purpose, and a number of research efforts have successfully applied them for texture segmentation [68–70]. The filter banks and time-frequency maps of Chapter 9 provide starting points for the spectral analysis of signal texture. The edges between differently textured regions are inferred as part of the higher-level interpretation steps.

**12.4.1.2 Time-Scale Strategies.** Better suited to edge detection are the time-scale transforms. Not only does the wavelet transform provide for narrowing the time-domain support of the analyzing wavelet, allowing it to zoom in on signal discontinuities, there are two theoretical results that support wavelet-based edge detection:

- (i) For certain continuous wavelet transforms, finding maximal response is identical to applying the optimal Canny edge detector [45].
- (ii) The decay of the wavelet transform maxima across scales determines the local regularity of the analyzed signal.

However, we also now know that edge-based descriptions of signal structure are not the final answer:

- (iii) Marr's conjecture is false [29, 51].

Yet, structural description by edges and extrema (ridge edges) remains a powerful tool for understanding signals. Both continuous and discrete wavelet transforms are closely related. For example, a wavelet transform can be built around spline wavelets

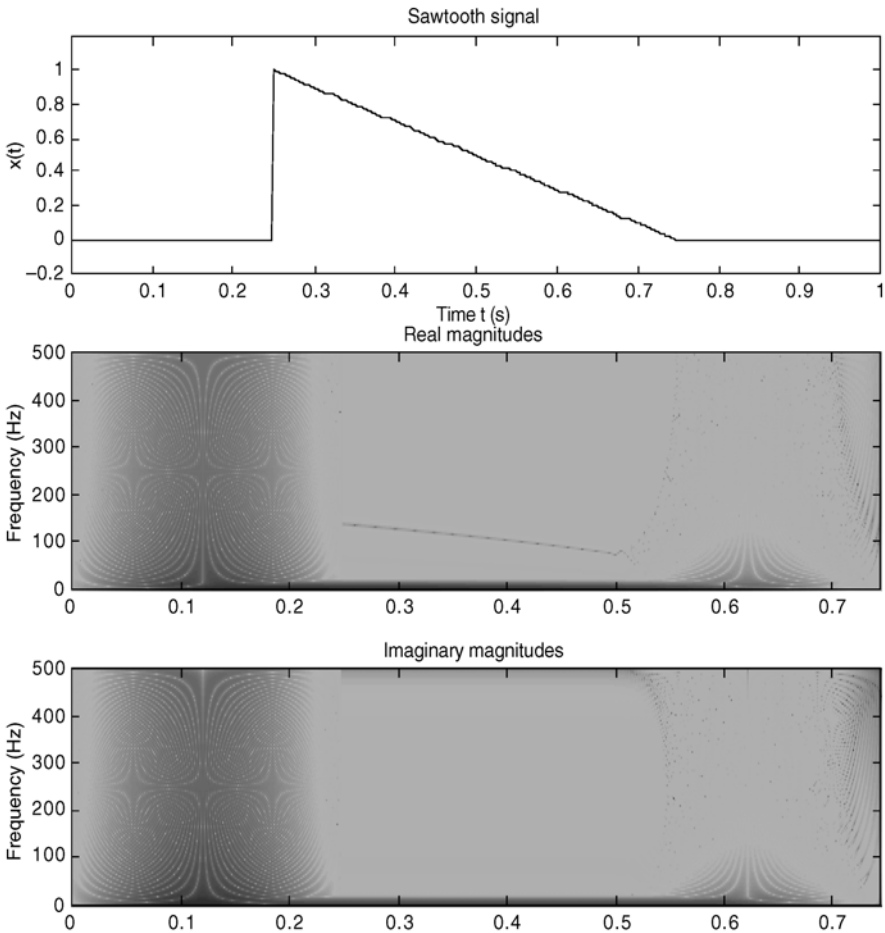


**Fig. 12.19.** A sawtooth edge (*top*); real and imaginary Gabor transform coefficient magnitudes (*middle*); and convolution of the discrete high-pass filter associated with the cubic spline orthogonal wavelet representation.

that mimic the optimal derivative of Gaussian [48]. The multiresolution decomposition of the signal supports a multiscale edge detector [50]. This is useful for discriminating background noise from substantive signal features according to perceptual criteria [71]. The discrete high-pass filters  $g_p(n)$  given in Figure 12.3 and Figure 12.4 function as edge detectors for the orthogonal wavelet pyramid (Figure 12.5).

Let us turn to the continuous wavelet transform. Suppose  $g(t) = Ae^{-Bt^2}$  is a Gaussian of zero mean. Set  $\psi(t) = \frac{d}{dt}g(t)$ . Then  $\psi(t)$  is a wavelet because it has zero mean, is integrable, and has finite energy. Let  $x_a(t) = ax(at)$  be the scaled dilation of  $x(t)$  by factor  $a$ . Typically,  $a = 2^i$  for  $i \in \mathbb{Z}$ , with  $i < 0$  in our notation [1].

Then, changing notations from Chapter 11 slightly, the wavelet transform of an analog signal  $x$  is

$$(W_{-i}x)(t) = (\Psi_{2^{-i}} * x)(t) \quad (12.29)$$

at time instant  $t$ . Consequently,

$$(W_{-i}x)(t) = (\Psi_{2^{-i}} * x)(t) = \left(2^{-i} \frac{d}{ds} g(2^{-i}s) * x\right)(t) = 2^{-i} \frac{d}{dt} (g_{2^{-i}} * x)(t). \quad (12.30)$$

So where  $|W_{-i}x|$  is large, the version of  $x$ , smoothed to resolution  $2^{-i}$ , is changing rapidly [72].

Let us recount the result (ii) above [72]. Suppose  $x(t)$  is a signal defined in a neighborhood of  $t_0$ ,  $0 \leq \alpha \leq 1$ , and there is a constant  $c$  such that for all  $t$  in an interval about  $t_0$ , we have

$$|x(t) - x(t_0)| \leq c|t - t_0|^\alpha. \quad (12.31)$$

Then  $x(t)$  is *Lipschitz*<sup>1</sup>  $\alpha$  at  $t = t_0$ . The *Lipschitz regularity* of  $x(t)$  at  $t = t_0$  is the least upper bound of all  $\alpha$  such that (12.31) holds. If there is an  $0 \leq \alpha \leq 1$  and an open interval such that (12.31) holds for all  $t \in (a, b)$ , then the signal  $x(t)$  is *uniformly Lipschitz*  $\alpha$  on  $(a, b)$ . In other words,  $x(t)$  is uniformly Lipschitz if it is as tame as an exponential function in some region.

Now suppose we have a continuous wavelet  $\psi(t)$  that decays at infinity as  $1/(1+t^2)$  and a square-integrable signal  $x(t)$ . Then it can be shown [73] that  $x(t)$  is uniformly Lipschitz  $\alpha$  on  $(a, b)$  if and only if there is a  $c > 0$  such that for all  $t \in (a, b)$

$$|(W_{-i}x)(t)| \leq c2^{i\alpha}. \quad (12.32)$$

The decay of wavelet transform maxima over many resolutions is essentially a study of the degree of singularity of the original signal. An extensive study of continuous wavelet transformation as a characterization of regularity is Ref. 74.

**12.4.1.3 Application: The Electrocardiogram.** Biomedical technology has investigated almost every avenue of signal analysis in order to improve electrocardiogram (ECG) interpretation. Researchers have experimented with time-domain, frequency domain, time-frequency domain, and now time-scale domain methods [75, 76]. Chapter 1 introduced ECG signal processing and analysis.

<sup>1</sup>Analyst Rudolf Lipschitz (1832–1903) was professor at the University of Bonn.

Frequency-domain methods are effective for many important tasks in computerized electrocardiography, such as convolutional noise removal and band rejection of noise from (50 or 60 Hz, for example) alternating current power sources [77]. Edges and transients in the ECG are crucial to interpreting abnormalities. In order to preserve these features, yet remove noise, research has turned to mixed-domain filtering techniques, such as we covered in Section 12.2 [78]. Compression techniques using wavelet transforms are also known [79]. The most important task in automated ECG analysis is QRS complex detection [80], essentially a ridge edge detection problem. The foundation of these application is the characterization of signal regularity by wavelet transform maxima across scales [74]. Algorithms for QRS detection and time-scale decomposition of ECGs using the orthogonal wavelet decomposition are shown in Ref. 81. The continuous wavelet transform is studied for QRS characterization in Ref. 82. The wavelet transform is effective in revealing abnormalities, such as the ventricular late potential (VLP) [83]. For example, in Ref. 84 a synthetic VLP is introduced into the ECG. The late potential is difficult to discern in the time-domain trace. However, wavelet transformation reveals that the defect is as an enlargement in the time-domain support of the QRS complex at certain scales.

### 12.4.2 Local Frequency Detection

Both the short-time Fourier and wavelet transforms perform local frequency detection. The STFT or Gabor transform relies on time-frequency cells of fixed size (Chapter 10). The wavelet transform adapts the time domain extent according to the frequency tuning (Chapter 11).

**12.4.2.1 Mixed-Domain Strategies.** The fixed window width of the short-time Fourier transform is useful when the range of frequencies in the analyzed signal is known to remain within fixed bounds (Figure 12.20). An example of this is in texture analysis, where the local frequencies of the signal pattern are expected within given spectral ranges. Small defects in the texture are not readily detected, but the time-frequency map displays the overall local pattern quite well.

On the other hand, the wavelet pyramid decomposition tends to mimic the coarse structure of the signal in the approximate coefficients and provides a range of highpass filters sensitive to local textures in the detail coefficients (Figure 12.21).

Finally, the continuous wavelet transform clearly shows the scale of the underlying pattern features in its amplitude (Figure 12.22).

**12.4.2.2 Application: Echo Cancellation.** One application of wavelet transform-based filter banks has been to improve echo canceller performance. Chapter 2 (Section 2.4.4) explained the need for echo cancellation in digital telephony. The echo arises from an impedance mismatch in the four-wire to two-wire hybrid transformer. This causes an echo, audible to the far-end listener, to pass into the speech signal from the near-end speaker. The classical time-domain approach for reducing the echo is to remove the echo by an adaptive convolutional filter [85]. One problem is getting the canceller to converge quickly to an accurate echo model when the

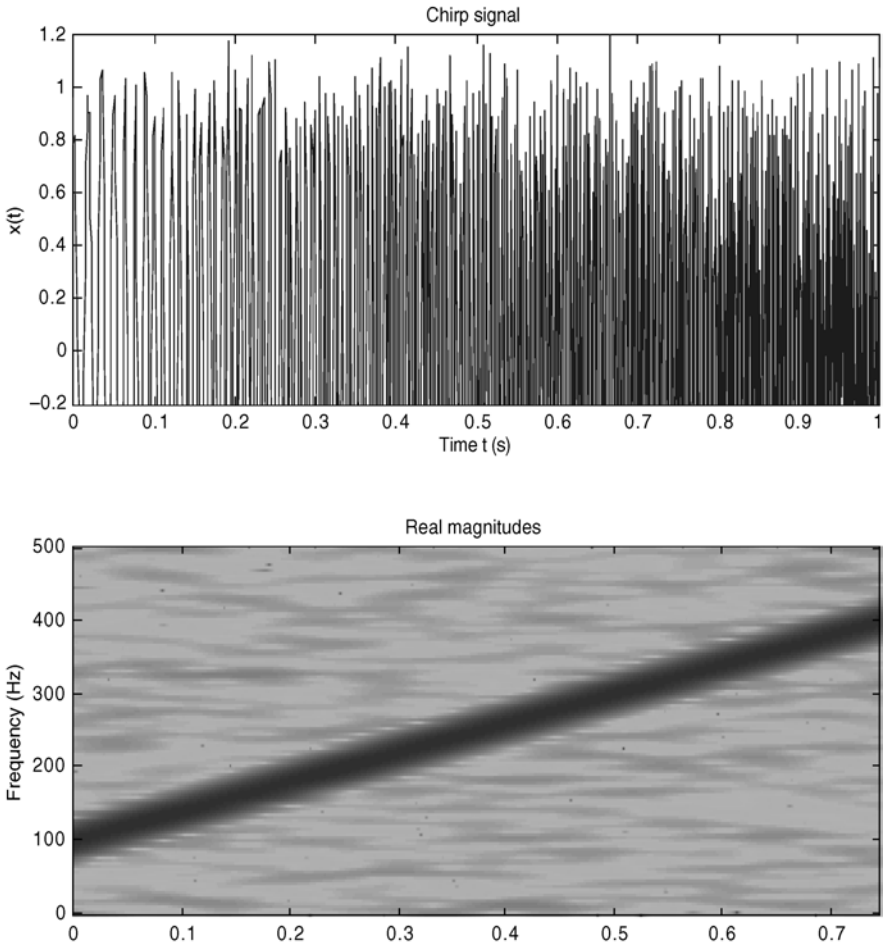


**Fig. 12.20.** A Gabor transform applied to a sinusoidal chirp signal embedded in noise.

echo path length varies. This can happen in digital telephony, and it is a problem in other applications, such as acoustic echo cancellers employed in teleconferencing systems. Both conventional quadrature mirror filter bank decompositions [86] and wavelet packet decompositions [87] have been used to replace the adaptive time-domain convolution in the classical echo canceller.

**12.4.2.3 Application: Seismic Signal Interpretation.** The continuous wavelet transform arose out of problematic attempts to use time-frequency methods in seismic data analysis [88]. Both the continuous wavelet transform and the discrete orthogonal pyramid decomposition are applicable to seismic signal interpretation. Early applications used the wavelet transform to improve visualization and interpretation of seismic sections [88–90].

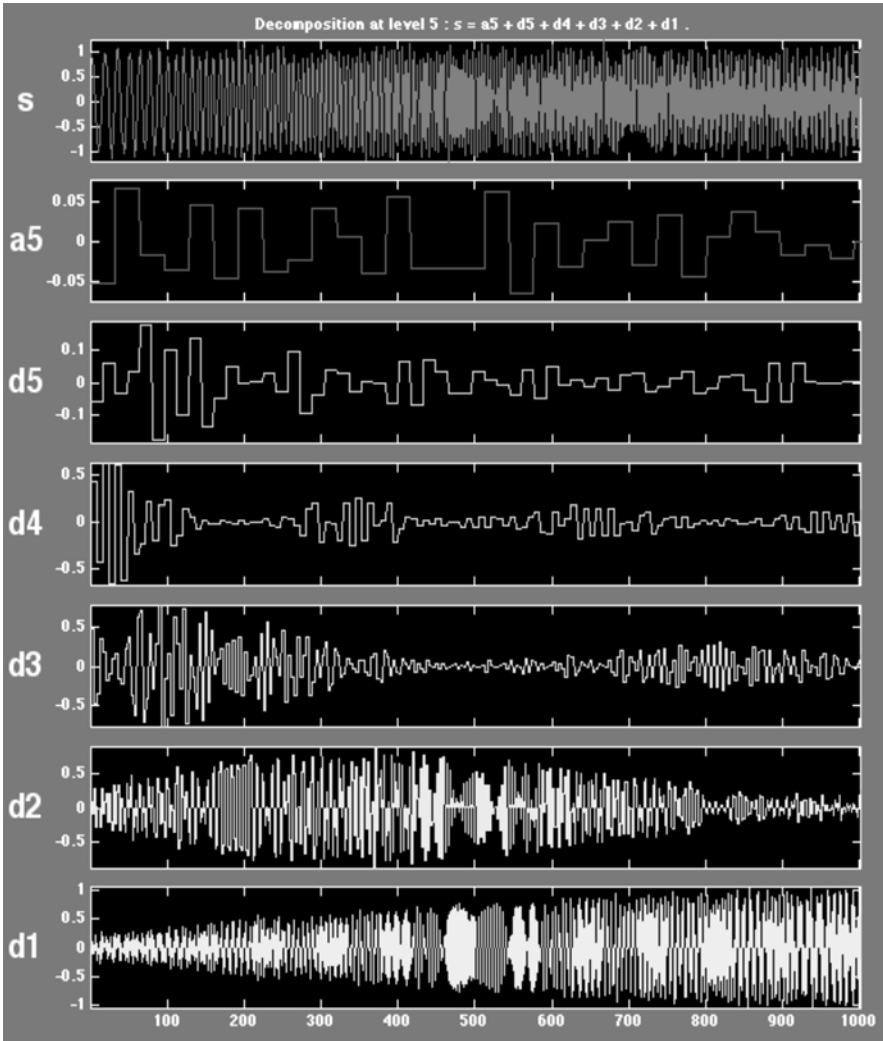


**Fig. 12.21.** An orthogonal wavelet transform applied to a sinusoidal chirp signal embedded in noise. Decomposition to five levels using the Haar wavelets.

Both the continuous and orthogonal wavelet transforms have been applied to seismic signal analysis. In Ref. 91, for example, researchers recommend the Morlet wavelet (12.33) for removing correlated ground roll noise from seismic exploration data sets.

$$\psi(t) = e^{-\frac{t^2}{2}} \cos(\omega_0 t). \tag{12.33}$$

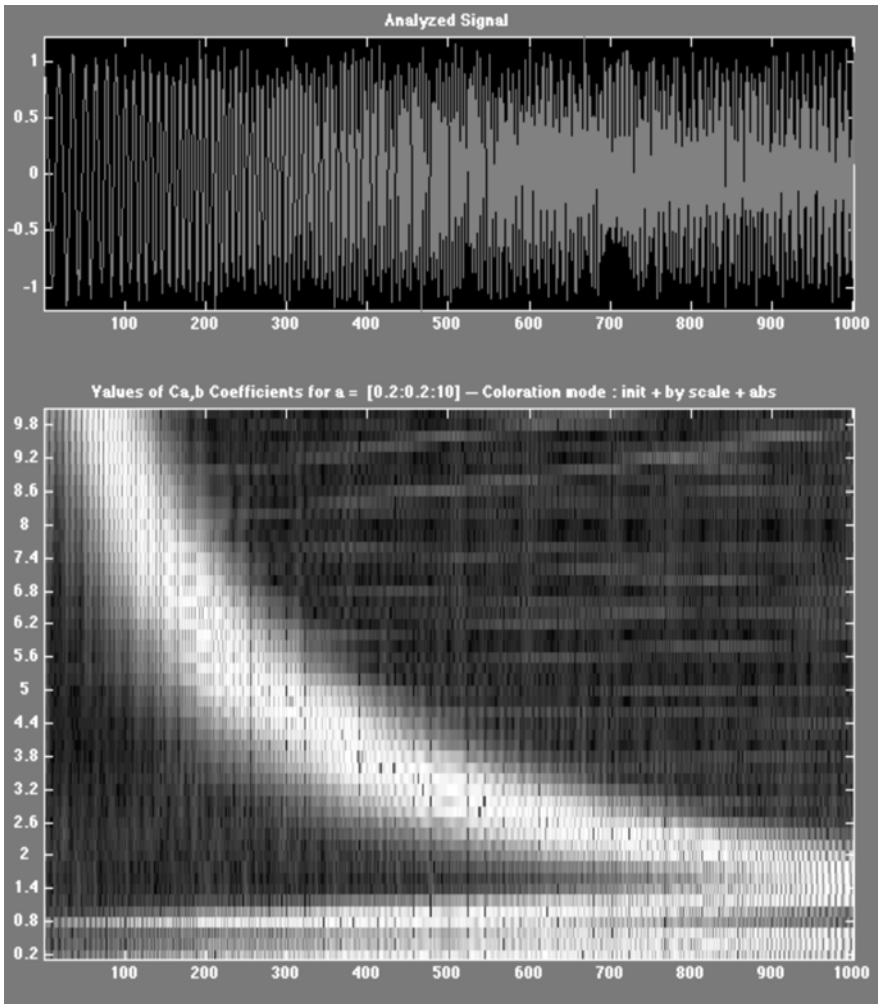


**Fig. 12.22.** A continuous wavelet transform applied to a sinusoidal chirp signal embedded in noise. Decomposition over 50 scale values using the Morlet wavelet.

The authors perform the continuous transformation by convolving the wavelet  $\psi(t)$  with the raw data, exclude the bands containing the ground roll noise, and reconstruct the signal using the inverse transform.

In Ref. 92 the wavelet pyramid transform is considered for analyzing arrival times estimation in seismic traces. The researchers conclude that preliminary de-noising is essential. The wavelet-based filtering preserves high-frequency components necessary for finding the boundaries between oscillatory components.

**12.4.2.4 Application: Phoneme Recognition.** The mixed-domain transforms offer different structural decomposition tools for the speech analyst. In Chapter 9, we considered two types of algorithm for localized frequency analysis: the filter bank and the time-frequency map. The wavelet pyramid decomposition (Figure 12.5) furnishes a filter bank scheme where the outputs are independent of one another and perfect reconstruction of the original signal is possible. In addition, both discrete time-frequency and time-scale transforms support a time-frequency map methodology. The difference between the two is that the time-frequency cells of the Gabor transform, for example, have a fixed time-domain extent (Chapter 10). The wavelet transform cells vary their time spans; cells tuned to higher frequencies have narrower time domain support. Local-frequency estimation, as a preliminary step for recognizing phonemes, remains an active area of research.

It is difficult to design a pitch detector that adapts to both high and low speech frequencies while maintaining adequate noise immunity [93–95]. Recently, the dyadic continuous wavelet transform, given by

$$F_{\Psi}(a, b) = W[x(t)](a, b) = \int_{-\infty}^{\infty} x(t) \overline{\Psi_{a,b}(t)} dt \equiv \langle x(t), \Psi_{a,b}(t) \rangle, \quad (12.34a)$$

where

$$\Psi_{a,b}(t) = \frac{1}{\sqrt{|a|}} \Psi\left(\frac{t-b}{a}\right), \quad (12.34b)$$

$x(t)$  has finite energy, and  $a = 2^i$  for some integer  $i$ , has been applied to this problem [96]. One advantage is that the analysis then corresponds to the apparent time-scale operation of the human auditory system [67]. Surprisingly, the researchers report that only a few scales  $a = 2^i$  are necessary for accurate detection [96]. Compared to conventional time- and frequency-domain methods, the dyadic wavelet pitch detector:

- (i) Is robust to nonstationary signals within its analysis window;
- (ii) Works on a wide range of pitch signals, such as from male and female speakers;
- (iii) Can detect the beginning of the voiced segment of the speech sample, making it the possible basis for a pitch detection algorithm that operates synchronously with the pitch bearing event;
- (iv) Is superior within low frequencies to pitch determination by the time-domain autocorrelation method [95];
- (v) Is superior within high frequencies to the frequency-domain cepstrum method [97].

### 12.4.3 Texture Analysis

Until recently, texture has been a persistently problematic area for signal and image analysis. Although the human subject readily distinguishes visual textures, it has

hitherto not been possible to classify them with computerized algorithms, let alone provide theoretical models for synthesizing visually realistic textures.

**12.4.3.1 Mixed-Domain Strategies.** Some promising early applications of the wavelet transform were to texture analysis [98]. An important contribution to texture analysis and synthesis has come from applying overcomplete wavelet pyramids to the problem [99]. A variety of statistics on the transform coefficients are used to characterize textures. Deletion of certain groups of statistical parameters and subsequent flawed reconstruction of the original image demonstrates that the necessity of the chosen statistics.

**12.4.3.2 Application: Defect Detection and Classification.** It is possible to apply the statistics of overcomplete pyramids to the problem of texture flaw detection. This application is important in manufacturing defect detection systems, for example. The algorithm of Ref. 99 is capable of synthesizing textures that appear to lie in between two others and offers the promise of a statistical divergence measure for textures. Defects in local regions can be detected by developing the statistical parameters from a prototype sample and comparing them to statistics extracted from candidate textures.

## 12.5 PATTERN RECOGNITION NETWORKS

This section explains pattern recognition methods that are useful for analyzing signals that have been decomposed through mixed domain transforms.

### 12.5.1 Coarse-to-Fine Methods

Pattern recognition where the time-domain size of the recognized signal structures are unknown present a variety of problems for the algorithm designer. In particular, the shape recognition computations can require more time than is available in real-time. We have already reviewed a variety of multiresolution methods for this purpose:

- Multiscale signal edge operators [45–48];
- Time-scale representations such as the wavelet multiresolution analysis [1] and the Laplacian pyramid decomposition [2];
- Scale-space smoothing with a range of kernel sizes [5].

Such decompositions demand large numbers of floating-point multiplications and additions. However, online process control and speech recognition software must keep a real-time pace and make a recognition decision with a fraction of a second. Sometimes, cost constrains the type of processor. One way to stay within the paradigms provided by time-scale signal analysis, yet achieve a real-time recognition time is to employ the classic Haar wavelet approximation [16–18] (Figure 12.23). How to do this is described in process control applications [100, 101].

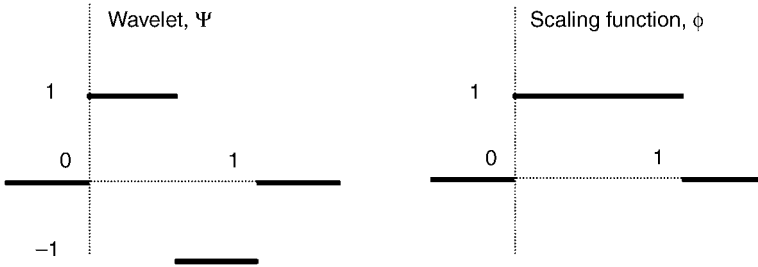


**Fig. 12.23.** The Haar MRA wavelet and scaling function. Translations and dilations of the wavelet form an orthonormal basis for all finite-energy signals, so the Haar representation can accommodate any signal shape. The scaling function can be used to develop step function approximations to signal shapes. The Fourier characteristics of these approximations are not as attractive as other decompositions, such as smooth spline functions. However, with this technique it is possible to implement a real-time signal decomposition with small industrial control computers.

It is possible to approximate signals by decomposing them into steps or to model them using the signal envelopes [101]. Figure 12.24 shows an example of an endpoint signal from the optical emission monitoring application in [101].

The idea behind using the Haar MRA for signal pattern recognition is that there is a simple relation between certain coarse and fine resolution patterns that allows the application to economize on matching.

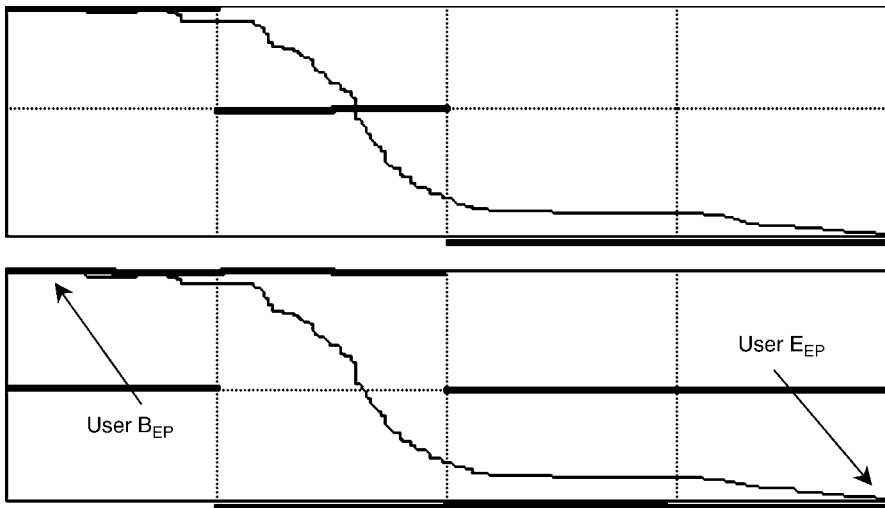


**Fig. 12.24.** Two methods to find Haar approximations for signal regions: projection to the mean (*top*) and the Haar envelope (*bottom*). In this figure, the shapes represent optical emission endpoint traces selected by users.

### 12.5.2 Pattern Recognition Networks

A pattern recognition network is a set of pattern detector elements or *neurons* tuned to different resolutions and different signal shapes [101].

Network *training* creates multiple resolution models of the signal shapes which are stored inside the neurons. The multiple resolution matching provides noise immunity during recognition, although linear and nonlinear smoothing operations help to clean acquired signals. To trim the number of pattern detectors in the network, the finest resolutions necessary for the model time and dynamic range divisions can be estimated as follows [101].

Given an input data file  $x(n)$  with  $N$  values, one computes the discrete Fourier transform:

$$X(k) = \sum_{n=0}^{N-1} x(n)e^{-2\pi jnk}. \quad (12.35)$$

Then, the non-DC coefficients representing the bulk of the signal's energy are selected:  $k = 1, 2, \dots, k_c, N-1, N-2, \dots, N-k_c$ . This selection is based on an energy percentage threshold. Then the signal detectors only need enough time-domain resolution so as to capture the shape of a single cycle of wavelength  $NT/k_c$  seconds, where  $T$  is the real-time application sampling rate. The length of a signal shape model, together with this minimum resolution value, determines the maximum length in samples of the discrete patterns stored in the detector elements.

The scheme of Ref. 101 also limits the dynamic range of signal models. Again using heuristic thresholds, typically modified by the application user, the amount of noise in the signal models is estimated. Then using a DFT approach again, the necessary dynamic range resolution in the step-shaped signal models is found. The result is a rectangular array of pattern detectors, from the lowest time resolution to the highest and from the lowest dynamic range division to the highest.

The projection of an acquired signal onto the step functions of the Haar representation are the coarse resolution representations used as models for pattern detection. Each "neuron" is a step function pattern detector. Before the network runs on real data, the patterns are checked against previously acquired data sets. One criterion is *stability*—how long a signal pattern persists in the data stream. Another criterion is the tendency to make false detections in the input data. Any neurons that fail to meet these criteria are disabled and not used by the network on real data.

The neurons of the network are interconnected with enabling and disabling links. When a coarse resolution node does not detect its established block shape pattern, it may disable certain finer resolution nodes. An example is shown in Figure 12.25.

At run time, the network presents the current and past signal data to each neuron. Each node computes the step pattern according to its particular resolutions. It compares the candidate pattern to its training pattern. When a node shows no match, higher-resolution nodes whose time or range resolutions are multiples of the non-matching unit cannot possibly activate and are disabled (Figure 12.25). When a node actually finds its pattern, all nodes of lesser resolution are disabled. The network continues to seek a more precise registration of the signal pattern. Any

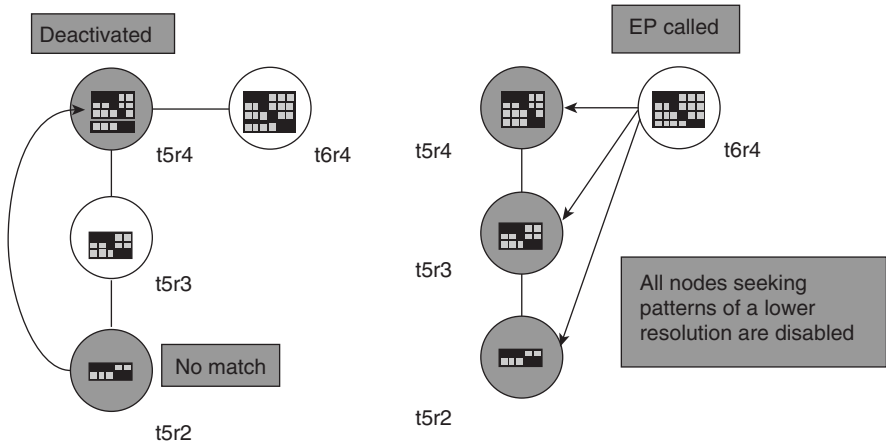


**Fig. 12.25.** Some interconnections of EP pattern detectors [101]. Node names indicate the time-domain and dynamic range resolutions of the Haar decomposition step functions that approximate the EP region. When a node shows no match, certain higher-resolution nodes cannot possibly activate and are disabled (*left*). When a node detects its pattern, the network disables all nodes of lesser resolution while it seeks a more precise registration of the signal shape. There is a single output node. Any enabled neuron that detects its own pattern can activate the output node to signal the detection of the prototype pattern.

enabled neuron that detects its own pattern can activate the output node to indicate a recognition success.

This is the key idea behind using the Haar step functions to model and compare signals. With a faster computer or freedom from the real-time processing requirement, other multiresolution approximations can be used. Of course, in this situation, the relation between detectors of different resolutions is not so easy to characterize and remains a potential problem for the algorithm design.

### 12.5.3 Neural Networks

Neural networks are an alternative to the structured design of the pattern recognition network above. Both supervised and unsupervised neural networks have been intensively studied in the last 20 years. An advantage of neural networks is that their training can be conditioned by training data, learning, as it were, the salient patterns present in the raw data [102]. The problem is that large amounts of data are sometimes necessary to train such networks. An example of applying neural networks to semiconductor process control is Ref. 103.

### 12.5.4 Application: Process Control

In semiconductor integrated circuit fabrication, plasma etch processes selectively remove materials from silicon wafers in a reactor [104]. The chemical species in the

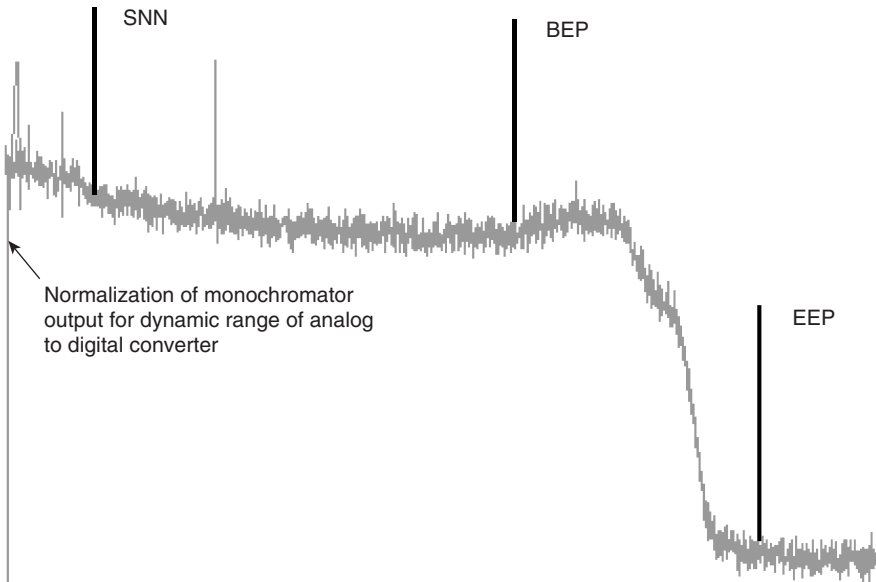


**Fig. 12.26.** Plasma etch optical emission trace from Ref. 101. The user acquires a sample trace and must indicate the points at which valid data begin (SNN), the endpoint is beginning (BEP), and the endpoint event is over (EEP). A Haar model can be made out of the data for training a pattern recognition network.

reaction emit characteristic wavelengths of light. It is typical to employ a monochromator and digitizer pass the light intensity signal to computer software algorithms to monitor and control the etch progress. When the target layer disappears, process endpoint occurs; the control computer extinguishes the plasma. For signal analysis, the problem is that process endpoints vary from wafer to wafer over a run. Both traditional neural networks [103] and the structured pattern recognition network [100, 101] have been used for this application. Extensive testing is reported in Ref. 101.

## 12.6 SIGNAL MODELING AND MATCHING

This final section mentions methods for extracting signal structure that have been particularly popular in conjunction with time-frequency and time-scale transforms.

### 12.6.1 Hidden Markov Models

The hidden Markov model (HMM) is a stochastic state machine that is especially useful for sequential analysis of data. Thus, it has been applied widely in speech recognition [105], handwriting recognition [106], and biological sequence analysis [107].

### 12.6.2 Matching Pursuit

The matching pursuit is a greedy, iterative algorithm [108]. In Ref. 109 the method is applied with overcomplete dictionaries of damped sinusoids. The method typically uses an overcomplete dictionary for numerical stability. It improves upon traditional techniques such as least squares, singular value decomposition, and orthonormal basis decompositions—for example, the orthogonal wavelet pyramid [1].

### 12.6.3 Applications

Two of the most important applications of hidden Markov models have been in speech recognition and biological sequence analysis.

**12.6.3.1 Speech Analysis.** Speech recognition applications are described in the classic tutorial [105].

**12.6.3.2 Protein Analysis.** A tutorial on protein analysis is Ref. 110.

## 12.7 AFTERWORD

There is no doubt that mixed-domain signal transforms, combining both time and either frequency or scale information, have altered the signal processing landscape. It is almost impossible today to browse an academic journal in the discipline and not find a contribution that concentrates on the theoretical or practical implications of these techniques. This text introduces the new methods into the mainstream of signal processing education.

Some of the trends we identified when contemplating the task of writing this book have become clearer and stronger. It is still true that learning windowed Fourier and wavelet transforms has its mathematical challenges. The entire signal processing research community has embraced the underlying mathematical tools—especially Hilbert space theory—even though they may entail a steep learning curve. Here we have developed the mathematics incrementally and colored it with terminology, notations, and concepts directly relevant to signal theory. This might relieve some anxiety and make the climb less daunting. Also, the selection of algorithms and applications in *signal analysis* not only reflects the modern mathematical slant but also emphasizes signal understanding as opposed to pure processing. We think that this too is timely, as more and more automated signal recognition technologies have intruded into our lives.

Of the new mixed-domain transforms, probably the most surprises came from orthogonal wavelets. These functions captivated researchers in so many areas. Today, however, the associated signal decomposition seem to be retreating into compression applications, with its analysis powers having been tested and found lacking for pattern recognition. But it does offer insights into texture characterization. On the other hand, the continuous wavelet transform rises up to be the better tool for

transient signals. The exponential short-time Fourier methods cannot be sparse and complete, as we now know, but this has not prevented them from becoming the tool of choice in a number of early processing applications. The time-frequency and time-scale tools are just alternative ways to break a signal into pieces and sort them out into a structural description. Beyond that, their importance is that they highlight the special global nature of the wellspring of them all—Fourier’s transform.

## REFERENCES

1. S. Mallat, A theory for multiresolution signal decomposition: The wavelet representation, *IEEE Transactions on Pattern Analysis and Machine Intelligence*, pp. 674–693, July 1989.
2. P. J. Burt and E. H. Adelson, The Laplacian pyramid as a compact image code, *IEEE Transactions on Communication*, vol. 31, no. 4, pp. 532–540, April 1983.
3. S. Mallat, *A Wavelet Tour of Signal Processing*, San Diego, CA: Academic Press, 1998.
4. O. Rioul and M. Vetterli, Wavelets and signal processing, *IEEE SP Magazine*, pp. 14–38, October 1991.
5. R. L. Allen, F. A. Kamangar, and E. M. Stokely, Laplacian and orthogonal wavelet pyramid decomposition in coarse-to-fine registration, *IEEE Transactions on Signal Processing*, vol. 41, no. 12, pp. 3536–3543, December 1993.
6. R. Y. Wong and E. L. Hall, Sequential hierarchical scene matching, *IEEE Transactions on Computers*, vol. C-27, no. 4, pp. 359–366, April 1978.
7. D. Marr, *Vision*, New York: W. H. Freeman, 1982.
8. T. Lindeberg, *Scale-Space Theory in Computer Vision*, Hingham, MA: Kluwer, 1994.
9. B. ter Haar Romeny, L. Florack, J. Koenderink, M. Viergever, eds., *Scale-Space Theory in Computer Vision* (Proceedings, First International Conference, Scale-Space ‘97, Utrecht, The Netherlands), Berlin: Springer-Verlag, 1997.
10. R. H. Bamberger and M. J. T. Smith, A filter bank for the directional decomposition of images: Theory and design, *IEEE Transactions on Signal Processing*, vol. 40, no. 4, pp. 882–893, April 1992.
11. E. P. Simoncelli, W. T. Freeman, E. H. Adelson, and D. J. Heeger, Shiftable multiscale transforms, *IEEE Transactions on Information Theory*, vol. 38, no. 2, pp. 587–607, March 1992.
12. P.-G. Lemarié, Ondelettes à localisation exponentielle, *Journal de Mathématiques Pures et Appliquées*, vol. 67, pp. 227–236, 1988.
13. F. Mokhtarian and A. Mackworth, Scale-based description and recognition of planar curves and two-dimensional shapes, *IEEE Transactions on Pattern Analysis and Machine Intelligence*, vol. PAMI-8, no. 1, pp. 34–43, January 1986.
14. M. P. do Carmo, *Differential Geometry of Curves and Surfaces*, Englewood Cliffs, NJ: Prentice-Hall, 1976.
15. J.-O. Strömberg, A modified Franklin system and higher order spline systems on  $R^n$  as unconditional bases for Hardy spaces, in W. Becker, A. P. Calderon, R. Fefferman, and P.W. Jones, eds., *Proceedings of the Conference in Honor of Antoni Zygmund*, vol. II, New York: Wadsworth, pp. 475–493, 1981.

16. A. Haar, Zur theorie der orthogonalen Functionensysteme, *Mathematische Annalen*, vol. 69, pp. 331–371, 1910.
17. I. Daubechies, *Ten Lectures on Wavelets*, Philadelphia: SIAM, 1992.
18. H. S. Stone, J. Le Moigne, and M. McGuire, The translation sensitivity of wavelet-based registration, *IEEE Transactions on Pattern Analysis and Machine Intelligence*, vol. 21, no. 10, pp. 1074–1081, October 1999.
19. M. Antonini, M. Barlaud, I. Daubechies, and P. Mathieu, Image coding using vector quantization in the wavelet transform domain, *Proceedings of the IEEE Conference on Acoustics, Speech, and Signal Processing*, pp. 2297–2300, April 1990.
20. S. G. Mallat and J. Froment, Second generation compact image coding with wavelets, in C. K. Chui, ed., *Wavelets: A Tutorial in Theory and Applications*, San Diego, CA: Academic Press, 1992.
21. D. Sinha, and A. H. Tewfik, Low bit rate transparent audio compression using adapted wavelets, *IEEE Transactions on Signal Processing*, vol. 41, no. 12, pp. 3463–3479, December 1993.
22. M. Vetterli and J. Kovacevic, *Wavelets and Subband Coding*, Upper Saddle River, NJ: Prentice-Hall, 1995.
23. A. Rosenfeld and A. C. Kak, *Digital Picture Processing*, San Diego, CA: Academic Press, 1982.
24. G. K. Wallace, The JPEG still picture compression standard, *Communications of the ACM*, vol. 34, no. 4, pp. 31–44, April 1991.
25. N. Ahmed, T. Natarajan, and K. R. Rao, Discrete cosine transform, *IEEE Transactions on Computers*, vol. C-23, no. 1, pp. 90–93, January 1974.
26. A. Gersho and A. M. Gray, *Vector Quantization and Signal Compression*, Boston: Kluwer, 1992.
27. F. W. C. Campbell and J. J. Kulikowski, Orientation selectivity of the human visual system, *Journal of Physiology*, vol. 197, pp. 437–441, 1966.
28. H. Malvar, Lapped transforms for efficient transform/subband coding, *IEEE Transactions on Acoustics, Speech, and Signal Processing*, vol. 38, no. 6, pp. 969–978, June 1990.
29. Y. Meyer: *Wavelets: Algorithms and Applications*, Philadelphia: Society for Industrial and Applied Mathematics, 1993.
30. R. R. Coifman, Y. Meyer, and V. Wickerhauser, Wavelet analysis and signal processing, in M. B. Ruskai, et al., eds., *Wavelets and Their Applications*, Boston: Jones and Bartlett, pp. 153–178, 1992.
31. R. R. Coifman, Y. Meyer, and V. Wickerhauser, Size properties of wavelet-packets, in M. B. Ruskai et al., eds., *Wavelets and Their Applications*, Boston: Jones and Bartlett, pp. 453–470, 1992.
32. D. L. Donoho and I. M. Johnstone, Ideal spatial adaptation by wavelet shrinkage, *Biometrika*, vol. 81, pp. 425–455, 1994.
33. D. L. Donoho, De-noising by soft-thresholding, *IEEE Transactions on Information Theory*, vol. 41, no. 3, pp. 613–627, March 1995.
34. D. L. Donoho, I. M. Johnstone, G. Kerkyacharian, and D. Picard, Density estimation by wavelet thresholding, *Annals of Statistics*, vol. 24, pp. 508–539, 1996.

35. C. M. Stein, Estimation of the mean of a multivariate normal distribution, *Annals of Statistics*, vol. 9, pp. 1135–1151, 1981.
36. K. R. Castleman, *Digital Image Processing*, Upper Saddle River, NJ: Prentice-Hall, 1996.
37. Nowak and Baraniuk, Wavelet-domain filtering for photon imaging systems, *IEEE Trans. IP*, pp. 666–678, May 1999.
38. D. A. Pollen and S. F. Ronner, Visual cortical neurons as localized spatial frequency filters, *IEEE Transactions on Systems, Man, and Cybernetics*, vol. SMC-13, no. 5, pp. 907–916, September–October 1983.
39. J. J. Kulikowski, S. Marcelja, and P. O. Bishop, Theory of spatial position and spatial frequency relations in the receptive fields of simple cells in the visual cortex, *Biological Cybernetics*, vol. 43, pp. 187–198, 1982.
40. F. Attneave, Some informational aspects of visual perception, *Psychological Review*, vol. 61, pp. 183–193, 1954.
41. H. Asada and M. Brady, The curvature primal sketch, *IEEE Transactions on Pattern Analysis and Machine Intelligence*, vol. PAMI-8, no. 1, pp. 2–14, January 1986.
42. I. Biedermann, Human image understanding: Recent research and a theory, *Computer Vision, Graphics, and Image Processing*, vol. 32, pp. 29–73, 1985.
43. A. P. Witkin, Scale-space filtering, *Proceedings of the 8th International Joint Conference on Artificial Intelligence*, Karlsruhe, W. Germany, 1983. See also A. P. Witkin, Scale-space filtering, in *From Pixels to Predicates*, A. P. Pentland, ed., Norwood, NJ: Ablex, 1986.
44. T. Lindeberg, Scale space for discrete signals, *IEEE Transactions on Pattern Analysis and Machine Intelligence*, vol. 12, no. 3, pp. 234–254, March 1990.
45. J. Canny, A computational approach to edge detection, *IEEE Transactions on Pattern Analysis and Machine Intelligence*, vol. PAMI-8, no. 6, pp. 679–698, November 1986.
46. H. D. Tagare and R. J. P. deFigueiredo, On the localization performance measure and optimal edge detection, *IEEE Transactions on Pattern Analysis and Machine Intelligence*, vol. 12, no. 12, pp. 1186–1190, 1990.
47. R. J. Qian and T. S. Huang, Optimal edge detection in two-dimensional images, *IEEE Transactions on Image Processing*, vol. 5, no. 7, pp. 1215–1220, 1996.
48. M. Gökmen and A. K. Jain,  $\lambda\tau$ -space representation of images and generalized edge detector, *IEEE Transactions on Pattern Analysis and Machine Intelligence*, vol. 19, no. 6, pp. 545–563, June 1997.
49. S. Mallat, Zero-crossings of a wavelet transform, *IEEE Transactions on Information Theory*, vol. 37, no. 4, pp. 1019–1033, July 1991.
50. S. Mallat and S. Zhong, Characterization of signals from multiscale edges, *IEEE Transactions on Pattern Analysis and Machine Intelligence*, vol. 14, no. 7, pp. 710–732, July 1992.
51. Z. Berman and J. S. Baras, Properties of the multiscale maxima and zero-crossings representations, *IEEE Transactions on Signal Processing*, vol. 41, no. 12, pp. 3216–3231, 1993.
52. G. A. Orban, *Neuronal Operations of the Visual Cortex*, Berlin: Springer-Verlag, 1984.
53. D. H. Hubel and T. N. Wiesel, Receptive fields, binocular interaction and functional architecture in the cat's visual cortex, *Journal of Physiology*, vol. 160, pp. 106–154, 1962.

54. F. W. C. Campbell and J. Robson, Application of Fourier analysis to the visibility of gratings, *Journal of Physiology*, vol. 197, pp. 551–566, 1968.
55. F. W. C. Campbell and J. J. Kulikowski, Orientation selectivity of the human visual system, *Journal of Physiology*, vol. 195, pp. 437–441, 1966.
56. C. Blakemore and F. W. C. Campbell, On the existence in the human visual system of neurons selectively sensitive to the orientation and size of retinal images, *Journal of Physiology*, vol. 203, pp. 237–260, 1969.
57. J. P. Jones and L. A. Palmer, The two-dimensional spatial structure of simple receptive fields in cat striate cortex, *Journal of Neurophysiology*, vol. 58, pp. 1187–1211, 1987.
58. J. P. Jones and L. A. Palmer, An evaluation of the two-dimensional Gabor filter model of simple receptive fields in cat striate cortex, *Journal of Neurophysiology*, vol. 58, pp. 1233–1258, 1987.
59. J. P. Jones, A. Stepnoski, and L. A. Palmer, The two-dimensional spectral structure of simple receptive fields in cat striate cortex, *Journal of Neurophysiology*, vol. 58, pp. 1212–1232, 1987.
60. S. Marcelja, Mathematical description of the responses of simple cortical cells, *Journal of the Optical Society of America*, vol. 70, pp. 1297–1300, 1980.
61. D. Gabor, Theory of communication, *Journal of the Institute of Electrical Engineers*, vol. 93, pp. 429–459, 1946.
62. M. Porat and Y. Y. Zeevi, The generalized Gabor scheme of image representation in biological and machine vision, *IEEE Transactions on Pattern Analysis and Machine Intelligence*, vol. 10, no. 4, pp. 452–468, July 1988.
63. D. A. Pollen and S. F. Ronner, Visual cortical neurons as localized spatial frequency filters, *IEEE Transactions on Systems, Man, and Cybernetics*, vol. SMC-13, no. 5, pp. 907–916, September/October 1983.
64. J. G. Daugman, Uncertainty relation for resolution in space, spatial frequency, and orientation optimized by two-dimensional visual cortical filters, *Journal of the Optical Society of America A*, vol. 2, no. 7, pp. 1160–1169, July 1985.
65. J. G. Daugman, Spatial visual channels in the Fourier plane, *Vision Research*, vol. 24, no. 9, pp. 891–910, 1984.
66. S. J. Anderson and D. C. Burr, Receptive field size of human motion detection units, *Vision Research*, vol. 27, no. 4, pp. 621–635, 1987.
67. X. Yang, K. Wang, and S.A. Shamma, Auditory representation of acoustic signals, *IEEE Transactions on Information Theory*, vol. 38, no. 2, pp. 824–839, March 1992.
68. M. R. Turner, Texture discrimination by Gabor functions, *Biological Cybernetics*, vol. 55, pp. 71–82, 1986.
69. A. C. Bovik, M. Clark, and W. S. Geisler, Multichannel texture analysis using localized spatial filters, *IEEE Transactions on Pattern Analysis and Machine Intelligence*, vol. 12, no. 1, pp. 55–73, January 1990.
70. T. Weldon and W. E. Higgins, Designing multiple Gabor filters for multitexture image segmentation, *Optical Engineering*, vol. 38, no. 9, pp. 1478–1489, September 1999.
71. J. Lu, J. B. Weaver, D. M. Healy, Jr., and Y. Xu, Noise reduction with a multiscale edge representation and perceptual criteria, *Proceedings of the IEEE-SP International Symposium on Time-Frequency and Time-Scale Analysis*, Victoria, BC, Canada, pp. 555–558, October 4–6, 1992.

72. S. Mallat and S. Zhong, Wavelet transform maxima and multiscale edges, in M. B. Ruskai, et al., eds., *Wavelets and Their Applications*, Boston: Jones and Bartlett, pp. 67–104, 1992.
73. M. Holschneider, *Wavelets: An Analysis Tool*, New York: Oxford University Press, 1995.
74. S. Mallat and W. L. Hwang, Singularity detection and processing with wavelets, *IEEE Transactions on Information Theory*, vol. 38, no. 2, pp. 617–643, March 1992.
75. M. Akay, ed., *Time-Frequency and Wavelets in Biomedical Signal Processing*, New York: Wiley-IEEE Press, 1997.
76. M. Unser and A. Aldroubi, A review of wavelets in biomedical applications, *Proceedings of the IEEE*, vol. 84, no. 4, pp. 626–638, April 1996.
77. J. R. Cox, Jr., F. M. Nolle, and R. M. Arthur, Digital analysis of electroencephalogram, the blood pressure wave, and the electrocardiogram, *Proceedings of the IEEE*, vol. 60, pp. 1137–1164, 1972.
78. P. E. Tikkanen, Nonlinear wavelet and wavelet packet denoising of electrocardiogram signal, *Biological Cybernetics*, vol. 80, no. 4, pp. 259–267, April 1999.
79. B. A. Rajoub, An efficient coding algorithm for the compression of ECG signals using the wavelet transform, *IEEE Transactions on Biomedical Engineering*, vol. 49, no. 4, pp. 255–362, April 2002.
80. B.-U. Kohler, C. Hennig, and R. Orglmeister, The principles of software QRS detection, *IEEE Engineering in Medicine and Biology Magazine*, vol. 21, no. 1, pp. 42–57, January/February 2002.
81. C. Li, C. Zheng, and C. Tai, Detection of ECG characteristic points using wavelet transforms, *IEEE Transactions on Biomedical Engineering*, vol. 42, no. 1, pp. 21–28, January 1995.
82. S. Kadambe, R. Murray, and G. F. Boudreaux-Bartels, Wavelet transform-based QRS complex detector, *IEEE Transactions on Biomedical Engineering*, vol. 46, no. 7, pp. 838–848, July 1999.
83. L. Khadra, M. Matalgah, B. El\_Asir, and S. Mawagdeh, Representation of ECG-late potentials in the time frequency plane, *Journal of Medical Engineering and Technology*, vol. 17, no. 6, pp. 228–231, 1993.
84. F. B. Tuteur, Wavelet transformations in signal detection, in *Wavelets: Time-Frequency Methods and Phase Space*, J. M. Combes, A. Grossmann, and P. Tchamitchian, eds., 2nd ed., Berlin: Springer-Verlag, pp. 132–138, 1990.
85. K. Murano, S. Unagami, and F. Amano, Echo cancellation and applications, *IEEE Communications Magazine*, vol. 28, no. 1, pp. 49–55, January 1990.
86. A. Gilloire and M. Vetterli, Adaptive filtering in sub-bands with critical sampling: Analysis, experiments and applications to acoustic echo cancellation, *IEEE Transactions on Signal Processing*, vol. 40, no. 8, pp. 1862–1875, August 1992.
87. O. Tanrikulu, B. Baykal, A. G. Constantinides, and J. A. Chambers, Residual echo signal in critically sampled subband acoustic echo cancellers based on IIR and FIR filter banks, *IEEE Transactions on Signal Processing*, vol. 45, no. 4, pp. 901–912, April 1997.
88. A. Grossmann and J. Morlet, Decomposition of Hardy functions into square Integrable wavelets of constant shape, *SIAM Journal of Mathematical Analysis*, vol. 15, pp. 723–736, July 1984.

89. P. Goupillaud, A. Grossmann, and J. Morlet, Cycle-octave and related transforms in seismic signal analysis, *Geoexploration*, vol. 23, pp. 85–102, 1984–1985.
90. J. L. Larssonneur and J. Morlet, Wavelets and seismic interpretation, in J. M. Combes, A. Grossmann, and P. Tchamitchian, eds., *Wavelets: Time-Frequency Methods and Phase Space*, 2nd ed., Berlin: Springer-Verlag, pp. 126–131, 1990.
91. X.-G. Miao and W. M. Moon, Application of wavelet transform in reflection seismic data analysis, *Geosciences Journal*, vol. 3, no. 3, pp. 171–179, September 1999.
92. G. Olmo and L. Lo Presti, Applications of the wavelet transform for seismic activity monitoring, in *Wavelets: Theory, Applications, and Applications*, C. K. Chui, L. Montefusco, and L. Puccio, eds., San Diego, CA: Academic Press, pp. 561–572, 1994.
93. M. Cooke, S. Beet, and M. Crawford, eds., *Visual Representations of Speech Signals*, Chichester: Wiley, 1993.
94. T. Parsons, *Voice and Speech Processing*, New York: McGraw-Hill, 1987.
95. W. Hess, *Pitch Determination of Speech Signals: Algorithms and Devices*, New York: Springer-Verlag, 1983.
96. S. Kadambe and G. F. Boudreaux-Bartels, Application of the wavelet transform for pitch detection of speech signals, *IEEE Transactions on Information Theory*, vol. 38, no. 2, pp. 917–924, March 1992.
97. A. M. Noll, Cepstrum pitch determination, *Journal of the Acoustical Society of America*, vol. 41, pp. 293–309, February 1967.
98. T. Chang and C.-C. J. Kuo, Texture analysis and classification with tree-structured wavelet transform, *IEEE Transactions on Image Processing*, vol. 2, no. 4, pp. 429–441, October 1993.
99. J. Portilla and E. P. Simoncelli, A parametric texture model based on joint statistics of complex wavelet coefficients, *International Journal of Computer Vision*, vol. 40, no. 1, pp. 49–71, October 2000.
100. R. L. Allen, R. Moore, and M. Whelan, Multiresolution pattern detector networks for controlling plasma etch reactors, *Process, Equipment, and Materials Control in Integrated Circuit Manufacturing*, Proceedings SPIE 2637, pp. 19–30, 1995.
101. R. L. Allen, R. Moore, and M. Whelan, Application of neural networks to plasma etch endpoint detection, *Journal of Vacuum Science and Technology (B)*, pp. 498–503, January–February 1996.
102. J. Hertz, A. Krogh, and R. G. Palmer, *Introduction to the Theory of Neural Computation*, Redwood City, CA: Addison-Wesley, 1991.
103. E. A. Rietman, R. C. Frye, E. R. Lory, and T. R. Harry, Active neural network control of wafer attributes in a plasma etch process, *Journal of Vacuum Science and Technology*, vol. 11, p. 1314, 1993.
104. D. M. Manos and G. K. Herb, Plasma etching technology—An overview, in D. M. Manos and D. L. Flamm, eds., *Plasma Etching: An Introduction*, Boston: Academic Press, 1989.
105. L. R. Rabiner, A tutorial on hidden Markov models and selected applications in speech recognition, *Proceedings of the IEEE*, vol. 77, no. 2, pp. 257–286, February 1989.
106. N. Arica and F. T. Yarman-Vural, Optical character recognition for cursive handwriting, *IEEE Transactions on Pattern Analysis and Machine Intelligence*, vol. 24, no. 6, pp. 801–813, June 2002.

- 107. R. Durbin, S. Eddy, A. Krogh, and G. Mitchison, *Biological Sequence Analysis*, Cambridge: Cambridge University Press, 1998.
- 108. S. Mallat and S. Zhang, Matching pursuits with time-frequency dictionaries, *IEEE Transactions on Signal Processing*, pp. 3397–3415, December 1993.
- 109. M. M. Goodwin and M. Vetterli, Matching pursuit and atomic signal models based on recursive filter banks, *IEEE Transactions on Signal Processing*, pp. 1890–1902, July 1999.
- 110. R. Karchin, *Hidden Markov Models and Protein Sequence Analysis*, Honors Thesis, Computer Engineering Department, University of California, Santa Cruz, June 1998.

**PROBLEMS**

1. Using material from Chapters 9 and 11, suppose we are given a multiresolution analysis of finite-energy signals.
  - (a) Show that the discrete lowpass filter  $H(\omega)$  associated to the MRA satisfies  $|H(\omega)|^2 + |H(\omega + \pi)|^2 = 1$ ;
  - (b) Let  $g(n) = g_1(n) = (-1)^{1-n}h(1-n)$  and  $G(\omega) = e^{-j\omega}\overline{H(\omega + \pi)}$ . Show that, indeed,  $g(n)$  is the inverse discrete-time Fourier transform of  $G(\omega)$ .
  - (c) Show that  $|H(\omega)|^2 + |G(\omega)|^2 = 1$ .
  - (d) Using the perfect reconstruction criterion of Chapter 9, show that  $\sqrt{2}h(n)$  is a quadrature mirror filter (QMF).
  - (e) Sketch a reconstruction diagram using  $h(n)$  and  $g(n)$  for the reconstruction of the original signal decomposed on the pyramid [1].
  
2. In the QMF pyramid decomposition (Figure 12.5), let  $\tilde{h}(n) = h(-n)$  be the reflection of  $h(n)$  and  $\tilde{H}(z)$  be its  $z$ -transform. Similarly, let  $\tilde{g}(n) = g(-n)$  and  $\tilde{G}(z)$  be the transfer function of the filter with impulse response  $\tilde{g}(n)$ .
  - (a) Show that subsampling a signal  $x(n)$  by two followed by  $\tilde{H}(z)$  filtering is the same discrete system as  $\tilde{H}(z^2)$  filtering followed by subsampling [4].
  - (b) Applying the same idea to  $\tilde{g}(n)$ , prove filtering with  $\tilde{H}(z)\tilde{H}(z^2)$  and  $\tilde{H}(z)\tilde{G}(z^2)$  and subsampling by four produces the level  $-2$  approximate and detail coefficients, respectively.
  - (c) Show that we can compute the impulse response of the filter with transfer function  $\tilde{H}(z)\tilde{H}(z^2)$  by convolving  $\tilde{h}(n)$  with the filter obtained by putting a zero between every  $h(n)$  value.
  - (d) State and prove a property similar to (c) for  $\tilde{H}(z)\tilde{G}(z^2)$ .
  - (e) State and prove properties for level  $l = -L$ , where  $L > 0$ , that generalize these results.
  
3. Suppose  $p > 0$  and define the filter  $G_p$  as in (12.13). Let  $O_i$  be the orthogonal complement of  $V_i$  inside  $V_{i+1}$ :  $V_i \perp O_i$  and  $V_{i+1} = V_i \oplus O_i$ .
  - (a) Show (12.16).

- (b) Show (12.17).  
 (c) Show (12.18).  
 (d) Since  $\{\phi(t-k)\}_{k \in \mathbb{Z}}$  is an orthogormal basis for  $V_0$ , explain the expansion (12.19).  
 (e) By Fourier transformation of (12.19), show that  $G_p(\omega) = \frac{\Psi(2^p \omega)}{\Phi(2\omega)}$ .
4. Suppose that  $y(n) = x(n-2)$  and both signal  $x(n)$  and  $y(n)$  are decomposed using the orthogonal wavelet pyramid.
- (a) How do the first-level  $L = -1$  coefficients for  $y(n)$  differ from the first-level coefficients for  $x(n)$ ?  
 (b) Generalize this result to delays that are higher powers of 2.
5. Show by simple convolutions on discrete steps and ridge edges that discrete highpass filters  $g_p(n)$  given in Figure 12.3 and Figure 12.4 function as edge detectors for the orthogonal wavelet pyramid.
6. Suppose  $g(t) = Ae^{-Bt^2}$  is a Gaussian of zero mean and  $\psi(t) = \frac{d}{dt}g(t)$ .
- (a) Show that  $\psi(t)$  is a wavelet.  
 (b) Let  $x_a(t) = ax(at)$  be the scaled dilation of  $x(t)$  by factor  $a = 2^{-i}$  for  $i \in \mathbb{Z}$ , with  $i > 0$ . Define the wavelet transform  $(W_{-i}x)(t) = (\psi_a * x)(t)$ . Show that

$$(W_{-i}x)(t) = a \frac{d}{dt}(g_a * x)(t). \quad (12.36)$$

- (c) Explain the significance of  $|W_{-i}x|$  being large.  
 (d) Explain the significance of large  $|W_{-i}x|$  when  $a$  is large. What if  $a$  is small?
7. Suppose  $x(t)$  is discontinuous at  $t = t_0$ . Show that its Libschitz regularity at  $t_0$  is zero.

Advanced problems and projects.

8. Implement the multiscale matching and registration algorithm of Section 12.1.3.
- (a) Use the cubic spline MRA as described in the text.  
 (b) Use the Laplacian pyramid.  
 (c) Use the MRA based on piecewise continuous functions.  
 (d) Develop matching and registration experiments using object boundaries or signal envelopes.  
 (e) Compare the performance of the above algorithms based on your chosen applications.  
 (f) Explore the effect of target shape support in the candidate signal data.

9. Derive the impulse responses for the  $h_p(n)$  and  $g_p(n)$  for the case where the MRA is
- Based on the Haar functions;
  - The Stromberg MRA.
10. Compare linear and nonlinear filtering of the electrocardiogram to the wavelet de-noising algorithms.
- Obtain and plot an ECG trace (for example, from the signal processing information base; see Section 1.9.2.2).
  - Develop algorithms based on wavelet noise removal as in Section 12.2.1. Compare hard and soft thresholding methods.
  - Compare your results in (b) to algorithms based on edge-preserving nonlinear filters, such as the median filter.
  - Compare your results in (b) and (c) to algorithms based on linear filters, such as the Butterworth, Chebyshev, and elliptic filters of Chapter 9.
  - Consider the requirements of real-time processing and analysis. Reevaluate your comparisons with this in mind.
11. Compare discrete and continuous wavelet transforms for QRS complex detection [81, 82].
- Using your data set from the previous problem, apply a nonlinear filter to remove impulse noise and a convolutional bandpass filter to further smooth the signal.
  - Decompose the filtered ECG signal using one of the discrete wavelet pyramid decompositions discussed in the text (the cubic spline multiresolution analysis, for instance). Describe the evolution of the QRS complexes across multiple scales [81]. Develop a threshold-based QRS detector and assess its usefulness with regard to changing scale and QRS pulse offset within the filtered data.
  - Select a scale for decomposition based on a continuous wavelet transform [82]. Compare this method of analysis to the discrete decomposition in (b).
  - Consider differentiating the smoothed ECG signals to accentuate the QRS peak within the ECG. Does this improve either the discrete or continuous algorithms?
  - Consider squaring the signal after smoothing to accentuate the QRS complex. Does this offer any improvement? Explain.
  - Do soft or hard thresholding with wavelet de-noising help in detecting the QRS complexes?
  - Synthesize some defects in the QRS pulse, such as ventricular late potentials, and explore how well the two kinds of wavelet transform perform in detecting this anomaly.



## INDEX

---

### A

Abel's function 256  
Absolutely integrable 66, 182  
Absolutely summable Signal 65  
Accumulator 177  
Adjoint  
  frame operator 220  
  Hilbert operator 210  
Admissibility condition 805  
Algebra 80  
   $\sigma$ - (sigma-) 80, 227  
Algebraic signals 25  
Almost everywhere 231  
Ambiguity function 769  
Amplitude 51  
  modulation (AM) 52, 469  
  spectrum 463  
Analog  
  convolution 176-177  
  filter 650  
  Gaussian 29  
  signal 1, 21-22  
  signal edge 334  
  sinusoid 51  
  system 174  
Analog-to-digital converter (ADC) 41  
Analytic 71  
  signal 692  
Analyzing wavelet 805  
Angle modulation 471  
Antisymmetric 63  
Approximate signal 875-876  
Approximating identity 253-256  
Approximation, ideal filter 624  
Arc 75  
Associated filter, multiresolution  
  analysis 852  
Atomic force microscope (AFM) 336  
Attneave 24  
Australia 887

Autocorrelation 176, 615-616  
Axiom of Choice 164-165

### B

Balian-Low theorem 771-787  
  frames 784  
  orthonormal basis 773-776  
Banach space 147-148, 198  
  construction 201-205  
  completion 203-205  
Bandlimited 538  
Bandpass filter 465, 599-601  
Bandwidth, 3-db 464  
Basis 154, 163  
  orthonormal 211-215  
  of translates 840  
Bat 645  
Bayes 82  
  classifier 346  
  decision rule 348  
  theorem 82, 91  
Bell, A. 93  
Bessel 612  
  function 475, 611-612  
  inequality 156-157  
Biased estimator 616  
Bilinear transformation 638  
Binomial distribution 87  
biological and computer vision 900  
Borel set 229  
Boundary curvature 368  
Bounded 65, 182  
  linear operator 197  
B-spline 189, 739  
  window 738  
Butterfly 68  
Butterworth, S. 654  
  filter 654-655

### C

$C^+$ , extended complex plane 555, 626

- C++ 507-508
  - Canny edge detector 335-336
  - Canonical linear map, multiresolution analysis 856
  - Cantor, G. 163
  - Cardano, G. 81
  - Cardinality 163
  - Carleson's theorem 529
  - Carrier frequency 52
  - Cat 24, 69
  - Cauchy
    - integral 76-77
    - principal value 689
    - residue 78
    - sequence 148, 198
  - Cauchy-Riemann equations 73
  - Cauchy-Schwarz inequality 146, 151
  - Cauer, W. 676
  - Cauer filter 676-680. *See also* elliptic filter
  - Causal 627
    - system 122, 183
  - Cepstral coefficient 345
  - Chain rule 72
  - Charge-coupled device (CCD) 897
  - Chebyshev, P. 664
  - Chebyshev
    - polynomial 664-665
    - Type I filter 664
    - Type II filter 670
  - Chemical mechanical planarization (CMP) 618
  - Chirp
    - detection 643
    - linear 730-732
  - Chirp z-transform (CZT) 573, 687
    - algorithm 574-575
  - City block metric 142
  - Classification 283-284, 346
  - Closed set 65, 148
  - Closing 326
  - Cohen, L. 789
  - Cohen class transform 771, 789
  - Comfort noise 79
  - Compact 65
    - support 65, 190
  - Complete 154, 158
  - Complete elliptic integral 677-678
  - Completion 203
  - Complex
    - integration 75-78
    - Lebesgue measure 230-231
    - numbers (C) 70
    - valued signal 22, 35
  - Component (channel) signal 9
  - Compression 894
  - Concavity 37, 354
  - Conditional probability 81
  - Congruential generator 591
    - linear 591
  - Conjugate
    - exponents 143-144
    - mirror filter 699
  - Contextual analysis 61
  - Continuous
    - mean 89
    - operator 197
    - random variable 88
    - variance 90
    - wavelet transform 803
  - Contour 75
    - integral 76, 566
  - Convolution 115, 176
    - discrete 498
    - of distributions 250-252
    - properties 131-132, 184-185
    - theorem 129, 182, 428, 460
  - Co-occurrence matrix 305-307
    - texture descriptors 307
  - Countable 163
  - Covering, open 230
  - Cross Wigner-Ville distribution 764
  - Cross-correlation 114, 176
  - Cross-terms (interference-) 761, 769-770
  - Cubic spline 46-50, 839, 851, 862
  - Curvature 354
  - Curve 75
  - Cut-off frequency 625
- D**
- DC (direct current) 405
    - waveform 442
  - Delay 605, 669
    - group 606-608
    - phase 605
  - Delta, *see also* Dirac
    - analog 179
    - discrete 39
  - Dense 154
  - Density Function 85
    - Wigner-Ville 766
  - Derivative 71, 241, 332
    - of Gaussian operator 330
  - Descartes, R. 140
  - Detail signal 879-880
  - Deterministic signal 78
  - Difference equation 130, 571-572, 627-628
  - Difference of boxes (DOB) filter 329

- Differentiable 71
- Digital
  - signal 1, 35
  - signal processor (DSP) 7, 507, 509
- Dilation 323-325, 803
- Dirac, P. 33
- Dirac
  - comb 452-454
  - delta 33-35, 241, 247-249, 443
  - delta, properties 186-188
- Direct current (DC) 405, 442
- Direct
  - form I 630
  - form II 631
  - sum 160
- Dirichlet, P. 392, 526
- Dirichlet kernel 392, 526
- Discrete
  - algebraic signal 37
  - convolution 498-499
  - cosine transform (DCT) 894
  - delta (impulse) 39
  - density function 86
  - Fourier series (DFS) 495-497
  - Fourier transform (DFT) 155-156, 482-484
    - inverse (IDFT) 485-487
    - properties 497-501
  - mean 88
  - random variable (RV) 85-86
  - rational function 37
  - signal 1, 35
    - edge 334
    - frequency 51, 55-56
  - sinusoid 38
  - system 109, 111
  - unit step 40
  - variance 88
- Discrete-time Fourier transform (DTFT)
  - 510-515, 555
  - existence 514-515
  - inverse (IDTFT) 517-519
  - for  $l^p$  528
  - and linear, translation-invariant systems 534
  - properties 529-534
- Discriminant function 350-351
- Distribution 84, 241-253
  - defined 242
  - equivalent 243
  - as limit 252
  - properties 244-246
- Dog 308
- Dolphin 52
- Doppler 53
- Dual-tone multi-frequency (DTMF) 281-282, 588-604
  - table of pairs 590
- E**
- Echo canceller 133-136, 908-909
- Echolocation 645
- Edge
  - analog and discrete 334
  - detection 326-338, 905-908
    - Canny 336
    - maximal response 336
- Eigenfunction 534-535
- Eigenvector 534
- Electrocardiogram (ECG, EKG) 12-16, 907-908
- Electroencephalogram (EEG) 8-9, 643
- Elliptic
  - filter 676-685
  - integral 677
    - complete 677-678
    - sine 678-680
- Endpoint detection 330, 344, 649
- Engine knock detection 344-345
- Enhancement 314
  - wavelet-based 897
- Envelope 692
  - detection 693
- Equiripple condition 664-665, 670
- Equivalence
  - class 202
  - relation 202
- Equivalent distributions 243
- Erosion 325-326
- Estimator 616
- Even and Odd Signals 59
- Even 63-64
- Event 81
- Exact frame 218
- Expectation 88-89
- Exponential
  - distribution 89
  - signal 26, 38, 212, 448
    - anti-causal 557
    - causal 556
- Extended complex plane ( $C^+$ ) 555
- F**
- Fast Fourier transform (FFT) 2, 501
  - decimation-in-frequency 505-507
  - decimation-in-time 502-505
  - implementation 507-510
- Fatou, P. 237

- Fatou's lemma 237-238  
 Feature extraction 342-346  
 Feature 279  
 Feller, W. 81  
 Fermat, P. 140  
 Filter 314-322, 460, 462-463.  
   analog 651  
   approximation 624-626  
   bank 589, 601-604  
     exact reconstruction 697  
     perfect reconstruction 694-695  
 Butterworth 654  
 Cauer (elliptic) 676  
 Chebyshev type I 664  
 Chebyshev type II (inverse) 670  
 design  
   analog 650-685  
   bilinear transformation 638  
   discrete 620-643  
   impulse invariance 633  
   Laplace transform 636-638  
   low-pass 632-639, 652  
   sampling analog 633-636  
   window 623-624  
 elliptic (Cauer) 676  
 frequency transformations 639-640  
 ideal 465-466, 621  
 inverse Chebyshev 670  
 low-pass 621-622, 653  
 median 322  
 morphological 322  
 nonlinear 321-326  
 optimal 316, 685  
 quadrature mirror (QMF) 699  
 wavelet-based 895  
 Finite energy 66, 138  
 Finite impulse response (FIR) 629, 641-642  
 Finitely supported 64  
 Finitely supported signals 60  
 Fischer, E. 166  
 Formant 54, 757  
 formants 50  
 Fourier, J. 384  
 Fourier  
   series (FS) 2, 166, 385-387  
     convergence 391, 394  
     partial 388  
     properties 389  
     trigonometric 397-399  
 transform (FT) 403  
   discrete, *see* Discrete Fourier transform  
   discrete-time, *see* Discrete-time Fourier transform  
   existence 409  
   generalized, *see* Generalized Fourier transform  
   Hertz 405  
   inverse (IFT) 408  
   for  $L^2(\mathbb{R})$  424-429  
   normalized 405  
   properties 411-421  
   properties table 421  
   radial 404  
   short-time, *see* Short-time Fourier transform  
   table 407  
   windowed, *see* Short-time Fourier transform  
 Fractal 69  
 Frame 216-225, 777  
   bounds 218, 821  
   dual 222, 782  
   exact 821  
   operator 219-223, 782  
     adjoint 220, 782  
   tight 821  
   wavelet 821-832  
   windowed Fourier 756-759  
 Frequency 38, 51  
   domain 20, 56  
   signal analysis 585  
   estimation 608  
   instantaneous 473-474  
   modulation (FM) 52  
   response 535, 604-605  
   transformations (filter) 639-640  
 Fubini, G. 240  
 Fubini's theorem 240  
 Functional 241  
 Fundamental period 51
- G**  
 Gabor, D. 30, 717  
   problem 759  
 Gabor  
   elementary function 30-31, 718-722, 903  
   transform (GT) 713-735, 903-904  
     adaptive 720  
     inverse (IGT) 723-725, 729  
     properties 735  
 Galileo Galilei 58  
 Gauss, K. 29, 501  
 Gaussian 29, 39, 353, 361, 367, 416, 467-468,  
   652, 737, 815-817, 819  
   filtering 695-696  
   smoothing 357  
 Generalized Fourier transform 440-443  
   inverse 443  
   properties 444-451  
 Geothermal gradient 17-18

- Gestalt psychology 301  
 Gibbs, J. 394, 523  
 Gibbs phenomenon 186, 394, 523-528  
 Gram-Schmidt orthogonalization 162  
 Grisey, G. 713  
 Group delay 606
- H**  
 Haar, A. 213  
 Haar basis 213-215, 837  
 Hamming distance classifier 346  
 Hartmann, N. 22  
 Heat diffusion equation 28, 365  
 Heine-Borel theorem 65, 190  
 Heisenberg, W. 743  
 Heisenberg uncertainty principle 743  
 Hertz, H. 51, 93  
 Hidden Markov model (HMM) 873, 917  
 High-definition television (HDTV) 3  
 Hilbert, D. 150, 688  
 Hilbert  
   adjoint operator 210  
   space 150, 158-168  
     separable 164, 206-210  
     two-dimensional 726-727  
   transform 688  
     associated analytic signal 692  
     discrete 690  
     properties 689-691  
 Histogram 289-292  
 Hölder inequality 145, 191  
 Hubble 54
- I**  
 Ideal filter 465-466, 621  
 Image 10, 726, 894  
 Impulse  
   invariance 633  
   response 128, 181, 605  
     finite (FIR) 629  
     infinite (IIR) 133, 629  
 Independent event 82  
 Infinite impulse response (IIR) 133, 629  
 Inner product 205  
   space 149-153, 205-206  
 Instantaneous  
   frequency 52, 473-474, 692  
   phase 692  
   radial frequency 692  
 Interference-term (cross-) 761, 769-770  
 Interferometry 618-620  
 Interpolation 42-50  
 Inverse  
   Chebyshev filter (Type II) 670  
   discrete Fourier transform (IDFT) 485-487  
   discrete-time Fourier transform (IDTFT)  
     517-519  
   Fourier transform (IFT) 408  
   Gabor transform (IGT) 729  
   short-time (windowed) Fourier transform 741  
   wavelet transform (IWT) 810  
 Isometry 210, 429-431  
 Isomorphism 210
- J**  
 Jacobi, C. 677  
 Jacobi elliptic sine 677  
 Joint  
   density 90, 613  
     normal 90  
   distribution function 613  
 Julesz's thesis 306-307
- K**  
 Khinchin, A. 615  
 Knot 45  
 Kolmogorov, A. 81  
 Kotelnikov, V. 94  
 Kronecker, L. 385  
 Kronecker delta 385
- L**  
 $l^1$  65  
 $L^1$  66  
 $l^2$  66  
 $L^1$  66  
 $l^p$  137  
 $l^\infty$  137  
 $L^p$  191, 193, 205, 239  
 $L$  191  
 Labeling 279  
 Lagrange, J. 45  
 Lagrange  
   interpolation 45-46  
   multipliers 316  
 Laplace, P. 27  
 Laplace  
   identity 27  
   transform 636  
     properties 637  
 Laplacian pyramid 695-697, 891-892  
 Laurent series 72, 557-558  
 Lebesgue, H. 260  
 Lebesgue  
   dominated convergence theorem 238  
   integral 225, 232-240  
   measurable set 229  
   measure 229-230

- lim inf 237, 558
- lim sup 237, 558
- Linear
  - congruential generator 591
  - interpolation 45
  - operator 197
    - bounded 197-198
    - norm 197
  - phase 640
  - system 177, 459
  - translation-invariant (LTI) 128, 178
- Liouville, J. 628
- Lipschitz, R. 907
- Lipschitz regularity 907
- Locality
  - frequency 546
  - time 546
- Localization
  - random signal 614
  - time-frequency 741, 746, 754
- Logon 714
- Loma Prieta earthquake 5-6
- Lorentzian 653
  
- M**
- Malvar wavelet 895
- Marconi, G. 93
- Marginals 767-768
- Marr, D. 24, 337, 352
- Marr's program 900
- Matched filter 341
- Matching pursuit 873, 918
- Mathematics, most important function 73
- Maxwell, J. 28, 93
- Maxwell's equations 28
- Mean 88, 89, 613
- Measurable function 227
- Measure 226-228
- Median Filter 15, 322
- Melville, H. 832
- Metric space 141-142
- Mexican hat 819-820
- Minimum distance classifier 346
- Minkowski inequality 146, 192
- Mixed-domain signal transform 712
- Mixed-domain signal analysis 873
- Modulation 114, 461, 468-469
  - amplitude 52, 469
  - angle 471-472
  - frequency 52, 537
  - phase 52
- Morphological filter 322-326
- Morse, S. 93 91
- Motorola 56001 DSP 507, 509
  
- Moving average
  - filter 15, 593-595
  - system 178
- Multichannel 9
- Multidimensional 10
- Multiresolution analysis (MRA) 835-842, 873
  - associated discrete low-pass filter 852
  - canonical map 856
  - orthonormal wavelet 857
  - scaling function 847
- Multivariate distribution 90
  
- N**
- Nearest-neighbor clustering 288
- Noise 589
- Nonmeasurable set 231-232
- Norm
  - inner product 151
  - operator 197
- Normalized cross-correlation 338-341
- Normed linear space 142-143, 195-198
- Numerical instability 224
- nverse Hertz Fourier Transform 466
- Nyquist, H. 2
- Nyquist
  - density 754
  - rate 542
  
- O**
- Odd 63-64
- Open
  - set 65, 148
  - covering 230
- Opening 326
- Operator
  - adjoint 210
  - continuous 197
  - ordering 210
- Optimal filter 316-321, 685
- Orthogonal 153
  - wavelet 857
    - representation 875
- Orthonormal 153
  - basis 163
  - translates theorem 843
  - wavelet 857-861
    - existence 860
  
- P**
- Parallelogram law 152, 205
- Parseval's theorem 428, 500, 533, 565
  - Gabor transform 728
  - short-time Fourier transform 740
  - wavelet transform 809
- Pascal, B. 81

- Pattern 279
    - detection 338-351
      - structural 342
      - statistical 346-351
    - recognition 873, 913-917
  - Periodic 51
  - Period, fundamental 51
  - Periodogram 616, 619
    - improvement 617
  - Phase 51
    - delay 605
    - estimation 608
    - factor ( $W_N$ ) 490
    - modulation 52
  - Phone 60
  - Phoneme 60, 285, 313, 912
    - classification 83
  - Piecewise linear function 838, 849
  - Pixel 10
  - Plancherel's theorem 428
    - Gabor transform 727
    - short-time Fourier transform 740
  - Planck, M. 22
  - Plasma etching 330
  - Poisson, S.-D. 88
  - Poisson distribution 88, 898
  - Polarization identity 206
  - Pole 77, 628
  - Polynomial signal 24, 37
  - Positive operator 210
  - Power
    - series 72, 557
    - set 163
    - spectral density (PSD) 613-614
  - Primary (P) wave 5
  - Probability 79-81
    - density function 613
    - distribution function 613
    - measure 80
    - space 81
  - Projection 160-161
  - Prony model 345
- Q**
- QRS complex 13-15
  - Quadratic time-frequency transform 760-771
  - Quadrature mirror filter (QMF) 699, 882
  - Quantization error 41
- R**
- Rademacher, H. 154
  - Rademacher signal 154
  - Radius of convergence 559
  - Random
    - signal 78, 91
    - variable 84, 613
  - Rapidly
    - decreasing 208
    - descending 242
  - Rational function 25, 37, 653
  - Receptive field (RF) 900-904
  - Reconstruction from samples 540-541
  - Region
    - of convergence (ROC) 626
    - merging 286-288
    - splitting 286-288
  - Registration 279
  - Remote sensing 10
  - Republic, Plato's 726
  - Residue 78
  - Richter, C. 303
  - Richter scale 303
  - Riemann, G. 225
  - Riemann
    - integral 225-226
    - Lebesgue lemma 258, 413
  - Riesz, F. 166
  - Riesz
    - basis 841
    - bound 841
    - of translates 845
    - Fischer theorem 166-167
    - representation theorem 209
  - Ripple 625
  - Rosenfeld, A. 274
- S**
- $\sigma$ -algebra 80, 227
  - Sample space 80-81
  - Sampling 40, 116
    - frequency 40
    - interval 40
    - theorem 538-542
  - Sawtooth signal 33, 400-403
  - Scale 67, 354, 803-804
    - domain 21
    - space 351-368
      - decomposition 360
      - kernel conditions 357
  - Scaling function 847-852
  - Scanning electron microscope (SEM) 899
  - Schwartz, L. 260
  - Schwarz
    - inequality 192
    - space 208-209
  - Secondary (S) wave 5
  - Segmentation 14, 277-278, 589

- Seismic
    - data analysis 909
    - section 804
  - Seismogram 5, 643
  - Shannon, C. 2
  - Shannon
    - function 465
    - Nyquist interpolation 544
  - Shape 354
    - recognition 883
  - Sharpness 625
  - Short-time (windowed) Fourier transform (STFT)
    - 736-747
    - discretized 747-760
    - inverse (ISTFT) 741
    - properties 740-741
    - sampling 749
  - Sifting property 40
  - Signal
    - analysis
      - narrow-band 586-608
      - wide-band 643-650
    - envelope 692
    - to-noise ratio 335
    - periodic 51
  - Signum 33, 446
  - Sinc function 215
  - Sinusoid 25, 38, 213, 587-588
  - Slowly increasing 243
  - Sobolev, S. 260
  - Spectrum estimation 608, 613-617
  - Speech 60-62, 912
    - analysis 646-650
      - endpoint 649
      - formants 647
      - pitch 647
    - envelope 693-694
    - segmentation 283
    - voiced and unvoiced 283, 649
  - Spline 46-50, 188-190. *See also* Cubic spline
    - B- 189, 739
    - natural 49
  - Spline Function 993
  - Splintering, QRS complex 15
  - Stable 138, 182, 627
  - Standard deviation 88, 90, 613
  - Step function 836, 849, 861
  - Structural analysis 18-20, 314
  - Structure 751, 904
  - Sunspot 57, 493
  - Surface
    - profilometer 302
    - wave 5
  - Symmetry 63
  - System function 563, 627
- T**
- Taylor, B. 25
  - Taylor series 25-26
  - Tempered distribution 243
  - Test function 242
  - Texture 300-314
    - analysis, mixed-domain 912-913
    - segmentation 301-314
      - spectral methods 308
      - statistical 301
      - structural 314
  - Thresholding 117, 119, 176, 288-300
    - hard 894
    - information theoretic 297-298
    - nonparametric 294-297
    - parametric 292-294
    - soft 896
  - Tight frame 218
  - Time domain 10
    - signal analysis 273
  - Time-frequency
    - (Nyquist) density 754
    - plane 589, 596-601, 751-753
    - transform 712
      - quadratic 760-771
      - kernel-based 770-771
  - Time-scale transform 802
  - Tone 733-735
    - detection 587
  - Top surface 324
  - Transfer (system) function 563, 627
  - Transient response 669-670
  - Translate of a set 323
  - Translation-invariant 127, 177
- U**
- Umbra 324
  - Unbiased estimator 319
  - Uncertainty principle 545-547, 743-746
  - Uncertainty principle 620, 855
  - Unconditional basis, *see* Riesz basis
  - Uncorrelated 613
  - Uncountable set 163
  - Uniform convergence 186
  - Uniformly continuous 194
  - Unit step 32, 40
  - Unvoiced 61, 283
- V**
- Variance 613
  - Vector space 140-141

Ville, J. 761, 789  
 Voiced 61, 283  
 Voxel 10

## W

Wavelet 802  
 analyzing 805  
 frames 824-832  
 Haar 214  
 Malvar 895  
 orthonormal 802  
 packet 895  
 pyramid decomposition 875  
 transform (WT) 803-821  
   continuous 803-805  
   discrete 874  
   discretization 822-824  
   inverse (IWT) 805  
   orthonormal 802  
   properties 810-815  
   properties, table 814  
 Waviness 308  
 Weyl, H. 745  
 Whale 52, 832  
 White  
   Gaussian noise 335  
   noise process 614  
 Wide sense stationary (WSS) 614-615  
 Wiener, N. 615, 686  
 Wiener  
   filter 686  
   -Khinchin theorem 615-616  
 Wigner, E. 761, 789  
 Wigner-Ville distribution (WVD) 760-766  
   cross 764  
   densities and marginals 766-769  
   interference- (cross-) term 761, 769-770  
   properties 763-766

## Window

Bartlett 611  
 Blackman 611-612  
 b-spline 738-740  
 function 609-612, 736-737  
   center and radius 742  
   diameter 742  
   table 739  
 Hamming 611-612  
 Hann 611-612, 624  
 Kaiser 611-612  
   rectangular 611  
 Windowed Fourier transform, *see*  
   Short-time Fourier transform  
 Wolf, J. 58  
 Wolf sunspot number 58, 493

## Z

Zak transform (ZT) 575-577,  
   777-781  
   isomorphism 576-577  
   properties 576  
 Zero 77, 628  
 Zero-crossing 356-359, 900  
 Zorn, M. 165  
 Zorn's lemma 165  
 z-Transform 554-560  
   existence 557-560  
   filter design 626-632  
   inverse 566-571  
     contour integration 566-567  
     Laurent series 567-568  
     partial fractions 570  
     table lookup 569-571  
   one-sided 556  
   properties 561-565  
   region of convergence (ROC) 555  
   table 569